SUBMICROSCOPIC CRACKING OF CEMENT PASTE AND MORTAR IN COMPRESSION

by

Emmanuel K. Attiogbe

David Darwin

A Report on Research Sponsored by

THE NATIONAL SCIENCE FOUNDATION

Research Grants

CME-7918414

CEE-8116349

AND

THE AIR FORCE OFFICE OF SCIENTIFIC RESEARCH

Research Grant

AFOSR-85-0194

UNIVERSITY OF KANSAS

LAWRENCE, KANSAS

November 1985

50272-101

REPORT DOCUMENTATION PAGE	1. REPORT NO.	2.	3. Recipient's Accession No.

4. Title and Subtitle
Submicroscopic Cracking of Cement Paste and Mortar in Compression

5. Report Date
November 1985

6.

7. Author(s)
Emmanuel K. Attiogbe and David Darwin

8. Performing Organization Rept. No.
SM Report No. 16

9. Performing Organization Name and Address
University of Kansas Center for Research, Inc.
2291 Irving Hill Drive, West Campus
Lawrence, KS 66045

10. Project/Task/Work Unit No.

11. Contract(C) or Grant(G) No.
NSF CME-7918414
(G) NSF CEE-8116349
AFOSR 85-0194

12. Sponsoring Organization Name and Address
National Science Foundation
Washington, D.C. 20550

Air Force Office of
Scientific Research
Bolling AFB
Washington, D.C. 20332

13. Type of Report & Period Covered

14.

15. Supplementary Notes

16. Abstract (Limit: 200 words)

Submicroscopic cracking of cement paste and mortar under uniaxial compression is measured and correlated with applied strain and load history. Cement paste specimens with water-cement ratios of 0.7, 0.5 and 0.3 were subjected to monotonic, sustained or cyclic loading, while mortar specimens with a water-cement ratio of 0.5 were subjected to monotonic loading. One hundred and thirty (130) specimens were tested at ages ranging from 27 to 29 days, using a closed-loop servo-hydraulic testing machine. After loading, slices of material were removed for study at a magnification of 1250x in a scanning electron microscope. Cracking on transverse and longitudinal surfaces was measured.

Statistical and stereological models are developed to convert the surface crack distributions to three-dimensional distributions. A self-consistent model is developed to estimate the elastic moduli of transversely isotropic cracked materials. These models are used to correlate submicrocracking with the reduction in stiffness and the shape of the stress-strain curve.

The surface crack densities in cement paste and mortar are about ten times the density of bond and mortar microcracks in concrete at the same value of compressive strain. Submicrocracking accounts for a significant portion (20% to 90%) of the nonlinear response of cement paste and mortar at all levels of applied compressive strain. As compressive strain increases, other mechanisms, such as large microcracks, macrocracks, and creep, play an increasingly greater role.

17. Document Analysis a. Descriptors

cement paste, compression, concrete, cracks (cracking), crack distribution, cyclic, engineering materials, engineering mechanics, microcracks, microstructure, monotonic, mortar, scanning electron microscope (SEM), self-consistent model, statistics, stereology, strains, stresses, stress-strain curve, submicrocracks, sustained, transverse isotropy

b. Identifiers/Open-Ended Terms

c. COSATI Field/Group

18. Availability Statement	19. Security Class (This Report)	21. No. of Pages
Release Unlimited	Unclassified	
	20. Security Class (This Page)	22. Price
	Unclassified	

(See ANSI-Z39.18) *See Instructions on Reverse*

OPTIONAL FORM 272 (4-77)
(Formerly NTIS-35)
Department of Commerce

ACKNOWLEDGMENTS

This report is based on a thesis submitted by Emmanuel K. Attiogbe to the Department of Civil Engineering of the University of Kansas in partial fulfillment of the requirements for the Ph.D. degree.

The research was supported by the National Science Foundation under grants CME-7918414 and CEE-8116349 and the Air Force Office of Scientific Research under grant AFOSR-85-0194.

Cement was donated by the Ash Grove Cement Company. Crack studies were carried out on the Philips 501 Scanning Electron Microscope of the University of Kansas Electron Microscope Facility. Numerical calculations were performed on the Harris 500 and 800 computer systems operated by the Computer Aided Engineering Laboratory at the University of Kansas.

TABLE OF CONTENTS

TABLE OF CONTENTS (continued)

TABLE OF CONTENTS (continued)

TABLE OF CONTENTS (continued)

LIST OF TABLES

LIST OF TABLES (continued)

LIST OF TABLES (continued)

LIST OF TABLES (continued)

LIST OF TABLES (continued)

LIST OF TABLES (continued)

LIST OF TABLES (continued)

LIST OF TABLES (continued)

LIST OF FIGURES

LIST OF FIGURES (continued)

LIST OF FIGURES (continued)

LIST OF FIGURES (continued)

LIST OF FIGURES (continued)

LIST OF FIGURES (continued)

LIST OF FIGURES (continued)

LIST OF FIGURES (continued)

LIST OF FIGURES (continued)

LIST OF FIGURES (continued)

LIST OF FIGURES (continued)

LIST OF FIGURES (continued)

LIST OF FIGURES (continued)

LIST OF FIGURES (continued)

LIST OF FIGURES (continued)

LIST OF FIGURES (continued)

CHAPTER 1
INTRODUCTION

1.1 General

Concrete is one of the most widely used engineering materials. In spite of its common use, the relationships between the behavior of concrete and the behavior of its constituent materials, and the factors that control the behavior of concrete under general types of loading are not well understood. The ever widening applications of concrete as a structural material make it increasingly important to improve both our understanding of the behavior of concrete and our ability to accurately predict its response under load.

Under various loading conditions, concrete exhibits a rate-dependent behavior. This phenomena is not well understood and explanations for it have been limited to the role of water within the structure of cement paste [45]. Complete explanations of rate dependency require an understanding of the internal behavior of concrete. Concrete for special applications, such as nuclear reactor pressure vessels, must meet strict performance standards. These standards can only be adequately ensured if the basic behavior of the material is well understood. Knowledge of the mechanisms which control the behavior of concrete and its constituent materials will provide a rational basis for developing material behavior laws.

Concrete is a highly heterogeneous material. Its response to loading is inelastic. Even for a relatively homogeneous and isotropic material, such as steel, external macroscopic observations do not provide sufficient information to explain its behavior, especially at strains where its response is inelastic. Thus, microscopic and submicroscopic dislocation processes in ductile metals have been used to explain macroscopic yielding [78]. An understanding of deformation mechanisms at the microscopic and submicroscopic levels in concrete will enable constitutive models to be formulated based on structural changes which actually take place.

The microscopic behavior of concrete under load has been studied during the last twenty-five years. Microscopic cracks (microcracks) exist in concrete prior to loading and propagate with load [17,27,32,42,60,76,77,78,82]. The term microcracking has, in general, been

limited to relatively large microcracks which are observed under low magnifications of up to 50x at the paste-aggregate interface and in the mortar constituent of concrete. The surface density of these microcracks has been shown to increase from about 1 in./in.^{2} for nonloaded specimens up to about 3.5 in./in.^{2} for specimens loaded to strains of 0.003 in uniaxial compression [17,42]. It has become clear that the behavior of concrete under compressive as well as tensile loads is closely related to the formation of microcracks.

During the early period of the microcracking studies, concrete was considered to be made up of two brittle materials, paste and aggregate, with the full nonlinearity being assigned to the microcracking [42,79]. More recently, however, investigators [22,57,58,59,85,86,87,88] have shown that the nonlinearity of concrete subjected to compressive loading is highly dependent upon the nonlinearity of its cement paste and mortar constituents. Cement paste is not a linear elastic and brittle material as previously thought [42,79], but is rather a nonlinear softening material that is damaged continuously under load [85,87,88]. The process of damage in mortar and concrete begins at very low strains and is also continuous [22,58,59,86,87]. These recent studies strongly indicate that microcracking does not fully explain the load-deformation behavior of concrete. Microcracking now appears to have its greatest effect on lateral strain [57].

The present study investigates, at the submicroscopic level (1250x magnification), the internal behavior of cement paste and mortar subjected to uniaxial compressive loading. The origin, causes and significance of cracks at the submicroscopic level in cement paste and mortar are explored. A better understanding of the engineering properties of concrete can be obtained if the behavior of its constituents is well understood. This could lead to improvements in the properties as well as improved use of the materials. The need for safe, economical concrete structures can best be satisfied if the behavior of concrete can be more accurately predicted.

1.2 Previous Work

1.2.1 Background

In 1963, Hsu, et al. [42] studied the formation and propagation of microcracks in concrete subjected to uniaxial compressive loading using

microscopic and x-ray techniques. One technique consisted of cutting a thin slice (0.15 inch thick) from a specimen and observing the cracks as shown in an x-ray photograph [81]. The other consisted of cutting the specimen, filling the cracks with a red dye, and examining the cross-section under an optical microscope at 40x magnification [42]. Hsu, et al. found that prior to loading, bond cracks at the interface between coarse aggregate and mortar exist in plain concrete. Above about 30% of the ultimate load, these bond cracks begin to increase appreciably in length, width and number with increasing strain. At this load, the stress-strain curve begins to deviate appreciably from a straight line. At 70% to 90% of the ultimate load, cracks through the mortar increase noticeably, and bridge between bond cracks to form continuous crack patterns. Mortar cracking continues at an accelerated rate until the material ultimately fails. They concluded that the shape of the stress-strain curve of plain concrete under short-term uniaxial compressive loading is related to microcracking.

Using the optical microscope technique, Shah and Chandra [77] and Meyers, Slate and Winter [60] have shown that microcracks increase under the effect of sustained and cyclic loading.

Carrasquillo, Slate and Nilson [17] found that the bond-mortar crack classification system, useful in studying behavior of normal strength concrete, is not highly relevant for microcrack studies of high strength concretes ($f'_c \geq 6000$ psi). They suggested that the classification of microcracks into simple and combined cracks, and the distinction between different types of combined cracks, is more appropriate for high strength concretes.

Derucher [27] used a scanning electron microscope (SEM) to obtain a somewhat different picture of the microscopic behavior of concrete. In order to observe microcracks with the SEM without having to unload the specimens (as did Hsu, et al.), he applied eccentric compressive loads to concrete specimens. The specimens had to be dried for proper operation of the SEM. In order to determine if the drying procedure caused additional microcracking in the specimens, Derucher used an optical microscope. He concluded that no cracks were induced by drying. Using the SEM, he found that bond cracks, with mortar microcrack extensions, exist in concrete prior to loading. Under increasing compression, the bond cracks propagate by a small amount and widen. At a stress as low as 15% of the ultimate strength,

the mortar cracks widen and propagate to the point where they begin to bridge bond cracks. Bridging of the bond cracks is about complete at 45% of the ultimate strength. At 75% of the ultimate strength, the mortar cracks start to bridge one another.

The importance of interfacial paste-aggregate bond strength on the behavior of concrete under load has been studied in a number of investigations [23,41,71,76,79,90]. Darwin and Slate [23] and Perry and Gillott [71] found from their studies that a large reduction in interfacial strength results in only about a 10 percent reduction in the compressive strength, as compared to similar concrete made with aggregate with normal interfacial strength. These two studies indicate that the interfacial strength plays a relatively minor role in controlling the stress-strain behavior and ultimate strength of concrete.

When concrete and cement paste are tested in uniaxial compression, concrete exhibits a general pattern of interlaced microcracks near its peak stress while cement paste fractures in an abrupt, even explosive, manner. The cracks in cement paste are fewer in number but of much greater length. This distinction between the modes of fracture of cement paste and concrete is responsible for the previous belief that cement paste is essentially a linear elastic, brittle material [88]. At a time when cement paste was thought to be linearly elastic, Spooner [85] proposed that the curvature of the stress-strain curve of concrete at low stresses might be due to creep of the cement paste and that cracking was responsible for further curvature as the stress was raised to failure. His attempt to calculate the uniaxial compressive stress-strain curve for cement pastes from data obtained from creep tests was only partially successful. The calculated curves were stiffer than the experimental curves. He suggested that the poor agreement between the calculated and experimental stress-strain curves might be attributed to structural damage in the specimens, causing greater strains to occur than accounted for by creep alone. He showed that cement paste is a nonlinear material.

Using a cyclic loading procedure, Spooner, et al. [86,87,88] demonstrated that both paste and concrete undergo measurable damage at strains as low as 0.0004 and that both materials are damaged progressively. Damage was measured in terms of the energy dissipated and changes in the modulus of elasticity. Cook and Chindaprasirt [22] and Maher and Darwin

[58,59] showed that the process of degradation of mortar during monotonic as well as cyclic compressive loading is continuous and begins at very low loads. Maher and Darwin measured residual strains for applied strains as low as 0.00027. When combined with the work of Derucher, in which he observed that mortar cracks widen and propagate at a stress level as low as 15% of the ultimate strength of concrete, these studies indicate that the nonlinear behavior of cement paste, mortar and concrete can be closely tied to damage sustained by these materials, even at very low loads.

The importance of mortar in controlling the stress-strain behavior of concrete is illustrated by the finite element work of Buyukozturk [16] and Maher and Darwin [57]. Maher and Darwin showed that by using a nonlinear representation for mortar in a finite element model of concrete, the nonlinear behavior of concrete can be closely matched. The finite element work of Buyukozturk could not duplicate the nonlinear experimental behavior of concrete using the formation of bond and mortar cracks as the only nonlinear effect.

A number of investigators [22,77,97] have found that sustained loading increases the strength and initial modulus of elasticity of cement paste, mortar and concrete. Shah and Chandra [77] showed that on reloading, paste and concrete specimens loaded to stress-strength ratios of 60% and 70% for four hours, exhibit strength increases in comparison with the controls. Cyclic loading [22] on other hand, results in decrease in strength and stiffness upon reloading. The structural changes due to cyclic loading may be of a different nature than those due to creep.

The physical nature of the damage that occurs in cement paste at the submicroscopic level is not well understood. Volumetric strain measurements by Spooner, et al. [88] indicate that a reduction in the rate of volume decrease, implying internal cracking, occurs in cement paste during compressive loading. Yoshimoto, et al. [103,104] observed microcracks in the cement matrix of concrete and mortar under flexural and compressive loading. They examined thin slices of mortar and concrete (about 37 μm thick) with an optical microscope at 150x magnification. The technique of slicing was similar to that of Slate and Olsefski [82] except that the slices were ground until light could penetrate through. They suggested that "hair-shaped" cracks occur at very low strains in the cement matrix of concrete. When the length of the "hair-shaped" cracks reaches a certain value, the

cracks stop extending in length but change in shape from a hair to a void. The "void-shaped" cracks propagate with the increasing of strain. They further suggested that mortar cracks develop from the "void-shaped" cracks, because the "void-shaped" cracks are the largest flaws in the cement matrix.

1.2.2 Work that Impacts on this Study

The studies discussed in the last section show that concrete is a nonlinear material, but only a small portion of its nonlinearity is explained by microcracking. Cement paste and mortar are also nonlinear materials. Thus, the nonlinearity of concrete can best be explained if the nonlinearity of its paste and mortar constituents is well understood. Load-induced changes in cement paste and mortar need to be studied in order to obtain a clear understanding of the nonlinear behavior of these materials.

Hsu, et al. [42] studied microcracks in concrete loaded in uniaxial compression using optical microscope and x-ray procedures. These two procedures suffer from the limitation that only cracks of widths larger than about 50 μm can be examined [63]. The scanning electron microscope (SEM) has a much higher degree of resolution than the optical microscope. In addition, the SEM has a depth of focus that is 30 to 40 times greater than that of the optical microscope [100]. Derucher [27] used the SEM to observe that mortar cracks in concrete widen and propagate at a stress level lower than that obtained by Hsu, et al. The superior resolution and depth of focus of the SEM may have enabled Derucher to observe mortar cracks which were finer than those observed by Hsu, et al.

Cracks have been observed in the cement matrix of mortar and concrete by Yoshimoto, et al. [103,104] using an optical microscope. They suggested that mortar cracks in concrete develop from the cracks they observed. The study of very small cracks in cement paste requires the use of an SEM.

In order to observe cracks in saturated specimens of cement paste and mortar, Mindess and Diamond [63] used an SEM equipped with an environmental chamber or "wet cell". They used a loading device which enabled them to subject the specimens to compressive loading within the SEM chamber. In both the paste and mortar specimens, cracks were first noted at an applied stress of about 5500 psi. These cracks were about the same size as those observed with optical microscope and x-ray procedures. From their micrographs, it is observed that the resolutions they obtained were not as

high as obtained with a conventional SEM with dry specimens [28,29,51,96,101]. It is therefore possible that cracks which might have formed at lower stresses were not detected. A different procedure is needed if smaller cracks are to be observed.

The microstructure of cement paste has been studied for several years with the aid of the SEM [19,28,29,51,62,89,96,97,101]. These studies have been done using fractured surfaces of the hardened paste. Sawed and polished surfaces are not recommended since the effects of smearing tend to make the identification of microstructural features difficult [51]. The two major products of hydration are calcium silicate hydrate (CSH) and calcium hydroxide (CH). It is generally agreed among the various investigators that calcium silicate hydrate gives cement paste most of its strength. Berger, et al. [9] and Diamond [29] identified four structural types of calcium silicate hydrate: Types I, II, III and IV. Flaws and stress concentrators which exist in cement paste have been identified by Williamson [101].

Constitutive models have been used to determine the effects of cracks on the stress-strain response of concrete [16,56,76,88]. Buyukozturk [16] used a linear finite element representation of a physical model of concrete. He could not duplicate the nonlinear experimental behavior of concrete using the formation of interfacial bond cracks and mortar cracks as the only nonlinearities. Testa and Stubbs [91] also used a linear representation of mortar in a mathematical model to determine the effects of bond failure on the stress-strain response of concrete. Their model could not match the behavior of concrete.

Shah and Winter [79] accounted for the inability of their linear elastic model to duplicate the nonlinear behavior of concrete by considering the statistical variations in the local strength of concrete. By the proper selection of these variations, they were able to duplicate the behavior of concrete. However, the major nonlinear behavior of concrete can also be matched by considering the nonlinearities of the mortar constituent, as shown by Maher and Darwin [57] in their finite element model. Thus, an understanding of the nonlinearities of mortar and cement paste should lead to a better understanding of the stress-strain behavior of concrete.

The models discussed above do not consider the three-dimensional crack size and orientation distributions. A complete cracking model should in-

clude these distributions. Constitutive models based on the "self-consistent method" [12,35] account for crack distributions and have been used to estimate the elastic moduli of cracked solids [14,38,40,67]. The method considers changes in the strain energy of a solid due to the formation of individual cracks. The changes in energy are based on material properties as they are modified by the cracks. Budiansky and O'Connell [14,67] and Horii and Nemat-Nasser [40] used the method to estimate the elastic moduli of solids containing isotropic distributions of cracks. Hoenig [38] estimated the elastic moduli of solids in which cracks are distributed with a single orientation.

Distributions of load-induced cracks in cement paste, mortar or concrete under uniaxial compressive loading should be symmetric about the longitudinal or loading axis of the specimen. These crack distributions would therefore render the material transversely isotropic with five independent elastic moduli. The self-consistent model has yet to be applied to such a transversely isotropic solid.

The nature of damage at the submicroscopic level in cement paste subjected to uniaxial compressive loading and its relationship to the nonlinear behavior of paste, mortar and concrete remains to be adequately investigated.

1.3 Techniques for Crack Studies

Two techniques have been used to study stress-induced microscopic cracks in concrete and its constituent materials.

In the first technique, the optical microscope and x-ray photographs are used to study the cracks [42,60,76,77,82,103,104]. Specimens of cement paste, mortar or concrete are loaded to predetermined strains and then unloaded. Sawed and polished surfaces of the specimens which are perpendicular to the direction of loading (transverse surfaces) are studied under low magnification (typically about 7x to 50x) using an optical microscope or without magnification using x-rays. By this procedure, cracks have been identified at the interface between coarse aggregate and mortar (bond cracks) and within mortar (mortar cracks). A major disadvantage of this procedure is that only cracks of widths larger than about 50 μm can be identified.

In the second technique, small specimens of cement paste, mortar or concrete are studied under load within an SEM [27,28,29,63]. Cracks are recorded as they form. The viewing plane is limited to a polished surface which is parallel to the loading direction (longitudinal surface). Transverse surfaces cannot be viewed. Saturated specimens are viewed using an SEM equipped with a "wet cell". The resolution obtained with saturated specimens is such that the magnification is limited to at most 500x. The poor resolution is due to gas (water vapor) in the SEM chamber. Because of the limited magnification, cracks observed in saturated specimens tend to be about the same size as those observed with the optical microscope and x-rays. Very high resolutions are obtained with the SEM when dry specimens are used [28,29,51,96,101]. Therefore, observations of cracks which are smaller than those observed in saturated specimens require the use of dry specimens. Derucher [27] used dry specimens in the SEM but limited his studies to a magnification of 100x. The cracks he studied were the same size as those studied by Hsu, et al. with the optical microscope [42]. High resolutions can be obtained with the SEM at magnifications on the order of 10000x when dry specimens are used.

The two techniques described above have been limited to providing a two-dimensional picture of cracks in concrete and its constituent materials, based on crack trace lengths on either transverse or longitudinal surfaces. A full understanding of material response to cracking requires a knowledge of three-dimensional crack distributions within the material volume. Since the materials are opaque, the three-dimensional crack distributions cannot be obtained directly. An accurate estimation of these distributions using stereological principles [94,98] requires that surface crack data on both transverse and longitudinal surfaces be obtained. This requirement suggests modifying the above techniques.

1.4 Object and Scope

The purpose of this investigation is to study submicroscopic cracking of cement paste and mortar under uniaxial compressive loading and to correlate the observed cracks with the applied strain and load history.

Cement paste and mortar specimens are subjected to uniaxial compressive loading. The cement pastes studied are representative of those found in low, normal and high strength concretes. Mixes with water-cement ratios of

0.7, 0.5 and 0.3 are used. The mortar studied corresponds to concrete with a water-cement ratio of 0.5. Tests on cement paste include "short-term" monotonic, sustained and cyclic loading, while tests on mortar are limited to "short-term" monotonic loading. Specimens are tested at ages of 27, 28 or 29 days.

Drying procedures are established to prepare nonloaded and preloaded specimens for viewing in the SEM. Cracking on transverse and longitudinal surfaces of the specimens is studied at a magnification of 1250x. Microstructural features in cement paste and mortar are also studied.

Statistical and stereological models are developed to convert the surface crack distributions to three-dimensional distributions. The extent of cracking in cement paste and mortar is compared.

A self-consistent model is developed for a transversely isotropic cracked material. Submicrocracking is correlated with the reduction in stiffness and the shape of the stress-strain curves of cement paste and mortar using the self-consistent model.

CHAPTER 2
EXPERIMENTAL STUDY

2.1 General

The experimental program was designed to study submicroscopic cracking of cement paste and mortar under uniaxial compression. Cement paste specimens were subjected to monotonic, sustained or cyclic loading. Mortar specimens were subjected to monotonic loading.

The cement pastes studied were representative of those found in low, normal and high strength concretes. Water-cement ratios (W/C) of 0.7, 0.5 and 0.3 were used. The mortar studied corresponded to concrete with a W/C of 0.5.

The test specimens were loaded in compression using a closed-loop servo-hydraulic testing machine. The average axial strain was obtained using a compressometer and the average lateral strain was obtained using an extensometer.

After the specimens were loaded, slices were removed and dried for viewing in a scanning electron microscope (SEM). This portion of the study provided data on cracks at the submicroscopic level in the materials.

In this report, the results of the experimental work are analyzed to determine the surface and volumetric densities of cracks in cement paste and mortar (Chapters 2 and 3) and the effects of the submicroscopic cracks on the load-deformation behavior of the materials (Chapters 4 and 5).

2.2 Materials

Cement: Type I portland cement, Ashgrove Brand, of the following composition was used: C_3S = 51.1%, C_2S = 22.3%, C_4AF = 9.5%, and C_3A = 8.6%.

Fine Aggregate: consists mainly of quartz, with 10% to 15% chert; larger particles contain some limestone and dolomite. Fineness Modulus = 2.9. Bulk Specific Gravity (Saturated Surface Dry) = 2.61. Absorption = 0.79%. Source: Kansas River, Lawrence, Kansas. The sand was passed through a #4 sieve before use.

Coarse Aggregate: Crushed limestone of 1/2 in. nominal size. Bulk Specific Gravity (Saturated Surface Dry) = 2.52. Absorption = 3.2%. Source: Hamm's Quarry, Perry, Kansas. The coarse aggregate was passed through a 1/2 in. sieve before use.

Concrete mixes were designed in order to obtain the proportions of the corresponding mortar constituent. Three water-cement ratios, 0.7, 0.5 and 0.3, were used for cement paste. A single mortar mix of W/C = 0.5 was used. The mix designs are given in Table 2.1.

2.3 Test Procedure

2.3.1 Test Specimen

Prismatic test specimens, 2 in. square by 8 in. long, were prepared. The paste and mortar specimens were mixed using a mechanical mixer following ASTM C 305-70 [2]. Sand for the mortar specimens was oven-dried during the twenty-four hour period prior to batching. The mix water was increased to correct for absorption of the sand. The sand was allowed to cool before being placed in the mixer.

Batching was performed at room temperature, which ranged from 68° to 84°F. Six specimens were prepared from each batch. The steel molds (Fig. 2.1) were oiled and sealed with modeling clay. The specimens were cast in a vertical position. The molds were filled in three equal layers. Each layer was rodded twenty-five times using a three-eighths in. diameter rod and the molds were then sealed at the top.

During the first twenty-four hours, the molds were stored in the laboratory in a horizontal position to reduce the effects of bleeding. The specimens were then removed from the molds and stored in lime saturated water until the time of test.

Prior to loading, the specimens were shortened to a length of 6 in. by removing equal portions from each end using a high speed masonry saw. Specimens were tested 27 to 29 days after casting. In preparation for testing, specimens were removed from the curing tank and wrapped in plastic to insure that they would remain in a saturated condition during the tests.

2.3.2 Instron Testing Machine

A 110,000 pound capacity closed-loop servo-hydraulic Instron testing machine (Model No. 1334) was used. The load was transmitted through flat rigid platens to insure that the imposed displacement was the same at all points across the width of the specimens. The testing machine allowed the

test to be controlled by either strain or load. Strain control at a constant strain rate was used for the monotonic tests, while load control was used for both the sustained and cyclic tests.

Alignment of the specimens in the testing machine was achieved using the following procedure. Both ends of the specimens were capped with a one-eighth in. layer of high strength gypsum cement (Hydrostone). A steel plate was fixed to the lower platen of the testing machine by means of Hydrostone and then oiled. Two layers of 4 mil polyethylene sheet were placed on this steel plate to reduce friction between the specimen and the steel plate. The specimen was then placed on the polyethylene sheets. Two more layers of polyethylene sheet were placed on top of the specimen. A second oiled steel plate was placed on top of these sheets. The surface of the upper platen was oiled. A thin layer of Hydrostone was spread on the top plate. By raising the lower platen, the specimen was slowly brought into contact with the upper platen. Fifty to one-hundred pounds of load were applied. The Hydrostone hardened in approximately thirty minutes, and then the load was removed.

2.3.3 Measurement of Axial and Lateral Strains

A five-inch gage length compressometer was used to measure the average axial strain (Fig. 2.2). An MTS extensometer, Model 632.11B-20, was installed on the compressometer to measure the strain and to provide closed-loop control for the testing machine. The gage length of the extensometer was 1.0 in., and the range of displacement was ± 0.15 in. Measurement of displacement over the five-inch gage length of the compressometer improved the sensitivity of the closed-loop control.

The compressometer was attached to wood strips on the test specimen using set-screws. The wood strips were attached to the specimen using a cyanoacrylate adhesive immediately after blotting off surface water at the selected locations on the specimen.

A second extensometer was mounted on each specimen to measure the average lateral strain. A one-inch gage extender was attached to the fixed leg of the extensometer to enable measurements to be made over a two-inch gage length. A cyanoacrylate adhesive was used to attach the extensometer to the specimen. A strong bond was obtained within one minute.

2.3.4 Data Acquisition

Data on load, axial strain and lateral strain were obtained using a Hewlett-Packard data acquisition system (3052B). A Hewlett-Packard desktop computer (9825B) was used to control the system and record the data. Software tailored to each loading regime automatically acquired data at specified time intervals.

2.4 Loading Regimes

2.4.1 General

The loading phase of the experimental work was designed to prepare specimens with known stress-strain histories for submicroscopic study. Specimens were subjected to monotonic, sustained or cyclic compressive load at ages of 27, 28 or 29 days. Sixteen batches of cement paste and two batches of mortar were tested. One specimen from each batch was used as a nonloaded control specimen for the submicroscopic studies.

The specimens are identified by batch and specimen number (e.g. 2-1), type of specimen and water-cement ratio (e.g. P-0.5), and type of test (e.g. M). A key to specimen identification is provided in Appendix A.

2.4.2 Monotonic Loading

This group of tests constituted the major thrust of the study. Cement paste and mortar specimens were loaded monotonically in compression to a specified strain and then immediately unloaded. The specimens were loaded and unloaded at a strain rate of 0.0004 per minute. The strain to which each specimen was loaded is shown in Tables 2.2-2.5.

Two batches of cement paste with a W/C = 0.7 and three batches each of cement paste with W/C = 0.5 and 0.3 were tested. Two batches of mortar with a W/C = 0.5 were also tested. Cement paste specimens were loaded to strains of 0.0005, 0.001, 0.002, 0.004 and 0.006, while mortar specimens were loaded to strains of 0.0005, 0.001, 0.002, 0.003 and 0.004. In addition, three specimens from each of the sustained and cyclic test batches were loaded monotonically: one specimen to failure, and two specimens to strains of 0.004 and 0.006 for the sustained batch, 0.002 and 0.004 for the cyclic batch.

Data was recorded at four second time intervals. Typical stress-strain curves for cement pastes with W/C = 0.7, 0.5 and 0.3 are shown in Fig. 2.3-2.5, and in Fig. 2.6 for mortar with a W/C = 0.5. Lateral strains were not measured for paste with a W/C = 0.7.

The stress-strain curves for cement paste and mortar are nonlinear (Fig. 2.3-2.6). Fig. 2.4 and 2.6 show that cement paste has a higher strain capacity than mortar with the same water-cement ratio. The stress-strain curves of cement pastes with W/C = 0.5 and 0.3 which were loaded to failure (Specimens 14-6/P-0.5/M and 16-3/P-0.3/M) are shown together in Fig. 2.7. This figure shows that cement paste with a W/C = 0.5 has a higher strain capacity than paste with a W/C = 0.3.

The initial modulus of elasticity, E_i, for each specimen is also given in Tables 2.2-2.5. In this study, E_i is the secant modulus obtained from the first two sets of stress-strain data recorded.

2.4.2.1 Poisson's Ratio and Volumetric Strain

Poisson's ratio, ν, is calculated as the ratio of transverse or lateral strain, ε_t, to longitudinal or axial strain, ε. Volumetric strain, ε_v, is calculated using the relation

$$\varepsilon_v = \varepsilon - 2\varepsilon_t \qquad (2.1)$$

Relationships between Poisson's ratio and axial strain, and between volumetric strain and axial strain, are shown in Fig. 2.8-2.13 for monotonically loaded cement paste and mortar specimens (Specimens 14-6/P-0.5/M, 16-3/P-0.3/M and 13-6/M-0.5/M).

Fig. 2.8 and 2.9 show that for cement pastes with W/C = 0.5 and 0.3, Poisson's ratio rapidly attains a value of about 0.24 and then gradually increases with increasing strain. For mortar with a W/C = 0.5 (Fig. 2.10), Poisson's ratio rapidly attains a value of about 0.20 and then increases more rapidly with increasing strain than for cement paste. The initial low values of Poisson's ratio are attributed to initial seating problems of the extensometer. It appears that some small load is required on the specimen in order for the extensometer to become properly seated on the specimen. Therefore, the values of 0.24 for the cement pastes and 0.20 for mortar are probably the true initial Poisson's ratios. These values agree well with values of 0.23-0.26 for cement paste and 0.19-0.21 for mortar obtained from

previous studies [3,58,59,68,71,76]. The single value for the initial Poisson's ratio of cement pastes with water-cement ratios of 0.5 and 0.3 is consistent with the findings of Anson [3] and Parrott [68] that Poisson's ratio does not vary with water-cement ratio for hardened cement pastes.

Fig. 2.11 and 2.12 show that volume decreases continuously in cement paste under uniaxial compression. At high applied strains, however, the figures show that a reduction in the rate of volume decrease occurs, as indicated by the increasing slope of the axial strain - volumetric strain curves. Fig. 2.13 shows that at low strains, volume decreases continuously in mortar under uniaxial compression, followed by an incremental volume increase at higher strains. These observations imply that some type of structural change takes place and opposes the normal reduction in volume which occurs under a compressive loading. This structural change is likely to be internal cracking.

2.4.3 Sustained Loading

In this group of tests, the stress-strength ratios were selected to enable strains of about 0.004 and 0.006 to be reached in four hours. Loading to the desired stress level took fifteen seconds. The stress-strength ratio and strain for each specimen are provided in Table 2.6. The data for a specimen with a W/C = 0.5 which failed in 3.5 hours at a strain of 0.0075 is also provided.

Two batches each for cement paste with water-cement ratios of 0.5 and 0.3 were tested. In each batch, one specimen was loaded monotonically to failure to determine the compressive strength and two specimens were subjected to sustained loading. Two specimens were loaded monotonically to strains of 0.004 and 0.006.

During the initial stage of loading, data was taken at one second intervals. The intervals were gradually increased up to 5 minutes as the test progressed. A typical stress-strain curve is shown in Fig. 2.14. As load is increased to the specified stress level, the stress-strain curve is nonlinear. Under constant stress, both the longitudinal and lateral strains increase.

2.4.3.1 Poisson's Ratio and Volumetric Strain

Fig. 2.15 and 2.16 show the Poisson's ratio versus axial strain relationships for cement pastes subjected to sustained loading. Fig. 2.17 and 2.18 show the corresponding volumetric strain versus axial strain relationships. Fig. 2.15 and 2.17 are for a specimen with a W/C = 0.5 (Specimen 15A-1/P-0.5/S) which failed at a strain of 0.0075 after a loading duration of 3.5 hours, while Fig. 2.16 and 2.18 are for a specimen with a W/C = 0.3 (Specimen 16-4/P-0.3/S) which was loaded for 4 hours to a strain of about 0.004. Fig. 2.15 and 2.16 show that during the initial stage of loading to the specified stress level, Poisson's ratio increases with increasing strain. Under constant stress, Poisson's ratio decreases with strain.

Parrott [68] subjected cement paste specimens to sustained loading for durations up to 500 days and obtained a value of 0.13 for the creep Poisson's ratio. He points out that this low value may be related to the porous nature of hardened cement paste. The decrease in Poisson's ratio obtained from the short-term creep tests in this study suggests that consolidation or deformation of solid phases into pores may occur, thus allowing substantial axial strains to develop without large lateral strains.

Fig. 2.17 and 2.18 show that the volume of the paste specimens decreases continuously for the stress levels used in this study. After the specified stress level is reached, the rate of consolidation increases as indicated by the decreased slope of each of the axial strain - volumetric strain curves.

2.4.4 Cyclic Loading

In this group of tests, the stress-strength ratios used enabled strains of 0.002 and 0.004 to be attained for specimens with a W/C = 0.5. For specimens with a W/C = 0.3, the selected stress-strength ratios enabled strains of 0.002, 0.0025 and 0.003 to be attained. Two attempts at loading specimens with a W/C = 0.3 to a strain of 0.004 were not successful; the specimens failed prior to reaching that strain. Each cycle (loading and unloading) took 30 seconds. The stress-strength ratio and strain for each specimen are provided in Table 2.7. The data for a specimen with a W/C = 0.5 which failed at a strain of 0.005 is also provided.

Two batches each for cement paste with W/C = 0.5 and 0.3 were tested. One specimen from each batch was loaded monotonically to failure to determine the compressive strength and two specimens were subjected to cyclic loading. Two specimens were loaded monotonically to strains of 0.002 and 0.004 for paste with a W/C = 0.5, and to strains of 0.002 and 0.003 for paste with a W/C = 0.3.

Data was recorded for selected cycles at one second intervals. Fig. 2.19 shows that the stress-strain curve for cyclic loading is nonlinear. As the number of cycles to the specified stress level increases, both the longitudinal and lateral strains increase.

2.4.4.1 Poisson's Ratio and Volumetric Strain

Relationships between Poisson's ratio and axial strain, and between volumetric strain and axial strain, are shown in Fig. 2.20-2.25 for cement pastes with W/C = 0.5 and 0.3. The relationships are shown for the loading portions of the cycles indicated in the figures.

Figs. 2.20 and 2.21 show the Poisson's ratio versus axial strain and volumetric strain versus axial strain relationships for a specimen with a W/C = 0.5 which was loaded to a stress-strength ratio of 0.865 and failed on the 31^{st} cycle at an axial strain of 0.005 (Specimen 19A-1/P-0.5/C). Fig. 2.20 shows that in each cycle, Poisson's ratio increases with strain. Poisson's ratio during the 29^{th} cycle is larger than that during the 1^{st} and 17^{th} cycles. As shown in Fig. 2.21, the increase in Poisson's ratio from the 17^{th} to 29^{th} cycles is accompanied by an incremental volume increase between the two cycles. Also, reductions in the rate of volume decrease occur during the 17^{th} and 29^{th} cycles, as indicated by the increasing slope of the axial strain - volumetric strain relationships for each of these cycles.

The Poisson's ratio versus axial strain and volumetric strain versus axial strain relationships for a specimen with a W/C = 0.5 loaded in 67 cycles (stress-strength ratio = 0.725) to a strain of 0.004 (Specimen 18-5/P-0.5/C) are shown in Fig. 2.22 and 2.23. With increasing strain within a single cycle, Poisson's ratio increases (Fig. 2.22) while the rate of volume decrease drops (Fig.2.23). Fig. 2.24 and 2.25 show the relationships between Poisson's ratio and axial strain and volumetric strain and axial strain, respectively, for a specimen with a W/C = 0.3 loaded in 85 cycles to

a strain of 0.003 (Specimen 21-5/P-0.3/C). Fig. 2.24 shows that Poisson's ratio is approximately constant during the 1^{st} cycle and decreases during later cycles. However, Poisson's ratio increases with increasing strain during the 42^{nd} and 85^{th} cycles. Fig. 2.25 shows that the volume decreases between the 1^{st} and 85^{th} cycles.

2.5 Submicrocracking Studies

2.5.1 Scanning Electron Microscope

A Philips 501 scanning electron microscope (SEM) [15] was used for the submicrocracking studies. An SEM produces a primary electron beam or probe which sweeps across the specimen, stimulating the emission of secondary electrons. Non-metallic materials, such as cement paste, must be coated with a metallic substance (e.g. gold-palladium) in order for a satisfactory quantity of secondary electrons to be emitted. The secondary electrons are collected to produce a signal which is then amplified. The resulting image, displayed on the viewing monitor, is similar to that obtained on a high quality television screen.

Specimens were coated with 200 angstroms, A, (0.02 μm) of gold-palladium using a Technics Hummer II sputter coater [15]. Specimens must be dried in order for a high vacuum to be reached in both the sputter coater and the SEM. A primary electron beam spot size of 200A and an accelerating voltage at the electron gun of 30kV were used. In order to insure close proximity of the emitted secondary electrons to the detector, the specimens were inclined at 45° to the primary beam by tilting the specimen stage [96]. A Polaroid camera attached to the SEM, with Polaroid type P/N 55 film, enabled photomicrographs of the specimens to be taken.

2.5.2 Specimen Preparation

After the test specimens were loaded, they were submerged in lime saturated water for a period of no longer than 24 hours. To prepare specimens for viewing in the SEM, 2 in. wide by 6 in. long by 1/8 in. thick slices were removed along the longitudinal (or loading) direction of the test specimens using a high speed diamond masonry saw, utilizing saturated calcium hydroxide solution as the lubricant. The middle portion of each slice, approximately 1 in. square, was removed by breaking the four sides of the slice with a pair of tongs. For proper identification during subsequent

preparation of the slice for viewing in the SEM, the perpendicular and parallel edges of the slice with respect to the direction of loading were labelled. The approximately 1 in. square by 1/8 in. thick slice was rinsed with lime saturated water and dried using one of three procedures: oven drying, solvent replacement drying, or silica gel drying. Of the three procedures, oven drying was selected for the main portion of the study. The latter two drying procedures saw limited use. They were used only for two batches of monotonically loaded paste specimens in order to compare the effects of the different drying conditions.

A description of the drying methods and the procedure for obtaining fractured surfaces for viewing in the SEM follow.

2.5.2.1 Oven Drying

The specimens was placed in an oven at a temperature of 217°F. A constant weight was attained in 24 hours.

2.5.2.2 Solvent Replacement Drying

This drying procedure involved placing a cement paste specimen in methanol, followed by placement in n-pentane and a vacuum desiccator [56,70]. For each storage medium, the specimen was weighed daily.

First, the paste specimen was placed in 25 ml of methanol. The methanol slowly replaced the water in the specimen. The methanol was changed every 3 days until the specimen weight began to increase instead of decreasing. At this point, the replacement of water by methanol was complete. The increase in weight is attributed to the polar nature of methanol which causes packing in the pore spaces of the specimen at a density greater than that in the bulk liquid state [70]. A total of 7 days was required for the complete replacement of water by methanol. Next, the specimen was placed in 25 ml of n-pentane. The n-pentane slowly replaced the methanol and was changed every 2 days. As in the case of the replacement of water by methanol, the replacement of methanol by n-pentane was complete when the specimen weight began to increase. A total of 5 days was required. Two days of continuous vacuum were required in order to reach constant weight in the vacuum desiccator. The total duration of this drying procedure was 14 days.

2.5.2.3 Silica Gel Drying

The specimen was placed in a desiccator which contained silica gel. A carbon dioxide absorbent (Ascarite) was also placed in the desiccator in order to prevent carbonation of the specimens. A constant weight was attained in 106 days.

2.5.2.4 Fracturing of the Specimens

After drying, the specimens were stored in a vacuum desiccator. One day prior to viewing in the SEM, the specimens were removed from the desiccator and fractured so that edges which were either perpendicular or parallel to the direction of loading (i.e., transverse or longitudinal edges) might be viewed. The viewing surfaces were about 1/8 in. thick.

The fracturing procedure involved holding one side of the specimen with a gloved hand and the opposite side with a pair of tongs so that a transverse fractured surface would be produced. The tip of the pair of tongs was positioned near the middle of the specimen and the specimen was then broken. One of the two broken pieces was selected and trimmed by slowly breaking off pieces of material from the sides. Care was taken so as not to handle the transverse fractured surface to be viewed. A longitudinal fractured surface was prepared in the same manner from the second broken piece. The two final specimens had dimensions of about 1/8 in. thick by 1/2 in. long by 1/4 in. high and were mounted on a stud using Pelco colloidal silver paste (Fig. 2.26).

The mounted specimens were stored in a vacuum desiccator to enable the colloidal paste to dry. Just prior to viewing, the fractured surfaces were coated with gold-palladium.

2.5.3 Crack Measurements

Within the SEM, each specimen was scanned at a magnification of 1250x in ten preselected bands across the specimen thickness. The width of the scanned area, w, was therefore equal to the specimen thickness; i.e., w ≈ 1/8 in. The actual thickness of each specimen was measured with a pair of calipers. The height of the fractured surface within each scanned area, h, was 0.0031 in. Fig. 2.27 shows a sketch of the specimen as positioned in the SEM.

To accurately select different bands for scanning, a grid was required. This was obtained by marking two pieces of masking tape at 1/2 in. intervals from 1 to 10. The marks corresponded to the ten bands to be viewed. The two pieces of masking tape were placed at the left and right edges of the SEM's viewing monitor. To select a particular band for scanning, a magnification of 10x was selected. At this magnification, the whole specimen was visible on the viewing monitor. A ruler was placed across opposite marks on the two pieces of masking tape to define the center of the band. A distinct feature along the center of the band was selected and positioned in the center of the viewing monitor. The magnification was increased to 1250x, and the selected feature was brought into clear view by an appropriate adjustment of the focus. By this procedure, the band to be scanned was clearly established. The left edge of the specimen was then brought into view and the scanning proceeded horizontally to the right edge. To select another band for scanning, the magnification was reduced to 10x and the procedure was repeated.

Crack trace lengths, widths, angles, and microstructural features through which cracks passed were recorded. Measurements were taken at a magnification of 1250x, except crack widths below 2.5 μm which were measured at 2500x. Only portions of cracks within the field of view were measured in order to obtain an accurate estimate of the density of cracks within the scanned areas. Crack trace lengths, ℓ, and widths, w_c, were measured on the viewing monitor with a ruler. Markers having units of μm were displayed on the viewing monitor to serve as a scale for measuring the true dimensions of objects. These markers were used to convert the ruler measurements to true dimensions. For ease of recording data, crack trace lengths were recorded in intervals of 1.5×10^{-4} in. or 3.8 μm (= 0.25 in. with the ruler). Crack trace angles, θ, were measured by means of the rotation control on the SEM. This control rotated the image appearing on the viewing monitor and was initially set at the 0° position. After a crack angle was measured, the control was reset to the 0° mark. For ease of recording data, the crack angles were recorded in 5° intervals from 0° to 180° (i.e., 5° is 2.5° to 7.5°, etc.).

The process of obtaining the crack data was quite tedious and required about 2.5 hours per specimen. To maintain objectivity, crack surveys were made at the same time each day and limited to a single specimen. To further

insure objectivity, specimens were selected and surveyed using a double blind coding system.

Table 2.8 illustrates the format used to record the data.

2.5.4 Results

2.5.4.1 Micrographs

Photomicrographs of key microstructural features are shown in Fig. 2.28-2.36 for cement paste, and in Fig. 2.37 and 2.38 for mortar. The descriptions of the various calcium silicate hydrate (CSH) structures follow that given by Berger, et al. [9] and Diamond [28,29].

Fig. 2.28 and 2.29 show typical Type I CSH for oven dried and solvent replacement dried specimens, respectively. The structure consists of fibrous globular clusters. The clusters in Fig. 2.28 look denser than those in Fig. 2.29. The different appearance of Type I CSH in Fig. 2.29 may indicate that the chemicals used in the solvent replacement drying process react with the hydration products of cement paste, as was found by Day [24]. Thus, the method of specimen drying appears to affect the nature of microstructural features. The balance of the micrographs represents oven dried specimens.

Type II CSH is shown in Fig. 2.30. This structure has a network-like morphology. It has been described by Diamond [28] as a "reticular network".

Fig. 2.31 shows the structure most commonly observed on the fractured surfaces. This is the equant grain morphology of Type III CSH. A typical crack is seen in the structure.

Inner product morphology, designated as Type IV CSH, is shown in the middle of the micrograph in Fig. 2.32.

Calcium hydroxide, CH, is shown in Fig. 2.33. This structure is characterized by distinct parallel cleavage planes. A crack is observed to have formed parallel to a cleavage plane. The total surface area of CH on the fractured surface of each of three paste specimens with a W/C = 0.5 was determined by measuring the area of CH regions. CH occupied about 3% of the fractured surface. A fundamental principle of stereology [94,98] shows that the area density of three-dimensional objects on a plane section through a volume is equal to the volume density of the objects. Hence, the 3% area density of CH converts to a 3% volume density. However, 15%-20% of the volume of hydrated cement paste is CH [8,48]. This observation suggests

that the fracture plane occurred preferentially through the softer CSH. Thus, the fractured surfaces are not fully representative of hydrated cement paste.

A crack through both Type III CSH and CH structures is shown in Fig. 2.34.

Fig. 2.35 shows an unhydrated cement grain, denoted in this study as UHC. This morphology is observed mainly in pastes with a W/C = 0.3, presumably because of the lower degree of hydration obtained at the low water-cement ratio. At low water-cement ratios, insufficient space for the hydration products and self-desiccation do not allow complete hydration to take place [64,65,84].

The interconnected rod-like morphology in Fig. 2.36 is that of ettringite. Ettringite is a reaction product of tricalcium aluminate and gypsum. Its formation prevents the flash set of tricalcium aluminate during the early hydration of cement [34]. The micrograph shown is for a 42-day old paste. It is generally believed that ettringite is completely converted into a low-sulphate sulphoaluminate, also referred to as monosulphate, about 1 day after the beginning of hydration [84]. Contrary to this belief, Fig. 2.36 shows that ettringite can remain in a hydrated cement paste as old as 42 days. Ettringite has also been observed by Diamond [28] in paste specimens at ages up to 28 days.

Fig. 2.37 and 2.38 are micrographs of mortar. In both micrographs, a sand grain, denoted in this study as SG, is observed adjacent to what is most likely Type III CSH. The Type III CSH observed here looks different than that observed in cement paste (Fig. 2.31 and 2.34). The Philips 501 SEM used in this study did not enable the composition of the Type III CSH in mortar to be analyzed. An SEM equipped with an energy-dispersive X-ray analyzer will enable the composition of this morphology to be determined. Cracks are observed at the interfaces between the sand grains and the Type III CSH and also within the Type III CSH.

2.5.4.2 Cracks

The cracks observed in the SEM ranged in length from about 0.0004 in. (10 μm) to about 0.008 in. (200 μm). Crack trace lengths and angles on the transverse and longitudinal surfaces of monotonically loaded specimens of

cement paste with a W/C = 0.5 (Batch #9) are given in Table 2.9 to illustrate the crack data obtained in the study. The total length of the cracks measured on each surface (transverse or longitudinal) is divided by the total area scanned to obtain a crack density in inches per square inch; i.e.,

$$\text{Crack Density} = \frac{\Sigma \ell}{10 \times w \times h} \text{ in./in.}^2$$

the denominator being the total area of the ten bands scanned.

The crack densities obtained in this study are given in Tables 2.10-2.17. The crack densities in cement paste range from about 20 in./in.^{2} to about 50 in./in.^{2}, which is one order of magnitude greater than obtained for bond and mortar microcracking in concrete [17,42].

Crack Density versus Water-Cement Ratio: Fig. 2.39 shows that the crack density of oven dried nonloaded cement paste specimens varies inversely with water-cement ratio. Specimens with a W/C = 0.3 show greater cracking at zero load than do specimens with a W/C = 0.5, which in turn is greater than specimens with a W/C = 0.7. This observation is discussed in Chapter 3.

Crack Density versus Strain: Fig. 2.40-2.47 show the variation in crack density of oven dried specimens as a function of applied compressive strain for all loading regimes. In all cases, crack density increases with strain.

The curves represent the least squares fit of the data. The equations of the lines are given in the figures. For cement pastes with W/C = 0.7 and 0.5 (Fig. 2.40-2.41), and mortar with a W/C = 0.5 (Fig. 2.43), the high values of the correlation coefficient, R, indicate that the relationships between crack density and applied strain are strongly linear.

Contrary to the linear trends exhibited by the other materials, cement paste with a W/C = 0.3 has a crack density - strain relationship that is curvilinear to the second order (Fig. 2.42). In these figures, the crack densities at strains of 0.0058 and 0.006 are from specimens which failed at those strains. The failure of these specimens was explosive and large surface cracks were seen just prior to failure. The curves in Fig. 2.42 suggest that a large increase in submicroscopic crack density occurs as the failure strain is reached.

For all monotonically loaded specimens, crack density begins to increase immediately, even for very small applied strains, suggesting that even low strains will result in some damage to cement paste and mortar. For sustained and cyclic loading, crack density increases with strain over the range of strains used, as shown in Fig. 2.44-2.47.

The average crack density at each applied strain in oven dried specimens are given in Tables 2.18-2.23 for all loading regimes.

Crack Density Based on Microscopic Structure: Crack density for each microscopic structure as a function of applied strain is shown in Tables 2.24-2.28 for cement pastes, and in Table 2.29 for mortar. The average values at each applied strain for the transverse and longitudinal surfaces of all specimens under each loading regime are given. The percentage of crack density for each structure in both cement paste and mortar remains nearly constant as the total density of cracking increases with strain.

For cement paste specimens, the dominant cracking on both the transverse and longitudinal surfaces occurs through the Type III CSH structure, independent of loading regime. About 80% of the total crack density occurs through the Type III CSH structure. The balance of the cracking is approximately evenly divided between CH and the CH-III boundary. About 1% of the cracking in cement paste with a W/C = 0.3 occurs at the UHC-III boundary.

The dominant cracking in mortar, about 70%, occurs through the Type III CSH structure (Table 2.29). About 18% of the cracking occurs at the SG-III boundary. The balance of the cracking is approximately evenly divided between CH and the CH-III boundary.

Crack Density versus Trace Angle: Typical relationships between crack density and crack angle for nonloaded and loaded specimens of paste and mortar are illustrated in Fig. 2.48-2.51 for values of θ from 0° to 90°. In obtaining these relationships, crack angles of $\theta \pm \Delta\theta/2$ and $180° - \theta \pm \Delta\theta/2$ ($\Delta\theta = 5°$) are grouped together. The crack density per degree is then calculated as

$$\text{Crack Density per degree} = \frac{\text{Crack Density for } \theta \text{ and } 180°-\theta}{2\ \Delta\theta}$$

As illustrated by the fairly constant least squares fits over the middle eighty-five degree range in Fig. 2.48-2.51, crack densities are

approximately equal at all angles for nonloaded specimens, and for the transverse surfaces of loaded specimens. The nearly uniform distributions of crack density with respect to trace angle on the transverse surfaces of loaded specimens suggest that cement paste and mortar under uniaxial compression are transversely isotropic, as expected. Crack density distributions on the longitudinal surfaces of loaded specimens are skewed towards $\theta = 90°$ (Fig. 2.49 and 2.51).

The larger crack densities within the ranges of θ from 0°-2.5° and 87.5°-90° are attributed to the procedures used in preparing specimens for viewing in the SEM and will be discussed in Chapter 3.

Crack Density Based on Drying Method: Crack density seems to depend upon the drying method, as evidenced by the relationships shown in Fig. 2.52. The average results at each applied strain for the transverse surfaces of oven dried, solvent replacement dried and silica gel dried paste specimens (W/C = 0.5) are shown. Fig. 2.52 indicates that the crack densities of solvent replacement dried specimens are larger than those of either oven dried or silica gel dried specimens. Oven drying, is a rapid drying process that causes high moisture gradients within a specimen. Thus it may cause drying cracks to initiate at weak locations at the surface as well as within the material. Solvent replacement drying, on the other hand, is a slow process that maintains a much more uniform moisture condition throughout the specimen. This may allow cracks to initiate at many locations, resulting in a larger crack density as compared to oven drying. Silica gel drying is a slow process, but th specimens are rapidly subjected to a high moisture gradient, and thus the effects of this method may be closer to those of oven drying. The crack densities of oven dried and silica gel dried specimens are about the same. The relative crack widths obtained with the three drying procedures support these arguments.

Crack Widths: The average values of crack width at each applied strain for the transverse and longitudinal surfaces of all specimens under each loading regime, are given in Tables 2.30-2.33. Crack widths increase with applied strain, and vary with drying method. For each applied strain, crack widths are largest in oven dried specimens and smallest in solvent replacement dried specimens.

The cracks range in width from 0.15 μm to 5.25 μm for solvent replacement dried pastes, from 0.20 μm to 6.25 μm for silica gel dried pastes, and

from 0.20 μm to 7.0 μm for oven dried pastes. Crack widths range from 0.15 μm to 7.5 μm for oven dried mortar. At the same strain level, mortar specimens have a larger average crack width than paste specimens.

If the total volume change due to drying is identical under different drying conditions due to removal of equal volumes of free water, the average crack width should decrease as the crack density increases. This observation is consistent with the measured crack widths and crack densities obtained with the three drying procedures.

2.5.5 Uniqueness of Submicroscopic Cracks

During preliminary studies, cracks were measured at magnifications up to 10000x. These studies showed that cracks which are visible at 10000x are also visible at 1250x and that crack densities obtained at the two magnifications are essentially the same. At the next lower magnification, 640x, some cracks are lost, and the crack density drops. A magnification of 1250x was used throughout this study since much more area could be covered than at 10000x.

These observations indicate that the submicroscopic cracks are unique to the particular level of microstructure studied. The uniqueness of these cracks also lies in the fact that magnification has to be increased by two orders of magnitude in order to observe cracks with a density one order of magnitude higher than that of bond and mortar microcracks in concrete.

2.5.6 Surface versus Volumetric Crack Distributions

The crack data discussed in this chapter, crack length, crack angle, and crack density, in fact, represent only the traces of three-dimensional cracks on selected planes. Thus, this data does not directly provide adequate information about cracking as it occurs throughout the volume of each specimen. Three-dimensional crack sizes and orientations, as opposed to surface trace lengths and angles, are needed if a full understanding of material response to cracking is to be obtained.

In the next chapter, the surface crack data is further analyzed to obtain estimates of the three-dimensional crack distributions. These three-dimensional distributions provide a clearer understanding of cracking as it occurs in cement paste and mortar under uniaxial compression, and are used

in Chapter 5 to estimate the effects of the cracks on the stress-strain behavior of the materials.

2.6 Summary of Observations

1. The stress-strain curves of cement paste and mortar are highly nonlinear.
2. Poisson's ratio increases continuously in cement paste and mortar under monotonic loading.
3. A reduction in the rate of volume decrease occurs in cement paste, and incremental volume increase occurs in mortar under monotonic loading.
4. For sustained loading, Poisson's ratio increases continuously in cement paste during the initial stage of loading to the specified stress level, and then decreases under constant stress.
5. For cyclic loading, Poisson's ratio increases continuously in cement paste during the loading portion of each cycle.
6. Incremental volume increase occurs in cement paste loaded to failure under cyclic loading.
7. The density and width of drying cracks in cement paste vary with the method of specimen drying.
8. Crack density in cement paste varies inversely with water-cement ratio for nonloaded specimens.
9. Crack density in cement paste and mortar increases with increasing uniaxial compressive strain.
10. Crack density in cement paste is about ten times the density of bond and mortar microcracks in concrete at the same value of compressive strain.
11. The dominant cracking in cement paste occurs through the Type III CSH structure with the balance approximately equally divided between CH and the CH-III boundary.
12. The dominant cracking in mortar occurs through the Type III CSH structure, followed by cracking at the sand grain - Type III CSH boundary. The balance of the cracking is approximately evenly divided between CH and the CH-III boundary.

CHAPTER 3
EVALUATION AND DISCUSSION OF EXPERIMENTAL RESULTS

3.1 General

In this chapter, the surface crack data of trace lengths and trace angles (examples in Table 2.9) are analyzed to (1) determine the effects of specimen preparation prior to viewing in the SEM and (2) estimate three-dimensional submicroscopic crack distributions in cement paste and mortar. For a given load regime and applied strain, the average surface crack data for all specimens loaded to that strain are used for the analyses which follow.

The accurate estimation of three-dimensional crack distributions requires that the surface crack distributions obtained with the SEM be converted to true surface crack distributions. As described in Chapter 2, only crack traces within the field of view of the SEM are measured in order to obtain an accurate estimate of the density of cracks within the scanned areas. However, since segments of some crack traces project outside the viewing area, their measured lengths are shorter than the true trace lengths, causing the length distribution to be skewed towards low values. A crack whose center is located outside the viewing area may have a portion within the field of view. A crack centered at the same point but at a lower angle, θ, may lie completely outside the viewing area. The observed number of cracks at low angles will therefore be relatively lower than the number at high angles, resulting in the angle distribution being skewed towards $\theta = 90°$. Thus, the observed or "apparent" distributions may not be good estimates of the true surface distributions. Since the fractured surfaces are scanned horizontally, there is no limitation imposed by the width of the viewing area on the measurement of cracks.

The true trace length and angle distributions are obtained from the observed surface distributions using statistical procedures described in Section 3.3. The detailed derivations of these procedures are presented in Appendix C.

The surface crack distributions must be converted to three-dimensional crack distributions in order to gain a full understanding of material response to cracking. The statistical procedures for this conversion are

described in Section 3.4. The detailed derivation of the procedures is presented in Appendix D.

The extent of cracking is compared for specimens with different water-cement ratios and load regimes.

3.2 Effects of Specimen Preparation

Prior to viewing in the SEM, the specimens are dried and fractured, as described in Section 2.5.2. Fig. 3.1 shows the variation of the number of cracks per unit area with trace angle on the transverse surface of nonloaded cement paste with a W/C = 0.5. The increased number of cracks over the ranges of θ from 0° to 2.5° and from 87.5° to 90° are typical of the results for all specimens.

The increased number of cracks over the range of θ from 0° to 2.5° is attributed to drying, since drying cracks form normal to the surface of the specimen due to differential drying rates between the exterior and interior of the specimen [5,6,7]. The direction normal to the surface of the specimen corresponds to θ = 0°, as measured in the SEM (Fig. 2.27). Drying can also cause randomly oriented cracks to form [6], as will be discussed in Section 3.5.1.

The increased number of cracks over the range of θ from 87.5° to 90° is attributed to fracturing of the specimen. The fracturing process induces tensile stresses in a direction parallel to the fracture crack, resulting in the formation of transverse cracks [54].

In order to reduce the effects of specimen preparation on the surface crack distributions, the specimen preparation cracks are removed from the total crack distributions using procedures described in Sections 3.3.4 and 3.4. The resulting surface distributions are used to estimate the three-dimensional distributions.

3.3 Surface Crack Distributions

As pointed out in Section 3.1, the true surface crack distributions cannot be obtained directly from the experimental data. In Sections 3.3.1 through 3.3.3, statistical procedures (details in Appendix C) are used to obtain the true surface crack distributions.

For uniaxially loaded paste and mortar specimens, trace length distributions of load-induced cracks on the transverse surface should be

independent of trace angle. Deviations from an isotropic distribution are attributed to specimen preparation. The mean lengths and variances of the estimated true trace length distributions on the transverse surface must therefore be modified to obtain an isotropic distribution with respect to trace angle. On the longitudinal surface, the mean trace length and variance of the distribution of load-induced cracks may vary with trace angle. The modifications for both the transverse and longitudinal surfaces are described in Section 3.3.4.

3.3.1 True Trace Length Distribution

A relative frequency distribution is defined by its form, mean, and variance. The form of the distribution, e.g. a normal or gamma distribution, describes its shape. An estimate of the true trace length distribution for each trace angle, $f(\ell|\theta)$, is obtained by determining its form, mean, $\langle \ell_\theta \rangle$, and variance, $\mathrm{var}(\ell_\theta)$. The equation (derived in Appendix C) relating the true trace length distribution to the apparent distribution is

$$f(\ell|\theta)_{ac} = \frac{(h-\ell\sin\theta)f(\ell|\theta) + 2\sin\theta\int_{\ell}^{\infty} f(\ell|\theta)d\ell}{h + \langle \ell_\theta \rangle \sin\theta} \tag{3.1}$$

in which $f(\ell|\theta)_{ac}$ is the calculated apparent trace length distribution for each trace angle, θ; ℓ is the trace length, and h is the height of the specimen surface within the regions viewed in the SEM (Section 2.5.3).

The experimental or known apparent trace length distribution for each trace angle, $f(\ell|\theta)_a$, is computed from the surface crack data as

$$f(\ell|\theta)_a = \frac{n}{n_\theta \Delta\ell} \tag{3.2}$$

in which n is the number of cracks with measured lengths of $\ell \pm \Delta\ell/2$ and angles of $\theta \pm \Delta\theta/2$, and n_θ is the number of cracks with angles of $\theta \pm \Delta\theta/2$. $\Delta\ell$ and $\Delta\theta$ are the experimental increments used for trace length and trace angle measurements, respectively; $\Delta\ell = 1.5\times10^{-4}$ in., and $\Delta\theta = 5°$. In computing $f(\ell|\theta)_a$ using Eq. (3.2), trace angles of θ and $180°-\theta$ are grouped together. The distributions are obtained for values of θ from 0° to 90° in five-degree intervals. Typical experimental distributions of crack trace

lengths for trace angles of 30°, 50°, 60° and 70° are represented by the histograms in Fig. 3.2. The data in this figure are obtained from the longitudinal surface of cement paste (W/C = 0.5) loaded monotonically to a compressive strain of 0.004.

As shown in Appendix C, the true mean trace length, $\langle \ell_\theta \rangle$, can be expressed in terms of the apparent mean trace length, $\langle \ell_\theta \rangle_a$, as

$$\langle \ell_\theta \rangle = \frac{h\langle \ell_\theta \rangle_a}{h - \langle \ell_\theta \rangle_a \sin\theta} \tag{3.3}$$

The true variance, $\mathrm{var}(\ell_\theta)$, can be expressed as

$$\mathrm{var}(\ell_\theta) = \frac{\langle \ell_\theta \rangle}{\langle \ell_\theta \rangle_a} \mathrm{var}(\ell_\theta)_a - \langle \ell_\theta \rangle(\langle \ell_\theta \rangle - \langle \ell_\theta \rangle_a) + \frac{\sin\theta}{3h} \int_0^\infty \ell^3 f(\ell|\theta)\, d\ell \tag{3.4}$$

in which $\mathrm{var}(\ell_\theta)_a$ is the variance of the observed distribution.

$\langle \ell_\theta \rangle$ can be obtained directly from Eq. (3.3) since h is known and $\langle \ell_\theta \rangle_a$ can be calculated from the measured crack data. The form and variance of $f(\ell|\theta)$, however, cannot be obtained directly, requiring the use of an iterative procedure (described below) involving Eqs. (3.1), (3.3) and (3.4). The objective of the procedure is to calculate an apparent distribution based on an assumed form of the true distribution. If a close match is obtained between the known and calculated apparent distributions, then the assumed form of the true distribution is the correct one.

A "goodness of fit" test, based on the chi-square distribution [31], is used to determine when a close match is obtained. In this test, a chi-square statistic or value is computed from the experimental and calculated apparent distributions. If this value is less than the value obtained from the chi-square distribution at a level of significance of 0.05, then a "close" match has been obtained. Further details of this test can be found in Reference 31 and in most statistics books.

The procedure for determining the true trace length distribution is outlined as follows:

1. Assume a form for $f(\ell|\theta)$.
2. The mean and variance of $f(\ell|\theta)$ are $\langle \ell_\theta \rangle$ and $\mathrm{var}(\ell_\theta)$, respectively. Calculate $\langle \ell_\theta \rangle$ using Eq. (3.3). As an initial guess, assume that $\mathrm{var}(\ell_\theta) = \mathrm{var}(\ell_\theta)_a$.

3. Calculate $var(\ell_\theta)$ using Eq. (3.4).
4. If the computed variance is not equal to the assumed variance, recompute $var(\ell_\theta)$ from Eq. (3.4) using the variance calculated in Step 3.
5. Repeat Steps 3 and 4 until the assumed and computed variances are equal.
6. Substitute $f(\ell|\theta)$, with parameters $\langle\ell_\theta\rangle$ and $var(\ell_\theta)$, into Eq. (3.1) in order to calculate $f(\ell|\theta)_{ac}$.
7. Use the "goodness of fit" test, based on the chi-square distribution to determine if there is a close agreement between the known, $f(\ell|\theta)_a$, and calculated, $f(\ell|\theta)_{ac}$, apparent distributions. A close agreement implies that a good estimate of $f(\ell|\theta)$ has been obtained.
8. If the "goodness of fit" test fails, assume a true distribution with a different form. Repeat Steps 2 to 7.

Application of this procedure for the surface crack data in this study indicates that the best form for the true trace length distribution is a gamma distribution. This distribution is represented as

$$f(\ell|\theta) = \frac{1}{\beta^\alpha \Gamma(\alpha)} \ell^{\alpha-1} e^{-\ell/\beta} \tag{3.5}$$

in which α and β are functions of the mean and the variance of the distribution, in this case $\langle\ell_\theta\rangle$ and $var(\ell_\theta)$.

$$\alpha = \frac{\langle\ell_\theta\rangle^2}{var(\ell_\theta)} \qquad \beta = \frac{var(\ell_\theta)}{\langle\ell_\theta\rangle} \tag{3.6}$$

$\Gamma(\alpha)$ is the gamma function and is defined as

$$\Gamma(\alpha) = \int_0^\infty y^{\alpha-1} e^{-y} dy \tag{3.7}$$

Gaussian quadrature with four integration points over the range of y from 0 to 50 is sufficient for the integration in Eq. (3.7). Also, four integration points over a length range of 0.0 to 0.006 in. are sufficient for integrating Eq. (3.1) and (3.4).

$f(\ell|\theta)$ and $f(\ell|\theta)_{ac}$ corresponding to the known apparent distributions, $f(\ell|\theta)_a$, for cement paste with a W/C = 0.5, are shown in Fig. 3.2. As expected, the estimated true trace length distributions are shifted to the

right with respect to the apparent distributions, showing that the effect of a finite height of the viewing area is to underestimate crack trace lengths.

3.3.2 True Trace Angle Distribution

The relationship (derived in Appendix C) between the true trace angle distribution, $f(\theta)$, and the apparent trace angle distribution is

$$f(\theta)_{ac} = \frac{(h + \langle \ell_\theta \rangle \sin\theta) f(\theta)}{h + \int_0^\pi \langle \ell_\theta \rangle \sin\theta \, f(\theta) d\theta} \tag{3.8}$$

in which $f(\theta)_{ac}$ is the calculated apparent distribution and $\langle \ell_\theta \rangle$ is the true mean trace length obtained in Eq. (3.3).

The known apparent trace angle distribution, $f(\theta)_a$, is computed from the surface crack data as

$$f(\theta)_a = \frac{n_\theta}{2N\Delta\theta} \tag{3.9}$$

in which n_θ is the number of cracks with angles of $\theta \pm \Delta\theta/2$, and N is the total number of cracks ($0° \leq \theta \leq 180°$). As before, trace angles of θ and $180°-\theta$ are grouped together. A typical known apparent distribution of crack trace angle is represented by the histogram in Fig. 3.3. As in the case of the trace length distributions in Fig. 3.2, the distribution in Fig. 3.3 is obtained from the longitudinal surface of cement paste (W/C = 0.5) loaded monotonically to a strain of 0.004.

In Eq. (3.8), the true trace angle distribution, $f(\theta)$, is the only unknown on the right side of the equation. An iterative procedure is used to estimate $f(\theta)$. The objective of the procedure is similar to that in the case of the trace length distribution. An apparent distribution is calculated based on an assumed expression for the true angle distribution. If a close match is obtained between the known and calculated apparent distributions, then the assumed expression for the true distribution is the correct estimate.

The procedure is outlined as follows:

1. Assume an expression for $f(\theta)$.
2. Compute $f(\theta)_{ac}$ using Eq. (3.8).

3. Use the "goodness of fit" test, based on the chi-square distribution to determine if there is close agreement between the known, $f(\theta)_a$, and calculated, $f(\theta)_{ac}$, apparent distributions.
4. Repeat Steps 1 to 3 until the "goodness of fit" test in Step 3 is successful. The true angle distribution which satisfies the test is the correct estimate of $f(\theta)$.

Fig. 3.3 shows that the known apparent trace angle distribution (the histogram) has spikes near 0° and 90°. As pointed out in Section 3.2, these spikes are due to specimen preparation. The form of the known apparent distribution suggests that constant functions should be assumed for $f(\theta)$ from 0° to 2.5° and from 87.5° to 90°, while a quadratic function may be assumed over the middle eighty-five degree range. This form of $f(\theta)$ gives a close match between $f(\theta)_{ac}$ and the histogram, as shown in Fig. 3.3.

3.3.3 True Number of Cracks per Unit Area

As explained in Section 3.1 and shown by the trace angle distributions in Fig. 3.3, the apparent number of cracks at low angles is less than the true number and the apparent number at high angles is greater than the true number. The apparent number of cracks per unit area, M_a, should, therefore, not be expected to equal the actual number of cracks per unit area, M.

The apparent number of cracks per unit area, M_a, is given by

$$M_a = \frac{N}{10 \times w \times h} \tag{3.10}$$

in which N is the number of cracks observed on a surface, and the denominator is the total area of surface observed. The expression (derived in Appendix C) for the true number of cracks per unit area is

$$M = \frac{N}{10w\left[h + \int_0^{\pi} \langle \ell_\theta \rangle \sin\theta \, f(\theta) d\theta\right]} \tag{3.11}$$

A comparison of Eq. (3.10) and (3.11) shows that $M_a > M$. Hence, the effect of the finite height of the viewing area is to overestimate the number of cracks per unit area.

For the cement paste specimens (W/C = 0.5) loaded to a strain of 0.004, M_a = 24568 per in.^{2} and M = 19813 per in.^{2}.

3.3.4 Modification of Mean Trace Length and Variance

As pointed out earlier, it is expected that the mean trace length and variance should be the same for all trace angles on transverse surfaces of uniaxially loaded specimens. Examples of the mean trace length, $\langle \ell_\theta \rangle$, and variance, $\text{var}(\ell_\theta)$, corresponding to the estimated true trace length distributions are illustrated in Fig. 3.4 and 3.5 for the transverse surface of cement paste (W/C = 0.5) loaded monotonically to a strain of 0.004. The curves shown are least squares fits through the data points. These examples are typical of the data obtained in this study.

Fig. 3.4 and 3.5 show that both the mean trace length and variance are not constant over the full range of trace angles. However, fairly uniform values are obtained for values of θ from 25° to 75°. It is assumed that these values of mean trace length and variance are not affected by specimen preparation, while the lower values of mean and variance for $\theta < 25°$ and the higher values for $\theta > 75°$ are the result of specimen preparation. The uniform values obtained from a least squares fit for θ from 25° to 75° are used for all θ ($0° \leq \theta \leq 90°$). These "modified" mean trace lengths and trace length variances, $\langle \ell \rangle_T$ and $\text{var} \langle \ell \rangle_T$, respectively, are illustrated in Fig. 3.6 and 3.7.

In the current analysis, it is further assumed that the effects of specimen preparation on the crack distributions for the transverse and longitudinal surfaces are the same. Hence, as for the transverse surface, the least squares fit for θ from 25° to 75° on the longitudinal surface is extrapolated to include all values of θ to obtain "modified" mean trace lengths and trace length variances $\langle \ell_\theta \rangle_L$ and $\text{var}(\ell_\theta)_L$. The linear variations with trace angle illustrated in Fig. 3.8 and 3.9 are typical of the results for longitudinal surfaces.

The modified experimental values of mean trace length and variance, obtained for all loading regimes and applied strains using the procedure described above, are given in Tables 3.1-3.6. These values, along with the form of the true trace length distributions obtained in Section 3.3.1 (the gamma distribution), completely describe the crack trace length distributions.

The trace length distributions on the transverse surface are denoted as $f(\ell)_T$, and those on the longitudinal surface are denoted as $f(\ell|\theta)_L$ for each trace angle, θ. The final trace length distribution for the transverse

surface of cement paste (W/C = 0.5) loaded monotonically to a strain of 0.004 is illustrated in Fig. 3.10.

The crack trace length distributions obtained above are used in the next section to estimate three-dimensional crack distributions in cement paste and mortar.

3.4 Estimates of Three-Dimensional Crack Distributions from Surface Crack Distributions

The procedure described here for obtaining estimates of three-dimensional crack distributions from surface crack distributions is an extended form of the procedure derived in Appendix D. The extension of the procedure in Appendix D is necessary in order to modify the trace angle distributions to reduce the effects of specimen preparation. These modified trace angle distributions are used in conjunction with the modified trace length distributions, calculated in the previous section, to obtain the three-dimensional distributions.

In the following presentation, the method for obtaining the modified trace angle distributions is described, the equations relating surface crack distributions to three-dimensional distributions are presented, and the overall procedure is outlined.

3.4.1 Modification of Trace Angle Distributions

The objective of this modification is to help remove the effects of specimen preparation from the trace angle distributions.

The method described in Section 3.3.2 is used to obtain true trace angle distributions on the transverse and longitudinal surfaces (as illustrated in Fig 3.3). Multiplication of the ordinates of the true trace angle distribution by the true number of cracks per unit area, M (obtained in Section 3.3.3), gives the variation of the true number of cracks per unit area per degree with trace angle. An example is shown in Fig. 3.11 for the transverse surface of cement paste (W/C = 0.5) loaded monotonically to a strain of 0.004. The figure shows spikes in the number of cracks over the ranges of θ from 0° to 2.5° and from 87.5° to 90°. These spikes are attributed to specimen preparation, as explained in Section 3.2.

Specimen preparation effects on the distribution in Fig. 3.11 can be reduced by removing the spikes and extrapolating the best fit (quadratic)

distribution in the middle eighty-five degree range to include all values of θ. The resulting distribution is shown by the solid curve in Fig. 3.12.

On the longitudinal surface, the spikes are also removed, and the middle eighty-five degree region of the distribution is also extrapolated to include all values of θ, as shown by the solid curve in Fig. 3.13. Like the transverse surface, the distribution on the longitudinal surface is also quadratic.

The distribution on the transverse surface (Fig. 3.12) is not uniform, as expected on the transverse surface of a uniaxially loaded specimen. This deviation from uniformity is considered to be another effect of specimen preparation. In order to reduce this specimen preparation effect, the quadratic distribution is replaced by a uniform distribution, shown by the dashed line in Fig. 3.12. The precise method for selecting this distribution is described in Section 3.4.3. The difference between the quadratic and uniform distributions gives an estimate of the number of cracks due to specimen preparation at each angle θ.

As stated in Section 3.3.4, the effects of specimen preparation are assumed to be the same on both the transverse and longitudinal surface crack distributions. This assumption implies that the number of specimen preparation cracks at a given angle θ is equal on the two surfaces. Therefore, once the uniform distribution is selected on the transverse surface, the distribution on the longitudinal surface (Fig. 3.13) is modified by an equal amount. If the assumed uniform distribution is lower than the measured distribution on the transverse surface, the difference is subtracted from the distribution on the longitudinal surface at the same angle θ. On the other hand, if the uniform distribution is larger than the measured distribution on the transverse surface, the difference is added to the distribution on the longitudinal surface. The modified trace angle distribution on the longitudinal surface is shown by the dashed line in Fig. 3.13. As indicated earlier, the distributions over the range of θ from 90° to 180° are identical to those in Fig. 3.12 and 3.13. Inherent in this procedures is the assumption that the trace length distributions, $f(\ell)_T$ and $f(\ell|\theta)_L$, need no further modification at this stage.

In order to obtain the correct estimates of the modified distributions on the transverse and longitudinal surfaces, the modification process

described above is tied to the iterative procedure used to estimate the three-dimensional crack distributions (Section 3.4.3).

The area under each of the distributions in Fig. 3.12 and 3.13, over the range $0° \leq \theta \leq 180°$, gives the number of cracks per unit area. The measured distributions for the transverse or longitudinal surfaces give the number of crack traces per unit area, $\bar{M}_T$ or $\bar{M}_L$, and include both load-induced cracks and specimen preparation cracks, not counting the preparation cracks removed when the spikes were excluded. The modified distribution for each surface gives an estimate of the number of cracks per unit area, M_T or M_L, which have had additional specimen preparation cracks removed.

Each ordinate of the modified distribution in Fig. 3.13, m_θ, is equal to the number of cracks per unit area per degree. The corresponding relative frequency distribution, $f(\theta)_L$ (Fig. 3.14), is obtained by dividing the ordinates of the modified distribution by the number of cracks per unit area, M_L.

$$f(\theta)_L = \frac{m_\theta}{M_L} \qquad (3.12a)$$
$$0° \leq \theta \leq 180°$$

Since transverse isotropy is expected for a uniaxially loaded specimen, the crack distributions should be symmetric with respect to the longitudinal or loading axis. It is therefore sufficient to consider $f(\theta)_L$ over the range $0° \leq \theta \leq 90°$. This requires that the right hand side of Eq. (3.12a) be multiplied by 2; i.e.,

$$f(\theta)_L = \frac{2m_\theta}{M_L} \qquad (3.12b)$$
$$0° \leq \theta \leq 90°$$

$f(\theta)_L$, defined over this condensed range, is used to estimate the three-dimensional crack distributions (Section 3.4.3).

3.4.2 Relationships between Surface and Three-Dimensional Crack Distributions

To derive relationships between surface and three-dimensional crack distributions (Appendix D), each crack is assumed to be elliptic with a

length of its major axis, 2a, aspect ratio, r, and angular coordinates ψ, ϕ and η (Fig. D.1). The length of the major semi-axis, a, is designated as the "characteristic crack size". Full descriptions of these parameters are provided in Appendix D.

The parameters which describe the three-dimensional crack distributions are the orientation distribution, $f(\psi)$, the size distribution, $f(a|\psi)$, at each orientation ψ, the mean and variance of $f(a|\psi)$, $\langle a_\psi \rangle$ and $\mathrm{var}(a_\psi)$, the crack aspect ratio, r, the rotation of the crack about its normal, defined by the angle η, and the number of cracks per unit volume, N_V.

For the crack distributions obtained in this study, the crack orientation distribution, $f(\psi)$, can be represented satisfactorily by a Marriott distribution [98]. This distribution describes the orientation of a transversely isotropic system of cracks with a mild degree of anisotropy. The Marriott distribution can be expressed as

$$f(\psi) = \frac{1}{1 - K/3} (1 + K \cos 2\psi) \sin \psi \qquad (3.13)$$

$$-1 \leq K \leq 1$$

The longitudinal direction (or direction of applied stress) corresponds to $\psi = 90°$. K is a measure of the degree of anisotropy. A negative value of K indicates a system in which more cracks are oriented in the longitudinal direction than in the transverse direction, while a positive value of K indicates a system in which more cracks are oriented in the transverse direction than in the longitudinal direction. K = 0 represents an isotropic distribution.

K can be obtained from the surface crack densities on the transverse and longitudinal surfaces as follows.

$$K = \frac{4\left[(M_L \langle \ell \rangle_L / M_T \langle \ell \rangle_T) - 1\right]}{2(M_L \langle \ell \rangle_L / M_T \langle \ell \rangle_T) - 1} \qquad (3.14)$$

in which $M_T \langle \ell \rangle_T$ and $M_L \langle \ell \rangle_L$ are the surface crack densities, i.e., total crack trace length per unit area, on the transverse and longitudinal surfaces, respectively. M_T and M_L are obtained from the experimental data as described in Section 3.4.1, while $\langle \ell \rangle_T$ is obtained as described in Section

3.3.4. $\langle \ell \rangle_L$, the mean trace length on the longitudinal surface over all trace angles, is computed as

$$\langle \ell \rangle_L = \int_0^{\pi/2} \langle \ell_\theta \rangle_L f(\theta)_L d\theta \tag{3.15}$$

in which $\langle \ell_\theta \rangle_L$ is the mean trace length for each trace angle on the longitudinal surface (See Section 3.3.4), and $f(\theta)_L$ is the trace angle distribution (Section 3.4.1).

Eq. (3.14) shows that an isotropic orientation distribution ($K = 0$) is indicated when the crack densities on the transverse and longitudinal surfaces are equal. An orientation distribution skewed towards the longitudinal direction ($K < 0$) is indicated when the crack density on the transverse surface is larger than that on the longitudinal surface, while a distribution skewed towards the transverse direction ($K > 0$) is indicated when the crack density on the transverse surface is lower than that on the longitudinal surface.

The following equations relate the crack trace angle and length distributions to the three-dimensional crack size and orientation distributions. These equations are used to establish the procedure for estimating the three-dimensional crack distributions. The equation (Appendix D) relating the trace angle distribution on the longitudinal surface to the three-dimensional distributions is

$$f(\theta)_{Lc} = \frac{\int_{-\eta'}^{\eta'} \int_0^{\pi} f(\psi(\theta,\phi)) \left|\frac{\partial \psi}{\partial \theta}\right| \langle s_{max} \rangle_{\psi(\theta,\phi)} \, d\phi d\eta}{\int_{-\eta'}^{\eta'} \int_0^{\pi} \int_0^{\pi/2} f(\psi) \langle s_{max} \rangle_{\psi} \, d\psi d\phi d\eta} \tag{3.16}$$

in which $f(\theta)_{Lc}$ is the calculated trace angle distribution on the longitudinal surface. $f(\psi)$ is the orientation distribution defined in Eq. (3.13). s is the distance between a crack centroid and a plane. s_{max} is the largest value of s for which the crack will intersect the plane. The expression relating θ, ψ and ϕ, as well as expressions for s_{max} and $\frac{\partial \psi}{\partial \theta}$, are given in Appendix D.

The trace length distribution on the longitudinal surface is related to the three-dimensional distributions as

$$f(\ell|\theta)_{Lc} = \frac{\int_{-\eta'}^{\eta'} \int_{0}^{\pi} \int_{a_{min}}^{\infty} f(a(\ell,\psi,\phi,\eta)|\psi(\theta,\phi))\, f(\psi(\theta,\phi))\, \left|\frac{\partial s}{\partial \ell}\right| \, da d\phi d\eta}{\int_{-\eta'}^{\eta'} \int_{0}^{\pi} \int_{0}^{\infty} f(a|\psi(\theta,\phi))\, f(\psi(\theta,\phi))\, s_{max}\, da d\phi d\eta} \tag{3.17}$$

in which $f(\ell|\theta)_{Lc}$ is the calculated trace length distribution on the longitudinal surface, and a_{min} is the smallest crack size that gives a trace length of ℓ on the plane. The expressions for a_{min}, s_{max} and $\frac{\partial s}{\partial \ell}$ are given in Appendix D.

The trace length distribution on the transverse surface is related to the three-dimensional distributions as

$$f(\ell)_{Tc} = \frac{\int_{-\eta'}^{\eta'} \int_{0}^{\pi/2} \int_{a_{min}}^{\infty} f(a(\ell,\psi,\eta)|\psi)\, f(\psi)\, \left|\frac{\partial s}{\partial \ell}\right| \, da d\psi d\eta}{\int_{-\eta'}^{\eta'} \int_{0}^{\pi/2} \int_{0}^{\infty} f(a|\psi)\, f(\psi)\, s_{max}\, da d\psi d\eta} \tag{3.18}$$

in which $f(\ell)_{Tc}$ is the calculated trace length distribution on the transverse surface. The expressions for a_{min}, s_{max} and $\frac{\partial s}{\partial \ell}$ are given in Appendix D.

The number of cracks per unit volume, N_V, is expressed as (Appendix D)

$$N_V = \frac{4}{3\pi^2 r \langle a^2 \rangle} \left(M_T \langle \ell \rangle_T + 2M_L \langle \ell \rangle_L\right) \tag{3.19}$$

in which $\langle a^2 \rangle$ is the mean squared value of the characteristic crack size over all orientations; i.e.

$$\langle a^2 \rangle = \int_{0}^{\infty} \int_{0}^{\pi/2} a^2 f(a|\psi) f(\psi) d\psi da \tag{3.20}$$

If the distributions $f(a|\psi)$ and $f(\psi)$ are known, Eq. (3.19) can be used to estimate the number of cracks per unit volume. The procedure for determining distributions $f(a|\psi)$ and $f(\psi)$ is described in the following section.

3.4.3 Procedure For Estimating the Three-Dimensional Distributions

An iterative procedure is used to estimate the three-dimensional crack parameters of the orientation distribution, $f(\psi)$, the size distribution, $f(a|\psi)$, the mean and variance of $f(a|\psi)$, $\langle a_\psi \rangle$ and $var(a_\psi)$, crack aspect ratio, r, and the range of the angle η. The procedure is set up in terms of

Eq. (3.13)-(3.18) and is based on minimizing the differences between the experimental trace distributions and the calculated trace distributions obtained using Eq. (3.16)-(3.18). The procedures is first summarized and then presented in detail.

The procedure begins by assuming a form for the crack size distribution, $f(a|\psi)$. Values of $\langle a_\psi \rangle$ and $var(a_\psi)$ are also assumed. A uniform distribution with respect to trace angle of the number of cracks per unit area per degree is assumed on the transverse surface. The experimental trace angle distribution for the longitudinal surface, $f(\theta)_L$, is then obtained as described in Section 3.4.1. The values of $M_T\langle \ell \rangle_T$ and $M_L\langle \ell \rangle_L$ are used in Eq. (3.14) to calculate the degree of anisotropy, K. The value of K enables the orientation distribution, $f(\psi)$, to be determined using Eq. (3.13). The calculated trace angle distribution on the longitudinal surface, $f(\theta)_{Lc}$, is obtained using Eq. (3.16).

The steps described above are repeated with different assumed uniform distributions on the transverse surface until the sum of the squared differences between the experimental, $f(\theta)_L$, and calculated, $f(\theta)_{Lc}$, trace angle distributions on the longitudinal surface is minimized; i.e. minimize

$$\sum_{\theta_i} [f(\theta_i)_L - f(\theta_i)_{Lc}]^2 \Delta\theta \qquad (3.21)$$

$\Delta\theta = 5°$; $\theta_i = 2.5°, 7.5°, 12.5°, \ldots\ldots, 87.5°$

The procedure then continues by determining the sum of the squared differences between the experimental, $f(\ell)_T$, and calculated, $f(\ell)_{Tc}$, trace length distributions for the transverse surface, as well as the sum of the squared differences between the experimental, $f(\ell|\theta)_L$, and calculated, $f(\ell|\theta)_{Lc}$, trace length distributions for the longitudinal surface. These sums are computed over the range of trace lengths, ℓ, from 0.0 to 0.006 in., since the trace length distributions virtually diminish to zero at a value of $\ell = 0.006$ (Fig. 3.2). For the transverse surface, the sum is

$$\sum_{\ell_i} [f(\ell_i)_T - f(\ell_i)_{Tc}]^2 \Delta\ell \qquad (3.22)$$

$\Delta\ell = 0.00015$ in.; $\ell_i = 0.000075, 0.000225, 0.000375, \ldots\ldots, 0.005925$ in.

and for the longitudinal surface, the sum is

$$\sum_{\theta} \left\{ \sum_{\ell_i} \left[f(\ell_i|\theta)_L - f(\ell_i|\theta)_{Lc} \right]^2 \Delta\ell \right\} \tag{3.23}$$

$\Delta\ell$ = 0.00015 in.; ℓ_i = 0.000075,0.000225,0.000375,.....,0.005925 in.

θ = 0°, 5°, 10°,....., 90°

The whole procedure may be repeated with different forms of $f(a|\psi)$ and with different values of $\langle a_\psi \rangle$ and $\text{var}(a_\psi)$ until the sums of the squared differences between the experimental and calculated trace length distributions on both surfaces are minimized. The three-dimensional crack parameters which enable the minimization process to attain a global minimum are the desired estimates.

The details of the procedure follow:

1. Assume a form for the crack size distribution, $f(a|\psi)$, such as a gamma distribution.
2. Assume expressions for $\langle a_\psi \rangle$ and $\text{var}(a_\psi)$ as functions of crack orientation.
3. Assume a value for the uniform distribution of the number of cracks per unit area per degree with respect to trace angle, θ, on the transverse surface, m_θ.
4. For each five-degree range, compute the difference in the areas under the uniform distribution assumed in Step 3 and the measured distribution of number of cracks per unit area per degree, $\bar{m}_\theta$, on the transverse surface. This difference is expressed as

$$(m_\theta - \bar{m}_\theta) \times 5° \tag{3.24}$$

5. Modify the distribution of number of cracks per unit area per degree with respect to trace angle on the longitudinal surface by algebraically adding to it the differences obtained in step 4.
6. Compute the degree of anisotropy, K, using Eq. (3.14), and determine the orientation distribution, $f(\psi)$ [Eq. (3.13)].
7. By varying the crack aspect ratio, r, compute the trace angle distribution on the longitudinal surface, $f(\theta)_{Lc}$, using Eq. (3.16), with η uniformly distributed over the range $-90° \leq \eta \leq 90°$. Determine the r which minimizes the sum of the squared differences between the experimental, $f(\theta)_L$, and calculated, $f(\theta)_{Lc}$, trace angle distributions

[Eq. (3.21)]. Reduce the range of η and again determine r which minimizes Eq. (3.21). Continue this process until Eq. (3.21) cannot be minimized further.

8. Repeat Steps 3-7 until the values computed using Eq. (3.21) reach a global minimum. The values of $f(\psi)$ and r, and the range of η for which Eq. (3.21) is fully minimized, are the estimates to be used in the following steps.
9. Use Eq. (3.18) to compute the trace length distribution on the transverse surface, $f(\ell)_{Tc}$. An improved estimate of the variance of $f(a|\psi)$ is obtained by assuming trial values for $var(a_\psi)$ until the sum of the squared differences between the experimental, $f(\ell)_T$, and calculated, $f(\ell)_{Tc}$, trace length distributions is minimized [Eq. (3.22)].
10. Compute the trace length distribution on the longitudinal surface, $f(\ell|\theta)_{Lc}$, using Eq. (3.17). Calculate the sum of the squared differences between the experimental, $f(\ell|\theta)_L$, and calculated, $f(\ell|\theta)_{Lc}$, trace length distributions [Eq. (3.23)].
11. Return to Step 2 and repeat the process until the values computed from Eq. (3.23) reach a global minimum. The parameters $\langle a_\psi \rangle$, $var(a_\psi)$, r, and the range of η which produce this global minimum are the best estimates for the three-dimensional crack distributions based on the form of $f(a|\psi)$ assumed in Step 1.
12. The iterative process may be restarted at Step 1 by assuming a different form for $f(a|\psi)$. The form of $f(a|\psi)$, the values of K, $\langle a_\psi \rangle$, $var(a_\psi)$ and r, and the range of η which minimize Eq. (3.23) are the desired estimates.

In the current study, the optimum solution for all loading regimes and applied strains yielded a value of $\eta = 0°$. This means that the cracks are predominantly oriented with the plane defined by the major axis of the crack and the crack normal parallel to the longitudinal (or loading) axis and perpendicular to the transverse plane. The best form of the crack size distribution, $f(a|\psi)$, turns out to be a gamma distribution. This is the same form of distribution obtained for the trace length distribution (Section 3.3.1). The size distribution is represented as

$$f(a|\psi) = \frac{1}{\beta^\alpha \, \Gamma(\alpha)} \, a^{\alpha-1} \, e^{-a/\beta} \qquad (3.25)$$

$$\text{in which } \alpha = \frac{\langle a_\psi \rangle^2}{\text{var}(a_\psi)}; \qquad \beta = \frac{\text{var}(a_\psi)}{\langle a_\psi \rangle} \tag{3.26}$$

Γ is defined in Eq. (3.7).

As illustrated in Fig. 3.15-3.17 for cement paste (W/C = 0.5) loaded monotonically to a strain of 0.004, the final calculated surface distributions closely match the modified experimental surface distributions. The deviations that do exist between the calculated and experimental distributions may be due to a number of causes. Primary among these is the rather bold assumption that the cracks are elliptic. In addition, all sources of the specimen preparation cracks are not known and therefore cannot be dealt with at this stage in the analysis. It should be noted that $f(\theta)_L$ used for comparison in Step 7 [Eq. (3.21)] is itself a product of the iteration scheme.

The calculated three-dimensional crack orientation and size distributions for a nonloaded specimen and for a specimen loaded to a strain of 0.004 are illustrated in Fig. 3.18 and 3.19. Fig. 3.18 shows that the orientation distribution for the loaded specimen is skewed more towards the direction of applied stress ($\psi = 90°$) than the corresponding distribution for the nonloaded specimen. Fig. 3.19 shows that the mean crack size in the loaded material is larger than that in the nonloaded material.

The final distributions obtained in Steps 4 and 5 of the iteration scheme produce the values of the modified numbers of cracks per unit area on the transverse and longitudinal surfaces, M_T and M_L, as well as the number of specimen preparation cracks, not counting those removed when the spikes were excluded, $\bar{M}_T$-M_T or $\bar{M}_L$-M_L. These are summarized along with the values of $\bar{M}_T$ and $\bar{M}_L$ in Tables 3.7-3.12. The final surface crack densities, $M_T\langle \ell \rangle_T$ and $M_L\langle \ell \rangle_L$, are given in Tables 3.13-3.16. The calculated three-dimensional crack parameters for nonloaded specimens and for all loading regimes and applied strains are presented in Tables 3.17-3.23. An additional parameter, $N_V\langle a^3 \rangle$, which is a measure of the volume density of the cracks, is added. $N_V\langle a^3 \rangle$ plays an important role in controlling material behavior, as will be shown in Chapters 4 and 5.

The data presented in Tables 3.7-3.23 are discussed for each loading regime in Section 3.5.

Effect of Averaging Surface Crack Data: As stated earlier, the average surface crack data for all specimens loaded to a specified strain are used to obtain the surface and three-dimensional crack parameters for each loading regime.. It is of interest to compare the results obtained using the average data with the extremes obtained in the tests. Monotonically loaded cement paste with a W/C = 0.5 is used for the comparison. To establish lower and upper bounds of the number of cracks per unit area on the transverse and longitudinal surfaces, M_T or M_L, and of the three-dimensional crack size parameters, $\langle a_\psi \rangle$ and $var(a_\psi)$, the surface crack data for individual specimens were analyzed. The results are presented in Tables 3.24 and 3.25. The values of the number of cracks per unit area, $\bar{M}_T$ and $\bar{M}_L$, are also given in Table 3.24. The values of M_T, M_L, $\langle a_\psi \rangle$, and $var(a_\psi)$ given in Tables 3.8 and 3.19 based on the average surface crack data are within 0.5% of the results in Tables 3.24 and 3.25. This indicates that the average data for all specimens are representative of the data for the individual specimens.

The upper bounds for the number of cracks per unit area before modification ($\bar{M}_T$ or $\bar{M}_L$) are about 6% to 8% larger than the lower bounds (Table 3.24). However, the upper bounds for the modified number of cracks per unit area (M_T or M_L) are only about 0.8% larger than the lower bounds. For specimens with the same strain, it is likely that the difference between the lower and upper bounds for $\bar{M}_T$ (or $\bar{M}_L$) is due to specimen preparation. Thus, the closeness of the lower and upper bounds for M_T and M_L suggests that the procedure for estimating M_T and M_L does a good job of removing specimen preparation cracks.

Multi-directional Crack Trace: In order for a multi-direction-al crack trace (Fig. 3.20) to be recorded as a single uni-directional crack, the differences in trace angle between the individual segments of the crack trace were required to be no bigger than the increment of angle measurement, $\Delta\theta/2 = \pm 2.5°$. Segments of a multi-directional crack trace which did not satisfy this requirement were recorded as separate crack traces. Thus, the recorded crack traces have a smaller mean length than would have been obtained if the total length of a multi-directional crack trace had been recorded as a single quantity, or if a multi-directional crack trace had been recorded as a single uni-directional crack.

This point is of some concern since in Chapter 4 it will be shown that, while material response depends on the number of cracks per unit volume, N_V, it depends on the average of the cube of the characteristic crack size, $\langle a^3 \rangle$. An overestimate of the number of surface cracks and corresponding underestimate of surface crack trace length will result in an overestimate of N_V and underestimate of $\langle a^3 \rangle$, which will substantially underestimate the effect of the cracks.

To rectify this problem, two specimens were studied to obtain a correlation between the multi-directional crack traces and the individual segments. For the current analysis a multi-directional crack trace must be represented as a single uni-directional trace since the surface to three-dimensional conversion procedure used in this study is based on linear surface cracks. The equivalent uni-directional crack trace is obtained by connecting the far ends of the attached segments (Fig. 3.20).

Based on the information obtained from the two specimens, it is estimated that if all multi-directional crack traces had been recorded as single cracks, the number of cracks per unit area would have been reduced by about 23% and the mean trace length would have been increased by about 30%. The variance of the trace lengths based on the large cracks is about 1% larger than the variance based on the small cracks.

To obtain an estimate of the crack parameters based on the larger, combined crack traces, the mean trace lengths and variances given in Tables 3.1-3.6 are increased by 30% and 1%, respectively, and the numbers of cracks per unit area, $\overline{M}_T$ and $\overline{M}_L$, given in Tables 3.7-3.12 are decreased by 23%. The surface to three-dimensional conversion procedure outlined above is then used to obtain estimates of $\langle a_\psi \rangle$ which are larger than those given in Tables 3.17-3.23. The estimates of $\langle a_\psi \rangle$, $\text{var}(a_\psi)$, N_V and $N_V\langle a^3 \rangle$ are presented in Tables 3.26-3.32. The effect of this conversion is substantial on the value of the key parameter $N_V\langle a^3 \rangle$, with increases ranging from 31% for mortar (W/C = 0.5) at a strain of 0.004 under monotonic loading to 44% for cement paste (W/C = 0.3) at a strain of 0.003 under cyclic loading. The estimates of K and r are unchanged from those given in Tables 3.17-3.23.

Unless stated otherwise, the discussions of three-dimensional crack parameters in the next section are based on the results which correspond to the larger estimate of $\langle a_\psi \rangle$.

3.5 Discussion of Results

In this section, the surface and three-dimensional crack parameters for cement paste and mortar are discussed for nonloaded specimens and for specimens under each loading regime. Crack densities and crack distributions are compared for specimens with different water-cement ratios and load regimes. For each loading regime, the implications of the results are discussed based on the three-dimensional crack parameters.

3.5.1 Nonloaded Specimens

Surface crack density, $M_T\langle \ell \rangle_T$ or $M_L\langle \ell \rangle_L$ (Table 3.13), as well as "volumetric crack density", $N_V\langle a^3 \rangle$ (Tables 3.17 and 3.26), vary inversely with water-cement ratio for nonloaded cement paste specimens, as shown in Fig. 3.21 and 3.22, respectively. Three reasons may be offered to explain these relationships: (1) The higher the water-cement ratio, the greater will be the degree of hydration at a given age. Therefore, upon drying, the higher water-cement ratio paste may undergo less differential volume change at the local level. (2) The more porous nature, and thus higher compliance, of the higher water-cement ratio paste may allow the material to deform with less cracking during the drying process. (3) A portion of the cracking may be due to self-desiccation, which will be higher for a lower water-cement ratio.

The existence of internal drying cracks in cement paste and mortar raises an interesting point about the significance of drying shrinkage measurements. Drying shrinkage measurements are carried out as external length measurements, and shrinkage values have been used as evidence in support of contrasting models of the hydration of portland cement paste [18,84]. If cracks form within the material, the external length change will be reduced, compared to the case without any cracks, by the total projected crack width in the direction of measurement. Also, the larger the crack density, the lower will be the externally measured shrinkage. Results in this study show that both crack density (Tables 2.12, 2.16 and Fig. 2.52) and crack width (Tables 2.30-2.32) vary with the method of specimen drying. Thus, shrinkage will be partly determined by the material and partly by the method used in drying the specimen. Drying shrinkage is, therefore, not a material property, but rather a composite or apparent property, and as such

may not be of much significance in proving or disproving any particular model of the hydration of cement paste.

Bazant, et al. [5,6,7] have shown analytically that due to differential drying rates between the exterior and interior of cement paste and concrete specimens, discontinuous random cracks, as well as a system of parallel drying cracks, form in the specimens. In this study, nearly uniform distributions of crack density with respect to trace angle have been obtained for the nonloaded specimens, as shown in Fig. 2.53 and 2.55. These observed crack distributions seem to support the formation of random drying cracks due to differential drying rates between the exterior and interior of the specimens, as proposed by Bazant, et al. However, some portion of the cracking can be due to differences in the properties of CH and CSH components in the hydrated cement paste. Since CH does not change volume during the drying process, and also has a higher stiffness than CSH [8,48], CH can act as a rigid inclusion surrounded by a shrinking matrix. The restraining effect of the CH can induce tensile stresses which are relaxed by the formation of cracks. This suggests that some cracking will occur, independent of the drying rate. An analytical study by Kawamura [48] supports this conclusion.

3.5.2 Monotonic Loading

For this loading regime, specimens were loaded to selected strains at a constant strain rate and then immediately unloaded. Typical stress-strain curves are shown in Fig. 2.3-2.6.

3.5.2.1 Surface Crack Density

The crack densities on the transverse and longitudinal surfaces of cement paste and mortar increase with applied compressive strain (Table 3.14). Fig. 3.23 and 3.24 show crack density on the transverse surface as a function of applied compressive strain for cement pastes with W/C = 0.7, 0.5 and 0.3. In Fig. 3.23, the linear least squares fits through the data points show that the average increase of surface crack density with strain is virtually the same for all the three cement pastes. However, if the data points are connected with straight lines, as shown in Fig. 3.24, it is observed that above a strain of 0.004, surface crack density increases more

rapidly in cement paste with a W/C = 0.3 than in pastes with W/C = 0.7 and 0.5.

Fig. 3.25 shows the transverse surface crack density - strain relationships for cement paste and mortar with a W/C = 0.5. The figure shows that surface crack density for nonloaded mortar specimens is lower than for nonloaded paste specimens. With applied compressive strain, however, the increase in surface crack density is more rapid in mortar than in cement paste. Beginning at a strain of about 0.002, the surface crack density in mortar exceeds the value for paste.

Specimen Preparation Cracks: The estimated number of specimen preparation cracks, not counting those removed when the spikes were excluded (Section 3.4.1), $\bar{M}_T - M_T$ or $\bar{M}_L - M_L$ (Tables 3.7-3.10), decreases with increasing applied strain. This relationship is illustrated in Fig. 3.26 for cement paste with a W/C = 0.5. The decrease in specimen preparation cracks with increasing strain implies that load-induced cracks relieve stresses due to specimen preparation, and that the greater the density of load-induced cracks the greater the relief.

3.5.2.2 Three-Dimensional Crack Parameters

The relationships between the mean characteristic crack size, $\langle a_\psi \rangle$, and strain, and between the coefficient of variation, $[\mathrm{var}(a_\psi)]^{1/2}/\langle a_\psi \rangle$, and strain are illustrated in Fig. 3.27 and 3.28 for cement paste with a W/C = 0.5. Crack orientations of 0°, 45° and 90° are used in these figures. The lines shown are least squares fits through the data points. Fig. 3.27 shows that $\langle a_\psi \rangle$ increases with increasing strain and with increasing orientation angle, ψ (Tables 3.18-3.21 and 3.27-3.30). The increase of $\langle a_\psi \rangle$ with increasing ψ indicates that the cracks are larger the more their orientation is skewed towards the direction of applied stress. The coefficients of variation are approximately constant, implying that crack sizes have the same spread relative to their means for all applied strains and crack orientations.

For nonloaded cement paste and mortar with a W/C = 0.5, the degree of anisotropy, K, is 0.00, while for nonloaded cement pastes with W/C = 0.7 and 0.3, the value of K is -0.02 (Table 3.17). As pointed out in Section 3.4.2, a value of K = 0 indicates an isotropic orientation distribution. The value of K = -0.02 for the pastes with W/C = 0.7 and 0.3 gives an orientation

distribution, $f(\psi)$, that is different from the distribution for K = 0 by less than 1%. This indicates that the orientation distributions in all the nonloaded materials are virtually isotropic.

The magnitude of K increases with increasing strain under monotonic loading (Tables 3.18-3.21), indicating that the crack distribution becomes skewed towards the direction of applied stress as strain increases. For cement paste with a W/C = 0.5, values of K range from 0.00 for nonloaded specimens to -0.30 for specimens at an applied strain of 0.006, while for paste with W/C = 0.7 and 0.3, they range from -0.02 for nonloaded specimens to -0.29 and -0.31 for specimens at an applied strain of 0.006. For mortar with a W/C = 0.5, the range of K is 0.00 for nonloaded specimens to -0.24 for specimens loaded to a strain of 0.004.

At low strains, the crack aspect ratio, r, is 1.0; i.e. the cracks are circular (Tables 3.18-3.21). At high applied strains, the cracks become elliptic (i.e. $r < 1.0$). At an applied strain of 0.006, the values of r are 0.90, 0.87 and 0.85 for cement pastes with W/C = 0.7, 0.5 and 0.3, respectively. At an applied strain of 0.004 in mortar with a W/C = 0.5, the value of r is 0.90. These results imply that each crack has a slightly preferred direction of propagation (or characteristic direction) in its plane. Since $\eta = 0°$ for all load cases (Section 3.4.2), that direction is parallel to the direction of loading.

The number of cracks per unit volume, N_V, decreases with increasing applied strain (Tables 3.18-3.21 and 3.27-3.30, Fig. 3.29). For example, for paste with a W/C = 0.5, N_V decreases from a value of 2.3×10^6 in.$^{-3}$ in nonloaded specimens to a value of 0.7×10^6 in.$^{-3}$ in specimens loaded to a strain of 0.006. For mortar with a W/C = 0.5, N_V decreases from a value of 1.5×10^6 in.$^{-3}$ in nonloaded specimens to a value of 0.6×10^6 in.$^{-3}$ in specimens loaded to a strain of 0.004. While the number of cracks per unit volume decreases with increasing applied strain (Fig. 3.29), the mean crack size increases (Fig. 3.27). The two results suggest that as the applied strain increases, small cracks join into a smaller number of larger cracks.

The variation of the volume density of cracks, $N_V\langle a^3\rangle$, with applied strain is shown in Fig. 3.30 and 3.31 for cement pastes with W/C = 0.7, 0.5 and 0.3. Both figures show that $N_V\langle a^3\rangle$ increases with increasing strain, suggesting that the paste materials are damaged progressively during loading. The linear least squares fits in Fig. 3.30, like the surface crack

density (Fig. 3.23), show that the average increase in $N_V\langle a^3\rangle$ with strain is virtually the same for all the three cement pastes. Fig. 3.31, in which the data points are connected with straight lines, shows that below a strain of 0.004, $N_V\langle a^3\rangle$ increases more rapidly the higher the water-cement ratio. Above a strain of 0.004 $N_V\langle a^3\rangle$, the trend is reversed, and $N_V\langle a^3\rangle$ increases most rapidly for cement paste with a W/C = 0.3. The larger rate of increase of volumetric crack density, $N_V\langle a^3\rangle$, at high strains in cement paste with a W/C = 0.3 may explain the lower strain capacity of this material when compared to pastes with higher water-cement ratios (Fig. 2.7).

Fig. 3.32 compares the relationships between $N_V\langle a^3\rangle$ and strain for cement paste and mortar with a W/C = 0.5. The value of $N_V\langle a^3\rangle$ for nonloaded mortar is lower than that for nonloaded cement paste. This reflects the lower percentage of paste in the cross-section of mortar and the restraint of shrinkage exerted by the sand grains. $N_V\langle a^3\rangle$ increases more rapidly in mortar than in cement paste. Under load, the sand appears to act as a stress raiser, resulting in a larger value of volumetric crack density and a lower strain capacity for mortar as compared to cement paste.

3.5.3 Sustained Loading

Under this loading regime, load was maintained at a specified stress level for four hours. Stress levels were selected in order to obtain specific strains. A typical stress-strain curve is shown in Fig. 2.14.

3.5.3.1 Surface Crack Density

For sustained loading of cement past, surface crack density increases with increasing applied strain, on both the transverse and longitudinal surfaces (Table 3.15). Crack density on the transverse surface versus strain is shown in Fig. 3.33 for cement pastes with W/C = 0.5 and 0.3. Surface crack density is larger and increases more rapidly in paste with a W/C = 0.3 than in paste with a W/C = 0.5.

The surface crack densities are compared at the same strain for monotonic and sustained loading regimes in Fig. 3.34. The figure shows that for loading to a fixed strain, surface crack density is larger under monotonic loading than under sustained loading.

3.5.3.2 Three-Dimensional Crack Parameters

The mean characteristic crack size, $\langle a_\psi \rangle$, increases with increases in strain and crack orientation under sustained loading (Tables 3.22 and 3.31). This relationship is illustrated in Fig. 3.35 for cement paste with a W/C = 0.5, and for crack orientations of 0°, 45° and 90°. Like the crack distributions for monotonic loading, the crack distributions for sustained loading are skewed more towards the direction of applied stress the higher the applied strain, as indicated by the increase in the magnitude of the degree of anisotropy, K, with an increase in strain (Table 3.22). For example, for cement paste with a W/C = 0.5 loaded to strains of 0.004 and 0.006, the values of K are -0.17 and -0.24, respectively. The crack distributions under sustained loading, however, are less skewed towards the direction of applied stress than the distributions under monotonic loading for which the corresponding values are -0.27 for a strain of 0.004 and -0.30 for a strain of 0.006.

The higher the strain under sustained loading, the smaller the number of cracks per unit volume, N_V (Fig. 3.36 and Table 3.31). The increase in $\langle a_\psi \rangle$ (Fig. 3.35) and the decrease in N_V (Fig. 3.36) with increase in strain suggest that small cracks join to form a smaller number of larger cracks in cement paste at higher applied strains, as occurs under monotonic loading.

The volume density of cracks, $N_V\langle a^3 \rangle$, at each strain (Table 3.31) is shown in Fig. 3.37 for the cement pastes. $N_V\langle a^3 \rangle$ is larger and increases more rapidly in paste with a W/C = 0.3 than in paste with a W/C = 0.5. This result is similar to that obtained for the surface crack density (Fig. 3.33). The greater value of $N_V\langle a^3 \rangle$ in the lower water-cement ratio paste is somewhat more extreme than the results obtained at high applied strains under monotonic loading (Fig. 3.31).

Fig. 3.38 shows that for the same applied strain, the volumetric crack density, $N_V\langle a^3 \rangle$, under monotonic loading ranges from 1.02 to 1.46 times $N_V\langle a^3 \rangle$ under sustained loading. The values of $N_V\langle a^3 \rangle$ are closer for paste with a W/C = 0.3 than for paste with W/C = 0.5. This result indicates that deformation mechanisms other than cracking play a role, and that under sustained loading at a lower stress, these mechanisms can reduce the amount of cracking. At higher strain rates, cracking would be expected to play an increasingly important role.

Fig. 3.39 compares $N_V\langle a^3\rangle$ for sustained loading to that for monotonic loading at the same stress-strength ratio. The data shown in this figure for monotonic loading is obtained by determining the strain which corresponds to a given stress-strength ratio, and then estimating the value of $N_V\langle a^3\rangle$ from the least squares fit shown in Fig. 3.30. Fig. 3.39 shows that $N_V\langle a^3\rangle$ is larger under sustained loading than under monotonic loading. This indicates the effect of the duration of loading. Under sustained loading, formation of new cracks and/or propagation of existing cracks may occur, resulting in a higher volumetric crack density for sustained loading as compared to monotonic loading at the same stress-strength ratio.

3.5.4 Cyclic Loading

This loading regime consisted of subjecting specimens to cyclic loading between stress levels of zero and a specified value until selected strains were reached. A typical stress-strain curve is shown in Fig. 2.19.

3.5.4.1 Surface Crack Density

Surface crack density is larger the higher the strain under cyclic loading (Fig. 3.40 and Table 3.16). Surface crack density increases more rapidly in cement paste with a W/C = 0.3 than in paste with a W/C = 0.5. This result is similar to results obtained for monotonic and sustained loading regimes.

Surface crack densities for monotonic and cyclic loading are compared at the same strain in Fig. 3.41. The figure shows that surface crack density is larger for cyclic loading than for monotonic loading.

3.5.4.2 Three-Dimensional Crack Parameters

For cyclic loading, as for monotonic and sustained loading, the mean characteristic crack size, $\langle a_\psi\rangle$, increases with increasing strain and crack orientation (Tables 3.23 and 3.32). This relationship is illustrated in Fig. 3.42 for cement paste with a W/C = 0.5, and for crack orientations of 0°, 45° and 90°.

The magnitude of the degree of anisotropy, K (Table 3.23), also increases with increasing strain, indicating that the crack distribution is skewed more towards the direction of applied stress the higher the strain under cyclic loading. For example, for cement paste with a W/C = 0.5 loaded

to strains of 0.002 and 0.004, the values of K are -0.14 and -0.20, respectively, are somewhat less than the corresponding values under monotonic loading of -0.16 and -0.27. As with the crack distributions obtained under sustained loading, the crack distributions under cyclic loading are less skewed towards the direction of applied stress than the distributions under monotonic loading.

The number of cracks per unit volume, N_V, decreases with increase in strain (Fig. 3.43 and Table 3.32). As in the case of monotonic and sustained loading regimes, the increase in $\langle a_\psi \rangle$ (Fig. 3.42) and the decrease in N_V (Fig. 3.43) with increase in strain suggest that a smaller number of larger cracks form at the higher applied strain.

The volumetric crack density, $N_V\langle a^3 \rangle$, increases with increased strain under cyclic loading (Fig. 3.44). Again, in the case of monotonic loading at high strains and sustained loading, $N_V\langle a^3 \rangle$ increases more rapidly in cement paste with a W/C = 0.3 than in paste with a W/C = 0.5. Fig. 3.45 shows that for loading to a fixed strain, $N_V\langle a^3 \rangle$ is larger under cyclic loading than under monotonic loading. Under cyclic loading, the repetitive nature of loading may cause new cracks to form and/or existing cracks to propagate in each cycle, resulting in a larger volumetric crack density for cyclic loading as compared to monotonic loading. This occurs even though a lower stress level is used for cyclic loading to attain the same strain. The increasing density of cracks with cyclic loading may explain the observed reduction in strength obtained for cyclically loaded cement past specimens upon reloading [22].

3.5.5 Expected Effects of Submicrocracking on Material Stiffness

In this section, the data of surface crack densities, $M_T\langle \ell \rangle_T$ and $M_L\langle \ell \rangle_L$, volumetric crack density, $N_V\langle a^3 \rangle$, and degree of anisotropy, K, which have been discussed in earlier sections are summarized in order to point out the expected effects of submicrocracking on material stiffness under different loading regimes. The data for monotonic loading of cement pastes with W/C = 0.7, 0.5 and 0.3 are compared in Table 3.33, while those for monotonic loading of cement paste and mortar with a W/C = 0.5 are compared in Table 3.34. The data for sustained and cyclic loading regimes are compared to those for monotonic loading in Tables 3.35 and 3.36, respectively.

Under monotonic loading, the surface crack densities of the three cement pastes are within 10% of each other at each strain (Table 3.33). The volumetric crack densities are also within 10% of each other. Linear least squares fits shown in Fig. 3.30 indicate that the increase of volumetric crack density with increasing strain is approximately the same for the three cement pastes. The crack orientation distributions for the cement pastes, $f(\psi)$, represented by the degrees of anisotropy, K, differ by less than 2% for most strains. The small differences in crack distributions indicated by these results, suggest that the degree of softening caused by submicrocracking under monotonic loading should be approximately the same for the cement pastes.

Above a strain of 0.001, both the surface and volumetric crack densities are larger in mortar than in cement paste (Table 3.34). The larger densities in mortar are associated with crack distributions which are less skewed towards the direction of applied stress than crack distributions in cement paste, as indicated by the degrees of anisotropy. The less skewed a crack distribution is towards the direction of applied stress, the larger is its effect on the stiffness modulus in that direction. Therefore, the degree of softening caused by submicrocracking under monotonic loading should be larger for mortar than for cement paste.

The surface and volumetric crack densities at each strain are larger for monotonic loading than for sustained loading (Table 3.35), suggesting a larger effect of cracks on the stiffness modulus under monotonic loading than under sustained loading. However, as indicated by the degrees of anisotropy, the crack distributions for sustained loading are less skewed towards the direction of applied stress than the distributions for monotonic loading, indicating a larger effect of cracks on stiffness modulus under sustained loading than under monotonic loading. Thus, the effect of the cracks on material stiffness under monotonic loading should be smaller than suggested by the values of volumetric crack density alone, while the effect on stiffness under sustained loading should be larger than suggested by the values of volumetric crack density alone.

The surface and volumetric crack densities at each strain are larger for cyclic loading than for monotonic loading (Table 3.36). The degrees of anisotropy indicate that the crack distributions are less skewed towards the direction of applied stress for cyclic loading than for monotonic loading.

These results suggest that the degree of softening caused by submicrocracking should be larger under cyclic loading than under monotonic loading.

In Chapter 5, the three-dimensional crack distributions discussed in this chapter are used in a material model to determine the effects of the cracks on the elastic moduli of cement paste and mortar. The material model is developed in the next chapter.

3.6 Summary of findings

The results discussed above can be summarized as follows. The term "crack density" refers to both the surface and volumetric crack densities.

1. The variations in crack density and crack width with the method of specimen drying suggest that drying shrinkage in cement paste is not a material property, but rather a property of the total cement paste composite.
2. Under monotonic loading, crack density increases more rapidly in mortar than in cement paste.
3. At high strains under uniaxial compressive loading, crack density seems to increase more rapidly in a low water-cement ratio paste (W/C = 0.3) than in higher water-cement ratio pastes (W/C = 0.7, 0.5).
4. For loading to a fixed strain, crack density in cement paste is larger under monotonic loading than under sustained loading, while at the stress-strength ratios investigated, crack density is larger under sustained loading than under monotonic loading.
5. For the same applied strain, crack density in cement paste under cyclic loading is larger than under monotonic loading.
6. Under uniaxial compressive loading, the mean size of submicroscopic cracks increases with increasing strain, while the number of cracks per unit volume decreases.
7. Under monotonic loading, the three-dimensional crack distributions in cement paste show only small variations with water-cement ratio; the volumetric crack densities are within 10% of each other and the orientation distributions are virtually the same.
8. Under uniaxial compressive loading, three-dimensional distributions of submicroscopic cracks become skewed towards the direction of applied stress as strain increases.

9. Under monotonic loading, the crack distributions in mortar are less skewed towards the direction of applied stress than the crack distributions in cement paste.
10. The crack distributions under sustained and cyclic loading of cement paste are less skewed towards the direction of applied stress than the crack distributions under monotonic loading.

CHAPTER 4

SELF-CONSISTENT MODEL FOR A TRANSVERSELY ISOTROPIC CRACKED SOLID

4.1 Introduction

A model based on the self-consistent method is developed to estimate the effective elastic moduli of a transversely isotropic solid containing many cracks. Such a solid has one axis of elastic symmetry.

The self-consistent method has been employed by various investigators [12,13,14,30,33,34,35,38,40,43,50,52,53,67] to estimate the elastic moduli of composite materials. The method accounts for inclusion interactions by estimating the actual behavior of an inclusion in the composite body as that of a single inclusion in an equivalent homogeneous body. There are two equivalent approaches for deriving the self-consistent equations. One approach, by Hill [35], involves the direct averaging of the components of stress and strain in the constituent phases of the solid. Average stress is related to average strain in the solid through the effective elastic moduli. The other approach, by Budiansky [12], involves the computation of the change in strain energy of the solid due to each representative inclusion. The change in strain energy is summed over all inclusions, and the result is set equal to the energy change produced by modification of the elastic moduli of the solid. Explicit formulations of the self-consistent method in the case of cracked solids have been obtained by Budiansky and O'Connell [14,67], Hoenig [38], and Horii and Nemat-Nasser [40].

Budiansky and O'Connell use the energy approach to estimate the elastic moduli of an isotropic cracked body permeated by many randomly distributed cracks. Hoenig considers non-randomly distributed cracks and employs Hill's approach to derive the self-consistent equations. He illustrates the results of his formulation with two examples. In each of the two examples, the cracked solid is transversely isotropic. The cracks are assumed to have a single orientation with respect to the plane of isotropy. Budiansky and O'Connell, and Hoenig, neglect the effects of crack closure in their studies. Horii and Nemat-Nasser assume a random crack distribution and use the self-consistent method to determine the effective moduli of a cracked solid when some cracks close, and when closed cracks undergo frictional sliding.

In this study, Budiansky's energy approach is used to formulate the self-consistent equations for a cracked transversely isotropic solid containing non-randomly distributed cracks. Crack closure effects are neglected. The cracks are assumed to be elliptic with known size and orientation distributions, and crack centroids are assumed to be randomly distributed throughout the solid. Both dry and saturated cracks are considered. The uncracked material is assumed to be locally isotropic and homogeneous. The cracks modify the material properties, and anisotropic distributions of crack size and orientation cause the cracked solid to become transversely isotropic. For opaque solids, procedures are established in Appendix D to estimate the three-dimensional crack distributions from crack trace distributions obtained on the exterior of the solid.

The results of the self-consistent formulations obtained in this study, are checked against those of Budiansky and O'Connell [14,67] and Hoenig [38]. Further, results are presented for a transversely isotropic cracked solid using assumed anisotropic crack distributions in which all orientations are represented. Results are also presented to show the sensitivity of the model to variations in three-dimensional crack parameters.

4.2 Overview of the Model

In the following presentation of the self-consistent model, the crack and global coordinate systems are defined. Stresses are applied to the cracked solid and the self-consistent equation is formulated for each applied stress. The energy change of the body-load system due to a single crack is expressed in terms of energy release rates for crack extension in an anisotropic material. The change in strain energy of the cracked solid due to all cracks is then obtained. Each of the self-consistent equations is expressed in a form which is appropriate for determining the effective moduli of solids containing either dry or saturated cracks.

The self-consistent equations are nonlinear in the unknown effective moduli. An iterative solution procedure is used. The solution process is stopped when the computed moduli converge.

4.3 Crack and Global Coordinate Systems

In the self-consistent method, the material properties are required for the directions associated with the individual crack orientations. The crack

and material coordinate systems are defined in Fig. 4.1. The figure shows an elliptic crack and a rectangular cartesian coordinate system in the principal material directions, with the 1-2 plane being the plane of isotropy. The 3-axis is the longitudinal axis of the cracked body, and it is also the axis of elastic symmetry. ψ is the orientation of the crack with respect to the plane of isotropy. The elliptic crack has a major semi-axis length of a and a minor semi-axis length of b. The length of the major semi-axis, a, is designated as the "characteristic crack size". In general, the characteristic crack size is a function of ψ; i.e. $a = a(\psi) = a_{\psi}$. The aspect ratio of the crack, r, is defined as the ratio b/a, and in this analysis, its value is assumed to be the same for all cracks. The aspect ratio varies between 0 and 1. A value of 1 indicates a circular crack. ϕ is the angle that the projection of the normal to the crack on a plane of isotropy, makes with the principal 1-direction. ϕ varies in a full circle about the axis of elastic symmetry. The angle η defines the degree of rotation of the crack about its normal. For $\eta = 0$, the plane defined by the major axis of the crack and the crack normal is parallel to the longitudinal axis and perpendicular to the transverse plane, while $\eta = \pi/2$ when the major axis is parallel to the transverse plane. For a circular crack, η is not defined since every axis of the crack is a major axis. The local reference frame of the crack is represented by the x, y and z axes. The x-y and y-z planes are normal to the crack plane, while the x-z plane is parallel to the crack plane. The crack displacements in the x, y and z directions are u, v and w, respectively.

In reference to the global coordinate system in Fig. 4.1, the strain-stress relations for a transversely isotropic material are

$$\begin{Bmatrix} \varepsilon_1 \\ \varepsilon_2 \\ \varepsilon_3 \\ \gamma_{12} \\ \gamma_{23} \\ \gamma_{31} \end{Bmatrix} = \begin{bmatrix} \frac{1}{E_1} & -\frac{\nu_{12}}{E_1} & -\frac{\nu_{31}}{E_3} & 0 & 0 & 0 \\ & \frac{1}{E_1} & -\frac{\nu_{31}}{E_3} & 0 & 0 & 0 \\ & & \frac{1}{E_3} & 0 & 0 & 0 \\ & & & \frac{1}{G_{12}} & 0 & 0 \\ & & & & \frac{1}{G_{31}} & 0 \\ \text{(symmetrical)} & & & & & \frac{1}{G_{31}} \end{bmatrix} \begin{Bmatrix} \sigma_1 \\ \sigma_2 \\ \sigma_3 \\ \tau_{12} \\ \tau_{23} \\ \tau_{31} \end{Bmatrix} \qquad (4.1)$$

in which E_1 and E_3 are stiffness moduli, ν_{12} and ν_{31} are Poisson's ratios, and G_{12} and G_{31} are shear moduli. The material is described by five independent elastic constants. These independent constants may be taken as E_1, E_3, ν_{12}, ν_{31} and G_{31}. ν_{ij} is Poisson's ratio which characterizes the strain in the j direction produced by stress in the i direction. G_{12} is dependent upon E_1 and ν_{12} through the relation

$$G_{12} = \frac{E_1}{2(1 + \nu_{12})} \tag{4.2}$$

4.4 Self-Consistent Scheme

The approach used in the self-consistent method to estimate the effective elastic moduli of a transversely isotropic cracked solid, follows that used by Budiansky and O'Connell [14,67] to determine the effective moduli of an isotropic cracked body. The change in strain energy due to each crack is computed based on the elastic moduli as modified by the full crack distribution. The strain energy change is summed over all cracks and the result is set equal to the energy change of the solid produced by the modification of the moduli.

If Φ is the strain energy of the uncracked solid under a prescribed loading and Φ_c is the corresponding quantity for the cracked body,

$$\Phi_c = \Phi + \Delta\Phi \tag{4.3}$$

in which $\Delta\Phi$ is the strain energy change due to the presence of cracks. The effective elastic constants are determined by using various load cases to obtain estimates for $\Delta\Phi$. For each load case, the self-consistent approximation is achieved by assuming that each crack contributes to $\Delta\Phi$ as if it were an isolated crack in an infinite matrix having the as yet unknown elastic moduli of the cracked solid.

In order to determine the five independent elastic constants of a transversely isotropic solid in which cracks are distributed at all orientations ($0° \leq \psi \leq 90°$), five load cases are needed. For example, the stiffness modulus in the plane of isotropy, E_1, is determined by applying a normal stress in the global 1-direction. The load cases are shown in Fig. 4.2. s is an applied normal stress and v is an applied shear stress.

By writing the strain energy for each load case, five different equations are generated using Eq. (4.3). The elastic moduli of the uncracked material are E, G and ν; V is the material volume. For each load case, the self-consistent equation and the resolved stresses, σ and τ, which are normal and tangential to the plane of the crack, are obtained. In the equations for the resolved stresses, τ_1 and τ_2 are perpendicular components of τ. τ_1 acts along a line defined by the intersection of the crack plane and a plane defined by the crack normal and the longitudinal axis. τ_2 acts within the crack plane and is perpendicular to τ_1.

Load case 1: E_1

$$\frac{s^2V}{2E_1} = \frac{s^2V}{2E} + \Delta\Phi_1 \tag{4.4}$$

$$\begin{aligned}\sigma &= s\cos^2\phi\sin^2\psi \\ \tau_1 &= s\cos^2\phi\sin\psi\cos\psi \\ \tau_2 &= s\sin\phi\cos\phi\end{aligned} \tag{4.5}$$

Load Case 2: E_3

$$\frac{s^2V}{2E_3} = \frac{s^2V}{2E} + \Delta\Phi_2 \tag{4.6}$$

$$\begin{aligned}\sigma &= s\cos^2\psi \\ \tau &= s\sin\psi\cos\psi\end{aligned} \tag{4.7}$$

Load case 3: ν_{12}

$$\frac{s^2V}{E_1}(1 - \nu_{12}) = \frac{s^2V}{E}(1 - \nu) + \Delta\Phi_3 \tag{4.8}$$

$$\begin{aligned}\sigma &= s\sin^2\psi \\ \tau &= s\sin\psi\cos\psi\end{aligned} \tag{4.9}$$

Load case 4: ν_{31}

$$\frac{s^2V}{2E_3}\left(1 - 2\nu_{31} + \frac{E_3}{E_1}\right) = \frac{s^2V}{E}(1 - \nu) + \Delta\Phi_4 \tag{4.10}$$

$$\sigma = s\,(\cos^2\phi\sin^2\psi+\cos^2\psi)$$
$$\tau_1 = s\,\sin^2\phi\sin\psi\cos\psi \qquad (4.11)$$
$$\tau_2 = s\,\sin\phi\cos\phi$$

Load case 5: G_{31}

$$\frac{v^2V}{2G_{31}} = \frac{v^2V}{2G} + \Delta\Phi_5 \qquad (4.12)$$

$$\sigma = 2\,v\,(\cos^2\phi-\sin^2\phi)\sin\psi\cos\psi$$
$$\tau = v\,(\cos^2\phi-\sin^2\phi)(\cos^2\psi-\sin^2\psi) \qquad (4.13)$$

For each load case, the energy change due to the cracks, $\Delta\Phi_i$, depends on the five independent elastic moduli of the cracked solid, and it is obtained by determining the energy change associated with a single crack. The energy change is affected by the presence of fluid in the crack. Both dry and saturated cracks are considered.

4.4.1 Dry Cracks

Budiansky and O'Connell [14] have shown that the energy change associated with a dry crack of arbitrary shape is given by

$$\xi = \frac{1}{3}\oint_{crack} \rho(J_1 + J_2 + J_3)dp \qquad (4.14)$$

in which J_1, J_2 and J_3 are the energy release rates associated with the three modes of crack deformation. These three modes are the opening mode (Mode I), the forward shear mode (Mode II), and the out-of-plane shear or tearing mode (Mode III) [73,81,102]. The expressions for the energy release rates for crack extension in an anisotropic material are given in a subsequent section. ρ is the perpendicular distance from the crack centroid to a point on the crack perimeter, and p is a distance measured along the crack perimeter (Fig. 4.3). The integration is carried out over the crack perimeter. For an elliptic crack [14,37],

$$\rho dp = abd\beta \qquad (4.15)$$

in which a and b are the lengths of the major and minor semi-axes, respectively. The angle β defines a point on the perimeter of the crack. For a crack aspect ratio b/a = r, the energy change associated with an elliptic crack is obtained from Eq. (4.14) as

$$\xi = \frac{4ra^2}{3}\int_0^{\pi/2}(J_1 + J_2 + J_3)d\beta \tag{4.16}$$

In the special case of an isotropic cracked solid, Budiansky and O'Connell [14] obtained the energy change due to an elliptic crack to be

$$\xi = \frac{4\pi r^2 a^3}{3E(k)}\left(\frac{1-\bar{\nu}^2}{E}\right)\{\sigma^2 + \tau^2[R(k,\bar{\nu})\cos^2\eta + Q(k,\bar{\nu})\sin^2\eta]\} \tag{4.17a}$$

in which

$$R(k,\bar{\nu}) = k^2E(k)[(k^2-\bar{\nu})E(k) + \bar{\nu}(1-k^2)K(k)]^{-1}$$

$$Q(k,\bar{\nu}) = k^2E(k)\{[k^2+\bar{\nu}(1-k^2)]E(k) - \bar{\nu}(1-k^2)K(k)\}^{-1} \tag{4.17b}$$

K(k) and E(k) are, respectively, the complete elliptic integrals of the first and second kind with argument $k = (1-r^2)^{1/2}$.

$$K(k) = \int_0^{\pi/2}(1 - k^2\sin^2\beta)^{-1/2}d\beta$$

$$E(k) = \int_0^{\pi/2}(1 - k^2\sin^2\beta)^{1/2}d\beta \tag{4.17c}$$

The expressions for the energy change due to the cracks, $\Delta\Phi_i$, which are required in the self-consistent equations, are obtained as follows.

Define a crack energy parameter, $W_i(a,\psi)$, as

$$W_i(a,\psi) = \frac{\xi}{P_i^2} \tag{4.18}$$

in which a and ψ are, respectively, the characteristic size and the orientation of the crack, ξ is the energy change associated with the crack, and P_i is the applied stress acting on the cracked solid; for load cases 1 through 4, P_i = s, and for load case 5, P_i = v, (see Fig. 4.2). Substituting Eq. (4.16) into (4.18),

$$W_i(a,\psi) = \frac{4ra^2}{3P_i^2}\int_o^{\pi/2}(J_1 + J_2 + J_3)d\beta \qquad (4.19)$$

$i = 1,..,5.$

The expressions for the energy release rates which are given in a subsequent section, show that J_1, J_2 and J_3 are proportional to P_i^2. Hence, the evaluation of Eq. (4.19) does not require a knowledge of the magnitude of the applied stress.

For load cases 1, 4 and 5, $W_i(a,\psi)$ is a function of the angle ϕ as indicated by the resolved stresses [see Eq. (4.5), (4.11) and (4.13)]. $W_i(a,\psi)$ must be averaged over all values of ϕ for each of these load cases.

The change in strain energy of the cracked solid due to all cracks within the volume is

$$\Delta\Phi_i = \Sigma\xi = P_i^2\,\Sigma W_i(a,\psi) \qquad (4.20)$$

in which the summation is over all cracks. The final forms of the self-consistent equations are now obtained.

Substituting Eq. (4.20) into Eq. (4.4), the self-consistent equation for the first load case is

$$\frac{V}{2E_1} = \frac{V}{2E} + \Sigma W_1(a,\psi) \qquad (4.21)$$

If N_V is the number of cracks per unit volume and $\langle W_1\rangle$ denotes the mean value of $W_1(a,\psi)$ over all crack sizes and orientations, then

$$\Sigma W_1(a,\psi) = N_V\, V\, \langle W_1\rangle \qquad (4.22)$$

Eq. (4.21) becomes

$$\frac{1}{2E_1} = \frac{1}{2E} + N_V\,\langle W_1\rangle \qquad (4.23)$$

$\langle W_1\rangle$ is expressed as

$$\langle W_1\rangle = \int_o^{\pi/2}\int_o^{\infty} W_1(a,\psi)f(a,\psi)da d\psi \qquad (4.24a)$$

or

$$\langle W_1 \rangle = \int_0^{\pi/2}\int_0^{\infty} W_1(a,\psi) f(a|\psi) f(\psi) da d\psi \qquad (4.24b)$$

$$0 < a < \infty$$

$$0 \leq \psi \leq \pi/2$$

in which $f(a|\psi)$ and $f(\psi)$ are, respectively, the size and orientation distributions of the cracks. Substitution of Eq. (4.24b) into Eq. (4.23) gives

$$\frac{1}{2E_1} = \frac{1}{2E} + N_V \int_0^{\pi/2}\int_0^{\infty} W_1(a,\psi) f(a|\psi) f(\psi) da d\psi \qquad (4.25)$$

Multiplying Eq. (4.25) through by $2E_1$ and rearranging, the self-consistent equation for the first load case is

$$E_1 = E \,/\, \left[1 + 2 N_V E \int_0^{\pi/2}\int_0^{\infty} W_1(a,\psi) f(a|\psi) f(\psi) da d\psi\right] \qquad (4.26)$$

Similarly, the formulations for load cases two through five are

$$E_3 = E \,/\, \left[1 + 2 N_V E \int_0^{\pi/2}\int_0^{\infty} W_2(a,\psi) f(a|\psi) f(\psi) da d\psi\right] \qquad (4.27)$$

$$\nu_{12} = 1 - E_1 \left[\frac{(1-\nu)}{E} + N_V \int_0^{\pi/2}\int_0^{\infty} W_3(a,\psi) f(a|\psi) f(\psi) da d\psi\right] \qquad (4.28)$$

$$\nu_{31} = \frac{1}{2} - E_3 \left[\frac{(1-\nu)}{E} - \frac{1}{2E_1} + N_V \int_0^{\pi/2}\int_0^{\infty} W_4(a,\psi) f(a|\psi) f(\psi) da d\psi\right] \qquad (4.29)$$

$$G_{31} = G \,/\, \left[1 + 2 N_V G \int_0^{\pi/2}\int_0^{\infty} W_5(a,\psi) f(a|\psi) f(\psi) da d\psi\right] \qquad (4.30)$$

Eq. (4.26)-(4.30) are nonlinear equations which can be solved for E_1, E_3, ν_{12}, ν_{31}, and G_{31} using an iterative scheme. The solution procedure is described in section 4.6.

4.4.2 Saturated Cracks

The derivations for a transversely isotropic solid with saturated cracks follow the procedure used by Budiansky and O'Connell [14,67] for an isotropic solid. The self-consistent equations are the same as for a body containing dry cracks [Eq. (4.26)-(4.30)]. Only the crack energy parameter for each load case, $W_i(a,\psi)$, needs to be modified.

If the cracks are filled with a fluid of bulk modulus K_f, the calculation of the change in strain energy due to the presence of the cracks must take into account the elastic energy of the fluid as well as the effect of the fluid on the elastic state of the surrounding material. As noted by Budiansky and O'Connell, a basic assumption in the calculations that follow is that the fluid in each crack is considered to be isolated. Hence, the effective moduli obtained here are only appropriate for stress changes that occur with sufficient rapidity so as to prevent communication of fluid pressure between cracks.

Due to the applied load, the fluid within the cracks will acquire a hydrostatic stress, σ_f. σ_f affects the normal mode (Mode I) deformation of the crack. Other modes are not affected since the fluid cannot carry shear stress. Hence, the energy release rates for Modes II and III deformations, J_2 and J_3, are the same as in the case of dry cracks.

Following Eq. (4.16), the increase in energy of the surrounding body-load system due to the hydrostatic pressure within the cracks is

$$\Delta\xi = \frac{4ra^2}{3}\int_0^{\pi/2} J_1' \, d\beta \tag{4.31}$$

in which J_1' is the energy release rate due to the hydrostatic stress, σ_f. The expression for J_1' is given in the next section.

The energy change associated with a saturated crack is obtained by subtracting the increase in energy of the body-load system due to the presence of the fluid from the energy change for the dry-crack case. Subtracting Eq. (4.31) from Eq. (4.16), the energy change due to a saturated elliptic crack is

$$\xi = \frac{4ra^2}{3}\int_0^{\pi/2}(J_1 + J_2 + J_3 - J_1')d\beta \tag{4.32}$$

Defining the crack energy parameter, $W_i(a,\psi)$, as in section 4.4.1,

$$W_i(a,\psi) = \frac{4ra^2}{3P_i^2}\int_0^{\pi/2}(J_1 + J_2 + J_3 - J_1')d\beta \tag{4.33}$$

$i = 1,..,5$

In the special case of an isotropic cracked solid, the energy change due to a saturated elliptic crack is [5]

$$\xi = \frac{4\pi r^2 a^3}{3E(k)}\left(\frac{1-\bar{\nu}^2}{E}\right)\{\tau^2[R(k,\bar{\nu})\cos^2\eta + Q(k,\bar{\nu})\sin^2\eta]\} \tag{4.34}$$

$R(k,\bar{\nu})$, $Q(k,\bar{\nu})$, and $E(k)$ are defined in Eq. (4.17b) and (4.17c).

The evaluation of Eq. (4.33) requires that J_1' be expressed as a function of P_i. This can be accomplished by expressing the hydrostatic stress, σ_f, in terms of σ, the normal stress acting on the crack surface due to the applied stress P_i. σ_f is expressed in terms of σ as follows.

The work done by the hydrostatic stress applied slowly to the crack surface is

$$\sigma_f^2 \, v_c/2K_m \tag{4.35}$$

in which v_c is the volume of the crack and K_m is the bulk modulus of the cracked material. The work done by σ_f is equal to the increase in energy of the body-load system. Thus equating (4.31) and (4.35),

$$\frac{\sigma_f^2 \, v_c}{2K_m} = \frac{4ra^2}{3}\int_0^{\pi/2} J_1' \, d\beta \tag{4.36}$$

Since v_c and K_m are, in general, dependent upon the size and the orientation of the cracks, the ratio v_c/K_m in Eq. (4.36) can be represented as $W_f(a,\psi)$. Eq. (4.36) is rearranged to become

$$W_f(a,\psi) = \frac{8ra^2}{3\sigma_f^2}\int_0^{\pi/2} J_1' \, d\beta \tag{4.37}$$

As in the case of Eq. (4.19), the evaluation of Eq. (4.37) does not require a knowledge of the magnitude of the hydrostatic stress, since J_1' is proportional to σ_f^2. The volume change of the crack is

$$(\sigma - \sigma_f)v_c/K_m \tag{4.38a}$$

or

$$(\sigma - \sigma_f)W_f(a,\psi) \tag{4.38b}$$

The volume change of the fluid is

$$\sigma_f v_c / K_f \tag{4.39}$$

The crack-volume change must be equal to the volume change of the fluid. Therefore, equating (4.38b) and (4.39) and rearranging, the desired relationship between σ_f and σ is obtained.

$$\sigma_f = \frac{W_f(a,\psi)}{v_c/K_f + W_f(a,\psi)}\,\sigma \tag{4.40}$$

If the crack opening is extremely small such that $W_f(a,\psi) >> v_c/K_f$, Eq. (4.40) yields $\sigma_f \approx \sigma$. Therefore in this case, $W_f(a,\psi)$ need not be determined.

As in the case of bodies containing dry cracks, the effective elastic moduli of bodies containing saturated cracks are calculated using Eq. (4.26)-(4.30). Here, the crack energy parameter, $W_i(a,\psi)$, is computed using Eq. (4.33).

4.5 Energy Release Rates

In this section, expressions are given for the energy release rates J_1, J_1', J_2 and J_3, which are required for the calculation of the crack energy parameters, $W_i(a,\psi)$ [Eq. (4.20) and (4.34)].

The energy release rates for crack extension in an anisotropic material have been derived by Sih, Paris and Irwin [81]. In the presence of all the three modes of crack deformation, the energy release rates, J_i, are

$$J_1 = -\frac{K_I}{2}\, c'_{33}\, \mathrm{Im}\left[\frac{K_I(\mu_1+\mu_2) + K_{II}}{\mu_1\mu_2}\right]$$

$$J_2 = \frac{K_{II}}{2}\, c'_{11}\, \mathrm{Im}\left[K_{II}(\mu_1+\mu_2) + K_I\mu_1\mu_2\right] \tag{4.41}$$

$$J_3 = \frac{K_{III}^2}{2}\,\frac{\mathrm{Im}\,(d_{45} + \mu_3 d_{55})}{d_{44}d_{55}}$$

in which μ_1, μ_2 and μ_3 are complex functions of c'_{ij} (i, j = 1,3,6) and d'_{ij} (i, j = 4,5), which are respectively elements of the constitutive compliance

and stiffness matrices in crack coordinates. Im denotes the imaginary part of the expression in brackets. K_I, K_{II} and K_{III} are the stress-intensity factors for Modes I, II and III, respectively. Stress-intensity factors characterize stresses at crack tips [37,39,46,47,73,80,81]. Expressions are given in the next section for determining these factors for elliptic cracks in an anisotropic material. μ_1, μ_2 and μ_3 are determined as follows.

For Modes I and II crack deformations, the equilibrium and compatibility equations of anisotropic elasticity [11,55,81] can be represented in terms of Airy's stress function, U, as

$$c'_{33}\frac{\partial^4 U}{\partial x^4} - 2c'_{36}\frac{\partial^4 U}{\partial x^3 \partial y} + (2c'_{13}+c'_{66})\frac{\partial^4 U}{\partial x^2 \partial y^2} - 2c'_{16}\frac{\partial^4 U}{\partial x \partial y^3} + c'_{11}\frac{\partial^4 U}{\partial y^4} = 0 \tag{4.42}$$

The solution of Eq. (4.42) for an anisotropic material containing a crack is obtained in terms of two analytic functions of two complex variables [11,81,102]. The complex variables are defined as

$$z_1 = x + \mu_1 y \ , \qquad z_2 = x + \mu_2 y \tag{4.43}$$

In Eq. (4.43), μ_1 and μ_2 are the roots (with positive imaginary parts) of the characteristic equation of (4.42). The characteristic equation of a differential equation is the algebraic equation obtained by replacing the differential operation with a variable [91]. The characteristic equation of Eq. (4.42) is

$$c'_{11}\mu^4 - 2c'_{16}\mu^3 + (2c'_{13} + c'_{66})\mu^2 - 2c'_{36}\mu + c'_{33} = 0 \tag{4.44}$$

The four roots of Eq. (4.44) are always complex or purely imaginary and occur in conjugate pairs [10,55,81]. The roots with positive imaginary parts, μ_1 and μ_2, can be written in the form

$$\begin{aligned} \mu_1 &= \alpha_1 + i\beta_1 \\ \mu_2 &= \alpha_2 + i\beta_2 \end{aligned} \tag{4.45}$$

in which α_j, β_j (j = 1,2) are real constants.

The elastic displacements associated with the tearing (Mode III) deformation of the crack are such that u = v = 0, w = w(x,y) [81]. Sih, et al. [81] have shown that the displacement w satisfies the following equation.

$$d'_{44}\frac{\partial^2 w}{\partial x^2} + 2d'_{45}\frac{\partial^2 w}{\partial x \partial y} + d'_{55}\frac{\partial^2 w}{\partial y^2} = 0 \tag{4.46}$$

The characteristic equation of (4.46) is

$$d'_{55}\mu^2 + 2d'_{45}\mu + d'_{44} = 0 \tag{4.47}$$

The two roots of Eq. (4.47) are complex conjugates [10,55,81]. The root with a positive imaginary part can be expressed as

$$\mu_3 = \alpha_3 + i\beta_3 \tag{4.48}$$

in which α_3 and β_3 are real constants.

Substitution of Eq. (4.45) and (4.48) into Eq. (4.41), gives the energy release rates as

$$J_1 = \frac{K_I\, c'_{33}}{2[(\alpha_1\alpha_2-\beta_1\beta_2)^2 + (\alpha_1\beta_2+\alpha_2\beta_1)^2]}[K_I(\alpha_1+\alpha_2)(\alpha_1\beta_2+\alpha_2\beta_1) - K_I(\beta_1+\beta_2)(\alpha_1\alpha_2-\beta_1\beta_2) + K_{II}(\alpha_1\beta_2+\alpha_2\beta_1)]$$

$$J_2 = \frac{K_{II}}{2}\, c'_{11}[K_{II}(\beta_1+\beta_2) + K_I(\alpha_1\beta_2+\alpha_2\beta_1)] \tag{4.49}$$

$$J_3 = \frac{K_{III}^2}{2}\frac{\beta_3}{d'_{44}}$$

For a dry crack, the expressions for the energy release rates are substituted into Eq. (4.20) in order to calculate $W_i(a,\psi)$, the crack energy parameter for each load case. For a saturated crack, the hydrostatic stress affects only the normal mode deformation of the crack. Therefore, the energy release rate due to the hydrostatic stress, J'_1, is a function only of

the stress-intensity factor corresponding to Mode I deformation, K_I. Hence, from the expression given in Eq. (4.49) for J_1,

$$J_1' = \frac{K_I^2}{2} c_{33}' \left[\frac{(\alpha_1+\alpha_2)(\alpha_1\beta_2+\alpha_2\beta_1) - (\beta_1+\beta_2)(\alpha_1\alpha_2-\beta_1\beta_2)}{(\alpha_1\alpha_2-\beta_1\beta_2)^2 + (\alpha_1\beta_2+\alpha_2\beta_1)^2} \right] \tag{4.50}$$

In the case of saturated cracks, therefore, Eq. (4.49) and (4.50) are substituted into Eq. (4.33) in order to calculate the crack energy parameter.

c_{ij}' (i, j = 1,3,6) and d_{ij}' (i, j = 4,5) which are required in Eq. (4.44) and (4.47) in order to determine μ_1, μ_2 and μ_3 (hence α_1, α_2 and α_3), are obtained as follows. If [C'] is the compliance matrix in crack coordinates, the two-dimensional strain-stress relations for plane deformations (Modes I and II) of the crack are

$$\begin{Bmatrix} \varepsilon_x \\ \varepsilon_y \\ \gamma_{xy} \end{Bmatrix} = \begin{bmatrix} c_{11}' & c_{13}' & c_{16}' \\ & c_{33}' & c_{36}' \\ (\text{sym}) & & c_{66}' \end{bmatrix} \begin{Bmatrix} \sigma_x \\ \sigma_y \\ \tau_{xy} \end{Bmatrix} \tag{4.51}$$

In global coordinates, the two-dimensional compliance matrix for the transversely isotropic material is

$$[\,C\,] = \begin{bmatrix} c_{11} & c_{13} & c_{16} \\ & c_{33} & c_{36} \\ (\text{sym}) & & c_{66} \end{bmatrix} = \begin{bmatrix} \frac{1}{E_1} & -\frac{\nu_{31}}{E_3} & 0 \\ & \frac{1}{E_3} & 0 \\ (\text{sym}) & & \frac{1}{G_{31}} \end{bmatrix} \tag{4.52}$$

The relationship between [C'] and [C] is

$$[\,C'\,] = [\,T_\varepsilon\,]\,[\,C\,]\,[\,T_\varepsilon\,]^T \tag{4.53}$$

in which $[T_\varepsilon]$ is the transformation matrix for strains and $[T_\varepsilon]^T$ is its transpose.

$$[\,T_\varepsilon\,] = \begin{bmatrix} \cos^2\psi & \sin^2\psi & \cos\psi\sin\psi \\ \sin^2\psi & \cos^2\psi & -\cos\psi\sin\psi \\ -2\cos\psi\sin\psi & 2\cos\psi\sin\psi & \cos^2\psi-\sin^2\psi \end{bmatrix} \tag{4.54}$$

Eq. (4.52) and (4.54) are substituted into Eq. (4.53) to obtain the elements of $[C']$.

$$c'_{11} = \frac{1}{E_1}\cos^4\psi + (\frac{1}{G_{31}} - \frac{2\nu_{31}}{E_3})\sin^2\psi\cos^2\psi + \frac{1}{E_3}\sin^4\psi$$

$$c'_{13} = -\frac{\nu_{31}}{E_3}(\sin^4\psi+\cos^4\psi) + (\frac{1}{E_1} + \frac{1}{E_3} - \frac{1}{G_{31}})\sin^2\psi\cos^2\psi$$

$$c'_{16} = 2\sin\psi\cos\psi\,[\frac{1}{E_3}\sin^2\psi - \frac{1}{E_1}\cos^2\psi + (\frac{\nu_{31}}{E_3} - \frac{1}{2G_{31}})(\sin^2\psi-\cos^2\psi)]$$

$$c'_{33} = \frac{1}{E_1}\sin^4\psi + \frac{1}{E_3}\cos^4\psi - (\frac{2\nu_{31}}{E_3} - \frac{1}{G_{31}})\sin^2\psi\cos^2\psi \qquad (4.55)$$

$$c'_{36} = 2\sin\psi\cos\psi\,[\frac{1}{E_3}\cos^2\psi - \frac{1}{E_1}\sin^2\psi - (\frac{\nu_{31}}{E_3} - \frac{1}{2G_{31}})(\sin^2\psi-\cos^2\psi)]$$

$$c'_{66} = 2(\frac{2}{E_1} + \frac{2}{E_3} + \frac{4\nu_{31}}{E_3} - \frac{1}{G_{31}})\sin^2\psi\cos^2\psi + \frac{1}{G_{31}}(\sin^4\psi+\cos^4\psi)$$

If $[D']$ is the stiffness matrix in crack coordinates, the stress-strain relations for Mode III crack deformation are

$$\begin{Bmatrix}\tau_{xz}\\ \tau_{yz}\end{Bmatrix} = \begin{bmatrix}d'_{44} & d'_{45}\\ d'_{45} & d'_{55}\end{bmatrix}\begin{Bmatrix}\gamma_{xz}\\ \gamma_{yz}\end{Bmatrix} \qquad (4.56)$$

In global coordinates, the corresponding stiffness matrix is

$$[\ D\ ] = \begin{bmatrix} d_{44} & d_{45} \\ d_{45} & d_{55} \end{bmatrix} = \begin{bmatrix} G_{12} & 0 \\ 0 & G_{31} \end{bmatrix} \tag{4.57}$$

The relationship between $[D']$ and $[D]$ is

$$[\ D'\ ] = [\ T_\sigma\ ]\ [\ D\ ]\ [\ T_\sigma\ ]^T \tag{4.58}$$

in which $[T_\sigma]$ is the transformation matrix for stresses and $[T_\sigma]^T$ is its transpose.

$$[\ T_\sigma\ ] = \begin{bmatrix} \cos\psi & \sin\psi \\ -\sin\psi & \cos\psi \end{bmatrix} \tag{4.59}$$

Eq. (4.57) and (4.59) are substituted into Eq. (4.58) to obtain the elements of $[D']$.

$$\begin{aligned} d'_{44} &= G_{31}\sin^2\psi + G_{12}\cos^2\psi \\ d'_{45} &= (G_{31} - G_{12})\cos\psi\sin\psi \\ d'_{55} &= G_{31}\cos^2\psi + G_{12}\sin^2\psi \end{aligned} \tag{4.60}$$

4.5.1 Stress-Intensity Factors

The stress-intensity factors required in the energy release rate expressions are given in this section.

Hoenig [37,39] derived the stress-intensity factors for an elliptic crack in an anisotropic body. His results are in conflict with earlier expressions developed by Kassir and Sih [47] for the stress-intensity factors for an elliptic crack in a transversely isotropic body. In his discussion, Hoenig [37] shows that the factors derived by Kassir and Sih are in error.

For a point on the perimeter of the crack whose location is defined by the angle β (Fig. 4.3), the stress-intensity factors are given by [37]

$$k_i = -(\pi a)^{1/2} Q_{ij} R_{jk} C^{-1}_{k\ell} \sigma^{\infty}_{\ell} \tag{4.61}$$

in which Q_{ij}, R_{jk} and $C_{k\ell}$ are tensors of second order, following standard summation notation ($i,j,k,\ell = 1,2,3$). a is the characteristic crack size. K_I is obtained by setting $i = 2$, K_{II} is obtained by setting $i = 1$, and K_{III}, by setting $i = 3$. σ^{∞}_{ℓ} represents the resolved stress acting either normal or tangential to the crack plane (see Fig. 4.2 and 4.4). $\ell = 1$ for a resolved stress acting parallel to the major axis of the crack, $\ell = 2$ for a resolved stress acting parallel to the minor axis, and $\ell = 3$ for a resolved stress acting normal to the crack plane. K_I corresponds to a stress acting normal to the crack plane. Therefore, $\sigma^{\infty}_3 = \sigma$ (see Fig. 4.2 and 4.4) for the computation of K_I. K_{II} corresponds to a shear stress acting parallel to the major axis of the crack, while K_{III} corresponds to a shear stress acting parallel to the minor axis. Hence, the component of the resolved stress in the direction of the major axis is used for computing K_{II}, while the component in the direction of the minor axis is used for computing K_{III}. For example, in Fig. 4.4, $\sigma^{\infty}_1 = \tau \cos\eta$ for the computation of K_{II}, and $\sigma^{\infty}_2 = \tau \sin\eta$ for the computation of K_{III}.

Expansion of Eq. (4.61) in accordance with the range and summation conventions of tensor notation [93], yields the complete expressions for K_I, K_{II} and K_{III}.

$$\begin{aligned}
K_I &= -(\pi a)^{1/2} \sigma^{\infty}_3 [Q_{21} R_{11} C^{-1}_{13} + Q_{21} R_{12} C^{-1}_{23} + Q_{21} R_{13} C^{-1}_{33} + Q_{22} R_{21} C^{-1}_{13} + \\
&\quad Q_{22} R_{22} C^{-1}_{23} + Q_{22} R_{23} C^{-1}_{33} + Q_{23} R_{31} C^{-1}_{13} + Q_{23} R_{32} C^{-1}_{23} + Q_{23} R_{33} C^{-1}_{33}] \\
K_{II} &= -(\pi a)^{1/2} \sigma^{\infty}_1 [Q_{11} R_{11} C^{-1}_{11} + Q_{11} R_{12} C^{-1}_{21} + Q_{11} R_{13} C^{-1}_{31} + Q_{12} R_{21} C^{-1}_{11} + \\
&\quad Q_{12} R_{22} C^{-1}_{21} + Q_{12} R_{23} C^{-1}_{31} + Q_{13} R_{31} C^{-1}_{11} + Q_{13} R_{32} C^{-1}_{21} + Q_{13} R_{33} C^{-1}_{31}] \\
K_{III} &= -(\pi a)^{1/2} \sigma^{\infty}_2 [Q_{31} R_{11} C^{-1}_{12} + Q_{31} R_{12} C^{-1}_{22} + Q_{31} R_{13} C^{-1}_{32} + Q_{32} R_{21} C^{-1}_{12} + \\
&\quad Q_{32} R_{22} C^{-1}_{22} + Q_{32} R_{23} C^{-1}_{32} + Q_{33} R_{31} C^{-1}_{12} + Q_{33} R_{32} C^{-1}_{22} + Q_{33} R_{33} C^{-1}_{33}]
\end{aligned} \tag{4.62}$$

C_{ij} is symmetric and represents a set of influence coefficients which connect the crack displacement magnitudes with the resolved stresses. C_{ij} is expressed as [37]

$$C_{ij} = \frac{-1}{4r^{1/2}} \oint_{crack} Q_{k\ell} R_{ki} R_{\ell j} d\beta \tag{4.63}$$

in which r is the aspect ratio of the crack. Expansion of Eq. (4.63) yields

$$C_{11} = -r^{-1/2}\int_0^{\pi/2}[Q_{11}R_{11}R_{11} + Q_{12}R_{11}R_{21} + Q_{13}R_{11}R_{31} + Q_{21}R_{21}R_{11} + Q_{22}R_{21}R_{21} + Q_{23}R_{21}R_{31} + Q_{31}R_{31}R_{11} + Q_{32}R_{31}R_{21} + Q_{33}R_{31}R_{31}]d\beta$$

$$C_{12} = -r^{-1/2}\int_0^{\pi/2}[Q_{11}R_{11}R_{12} + Q_{12}R_{11}R_{22} + Q_{13}R_{11}R_{32} + Q_{21}R_{21}R_{12} + Q_{22}R_{21}R_{22} + Q_{23}R_{21}R_{32} + Q_{31}R_{31}R_{12} + Q_{32}R_{31}R_{22} + Q_{33}R_{31}R_{32}]d\beta$$

$$C_{13} = -r^{-1/2}\int_0^{\pi/2}[Q_{11}R_{11}R_{13} + Q_{12}R_{11}R_{23} + Q_{13}R_{11}R_{33} + Q_{21}R_{21}R_{13} + Q_{22}R_{21}R_{23} + Q_{23}R_{21}R_{33} + Q_{31}R_{31}R_{13} + Q_{32}R_{31}R_{23} + Q_{33}R_{31}R_{33}]d\beta$$

$$C_{22} = -r^{-1/2}\int_0^{\pi/2}[Q_{11}R_{12}R_{12} + Q_{12}R_{12}R_{22} + Q_{13}R_{12}R_{32} + Q_{21}R_{22}R_{12} + Q_{22}R_{22}R_{22} + Q_{23}R_{22}R_{32} + Q_{31}R_{32}R_{12} + Q_{32}R_{32}R_{22} + Q_{33}R_{32}R_{32}]d\beta \tag{4.64}$$

$$C_{23} = -r^{-1/2}\int_0^{\pi/2}[Q_{11}R_{12}R_{13} + Q_{12}R_{12}R_{23} + Q_{13}R_{12}R_{33} + Q_{21}R_{22}R_{13} + Q_{22}R_{22}R_{23} + Q_{23}R_{22}R_{33} + Q_{31}R_{32}R_{13} + Q_{32}R_{32}R_{23} + Q_{33}R_{32}R_{33}]d\beta$$

$$C_{33} = -r^{-1/2}\int_0^{\pi/2}[Q_{11}R_{13}R_{13} + Q_{12}R_{13}R_{23} + Q_{13}R_{13}R_{33} + Q_{21}R_{23}R_{13} + Q_{22}R_{23}R_{23} + Q_{23}R_{23}R_{33} + Q_{31}R_{33}R_{13} + Q_{32}R_{33}R_{23} + Q_{33}R_{33}R_{33}]d\beta$$

Q_{ij} is a symmetric set of six real constants which are functions of the elastic moduli [37].

$$Q_{ij}^{-1} = t_{ik}U_{kj} + s_{ik}V_{kj} \tag{4.65}$$

in which s_{jk}, U_{jk}, and t_{jk}, V_{jk} are, respectively, the real and the imaginary components of two matrices, p_{jk} and N_{jk}, which are expressed as

$$p_{jk} = s_{jk} + it_{jk}$$
$$N_{jk} = U_{jk} + iV_{jk} \tag{4.66}$$

Eq. (4.65) is expanded to yield

$$Q_{11}^{-1} = t_{11}U_{11} + t_{12}U_{21} + t_{13}U_{31} + s_{11}V_{11} + s_{12}V_{21} + s_{13}V_{31}$$

$$
\begin{aligned}
Q_{12}^{-1} &= t_{11}U_{12} + t_{12}U_{22} + t_{13}U_{32} + s_{11}V_{12} + s_{12}V_{22} + s_{13}V_{32} \\
Q_{13}^{-1} &= t_{11}U_{13} + t_{12}U_{23} + t_{13}U_{33} + s_{11}V_{13} + s_{12}V_{23} + s_{13}V_{33} \\
Q_{22}^{-1} &= t_{21}U_{12} + t_{22}U_{22} + t_{23}U_{32} + s_{21}V_{12} + s_{22}V_{22} + s_{23}V_{32} \\
Q_{23}^{-1} &= t_{21}U_{13} + t_{22}U_{23} + t_{23}U_{33} + s_{21}V_{13} + s_{22}V_{23} + s_{23}V_{33} \\
Q_{33}^{-1} &= t_{31}U_{13} + t_{32}U_{23} + t_{33}U_{33} + s_{31}V_{13} + s_{32}V_{23} + s_{33}V_{33}
\end{aligned}
\tag{4.67}
$$

The matrix p_{jk}, which is expressed in Eq. (4.66), is defined in the following manner [39].

$$
\begin{aligned}
p_{11} &= c'_{11}\mu_1^2 + c'_{13} - c'_{16}\mu_1 \\
p_{13} &= c'_{11}\mu_2^2 + c'_{13} - c'_{16}\mu_2 \\
p_{22} &= c'_{45} - c'_{55}/\mu_3 \\
p_{31} &= c'_{13}\mu_1 + c'_{33}/\mu_1 - c'_{36} \\
p_{33} &= c'_{13}\mu_2 + c'_{33}/\mu_2 - c'_{36} \\
p_{12} &= p_{21} = p_{23} = p_{32} = 0
\end{aligned}
\tag{4.68}
$$

The elastic constants, c'_{ij}, are expressed in Eq. (4.55). μ_1, μ_2 and μ_3, the complex roots of Eq. (4.44) and (4.47), were discussed in the last section. Expressing μ_1, μ_2 and μ_3 as quantities with real and imaginary parts [see Eq. (4.45) and (4.48)], Eq. (4.68) can be rewritten in the form of Eq. (4.66) to yield

$$
\begin{aligned}
s_{11} &= c'_{11}(\alpha_1^2-\beta_1^2) + c'_{13} - c'_{16}\alpha_1 \\
t_{11} &= \beta_1(2c'_{11}\alpha_1 - c'_{16}) \\
s_{13} &= c'_{11}(\alpha_2^2-\beta_2^2) + c'_{13} - c'_{16}\alpha_2
\end{aligned}
$$

$$t_{13} = \beta_2(2c'_{11}\alpha_2 - c'_{16})$$

$$s_{22} = c'_{45} - c'_{55}\left(\frac{\alpha_3}{\alpha_3^2 + \beta_3^2}\right)$$

$$t_{22} = c'_{55}\left(\frac{\beta_3}{\alpha_3^2 + \beta_3^2}\right) \qquad (4.69)$$

$$s_{31} = c'_{13}\alpha_1 + c'_{33}\left(\frac{\alpha_1}{\alpha_1^2 + \beta_1^2}\right) - c'_{36}$$

$$t_{31} = \beta_1\left(c'_{13} - \frac{c'_{33}}{\alpha_1^2 + \beta_1^2}\right)$$

$$s_{33} = c'_{13}\alpha_2 + c'_{33}\left(\frac{\alpha_2}{\alpha_2^2 + \beta_2^2}\right) - c'_{36}$$

$$t_{33} = \beta_2\left(c'_{13} - \frac{c'_{33}}{\alpha_2^2 + \beta_2^2}\right)$$

$$s_{12} = s_{21} = s_{23} = s_{32} = t_{12} = t_{21} = t_{23} = t_{32} = 0$$

The matrix N^{-1}_{jk} is defined as [39]

$$N^{-1}_{11} = \frac{\mu_2}{\mu_2 - \mu_1}$$

$$N^{-1}_{13} = \frac{1}{\mu_2 - \mu_1}$$

$$N^{-1}_{22} = -1$$

$$N^{-1}_{31} = -\frac{\mu_1}{\mu_2 - \mu_1} \qquad (4.70)$$

$$N^{-1}_{33} = -\frac{1}{\mu_2 - \mu_1}$$

$$N_{12}^{-1} = N_{21}^{-1} = N_{23}^{-1} = N_{32}^{-1} = 0$$

Expressing μ_1 and μ_2 as in Eq. (4.45), Eq. (4.70) can be rewritten in the form of Eq. (4.66) to yield

$$U_{11} = \frac{\alpha_2(\alpha_2-\alpha_1) + \beta_2(\beta_2-\beta_1)}{(\alpha_2-\alpha_1)^2 + (\beta_2-\beta_1)^2}$$

$$V_{11} = \frac{\beta_2(\alpha_2-\alpha_1) - \alpha_2(\beta_2-\beta_1)}{(\alpha_2-\alpha_1)^2 + (\beta_2-\beta_1)^2}$$

$$U_{13} = \frac{\alpha_2 - \alpha_1}{(\alpha_2-\alpha_1)^2 + (\beta_2-\beta_1)^2}$$

$$V_{13} = \frac{\beta_1 - \beta_2}{(\alpha_2-\alpha_1)^2 + (\beta_2-\beta_1)^2}$$

$$U_{22} = -1$$

$$V_{22} = 0$$

$$U_{31} = \frac{\alpha_1(\alpha_1-\alpha_2) + \beta_1(\beta_1-\beta_2)}{(\alpha_1-\alpha_2)^2 + (\beta_1-\beta_2)^2} \qquad (4.71)$$

$$V_{31} = \frac{\beta_1(\alpha_1-\alpha_2) - \alpha_1(\beta_1-\beta_2)}{(\alpha_1-\alpha_2)^2 + (\beta_1-\beta_2)^2}$$

$$U_{33} = \frac{\alpha_1 - \alpha_2}{(\alpha_1-\alpha_2)^2 + (\beta_1-\beta_2)^2}$$

$$V_{33} = \frac{\beta_1 - \beta_2}{(\alpha_1-\alpha_2)^2 + (\beta_1-\beta_2)^2}$$

$$U_{12} = U_{21} = U_{23} = U_{32} = V_{12} = V_{21} = V_{23} = V_{32} = 0$$

Q_{ij} is obtained by substituting the expressions in Eq. (4.69) and (4.71) into Eq. (4.67) and inverting the resulting matrix.

R_{ij} is defined as [37]

$$R_{ij} = (\sin^2\beta + r^2\cos^2\beta)^{-1/4} \begin{bmatrix} r\cos\beta & \sin\beta & 0 \\ 0 & 0 & (\sin^2\beta + r^2\cos^2\beta)^{1/2} \\ -\sin\beta & r\cos\beta & 0 \end{bmatrix} \tag{4.72}$$

With Q_{ij}, C_{ij} and R_{ij} defined above, the stress-intensity factors can be determined using Eq. (4.62)

4.6 Solution of the Self-Consistent Equations

4.6.1 Transversely Isotropic Solid

For a transversely isotropic solid containing either dry or saturated cracks which are distributed at all orientations ($0° \leq \psi \leq 90°$), Eq. (4.26)-(4.30) are the self-consistent equations from which the five independent elastic moduli can be determined. The crack parameters which are required in order to determine the moduli are the crack size and orientation distributions, $f(a|\psi)$ and $f(\psi)$, respectively, the number of cracks per unit volume, N_V, the aspect ratio of the cracks, r, and the range of the angle η which defines the characteristic directions of the cracks. These parameters are three-dimensional in nature and are therefore not amenable to direct measurements for opaque bodies. Procedures are established in Appendix D for the estimation of the parameters from crack distributions on plane sections.

The orientation distribution function used in this study is that of the Marriott distribution [98]. This distribution represents a mildly anisotropic system of cracks.

$$f(\psi) = \frac{1}{1 - K/3}(1 + K\cos 2\psi)\sin\psi \tag{4.73}$$

$$-1 \leq K \leq 1$$

in which K is a measure of the degree of anisotropy. Defining "high angles" as angles, ψ, close to 90° and "low angles" as ψ close to 0°, a negative K

indicates a system in which more cracks are oriented at high angles than at low angles, while a positive K indicates a system in which fewer cracks are oriented at high angles than at low angles. Further details of this distribution are presented in Appendix D.

A more general orientation distribution function, the Fisher distribution, allows for all degrees of anisotropy [98]. This distribution is expressed as

$$f(\psi) = \frac{1}{\sum_{n=0}^{\infty}(2K)^n/[n!(2n+1)]} \sin\psi\, e^{2K\cos^2\psi} \qquad (4.74)$$

$$-\infty < K < \infty$$

As $K \to -\infty$, the cracks are distributed such that their normals lie in planes which are perpendicular to the longitudinal axis of the solid; i.e. the crack orientation corresponds to $\psi = 90°$. On the other hand, as $K \to \infty$, the cracks are distributed such that their normals are parallel to the longitudinal axis of the solid; i.e. the crack orientation corresponds to $\psi = 0°$. Hoenig [38] describes the first distribution ($K \to -\infty$) as cylindrical transverse isotropy (CTI), while he describes the second ($K \to \infty$) as planar transverse isotropy (PTI).

The forms of the integrands in Eq. (4.26)-(4.30) do not allow direct integration. A numerical integration scheme is therefore required for their evaluation. Gaussian quadrature [72] is used for the examples presented in a subsequent section.

Since Eq. (4.26)-(4.30) are nonlinear in the unknown moduli, an iterative solution scheme is required. Picard iteration with successive displacements [72] is used; during each iteration, the newly computed value of each of the moduli is immediately substituted into the remaining equations for the computation of the other moduli. In the current study, convergence is achieved when all five computed moduli satisfy the criterion that the values computed during the current iteration lie within 0.1% of the values obtained during the previous iteration.

4.6.2 Special Cases

4.6.2.1 Cylindrical Transverse Isotropy

The self-consistent formulations can be simplified for the special case of the transversely isotropic solid in which the distribution of cracks is that of cylindrical transverse isotropy ($K \to \infty$). Hoenig [38] obtained results for this case. This type of crack distribution ($\psi = 90°$ for all cracks) affects three of the independent elastic moduli of the solid, E_1, ν_{12} and G_{31}, while $E_3 = E$ and $\nu_{31} = \nu$. The corresponding self-consistent equations are obtained from Eq. (4.26), (4.28) and (4.30) to be

$$E_1 = E \,/\, \left[1 + 2\, N_V\, E \int_0^\infty W_1(a) f(a) da\right] \tag{4.75}$$

$$\nu_{12} = 1 - E_1 \left[\frac{(1-\nu)}{E} + N_V \int_0^\infty W_3(a) f(a) da\right] \tag{4.76}$$

$$G_{31} = G \,/\, \left[1 + 2\, N_V\, G \int_0^\infty W_5(a) f(a) da\right] \tag{4.77}$$

in which $f(a)$ is the size distribution of the cracks. As in the case of five independent moduli, the crack energy parameters, $W_i(a)$ ($i = 1,3,5$), are obtained using Eq. (4.19) for dry cracks and Eq. (4.33) for saturated cracks.

4.6.2.2 Isotropic Solid

The self-consistent formulations obtained in this study can also be simplified for the special case of the isotropic cracked solid. The moduli for such a body have been obtained by Budiansky and O'Connell [14,67]. An isotropic material is described by two independent elastic constants. Thus, two self-consistent equations need to be solved to obtain the elastic moduli. If $\bar{E}$, $\bar{G}$ and $\bar{\nu}$ are the effective moduli of the isotropic cracked solid, $\bar{G}$ may be taken as the dependent modulus. The moduli are related by the standard elasticity relation

$$\bar{G} = \frac{\bar{E}}{2(1 + \bar{\nu})} \tag{4.78}$$

Substituting $\bar{E}$ in place of E_3 in Eq. (4.27) and $\bar{\nu}$ in place of ν_{31} in Eq. (4.29), the self-consistent equations reduce to

$$\bar{E} = E \,/\, \left[1 + 2\, N_V\, E \int_0^{\pi/2}\int_0^{\infty} W_2(a,\psi) f(a) f(\psi)\, da\, d\psi\right] \tag{4.79}$$

$$\bar{\nu} = \frac{1}{2} - \bar{E}\left[\frac{(1-\nu)}{E} - \frac{1}{2\bar{E}} + N_V \int_0^{\pi/2}\int_0^{\infty} W_4(a,\psi) f(a) f(\psi)\, da\, d\psi\right] \tag{4.80}$$

Here, the expressions for computing the energy change associated with a single crack, ξ, are given by Eq. (4.17a) for dry cracks and Eq. (4.34) for saturated cracks. The crack energy parameter, $W_i(a,\psi)$ $(i = 2,4)$, is defined by Eq. (4.18).

The orientation distribution of an isotropic system is expressed as [98]

$$f(\psi) = \sin \psi \tag{4.81}$$

This distribution is used in Eq. (4.79) and (4.80). Eq. (4.81) can be obtained from the Marriott and Fisher distributions by setting K = 0.

4.6.3 Solution Procedure

The general method for solving the self-consistent equations numerically, is outlined as follows.

1. Assume values for the independent elastic moduli which are affected by the presence of cracks.
2. Use these values to determine the crack energy parameter, $W_i(a,\psi)$, associated with each crack. For each load case, this computation may have to be carried out many times corresponding to cracks of different orientations.
3. Using an iterative scheme (e.g. Picard iteration), the self-consistent equations are used to refine the initial guesses for the effective elastic moduli.
4. Test for convergence of each modulus based upon an appropriate tolerance.
5. Return to Step 1 if any of the convergence tests fail.

4.7 Results

4.7.1 Isotropic Solid

Budiansky and O'Connell [14,67] obtained relationships between the effective moduli of a cracked solid and a parameter representing the crack

density. This crack density parameter is $N_V\langle a^3\rangle$, in which N_V is the number of cracks per unit volume, and $\langle a^3\rangle$ is the mean cubed value of the characteristic crack size. The variation of the effective moduli with $N_V\langle a^3\rangle$ implies that if small cracks join into a smaller number of larger cracks, a substantial increase will occur in $N_V\langle a^3\rangle$ resulting in a corresponding reduction in the effective moduli. $N_V\langle a^3\rangle$ is proportional to the volume of cracks per unit volume of the material.

The relationships between effective moduli and $N_V\langle a^3\rangle$ for an isotropic cracked solid containing either dry or saturated circular cracks, obtained from the current procedures, are compared to Budiansky and O'Connell's results in Fig. 4.5 and 4.6. The results match in each case. In the case of dry cracks, the moduli decrease continuously with the increasing crack density parameter. The reductions in $\bar{E}$ indicate continuous loss of coherence of the material as caused by the cracks. For saturated cracks, $\bar{E}$ decreases continuously with increasing crack density parameter, while $\bar{\nu}$ increases to a limiting value of 0.5.

4.7.2 Transversely Isotropic Solid

4.7.2.1 Cylindrical Transverse Isotropy

The results for a transversely isotropic cracked solid, in which the distribution of circular cracks is that of cylindrical transverse isotropy, are shown in Fig. 4.7-4.9 for dry and saturated cracks. These results match those obtained by Hoenig [38] for this type of crack distribution, as shown in the figures. In the case of dry cracks, all of the moduli decrease with the increasing crack density parameter, $N_V\langle a^3\rangle$. ν_{12} reduces to zero at a value of $N_V\langle a^3\rangle$ of about 0.65, but E_1 and G_{31} do not vanish, even at a value of $N_V\langle a^3\rangle$ of 1.0.

For saturated cracks, Fig. 4.7 and 4.9 show that the effective moduli, E_1 and G_{31}, decrease with the increasing crack density parameter, as in the case of dry cracks. On the other hand, Poisson's ratio, ν_{12}, increases with $N_V\langle a^3\rangle$. As shown in Fig. 4.8, the value of ν_{12} exceeds 0.5 at a value of $N_V\langle a^3\rangle$ of about 0.4, attaining a value of 0.813 at $N_V\langle a^3\rangle$ of 1.0.

A comparison of the results for dry and saturated cracks indicates that dry cracks cause greater reductions in the moduli than saturated cracks. In a saturated crack, the effect of the fluid is to prevent relative normal

displacement of the crack faces. As a result, a saturated cracked solid is stiffer than a dry solid with the same crack distribution.

As pointed out in Section 4.6.2.1, E_3 and ν_{31} are unaffected by a cylindrically transverse isotropic distribution of cracks ($\psi = 90°$ for all cracks). When materials like cement paste and mortar are loaded in uniaxial compression, E_3 and ν_{31} change with increasing applied load, while cracks form at all orientations (Chapter 3). For these materials, it appears that cracks which form at orientations other than the direction of applied compression play an important role in the material behavior.

4.7.2.2 Marriott Distribution with K = -0.3

The crack orientation and size distributions used for the example described in this section are typical of the spatial distributions of cracks in cement paste and mortar loaded in uniaxial compression (Chapter 3). Fig. 4.10-4.14 show the results for a transversely isotropic cracked solid in which circular cracks are distributed according to a Marriott distribution [Eq. (4.73)] with K = -0.3. The negative value of K implies that the orientation distribution is skewed towards the longitudinal direction. The crack size distribution at each orientation is assumed to have the form of a gamma distribution. This distribution is represented as

$$f(a|\psi) = \frac{1}{\beta^{\alpha}\Gamma(\alpha)} a^{\alpha-1} e^{-a/\beta} \tag{4.82}$$

with $a = a_{\psi}$. α and β are functions of the mean and the variance of the distribution, $\langle a_{\psi} \rangle$ and $\mathrm{var}(a_{\psi})$.

$$\alpha = \frac{\langle a_{\psi} \rangle^2}{\mathrm{var}(a_{\psi})} \qquad \beta = \frac{\mathrm{var}(a_{\psi})}{\langle a_{\psi} \rangle} \tag{4.83}$$

$\Gamma(\alpha)$ is the gamma function and is defined as

$$\Gamma(\alpha) = \int_0^{\infty} y^{\alpha-1} e^{-y} dy \tag{4.84}$$

Gaussian quadrature with four integrations points over the range of y from 0 to 50 is sufficient for the integration in Eq. (4.84). For this example, the mean and the variance of the gamma distribution are, respectively,

$\langle a_\psi \rangle = 1.0\times10^{-5}\psi + 5.0\times10^{-3}$in., $\quad var(a_\psi) = 1.0\times10^{-9}\psi + 1.0\times10^{-6}$in.^{2}.

Fig. 4.10 and 4.14 show that the effective moduli, E_1 and G_{31}, reduce to zero at a value of $N_V\langle a^3 \rangle$ of about 0.44 for dry cracks. For saturated cracks, E_1 reduces to zero at a value of $N_V\langle a^3 \rangle$ of about 0.46. For both dry and saturated cracks, E_3 decreases continuously with increasing $N_V\langle a^3 \rangle$, but does not reduce to zero (Fig. 4.11). At the values of $N_V\langle a^3 \rangle$ at which E_1 reduces to zero, E_3 attains a value of 0.475E in the case of dry cracks and a value of 0.675E in the case of saturated cracks.

The Poisson's ratios, ν_{12} and ν_{31} (Fig. 4.12 and 4.13), increase with $N_V\langle a^3 \rangle$ for both dry and saturated cracks. For dry cracks, ν_{12} and ν_{31} increase up to 0.833 and 0.368, respectively, while for saturated cracks, ν_{12} and ν_{31} increase up to 0.913 and 0.541, respectively. A value of Poisson's ratio above 0.5 for applied compressive loads indicates a volume expansion of the solid due to the internal cracking. Under uniaxial compressive loading, volume increase has been observed in mortar and concrete, and a reduction in the rate of volume decrease has been observed in cement paste (Chapter 3 and [58,59,76,87,88]).

A comparison of the results in Fig. 4.7-4.9 with those in Fig. 4.10-4.14 indicates that a multi-orientation crack distribution (in this case a Marriott distribution with K = -0.3), results in greater changes in effective moduli, E_1 and G_{31}, with increasing crack density than obtained with cracks distributed with a single orientation. In addition, there appears to be less relative difference between dry and saturated cracks for the multi-orientation distribution than for the single orientation distribution.

4.8 Sensitivity of the Moduli to Variations in Crack Parameters

This section illustrates the effects of crack parameters on the computed effective moduli of a transversely isotropic solid. Variations in the mean and variance of crack size distributions, $\langle a_\psi \rangle$ and $var(a_\psi)$, the number of cracks per unit volume, N_V, the aspect ratio of the cracks, r, and the range of orientation η, are considered. The value of each parameter is varied independently for a solid containing dry cracks which are distributed according to a Marriott distribution with K = -0.3. The crack size distribution has the form of a gamma distribution, and its mean and variance are the same as those used for the example in Section 4.7.2.2. Both the

Marriott and the gamma distributions are typical of spatial crack distributions found in cement paste and mortar.

The data used in the analysis, and the calculated values of E_3/E are given in Table 4.1. The values of E_3/E are determined for 5%, 10%, 20% and 30% variations in $\langle a_\psi \rangle$, $var(a_\psi)$, N_V and r, and for ranges of η of 20°, 90° and 180° (assuming a uniform distribution within the range).

The results indicate that the modulus E_3 is particularly sensitive to variations in mean crack size, $\langle a_\psi \rangle$. For a 30% increase in $\langle a_\psi \rangle$, E_3/E decreases by 35.8%. A 30% increase in N_V results in only a 10.4% decrease in E_3/E. The greater sensitivity of the effective moduli to crack size is reflected in the variation of the effective moduli with $N_V\langle a^3 \rangle$.

E_3/E decreases by 13.8% for a 30% increase in the variance, $var(a_\psi)$. The effect of $var(a_\psi)$ on the moduli is a reflection of the sensitivity of the value of $\langle a^3 \rangle$ to $var(a_\psi)$. A 30% decrease in aspect ratio, r, results in a 10.5% increase in E_3/E. The increase in E_3/E with decreasing aspect ratio, r, indicates that the smaller the surface area of the cracks, the smaller the change in the moduli of the solid. An increase in the range of η from 0° to 180° results in a 7.1% decrease in E_3/E. This result is an indication of the sensitivity of the effective moduli to the value of η.

As pointed out above, the effects of $\langle a_\psi \rangle$ and $var(a_\psi)$ on the moduli are accounted for in the value of $\langle a^3 \rangle$. Therefore, for a transversely isotropic crack distribution, the four crack parameters, K, $N_V\langle a^3 \rangle$, r and the range of η, determine the effective moduli. This implies that a single relationship is obtained for the variation of the effective moduli with $N_V\langle a^3 \rangle$, if the values of K, r and η are constant. If the value of K, r or η is changed, a different relationship results. In the following section, the effects of variations in K are demonstrated.

4.8.1 Degree of Anisotropy, K

In this section, the sensitivity of the effective moduli to variations in the degree of anisotropy, K, is investigated. Transversely isotropic solids containing dry circular cracks distributed according to the Marriott distribution are considered. Values of K of -1.0, -0.3, 0, +0.3 and +1.0 are used. The crack size distribution is uniform over all crack sizes within a range of 0 to 0.01 in. and is independent of crack orientation.

A spatial distribution with K = -1.0 is skewed more towards the longitudinal direction than a distribution with K= -0.3, and a distribution with K = +1.0 is skewed more towards the plane of isotropy than one with K = +0.3.

The relationships between the effective moduli and the crack density parameter, $N_V\langle a^3\rangle$, are shown in Fig. 4.15-4.19. As expected, Fig. 4.15 shows that cracks cause bigger changes in the stiffness modulus in the plane of isotropy, E_1, when the crack orientation distribution is skewed towards the longitudinal direction (K = -0.3, -1.0) than when the orientation is skewed towards the plane of isotropy (K = +0.3, +1.0). On the other hand, Fig. 4.16 shows that cracks cause bigger changes in the stiffness modulus in the longitudinal direction, E_3, for K values of +0.3 and +1.0 than for K values of -0.3 and -1.0. For K values of -1.0 and -0.3, E_1 reduces to zero at values of $N_V\langle a^3\rangle$ of about 0.32 and 0.44, respectively, while for K values of +1.0 and +0.3, E_3 reduces to zero at values of $N_V\langle a^3\rangle$ of about 0.22 and 0.47, respectively.

For solids containing cracks distributed with negative values of K, the fact that E_1 vanishes while E_3 does not implies that no additional load can be carried in the lateral direction, even though the longitudinal direction can support additional load. This suggests that materials, such as cement paste, mortar and concrete, in which crack distributions are skewed towards the longitudinal direction due to uniaxial compression (negative K), are greatly weakened for tensile loading in the lateral direction.

Fig. 4.17 and 4.18 show that Poisson's ratios, ν_{12} and ν_{31}, increase with increasing $N_V\langle a^3\rangle$ for K values of -1.0 and -0.3, and decrease for K values of 0, +0.3 and +1.0. The increase in Poisson's ratio for the negative values of K implies that under uniaxial compressive loading, a volume increase of the cracked solid could occur for a crack distribution that is skewed towards the direction of applied compression. Such behavior has been observed for cement paste and mortar (Chapter 3).

4.9 Summary and Conclusions

4.9.1 Summary

The self-consistent energy method is used to develop a model for determining the effective moduli of a transversely isotropic cracked solid. Both

dry and saturated cracks are considered. To apply the technique, the three-dimensional crack distributions must be known.

The moduli for an isotropic cracked solid match the results obtained by Budiansky and O'Connell [14,67]. The results for a transversely isotropic solid, in which the cracks are distributed with a single orientation, match those obtained by Hoenig [38]. Results are also presented for a series of transversely isotropic solids with mild degrees of anisotropy. The sensitivity of the model to variations in crack parameters is discussed.

4.9.2 Conclusions

1. The effective moduli of a cracked solid containing elliptic cracks depend on the degree of anisotropy, K, the crack density parameter, $N_V\langle a^3\rangle$, the aspect ratio, r, and the range of orientation, η. The degree of anisotropy and the crack density parameter are dominant.
2. Dry cracks cause larger reductions in the moduli than saturated cracks.
3. For the same value of $N_V\langle a^3\rangle$, a multi-orientation crack distribution affects the moduli of a solid more than a single-orientation distribution.
4. In materials such as cement paste, mortar and concrete, cracks which are oriented in directions other than the direction of applied compression influence material behavior.
5. Materials, such as cement paste, mortar and concrete, in which crack distributions are skewed towards the direction of uniaxial compression should exhibit a reduced strength under lateral tensile loading.

CHAPTER 5
APPLICATION OF THE SELF-CONSISTENT MODEL

5.1 General

In Chapter 3, three-dimensional distributions of submicroscopic cracks in cement paste and mortar were estimated from observed surface crack distributions. In this Chapter, these three-dimensional crack distributions are used in conjunction with the self-consistent model developed in Chapter 4 to estimate the effect of the cracks on the elastic moduli of these materials and to estimate the portion of the applied strain that can be attributed to the cracking. Material response under monotonic, sustained and cyclic loading is investigated.

In applying the self-consistent model, both dry and saturated cracks are considered. However, under the slow rates of loading used in this study, there is likely to be sufficient time for water to diffuse out of saturated cracks. Hence, a dry crack assumption seems to be more appropriate.

For the initial application of the self-consistent model, it is assumed that the material between cracks (i.e. the matrix material) is homogeneous, linearly elastic, isotropic, and unaffected by the load history. With these assumptions, cracking is the only nonlinear effect.

If we further assume that the self-consistent model accurately accounts for the cracks and that the submicroscopic cracking recorded in this study is, in fact, the only nonlinear effect, then the experimental stress-strain curves should be duplicated exactly by the curves obtained using the self-consistent model. If the curves cannot be duplicated, then one or more of the assumptions is incorrect.

As we will see, the curves cannot be duplicated based on these assumptions, and only a portion of the nonlinear behavior can be explained by submicroscopic cracking.

As a second step, the assumptions are altered to allow the matrix material to soften due to nonlinear effects that are not accounted for by the submicrocracks. These other effects could include submicroscopic cracks that are not recorded, time dependent behavior, large microcracks, and macrocracks. This altered assumption is then used to obtain a closer estimate of the portion of inelastic strain that can be attributed to the

submicroscopic cracks. Before this step is taken, however, the results obtained with the initial assumptions are carefully studied.

The initial assumptions also suggest that the self-consistent model will be less valid for mortar than for cement paste, since the presence of sand grains makes mortar highly heterogeneous.

The anisotropic crack distributions which are induced in cement paste and mortar by uniaxial compressive loading, render the materials transversely isotropic. As discussed in Chapter 4, a transversely isotropic material has five independent elastic moduli: the stiffness modulus in the plane of isotropy, E_1, the stiffness modulus in the longitudinal direction which is also the direction of the applied stress, E_3, the Poisson's ratio in the plane of isotropy, ν_{12}, the Poisson's ratio in a plane perpendicular to the plane of isotropy, ν_{31}, and the shear modulus in a longitudinal plane, G_{31}. For a given three-dimensional distribution of cracks, values for these moduli are obtained using the self-consistent model.

The parameters which describe the three-dimensional crack distribution are the crack size distribution at each orientation ψ, $f(a|\psi)$, the mean and variance of $f(a|\psi)$, $\langle a_\psi \rangle$ and $\text{var}(a_\psi)$, respectively, the crack orientation distribution, $f(\psi)$, the crack aspect ratio, r, the rotation of the crack about its normal as defined by the angle η, and the number of cracks per unit volume, N_V. The details of these three-dimensional distributions and how they are estimated from surface crack distributions are presented in Chapter 3 and Appendix D. As described in Chapter 3, $f(a|\psi)$ for cement paste and mortar can be approximated by a gamma distribution, and $f(\psi)$ by a Marriott distribution. The crack parameters for cement paste and mortar are summarized in Tables 3.17-3.23 and 3.26-3.32.

For the uniaxially loaded paste and mortar specimens, the effective moduli of interest are E_3 and ν_{31}. Values for these moduli are obtained corresponding to both the smaller and larger estimates of the mean characteristic crack size, $\langle a_\psi \rangle$. As explained in Chapter 3 (Section 3.4.3), the smaller estimate of $\langle a_\psi \rangle$ is obtained when segments of a multi-directional crack trace are recorded as separate crack traces, while the larger estimate is obtained when a multi-directional crack trace is recorded as a single uni-directional crack. For the surface to three-dimensional crack distribution conversion procedure used in this study (Chapter 3 and Appendix D), the larger estimate of $\langle a_\psi \rangle$ is more correct. Hence, discussions in subsequent

sections are based primarily on results which correspond to the larger estimate of $\langle a_\psi \rangle$.

5.2 Application of the Model

The work described in this section and Section 5.3 is based on the assumption that the material between the cracks remains unchanged by the applied stresses.

In order to calculate the effective moduli using the self-consistent model, the stiffness modulus, E, and the Poisson's ratio, ν, of the undamaged material need to be known.

The moduli of the undamaged material are estimated based on two separate assumptions. These assumptions are made with regards to whether or not cracks exist in the cement paste and mortar specimens prior to loading. The two assumptions involve two different approaches to calculating the effective moduli. These approaches are described in Sections 5.2.1 and 5.2.2. It will be demonstrated that the effective moduli calculated using the two approaches are virtually identical.

5.2.1 First Approach

In the first approach, we assume that the cracks observed in a non-loaded specimen exist prior to loading. This assumption is not unreasonable since self-desiccation occurs in hydrated cement paste and may lead to internal cracking [18,84]. Self-desiccation is the decrease in the water content of the paste due to the ongoing hydration process. This assumption implies that the estimated three-dimensional crack distribution within a loaded specimen is due both to cracks which exist in the specimen prior to loading and cracks which are induced by the loading. The calculation of the effective moduli of the loaded material must account for both types of cracks. This is accomplished by estimating the moduli of the completely uncracked material, E and ν, and using the full three-dimensional crack distribution at any stage of loading to calculate the effective moduli.

If cracks exist in a specimen prior to loading, then the stiffness modulus and the Poisson's ratio prior to loading, E_i and ν_i, are the effective moduli as influenced by the existing crack distribution. For the uniaxially loaded specimens, E_i and ν_i are taken equal to the experimental values of the initial modulus of elasticity and Poisson's ratio. To obtain

estimates of the moduli of the uncracked material, values of E and ν are selected which, when combined with the three-dimensional crack distribution obtained for the nonloaded specimen, produce the measured values of E_i and ν_i. With the values of E and ν obtained, the full three-dimensional crack distribution obtained for specimens loaded to a given axial strain is used in the self-consistent model to calculate E_3 and ν_{31}.

For each material, E_i and ν_i are taken as the average of the values of the initial moduli given in Tables 2.2-2.7. The values of E_i are 1.78×10^6 psi, 2.54×10^6 psi, and 3.31×10^6 psi for cement pastes with W/C = 0.7, 0.5, and 0.3, respectively, and 4.79×10^6 psi for mortar with a W/C = 0.5. ν_i is 0.24 for the cement pastes, and 0.20 for mortar.

5.2.2 Second Approach

In this approach, the assumption is made that cracks do not exist in the specimens prior to loading. Therefore, the moduli of the uncracked material are equal to the moduli prior to loading; i.e. $E = E_i$ and $\nu = \nu_i$.

In Section 3.2, it was pointed out that the procedures used to prepare the specimens for viewing in the scanning electron microscope introduced additional cracks in the cement paste and mortar. If no cracks exist in the specimens prior to loading, the crack density measured in a nonloaded specimen is assumed to represent preparation cracks which are superimposed on any load-induced cracks and which are not accounted for by the procedure described in Section 3.4.3. The estimated three-dimensional crack distribution in a loaded specimen is, therefore, due both to load-induced cracks and specimen preparation cracks. The calculation of the effective moduli of the loaded material must account for only the load-induced cracks. The load-induced cracks are obtained here by subtracting the three-dimensional crack distribution (size, orientation and density) obtained for the nonloaded specimen from the distribution obtained for the loaded specimen. The altered distribution is used to calculate E_3 and ν_{31} for each applied strain.

During the subtraction of the three-dimensional distributions, negative values are obtained for the resulting distribution over those crack sizes for which the distribution in the nonloaded specimen is larger than the distribution in the loaded specimen. A value of zero is used for the distribution obtained after subtraction wherever a negative value occurs.

5.3 Material Response Due to Submicrocracking

In the self-consistent model, the effective stiffness modulus, E_3, is the predicted secant modulus at an applied stress, σ, at which the given three-dimensional crack distribution is obtained. The strain, ε_{ec}, associated with E_3 and σ includes a component due to elastic deformation and a component due to submicrocracking. ε_{ec} is calculated as

$$\varepsilon_{ec} = \frac{\sigma}{E_3} \tag{5.1}$$

The portion of ε_{ec} due to submicroscopic cracking, ε_c, is

$$\varepsilon_c = \varepsilon_{ec} - \varepsilon_e = \frac{\sigma}{E_3} - \frac{\sigma}{E_i} = \sigma\left(\frac{E_i - E_3}{E_i E_3}\right) \tag{5.2}$$

in which ε_e is the elastic strain. The total inelastic strain, $\varepsilon - \varepsilon_e$, is the difference between the applied strain, ε, and the elastic strain. For monotonically loaded specimens with a given water-cement ratio, the average applied stress for all specimens loaded to a particular axial strain is used as the value of σ in Eq. (5.1) and (5.2).

In the following section, the results obtained for monotonic loading are presented and discussed.

5.3.1 Monotonic Loading

The calculated values of the effective moduli and the axial strains obtained from the self-consistent model are presented in Tables 5.1-5.8 for cement pastes with W/C of 0.7, 0.5 and 0.3, and for mortar with a W/C of 0.5. These values are obtained using the assumption that cracks exist in the materials prior to loading (first approach). The values obtained using the assumption that cracks do not exist in the materials prior to loading (second approach) are given in Tables 5.9-5.12. Tables 5.1-5.12 include results for both the smaller and larger estimates of $\langle a_\psi \rangle$. The results indicate that submicroscopic cracks will cause a progressive softening of the materials under increasing strain, but that submicrocracks do not alone account for the nonlinear behavior of the materials.

Separate calculations based on dry and saturated cracks are discussed. Unless stated otherwise, the discussions are based on results which correspond to the larger estimate of $\langle a_\psi \rangle$.

Dry Cracks: The results for the dry crack assumption using the first approach (Tables 5.1-5.4) show that the calculated stiffness modulus, E_3, decreases with increasing applied strain. For example, for cement paste with a W/C = 0.5, E_3 decreases from a value of 2.54×10^6 psi at initial loading to a value of 2.156×10^6 psi at an applied strain of 0.006. For mortar with a W/C = 0.5, E_3 decreases from a value of 4.79×10^6 psi at initial loading to a value of 4.06×10^6 psi at an applied strain of 0.004.

To compare the effect of the cracks on E_3 for the different materials, the normalized stiffness modulus, E_3/E_i, is also calculated for each applied strain (Tables 5.1-5.4). The variation of E_3/E_i with applied strain is shown in Fig. 5.1 for all three cement pastes.

Fig. 5.1 shows that the variation of E_3/E_i with applied strain is virtually identical for the three cement pastes. The calculated percentage reduction in stiffness caused by the submicroscopic cracks appears to be independent of water-cement ratio. As discussed in Section 3.5.5, this result is expected because of the nearly identical crack distributions obtained in the cement pastes (Table 3.33). At the maximum applied strain of 0.006, the calculated reduction in stiffness of each of the cement pastes is 15%.

Fig. 5.2 compares the variation of E_3/E_i with applied strain for cement paste and mortar with a W/C = 0.5. This comparison indicates that the calculated percentage reduction in stiffness caused by the cracks is larger in mortar than in cement paste. At the maximum applied strain of 0.004 in mortar, the calculated reduction in stiffness of mortar is 15%, while at the same strain in cement paste, the reduction is 11%. This result is consistent with the crack density comparisons for cement paste and mortar in Table 3.34. The larger density of cracks in mortar causes a larger percentage reduction in the stiffness of mortar as compared to that of paste.

The calculated stress-strain (σ,ε_{ec}) curve due to submicrocracking is compared with the experimental stress-strain (σ,ε) curve and the linear elastic stress-strain relationship based on the initial stiffness in Fig. 5.3-5.6. The curves illustrate that the submicroscopic cracks account for just a portion of the nonlinear response of the materials. The total strain may be considered as consisting of elastic and inelastic components. The

inelastic component consists of a portion due to submicrocracking, ε_c, and a portion due to other causes, $\varepsilon - \varepsilon_e - \varepsilon_c$. This latter portion may be due to mechanisms other than submicrocracking, such as macrocracking and deformation or consolidation within the material between cracks.

For mortar (Fig. 5.6), unlike the applied strain, the value of ε_{ec} after the peak stress is smaller than the value at the peak stress, indicating that the material is unloading with a decreasing strain. This response of the model is due in large part to the assumption that the material between the cracks remains unchanged by the applied strain. This point is discussed further in Section 5.4.1 along with the results obtained by allowing the matrix material to soften.

Calculated values of the strain due to submicrocracking, ε_c, are presented in Tables 5.1 - 5.8. ε_c is also presented as a percentage of inelastic strain, $\varepsilon_c/(\varepsilon - \varepsilon_e)$. ε_c increases with increasing applied strain in both cement paste and mortar. As illustrated by cement paste with a W/C = 0.5 (Table 5.2), the value of ε_c increases from 0.000005 at an applied strain of 0.0005 to 0.000469 at an applied strain of 0.006. $\varepsilon_c/(\varepsilon - \varepsilon_e)$, on the other hand, decreases with increasing applied strain in both cement paste and mortar. For cement paste with a W/C = 0.5, the value of ε_c is 18% of the inelastic strain at an applied strain of 0.0005 and drops to 13% of the inelastic strain at a strain of 0.006. Similar values are obtained for paste with a W/C = 0.7. For cement paste with a W/C = 0.3, the submicroscopic cracks account for as high as 86% of the inelastic strain at an applied strain of 0.0005. This value drops to 29% at a strain of 0.006. The implications of these observations are discussed under the alternate application of the model in which the matrix material is allowed to soften (Section 5.4).

The fact that the calculated strain due to submicroscopic cracking accounts for only a portion of the inelastic strain in cement paste and mortar suggests that the initial assumption of a linear, elastic matrix material is incorrect. Rather, the matrix material appears to become inelastic with increasing applied strain. The probable mechanisms and effects of an inelastic matrix material are addressed in a subsequent section.

The results illustrated so far have been based on the larger estimate of $\langle a_\psi \rangle$. A comparison of E_3/E_i obtained with the smaller estimate of $\langle a_\psi \rangle$ for the cement paste with E_3/E_i for the larger estimate (Fig. 5.7) shows

that the calculated percentage reduction in stiffness caused by the submicroscopic cracks is lower for the smaller estimate of $\langle a_\psi \rangle$. As pointed out in Section 5.1, the estimates of the elastic moduli obtained with the larger estimates of $\langle a_\psi \rangle$ are considered to be more realistic. This comparison emphasizes that multi-directional crack traces must be properly accounted for in order to correctly estimate the effect of the cracks on material behavior.

Fig. 5.8-5.10 show the variations of the experimental and calculated Poisson's ratios, ν_{31}, with applied strain for cement pastes with W/C = 0.5 and 0.3, and for mortar with a W/C = 0.5.

Both the experimental and calculated Poisson's ratios for the cement pastes (Fig. 5.8 and 5.9) increase gradually with increasing compressive strain. For paste with a W/C = 0.5, the experimental Poisson's ratio starts at a value of 0.24 and rises to a value of 0.27, while for paste with a W/C = 0.3, the experimental Poisson's ratio starts at a value of 0.24 and rises to a value of 0.29. For both pastes, the calculated Poisson's ratio starts at a value of 0.24 and rises just slightly to a value of about 0.25.

The experimental values differ from the calculated values most distinctly at strains above 0.004, particularly for paste with a W/C = 0.3 (Fig. 5.9). The experimental results illustrated in Fig. 5.9 are for a specimen which failed at a strain of 0.006 (Specimen 17-3/P-0.3/M). Just prior to failure, macroscopic cracks (or macrocracks), which typically have trace lengths in the order of 1 in. or more [95], were visible on the surface of this specimen. Macrocracks are not accounted for in this study. Since cracking seems to have its greatest effect on lateral strain as reported by Maher and Darwin [57], the larger values of Poisson's ratio obtained experimentally for the cement pastes are likely due to cracks longer than those recorded with the scanning electron microscope.

For mortar (Fig. 5.10), the experimental Poisson's ratio increases rapidly with increasing compressive strain, while the calculated Poisson's ratio increases gradually with increasing compressive strain. The experimental Poisson's ratio starts at a value of 0.20 and rises to a value of 0.48, while the calculated Poisson's ratio starts at a value of 0.20 and rises to a value of about 0.22. As in the case of the cement pastes, the experimental Poisson's ratio is clearly larger than the calculated Poisson's ratio. The experimental results illustrated in Fig. 5.10 are for a mortar

specimen which was loaded beyond the peak stress to a maximum strain of 0.004 (Specimen 13-6/M-0.5/M). Macrocracks were visible on the surface of the specimen just beyond the peak stress, which corresponds to a strain of 0.003. Like the results for cement paste, the larger values of Poisson's ratio obtained experimentally are attributed to the cracks not accounted for in the current study.

Saturated Cracks: The results obtained with the self-consistent model for saturated cracks are presented in Tables 5.5-5.8. A comparison of the calculated normalized stiffness moduli, E_3/E_1, for dry and saturated cracks in cement pastes is shown in Fig. 5.11. This comparison shows that a material containing saturated cracks is stiffer than one containing dry cracks. In a saturated crack, the fluid prevents relative normal displacement of the crack faces, resulting in a smaller effect of the cracks on the stiffness modulus. Fig. 5.11 also shows that for the saturated cracks, the calculated effect of submicroscopic cracks on the stiffness of cement paste is independent of water-cement ratio, as it was for the dry cracks.

The calculated Poisson's ratios based on saturated cracks are slightly larger than those based on dry cracks, since the presence of fluid within the cracks enables the crack faces to interact. For example, at an applied strain of 0.006 in cement paste with a W/C = 0.5, the values of ν_{31} are 0.25 and 0.26 based on assumptions of dry and saturated cracks, respectively, compared to the experimental value of 0.27.

Fig. 5.12-5.14 show that, as for dry cracks, the calculated Poisson's ratios obtained with saturated cracks are smaller than the experimental Poisson's ratios, demonstrating that the presence of fluid within the cracks does not explain the increased Poisson effect obtained experimentally.

Second Approach: The calculated effective moduli obtained with the assumption that cracks do not exist in the materials prior to loading are presented in Tables 5.9-5.12 for dry cracks. The values of the stiffness modulus, E_3, calculated with the first and second approaches are compared in Fig. 5.15 for cement paste with a W/C = 0.5. Fig. 5.15 shows that the values of E_3 are virtually the same for the two approaches. At the most, the value of E_3 for the second approach is 0.7% larger than the corresponding value for the first approach. Fig. 5.16 shows that the calculated Poisson's ratios, ν_{31}, are the same for the two approaches.

Based on the assumptions used in the two approaches, as described in Sections 5.2.1 and 5.2.2, an analysis using the second approach starts with a lower calculated stiffness for the matrix material, E. The fact that the estimates of E_3 and ν_{31} for the two approaches are virtually identical indicates that the smaller number of cracks used in the second approach compensates for the lower value of E.

5.3.2 Other Inelastic Deformation

In the earlier discussions of Fig. 5.3-5.6 in Section 5.3.1, it was pointed out that inelastic deformations in cement paste and mortar include sizeable strains that cannot be attributed to the recorded submicrocracking. Fig. 5.3-5.6 show that the assumption of a linear elastic matrix, as used in the self-consistent model, is not correct. If it were, and all submicrocracks were accounted for, then the calculated axial strain, ε_{ec}, would be equal to the applied strain, ε. The following discussion pinpoints the probable sources of the inelastic deformation which is in excess of the deformation calculated for submicrocracking.

It is possible that not all of the submicroscopic cracks on the specimen surfaces were seen. Since the microstructure of cement paste consists of different features (e.g. calcium silicate hydrate and calcium hydroxide), some cracks may be obscured by the boundaries between these features. This may be even more so in mortar, which contains many sand grains. The increased crack density due to these cracks would result in a larger portion of the inelastic strain being due to submicrocracking.

Large microcracks and macrocracks, which were visible on the surface of some specimens at high stress levels, were not included in this study. These cracks will make an important contribution at high strains. As demonstrated in Chapter 4, large cracks are especially important since the change in material properties depends on the average value of the cube of the characteristic crack size, $\langle a^3 \rangle$.

A study by Spooner [85] showed that some portion of the inelastic strain in cement paste subjected to monotonic loading is due to flow or creep of the material. Thus, the mechanism of creep may account for a portion of the inelastic deformation that is not due to submicrocracking.

These observations should not come as a surprise. In fact, we should expect that the properties of the matrix material should change under load.

The resulting inelasticity of the matrix material and the effects of larger cracks, need to be accounted for in order to understand the role of submicrocracks in the nonlinear behavior of cement paste and mortar. These points are addressed in the next section.

5.4 Material Response with Inelastic Matrix Material

To obtain an improved estimate of the role of submicroscopic cracking in the stress-strain response of cement paste and mortar, the procedures used in the previous section are altered to allow the properties of the matrix material to change. For simplicity, all of the nonlinear response of cement paste and mortar that is not accounted for by submicrocracking is considered to be due to changes in the matrix. This is clearly a simplying assumption since it lumps large microcracks and macrocracks in with flow or creep. Although its properties may change, the matrix material is assumed to remain isotropic.

Using these assumptions, the self-consistent model is used to back-calculate the stiffness modulus, E_{mat}, and Poisson's ratio, ν_{mat}, of the matrix material that yield the experimentally measured strains when coupled with the three dimensional crack distributions. In this case, the portion of the stress-strain response of the material not due to the matrix is due to the submicroscopic cracks.

To calculate E_{mat} and ν_{mat} for a given distribution of submicroscopic cracks, the effective stiffness modulus of the cracked material, E_3, is set equal to the measured secant modulus, which corresponds to the applied stress, σ, and strain, ε, at which the crack distribution is obtained; i.e. $E_3 = \sigma/\varepsilon$. The effective Poisson's ratio, ν_{31}, is set equal to the measured Poisson's ratio. Values of E_{mat} and ν_{mat} are selected which, when combined with the full three-dimensional crack distribution obtained for specimens loaded to a given axial strain, produce the measured values of E_3 and ν_{31}.

This computation process is similar to the "first approach" procedure described in Section 5.2.1. If, however, the computation process utilizes a crack distribution equal to the difference between the three-dimensional crack distributions in the loaded and nonloaded specimens, a procedure similar to the "second approach" of Section 5.2.2 is obtained. The discussions that follow in Sections 5.4.1 through 5.4.3 follow the first

approach. The results for the second approach are presented in Section 5.4.4.

The strain, ε_{mat}, associated with E_{mat} and σ includes a component due to elastic deformation and a component due to inelastic deformation within the matrix material.

$$\varepsilon_{mat} = \sigma/E_{mat} \tag{5.3}$$

As in the case of Eq. (5.1) and (5.2), the value of σ used in calculating ε_{mat} for monotonic loading is the average applied stress for all specimens with a given water-cement ratio which have been loaded to the particular axial strain. For sustained or cyclic loading, σ is the stress which corresponds to the stress-strength ratio used in the test.

The component of the strain due to submicrocracking, ε_c, is the difference between the applied strain, ε, and ε_{mat}.

$$\varepsilon_c = \varepsilon - \varepsilon_{mat} \tag{5.4}$$

The total inelastic strain, $\varepsilon - \varepsilon_e$, is the difference between the applied strain, ε, and the elastic strain, $\varepsilon_e = \sigma/E_i$.

In subsequent sections, the results obtained for the moduli of the matrix material, E_{mat} and ν_{mat}, and the strain due to submicrocracking, ε_c, are presented and discussed for each loading regime. These results correspond to the larger estimate of $\langle a_\psi \rangle$, and the cracks are assumed to be dry.

5.4.1 Monotonic Loading

The calculated values of the moduli of the matrix material and the strain due to submicrocracking are presented in Tables 5.13-5.16 for cement paste and mortar. Softening within the matrix accounts for a significant portion of the nonlinearity at all values of applied strain. Typical changes in E_{mat} are illustrated by cement paste with a W/C = 0.5; E_{mat} decreases from a value of 2.54×10^6 psi at initial loading to a value of 1.375×10^6 psi at an applied strain of 0.006.

The calculated stress-strain (σ,ε_{mat}) curve due to softening within the matrix material is compared with the experimental stress-strain (σ,ε) curve

and the linear elastic stress-strain relationship based on the initial stiffness in Fig. 5.17-5.20. When compared with the stress-strain curves in Fig. 5.3-5.6, the curves in Fig. 5.17-5.20 show the importance of including the nonlinearity of the material between the submicroscopic cracks. This observation is similar to that of Maher and Darwin [57], who found from their finite element study that the nonlinear behavior of concrete requires an accurate representation for the nonlinear behavior of the mortar constituent, in addition to nonlinearity caused by bond and mortar cracks.

A comparison of the calculated stress-strain curves for mortar (Fig. 5.6 and 5.20) indicates that the increase in average strain obtained experimentally on the descending branch of the stress-strain curve, is due largely to aspects other than submicrocracking. Macroscopic cracks which form in a mortar specimen under uniaxial compression are visible on the surface of the specimen during the descending branch of the stress-strain curve. If the post-peak softening of the material is due to macrocracks only, based on the concept of strain localization as proposed in an analytical study by Bazant [4] and an experimental study by Van Mier [95], then categorizing all nonlinear responses other than submicrocracking as softening of the matrix material will overestimate the strain due to submicrocracking (Fig. 5.20).

From the concept of strain localization for materials which show strain-softening in compression, the relatively undamaged portions of the material should unload with a decreasing strain, while the average strain continues to increase on the descending branch. Thus, the strain due to submicrocracking on the descending branch should at most be equal to that at the peak of the stress-strain curve. The unloading response of the model shown in Fig. 5.6 is due in large part to the assumption that the material between the submicroscopic cracks remains unchanged by the applied strain, but it may support the existence of a region of localized deformation during the post-peak softening of mortar.

The strain due to submicrocracking, ε_c, is indicated on Fig. 5.17-5.20. ε_c as a percentage of the inelastic strain, $\varepsilon_c/(\varepsilon - \varepsilon_e)$, is presented in Tables 5.13-5.16 and Fig. 5.21. Fig. 5.21 and the data in Tables 5.13-5.15 show that for cement paste, $\varepsilon_c/(\varepsilon - \varepsilon_e)$ is the greatest at low strains, accounting for as high as 85% of the inelastic strain for 0.3 W/C paste at a strain of 0.0005. $\varepsilon_c/(\varepsilon - \varepsilon_e)$ decreases with increasing applied strain,

dropping to values of 30%, 34%, and 45% at a strain of 0.006 for pastes with W/C = 0.7, 0.5 and 0.3, respectively. This indicates that while the contribution of submicrocracking to the nonlinear response of cement paste is significant at all levels of applied strain, the relative importance of other mechanisms, large microcracks, macrocracks, and creep, increases with increasing strain until they play a dominant role. The relative importance of the submicrocracks increases with a decrease in water-cement ratio; the majority of the nonlinear strain in 0.3 W/C paste is due to submicrocracking at all strains except 0.006, at which strain presumably macrocracks play the major role. This observation is in line with the observation by Ngab, et al. [66] that, for specimens of the same age and at the same stress-strength ratio, creep is lower the higher the compressive strength (i.e., the lower the water-cement ratio).

For mortar, Fig. 5.21 and the data in Table 5.16 show that $\varepsilon_c/(\varepsilon - \varepsilon_e)$ decreases with increasing applied strain from 45% at a strain of 0.0005 to 17% at a strain of 0.003, the strain at the peak stress. At a strain of 0.004, which corresponds to the descending branch of the stress-strain curve, the value of $\varepsilon_c/(\varepsilon - \varepsilon_e)$ increases to 22%, implying that the portion of the inelastic strain due to submicrocracking is larger on the descending branch of the stress-strain curve than at the peak of the stress-strain curve. However, as pointed out earlier, the strain due to submicrocracking may have been overestimated on the descending branch. The smaller values of $\varepsilon_c/(\varepsilon - \varepsilon_e)$ for mortar as compared to those for cement paste may indicate that large microcracks and macrocracks play a more dominant role in mortar.

The variations of the experimental Poisson's ratio and the calculated Poisson's ratio of the matrix material with applied strain are shown in Fig. 5.22-5.24. These figures demonstrate that aspects other than submicrocracking control the Poisson effect in these materials.

5.4.2 Sustained Loading

The calculated values of the moduli of the matrix material and the strain due to submicrocracking are presented in Table 5.17 for cement pastes with W/C = 0.5 and 0.3. As for the monotonic tests, the stiffness modulus of the matrix material, E_{mat}, decreases with an increase in strain under sustained loading. For example, for paste with a W/C = 0.5, E_{mat} decreases

from a value of 2.54×10^6 psi at initial loading to a value of 0.975×10^6 psi at an applied strain of 0.006.

The calculated strain (elastic and inelastic) within the matrix material, ε_{mat}, is plotted against the applied stress, along with the experimental stress-strain curve and the linear elastic stress-strain relationship based on the initial stiffness, in Fig. 5.25-5.28. The figures show that the applied axial strain is made up of components of elastic strain, ε_e, inelastic strain due to submicrocracking, ε_c, and inelastic strain within the matrix material, $\varepsilon_{mat} - \varepsilon_e$.

For the experimental results considered here, the percentage of inelastic strain due to submicrocracking, $\varepsilon_c/(\varepsilon - \varepsilon_e)$, ranges from 20% to 34%, depending on the strain and the water-cement ratio. As for monotonic loading, $\varepsilon_c/(\varepsilon - \varepsilon_e)$ decreases with an increase in strain under sustained loading. For cement paste with a W/C = 0.5, $\varepsilon_c/(\varepsilon - \varepsilon_e)$ decreases from 24% at a strain of 0.004 to 20% at a strain of 0.006. For similar strains in cement paste with a W/C = 0.3, $\varepsilon_c/(\varepsilon - \varepsilon_e)$ decreases from 34% to 29%. Also, as for monotonic loading, the percentage of inelastic strain due to submicrocracking is larger for the lower water-cement ratio paste.

Fig. 5.29 and the data in Tables 5.14, 5.15 and 5.17 show that at a strain of 0.004, ε_c is virtually the same for monotonic and sustained loading. However, at a strain of 0.006, ε_c is greater for the monotonic specimens. For cement paste with a W/C = 0.5 at an applied strain of 0.004, ε_c is 0.000567 for monotonic loading and 0.000535 for sustained loading. At a strain of 0.006, ε_c increases to 0.001137 for monotonic loading but only to 0.000824 for sustained loading. For W/C = 0.3, the relative change in ε_c is less, with ε_c = 0.000564 and 0.000547, respectively, for monotonic and sustained loading to 0.004, and ε_c = 0.001132 and 0.001036, respectively, for loading to 0.006. These observations parallel those based on crack densities in Chapter 3 (Section 3.5.3.2).

At the same stress-strength ratio, ε_c is noticeably greater for sustained loading than for monotonic loading (Fig. 5.30), with values of ε_c for sustained loading ranging from 1.72 to 3.46 times the value of ε_c for monotonic loading. For this comparison, the value of ε_c for monotonic loading is obtained by linear interpolation of the data in Tables 5.14 and 5.15. The higher value of ε_c for sustained loading indicates that the strain due to submicrocracking increases with the duration of loading. This

increase in ε_c corresponds to the observed increase in crack density (Section 3.5.3.2).

The calculated and experimental Poisson's ratios are compared in Fig. 5.31 for cement pastes with W/C = 0.5 and 0.3, respectively. The calculated values of Poisson's ratio for the matrix material account for most of the observed changes, demonstrating that mechanisms other than submicrocracking control the Poisson effect in cement paste under sustained loading, as under monotonic loading. As pointed out in Chapter 2 (Section 2.4.3.1), the decrease in Poisson's ratio with an increase in applied strain under sustained loading may be due to volume consolidation, with the development of substantial axial strains but without corresponding large lateral strains.

5.4.3 Cyclic Loading

The calculated values of the moduli of the matrix material and the strain due to submicrocracking are presented in Table 5.18 for cement pastes with W/C = 0.5 and 0.3. The calculated stiffness modulus of the matrix material, E_{mat}, decreases with an increase in strain under cyclic loading, as it does under monotonic and sustained loading. For example, for paste with a W/C = 0.5, E_{mat} decreases from a value of 2.54×10^6 psi at initial loading to a value of 1.473×10^6 psi at an applied strain of 0.004.

The calculated strain within the matrix material, ε_{mat}, is plotted against the peak stress, along with the experimental stress-strain curve and the linear elastic stress-strain relationship based on the initial stiffness, in Fig. 5.32-5.36. As for the monotonic and sustained tests, the figures show that the applied axial strain for cyclic loading is made up of components of elastic strain, ε_e, inelastic strain due to submicrocracking, ε_c, and inelastic strain due to other mechanisms, $\varepsilon_{mat} - \varepsilon_e$. Softening within the matrix and submicrocracking both play major roles. Submicrocracking is especially important for the higher strength paste.

As for monotonic and sustained loading, the portion of inelastic strain due to submicrocracking, $\varepsilon_c/(\varepsilon - \varepsilon_e)$, decreases with an increase in strain under cyclic loading. For cement paste with a W/C = 0.5, $\varepsilon_c/(\varepsilon - \varepsilon_e)$ decreases from a value of 40% at a strain of 0.002 to a value of 25% at a strain of 0.004. For strains of 0.002, 0.0025 and 0.003 in cement paste with a W/C = 0.3, the values of $\varepsilon_c/(\varepsilon - \varepsilon_e)$ are 91%, 69% and 41%,

respectively. At low strains, 0.002 and 0.0025, the major portion of the nonlinear strain in 0.3 W/C paste is due to submicrocracking.

Fig. 5.37 compares ε_c under cyclic and monotonic loading regimes for cement pastes with W/C = 0.5 and 0.3, respectively. For the same applied strain in paste with a W/C = 0.5, ε_c is larger under cyclic loading than under monotonic loading. The values of ε_c are 0.00025 and 0.00058 for cyclic loading compared to 0.00014 and 0.00056 for monotonic loading, at strains of 0.002 and 0.004. At a strain of 0.002 in paste with a W/C = 0.3, the values of ε_c are 0.00007 for cyclic loading and 0.00013 for monotonic loading. But at a strain of 0.003, ε_c is larger for cyclic loading than for monotonic loading, with values of 0.00038 and 0.00030, respectively. The inelastic strain in the matrix, $\varepsilon_{mat} - \varepsilon_e$, is also larger for cyclic loading than for monotonic loading at all values of maximum strain (Fig. 5.38).

As observed by Maher and Darwin [58,59], material degradation is greater the greater the range of strain (loading strain plus unloading strain). If inelastic strains due to submicrocracking and other mechanisms are presumed to be indicators of damage, then Maher and Darwin's study indicates that the larger values of these strains under cyclic loading compared to monotonic loading (Fig. 5.37 and 5.38) are due to the fact that the range of strain for cyclic loading is larger than for monotonic loading.

For cyclic loading, as for monotonic and sustained loading, the decrease in the percentage of inelastic strain due to submicrocracking, $\varepsilon_c/(\varepsilon - \varepsilon_e)$, with an increase in applied strain indicates that the relative importance of other nonlinear responses increases with an increase in strain. But clearly, the density of submicrocracks (Fig. 3.45) and their effect (Fig. 5.37) continue to increase with continuing cycles as suggested by Maher and Darwin [58,59]. Also, the larger values of $\varepsilon_c/(\varepsilon - \varepsilon_e)$ for the lower water-cement ratio paste indicate that submicrocracks are relatively more important for higher strength materials than for lower strength materials for virtually all uniaxial loading regimes.

The calculated values of Poisson's ratio of the matrix material are compared with the experimental values in Fig. 5.39 for cement pastes with W/C = 0.5 and 0.3. The results show that the nonlinear responses other than submicrocracking control the Poisson effect in cement paste.

5.4.4 Comparison of Calculated Effects of Submicrocracks for First and Second Approaches

The calculated values of the moduli of the matrix material and the strain due to submicrocracking obtained with the second approach are presented in Tables 5.19-5.24. For the second approach, the percentage of inelastic strain due to submicrocracking, $\varepsilon_c/(\varepsilon - \varepsilon_e)$, is lower than obtained with the first approach. $\varepsilon_c/(\varepsilon - \varepsilon_e)$ for the second approach ranges from 10% to 80% compared with 20% to 90% for the first approach. The fact that the first and second approaches produce different results with an inelastic matrix is in contrast to the results obtained for an elastic matrix (Section 5.3.1). With an elastic matrix, both approaches produce the same results.

In the computation process with an elastic matrix, the second approach uses a lower value of matrix material stiffness, E, than the first approach [Section 5.2.2]. This lower value of E compensates for the reduced softening obtained with the lower crack density, and as a result, the calculated stiffness, E_3, and strain due to submicrocracking, ε_c, are the same for both approaches [Eq. (5.1) and (5.2)]. With an inelastic matrix, however, the crack density is used to back-calculate the matrix stiffness at each strain. As a result, the matrix stiffness and the strain due to submicrocracking, ε_c, [Eq. (5.3) and (5.4)] are different for the two approaches.

The difference in ε_c obtained with the two approaches increases as the applied strain increases. For example, for cement paste with W/C = 0.5 (Fig. 5.40), at a strain of 0.0005, ε_c for the first approach is 1.08 times the value for the second approach, while at a strain of 0.006, ε_c for the first approach is 1.26 times the value for the second approach. Considering the extreme assumptions used for the two approaches, these differences are not large.

At this point, it is not clear which approach is correct. The correct approach depends on the actual amount of cracking that exists prior to loading, a question not answered in the current study. As discussed in Sections 3.5.1 and 5.2.1, it is likely that some cracks do exist prior to loading. However, it is also likely that all preparation cracks are not removed by the procedure described in Section 3.4.3. Therefore, the true effect of load-induced submicrocracking should lie somewhere between the

results obtained with the two approaches. Future studies should continue to explore this issue.

5.5 Summary of Findings

1. Under uniaxial compressive loading of cement paste and mortar, submicroscopic cracks contribute to the decrease in the modulus of elasticity with increasing applied strain.
2. For monotonic loading, if submicrocracking is the only nonlinear effect, then the calculated percentage reduction in the stiffness of cement paste due to these cracks is nearly independent of water-cement ratio. The calculated percentage reduction in stiffness is larger for mortar than for cement paste.
3. For monotonic loading, the calculated stress-strain curves for cement paste and mortar, based on submicrocracking as the only nonlinear effect, are much stiffer than the experimental curves. The nonlinear behavior of the materials is more closely matched by accounting for the inelasticity of the material between the submicroscopic cracks.
4. The increase in average strain on the descending branch of the stress-strain curve of mortar is due largely to mechanisms other than submicrocracking.
5. Under uniaxial compressive loading of cement paste, the percentage of inelastic strain due to submicrocracking decreases with increasing applied strain. This indicates that other softening mechanisms, macrocracks and creep, play a larger role in the inelastic deformation of cement paste the higher the applied strain.
6. For uniaxial compressive loading of cement pastes of the same age at a given strain, the percentage of inelastic strain due to submicrocracking is larger the lower the water-cement ratio.
7. Under uniaxial compression, the Poisson effect in cement paste and mortar appears to be controlled by mechanisms other than submicrocracking.
8. For uniaxial compressive loading of cement paste to a fixed strain, a greater portion of the total strain is due to submicrocracking for monotonic loading than for sustained loading. Other nonlinear responses play a larger role under sustained loading.

9. At the same stress-strength ratio in cement paste, the strain caused by submicroscopic cracks is larger for sustained loading than for monotonic loading, implying that the degree of softening due to submicrocracking increases with the duration of loading.
10. For uniaxial compressive loading of cement paste to a fixed strain, the strain caused by submicroscopic cracks is larger for cyclic loading than for monotonic loading, implying that the degree of softening due to submicrocracking increases with repetition of load. Inelastic strain caused by other nonlinear mechanisms is also larger for cyclic loading.

CHAPTER 6
SUMMARY AND CONCLUSIONS

6.1 Summary

The purpose of this investigation is to study submicroscopic cracking of cement paste and mortar under uniaxial compression and to correlate the observed cracks with the applied strain and load history. Cement paste specimens are subjected to monotonic, sustained or cyclic loading. Mortar specimens are subjected to monotonic loading.

The cement pastes are representative of those found in low, normal and high strength concretes. Mixes with water-cement ratios of 0.7, 0.5 and 0.3 are used. The mortar corresponds to concrete with a water-cement ratio of 0.5. One hundred and thirty (130) specimens are tested at ages ranging from 27 to 29 days.

Specimens are loaded in compression using a closed-loop servo-hydraulic testing machine. Average axial strain is obtained using a compressometer and average lateral strain is obtained using an extensometer. After the specimens are loaded, slices are removed and dried for viewing in a scanning electron microscope. Cracking on transverse and longitudinal surfaces is studied at a magnification of 1250x.

Statistical and stereological models are developed to convert the surface crack distributions to three-dimensional distributions. The extent of cracking is compared in cement paste and mortar under different loading regimes.

A self-consistent model is developed to estimate the elastic moduli of transversely isotropic cracked materials. The model is used to correlate submicrocracking with the reduction in stiffness and the shape of the stress-strain curves of cement paste and mortar.

6.2 Conclusions

Based on the study presented in this report, the following conclusions can be made. The term "crack density" refers to both surface and volumetric submicroscopic crack densities.

1. The density and width of drying cracks in cement paste vary with the method of specimen drying. This suggests that drying shrinkage

in cement paste is not a material property, but rather a property of the total cement paste composite.

2. Crack density in cement paste varies inversely with water-cement ratio for nonloaded specimens.
3. Crack density in cement paste and mortar increases with increasing uniaxial compressive strain.
4. Surface crack density in cement paste is about ten times the density of bond and mortar microcracks in concrete at the same value of compressive strain.
5. About 80% of the surface crack density in cement paste occurs through the Type III CSH structure, with the balance approximately evenly divided between CH and the CH-III boundary.
6. About 70% of the surface crack density in mortar occurs through the Type III CSH structure, followed by about 18% at the sand grain - Type III CSH boundary. The balance of the cracking is approximately evenly divided between CH and the CH-III boundary.
7. Under uniaxial compressive loading, the mean size of submicroscopic cracks increases with increasing strain, while the number of cracks per unit volume decreases. This suggests that as the applied strain increases, small cracks join into a smaller number of larger cracks.
8. Under uniaxial compressive loading of cement paste and mortar, three-dimensional orientation distributions of submicroscopic cracks become skewed towards the direction of applied stress as strain increases.
9. Under monotonic loading, the crack orientation distributions in mortar are less skewed towards the direction of applied stress than the crack distributions in cement paste.
10. The crack orientation distributions under sustained and cyclic loading of cement paste are less skewed towards the direction of applied stress than the crack distributions under monotonic loading.
11. The effective moduli of a cracked solid depend primarily on the orientation distribution of the cracks, represented by the degree of anisotropy, K, and the measure of volumetric crack density, $N_V\langle a^3\rangle$.

12. In cement paste, mortar and concrete, cracks which are oriented in directions other than the direction of applied compression influence material behavior.
13. Cement paste, mortar and concrete in which crack orientation distributions are skewed towards the direction of uniaxial compression should exhibit a reduced strength under lateral tensile loading.
14. Submicrocracking accounts for a significant portion (20% to 90%) of the nonlinear response of cement paste and mortar at all levels of applied compressive strain. The role of submicrocracking decreases in relation to other mechanisms, such as large microcracks, macrocracks, and creep, with increasing applied strain.
15. For uniaxial compressive loading of cement paste and mortar, submicroscopic cracks contribute to the decrease in the modulus of elasticity with increasing strain.
16. Under monotonic loading, the submicroscopic crack distributions in cement paste show only small variations with water-cement ratio. As a result, if submicrocracking is the only nonlinear effect, then the calculated percentage reduction in the stiffness of cement paste due to these cracks is nearly independent of water-cement ratio.
17. For uniaxial compressive loading of cement pastes of the same age at a given strain, the percentage of inelastic strain due to submicrocracking is larger the lower the water-cement ratio. This suggests that submicrocracks are relatively more important for higher strength materials than for lower strength materials.
18. Under monotonic loading, crack density increases more rapidly in mortar than in cement paste, resulting in a larger percentage reduction in stiffness.
19. The calculated stress-strain curves for cement paste and mortar, based on submicrocracking as the only nonlinear effect, are much stiffer than the experimental curves. The nonlinear behavior of the materials is more closely matched by accounting for the inelasticity of the material between the submicroscopic cracks.
20. The increase in average strain on the descending branch of the stress-strain curve of mortar is due largely to mechanisms other than submicrocracking.

21. For uniaxial compressive loading of cement paste to a fixed strain, both crack density and strain due to submicrocracking are larger for monotonic loading than for sustained loading. Other nonlinear responses play a larger role under sustained loading.
22. At the same stress-strength ratio, both crack density and strain due to submicrocracking are larger for sustained loading than for monotonic loading, implying that the degree of softening due to submicrocracking increases with the duration of loading.
23. For uniaxial compressive loading of cement paste to a fixed strain, both crack density and strain due to submicrocracking are larger for cyclic loading than for monotonic loading. This implies that the degree of softening due to submicrocracking increases with repetition of load.
24. Under uniaxial compression, the Poisson effect in cement paste and mortar appears to be controlled by mechanisms other than submicrocracking.

6.3 Recommendations for Future Study

1. The role of cracking in the rate-dependent behavior of concrete should be investigated by studying submicrocracking in cement paste and mortar at different strain rates.
2. The relationship between submicrocracks and macrocracks in cement paste and mortar under uniaxial compression should be investigated using both experimental and analytical procedures. Such an investigation could provide a complete understanding of the mechanism of load-induced cracking in concrete.
3. Techniques need to be developed for performing crack surveys with saturated specimens in order to minimize cracking due to specimen preparation.
4. The surface to three-dimensional conversion procedure used in this study can handle only crack distributions with mild degrees of anisotropy. The possibility of modifying the procedure to handle crack distributions with more general degrees of anisotropy should be investigated.

REFERENCES

1. Allio, R. J. and Randall, C. H., "The Quantitative Analysis of Microstructure with Densitometer Data," Transactions of the American Institute of Mining, Metallurgical and Petroleum Engineers, Vol. 224, 1962, pp. 221-227.

2. American Society for Testing and Materials, Annual Book of ASTM Standards, Cement; Lime; Gypsum, Part 13, Philadelphia, Pennsylvania, 1981, pp. 246-247.

3. Anson, M., "An Investigation into a Hypothetical Deformation and Failure Mechanism for Concrete," Magazine of Concrete Research, Vol. 16, No. 47, June 1964, pp. 73-82.

4. Bazant, Z. P., "Instability, Ductility, and Size Effects in Strain-Softening Concrete," Journal of the Engineering Mechanics Division, ASCE, Vol. 102, No. EM2, April 1976, pp. 331-344.

5. Bazant, Z. P., Ohtsubo, H., and Aoh, K., "Stability and Post-Critical Growth of a System of Cooling or Shrinkage Cracks," International Journal of Fracture, Vol. 15, No. 5, October 1979, pp. 443-455.

6. Bazant, Z. P. and Raftshol, W. J., "Effect of Cracking in Drying and Shrinkage Specimens," Cement and Concrete Research, Vol. 12, No. 2, March 1982, pp. 209-226.

7. Bazant, Z. P. and Wahab, A. B., "Instability and Spacing of Cooling or Shrinkage Cracks," Journal of the Engineering Mechanics Division, ASCE, Vol. 105, No. EM5, October 1979, pp. 873-889.

8. Beaudoin, J. J., "Comparison of Mechanical Properties of Compacted Calcium Hydroxide and Portland Cement Paste Systems," Cement and Concrete Research, Vol. 13, No. 3, May 1983, pp. 319-324.

9. Berger, R. L., Young, J. F., and Lawrence, F. V., Discussion of "Morphology and Surface Properties of Hydrated Tricalcium Silicate Paste," by M. Collepardi and B. Marchese, Cement and Concrete Research, Vol. 2, No. 5, Sept. 1972, pp. 633-636.

10. Birkhoff, G. and Mac Lane, S., A Survey of Modern Algebra, Third Edition, Wiley, 1963, pp. 89-109.

11. Bowie, O. L., "Solutions of Plane Crack Problems by Mapping Technique," Mechanics of Fracture : Methods of Analysis and Solutions of Crack Problems, Edited by Sih, G.C., Vol. 1, 1973, pp. 8-9.

5. The self-consistent method should be applied to solids containing anisotropic crack distributions with closed cracks that undergo frictional sliding.

12. Budiansky, B., "On the Elastic Moduli of some Heterogeneous Materials," Journal of Mechanics and Physics of Solids, Vol. 13, 1965, pp. 223-226.

13. Budiansky, B., "Thermal and Thermoelastic Properties of Isotropic Composites," Journal of Composite Materials, Vol. 4, July 1970, pp. 286-290.

14. Budiansky, B. and O'Connell, R. J., "Elastic Moduli of a Cracked Solid," International Journal of Solids and Structures, Vol. 12, No. 2, 1976, pp. 81-97.

15. Burton, P. R., Manual for Scanning Electron Microscopy - An Outline of Preparation Methods and An Operation Manual for the Philips 501 Scanning Electron Microscope, University of Kansas, Lawrence, Kansas, 1978.

16. Buyukozturk, O., "Stress-Strain Response and Fracture of a Model of Concrete in Biaxial Loading," Thesis presented to Cornell University, Ithaca, NY, June 1970, in partial fulfillment of the requirements for the degree of Doctor of Philosophy.

17. Carrasquillo, R. L., Slate, F. O., and Nilson, A. H., "Microcracking and Behavior of High Strength Concrete Subject to Short-Term Loading," Journal of the American Concrete Institute, Proc. Vol. 78, No. 3, May-June 1981, pp. 179-186.

18. Chatterji, S., "Drying Shrinkage of Cement Paste and Concrete: A Reappraisal of the Measurement Technique and its Significance," Cement and Concrete Research, Vol. 6, No. 1, Jan. 1976, pp. 145-148.

19. Chatterji, S. and Jeffery, J. W., "Strength Development in Calcarious Cement," Nature, Vol. 214, No. 1, May 1967, pp. 559-561.

20. Chatterji, S., Thaulow, N., and Christensen, P., "Formation of Shrinkage Cracks in Thin Specimens of Cement Paste," Cement and Concrete Research, Vol. 11, No. 1, Jan. 1981, pp. 155-157.

21. Cleary, M. P., Chen, I-Wei, and Lee, Shaw-Ming, "Self-Consistent Techniques for Heterogeneous Media," Journal of the Engineering Mechanics Division, ASCE, Vol. 106, No. EM5, Oct. 1980, pp. 861-887.

22. Cook, D. J. and Chindaprasirt, P., "Influence of Loading History Upon the Compressive Properties of Concrete," Magazine of Concrete Research, Vol. 32, No. 111, June 1980, pp. 89-100.

23. Darwin, D. and Slate, F. O., "Effect of Paste-Aggregate Bond Strength on Behavior of Concrete," Journal of Materials, Vol. 5, No. 1, March 1970, pp. 86-98.

24. Day, R. L., "Reactions between Methanol and Portland Cement Paste," Cement and Concrete Research, Vol. 11, No. 3, May 1981, pp. 341-349.

25. De Hoff, R. T., "The Determination of the Size Distribution of Ellipsoidal Particles from Measurements made on Random Plane Sections," Transactions of the American Institute of Mining, Metallurgical and Petroleum Engineers, Vol. 224, June 1962, pp. 474-477.

26. De Hoff, R. T. and Rhines, F. N., "Determination of the Number of Particles per Unit Volume from Measurements made on Random Plane Sections: The General Cylinder and the Ellipsoid," Transactions of the American Institute of Mining, Metallurgical and Petroleum Engineers, Vol. 221, Oct. 1961, pp. 975-982.

27. Derucher, K. N., "Application of the Scanning Electron Microscope to Fracture Studies of Concrete," Building and Environment, Vol. 13, No. 2, 1978, pp. 135- 141.

28. Diamond, S., "Application of Scanning Electron Microscopy to the Study of Hydrated Cement," Proceedings, Third Annual Scanning Electron Microscope Symposium, IIT Research Institute, Chicago, Illinois, April 1970, pp. 385-392.

29. Diamond, S., "Cement Paste Microstructure--an Overview at Several Levels," Proceedings, Conference on Hydraulic Cement Pastes: Their Structure and Properties, Cement and Concrete Association, University of Sheffield, England, April 1976, pp. 2-30.

30. Domany, E., Gubernatis, J. E., and Krumhansi, J. A., "The Elasticity of Polycrystals and Rocks," Journal of Geophysical Research, Vol. 80, No. 39, Dec. 1975, pp. 4851-4856.

31. Freund, John E. and Walpole, Ronald E., Mathematical Statistics, Third Edition, Prentice-Hall, 1980, 548 pp.

32. Hansen, T. C., "Microcracking of Concrete," Journal of the American Concrete Institute, Vol. 64, No. 2, Feb. 1968, pp. 9-12.

33. Hershey, A. V., "The Elasticity of an Isotropic Aggregate of Anisotropic Cubic Crystals," Journal of Applied Mechanics, Vol. 21, No. 2, June 1954, pp. 236-242.

34. Hill, R., "Continuum Micro-Mechanics of Elastic-Plastic Polycrystals," Journal of the Mechanics and Physics of Solids, Vol. 13, No. 2, 1965, pp. 89-101.

35. Hill R., "A Self-Consistent Mechanics of Composite Materials," Journal of Mechanics and Physics of Solids, Vol. 13, No. 2, 1965, pp. 213-222.

36. Hilliard, J. E., "Specification and Measurement of Microstructural Anisotropy," Transactions of the American Institute of Mining, Metallurgical and Petroleum Engineers, Vol. 224, Dec. 1962, pp. 1201-1211.

37. Hoenig, A., "The Behavior of a Flat Elliptical Crack in an Anisotropic Elastic Body," International Journal of Solids and Structures, Vol. 14, No. 11, 1978, pp. 925-934.

38. Hoenig, A., "Elastic Moduli of a Non-Randomly Cracked Body," International Journal of Solids and Structures, Vol. 15, No. 2, 1979, pp. 137-154.

39. Hoenig, A., "Near-Tip Behavior of a Crack in a Plane Anisotropic Elastic Body," Engineering Fracture Mechanics, Vol. 16, No. 3, 1982, pp. 393-403.

40. Horii, H. and Nemat-Nasser, S., "Overall Moduli of Solids with Microcracks: Load-Induced Anisotropy," Journal of Mechanics and Physics of Solids, Vol. 31, No. 2, 1983, pp. 155-171.

41. Hsu, T. C. and Slate, F. O., "Tensile Strength between Aggregate and Cement Paste or Mortar," Journal of the American Concrete Institute, Proc. Vol. 60, No. 4, April 1963, pp. 465-486.

42. Hsu, T. C., Slate, F. O., Sturman, G. M., and Winter, G., "Microcracking of Plain Concrete and the Shape of the Stress-Strain Curve," Journal of the American Concrete Institute, Proc. Vol. 60, No. 2, Feb. 1963, pp. 209-224.

43. Hutchinson, J. W., "Bounds and Self-Consistent Estimates for Creep of Polycrystalline Materials," Proceedings of the Royal Society of London, Vol. 348, 1976, pp. 101-127.

44. Kaechele, L. E. and Tetelman, A. S., "A Statistical Investigation of Microcrack Formation," Acta Metallurgica, Vol. 17, March 1969, pp. 463-475.

45. Kaplan, S. A., "Factors Affecting the Relationship between Rate of Loading and Measured Compressive Strength of Concrete," Magazine of Concrete Research (London), Vol. 32, No. 111, June 1980, pp. 79-88.

46. Kassir, M. K. and Sih, G. C., "Three-Dimensional Stress Distribution Around an Elliptical Crack Under Arbitrary Loadings," Journal of Applied Mechanics, Vol. 33, No. 3, Sept. 1966, pp. 601-608.

47. Kassir, M. K. and Sih, G. C., "Three-Dimensional Stresses Around Elliptical Cracks in Transversely Isotropic Solids," Engineering Fracture Mechanics, Vol. 1, 1968, pp. 327-345.

48. Kawamura, M., "Internal Stresses and Microcrack Formation caused by Drying in Hardened Cement Pastes," Journal of the American Ceramic Society, Vol. 61, No. 7-8, July-Aug. 1978, pp.281-283.

49. Kendall, M. G. and Moran, P. A. P., Geometrical Probability, Griffin's Statistical Monographs and Courses, No. 10, 1963, 125 pp.

50. Kroner, E., "Self-Consistent Schemes and Graded Disorder in Polycrystal Elasticity," Journal of Physics, Vol. 8, No. 6, Sept. 1978, pp. 2261-2267.

51. Lawrence, F. V. and Young, J. F., "Studies on the Hydration of Tricalcium Silicate Pastes: Scanning Electron Microscopic Examination of Microstructural Features," Cement and Concrete Research, Vol. 3, No. 2, March 1973, pp. 149-161.

52. Laws, N., "The Over-all Thermoelastic Moduli of Transversely Isotropic Composites According to the Self-Consistent Method," International Journal of Engineering Science, Vol. 12, No. 1, Jan. 1974, pp. 79-87.

53. Laws, N. and McLaughlin, R., "Self-Consistent Estimates for the Viscoelastic Creep Compliances of Composite Materials," Proceedings of the Royal Society of London, Series A, 1978, pp. 251-273.

54. Leibengood, L., Darwin, D., and Dodds, R. H., "Finite Element Analysis of Concrete Fracture Specimens," Structural Engineering and Engineering Materials, SM Report No. 11, University of Kansas, Lawrence, Kansas, May 1984.

55. Lekhnitskii, S. G., Theory of Elasticity of An Anisotropic Elastic Body, Holden-Day, San-Francisco, 1963, Chapter 3.

56. Litvan, G. G., "Variability of the Nitrogen Surface Area of Hydrated Cement Paste," Cement and Concrete Research, Vol. 6, No. 1, Jan. 1976, pp. 139-144.

57. Maher, A. and Darwin, D., "Microscopic Finite Element Model of Concrete," Proceedings, First International Conference on Mathematical Modeling (St. Louis, Aug.-Sept. 1977), University of Missouri-Rolla, Vol. III, 1977, pp. 1705-1714.

58. Maher, A. and Darwin, D., "Mortar Constituent of Concrete under Cyclic Compression," Structural Engineering and Engineering Materials, SM Report No. 5, University of Kansas, Lawrence, Kansas, Oct. 1980.

59. Maher, A. and Darwin, D., "Mortar Constituent of Concrete in Compression," Journal of the American Concrete Institute, Vol. 79, No. 2, March-April 1982, pp. 100-109.

60. Meyers, B. L., Slate, F. O., and Winter, G., "Relationship between Time Dependent Deformation and Microcracking of Plain Concrete," Journal of the American Concrete Institute, Proc. Vol. 66, No. 1, Jan. 1969, pp. 60-68.

61. Miles, R. E. and Davy, P., "Particle Number or Density can be Stereologically Estimated by Wedge Sections," Journal of Microscopy, Vol. 113, No. 12, Nov. 1978, pp. 45-52.

62. Mills, R. H., "Collapse of Structure and Creep in Concrete," Proceedings, Conference on Structure, Solid Mechanics and Engineering Design, Part 1, University of Southampton, England, 1969, pp. 751-768.

63. Mindess, S. and Diamond, S., "A Device for Direct Observation of Cracking of Cement Paste or Mortar under Compressive Loading within a Scanning Electron Microscope," Cement and Concrete Research, Vol. 12, No. 5, Sept. 1982, pp. 569-576.

64. Mindess, S. and Young, F. J., Concrete, Prentice Hall, 1981, pp. 103-106.

65. Neville, A. M., Properties of Concrete, Pitman Publishing Inc., 1981, pp. 308-309.

66. Ngab, A. S., Nilson, A. H., Slate, F. O., "Shrinkage and Creep of High Strength Concrete," Journal of the American Concrete Institute, Proc. Vol. 78, No. 4, July 1981, pp. 255-261.

67. O'Connell, R. J. and Budiansky, B., "Seismic Velocities in Dry and Saturated Cracked Solids," Journal of Geophysical Research, Vol. 79, No. 35, Dec. 1974, pp. 5412-5425.

68. Parrott, L. J., "Lateral Strains in Hardened Cement Paste Under Short- and Long-Term Loading," Magazine of Concrete Research, Vol. 26, No. 89, Dec. 1974, pp. 198-202.

69. Parrott, L. J., "Effect of Drying History Upon the Exchange of Pore Water with Methanol and Upon Subsequent Methanol Sorption Behavior in Hydrated Alite Paste," Cement and Concrete Research, Vol.11, No. 5/6, Sept./Nov. 1981, pp. 651-658.

70. Parrott, L. J., Hansen, W., and Berger, R. L., "Effect of First Drying Upon the Pore Structure of Hydrated Pastes," Cement and Concrete Research, Vol. 10, No. 5, Sept. 1980, pp. 647-655.

71. Perry, C. and Gillott, J. E., "The Influence of Mortar-Aggregate Bond Strength on the Behavior of Concrete in Uniaxial Compression," Cement and Concrete Research, Vol. 7, No. 5, Sept. 1977, pp. 553-564.

72. Pizer, S. M., Numerical Computing and Mathematical Analysis, Prentice-Hall, 1975, 529 pp.

73. Rolfe, S. T. and Barsom, J. M., Fracture and Fatigue Control in Structures : Applications of Fracture Mechanics, Prentice-Hall, 1977, pp. 30-39.

74. Saltykov, S. A., "The Determination of the Size Distribution of Particles in an Opaque Material from a Measurement of the Size Distribution of their Sections," Stereology, Proceedings of the Second International Congress for Stereology, Edited by Elias, H., Spriger Verlag, New York, 1967, pp. 163-171.

75. Seaman, L., Curran, D. R., and Crewdson, R. C., "Transformation of Observed Crack Traces on a Section to True Crack Density for Fracture Calculations," Journal of Applied Physics, Vol. 49, No. 10, Sept. 1978, pp. 5221-5229.

76. Shah, S. P. and Chandra, S., "Critical Stress, Volume Change, and Microcracking of Concrete," Journal of the American Concrete Institute, Proc. Vol. 65, No. 9, Sept. 1968, pp. 770-781.

77. Shah, S. P. and Chandra, S., "Fracture of Concrete Subjected to Cyclic and Sustained Loading," Journal of the American Institute, Proc. Vol. 67, No. 10, Oct. 1970, pp. 816-824.

78. Shah, S. P. and Slate F. O., "Internal Microcracking, Mortar-Aggregate Bond and the Stress-Strain Curve of Concrete," Proceedings, International Conference on the Structure of Concrete, Cement and Concrete Association, University of London, England, Sept. 1965, pp. 82-92.

79. Shah, S. P. and Winter, G., "Inelastic Behavior and Fracture of Concrete," Journal of the American Concrete Institute, Proc. Vol. 63, No. 9, Sept. 1966, pp. 925-980.

80. Sih, G. C., Paris, P. C., and Erdogan, F., "Crack-Tip, Stress-Intensity Factors for Plane Extension and Plate Bending Problems," Journal of Applied Mechanics, Vol. 29, No. 2, June 1962, pp. 306-311.

81. Sih, G. C., Paris, P. C., and Irwin, G. R., "On Cracks in Rectilinearly Anisotropic Bodies," International Journal of Fracture Mechanics, Vol. 1, No. 3, Sept. 1965, pp. 189-202.

82. Slate, F. O. and Olsefski, S., "X-Rays for Study of Internal Structure and Microcracking of Concrete," Journal of the American Concrete Institute, Proc. Vol. 60, No. 5, May 1963, pp. 575-588.

83. Smith, C. S. and Guttman, L., "Measurement of Internal Boundaries in Three-Dimensional Structures by Random Sectioning," Transactions of the American Intitute of Mining, Metallurgical and Petroleum Engineers, Vol. 197, Jan. 1953, pp. 81-87.

84. Soroka, I., Portland Cement Paste and Concrete, Chemical Publishing Co., 1979, pp. 32-34.

85. Spooner, D. C., "The Stress-Strain Relationship for Hardened Cement Pastes in Compression," Magazine of Concrete Research (London), Vol. 24, No. 79, June 1972, pp. 85-92.

86. Spooner, D. C. and Dougill, J. W., "A Quantitative Assessment of Damage Sustained in Concrete During Compressive Loading," Magazine of Concrete Research (London), Vol. 27, No. 92, Sept. 1975, pp. 151-160.

87. Spooner, D. C., Pomeroy, C. D., and Dougill, J. W., "The Deformation and Progressive Fracture of Concrete," Proc. British Ceramic Society, No. 25, May 1975; Mechanical Properties of Ceramics (2), Joint Meeting of the Basic Sciences Section of the British Ceramic Society and the Materials and Testing Group of the Institute of Physics, London, England, Dec. 17-18, 1974, pp. 101-107.

88. Spooner, D. C., Pomeroy, C. D., and Dougill, J. W., "Damage and Energy Dissipation in Cement Pastes in Compression," Magazine of Concrete Research (London), Vol. 28, No. 94, March 1976, pp. 21-29.

89. Taylor, D. H., "A New Technique for the Study of Cement Hydration by Scanning Electron Microscopy," Journal of Testing and Evaluation, JTEVA, Vol. 5, No. 2, March 1977, pp. 102-105.

90. Taylor, M. A. and Broms, B. B., "Shear-Bond Strength between Coarse Aggregate and Cement Paste or Mortar," Journal of the American Concrete Institute, Proc. Vol. 61, No. 8, Aug. 1964, pp. 939-958.

91. Testa, R. B. and Stubbs, N., "Bond Failure and Inelastic Response of Concrete," Journal of the Engineering Mechanics Division, ASCE, Vol. 103, No. EM2, April 1977, pp. 296-310.

TABLE 2.4

MONOTONIC LOADING TESTS.

CEMENT PASTE WITH A W/C = 0.3

Specimen*	Age at Testing, days	Maximum Strain	Initial Modulus, E_i, 10^6 psi
5-2/P-0.3/M	27	0.0005	3.22
5-3/P-0.3/M	28	0.001	3.30
5-4/P-0.3/M	28	0.002	3.32
5-5/P-0.3/M	29	0.004	3.29
10-2/P-0.3/M	28	0.0005	3.24
10-3/P-0.3/M	28	0.001	3.32
10-4/P-0.3/M	28	0.002	3.34
10-5/P-0.3/M	29	0.004	3.38
11-2/P-0.3/M	27	0.0005	3.32
11-3/P-0.3/M	27	0.001	2.99
11-4/P-0.3/M	28	0.002	3.27
11-5/P-0.3/M	28	0.004	3.32
16-2/P-0.3/M	28	0.004	3.34
16-3/P-0.3/M	28	0.0058	3.37
17-2/P-0.3/M	27	0.004	3.27
17-3/P-0.3/M	27	0.006	3.32
20-2/P-0.3/M	28	0.002	3.00
20-3/P-0.3/M	28	0.003	3.35
20-6/P-0.3/M	28	0.0057	3.19
21-2/P-0.3/M	28	0.002	3.31
21-3/P-0.3/M	29	0.003	3.35

* See Appendix A

TABLE 2.5

MONOTONIC LOADING TESTS.

MORTAR WITH A W/C = 0.5

Specimen*	Age at Testing, days	Maximum Strain	Initial Modulus, E_i, 10^6psi
12-2/M-0.5/M	27	0.0005	4.84
12-3/M-0.5/M	27	0.001	4.76
12-4/M-0.5/M	28	0.002	5.04
12-5/M-0.5/M	28	0.003	4.79
13-2/M-0.5/M	28	0.0005	4.55
13-3/M-0.5/M	28	0.001	4.82
13-4/M-0.5/M	28	0.002	4.73
13-5/M-0.5/M	29	0.003	4.81
13-6/M-0.5/M	29	0.004	4.77

* See Appendix A

TABLE 2.6

SUSTAINED LOADING TESTS.

CEMENT PASTES WITH W/C = 0.5, 0.3

Specimen*	Age at Testing, days	Maximum Strain	Stress/Strength	Test Duration, hours	Initial Modulus, E_i, 10^6psi
14-4/P-0.5/S	28	0.0039	0.675	4	2.51
14-5/P-0.5/S	29	0.0062	0.725	4	2.80
15-4/P-0.5/S	28	0.0040	0.675	4	2.37
15-5/P-0.5/S	29	0.0059	0.725	4	2.69
15A-1/P-0.5/S	29	0.0075	0.8	3.5	2.54
16-4/P-0.3/S	28	0.0042	0.675	4	3.36
16-5/P-0.3/S	29	0.0061	0.715	2.75	3.36
17-4/P-0.3/S	28	0.0039	0.675	4	3.13
17-5/P-0.3/S	28	0.0059	0.71	2.25	3.34

* See Appendix A

TABLE 2.7

CYCLIC LOADING TESTS.

CEMENT PASTES WITH W/C = 0.5, 0.3

Specimen*	Age at Testing, days	Maximum Strain	Stress/Strength	No. of Cycles**	Initial Modulus, E_i, 10^6 psi
18-4/P-0.5/C	28	0.002	0.5	75	2.36
18-5/P-0.5/C	28	0.004	0.725	67	2.55
19-4/P-0.5/C	27	0.002	0.5	72	2.48
19-5/P-0.5/C	28	0.004	0.725	70	2.73
19A-1/P-0.5/C	29	0.005	0.865	31	2.52
20-4/P-0.3/C	27	0.002	0.65	38	3.37
20-5/P-0.3/C	27	0.003	0.60	85	3.28
21-4/P-0.3/C	28	0.0025	0.65	47	3.29
21-5/P-0.3/C	29	0.003	0.60	81	3.33

* See Appendix A
** Test duration in minutes is the number of cycles divided by 2.

TABLE 2.8

FORMAT FOR RECORDING CRACK DATA

Band No.	Type of Data	Crack data					
	Length, .0006 in.	0.75	1.5	1	2.25	3.5	0.5 .....
i*	Width, .00004 in.	0.2	0.25	0.2	1.5	1	0.75 .....
	Angle, degrees	50	30	75	45	30	10 .....
	Structure**	III	III	CH	CH-III	III	UHC-III ...

* : i = 1, 2, ..., 10
** : III = Type III Calcium Silicate Hydrate (CSH).
CH = Calcium Hydroxide.
UHC = Unhydrated Cement.
CH-III denctes a crack at the interface between CH and Type III CSH. Similar interpretation for UHC-III. See section 2.5.4.1 for full descriptions of the microscopic structures.

TABLE 2.9a

SURFACE CRACK DATA FOR MONOTONIC LOADING OF CEMENT PASTE WITH A W/C = 0.5 (BATCH #9). TRANSVERSE SURFACE.

NONLOADED

Band No.	Type of Data	Crack Data Trace Length, ℓ, 0.0006 in.; Trace Angle, θ, deg. (1 in. = 25400 μm)						
	ℓ	1	0.75	0.75	1.5	1.25	3.75	3.5
1	θ	100	0	165	140	35	130	90
	ℓ	4	3	2.25	3	2	1	1
	θ	0	155	60	60	125	175	165
	ℓ	1	3	1.25	0.5	1.5	0.75	2.25
2	θ	155	145	0	90	65	175	0
	ℓ	1.25	0.75	1.5	1.25	0.5		
	θ	0	60	85	50	85		
	ℓ	0.75	1.75	5	2.5	0.75	2.5	3
3	θ	160	90	10	120	140	90	40
	ℓ	2	1.25	2.5				
	θ	120	75	0				
	ℓ	2.5	1.25	2	1	1.25	1.5	3
4	θ	55	0	110	30	55	140	25
	ℓ	0.5	0.5	0.75	1.25	2	1.25	1.25
	θ	90	175	125	60	60	155	0
	ℓ	1	1.5	3	4	2	2.75	1
5	θ	90	130	35	140	165	0	100
	ℓ	0.75	1	0.5	2.5	0.75		
	θ	25	140	55	30	110		
	ℓ	1	2.75	1.5	2	1	2.5	3.25
6	θ	0	55	0	75	120	40	90
	ℓ	1	0.75	0.5	1	1	1.25	
	θ	140	120	10	90	160	85	
	ℓ	2	1.5	1	1	1.25	2.5	1.75
7	θ	50	85	60	0	0	175	65
	ℓ	2	1	1.25	1			
	θ	90	0	145	155			
	ℓ	1.75	2.25	4.5	1	2	3.75	2.5
8	θ	165	175	125	60	60	155	0

	ℓ	1	0.75	1.75	2	4.75	1	5.75
	θ	90	130	35	140	165	0	40
	ℓ	2.25	1	2	3.25	1	2.75	2
9	θ	120	55	30	110	0	25	80
	ℓ	2.5	1	1.5	3.25	2	1	1.25
10	θ	85	50	85	160	90	10	120
	ℓ	2.5	1	0.75	2	1	2.5	2.75
	θ	140	90	155	0	90	140	35

MAXIMUM STRAIN = 0.0005

Band No.	Type of Data	Crack Data Trace Length, ℓ, 0.0006 in.; Trace Angle, θ, deg. (1 in. = 25400 μm)						
	ℓ	2	1.25	1.25	1.5	2.25	2	3
1	θ	170	150	105	40	70	90	80
	ℓ	2	2.25	2	2.5	2.25		
	θ	115	100	0	0	155		
	ℓ	3.5	1.5	2	1.25	1	3	5
2	θ	50	130	40	110	125	130	155
	ℓ	2.5	1.25	2	6	1.75	1	1.5
	θ	85	0	50	95	25	100	55
3	ℓ	2.75	3.5	1.25	2	1	1.75	1.5
	θ	100	70	120	90	50	20	5
	ℓ	1.5	3	2.5	2.25			
	θ	20	45	75	65			
	ℓ	5.5	2.5	1	0.75	2	1.5	1.5
4	θ	55	30	35	5	0	15	80
	ℓ	1.5	1	1.25	2.5	1.75	3	3
5	θ	20	45	25	125	115	35	30
	ℓ	1	2.5	1.75	3.25	2.75	1.5	2
	θ	20	135	25	125	65	90	70
	ℓ	1.5	5	5	2.5	2	2	2
6	θ	15	70	105	65	5	60	25
	ℓ	5	1.5	1.75	3.5	0.75	1.25	1.25
7	θ	20	5	155	140	90	120	70
	ℓ	1.5	1.5	3.5	1.5			
	θ	100	55	80	85			
	ℓ	1.25	3.5	1	1.25	2.5	3.75	1
8	θ	50	130	25	0	100	0	65
	ℓ	1.25	2	3.5	0.75	1.5	2	1.75
	θ	80	90	70	40	105	150	20

	ℓ	3.5	2	1.5	2	1	1.25	3.75
9	θ	170	70	55	50	25	120	85
	ℓ	2	3	1.25	1	2	2.25	4.5
	θ	0	50	25	60	70	55	90
	ℓ	2.5	1	2.75	3.25	2	1.25	1
10	θ	90	10	85	150	30	35	45
	ℓ	0.75	0.75	1	2.5	1.75	1.5	
	θ	65	55	25	45	20	80	

MAXIMUM STRAIN = 0.001

Band No.	Type of Data	Crack Data Trace Length, ℓ, 0.0006 in.; Trace Angle, θ, deg. (1 in. = 25400 μm)						
	ℓ	3.5	2	3	3	4.5	2	1.5
	θ	55	55	90	150	65	0	85
1	ℓ	1.5	2.5	2	1.75	0.75	1.5	1
	θ	30	90	55	0	0	10	170
	ℓ	2	0.75	1	0.75	3		
	θ	120	50	0	70	45		
	ℓ	2.5	1.25	2	6	1.75	1	1.5
	θ	85	0	50	95	25	100	55
2	ℓ	2.75	3.5	1.25	2	1	1.75	1.5
	θ	100	70	120	90	50	20	5
	ℓ	1.5	3	2.5	2.25			
	θ	20	45	75	65			
	ℓ	5.5	2.5	1	0.75	2	1.5	1.5
3	θ	55	30	35	5	0	15	80
	ℓ	1.5	1	1.25	2.5	1.75	3	3
4	θ	20	45	25	125	115	35	30
	ℓ	1	2.5	1.75	3.25	2.75	1.5	2
	θ	20	135	25	125	65	90	70
	ℓ	1.5	5	5	2.5	2	2	2
5	θ	15	70	105	65	5	60	25
	ℓ	5	1.5	1.75	3.5	0.75	1.25	1.25
6	θ	20	5	155	140	90	120	70
	ℓ	1.5	1.5	3.5	1.5			
	θ	100	55	80	85			
	ℓ	3.5	1.5	2	1.25	1	3	5
7	θ	50	130	40	110	125	130	155
	ℓ	1.25	3.5	1	1.25	2.5	3.75	1
8	θ	50	130	25	0	100	0	65
	ℓ	1.25	2	3.5	0.75	1.5	2	1.75

	θ	80	90	70	40	105	150	20
	ℓ	3.5	2	1.5	2	1	1.25	3.75
9	θ	170	70	55	50	25	120	85
	ℓ	2	3	1.25	1	2	2.25	4.5
	θ	0	50	25	60	70	55	90
	ℓ	1.25	2.5	1.75	2	3.25	2.5	2.75
10	θ	50	165	120	85	25	65	50
	ℓ	1	1	1.25	1	1.75	3	1.25
	θ	90	40	0	45	50	35	65

MAXIMUM STRAIN = 0.002

Band No.	Type of Data	Crack Data Trace Length, ℓ, 0.0006 in.; Trace Angle, θ, deg. (1 in. = 25400 μm)						
	ℓ	2	2.5	1.25	2.5	7.25	5.75	3.5
1	θ	100	0	165	140	35	130	90
	ℓ	4	3	2.25	3	2	1	1
	θ	5	0	60	0	140	90	165
	ℓ	0.75	1.75	5	2.5	0.75	2.5	3
2	θ	160	90	10	120	140	90	40
	ℓ	2	1.25	2.5				
	θ	120	75	0				
	ℓ	2.5	1.25	2	1	1.25	1.5	3
3	θ	55	0	110	30	55	140	25
	ℓ	0.5	0.5	0.75	1.25	2	1.25	1.25
	θ	90	175	125	60	60	155	0
	ℓ	1	1.5	3	4	2	2.75	1
4	θ	90	130	35	140	165	0	100
	ℓ	0.75	1	0.5	2.5	0.75		
	θ	25	140	55	30	110		
	ℓ	1	2.75	1.5	2	1	2.5	3.25
5	θ	0	55	0	75	120	40	90
	ℓ	1	0.75	0.5	1	1	1.25	
	θ	140	120	10	90	160	85	
	ℓ	2	1.5	1	1	1.25	2.5	1.75
6	θ	50	85	60	0	0	175	65
	ℓ	2	1	1.25	1			
	θ	90	0	145	155			
	ℓ	1.75	2.25	4.5	1	2	3.75	2.5
7	θ	165	175	125	60	60	155	0
	ℓ	1	0.75	1.75	2	4.75	1	5.75
	θ	90	130	35	140	165	0	40

	ℓ	2.25	1	10.25	3.25	1	2.75	2
8	θ	120	55	30	110	0	25	80
	ℓ	2.5	1	0.75	2	1	2.5	2.75
	θ	140	90	155	0	90	140	35
	ℓ	1	3	1.25	0.5	1.5	0.75	2.25
9	θ	155	145	0	90	65	175	0
	ℓ	1.25	0.75	1.5	1.25	0.5		
	θ	0	60	85	50	85		
	ℓ	5.5	1	3.5	3.25	2	4	1.25
10	θ	85	35	15	160	90	10	120

MAXIMUM STRAIN = 0.004

Band No.	Type of Data	Crack Data Trace Length, ℓ, 0.0006 in.; Trace Angle, θ, deg. (1 in. = 25400 μm)						
	ℓ	4.5	2	1.25	1.5	2.25	2	3
1	θ	170	150	105	40	70	90	80
	ℓ	2	2.25	2	2.5	2.25		
	θ	115	20	5	0	155		
	ℓ	3.5	2.5	5	1.25	1	2	5
2	θ	50	130	40	145	125	130	155
	ℓ	2.5	1.25	2	6	1.75	1	1.5
	θ	85	0	50	95	25	100	55
3	ℓ	2.75	3.5	1.25	2	1	1.75	1.5
	θ	90	10	85	150	30	35	45
	ℓ	1.5	3	2.5	2.25			
	θ	20	45	75	65			
	ℓ	5.5	2.5	1	0.75	2	1.5	1.5
4	θ	55	30	35	5	0	15	80
	ℓ	1.5	1	1.25	2.5	1.75	3	3
5	θ	20	45	25	125	115	35	30
	ℓ	1	2.5	1.75	3.25	2.75	1.5	2
	θ	20	135	25	125	65	90	70
	ℓ	1.5	5	5	2.5	2	2	2
6	θ	15	70	105	65	5	60	25
	ℓ	1.25	2	3.5	0.75	1.5	2	1.75
	θ	80	90	70	40	105	150	20
	ℓ	5	1.5	1.75	3.5	0.75	1.25	1.25
7	θ	20	5	155	140	90	120	70
	ℓ	1.5	1.5	6.5	1.5			
	θ	100	55	80	85			

	ℓ	1.25	3.5	1	1.25	2.5	3.75	1
8	θ	50	130	25	0	100	0	65
	ℓ	3.5	2	1.5	2	1	1.25	3.75
9	θ	170	70	55	50	25	120	85
	ℓ	2	3	1.25	1	2	2.25	4.5
	θ	0	50	25	60	70	55	90
	ℓ	2.5	1	5.75	3.25	2	1.25	1
10	θ	100	70	120	90	50	20	5
	ℓ	0.75	0.75	1	2.5	1.75	1.5	
	θ	65	55	25	45	20	80	

MAXIMUM STRAIN = 0.006

Band No.	Type of Data	Crack Data Trace Length, ℓ, 0.0006 in.; Trace Angle, θ, deg. (1 in. = 25400 μm)						
	ℓ	1.5	4	6	3	2.5	2	3.5
	θ	55	55	90	150	65	0	85
1	ℓ	1.5	2.5	2	1.75	0.75	1.5	1
	θ	20	90	45	5	0	30	150
	ℓ	2	0.75	1	0.75	3	3.75	1.5
	θ	120	50	0	70	45	105	40
2	ℓ	2.75	3.5	1.25	2	1	1.75	1.5
	θ	100	70	120	90	50	20	5
	ℓ	1.5	3	2.5	2.25			
	θ	20	45	75	65			
	ℓ	5.5	2.5	1	0.75	2	1.5	1.5
3	θ	55	30	35	5	0	15	80
	ℓ	2.5	1.25	2	6	1.75	1	1.5
	θ	85	0	50	95	25	100	55
	ℓ	1.5	1	1.25	2.5	1.75	3	3
4	θ	20	45	25	125	115	35	30
	ℓ	1	2.5	1.75	3.25	2.75	1.5	2
	θ	20	135	25	125	65	90	70
	ℓ	3.5	5	7	1.5	5	2	3
5	θ	35	70	105	65	5	55	25
	ℓ	5	1.5	1.75	3.5	0.75	1.25	1.25
6	θ	20	5	155	140	90	120	70
	ℓ	1.5	1.5	3.5	1.5			
	θ	100	55	80	85			
	ℓ	3.5	1.5	2	1.25	1	3	5
7	θ	50	130	40	110	125	130	155

	ℓ	1.25	3.5	1	1.25	2.5	3.75	1
8	θ	50	130	25	0	100	0	65
	ℓ	1.25	2	3.5	0.75	1.5	2	1.75
	θ	80	90	70	40	105	150	20
	ℓ	3.5	2	1.5	2	1	1.25	3.75
9	θ	170	70	55	50	25	120	85
	ℓ	2	3	1.25	1	2	2.25	4.5
	θ	0	50	25	60	70	55	90
	ℓ	3.25	3.75	2.75	8.25	3.25	2.5	2.75
10	θ	50	165	120	85	25	65	50
	ℓ	5.5	1	1.25	4	1.75	3	2.25
	θ	90	40	0	45	50	35	35

TABLE 2.9b

SURFACE CRACK DATA FOR MONOTONIC LOADING OF CEMENT PASTE WITH A W/C = 0.5 (BATCH #9). LONGITUDINAL SURFACE.

NONLOADED

Band No.	Type of Data	Crack Data Trace Length, ℓ, 0.0006 in.; Trace Angle, θ, deg. (1 in. = 25400 μm)						
	ℓ	0.75	1.75	5	2.5	0.75	2.5	3
1	θ	95	5	135	20	25	100	85
	ℓ	4	3	2.25	3	2	1	1
	θ	0	155	60	60	125	175	165
	ℓ	1	3	1.25	0.5	1.5	0.75	2.25
2	θ	155	145	0	90	65	175	0
	ℓ	1.25	0.75	1.5	1.25	0.5		
	θ	0	60	85	50	85		
	ℓ	2	0.75	0.75	1.5	1.25	3.75	3.5
3	θ	160	90	10	120	140	90	40
	ℓ	2	1.25	2.5				
	θ	120	75	0				
	ℓ	3.5	1.25	2	1	1.25	1.5	3
4	θ	65	0	110	30	55	140	25
	ℓ	0.5	0.5	0.75	1.25	2	1.25	1.25
	θ	90	175	125	60	60	155	0
	ℓ	3.5	1	1.5	3.25	2	1	1.25
5	θ	85	130	35	140	165	0	100
	ℓ	1.75	1	0.5	2.5	0.75		
	θ	25	140	55	30	110		
	ℓ	2	2.75	1.5	2	1	2.5	3.25
6	θ	0	55	0	75	120	40	90
	ℓ	1	0.75	0.5	1	1	1.25	
	θ	125	120	10	90	160	85	
	ℓ	2	1.5	1	1	1.25	2.5	1.75
7	θ	50	85	60	0	0	175	65
	ℓ	1	0.75	1.75	2	4.75	1	5.75
	θ	90	130	35	140	165	0	40
	ℓ	1.75	2.25	4.5	1	2	3.75	2.5
8	θ	165	175	125	60	60	155	0
	ℓ	1	3	1.25	1			
	θ	90	0	145	155			

	ℓ	2.25	1	2	3.25	1	2.75	2
9	θ	85	55	30	110	0	25	80
	ℓ	1	1.5	3	4	2	2.75	1
10	θ	75	40	85	160	90	10	120
	ℓ	1.5	2	0.75	3	0.75	2.5	2.75
	θ	130	80	145	5	90	40	25

MAXIMUM STRAIN = 0.0005

Band No.	Type of Data	Crack Data Trace Length, ℓ, 0.0006 in.; Trace Angle, θ, deg. (1 in. = 25400 μm)						
	ℓ	2.5	1.25	2	6	1.75	1	1.5
1	θ	155	50	105	35	75	90	70
	ℓ	2	2.25	2	2.5	2.25		
	θ	105	100	0	5	135		
	ℓ	5.5	0.5	3	1.25	1	3	5
2	θ	45	130	45	100	125	130	155
	ℓ	2.75	3.5	1.25	2	1	1.75	1.5
3	θ	100	70	120	90	50	20	5
	ℓ	1.5	3	2.5	2.25			
	θ	20	45	75	65			
	ℓ	4.5	2.5	3	0.75	2	1.5	1.5
4	θ	50	30	35	5	0	15	80
	ℓ	1.5	1	1.25	2.5	1.75	3	3
5	θ	20	45	25	125	115	35	30
	ℓ	1	2.5	1.75	3.25	2.75	1.5	2
	θ	30	135	25	125	65	90	70
	ℓ	2	1.25	1.25	1.5	2.25	2	3
6	θ	85	0	50	95	25	100	55
	ℓ	1.5	5	5	2.5	2	2	2
	θ	15	70	105	65	5	60	25
	ℓ	4	1.5	1.75	2.5	1.75	1.25	1.25
7	θ	20	5	145	140	80	120	70
	ℓ	0.75	0.75	1	2.5	1.75	1.5	
	θ	65	45	25	45	20	80	
	ℓ	3.25	1.5	1	1.25	2.5	3.75	1
8	θ	50	130	25	0	100	0	65
	ℓ	1.25	2	3.5	0.75	1.5	2	1.75
	θ	80	90	70	40	105	150	20

	ℓ	3.5	2	1.5	2	1	1.25	3.75
9	θ	170	70	55	50	25	120	85
	ℓ	2	3	1.25	1	2	2.25	4.5
	θ	0	50	25	60	70	55	90
	ℓ	1.5	2	3.25	3.25	2	2.25	1
10	θ	90	10	85	145	30	45	45
	ℓ	1.5	1.5	3.5	1.5			
	θ	100	55	80	85			

MAXIMUM STRAIN = 0.001

Band No.	Type of Data	Crack Data Trace Length, ℓ, 0.0006 in.; Trace Angle, θ, deg. (1 in. = 25400 μm)						
	ℓ	2.5	0.5	2	2.75	1.75	1.5	1
1	θ	40	90	55	0	5	10	170
	ℓ	2	0.75	1	0.75	3		
	θ	120	50	0	70	45		
	ℓ	3.5	1.25	1	6	1.75	1	1.5
	θ	75	0	50	95	25	100	55
2	ℓ	2.75	3.5	1.25	2	1	1.75	1.5
	θ	100	70	120	90	50	20	5
	ℓ	1.5	3	2.5	2.25			
	θ	20	45	75	65			
	ℓ	3.5	2	3	3	4.5	2	1.5
3	θ	55	55	90	150	65	0	85
	ℓ	5.5	2.5	1	0.75	2	1.5	1.5
	θ	55	30	35	5	0	15	80
	ℓ	2.5	1	1.25	2.5	1.75	3	3
4	θ	30	45	25	125	115	35	30
	ℓ	3	1.5	1.75	3.25	2.75	1.5	2
	θ	20	105	25	125	65	90	70
	ℓ	1.5	5	3	2.5	2	2	2
5	θ	15	60	105	65	5	45	25
	ℓ	5	1.5	1.75	3.5	0.75	1.25	1.25
6	θ	20	5	155	140	90	120	70
	ℓ	1.5	1.5	3.5	1.5			
	θ	100	55	80	85			
	ℓ	1.25	2.5	1.75	2	3.25	2.5	2.75
7	θ	50	165	120	85	25	65	50
	ℓ	3.5	1.5	2	1.25	1	3	5
	θ	50	130	40	110	125	130	155

	ℓ	1.25	3.5	1	1.25	2.5	3.75	1
8	θ	50	130	25	0	100	0	65
	ℓ	1.25	2	3.5	0.75	1.5	2	1.75
	θ	80	90	70	40	105	150	20
	ℓ	3.5	2	1.5	2	1	1.25	3.75
9	θ	170	70	55	50	25	120	85
	ℓ	2	3	1.25	1	2	2.25	4.5
	θ	0	50	25	60	70	55	90
	ℓ	1	1	1.25	1	1.75	3	1.25
10	θ	90	40	0	45	50	35	65

MAXIMUM STRAIN = 0.002

Band No.	Type of Data	Crack Data Trace Length, ℓ, 0.0006 in.; Trace Angle, θ, deg. (1 in. = 25400 μm)						
	ℓ	2.5	1.25	2	1	1.25	1.5	3
1	θ	55	0	110	30	55	140	25
	ℓ	2	1	4.25	3	2	3	1
	θ	5	0	30	0	120	90	165
	ℓ	1.75	2.75	3	2.5	0.75	2.5	3
2	θ	60	90	10	120	140	90	40
	ℓ	3	1.25	1.5				
	θ	110	75	0				
	ℓ	2	2.5	1.25	2.5	7.25	5.75	3.5
	θ	100	0	165	140	35	130	90
3	ℓ	0.5	0.5	0.75	1.25	2	1.25	1.25
	θ	90	175	125	60	60	155	0
	ℓ	1.5	1.5	2	3	3	3.75	2
4	θ	90	120	35	140	165	0	105
	ℓ	1.75	1	0.5	2.5	0.75		
	θ	35	140	45	30	110		
	ℓ	1	2.75	1.5	2	1	2.5	3.25
5	θ	0	55	0	75	120	40	90
	ℓ	1	0.75	0.5	1	1	1.25	
	θ	140	120	10	90	160	85	
	ℓ	1	1.5	1	1	1.25	2.5	1.75
6	θ	50	85	60	0	0	175	65
	ℓ	2.5	1	1.25	1			
	θ	90	0	145	155			

	ℓ	1.75	2.25	4.5	1	2	3.75	2.5
7	θ	165	175	125	60	60	155	0
	ℓ	1	0.75	1.75	2	4.75	1	5.75
	θ	90	130	35	140	165	0	40
	ℓ	3.25	2	10.25	3.25	1	2.75	2
8	θ	120	55	30	110	0	25	80
	ℓ	1.5	1	0.75	1	1	2.5	2.75
	θ	120	90	145	0	90	130	35
	ℓ	3.5	3	3.5	3.25	1	4	1.25
9	θ	75	35	15	140	90	10	120
	ℓ	1	2	1.25	1.5	1.5	0.75	2.25
10	θ	145	145	0	90	65	175	0
	ℓ	2.25	0.75	1.5	1.25	0.5		
	θ	0	60	85	50	85		

MAXIMUM STRAIN = 0.004

Band No.	Type of Data	Crack Data Trace Length, ℓ, 0.0006 in.; Trace Angle, θ, deg. (1 in. = 25400 μm)						
	ℓ	1.5	1.25	2	6	1.75	1	1.5
1	θ	75	0	60	95	25	100	55
	ℓ	1	1.25	2	2.5	2.25		
	θ	15	30	5	0	155		
	ℓ	1.5	2	1.25	1.5	2.25	2	2
2	θ	150	10	105	40	60	90	80
	ℓ	3.5	2.5	5	1.25	1	2	5
	θ	50	20	40	145	125	130	155
	ℓ	1.75	3.5	2.25	2	1	1.75	1.5
3	θ	90	10	75	150	30	35	45
	ℓ	2.5	2	2.5	2.25			
	θ	20	45	75	65			
	ℓ	4.5	2.5	1	0.75	2	1.5	1.5
4	θ	65	30	35	5	0	15	80
	ℓ	2.5	1	2.25	2.5	1.75	3	3
5	θ	30	45	25	125	115	35	30
	ℓ	1	2.5	1.75	3.25	2.75	1.5	2
	θ	20	135	25	125	65	90	70
6	ℓ	1.25	2	3.5	0.75	1.5	2	1.75
	θ	80	90	70	40	105	150	20

	ℓ	6	2.5	1.75	3.5	0.75	1.25	1.25
7	θ	20	5	155	140	90	120	70
	ℓ	2.5	1.5	6.5	1.5			
	θ	90	55	80	85			
	ℓ	2.5	5	5	2.5	2	2	2
8	θ	30	70	115	65	5	60	25
	ℓ	2.25	3.5	1	1.25	2.5	3.75	1
	θ	45	120	25	0	100	0	65
	ℓ	2.5	1	5.75	3.25	2	1.25	1
9	θ	100	70	120	90	50	20	5
	ℓ	2	3	1.25	1	2	2.25	4.5
	θ	0	50	25	60	70	55	90
	ℓ	3.5	2	1.5	2	1	1.25	3.75
10	θ	170	70	55	50	25	120	85
	ℓ	0.75	0.75	1	2.5	1.75	1.5	
	θ	65	55	25	45	20	80	

MAXIMUM STRAIN = 0.006

Band No.	Type of Data	Crack Data Trace Length, ℓ, 0.0006 in.; Trace Angle, θ, deg. (1 in. = 25400 μm)						
	ℓ	3.5	2.5	1	0.75	2	1.5	1.5
	θ	75	30	35	5	0	15	80
1	ℓ	2.5	3	6	3	2.5	2	3.5
	θ	65	75	90	150	65	0	85
	ℓ	1.5	1.5	1	1.75	0.75	1.5	1
	θ	20	90	45	5	0	30	150
	ℓ	3.75	3.5	1.25	2	1	1.75	1.5
2	θ	90	70	120	90	50	20	5
	ℓ	3.5	3	2.5	2.25			
	θ	40	20	75	65			
	ℓ	2.5	1.25	2	6	1.75	1	1.5
3	θ	95	0	50	95	35	100	55
	ℓ	2	1.75	1	0.75	3	3.75	1.5
	θ	20	40	0	70	45	105	40
	ℓ	3.5	5	7	1.5	5	2	3
4	θ	35	70	105	65	5	55	25
	ℓ	1.5	1	1.25	2.5	1.75	3	3
	θ	20	45	25	125	115	35	30
	ℓ	1	2.5	1.75	3.25	2.75	1.5	2
5	θ	20	135	25	125	65	90	70

	ℓ	2	1.5	1.75	3.5	0.75	1.25	1.25
6	θ	30	5	135	140	90	120	70
	ℓ	1.5	1.5	3.5	1.5			
	θ	100	55	90	85			
	ℓ	2.5	1.5	2	1.25	1	2.5	5
7	θ	60	130	40	55	125	130	155
	ℓ	2.25	3.5	2	1.25	2.5	3.75	1
8	θ	50	130	25	0	100	0	65
	ℓ	3.25	2	3.5	0.75	1.5	2	1.75
	θ	60	90	75	40	105	150	20
	ℓ	3.5	2	1.5	2	3	1.25	3.75
9	θ	160	70	65	50	25	120	85
	ℓ	5.5	1	1.25	4	1.75	3	2.25
	θ	90	40	0	45	50	35	35
	ℓ	3.25	3.75	2.75	8.25	3.25	2.5	2.75
10	θ	60	125	120	85	35	65	50
	ℓ	2	3	1.25	1	2	2.25	4.5
	θ	0	50	25	60	70	55	90

TABLE 2.10

CRACK DENSITY OF NONLOADED, OVEN DRIED CEMENT PASTE AND MORTAR SPECIMENS

Specimen*	Crack Density, in./in.^{2}	
	Transverse Surface	Longitudinal Surface
1-1/P-0.7/NL	--	18.4
2-1/P-0.7/NL	--	19.9
2-2/P-0.7/NL	--	16.9
3-1/P-0.7/NL	--	19.5
6-1/P-0.7/NL	20.2	19.4
7-1/P-0.7/NL	19.1	17.8
4-1/P-0.5/NL	--	18.9
8-1/P-0.5/NL	22.7	20.6
9-1/P-0.5/NL	20.3	19.8
14-1/P-0.5/NL	21.2	19.1
15-1/P-0.5/NL	22.3	18.5
18-1/P-0.5/NL	21.1	20.8
19-1/P-0.5/NL	18.2	19.5
5-1/P-0.3/NL	--	20.2
10-1/P-0.3/NL	23.7	20.6
11-1/P-0.3/NL	21.2	22.3
16-1/P-0.3/NL	24.1	25.7
17-1/P-0.3/NL	23.3	20.3
20-1/P-0.3/NL	22.5	20.4
21-1/P-0.3/NL	20.3	24.7
12-1/M-0.5/NL	12.0	10.5
13-1/M-0.5/NL	15.2	14.6

* See Appendix A

TABLE 2.11

CRACK DENSITY OF OVEN DRIED SPECIMENS.

MONOTONIC LOADING : CEMENT PASTE WITH A W/C = 0.7

Specimen*	Maximum Strain	Crack Density, in./in.^{2} Transverse Surface	Longitudinal Surface
1-1/P-0.7/NL	0.0	--	18.4
2-1/P-0.7/NL	0.0	--	19.9
2-2/P-0.7/NL	0.0	--	16.9
3-1/P-0.7/NL	0.0	--	19.5
6-1/P-0.7/NL	0.0	20.2	19.4
6-2/P-0.7/M	0.0005	24.0	22.5
6-3/P-0.7/M	0.001	25.2	23.1
6-4/P-0.7/M	0.002	28.3	29.2
6-5/P-0.7/M	0.004	36.5	34.9
7-1/P-0.7/NL	0.0	19.1	17.8
7-2/P-0.7/M	0.0005	24.1	23.2
7-3/P-0.7/M	0.001	26.3	24.6
7-4/P-0.7/M	0.002	32.4	29.5
7-5/P-0.7/M	0.004	41.3	37.6
7-6/P-0.7/M	0.006	43.6	40.9

* See Appendix A

TABLE 2.12

CRACK DENSITY OF OVEN DRIED SPECIMENS.

MONOTONIC LOADING : CEMENT PASTE WITH A W/C = 0.5

Specimen*	Maximum Strain	Crack Density, in./in.^{2} Transverse Surface	Longitudinal Surface
4-1/P-0.5/NL	0.0	--	18.9
4-2/P-0.5/M	0.0005	--	18.3
4-3/P-0.5/M	0.001	--	20.1
4-4/P-0.5/M	0.002	--	27.8
4-5/P-0.5/M	0.004	--	37.6
8-1/P-0.5/NL	0.0	22.7	20.6
8-2/P-0.5/M	0.0005	27.1	21.8
8-3/P-0.5/M	0.001	27.7	24.7
8-4/P-0.5/M	0.002	30.5	28.9
8-5/P-0.5/M	0.004	39.4	30.7
8-6/P-0.5/M	0.006	45.4	43.6
9-1/P-0.5/NL	0.0	20.3	19.8
9-2/P-0.5/M	0.0005	23.6	22.3
9-3/P-0.5/M	0.001	26.2	25.4
9-4/P-0.5/M	0.002	30.2	27.5
9-5/P-0.5/M	0.004	39.4	38.7
9-6/P-0.5/M	0.006	43.5	42.3
14-1/P-0.5/NL	0.0	21.2	19.1
14-2/P-0.5/M	0.004	34.7	29.8
14-3/P-0.5/M	0.006	47.1	42.5
15-1/P-0.5/NL	0.0	22.3	18.5
15-2/P-0.5/M	0.004	35.6	27.2
15-3/P-0.5/M	0.006	41.3	39.4
18-1/P-0.5/NL	0.0	21.1	20.8
18-2/P-0.5/M	0.002	29.6	25.8
18-3/P-0.5/M	0.004	30.3	28.5
19-1/P-0.5/NL	0.0	18.2	19.5
19-2/P-0.5/M	0.002	30.2	27.5
19-3/P-0.5/M	0.004	37.7	32.4

* See Appendix A

TABLE 2.13

CRACK DENSITY OF OVEN DRIED SPECIMENS.

MONOTONIC LOADING : CEMENT PASTE WITH A W/C = 0.3

Specimen*	Maximum Strain	Crack Density, in./in.^{2} Transverse Surface	Longitudinal Surface
5-1/P-0.3/NL	0.0	--	20.2
5-2/P-0.3/M	0.0005	--	20.4
5-3/P-0.3/M	0.001	--	22.8
5-4/P-0.3/M	0.002	--	23.5
5-5/P-0.3/M	0.004	--	31.6
10-1/P-0.3/NL	0.0	23.7	20.6
10-2/P-0.3/M	0.0005	22.8	21.4
10-3/P-0.3/M	0.001	23.9	24.3
10-4/P-0.3/M	0.002	29.4	26.5
10-5/P-0.3/M	0.004	35.2	33.9
11-1/P-0.3/NL	0.0	21.2	22.3
11-2/P-0.3/M	0.0005	23.5	23.4
11-3/P-0.3/M	0.001	25.7	27.4
11-4/P-0.3/M	0.002	26.6	26.2
11-5/P-0.3/M	0.004	37.4	34.3
16-1/P-0.3/NL	0.0	24.1	25.7
16-2/P-0.3/M	0.004	30.6	31.8
16-3/P-0.3/M	0.0058	44.3	39.7
17-1/P-0.3/NL	0.0	23.3	20.3
17-2/P-0.3/M	0.004	33.6	27.8
17-3/P-0.3/M	0.006	47.8	44.0
20-1/P-0.3/NL	0.0	22.5	20.4
20-2/P-0.3/M	0.002	30.4	26.7
20-3/P-0.3/M	0.003	28.9	30.4
21-1/P-0.3/NL	0.0	20.3	24.7
21-2/P-0.3/M	0.0025	25.3	20.1
21-3/P-0.3/M	0.003	31.2	27.5

* See Appendix A

TABLE 2.14

CRACK DENSITY OF OVEN DRIED SPECIMENS.

MONOTONIC LOADING : MORTAR WITH A W/C = 0.5

Specimen*	Maximum Strain	Crack Density, in./in.^{2} Transverse Surface	Longitudinal Surface
12-1/M-0.5/NL	0.0	12.0	10.5
12-2/M-0.5/M	0.0005	17.6	17.1
12-3/M-0.5/M	0.001	23.9	22.1
12-4/M-0.5/M	0.002	33.6	29.3
12-5/M-0.5/M	0.003	32.8	29.6
13-1/M-0.5/NL	0.0	14.6	15.2
13-2/M-0.5/M	0.0005	16.8	27.4
13-3/M-0.5/M	0.001	25.6	28.3
13-4/M-0.5/M	0.002	34.3	26.7
13-5/M-0.5/M	0.003	38.6	35.6
13-6/M-0.5/M	0.004	47.7	43.4

* See Appendix A

TABLE 2.15

CRACK DENSITY OF OVEN DRIED SPECIMENS.

SUSTAINED AND CYCLIC LOADING : CEMENT PASTE WITH W/C = 0.5, 0.3

Specimen*	Maximum Strain	Crack Density, in./in.^{2} Transverse Surface	Longitudinal Surface
14-4/P-0.5/S	0.0039	22.6	27.4
14-5/P-0.5/S	0.0062	34.1	26.7
15-4/P-0.5/S	0.0040	28.6	25.7
15-5/P-0.5/S	0.0059	37.2	35.9
16-4/P-0.3/S	0.0042	38.9	38.4
16-5/P-0.3/S	0.0061	46.8	42.4
17-4/P-0.3/S	0.0039	42.7	37.7
17-5/P-0.3/S	0.0059	46.2	50.5
18-4/P-0.5/C	0.002	28.4	27.3
18-5/P-0.5/C	0.004	40.7	39.4
19-4/P-0.5/C	0.002	34.1	26.5
19-5/P-0.5/C	0.004	41.4	35.2
20-4/P-0.3/C	0.002	32.4	27.8
20-5/P-0.3/C	0.003	49.1	48.6
21-4/P-0.3/C	0.0025	34.2	29.7
21-5/P-0.3/C	0.003	57.8	43.4

* See Appendix A

TABLE 2.16

CRACK DENSITY OF SOLVENT REPLACEMENT DRIED SPECIMENS.

MONOTONIC LOADING : CEMENT PASTE WITH A W/C = 0.5

Specimen*	Maximum Strain	Crack Density, in./in.^{2} Transverse Surface	Longitudinal Surface
8-1/P-0.5/NL	0.0	23.6	25.2
8-2/P-0.5/M	0.0005	26.8	27.3
8-3/P-0.5/M	0.001	28.4	28.1
8-4/P-0.5/M	0.002	32.3	31.6
8-5/P-0.5/M	0.004	41.7	40.5
8-6/P-0.5/M	0.006	53.4	49.4
9-1/P-0.5/M	0.0	22.9	22.5
9-2/P-0.5/M	0.0005	26.2	25.8
9-3/P-0.5/M	0.001	27.5	27.2
9-4/P-0.5/M	0.002	31.4	31.7
9-5/P-0.5/M	0.004	39.6	38.2
9-6/P-0.5/M	0.006	50.7	49.8

* See Appendix A

TABLE 2.17

CRACK DENSITY OF SILICA GEL DRIED SPECIMENS.

MONOTONIC LOADING : CEMENT PASTE WITH A W/C = 0.5

Specimen*	Maximum Strain	Crack Density, in./in.^{2} Transverse Surface	Longitudinal Surface
9-1/P-0.5/NL	0.0	19.4	21.8
9-2/P-0.5/M	0.0005	25.3	23.6
9-3/P-0.5/M	0.001	26.8	26.1
9-4/P-0.5/M	0.002	27.6	27.8
9-5/P-0.5/M	0.004	33.9	31.4
9-6/P-0.5/M	0.006	40.5	37.6

* See Appendix A

TABLE 2.18

AVERAGE CRACK DENSITY OF OVEN DRIED SPECIMENS AT EACH STRAIN.

MONOTONIC LOADING : CEMENT PASTE WITH A W/C = 0.7

Maximum Strain	Crack Density, in./in.^{2} Transverse* Surface	Longitudinal* Surface
0.0	19.7	18.6
0.0005	24.1	22.8
0.001	25.8	23.9
0.002	30.4	29.4
0.004	38.9	36.3
0.006	43.6	40.9

* Each value is an average of two specimens.

TABLE 2.19

AVERAGE CRACK DENSITY OF OVEN DRIED SPECIMENS AT EACH STRAIN.

MONOTONIC LOADING : CEMENT PASTE WITH A W/C = 0.5

Maximum Strain	Crack Density, in./in.^{2} Transverse* Surface	Longitudinal* Surface
0.0	20.6	19.7
0.0005	22.4	22.1
0.001	25.1	25.0
0.002	28.1	27.4
0.004	34.4	33.1
0.006	44.0	42.0

* Each value is an average of three specimens.

TABLE 2.20

AVERAGE CRACK DENSITY OF OVEN DRIED SPECIMENS AT EACH STRAIN.

MONOTONIC LOADING : CEMENT PASTE WITH A W/C = 0.3

Maximum Strain	Crack Density, in./in.^{2} Transverse* Surface	Longitudinal* Surface
0.0	22.5	22.3
0.0005	22.7	22.6
0.001	24.9	25.2
0.002	26.2	25.9
0.003	28.9	30.4
0.004	33.2	32.7
0.006	46.1	44.3

* Each value is an average of three specimens.

TABLE 2.21

AVERAGE CRACK DENSITY OF OVEN DRIED SPECIMENS AT EACH STRAIN.

MONOTONIC LOADING : MORTAR WITH A W/C = 0.5

Maximum Strain	Crack Density, in./in.^{2} Transverse* Surface	Longitudinal* Surface
0.0	13.3	12.9
0.0005	17.2	22.3
0.001	24.8	25.2
0.002	26.2	25.3
0.003	35.7	32.6
0.004	47.7	43.4

* Each value is an average of two specimens.

TABLE 2.22

AVERAGE CRACK DENSITY OF OVEN DRIED SPECIMENS AT EACH STRAIN.

SUSTAINED LOADING

Maximum Strain	Crack Density, in./in.^{2} Transverse* Surface	Longitudinal* Surface
	CEMENT PASTE WITH A W/C = 0.5	
0.004	26.6	25.6
0.006	35.7	33.3
	CEMENT PASTE WITH A W/C = 0.3	
0.004	36.8	35.1
0.006	46.7	46.5

* Each value is an average of two specimens.

TABLE 2.23

AVERAGE CRACK DENSITY OF OVEN DRIED SPECIMENS AT EACH STRAIN.

CYCLIC LOADING

Maximum Strain	Crack Density, in./in.^{2} Transverse* Surface	Longitudinal* Surface
	CEMENT PASTE WITH A W/C = 0.5	
0.002	31.3	26.9
0.004	41.1	37.3
	CEMENT PASTE WITH A W/C = 0.3	
0.002	33.3	28.8
0.003	53.5	46.0

* Each value is an average of two specimens.

TABLE 2.24

AVERAGE CRACK DENSITY BASED ON MICROSCOPIC STRUCTURES.

MONOTONIC LOADING : TRANSVERSE AND LONGITUDINAL SURFACES OF

OVEN DRIED CEMENT PASTE WITH A W/C = 0.7

Maximum Strain	Structure*	Crack Density, in./in.^{2}**		% of Total Crack Density**	
		Transverse	Longitudinal	Transverse	Longitudinal
0.0	III	15.2	14.5	77.2	78.2
	CH-III	2.3	2.2	11.7	11.4
	CH	2.2	1.9	11.1	10.4
0.0005	III	17.9	17.4	74.3	76.3
	CH-III	3.7	3.1	15.3	13.5
	CH	2.5	2.3	10.4	10.2
0.001	III	19.4	18.4	75.2	76.8
	CH-III	3.5	2.8	13.6	11.9
	CH	2.9	2.7	11.2	11.3
0.002	III	25.3	24.9	83.2	84.7
	CH-III	2.7	2.4	8.9	8.2
	CH	2.4	2.1	7.9	7.1
0.004	III	30.8	29.5	79.2	81.3
	CH-III	4.3	3.8	11.0	10.4
	CH	3.8	3.0	9.8	8.3
0.006	III	35.6	34.2	81.7	83.5
	CH-III	4.2	3.7	9.6	9.1
	CH	3.8	3.0	8.7	7.4

* See Section 2.5.4.1 for descriptions of structures.
** Each value is an average of two specimens.

TABLE 2.25

AVERAGE CRACK DENSITY BASED ON MICROSCOPIC STRUCTURES.

MONOTONIC LOADING : TRANSVERSE AND LONGITUDINAL SURFACES OF

OVEN DRIED CEMENT PASTE WITH A W/C = 0.5

Maximum Strain	Structure*	Crack Density, in./in.^{2}**		% of Total Crack Density**	
		Transverse	Longitudinal	Transverse	Longitudinal
0.0	III	17.2	16.2	83.5	82.3
	CH-III	2.1	2.0	10.2	9.9
	CH	1.3	1.5	6.3	7.8
0.0005	III	17.4	16.8	77.7	75.9
	CH-III	2.9	2.9	13.0	12.9
	CH	2.1	2.5	9.3	11.2
0.001	III	21.0	21.2	83.7	84.6
	CH-III	2.0	1.9	8.0	7.6
	CH	2.1	1.9	8.3	7.8
0.002	III	23.9	23.3	85.0	85.1
	CH-III	1.9	1.8	6.8	6.5
	CH	2.3	2.3	8.2	8.4
0.004	III	27.1	25.7	78.8	77.6
	CH-III	3.2	3.4	9.3	10.3
	CH	4.1	4.0	11.9	12.1
0.006	III	34.7	33.4	78.9	79.4
	CH-III	4.9	4.7	11.1	11.2
	CH	4.4	3.9	10.0	9.4

* See Section 2.5.4.1 for descriptions of structures.
** Each value is an average of three specimens.

TABLE 2.26

AVERAGE CRACK DENSITY BASED ON MICROSCOPIC STRUCTURES.

MONOTONIC LOADING : TRANSVERSE AND LONGITUDINAL SURFACES OF

OVEN DRIED CEMENT PASTE WITH A W/C = 0.3

Maximum Strain	Structure*	Crack Density, in./in.^{2}**		% of Total Crack Density**	
		Transverse	Longitudinal	Transverse	Longitudinal
0.0	III	17.4	17.5	77.3	78.4
	CH-III	2.2	1.9	9.8	8.6
	CH	2.7	2.7	12.0	12.1
	UHC-III	0.2	0.2	0.9	0.9
0.0005	III	18.1	17.9	79.7	79.2
	CH-III	2.1	2.3	9.2	10.3
	CH	2.0	2.1	8.8	9.4
	UHC-III	0.3	0.2	1.3	1.1
0.001	III	19.8	21.0	79.5	83.4
	CH-III	2.4	2.0	9.6	8.1
	CH	2.3	1.9	9.3	7.6
	UHC-III	0.4	0.2	1.6	0.9
0.002	III	20.2	19.9	77.1	76.7
	CH-III	3.0	3.2	11.4	12.4
	CH	2.6	2.5	10.0	9.6
	UHC-III	0.4	0.3	1.5	1.3
0.004	III	27.5	26.5	82.9	81.1
	CH-III	2.6	2.9	7.8	8.9
	CH	2.6	2.8	7.8	8.7
	UHC-III	0.5	0.4	1.5	1.3
0.006	III	37.0	35.4	80.2	79.8
	CH-III	4.5	4.7	9.8	10.5
	CH	4.0	3.6	8.7	8.2
	UHC-III	0.6	0.5	1.3	1.2

* See Section 2.5.4.1 for descriptions of structures.
** Each value is an average of three specimens.

TABLE 2.27

AVERAGE CRACK DENSITY BASED ON MICROSCOPIC STRUCTURES.

SUSTAINED AND CYCLIC LOADING : TRANSVERSE AND LONGITUDINAL SURFACES OF OVEN DRIED CEMENT PASTE WITH A W/C = 0.5

Loading Regime	Maximum Strain	Structure*	Crack Density, in./in.^{2}**		% of Total Crack Density**	
			Trans.	Long.	Trans.	Long.
		III	21.8	21.2	82.0	82.7
	0.004	CH-III	2.6	2.6	9.8	10.1
		CH	2.2	1.8	8.2	7.2
Sustained						
		III	27.6	26.4	77.3	79.4
	0.006	CH-III	4.3	3.8	12.0	11.3
		CH	3.8	3.1	10.7	9.3
		III	24.6	21.8	78.6	81.1
	0.002	CH-III	3.3	2.4	10.5	8.8
		CH	3.4	2.7	10.9	10.1
Cyclic						
		III	33.6	31.1	81.8	83.2
	0.004	CH-III	3.9	3.5	9.5	9.5
		CH	3.6	2.7	8.7	7.3

* See Section 2.5.4.1 for descriptions of structures.

** Each value is an average of two specimens.

TABLE 2.28

AVERAGE CRACK DENSITY BASED ON MICROSCOPIC STRUCTURES.

SUSTAINED AND CYCLIC LOADING : TRANSVERSE AND LONGITUDINAL SURFACES OF OVEN DRIED CEMENT PASTE WITH A W/C = 0.3

Loading Regime	Maximum Strain	Structure*	Crack Density, in./in.^{2}**		% of Total Crack Density**	
			Trans.	Long.	Trans.	Long.
		III	30.7	28.2	83.4	80.4
	0.004	CH-III	3.4	3.9	9.2	11.2
		CH	2.2	2.6	6.0	7.2
		UHC-III	0.5	0.4	1.4	1.2
Sustained						
		III	38.9	38.9	83.3	83.6
	0.006	CH-III	3.8	3.7	8.1	8.1
		CH	3.5	3.4	7.5	7.3
		UHC-III	0.5	0.5	1.1	1.0
		III	27.6	24.0	82.9	83.2
	0.002	CH-III	2.9	2.6	8.7	9.1
		CH	2.8	2.2	8.4	7.7
Cyclic						
		III	41.1	36.2	76.8	78.7
	0.003	CH-III	6.2	5.2	11.6	11.2
		CH	5.5	4.1	10.3	9.0
		UHC-III	0.7	0.5	1.3	1.1

* See Section 2.5.4.1 for descriptions of structures.
** Each value is an average of two specimens.

TABLE 2.29

AVERAGE CRACK DENSITY BASED ON MICROSCOPIC STRUCTURES.

MONOTONIC LOADING : TRANSVERSE AND LONGITUDINAL SURFACES OF

OVEN DRIED MORTAR WITH A W/C = 0.5

Maximum Strain	Structure*	Crack Density, in./in.^{2}**		% of Total Crack Density**	
		Transverse	Longitudinal	Transverse	Longitudinal
0.0	III	9.5	9.3	71.4	72.3
	SG-III	2.4	2.2	18.0	16.7
	CH-III	0.8	0.8	6.0	6.1
	CH	0.6	0.6	4.6	4.9
0.0005	III	12.4	16.3	72.1	73.1
	SG-III	2.7	3.6	15.7	16.2
	CH-III	1.0	1.2	5.8	5.3
	CH	1.1	1.2	6.4	5.4
0.001	III	17.6	17.7	71.0	70.5
	SG-III	4.4	4.6	17.7	17.7
	CH-III	1.6	1.7	6.5	6.9
	CH	1.2	1.2	4.8	4.9
0.002	III	20.1	18.0	76.7	71.2
	SG-III	2.5	4.0	9.5	15.8
	CH-III	1.9	1.9	7.3	7.4
	CH	1.7	1.4	6.5	5.6
0.003	III	24.3	22.3	68.1	68.3
	SG-III	6.7	5.9	18.8	18.1
	CH-III	2.5	2.3	7.0	7.2
	CH	2.2	2.1	6.1	6.4
0.004	III	32.0	28.5	67.1	65.8
	SG-III	9.4	8.9	19.7	20.4
	CH-III	3.5	3.3	7.3	7.6
	CH	2.8	2.7	5.9	6.2

* See Section 2.5.4.1 for descriptions of structures.
** Each value is an average of two specimens.

TABLE 2.30

AVERAGE CRACK WIDTH AT EACH STRAIN FOR MONOTONIC, SUSTAINED AND CYCLIC LOADING. OVEN DRIED CEMENT PASTE WITH A W/C = 0.5

Loading Regime	Maximum Strain	Avg. Crack Width, μm* Trans. Surface (Long. Surface)	Width Range, μm Trans. Surface (Long. Surface)
Monotonic	0.0	1.01 (1.03)	0.20-5.50 (0.20-5.50)
	0.0005	0.94 (1.01)	0.20-5.75 (0.20-6.00)
	0.001	1.02 (1.02)	0.20-5.75 (0.20-5.50)
	0.002	1.02 (1.05)	0.20-5.75 (0.20-5.75)
	0.004	1.22 (1.21)	0.20-6.25 (0.20-6.25)
	0.006	1.38 (1.39)	0.20-7.00 (0.20-6.50)
Sustained	0.004	1.21 (1.18)	0.20-6.00 (0.20-6.00)
	0.006	1.37 (1.41)	0.20-6.50 (0.20-6.00)
Cyclic	0.002	1.02 (1.01)	0.20-5.50 (0.20-6.00)
	0.004	1.22 (1.19)	0.20-6.50 (0.20-6.00)

* Each value is an average of three specimens for monotonic loading, and two specimens for sustained and cyclic loading.

1 μm = 0.04×10^{-3} in.

TABLE 2.31

AVERAGE CRACK WIDTH AT EACH STRAIN FOR MONOTONIC, SUSTAINED AND CYCLIC LOADING. OVEN DRIED CEMENT PASTE WITH A W/C = 0.3

Loading Regime	Maximum Strain	Avg. Crack Width, μm* Trans. Surface (Long. Surface)	Width Range, μm Trans. Surface (Long. Surface)
Monotonic	0.0	0.97 (1.01)	0.20-5.00 (0.20-5.00)
	0.0005	1.02 (1.02)	0.20-5.25 (0.20-5.25)
	0.001	1.01 (1.03)	0.20-5.50 (0.20-6.00)
	0.002	1.02 (1.05)	0.20-6.00 (0.20-6.00)
	0.004	1.17 (1.14)	0.20-7.00 (0.20-6.00)
	0.006	1.36 (1.38)	0.20-6.75 (0.20-6.50)
Sustained	0.004	1.21 (1.23)	0.20-6.25 (0.20-6.25)
	0.006	1.35 (1.34)	0.20-7.00 (0.20-7.00)
Cyclic	0.002	1.04 (1.05)	0.20-6.25 (0.20-6.00)
	0.003	1.15 (1.15)	0.20-6.25 (0.20-6.50)

* Each value is an average of three specimens for monotonic loading, and two specimens for sustained and cyclic loading.

1 μm = 0.04×10^{-3} in.

TABLE 2.32

AVERAGE CRACK WIDTH AT EACH STRAIN FOR MONOTONIC, SUSTAINED AND CYCLIC LOADING. SOLVENT REPLACEMENT AND SILICA GEL DRIED CEMENT PASTES WITH A W/C = 0.5

Drying Method	Maximum Strain	Avg. Crack Width, μm* Trans. Surface (Long. Surface)	Width Range, μm Trans. Surface (Long. Surface)
Solvent Replacement	0.0	0.71 (0.75)	0.15-5.00 (0.15-5.00)
	0.0005	0.70 (0.75)	0.20-5.00 (0.20-5.00)
	0.001	0.74 (0.81)	0.15-5.25 (0.20-5.00)
	0.002	0.82 (0.82)	0.15-5.00 (0.15-5.00)
	0.004	0.87 (0.85)	0.15-5.25 (0.15-5.25)
	0.006	0.95 (0.95)	0.15-5.25 (0.15-6.50)
Silica Gel	0.0	0.77 (0.70)	0.25-5.25 (0.25-6.00)
	0.0005	0.81 (0.81)	0.20-5.25 (0.20-5.25)
	0.001	0.94 (0.95)	0.20-5.50 (0.20-5.50)
	0.002	1.01 (1.05)	0.20-5.75 (0.20-5.75)
	0.004	1.10 (1.10)	0.25-6.25 (0.15-6.25)
	0.006	1.21 (1.24)	0.20-5.75 (0.20-6.25)

* Each value is an average of two specimens for solvent replacement drying. The values for silica gel drying are from a single specimen at each strain.

1 μm = 0.04×10^{-3} in.

TABLE 2.33

AVERAGE CRACK WIDTH AT EACH STRAIN FOR MONOTONIC LOADING.

OVEN DRIED MORTAR WITH A W/C = 0.5

Maximum Strain	Avg. Crack Width, μm* Trans. Surface (Long. Surface)	Width Range, μm Trans. Surface (Long. Surface)
0.0	1.04	0.15-5.00
	(1.01)	(0.15-5.00)
0.0005	1.03	0.15-5.00
	(1.07)	(0.15-5.00)
0.001	1.08	0.20-5.50
	(1.11)	(0.15-6.00)
0.002	1.13	0.15-6.00
	(1.09)	(0.15-6.00)
0.003	1.25	0.15-7.50
	(1.27)	(0.15-7.00)
0.004	1.23	0.15-6.75
	(1.28)	(0.15-7.00)

* Each value is an average of two specimens.

1 μm = 0.04×10^{-3} in.

TABLE 3.1

MEAN TRACE LENGTH AND VARIANCE OF CRACK TRACE LENGTH DISTRIBUTION

FOR MONOTONIC LOADING OF CEMENT PASTE WITH A W/C = 0.7

	Transverse Surface		Longitudinal Surface	
Maximum Strain	$\langle \ell \rangle_T$, 10^{-3}in.	$var(\ell)_T$, 10^{-6}in.^{2}	$\langle \ell_\theta \rangle_L^*$, 10^{-3}in.	$var(\ell_\theta)_L^*$, 10^{-6}in.^{2}
0.0	1.54	0.47	1.52	0.67
0.0005	1.55	0.72	1.52	0.59
0.001	1.63	0.54	1.69	1.02
0.002	2.07	1.21	$0.68\times10^{-2}\theta+2.02$	$1.21\times10^{-3}\theta+1.07$
0.004	2.24	1.15	$0.73\times10^{-2}\theta+2.11$	$1.18\times10^{-3}\theta+1.24$
0.006	2.38	1.32	$0.76\times10^{-2}\theta+2.22$	$1.04\times10^{-3}\theta+1.65$

TABLE 3.2

MEAN TRACE LENGTH AND VARIANCE OF CRACK TRACE LENGTH DISTRIBUTION

FOR MONOTONIC LOADING OF CEMENT PASTE WITH A W/C = 0.5

	Transverse Surface		Longitudinal Surface	
Maximum Strain	$\langle \ell \rangle_T$, 10^{-3}in.	$var(\ell)_T$, 10^{-6}in.^{2}	$\langle \ell_\theta \rangle_L^*$, 10^{-3}in.	$var(\ell_\theta)_L^*$, 10^{-6}in.^{2}
0.0	1.49	0.64	1.50	0.71
0.0005	1.49	0.78	1.51	0.68
0.001	1.51	0.66	1.58	0.72
0.002	2.01	1.37	$0.75\times10^{-2}\theta+1.90$	$1.15\times10^{-3}\theta+1.35$
0.004	2.23	0.82	$0.62\times10^{-2}\theta+2.07$	$1.20\times10^{-3}\theta+1.58$
0.006	2.31	1.45	$0.65\times10^{-2}\theta+2.14$	$1.08\times10^{-3}\theta+1.79$

* θ in degrees.

TABLE 3.3

MEAN TRACE LENGTH AND VARIANCE OF CRACK TRACE LENGTH DISTRIBUTION

FOR MONOTONIC LOADING OF CEMENT PASTE WITH A W/C = 0.3

	Transverse Surface		Longitudinal Surface	
Maximum Strain	$\langle \ell \rangle_T$, 10^{-3}in.	$var(\ell)_T$, 10^{-6}in.^{2}	$\langle \ell_\theta \rangle_L^*$, 10^{-3}in.	$var(\ell_\theta)_L^*$, 10^{-6}in.^{2}
0.0	1.48	0.58	1.52	0.55
0.0005	1.51	0.82	1.54	0.71
0.001	1.62	0.71	1.67	0.77
0.002	1.94	0.94	$0.64\times10^{-2}\theta+1.78$	0.96
0.003	1.98	0.91	$0.67\times10^{-2}\theta+1.86$	$1.03\times10^{-3}\theta+1.25$
0.004	2.11	1.33	$0.59\times10^{-2}\theta+1.92$	$1.09\times10^{-3}\theta+1.27$
0.006	2.42	1.24	$0.61\times10^{-2}\theta+2.10$	$1.21\times10^{-3}\theta+1.52$

TABLE 3.4

MEAN TRACE LENGTH AND VARIANCE OF CRACK TRACE LENGTH DISTRIBUTION

FOR MONOTONIC LOADING OF MORTAR WITH A W/C = 0.5

	Transverse Surface		Longitudinal Surface	
Maximum Strain	$\langle \ell \rangle_T$, 10^{-3}in.	$var(\ell)_T$, 10^{-6}in.^{2}	$\langle \ell_\theta \rangle_L^*$, 10^{-3}in.	$var(\ell_\theta)_L^*$, 10^{-6}in.^{2}
0.0	1.21	0.43	1.20	0.47
0.0005	1.53	0.51	1.51	0.49
0.001	1.55	0.64	1.56	0.58
0.002	1.98	1.32	2.13	1.36
0.003	2.06	1.35	$0.65\times10^{-2}\theta+2.05$	$1.05\times10^{-3}\theta+1.41$
0.004	2.25	1.51	$0.70\times10^{-2}\theta+2.08$	$1.22\times10^{-3}\theta+1.53$

* θ in degrees.

TABLE 3.5

MEAN TRACE LENGTH AND VARIANCE OF CRACK TRACE LENGTH DISTRIBUTION

FOR SUSTAINED LOADING OF CEMENT PASTE

	Transverse Surface		Longitudinal Surface	
Maximum Strain	$\langle \ell \rangle_T$, 10^{-3}in.	$var(\ell)_T$, 10^{-6}in.^{2}	$\langle \ell_\theta \rangle_L^*$, 10^{-3}in.	$var(\ell_\theta)_L^*$, 10^{-6}in.^{2}
		CEMENT PASTE WITH A W/C = 0.5		
0.004	1.98	1.23	$0.55\times10^{-2}\theta+1.93$	$1.21\times10^{-3}\theta+1.77$
0.006	2.11	1.24	$0.50\times10^{-2}\theta+1.96$	$1.36\times10^{-3}\theta+1.65$
		CEMENT PASTE WITH A W/C = 0.3		
0.004	1.92	1.22	$0.67\times10^{-2}\theta+1.89$	$1.18\times10^{-3}\theta+1.64$
0.006	2.03	1.25	$0.73\times10^{-2}\theta+1.97$	$1.27\times10^{-3}\theta+1.72$

TABLE 3.6

MEAN TRACE LENGTH AND VARIANCE OF CRACK TRACE LENGTH DISTRIBUTION

FOR CYCLIC LOADING OF CEMENT PASTE

	Transverse Surface		Longitudinal Surface	
Maximum Strain	$\langle \ell \rangle_T$, 10^{-3}in.	$var(\ell)_T$, 10^{-6}in.^{2}	$\langle \ell_\theta \rangle_L^*$, 10^{-3}in.	$var(\ell_\theta)_L^*$, 10^{-6}in.^{2}
		CEMENT PASTE WITH A W/C = 0.5		
0.002	2.03	0.73	$0.80\times10^{-2}\theta+1.95$	1.50
0.004	2.27	1.25	$0.72\times10^{-2}\theta+2.11$	1.70
		CEMENT PASTE WITH A W/C = 0.3		
0.002	1.91	0.80	2.13	0.78
0.0025	1.97	0.75	2.17	0.82
0.003	2.28	1.02	$0.51\times10^{-2}\theta+2.23$	0.91

* θ in degrees.

TABLE 3.7

NUMBER OF CRACKS PER UNIT AREA FOR MONOTONIC LOADING OF CEMENT PASTE WITH A W/C = 0.7

Maximum Strain	Measured, $\bar{M}_T$ or $\bar{M}_L$, and Modified, M_T or M_L, Number of Cracks				Number of Specimen Preparation Cracks
	Transverse Surface		Longitudinal Surface		
	$\bar{M}_T$, in.$^{-2}$	M_T, in.$^{-2}$	$\bar{M}_L$, in.$^{-2}$	M_L, in.$^{-2}$	$\bar{M}_T - M_T$ or $\bar{M}_L - M_L$, in.$^{-2}$
0.0	15584	9610	15564	9590	5974
0.0005	15756	10129	15921	10294	5627
0.001	15961	10491	15477	10007	5470
0.002	16349	11836	15167	10654	4513
0.004	16548	13393	15138	11983	3155
0.006	17684	15336	15671	13323	2348

TABLE 3.8

NUMBER OF CRACKS PER UNIT AREA FOR MONOTONIC LOADING OF CEMENT PASTE WITH A W/C = 0.5

Maximum Strain	Measured, $\bar{M}_T$ or $\bar{M}_L$, and Modified, M_T or M_L, Number of Cracks				Number of Specimen Preparation Cracks
	Transverse Surface		Longitudinal Surface		
	$\bar{M}_T$, in.$^{-2}$	M_T, in.$^{-2}$	$\bar{M}_L$, in.$^{-2}$	M_L, in.$^{-2}$	$\bar{M}_T - M_T$ or $\bar{M}_L - M_L$, in.$^{-2}$
0.0	17123	10811	17051	10739	6312
0.0005	17207	11012	17074	10879	6195
0.001	17434	11505	16765	10836	5929
0.002	17694	12017	17118	11441	5677
0.004	18509	13273	17903	13167	4736
0.006	18900	15887	17711	14698	3013

TABLE 3.9

NUMBER OF CRACKS PER UNIT AREA FOR MONOTONIC LOADING OF CEMENT PASTE WITH A W/C = 0.3

Maximum Strain	Measured, $\bar{M}_T$ or $\bar{M}_L$, and Modified, M_T or M_L, Number of Cracks				Number of Specimen Preparation Cracks
	Transverse Surface		Longitudinal Surface		
	$\bar{M}_T$, in.$^{-2}$	M_T, in.$^{-2}$	$\bar{M}_L$, in.$^{-2}$	M_L, in.$^{-2}$	$\bar{M}_T-M_T$ or $\bar{M}_L-M_L$, in.$^{-2}$
0.0	18497	11959	17825	11287	6538
0.0005	18103	11854	17661	11412	6249
0.001	17362	11235	16643	10516	6127
0.002	17178	11495	16140	10457	5683
0.003	17194	12727	16155	11688	4467
0.004	17016	13175	16090	12249	3841
0.006	19214	16198	18728	15712	3016

TABLE 3.10

NUMBER OF CRACKS PER UNIT AREA FOR MONOTONIC LOADING OF MORTAR WITH A W/C = 0.5

Maximum Strain	Measured, $\bar{M}_T$ or $\bar{M}_L$, and Modified, M_T or M_L, Number of Cracks				Number of Specimen Preparation Cracks
	Transverse Surface		Longitudinal Surface		
	$\bar{M}_T$, in.$^{-2}$	M_T, in.$^{-2}$	$\bar{M}_L$, in.$^{-2}$	M_L, in.$^{-2}$	$\bar{M}_T-M_T$ or $\bar{M}_L-M_L$, in.$^{-2}$
0.0	10931	7686	10923	7678	3245
0.0005	10979	8105	10953	8079	2874
0.001	13243	10710	12982	10449	2533
0.002	14959	12777	13684	11502	2182
0.003	17061	15194	14286	12419	1867
0.004	17449	16178	14286	14335	1271

TABLE 3.11

NUMBER OF CRACKS PER UNIT AREA FOR SUSTAINED LOADING OF CEMENT PASTE

Maximum Strain	Measured, $\bar{M}_T$ or $\bar{M}_L$, and Modified, M_T or M_L, Number of Cracks				Number of Specimen Preparation Cracks
	Transverse Surface		Longitudinal Surface		
	$\bar{M}_T$, in.$^{-2}$	M_T, in.$^{-2}$	$\bar{M}_L$, in.$^{-2}$	M_L, in.$^{-2}$	$\bar{M}_T-M_T$ or $\bar{M}_L-M_L$, in.$^{-2}$
			CEMENT PASTE WITH A W/C = 0.5		
0.004	13168	10303	11714	8849	2865
0.006	14829	12417	13619	11207	2412
			CEMENT PASTE WITH A W/C = 0.3		
0.004	17188	14167	16578	13557	3021
0.006	21040	18126	18256	15342	2914

TABLE 3.12

NUMBER OF CRACKS PER UNIT AREA FOR CYCLIC LOADING OF CEMENT PASTE

Maximum Strain	Measured, $\bar{M}_T$ or $\bar{M}_L$, and Modified, M_T or M_L, Number of Cracks				Number of Specimen Preparation Cracks
	Transverse Surface		Longitudinal Surface		
	$\bar{M}_T$, in.$^{-2}$	M_T, in.$^{-2}$	$\bar{M}_L$, in.$^{-2}$	M_L, in.$^{-2}$	$\bar{M}_T-M_T$ or $\bar{M}_L-M_L$, in.$^{-2}$
			CEMENT PASTE WITH A W/C = 0.5		
0.002	15951	12167	13991	10207	3784
0.004	15836	13304	14304	11772	2532
			CEMENT PASTE WITH A W/C = 0.3		
0.002	15708	11812	14024	10137	3887
0.0025	15721	11827	14036	10142	3894
0.003	19655	16930	19102	16377	2725

TABLE 3.13

SURFACE CRACK DENSITY FOR NONLOADED SPECIMENS OF CEMENT PASTE AND MORTAR

Material	Water-Cement Ratio	Trans. Surface $M_T\langle \ell \rangle_T$, in./in.^{2}	Long. Surface $M_L\langle \ell \rangle_L$, in./in.^{2}
Cement Paste	0.7	14.8	14.7
	0.5	16.2	16.2
	0.3	17.7	17.6
Mortar	0.5	9.3	9.3

TABLE 3.14

SURFACE CRACK DENSITY FOR MONOTONIC LOADING OF CEMENT PASTE AND MORTAR

Maximum Strain	Transverse Surface $M_T\langle \ell \rangle_T$, in./in.^{2}				Longitudinal Surface $M_L\langle \ell \rangle_L$, in./in.^{2}			
	Paste W/C=0.7	Paste W/C=0.5	Paste W/C=0.3	Mortar W/C=0.5	Paste W/C=0.7	Paste W/C=0.5	Paste W/C=0.3	Mortar W/C=0.5
0.0	14.8	16.2	17.7	9.3	14.7	16.2	17.6	9.3
0.0005	15.7	16.5	17.9	12.4	15.5	16.3	17.7	12.2
0.001	17.1	17.3	18.2	16.6	16.8	16.9	17.8	16.3
0.002	24.5	24.0	22.3	25.4	23.6	23.1	21.5	24.5
0.003	--	--	25.2	31.3	--	--	24.1	29.5
0.004	30.0	29.6	27.8	36.1	28.3	27.9	26.8	34.2
0.006	36.5	36.7	39.2	--	34.2	34.3	36.6	--

TABLE 3.15

SURFACE CRACK DENSITY FOR SUSTAINED LOADING OF CEMENT PASTE

Maximum Strain	Transverse Surface $M_T\langle \ell \rangle_T$, in./in.^{2}		Longitudinal Surface $M_L\langle \ell \rangle_L$, in./in.^{2}	
	W/C=0.5	W/C=0.3	W/C=0.5	W/C=0.3
0.004	20.4	27.2	19.6	26.1
0.006	26.2	36.8	24.8	35.2

TABLE 3.16

SURFACE CRACK DENSITY FOR CYCLIC LOADING OF CEMENT PASTE

Maximum Strain	Transverse Surface $M_T\langle \ell \rangle_T$, in./in.^{2}	Longitudinal Surface $M_L\langle \ell \rangle_L$, in./in.^{2}
	CEMENT PASTE WITH A W/C = 0.5	
0.002	24.7	23.9
0.004	30.2	28.8
	CEMENT PASTE WITH A W/C = 0.3	
0.002	22.9	22.1
0.0025	23.3	22.4
0.003	38.6	37.1

TABLE 3.17

THREE-DIMENSIONAL CRACK PARAMETERS FOR NONLOADED SPECIMENS OF CEMENT PASTE AND MORTAR

Material	Water Cement Ratio	K	r	$\langle a_\psi \rangle$, 10^{-3}in	var(a_ψ), 10^{-6}in^2	N_V, 10^6in^{-3}	$N_V\langle a^3 \rangle$
Cement Paste	0.7	-0.02	1.0	1.12	0.70	3.57	0.009
	0.5	0.0	1.0	1.03	0.82	4.63	0.010
	0.3	-0.02	1.0	1.05	0.61	4.89	0.012
Mortar	0.5	0.0	1.0	0.95	0.51	3.22	0.006

TABLE 3.18

THREE-DIMENSIONAL CRACK PARAMETERS FOR MONOTONIC LOADING OF CEMENT PASTE WITH A W/C = 0.7

Maximum Strain	K	r	$\langle a_\psi \rangle^*$, 10^{-3}in.	var(a_ψ)*, 10^{-6}in.^{2}	N_V, 10^6in^{-3}	$N_V\langle a^3 \rangle$
0.0	-0.02	1.0	1.12	0.70	3.57	0.009
0.0005	-0.05	1.0	1.46	0.62	2.91	0.013
0.001	-0.07	1.0	$1.5\times10^{-3}\psi+1.52$	0.90	2.34	0.014
0.002	-0.16	0.92	$1.0\times10^{-2}\psi+1.67$	$1.3\times10^{-3}\psi+1.21$	2.41	0.025
0.004	-0.26	0.95	$1.1\times10^{-2}\psi+2.43$	$1.7\times10^{-3}\psi+1.55$	1.23	0.057
0.006	-0.31	0.90	$1.0\times10^{-2}\psi+2.56$	$1.6\times10^{-3}\psi+2.33$	1.12	0.068

* ψ in degrees.

TABLE 3.19

THREE-DIMENSIONAL CRACK PARAMETERS FOR MONOTONIC LOADING OF CEMENT PASTE WITH A W/C = 0.5

Maximum Strain	K	r	$\langle a_\psi \rangle^*$, 10^{-3}in.	$var(a_\psi)^*$, 10^{-6}in.^{2}	N_V, 10^6in^{-3}	$N_V\langle a^3 \rangle$
0.0	0.00	1.0	1.03	0.82	4.63	0.010
0.0005	-0.07	1.0	1.43	0.77	3.92	0.013
0.001	-0.11	1.0	$1.3\times10^{-3}\psi+1.47$	1.21	3.02	0.015
0.002	-0.16	0.9	$1.0\times10^{-2}\psi+1.69$	$1.6\times10^{-3}\psi+1.43$	2.31	0.022
0.004	-0.27	0.85	$1.0\times10^{-2}\psi+2.35$	$1.5\times10^{-3}\psi+1.71$	1.42	0.053
0.006	-0.30	0.87	$1.2\times10^{-2}\psi+2.50$	$1.8\times10^{-3}\psi+2.10$	1.28	0.076

TABLE 3.20

THREE-DIMENSIONAL CRACK PARAMETERS FOR MONOTONIC LOADING OF CEMENT PASTE WITH A W/C = 0.3

Maximum Strain	K	r	$\langle a_\psi \rangle^*$, 10^{-3}in.	$var(a_\psi)^*$, 10^{-6}in.^{2}	N_V, 10^6in^{-3}	$N_V\langle a^3 \rangle$
0.0	-0.02	1.0	1.05	0.61	4.89	0.012
0.0005	-0.05	1.0	1.36	0.81	4.11	0.015
0.001	-0.09	1.0	1.45	0.88	3.37	0.016
0.002	-0.15	0.95	$0.9\times10^{-2}\psi+1.68$	1.32	2.62	0.021
0.003	-0.18	0.90	$1.0\times10^{-2}\psi+2.08$	1.57	2.13	0.028
0.004	-0.24	0.90	$1.0\times10^{-2}\psi+2.10$	$1.4\times10^{-3}\psi+1.48$	1.67	0.047
0.006	-0.31	0.85	$1.1\times10^{-2}\psi+2.35$	$1.6\times10^{-3}\psi+1.79$	1.42	0.078

* ψ in degrees.

TABLE 3.21

THREE-DIMENSIONAL CRACK PARAMETERS FOR MONOTONIC LOADING OF MORTAR WITH A W/C = 0.5

Maximum Strain	K	r	$\langle a_\psi \rangle^*$, 10^{-3}in.	$var(a_\psi)^*$, 10^{-6}in.^{2}	N_V, 10^6in^{-3}	$N_V\langle a^3 \rangle$
0.0	0.00	1.0	0.95	0.51	3.22	0.006
0.0005	-0.07	1.0	1.27	0.49	2.54	0.010
0.001	-0.08	1.0	1.42	0.78	2.49	0.014
0.002	-0.15	0.95	1.83	1.13	2.31	0.028
0.003	-0.18	1.0	$0.9\times10^{-2}\psi+2.27$	$1.2\times10^{-3}\psi+0.88$	1.33	0.051
0.004	-0.24	0.90	$1.0\times10^{-2}\psi+2.46$	$1.4\times10^{-3}\psi+1.71$	1.28	0.067

TABLE 3.22

THREE-DIMENSIONAL CRACK PARAMETERS FOR SUSTAINED LOADING OF CEMENT PASTE

Maximum Strain	K	r	$\langle a_\psi \rangle^*$, 10^{-3}in.	$var(a_\psi)^*$, 10^{-6}in.^{2}	N_V, 10^6in^{-3}	$N_V\langle a^3 \rangle$
			CEMENT PASTE WITH A W/C = 0.5			
0.004	-0.17	0.95	$0.9\times10^{-2}\psi+2.02$	$1.2\times10^{-3}\psi+1.57$	1.14	0.041
0.006	-0.24	0.90	$1.1\times10^{-2}\psi+2.37$	$1.2\times10^{-3}\psi+1.80$	1.12	0.050
			CEMENT PASTE WITH A W/C = 0.3			
0.004	-0.18	1.0	$1.0\times10^{-2}\psi+2.08$	$0.9\times10^{-3}\psi+1.79$	1.73	0.047
0.006	-0.19	0.92	$1.0\times10^{-2}\psi+2.31$	$1.2\times10^{-3}\psi+1.62$	1.49	0.070

* ψ in degrees.

TABLE 3.23

THREE-DIMENSIONAL CRACK PARAMETERS FOR CYCLIC LOADING OF CEMENT PASTE

Maximum Strain	K	r	$\langle a_\psi \rangle^*$, 10^{-3}in.	$var(a_\psi)^*$, 10^{-6}in.^{2}	N_V, 10^6in.$^{-3}$	$N_V\langle a^3 \rangle$
			CEMENT PASTE WITH A W/C = 0.5			
0.002	-0.14	1.0	$1.0\times10^{-2}\psi+1.65$	0.70	1.71	0.031
0.004	-0.20	1.0	$1.2\times10^{-2}\psi+2.29$	1.28	1.13	0.059
			CEMENT PASTE WITH A W/C = 0.3			
0.002	-0.15	1.0	$0.6\times10^{-2}\psi+2.05$	0.81	1.52	0.032
0.0025	-0.15	1.0	$0.7\times10^{-2}\psi+2.09$	0.78	1.50	0.034
0.003	-0.17	1.0	$0.9\times10^{-2}\psi+2.38$	$1.1\times10^{-3}\psi+1.14$	1.22	0.063

* ψ in degrees.

TABLE 3.24

BOUNDS ON NUMBER OF CRACKS PER UNIT AREA FOR MONOTONIC LOADING OF CEMENT PASTE WITH A W/C = 0.5

Maximum Strain	Transverse Surface: Modified No. of Cracks, M_T, in.$^{-2}$ (No. before Modification, $\bar{M}_T$, in.$^{-2}$)		Longitudinal Surface: Modified No. of Cracks, M_L, in.$^{-2}$ (No. before Modification, $\bar{M}_L$, in.$^{-2}$)	
	Lower Bound	Upper Bound	Lower Bound	Upper Bound
0.00	10764 (16238)	10839 (17546)	10732 (16206)	10788 (17495)
0.0005	10956 (16491)	11048 (17632)	10740 (16275)	10832 (17416)
0.001	11468 (16856)	11566 (18002)	10674 (16062)	10752 (17188)
0.002	11969 (16978)	12037 (18104)	11508 (16517)	11597 (17664)
0.004	14786 (17883)	14885 (19046)	13923 (17020)	13995 (18156)
0.006	18262 (21478)	18418 (22734)	17113 (20329)	17207 (21523)

TABLE 3.25

BOUNDS ON MEAN CHARACTERISTIC CRACK SIZE AND VARIANCE FOR

MONOTONIC LOADING OF CEMENT PASTE WITH W/C = 0.5

Maximum	$\langle a_\psi \rangle^*$, 10^{-3}in.		$var(a_\psi)^*$, 10^{-6}in.^{2}	
Strain	Lower Bound	Upper Bound	Lower Bound	Upper Bound
0.00	1.03	1.03	0.82	0.82
0.0005	1.42	1.43	0.87	0.84
0.001	$1.3\times10^{-3}\psi+1.45$	$1.3\times10^{-2}\psi+1.48$	1.05	1.25
0.002	$1.0\times10^{-2}\psi+1.66$	$1.0\times10^{-2}\psi+1.03$	$1.6\times10^{-3}\psi+1.38$	$1.6\times10^{-3}\psi+1.45$
0.004	$1.0\times10^{-2}\psi+2.33$	$1.0\times10^{-2}\psi+2.36$	$1.5\times10^{-3}\psi+1.70$	$1.5\times10^{-3}\psi+1.74$
0.006	$1.2\times10^{-2}\psi+2.47$	$1.2\times10^{-2}\psi+2.52$	$1.8\times10^{-3}\psi+2.08$	$1.8\times10^{-3}\psi+2.30$

* ψ in degrees.

TABLE 3.26

THREE-DIMENSIONAL CRACK PARAMETERS : MULTI-DIRECTIONAL CRACK TRACES

TREATED AS SINGLE UNI-DIRECTIONAL TRACES.

NONLOADED SPECIMENS OF CEMENT PASTE AND MORTAR

Material	Water Cement Ratio	K	r	$\langle a_\psi \rangle$, 10^{-3}in	$var(a_\psi)$, 10^{-6}in^2	N_V, 10^6in^{-3}	$N_V\langle a^3 \rangle$
Cement Paste	0.7	-0.02	1.0	1.58	0.73	1.73	0.014
	0.5	0.0	1.0	1.50	0.84	2.32	0.015
	0.3	-0.02	1.0	1.51	0.63	2.41	0.017
Mortar	0.5	0.0	1.0	1.35	0.55	1.54	0.008

TABLE 3.27

THREE-DIMENSIONAL CRACK PARAMETERS : MULTI-DIRECTIONAL CRACK TRACES TREATED AS SINGLE UNI-DIRECTIONAL TRACES.

MONOTONIC LOADING OF CEMENT PASTE WITH A W/C = 0.7

Maximum Strain	K	r	$\langle a_\psi \rangle^*$, 10^{-3}in.	$var(a_\psi)^*$, 10^{-6}in.^{2}	N_V, 10^6in^{-3}	$N_V\langle a^3 \rangle$
0.0	-0.02	1.0	1.58	0.73	1.73	0.014
0.0005	-0.05	1.0	2.10	0.64	1.40	0.020
0.001	-0.07	1.0	$1.5\times10^{-3}\psi+2.16$	0.93	1.12	0.021
0.002	-0.16	0.92	$1.0\times10^{-2}\psi+2.23$	$1.3\times10^{-3}\psi+1.26$	1.19	0.036
0.004	-0.26	0.95	$1.1\times10^{-2}\psi+3.47$	$1.7\times10^{-3}\psi+1.58$	0.63	0.082
0.006	-0.31	0.90	$1.0\times10^{-2}\psi+3.68$	$1.6\times10^{-3}\psi+2.37$	0.51	0.097

TABLE 3.28

THREE-DIMENSIONAL CRACK PARAMETERS : MULTI-DIRECTIONAL CRACK TRACES TREATED AS SINGLE UNI-DIRECTIONAL TRACES.

MONOTONIC LOADING OF CEMENT PASTE WITH A W/C = 0.5

Maximum Strain	K	r	$\langle a_\psi \rangle^*$, 10^{-3}in.	$var(a_\psi)^*$, 10^{-6}in.^{2}	N_V, 10^6in^{-3}	$N_V\langle a^3 \rangle$
0.0	0.00	1.0	1.50	0.84	2.32	0.015
0.0005	-0.07	1.0	2.06	0.83	1.91	0.020
0.001	-0.11	1.0	$1.3\times10^{-3}\psi+2.12$	1.25	1.38	0.024
0.002	-0.16	0.9	$1.0\times10^{-2}\psi+2.27$	$1.6\times10^{-3}\psi+1.47$	1.03	0.033
0.004	-0.27	0.85	$1.0\times10^{-2}\psi+3.13$	$1.5\times10^{-3}\psi+1.75$	0.72	0.076
0.006	-0.30	0.87	$1.2\times10^{-2}\psi+3.60$	$1.8\times10^{-3}\psi+2.14$	0.68	0.105

* ψ in degrees.

TABLE 3.29

THREE-DIMENSIONAL CRACK PARAMETERS : MULTI-DIRECTIONAL CRACK TRACES TREATED AS SINGLE UNI-DIRECTIONAL TRACES.

MONOTONIC LOADING OF CEMENT PASTE WITH A W/C = 0.3

Maximum Strain	K	r	$\langle a_\psi \rangle^*$, 10^{-3}in.	$var(a_\psi)^*$, 10^{-6}in.^{2}	N_V, 10^6in^{-3}	$N_V\langle a^3 \rangle$
0.0	-0.02	1.0	1.51	0.63	2.41	0.017
0.0005	-0.05	1.0	1.96	0.85	1.93	0.021
0.001	-0.09	1.0	2.09	0.92	1.41	0.024
0.002	-0.15	0.95	$0.9\times10^{-2}\psi+2.27$	1.36	1.32	0.031
0.003	-0.18	0.90	$1.0\times10^{-2}\psi+2.75$	1.57	1.14	0.042
0.004	-0.24	0.90	$1.0\times10^{-2}\psi+3.01$	$1.4\times10^{-3}\psi+1.53$	0.92	0.071
0.006	-0.31	0.85	$1.1\times10^{-2}\psi+3.56$	$1.6\times10^{-3}\psi+1.84$	0.81	0.109

TABLE 3.30

THREE-DIMENSIONAL CRACK PARAMETERS : MULTI-DIRECTIONAL CRACK TRACES TREATED AS SINGLE UNI-DIRECTIONAL TRACES.

MONOTONIC LOADING OF MORTAR WITH A W/C = 0.5

Maximum Strain	K	r	$\langle a_\psi \rangle^*$, 10^{-3}in.	$var(a_\psi)^*$, 10^{-6}in.^{2}	N_V, 10^6in^{-3}	$N_V\langle a^3 \rangle$
0.0	0.00	1.0	1.35	0.55	1.54	0.008
0.0005	-0.07	1.0	2.08	0.54	1.22	0.018
0.001	-0.08	1.0	2.14	0.82	1.19	0.022
0.002	-0.15	0.95	2.54	1.16	1.13	0.040
0.003	-0.18	1.0	$0.9\times10^{-2}\psi+3.21$	$1.2\times10^{-3}\psi+0.92$	0.71	0.072
0.004	-0.24	0.90	$1.0\times10^{-2}\psi+3.52$	$1.4\times10^{-3}\psi+1.74$	0.60	0.088

* ψ in degrees.

TABLE 3.31

THREE-DIMENSIONAL CRACK PARAMETERS : MULTI-DIRECTIONAL CRACK TRACES TREATED AS SINGLE UNI-DIRECTIONAL TRACES.

SUSTAINED LOADING OF CEMENT PASTE

Maximum Strain	K	r	$\langle a_\psi \rangle^*$, 10^{-3}in.	$var(a_\psi)^*$, 10^{-6}in.^{2}	N_V, 10^6in^{-3}	$N_V\langle a^3 \rangle$
			CEMENT PASTE WITH A W/C = 0.5			
0.004	-0.17	0.95	$0.9\times10^{-2}\psi+2.89$	$1.2\times10^{-3}\psi+1.61$	0.62	0.063
0.006	-0.24	0.90	$1.1\times10^{-2}\psi+3.41$	$1.2\times10^{-3}\psi+1.83$	0.51	0.072
			CEMENT PASTE WITH A W/C = 0.3			
0.004	-0.18	1.0	$1.0\times10^{-2}\psi+2.89$	$0.9\times10^{-3}\psi+1.82$	0.84	0.070
0.006	-0.19	0.92	$1.0\times10^{-2}\psi+3.32$	$1.2\times10^{-3}\psi+1.64$	0.73	0.099

TABLE 3.32

THREE-DIMENSIONAL CRACK PARAMETERS : MULTI-DIRECTIONAL CRACK TRACES TREATED AS SINGLE UNI-DIRECTIONAL TRACES.

CYCLIC LOADING OF CEMENT PASTE

Maximum Strain	K	r	$\langle a_\psi \rangle^*$, 10^{-3}in.	$var(a_\psi)^*$, 10^{-6}in.^{2}	N_V, 10^6in^{-3}	$N_V\langle a^3 \rangle$
			CEMENT PASTE WITH A W/C = 0.5			
0.002	-0.14	1.0	$1.0\times10^{-2}\psi+2.39$	0.73	0.91	0.044
0.004	-0.20	1.0	$1.2\times10^{-2}\psi+3.38$	1.33	0.52	0.083
			CEMENT PASTE WITH A W/C = 0.3			
0.002	-0.15	1.0	$0.6\times10^{-2}\psi+2.97$	0.85	0.74	0.045
0.0025	-0.15	1.0	$0.7\times10^{-2}\psi+3.01$	0.84	0.71	0.049
0.003	-0.17	1.0	$0.9\times10^{-2}\psi+3.39$	$1.1\times10^{-3}\psi+1.17$	0.62	0.091

* ψ in degrees.

TABLE 3.33

COMPARISONS OF CRACK DENSITIES AND DEGREE OF ANISOTROPY FOR CRACK DISTRIBUTIONS IN CEMENT PASTES UNDER MONOTONIC LOADING. RESULTS CORRESPOND TO LARGER ESTIMATE OF $\langle a_\psi \rangle$

Maximum Strain	Surface Crack Density, $M_T\langle \ell \rangle_T$, in./in.^{2} ($M_L\langle \ell \rangle_L$)			Volume Density, $N_V\langle a^3 \rangle$			Degree of Anisotropy, K		
	W/C			W/C			W/C		
	0.7	0.5	0.3	0.7	0.5	0.3	0.7	0.5	0.3
0.0	14.8 (14.7)	16.2 (16.2)	17.7 (17.6)	.014	.015	.017	-.02	.0	-.02
0.0005	15.7 (15.5)	16.5 (16.3)	17.9 (17.7)	.020	.020	.021	-.05	-.07	-.05
0.001	17.1 (16.8)	17.3 (16.9)	18.2 (17.8)	.021	.024	.024	-.07	-.11	-.09
0.002	24.5 (23.6)	24.0 (23.1)	22.3 (21.5)	.036	.033	.031	-.16	-.16	-.15
0.004	30.0 (28.3)	29.6 (27.9)	27.8 (26.8)	.082	.076	.071	-.26	-.27	-.24
0.006	36.5 (34.2)	36.7 (34.3)	39.2 (36.6)	.097	.105	.109	-.29	-.30	-.31

TABLE 3.34

COMPARISONS OF CRACK DENSITIES AND DEGREE OF ANISOTROPY FOR CRACK DISTRIBUTIONS IN CEMENT PASTE AND MORTAR WITH A W/C = 0.5. MONOTONIC LOADING. RESULTS CORRESPOND TO LARGER ESTIMATE OF $\langle a_\psi \rangle$.

Maximum Strain	Surface Crack Density, $M_T\langle \ell \rangle_T$, in./in.^{2} ($M_L\langle \ell \rangle_L$)		Volume Density, $N_V\langle a^3 \rangle$		Degree of Anisotropy, K	
	Paste	Mortar	Paste	Mortar	Paste	Mortar
0.0	16.2	9.3	.015	.008	.0	.0
	(16.2)	(9.3)				
0.0005	16.5	12.4	.020	.018	-.07	-.07
	(16.3)	(12.2)				
0.001	17.3	16.6	.024	.022	-.11	-.08
	(16.9)	(16.3)				
0.002	24.0	25.4	.033	.040	-.16	-.15
	(23.1)	(24.5)				
0.004	29.6	36.1	.076	.088	-.27	-.24
	(27.9)	(34.2)				

TABLE 3.35

COMPARISONS OF CRACK DENSITIES AND DEGREE OF ANISOTROPY FOR CRACK DISTRIBUTIONS IN CEMENT PASTE UNDER MONOTONIC AND SUSTAINED LOADING. RESULTS CORRESPOND TO LARGER ESTIMATE OF $\langle a_\psi \rangle$.

Maximum Strain	Surface Crack Density, $M_T\langle \ell \rangle_T$, in./in.^{2} ($M_L\langle \ell \rangle_L$)		Volume Density, $N_V\langle a^3 \rangle$		Degree of Anisotropy, K	
	Monotonic	Sustained	Monotonic	Sustained	Monotonic	Sustained
			CEMENT PASTE WITH A W/C = 0.5			
0.004	29.6 (27.9)	20.4 (19.6)	.076	.063	-.27	-.17
0.006	36.7 (34.3)	26.2 (24.8)	.105	.072	-.30	-.24
			CEMENT PASTE WITH A W/C = 0.3			
0.004	27.8 (26.8)	27.2 (26.1)	.071	.070	-.24	-.18
0.006	39.2 (36.6)	36.8 (35.2)	.109	.099	-.31	-.19

TABLE 3.36

COMPARISONS OF CRACK DENSITIES AND DEGREE OF ANISOTROPY FOR CRACK DISTRIBUTIONS IN CEMENT PASTE UNDER MONOTONIC AND CYCLIC LOADING. RESULTS CORRESPOND TO LARGER ESTIMATE OF $\langle a_\psi \rangle$.

Maximum Strain	Surface Crack Density, $M_T\langle \ell \rangle_T$, in./in.^{2} ($M_L\langle \ell \rangle_L$)		Volume Density, $N_V\langle a^3 \rangle$		Degree of Anisotropy, K	
	Monotonic	Cyclic	Monotonic	Cyclic	Monotonic	Cyclic
			CEMENT PASTE WITH A W/C = 0.5			
0.002	24.0 (23.1)	24.7 (23.9)	.033	.044	-.16	-.14
0.004	29.6 (27.9)	30.2 (28.8)	.076	.083	-.27	-.20
			CEMENT PASTE WITH A W/C = 0.3			
0.002	22.3 (21.5)	23.3 (22.4)	.031	.045	-.15	-.15
0.003	25.2 (24.1)	38.6 (37.1)	.042	.091	-.18	-.17

TABLE 4.1

SENSITIVITY OF THE STIFFNESS MODULUS, E_3, TO VARIATIONS IN CRACK PARAMETERS.

$\langle a_\psi \rangle = 1.0\times10^{-5}\psi + 5.0\times10^{-3}$ in. $\quad r = 0.9$

$var(a_\psi) = 1.0\times10^{-9}\psi + 1.0\times10^{-6}$ in.^{2} $\quad K = -0.3$

$N_V = 4\times10^{5}$ in.$^{-3}$ $\quad \eta = 0°$

Crack Parameter	% Increase in Crack Parameter				
	0	5	10	20	30
			E_3/E		
$\langle a_\psi \rangle$	0.827	0.779	0.731	0.650	0.531
$var(a_\psi)$	0.827	0.818	0.784	0.740	0.713
N_V	0.827	0.820	0.798	0.764	0.741

	% Decrease in Crack Parameter				
	0	5	10	20	30
			E_3/E		
r	0.827	0.849	0.875	0.893	0.914

	Range of η			
	$\eta = 0°$	$-10° \leq \eta \leq 10°$	$-45° \leq \eta \leq 45°$	$-90° \leq \eta \leq 90°$
			E_3/E	
η	0.827	0.820	0.797	0.768

TABLE 5.1

EFFECTIVE MODULI AND AXIAL STRAIN DUE TO SUBMICROCRACKING FOR MONOTONIC LOADING OF CEMENT PASTE WITH A W/C = 0.7.

FIRST APPROACH*; DRY CRACKS.

$E_i = 1.78\times10^6$ psi; $\nu_i = 0.24$

ε	σ, psi	$E_3, 10^6$ psi	$\frac{E_3}{E_i}$	ν_{31}	$\varepsilon_{ec}=\frac{\sigma}{E_3}$	$\varepsilon_c=\sigma\left(\frac{E_i-E_3}{E_iE_3}\right)$	$\frac{\varepsilon_c}{\varepsilon-\varepsilon_e}$, %
RESULTS CORRESPONDING TO SMALLER ESTIMATE OF $\langle a_\psi \rangle$.							
		$E = 1.816\times10^6$ psi; $\nu = 0.242$					
.0005	830	1.767	.9921	.240	.000469	.000004	11.1
.001	1581	1.763	.9899	.240	.000897	.000013	10.5
.002	2657	1.752	.9837	.241	.001516	.000058	10.0
.004	3740	1.633	.9169	.245	.002290	.000189	9.9
.006	4070	1.564	.8782	.248	.002602	.000315	8.5
RESULTS CORRESPONDING TO LARGER ESTIMATE OF $\langle a_\psi \rangle$.							
		$E = 1.837\times10^6$ psi; $\nu = 0.243$					
.0005	830	1.763	.9899	.241	.000471	.000006	16.7
.001	1581	1.758	.9871	.241	.000899	.000016	14.5
.002	2657	1.750	.9826	.242	.001518	.000061	12.0
.004	3740	1.578	.8860	.246	.002370	.000269	14.2
.006	4070	1.512	.8490	.249	.002692	.000405	10.9

* Cracks are assumed to exist in the specimens prior to loading.

TABLE 5.2

EFFECTIVE MODULI AND AXIAL STRAIN DUE TO SUBMICROCRACKING FOR MONOTONIC LOADING OF CEMENT PASTE WITH A W/C = 0.5.

FIRST APPROACH*; DRY CRACKS.

$E_i = 2.54\times10^6$ psi; $\nu_i = 0.24$

ε	σ, psi	$E_3, 10^6$ psi	$\frac{E_3}{E_i}$	ν_{31}	$\varepsilon_{ec}=\frac{\sigma}{E_3}$	$\varepsilon_c=\sigma\left(\frac{E_i-E_3}{E_iE_3}\right)$	$\frac{\varepsilon_c}{\varepsilon-\varepsilon_e}$, %

RESULTS CORRESPONDING TO SMALLER ESTIMATE OF $\langle a_\psi \rangle$.

$E = 2.590\times10^6$ psi; $\nu = 0.242$

.0005	1195	2.520	.9921	.240	.000474	.000004	14.0
.001	2310	2.515	.9902	.240	.000918	.000009	12.5
.002	4128	2.499	.9839	.240	.001652	.000027	12.7
.004	6036	2.328	.9165	.243	.002593	.000217	11.8
.006	6687	2.230	.8780	.245	.002999	.000366	10.9

RESULTS CORRESPONDING TO LARGER ESTIMATE OF $\langle a_\psi \rangle$.

$E = 2.620\times10^6$ psi; $\nu = 0.243$

.0005	1195	2.515	.9894	.240	.000475	.000005	18.1
.001	2310	2.507	.9862	.240	.000921	.000012	16.8
.002	4128	2.490	.9795	.241	.001658	.000033	15.7
.004	6036	2.309	.8855	.244	.002614	.000238	14.6
.006	6687	2.156	.8482	.253	.003102	.000469	13.9

* Cracks are assumed to exist in the specimens prior to loading.

TABLE 5.3

EFFECTIVE MODULI AND AXIAL STRAIN DUE TO SUBMICROCRACKING FOR MONOTONIC LOADING OF CEMENT PASTE WITH A W/C = 0.3.

FIRST APPROACH*; DRY CRACKS.

$E_i = 3.31\times10^6$ psi; $\nu_i = 0.24$

ε	σ, psi	$E_3, 10^6$ psi	$\frac{E_3}{E_i}$	ν_{31}	$\varepsilon_{ec}=\frac{\sigma}{E_3}$	$\varepsilon_c=\sigma\left(\frac{E_i-E_3}{E_iE_3}\right)$	$\frac{\varepsilon_c}{\varepsilon-\varepsilon_e}$, %
RESULTS CORRESPONDING TO SMALLER ESTIMATE OF $\langle a_\psi \rangle$.							
		$E = 3.385\times10^6$ psi; $\nu = 0.242$					
.0005	1581	3.294	.9953	.240	.000480	.000016	72.9
.001	3137	3.287	.9931	.239	.000954	.000037	69.1
.002	6051	3.268	.9872	.239	.001851	.000080	46.5
.003	8195	3.155	.9533	.241	.002597	.000204	38.5
.004	9860	3.044	.9197	.244	.003239	.000360	35.2
.006	11503	2.915	.8807	.246	.003946	.000592	23.4
RESULTS CORRESPONDING TO LARGER ESTIMATE OF $\langle a_\psi \rangle$.							
		$E = 3.423\times10^6$ psi; $\nu = 0.243$					
.0005	1581	3.288	.9935	.240	.000481	.000017	76.7
.001	3137	3.280	.9910	.241	.000956	.000039	72.3
.002	6051	3.264	.9860	.241	.001854	.000083	48.2
.003	8195	3.105	.9380	.242	.002639	.000248	46.8
.004	9860	2.942	.8890	.245	.003351	.000476	46.6
.006	11503	2.819	.8518	.254	.004080	.000605	28.9

* Cracks are assumed to exist in the specimens prior to loading.

TABLE 5.4

EFFECTIVE MODULI AND AXIAL STRAIN DUE TO SUBMICROCRACKING FOR MONOTONIC LOADING OF MORTAR WITH A W/C = 0.5.

FIRST APPROACH*; DRY CRACKS.

$E_i = 4.79\times10^6$ psi; $\nu_i = 0.20$

ε	σ, psi	$E_3, 10^6$ psi	$\frac{E_3}{E_i}$	ν_{31}	$\varepsilon_{ec}=\frac{\sigma}{E_3}$	$\varepsilon_c=\sigma\left(\frac{E_i-E_3}{E_iE_3}\right)$	$\frac{\varepsilon_c}{\varepsilon-\varepsilon_e}$, %

RESULTS CORRESPONDING TO SMALLER ESTIMATE OF $\langle a_\psi \rangle$.

$E = 4.838\times10^6$ psi; $\nu = 0.201$

.0005	2205	4.731	.9877	.198	.000466	.000006	14.5
.001	3697	4.698	.9808	.198	.000787	.000015	6.7
.002	5398	4.644	.9695	.199	.001162	.000035	4.1
.003	5804	4.403	.9192	.205	.001318	.000106	5.9
.004	4066	4.209	.8787	.208	.000966	.000117	3.7

RESULTS CORRESPONDING TO LARGER ESTIMATE OF $\langle a_\psi \rangle$.

$E = 4.874\times10^6$ psi; $\nu = 0.202$

.0005	2205	4.718	.9844	.199	.000467	.000007	17.7
.001	3697	4.664	.9731	.199	.000793	.000021	9.3
.002	5398	4.628	.9656	.200	.001166	.000039	8.9
.003	5804	4.216	.8796	.207	.001377	.000165	9.2
.004	4066	4.060	.8471	.218	.001002	.000153	4.8

* Cracks are assumed to exist in the specimens prior to loading.

TABLE 5.5

EFFECTIVE MODULI AND AXIAL STRAIN DUE TO SUBMICROCRACKING FOR MONOTONIC LOADING OF CEMENT PASTE WITH A W/C = 0.7.

FIRST APPROACH*; SATURATED CRACKS.

$E_i = 1.78\times10^6$ psi; $\nu_i = 0.24$

RESULTS CORRESPONDING TO LARGER ESTIMATE OF $\langle a_\psi \rangle$.

$E = 1.812\times10^6$ psi; $\nu = 0.235$

ε	σ, psi	$E_3, 10^6$ psi	$\frac{E_3}{E_i}$	ν_{31}	$\varepsilon_{ec} = \frac{\sigma}{E_3}$	$\varepsilon_c = \sigma\left(\frac{E_i - E_3}{E_i E_3}\right)$	$\frac{\varepsilon_c}{\varepsilon - \varepsilon_e}$, %
.0005	830	1.768	.9927	.243	.000469	.000004	11.1
.001	1581	1.764	.9905	.244	.000896	.000013	11.8
.002	2657	1.755	.9854	.248	.001514	.000057	11.2
.004	3740	1.645	.9236	.262	.002274	.000173	9.1
.006	4070	1.600	.8984	.267	.002544	.000257	6.9

TABLE 5.6

EFFECTIVE MODULI AND AXIAL STRAIN DUE TO SUBMICROCRACKING FOR MONOTONIC LOADING OF CEMENT PASTE WITH A W/C = 0.5.

FIRST APPROACH*; SATURATED CRACKS.

$E_i = 2.54\times10^6$ psi; $\nu_i = 0.24$

RESULTS CORRESPONDING TO LARGER ESTIMATE OF $\langle a_\psi \rangle$.

$E = 2.590\times10^6$ psi; $\nu = 0.235$

ε	σ, psi	$E_3, 10^6$ psi	$\frac{E_3}{E_i}$	ν_{31}	$\varepsilon_{ec} = \frac{\sigma}{E_3}$	$\varepsilon_c = \sigma\left(\frac{E_i - E_3}{E_i E_3}\right)$	$\frac{\varepsilon_c}{\varepsilon - \varepsilon_e}$, %
.0005	1195	2.528	.9945	.241	.000473	.000003	10.9
.001	2310	2.523	.9925	.242	.000916	.000007	9.8
.002	4128	2.512	.9882	.244	.001643	.000020	9.5
.004	6036	2.352	.9253	.250	.002566	.000170	9.4
.006	6687	2.287	.8992	.261	.002924	.000291	8.6

* Cracks are assumed to exist in the specimens prior to loading.

TABLE 5.7

EFFECTIVE MODULI AND AXIAL STRAIN DUE TO SUBMICROCRACKING FOR MONOTONIC LOADING OF CEMENT PASTE WITH A W/C = 0.3.

FIRST APPROACH*; SATURATED CRACKS.

$E_i = 3.31\times10^6$ psi; $\nu_i = 0.24$

ε	σ, psi	$E_3, 10^6$ psi	$\frac{E_3}{E_i}$	ν_{31}	$\varepsilon_{ec}=\frac{\sigma}{E_3}$	$\varepsilon_c=\sigma(\frac{E_i-E_3}{E_iE_3})$	$\frac{\varepsilon_c}{\varepsilon-\varepsilon_e}$, %

RESULTS CORRESPONDING TO LARGER ESTIMATE OF $\langle a_\psi \rangle$.

$E = 3.377\times10^6$ psi; $\nu = 0.235$

.0005	1581	3.297	.9960	.242	.000480	.000016	72.9
.001	3137	3.290	.9938	.243	.000954	.000037	69.1
.002	6051	3.276	.9897	.245	.001847	.000076	44.1
.003	8195	3.169	.9573	.248	.002586	.000195	36.8
.004	9860	3.067	.9265	.256	.003215	.000340	33.3
.006	11502	2.978	.8997	.263	.003863	.000388	18.5

TABLE 5.8

EFFECTIVE MODULI AND AXIAL STRAIN DUE TO SUBMICROCRACKING FOR MONOTONIC LOADING OF MORTAR WITH A W/C = 0.5.

FIRST APPROACH*; SATURATED CRACKS.

$E_i = 4.79\times10^6$ psi; $\nu_i = 0.20$

ε	σ, psi	$E_3, 10^6$ psi	$\frac{E_3}{E_i}$	ν_{31}	$\varepsilon_{ec}=\frac{\sigma}{E_3}$	$\varepsilon_c=\sigma(\frac{E_i-E_3}{E_iE_3})$	$\frac{\varepsilon_c}{\varepsilon-\varepsilon_e}$, %

RESULTS CORRESPONDING TO LARGER ESTIMATE OF $\langle a_\psi \rangle$.

$E = 4.858\times10^6$ psi; $\nu = 0.196$

.0005	2205	4.761	.9933	.203	.000463	.000003	7.6
.001	3697	4.731	.9871	.209	.000781	.000016	7.1
.002	5398	4.716	.9839	.214	.001145	.000018	4.1
.003	5804	4.460	.9305	.221	.001301	.000089	5.0
.004	4066	4.285	.9051	.227	.000949	.000100	3.1

* Cracks are assumed to exist in the specimens prior to loading.

TABLE 5.9

EFFECTIVE MODULI FOR MONOTONIC LOADING OF CEMENT PASTE, W/C = 0.7.

SECOND APPROACH*; DRY CRACKS.

$E = E_i = 1.78 \times 10^6$ psi; $\nu = \nu_i = 0.24$

ε	σ, psi	E_3, 10^6psi	ν_{31}
RESULTS CORRESPONDING TO LARGER ESTIMATE OF $\langle a_\psi \rangle$.			
.0005	830	1.766	.239
.001	1581	1.760	.240
.002	2657	1.752	.241
.004	3740	1.587	.245
.006	4070	1.523	.248

TABLE 5.10

EFFECTIVE MODULI FOR MONOTONIC LOADING OF CEMENT PASTE, W/C = 0.5.

SECOND APPROACH*; DRY CRACKS.

$E = E_i = 2.54 \times 10^6$ psi; $\nu = \nu_i = 0.24$

ε	σ, psi	E_3, 10^6psi	ν_{31}
RESULTS CORRESPONDING TO LARGER ESTIMATE OF $\langle a_\psi \rangle$.			
.0005	1195	2.518	.240
.001	2310	2.510	.240
.002	4128	2.498	.241
.004	6036	2.322	.243
.006	6687	2.172	.252

* Cracks are assumed not to exist in the specimens prior to loading.

TABLE 5.11

EFFECTIVE MODULI FOR MONOTONIC LOADING OF CEMENT PASTE, W/C = 0.3.

SECOND APPROACH*; DRY CRACKS.

$E = E_i = 3.31 \times 10^6$ psi; $\nu = \nu_i = 0.24$

ε	σ, psi	E_3, 10^6psi	ν_{31}
RESULTS CORRESPONDING TO LARGER ESTIMATE OF $\langle a_\psi \rangle$.			
.0005	1581	3.289	.240
.001	3137	3.277	.240
.002	6051	3.259	.241
.003	8195	3.108	.242
.004	9860	2.950	.244
.006	11503	2.832	.253

TABLE 5.12

EFFECTIVE MODULI FOR MONOTONIC LOADING OF MORTAR, W/C = 0.5.

SECOND APPROACH*; DRY CRACKS.

$E = E_i = 4.79 \times 10^6$ psi; $\nu = \nu_i = 0.20$

ε	σ, psi	E_3, 10^6psi	ν_{31}
RESULTS CORRESPONDING TO LARGER ESTIMATE OF $\langle a_\psi \rangle$.			
.0005	2205	4.721	.200
.001	3697	4.669	.200
.002	5398	4.635	.201
.003	5804	4.220	.205
.004	4066	4.112	.214

* Cracks are assumed not to exist in the specimens prior to loading.

TABLE 5.13

MODULI OF INELASTIC MATRIX AND STRAIN DUE TO SUBMICROCRACKING FOR MONOTONIC LOADING OF CEMENT PASTE WITH A W/C = 0.7. FIRST APPROACH*. RESULTS CORRESPOND TO LARGER ESTIMATE OF $\langle a_\psi \rangle$;DRY CRACKS.

$E_i = 1.78 \times 10^6$ psi

ε	σ, psi	$E_{mat}, 10^6$ psi	ν_{mat}	$\varepsilon_{mat} = \frac{\sigma}{E_{mat}}$	$\varepsilon_c = \varepsilon - \varepsilon_{mat}$	$\frac{\varepsilon_c}{\varepsilon - \varepsilon_e}$, %
.0005	830	1.725	.242	.000481	.000019	55.9
.001	1581	1.654	.242	.000956	.000044	39.4
.002	2657	1.450	.243	.001832	.000168	33.2
.004	3740	1.094	.246	.003419	.000581	30.6
.006	4070	0.835	.264	.004875	.001125	30.2

TABLE 5.14

MODULI OF INELASTIC MATRIX AND STRAIN DUE TO SUBMICROCRACKING FOR MONOTONIC LOADING OF CEMENT PASTE WITH A W/C = 0.5. FIRST APPROACH*. RESULTS CORRESPOND TO LARGER ESTIMATE OF $\langle a_\psi \rangle$;DRY CRACKS.

$E_i = 2.54 \times 10^6$ psi

ε	σ, psi	$E_{mat}, 10^6$ psi	ν_{mat}	$\varepsilon_{mat} = \frac{\sigma}{E_{mat}}$	$\varepsilon_c = \varepsilon - \varepsilon_{mat}$	$\frac{\varepsilon_c}{\varepsilon - \varepsilon_e}$, %
.0005	1195	2.485	.242	.000481	.000019	64.6
.001	2310	2.416	.241	.000956	.000044	48.6
.002	4127	2.217	.242	.001862	.000138	36.7
.004	6036	1.758	.246	.003433	.000567	34.9
.006	6687	1.375	.262	.004863	.001137	33.8

* Cracks are assumed to exist in the specimens prior to loading.

TABLE 5.15

MODULI OF INELASTIC MATRIX AND STRAIN DUE TO SUBMICROCRACKING FOR MONOTONIC LOADING OF CEMENT PASTE WITH A W/C = 0.3. FIRST APPROACH*. RESULTS CORRESPOND TO LARGER ESTIMATE OF $\langle a_\psi \rangle$;DRY CRACKS.

$E_i = 3.31 \times 10^6$ psi

ε	σ, psi	$E_{mat}, 10^6$ psi	ν_{mat}	$\varepsilon_{mat} = \frac{\sigma}{E_{mat}}$	$\varepsilon_c = \varepsilon - \varepsilon_{mat}$	$\frac{\varepsilon_c}{\varepsilon - \varepsilon_e}$, %
.0005	1581	3.286	.242	.000481	.000019	85.4
.001	3137	3.271	.244	.000959	.000041	78.5
.002	6051	3.198	.247	.001892	.000108	62.8
.003	8195	3.034	.250	.002701	.000299	57.0
.004	9860	2.870	.258	.003436	.000564	55.2
.006	11503	2.363	.289	.004868	.001132	44.8

TABLE 5.16

MODULI OF INELASTIC MATRIX AND STRAIN DUE TO SUBMICROCRACKING FOR MONOTONIC LOADING OF MORTAR WITH A W/C = 0.5. FIRST APPROACH*. RESULTS CORRESPOND TO LARGER ESTIMATE OF $\langle a_\psi \rangle$;DRY CRACKS.

$E_i = 4.79 \times 10^6$ psi

ε	σ, psi	$E_{mat}, 10^6$ psi	ν_{mat}	$\varepsilon_{mat} = \frac{\sigma}{E_{mat}}$	$\varepsilon_c = \varepsilon - \varepsilon_{mat}$	$\frac{\varepsilon_c}{\varepsilon - \varepsilon_e}$, %
.0005	2205	4.575	.214	.000482	.000018	45.4
.001	3697	3.855	.249	.000959	.000041	18.0
.002	5398	2.919	.290	.001880	.000151	17.3
.003	5804	2.150	.352	.002700	.000300	16.8
.004	4066	1.231	.441	.003303	.000697	22.1

* Cracks are assumed to exist in the specimens prior to loading.

TABLE 5.17

MODULI OF INELASTIC MATRIX AND STRAIN DUE TO SUBMICROCRACKING FOR SUSTAINED LOADING OF CEMENT PASTE. FIRST APPROACH*.

RESULTS CORRESPOND TO LARGER ESTIMATE OF $\langle a_\psi \rangle$;DRY CRACKS.

ε	σ, psi	$E_{mat}, 10^6$ psi	ν_{mat}	$\varepsilon_{mat} = \frac{\sigma}{E_{mat}}$	$\varepsilon_c = \varepsilon - \varepsilon_{mat}$	$\frac{\varepsilon_c}{\varepsilon - \varepsilon_e}$, %
CEMENT PASTE WITH A W/C = 0.5; $E_i = 2.54 \times 10^6$ psi						
.004	4572	1.319	.229	.003465	.000535	24.3
.006	4884	0.943	.165	.005176	.000824	20.2
CEMENT PASTE WITH A W/C = 0.3; $E_i = 3.31 \times 10^6$ psi						
.004	7856	2.275	.243	.003453	.000547	33.6
.006	8091	1.630	.175	.004964	.001036	29.1

TABLE 5.18

MODULI OF INELASTIC MATRIX AND STRAIN DUE TO SUBMICROCRACKING FOR CYCLIC LOADING OF CEMENT PASTE. FIRST APPROACH*.

RESULTS CORRESPOND TO LARGER ESTIMATE OF $\langle a_\psi \rangle$;DRY CRACKS.

ε	σ, psi	$E_{mat}, 10^6$ psi	ν_{mat}	$\varepsilon_{mat} = \frac{\sigma}{E_{mat}}$	$\varepsilon_c = \varepsilon - \varepsilon_{mat}$	$\frac{\varepsilon_c}{\varepsilon - \varepsilon_e}$, %
CEMENT PASTE WITH A W/C = 0.5; $E_i = 2.54 \times 10^6$ psi						
.002	3017	1.725	.212	.001749	.000251	39.9
.004	5033	1.437	.281	.003503	.000583	24.6
CEMENT PASTE WITH A W/C = 0.3; $E_i = 3.31 \times 10^6$ psi						
.002	6383	3.302	.149	.001933	.000067	91.3
.0025	7285	3.177	.150	.002293	.000207	69.2
.003	6902	2.632	.172	.002622	.000378	41.3

* Cracks are assumed to exist in the specimens prior to loading.

TABLE 5.19

MODULI OF INELASTIC MATRIX AND STRAIN DUE TO SUBMICROCRACKING FOR MONOTONIC LOADING OF CEMENT PASTE WITH A W/C = 0.7. SECOND APPROACH*. RESULTS CORRESPOND TO LARGER ESTIMATE OF $\langle a_\psi \rangle$;DRY CRACKS.

$E_i = 1.78 \times 10^6$ psi

ε	σ, psi	$E_{mat}, 10^6$ psi	ν_{mat}	$\varepsilon_{mat} = \frac{\sigma}{E_{mat}}$	$\varepsilon_c = \varepsilon - \varepsilon_{mat}$	$\frac{\varepsilon_c}{\varepsilon - \varepsilon_e}$, %
.0005	830	1.718	.242	.000483	.000017	50.2
.001	1581	1.642	.243	.000963	.000037	33.7
.002	2657	1.428	.244	.001861	.000139	27.4
.004	3740	1.054	.248	.003548	.000452	23.8
.006	4070	0.790	.267	.005154	.000846	22.7

TABLE 5.20

MODULI OF INELASTIC MATRIX AND STRAIN DUE TO SUBMICROCRACKING FOR MONOTONIC LOADING OF CEMENT PASTE WITH A W/C = 0.5. SECOND APPROACH*. RESULTS CORRESPOND TO LARGER ESTIMATE OF $\langle a_\psi \rangle$;DRY CRACKS.

$E_i = 2.54 \times 10^6$ psi

ε	σ, psi	$E_{mat}, 10^6$ psi	ν_{mat}	$\varepsilon_{mat} = \frac{\sigma}{E_{mat}}$	$\varepsilon_c = \varepsilon - \varepsilon_{mat}$	$\frac{\varepsilon_c}{\varepsilon - \varepsilon_e}$, %
.0005	1195	2.474	.242	.000483	.000017	59.8
.001	2310	2.401	.242	.000962	.000038	42.3
.002	4127	2.189	.243	.001885	.000115	30.7
.004	6036	1.703	.248	.003544	.000456	28.1
.006	6687	1.313	.265	.005093	.000907	26.9

* Cracks are assumed not to exist in the specimens prior to loading.

TABLE 5.21

MODULI OF INELASTIC MATRIX AND STRAIN DUE TO SUBMICROCRACKING FOR MONOTONIC LOADING OF CEMENT PASTE WITH A W/C = 0.3. SECOND APPROACH*. RESULTS CORRESPOND TO LARGER ESTIMATE OF $\langle a_\psi \rangle$;DRY CRACKS.

$E_i = 3.31 \times 10^6$ psi

ε	σ, psi	$E_{mat}, 10^6$ psi	ν_{mat}	$\varepsilon_{mat} = \frac{\sigma}{E_{mat}}$	$\varepsilon_c = \varepsilon - \varepsilon_{mat}$	$\frac{\varepsilon_c}{\varepsilon - \varepsilon_e}$, %
.0005	1581	3.280	.242	.000482	.000018	80.9
.001	3137	3.268	.244	.000960	.000040	76.6
.002	6051	3.168	.248	.001910	.000090	52.3
.003	8195	2.987	.251	.002743	.000257	49.1
.004	9860	2.808	.260	.003512	.000488	47.7
.006	11503	2.251	.292	.005110	.000890	35.2

TABLE 5.22

MODULI OF INELASTIC MATRIX AND STRAIN DUE TO SUBMICROCRACKING FOR MONOTONIC LOADING OF MORTAR WITH A W/C = 0.5. SECOND APPROACH*. RESULTS CORRESPOND TO LARGER ESTIMATE OF $\langle a_\psi \rangle$;DRY CRACKS.

$E_i = 4.79 \times 10^6$ psi

ε	σ, psi	$E_{mat}, 10^6$ psi	ν_{mat}	$\varepsilon_{mat} = \frac{\sigma}{E_{mat}}$	$\varepsilon_c = \varepsilon - \varepsilon_{mat}$	$\frac{\varepsilon_c}{\varepsilon - \varepsilon_e}$, %
.0005	2205	4.556	.214	.000484	.000016	41.1
.001	3697	3.819	.250	.000968	.000032	14.2
.002	5398	2.858	.292	.001889	.000111	12.7
.003	5804	2.069	.355	.002805	.000195	10.9
.004	4066	1.198	.446	.003394	.000606	19.2

* Cracks are assumed not to exist in the specimens prior to loading.

TABLE 5.23

MODULI OF INELASTIC MATRIX AND STRAIN DUE TO SUBMICROCRACKING FOR SUSTAINED LOADING OF CEMENT PASTE. SECOND APPROACH*.

RESULTS CORRESPOND TO LARGER ESTIMATE OF $\langle a_\psi \rangle$;DRY CRACKS.

ε	σ, psi	$E_{mat}, 10^6$ psi	ν_{mat}	$\varepsilon_{mat} = \frac{\sigma}{E_{mat}}$	$\varepsilon_c = \varepsilon - \varepsilon_{mat}$	$\frac{\varepsilon_c}{\varepsilon - \varepsilon_e}$, %
CEMENT PASTE WITH A W/C = 0.5; $E_i = 2.54 \times 10^6$ psi						
.004	4572	1.278	.231	.003577	.000423	19.2
.006	4884	0.905	.168	.005396	.000604	14.8
CEMENT PASTE WITH A W/C = 0.3; $E_i = 3.31 \times 10^6$ psi						
.004	7856	2.204	.245	.003565	.000435	26.7
.006	8091	1.546	.179	.005235	.000765	21.5

TABLE 5.24

MODULI OF INELASTIC MATRIX AND STRAIN DUE TO SUBMICROCRACKING FOR CYCLIC LOADING OF CEMENT PASTE. SECOND APPROACH*.

RESULTS CORRESPOND TO LARGER ESTIMATE OF $\langle a_\psi \rangle$;DRY CRACKS.

ε	σ, psi	$E_{mat}, 10^6$ psi	ν_{mat}	$\varepsilon_{mat} = \frac{\sigma}{E_{mat}}$	$\varepsilon_c = \varepsilon - \varepsilon_{mat}$	$\frac{\varepsilon_c}{\varepsilon - \varepsilon_e}$, %
CEMENT PASTE WITH A W/C = 0.5; $E_i = 2.54 \times 10^6$ psi						
.002	3017	1.696	.212	.001779	.000221	35.1
.004	5033	1.425	.283	.003531	.000469	19.8
CEMENT PASTE WITH A W/C = 0.3; $E_i = 3.31 \times 10^6$ psi						
.002	6383	3.295	.150	.001937	.000063	86.2
.0025	7285	3.148	.150	.002314	.000186	62.1
.003	6902	2.572	.175	.002684	.000316	34.5

* Cracks are assumed not to exist in the specimens prior to loading.

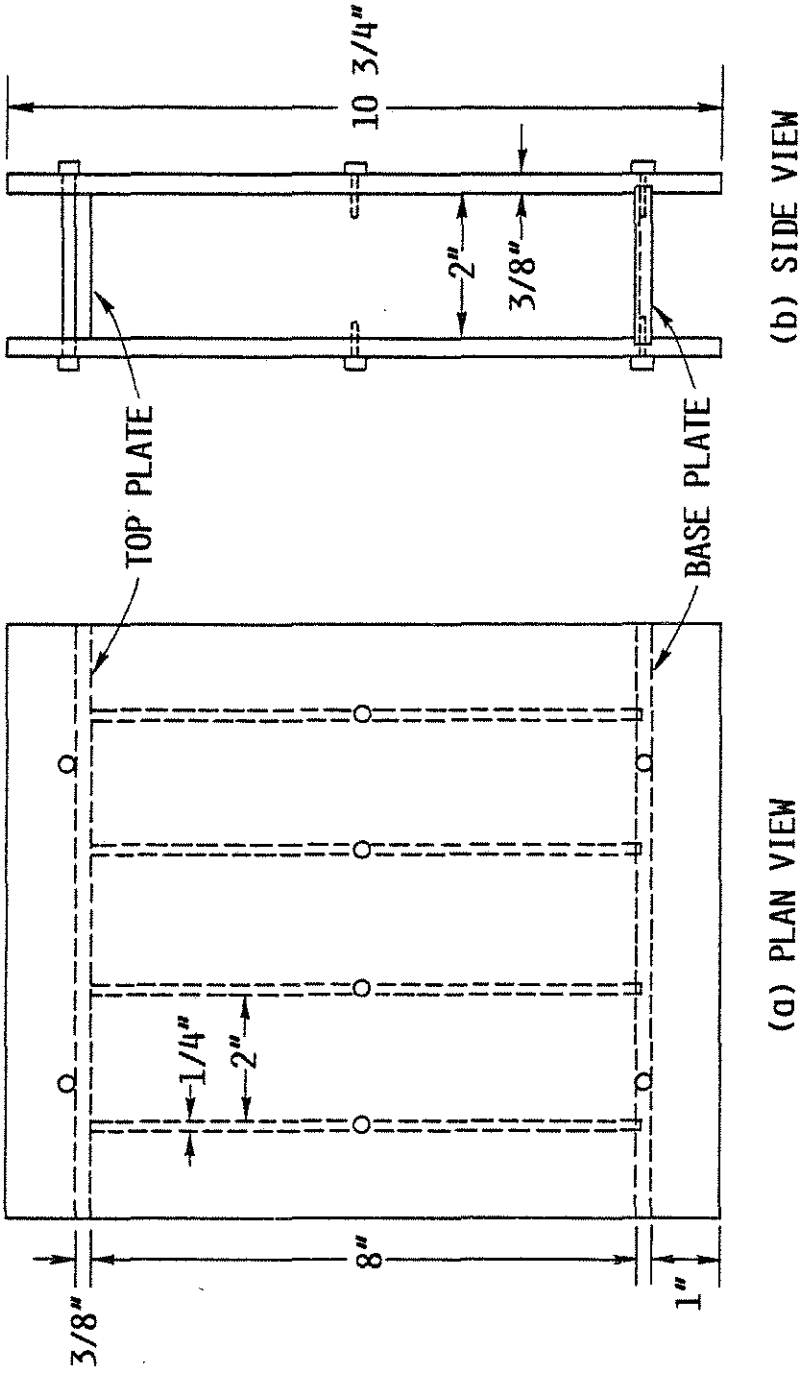

Fig. 2.1. Steel Mold

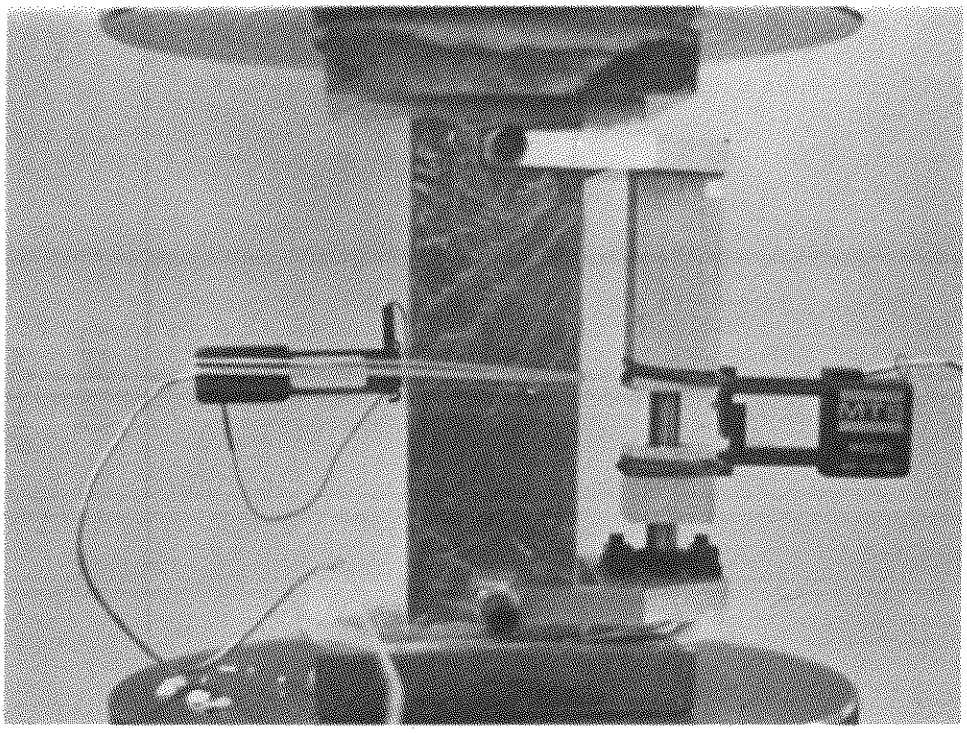

Fig. 2.2. Compressometer and Extensometers as Mounted on Test Specimen

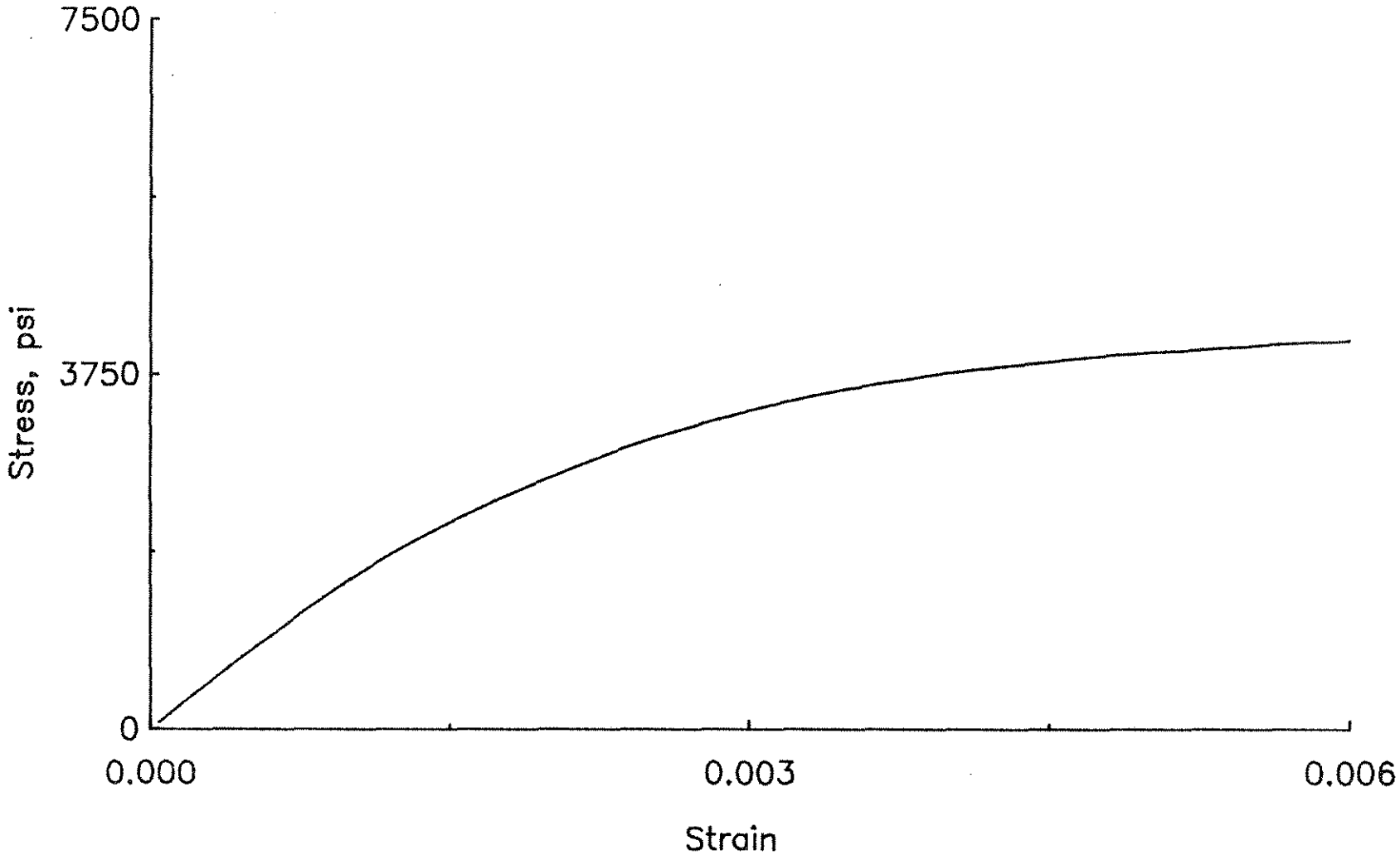

Fig. 2.3. Stress versus Longitudinal Strain for Monotonic Loading of Cement with a W/C = 0.7: Specimen 7-6/P-0.7M

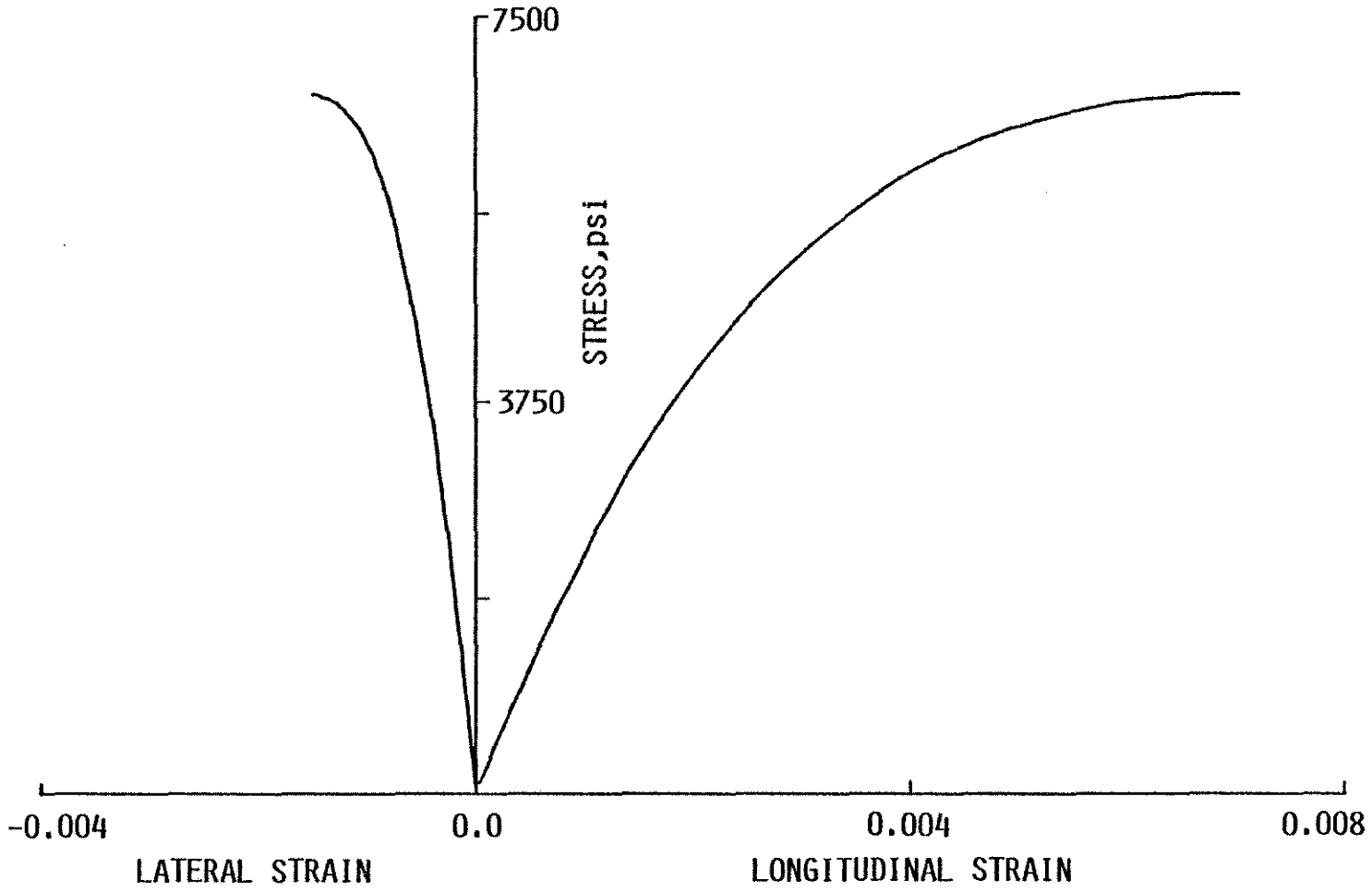

Fig. 2.4. Stress versus Longitudinal and Lateral Strains for Monotonic Loading of Cement Paste with a W/C = 0.5: Specimen 14-6/P-0.5/M

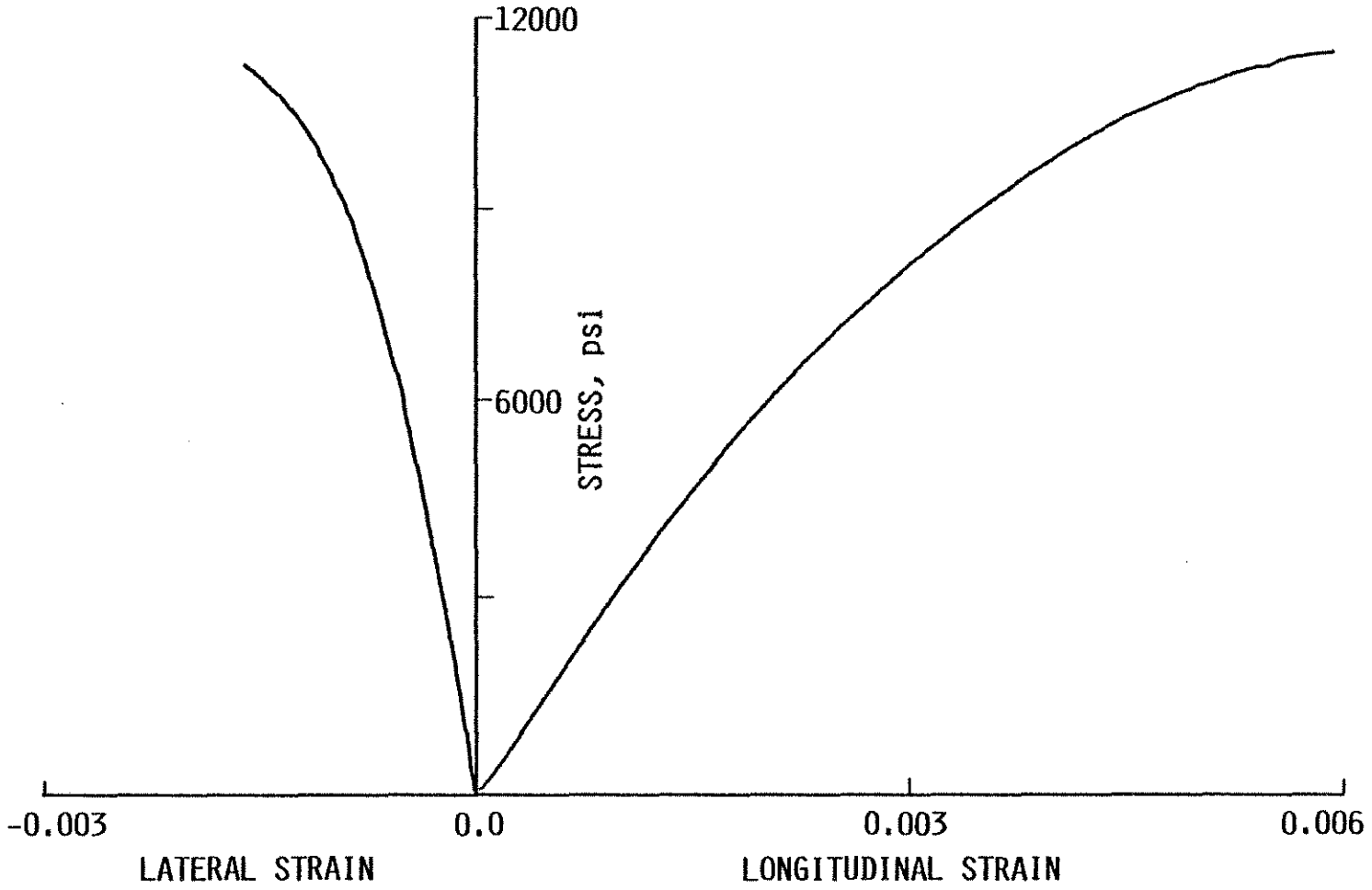

Fig. 2.5. Stress versus Longitudinal and Lateral Strains for Monotonic Loading of Cement Paste with a W/C = 0.3: Specimen 16-3/P-0.3/M

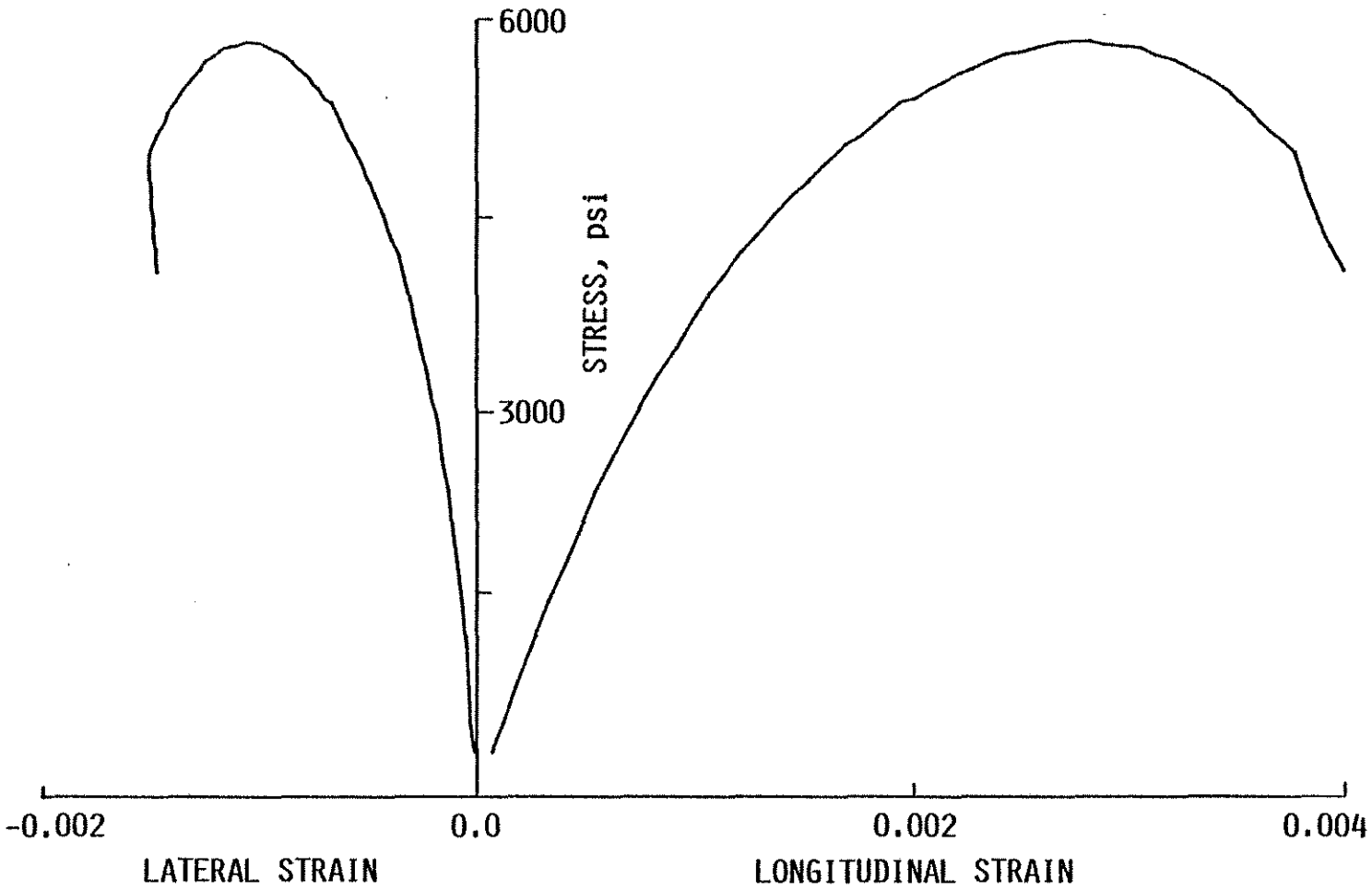

Fig. 2.6. Stress versus Longitudinal and Lateral Strains for Monotonic Loading of Mortar with a W/C = 0.5: Specimen 13-6/M-0.5/M

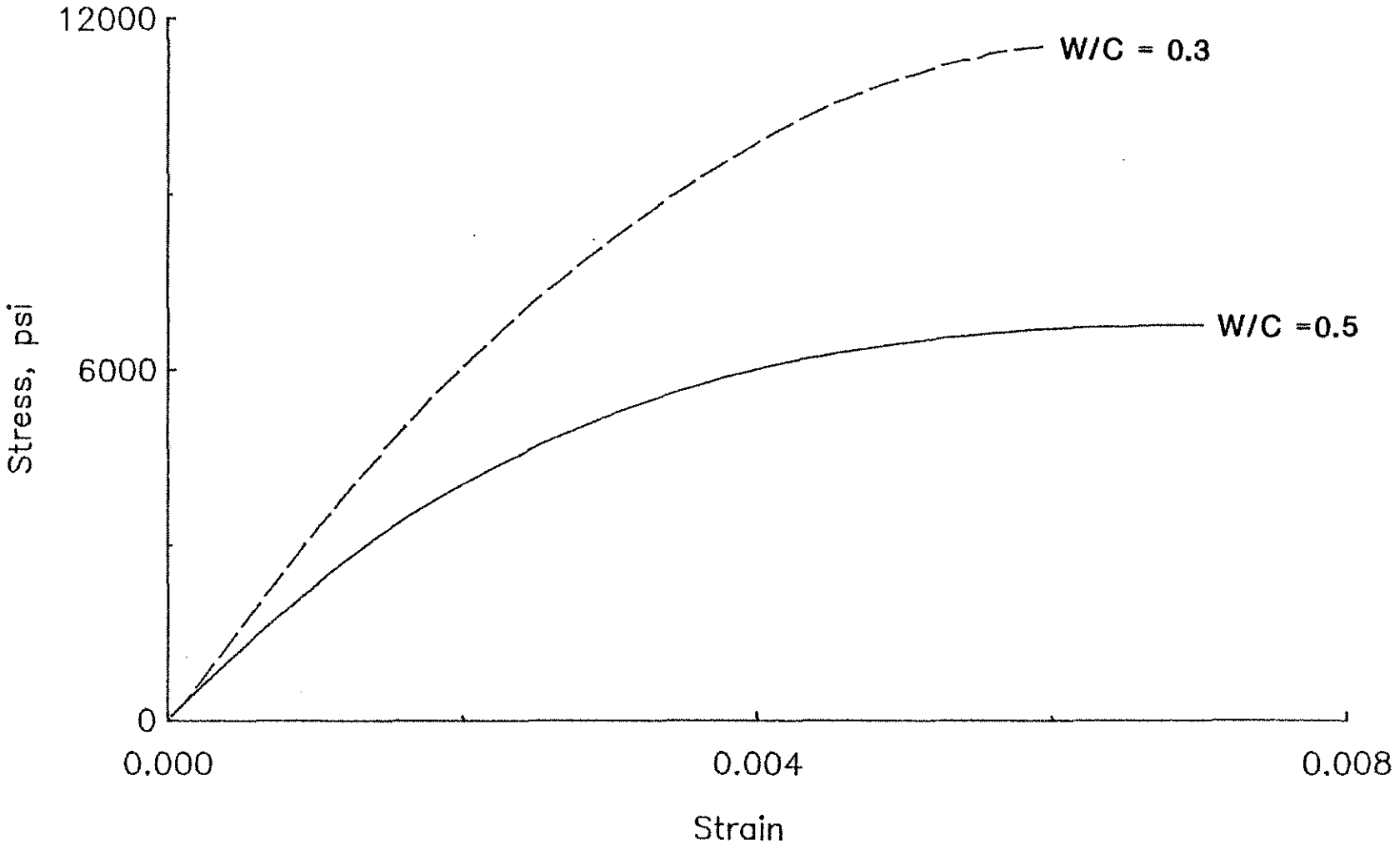

Fig. 2.7. Stress-Strain Curves for Cement Pastes with W/C = 0.5 and 0.3

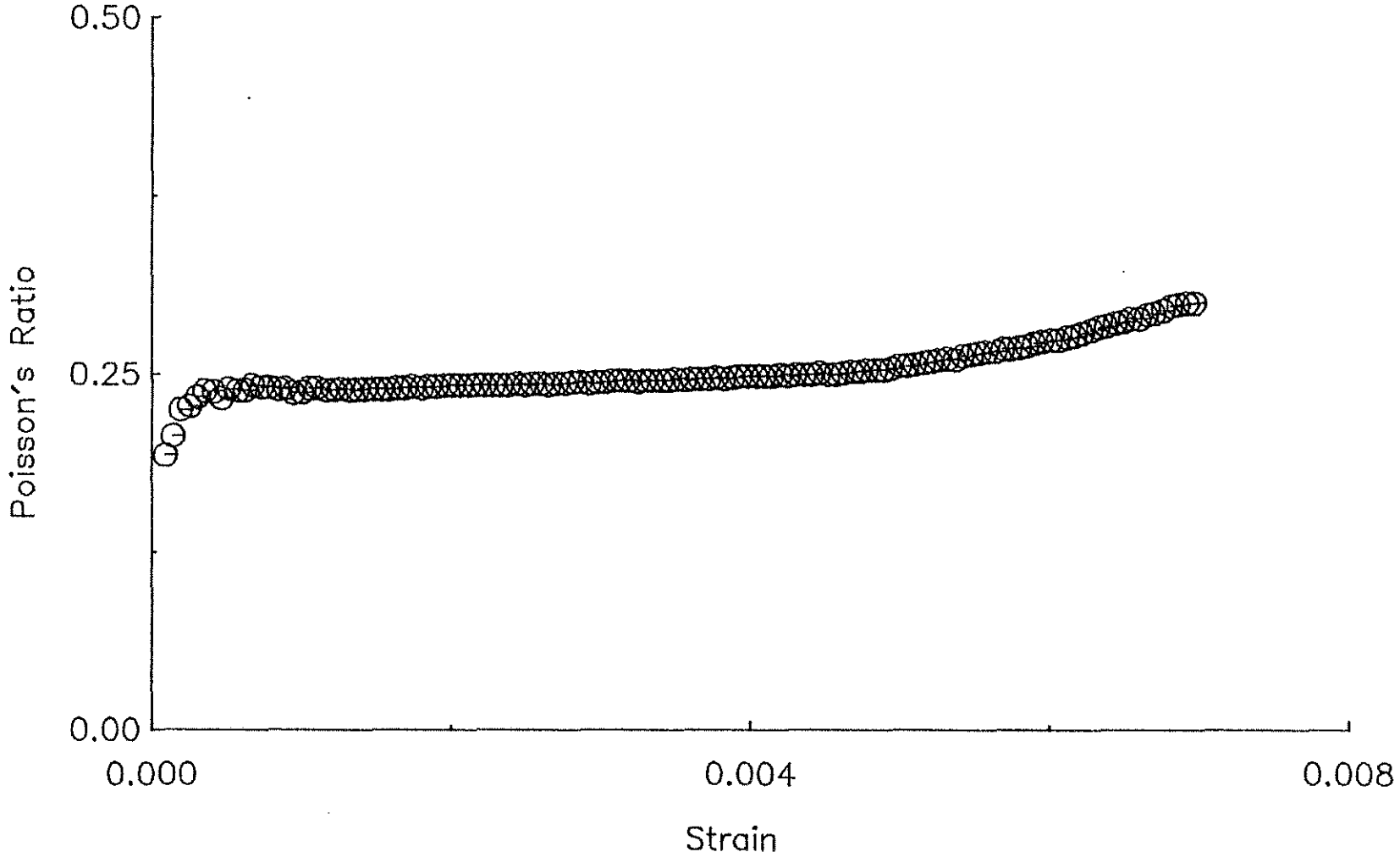

Fig. 2.8. Poisson's Ratio versus Axial Strain for Monotonic Loading of Cement Paste with a W/C = 0.5: Specimen 14-6/P-0.5/M

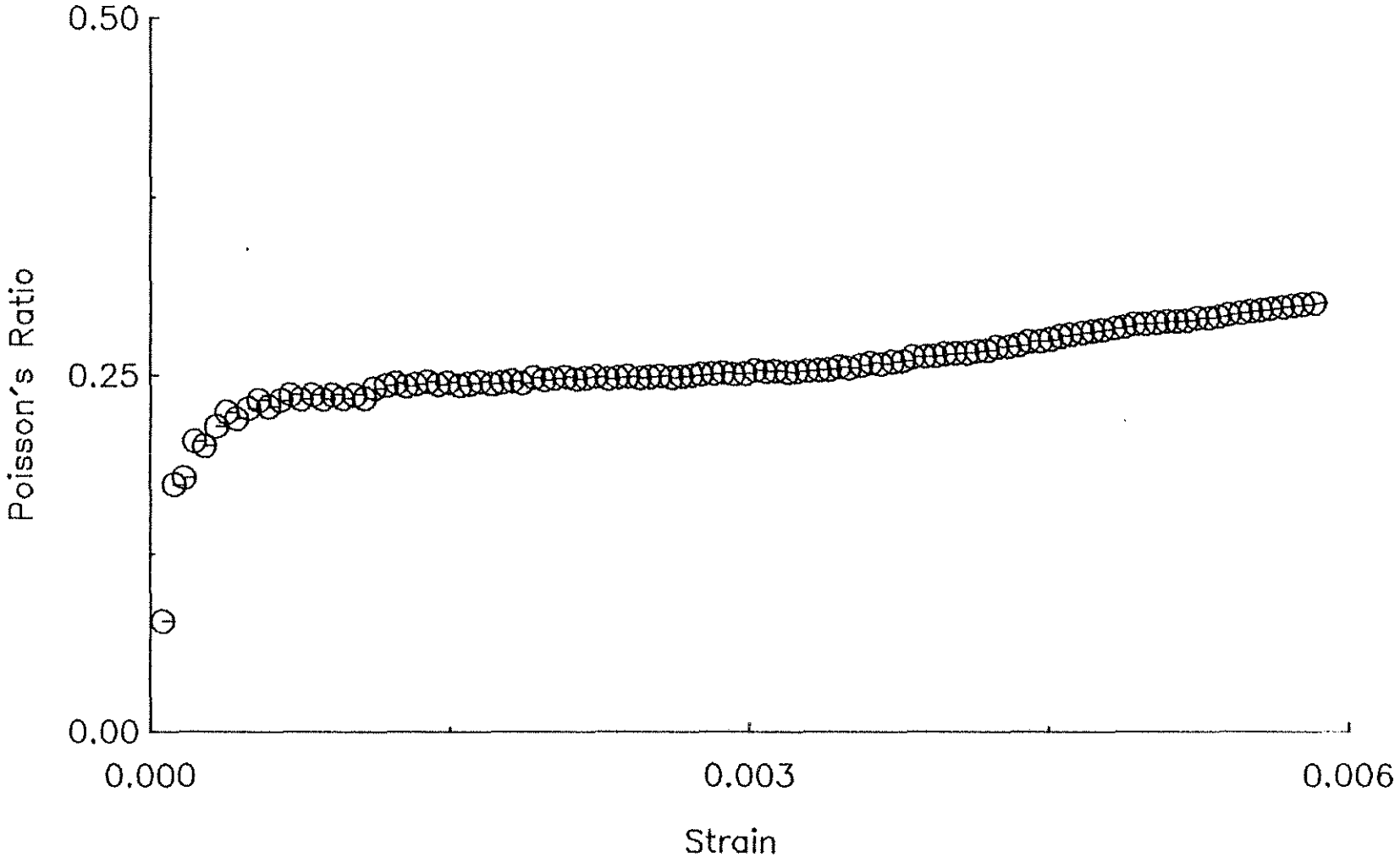

Fig. 2.9. Poisson's Ratio versus Axial Strain for Monotonic Loading of Cement Paste with a W/C = 0.3: Specimen 16-3/P-0.3/M

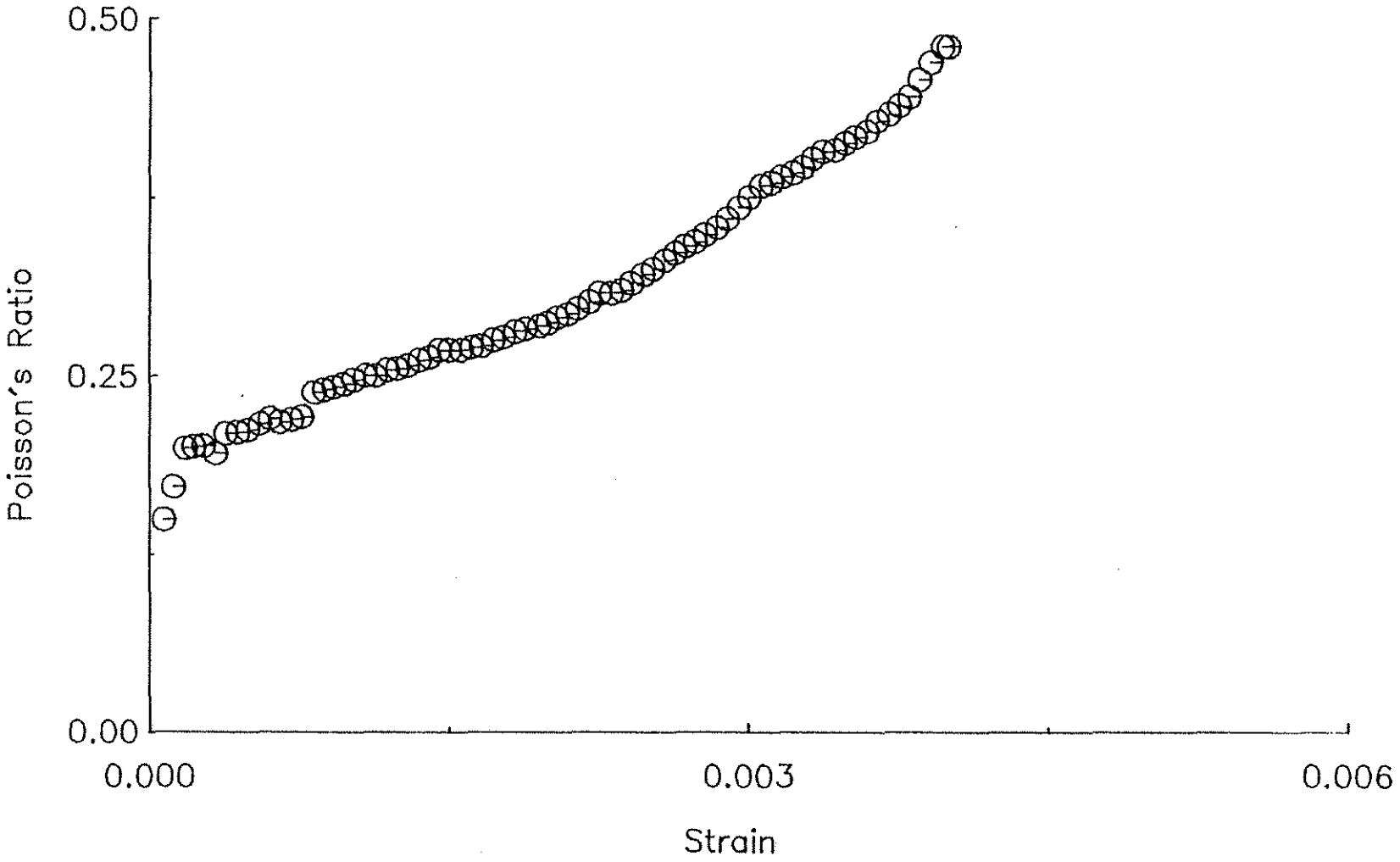

Fig. 2.10. Poisson's Ratio versus Axial Strain for Monotonic Loading of Mortar with a W/C = 0.5: Specimen 13-6/M-0.5/M

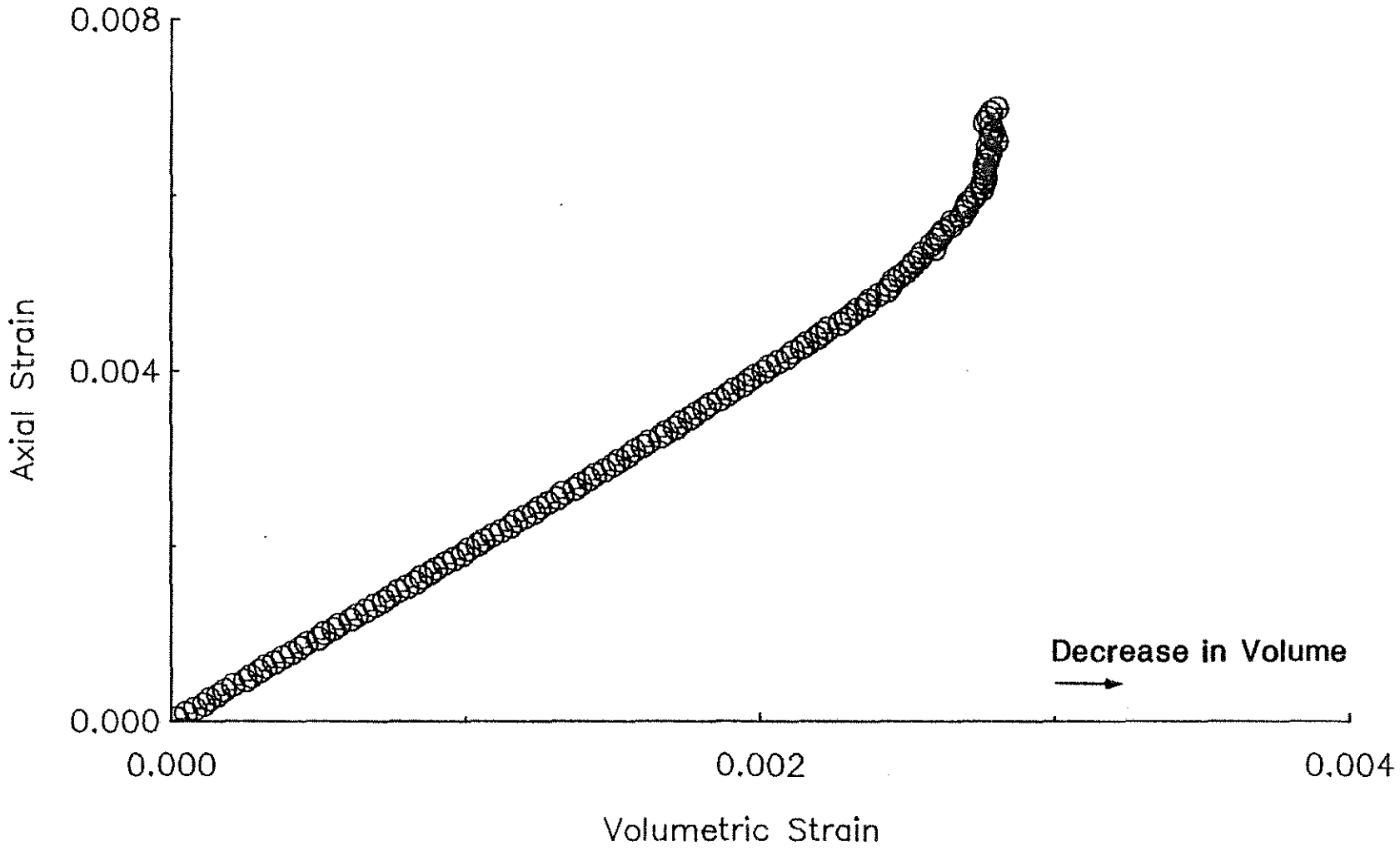

Fig. 2.11. Volumetric Strain versus Axial Strain for Monotonic Loading of Cement Paste with a W/C = 0.5: Speciment 14-6/P-0.5/M

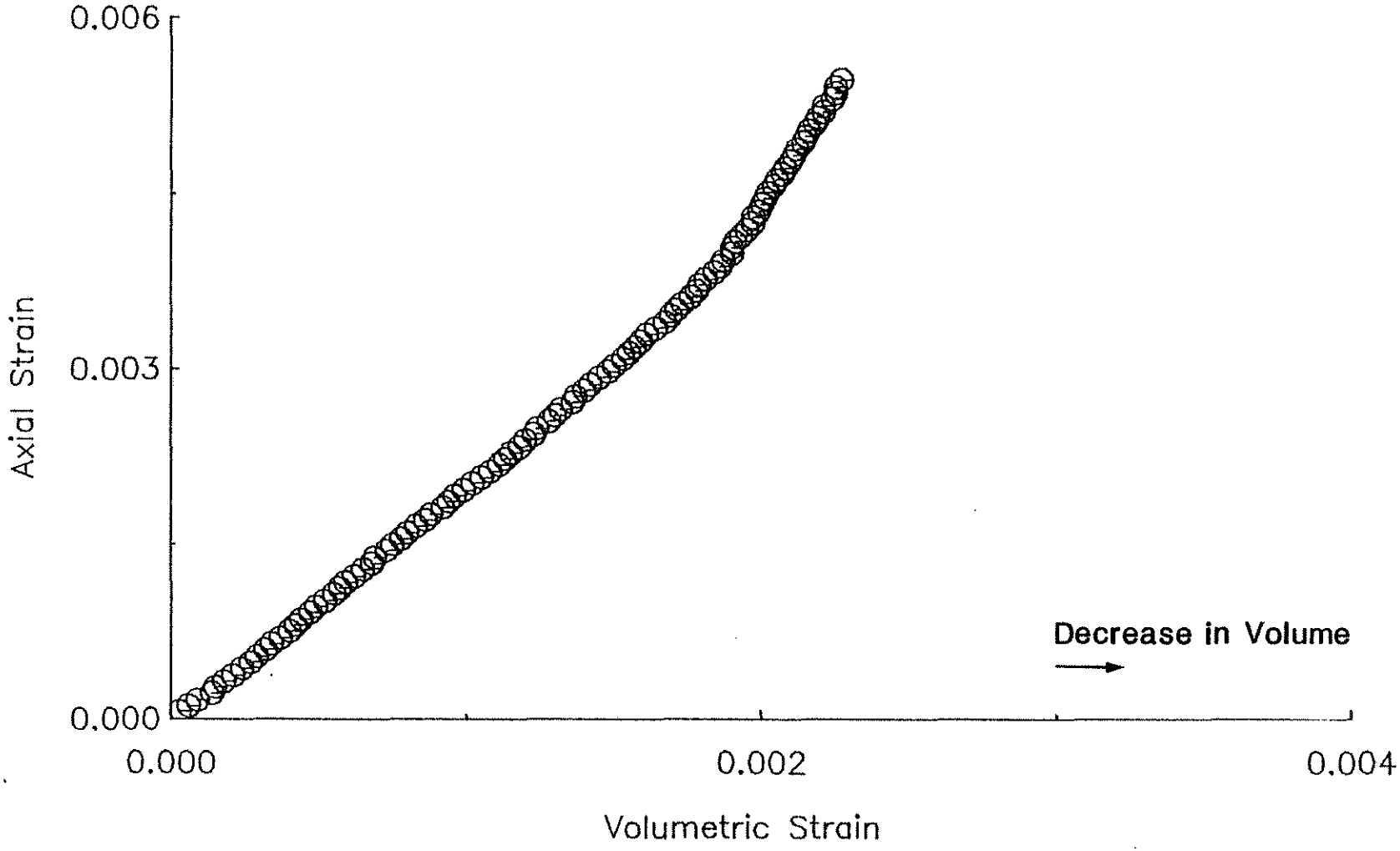

Fig. 2.12. Volumetric STrain versus Axial Strain for Monotonic Loading of Cement Paste with a W/C = 0.3: Specimen 16-3/P-0.3/M

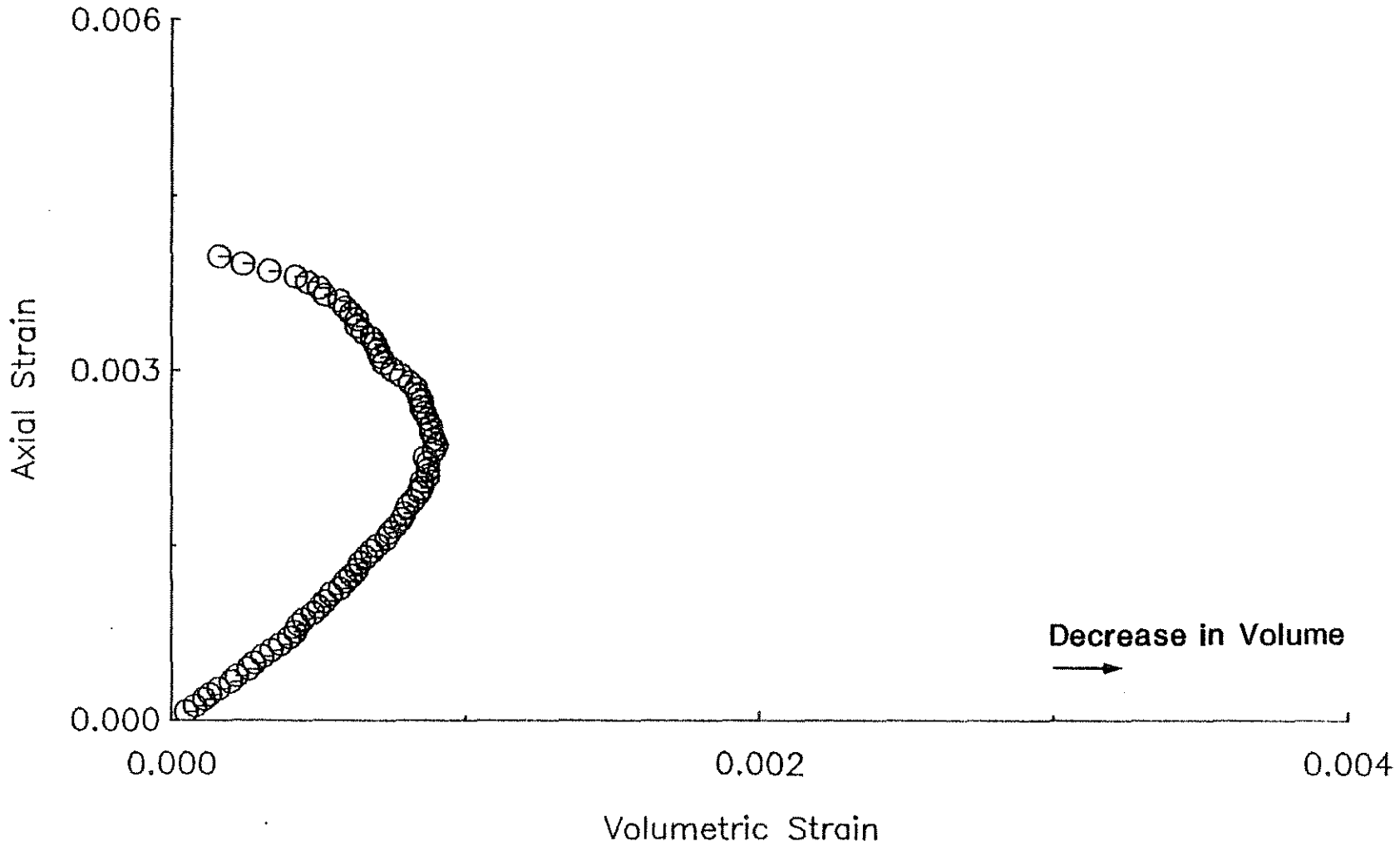

Fig. 2.13. Volumetric Strain versus Axial Strain for Monotonic Loading of Mortar with a W/C = 0.5: Specimen 13-6/M-0.5/M

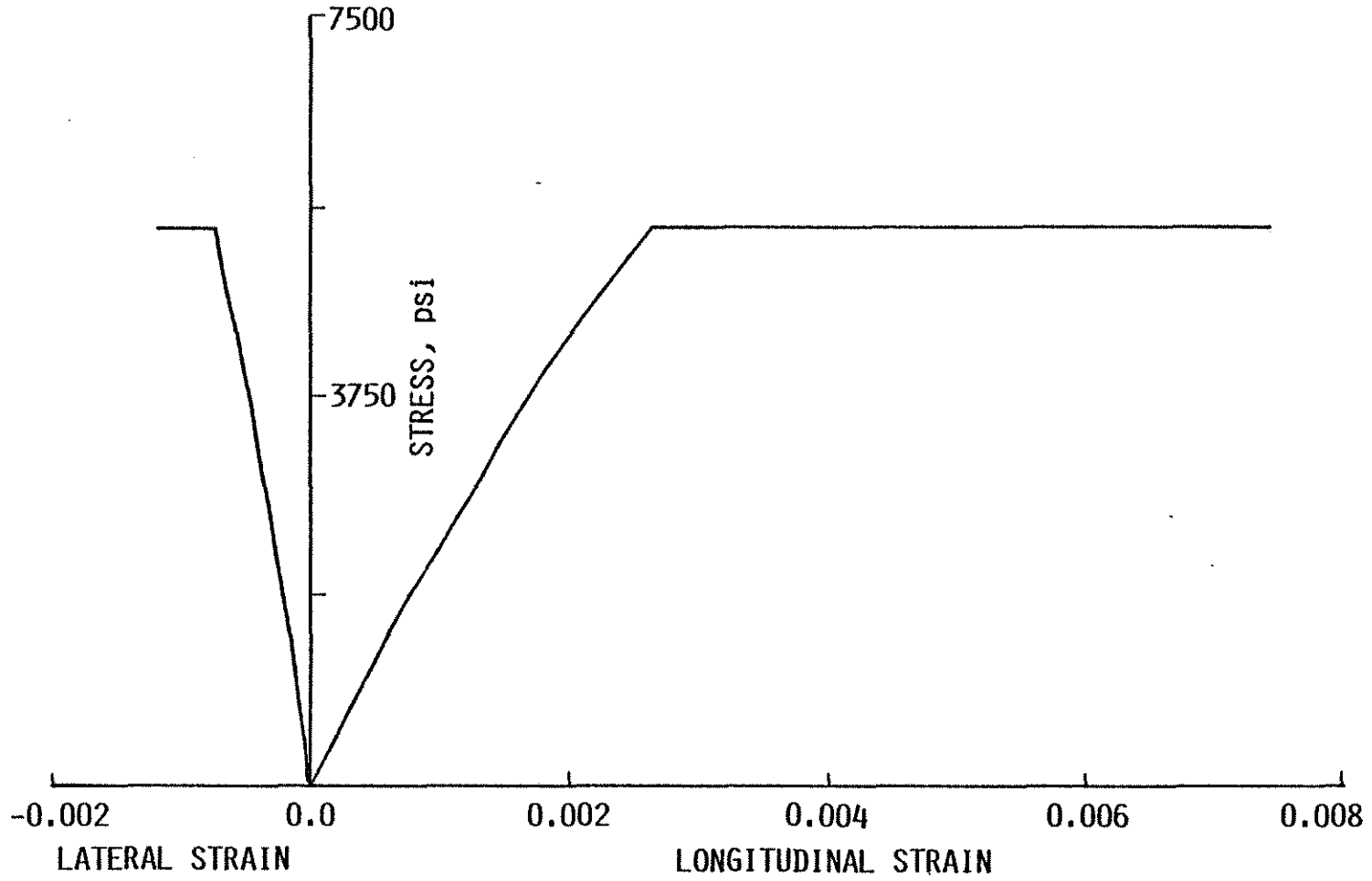

Fig. 2.14. Stress versus Longitudinal and Lateral Strains for Sustained Loading of Cement Paste with a W/C = 0.5: Specimen 15A-1/P-0.5/S

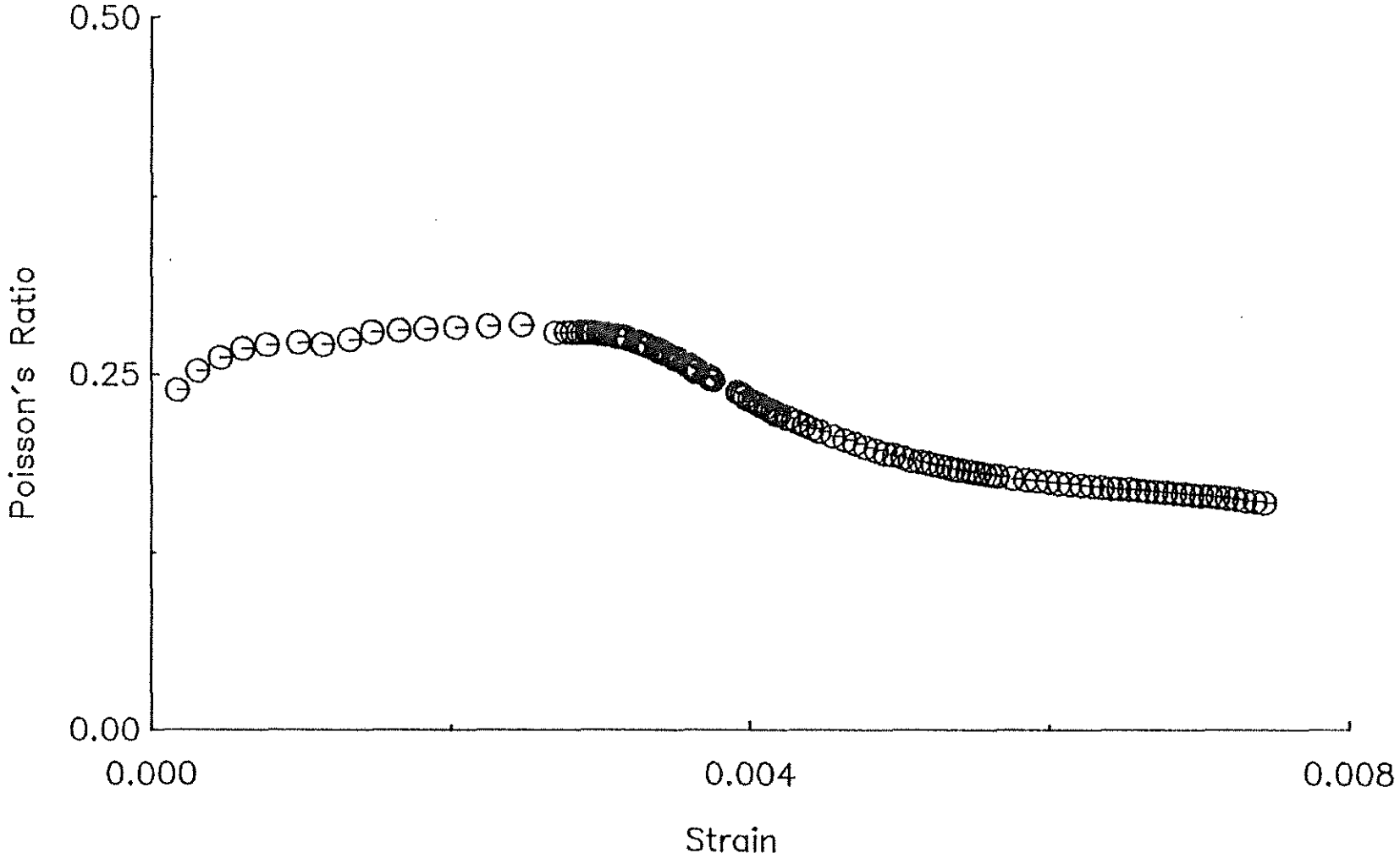

Fig. 2.15. Poisson's Ratio versus Axial Strain for Sustained Loading of Cement Paste with a W/C = 0.5: Specimen 15A-1/P-0.5/S

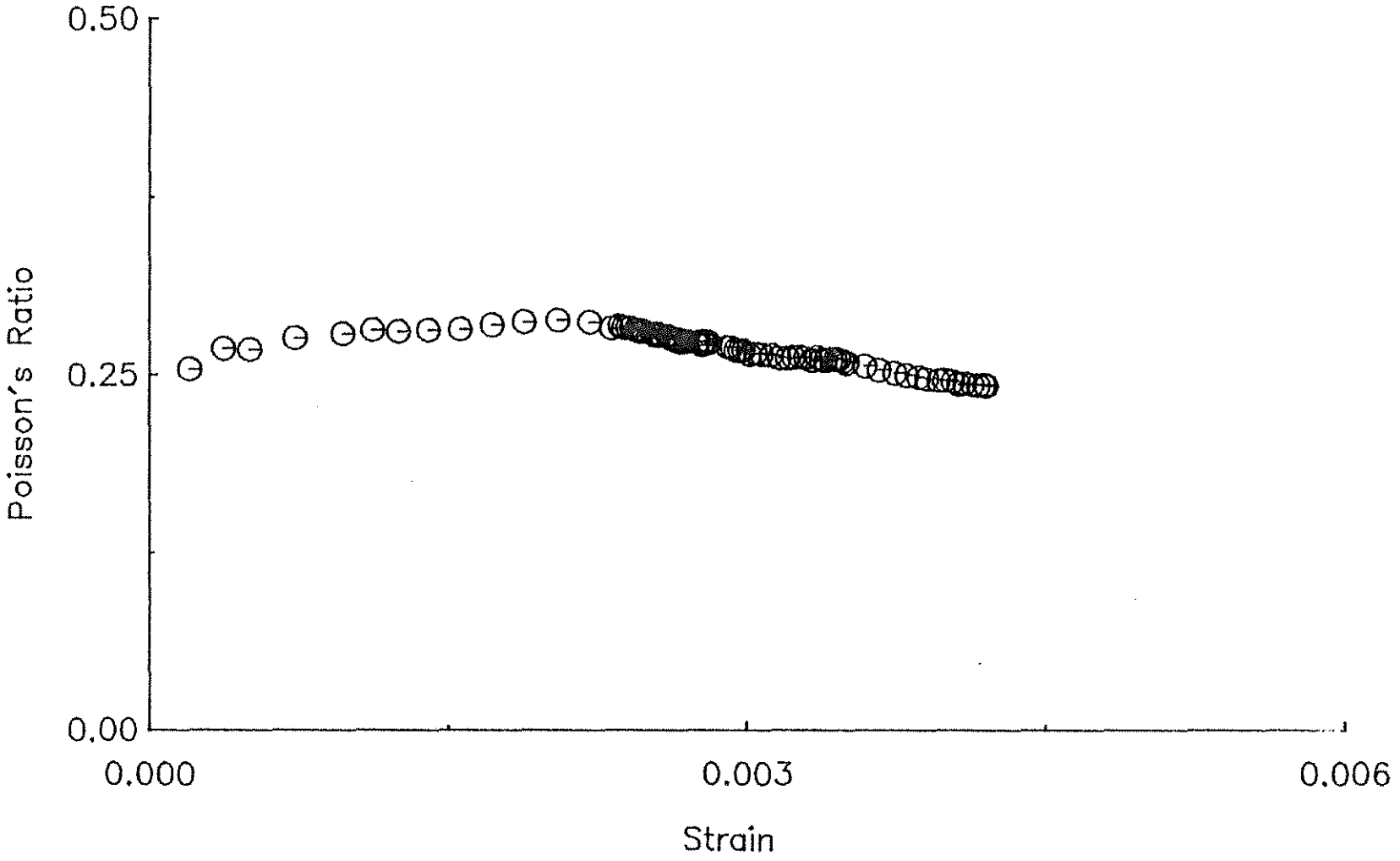

Fig. 2.16. Poisson's Ratio versus Axial Strain for Sustained Loading of Cement Paste with a W/C = 0.3: Specimen 16-4/P-0.3/S

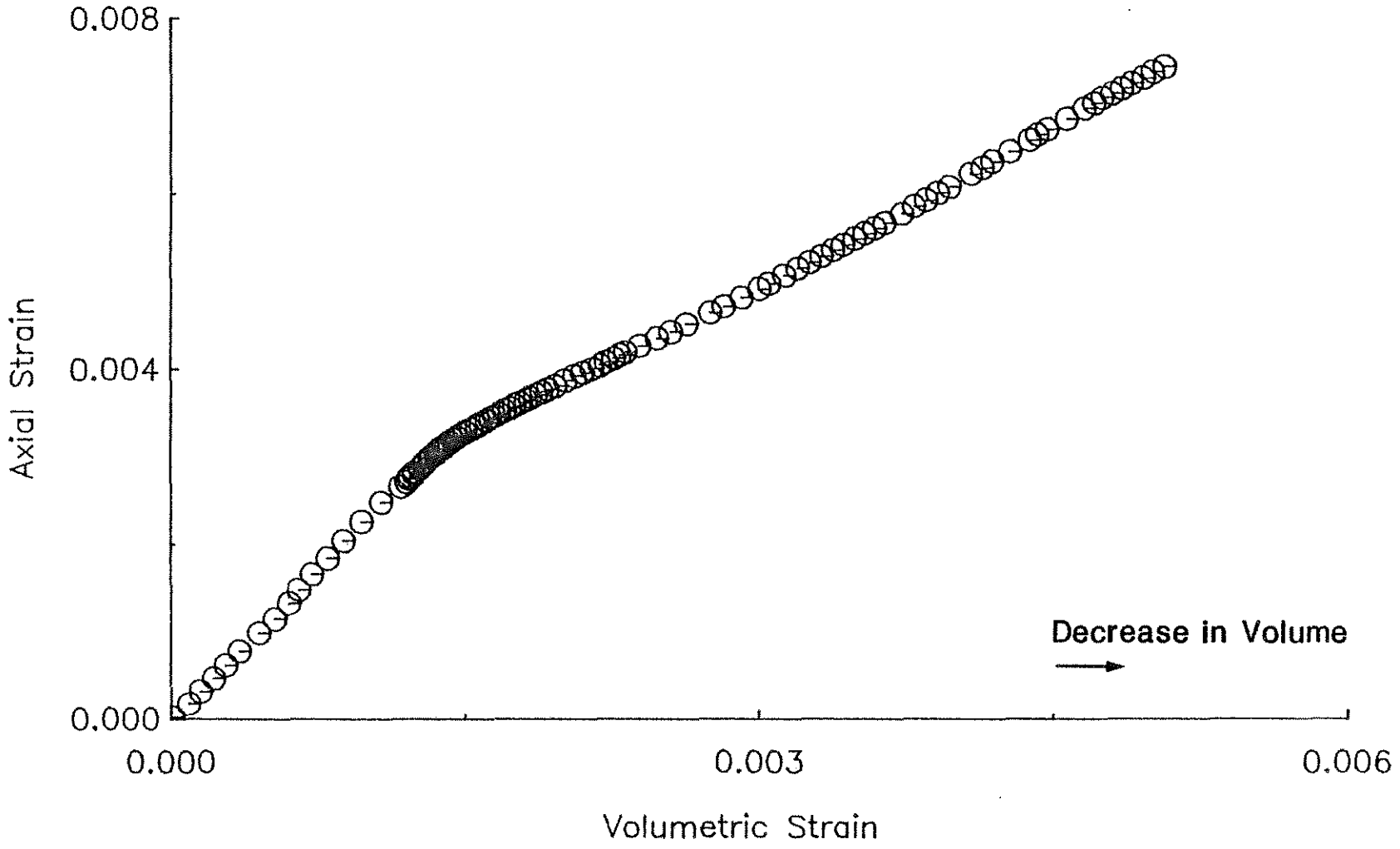

Fig. 2.17. Volumetric Strain versus Axial Strain for Sustained Loading of Cement Paste with a W/C = 0.5: Specimen 15A-1/P-0.5/S

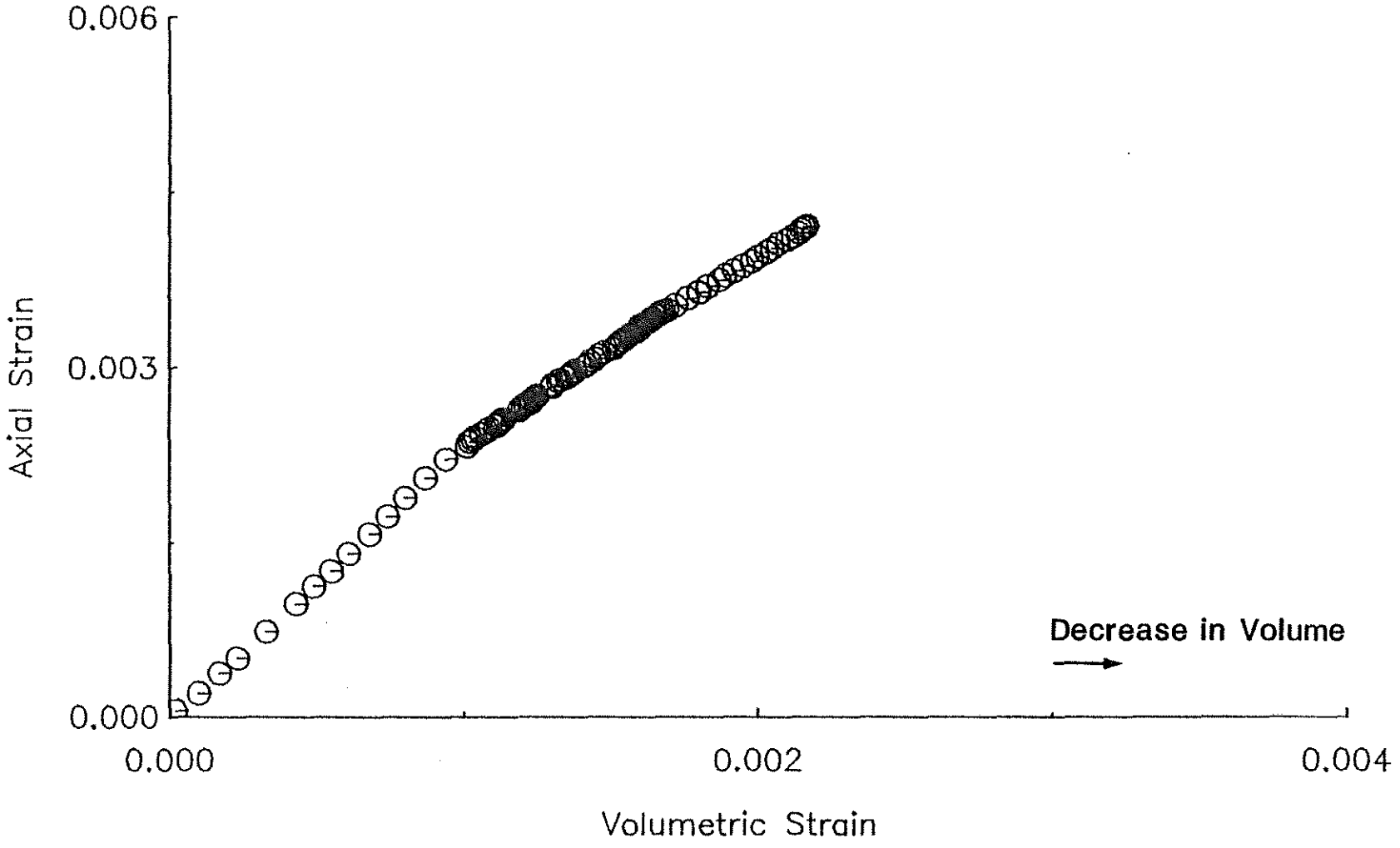

Fig. 2.18. Volumetric STrain versus Axial STrain for Sustained Loading of Cement Paste with a W/C = 0.3: Specimen 16-4/P-0.3/S

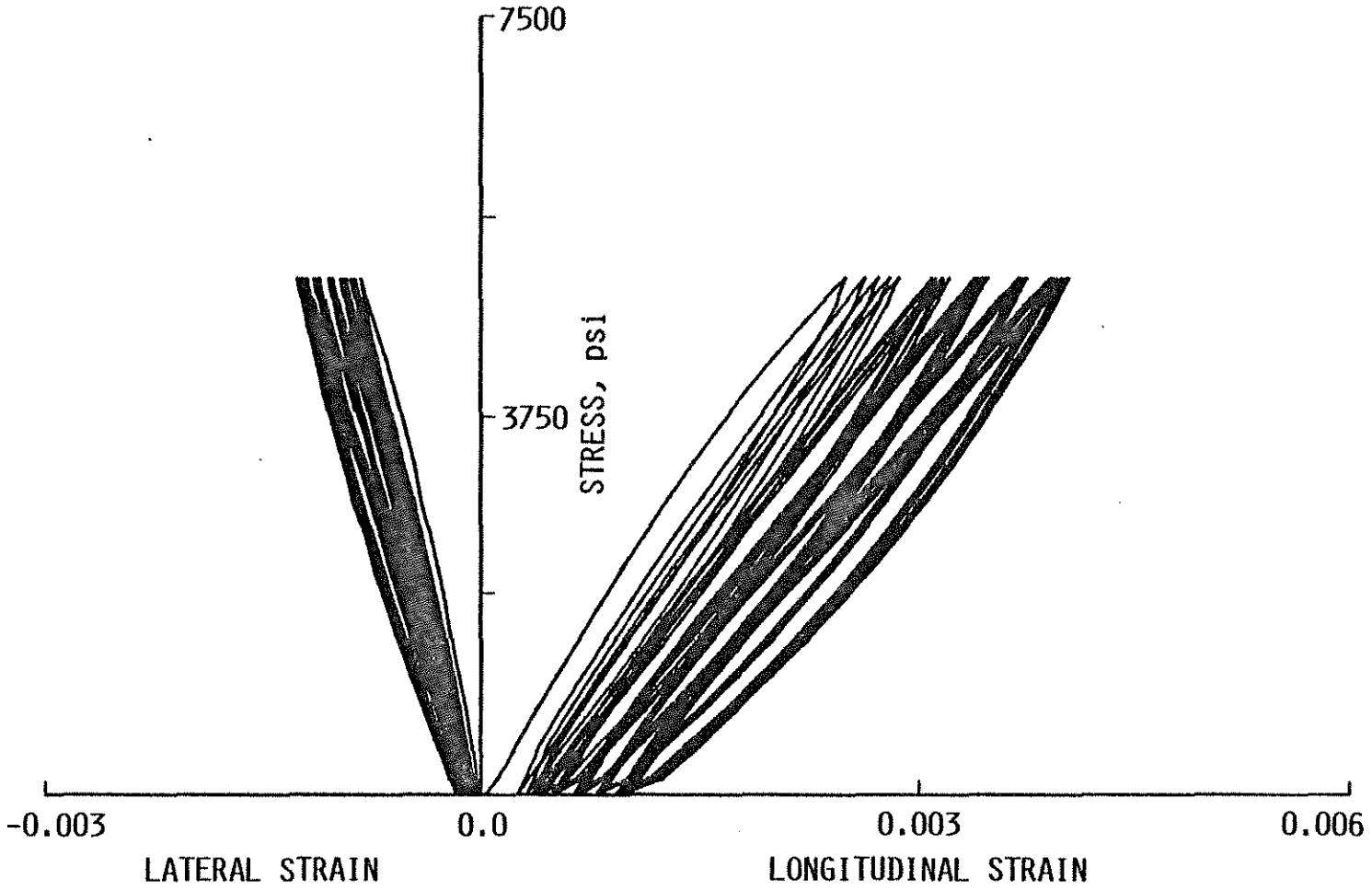

Fig. 2.19. Stress versus Longitudinal and Lateral Strains for Cyclic Loading of Cement Paste with a W/C = 0.5: Selected Cycles: Specimen 18-5/P-0.5/C

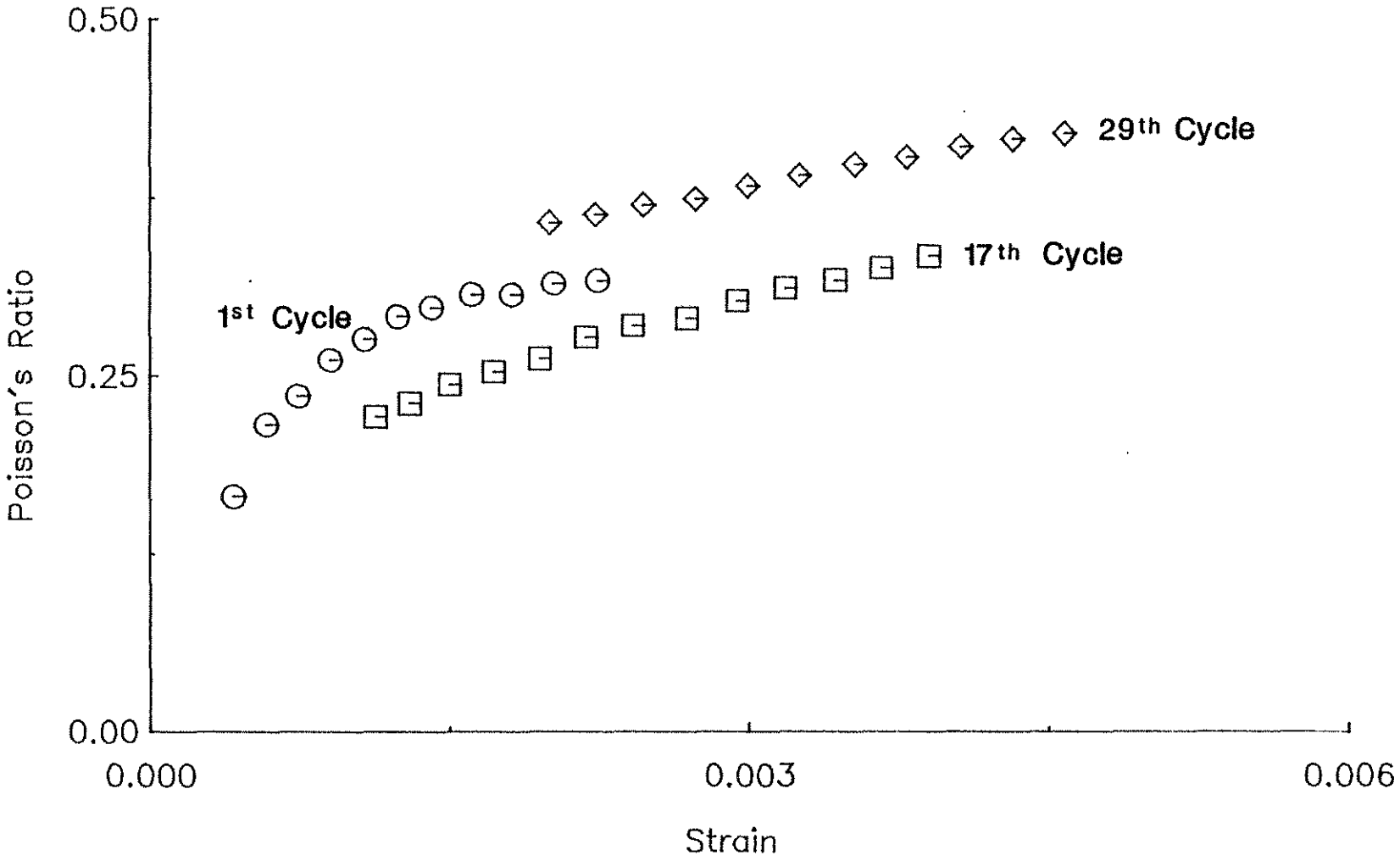

Fig. 2.20. Poisson's Ratio versus Axial Strain for Cyclic Loading: 1st, 17th and 29th Cycles; Cement Paste with a W/C = 0.5: Specimen 19A-1/P-0.5/C

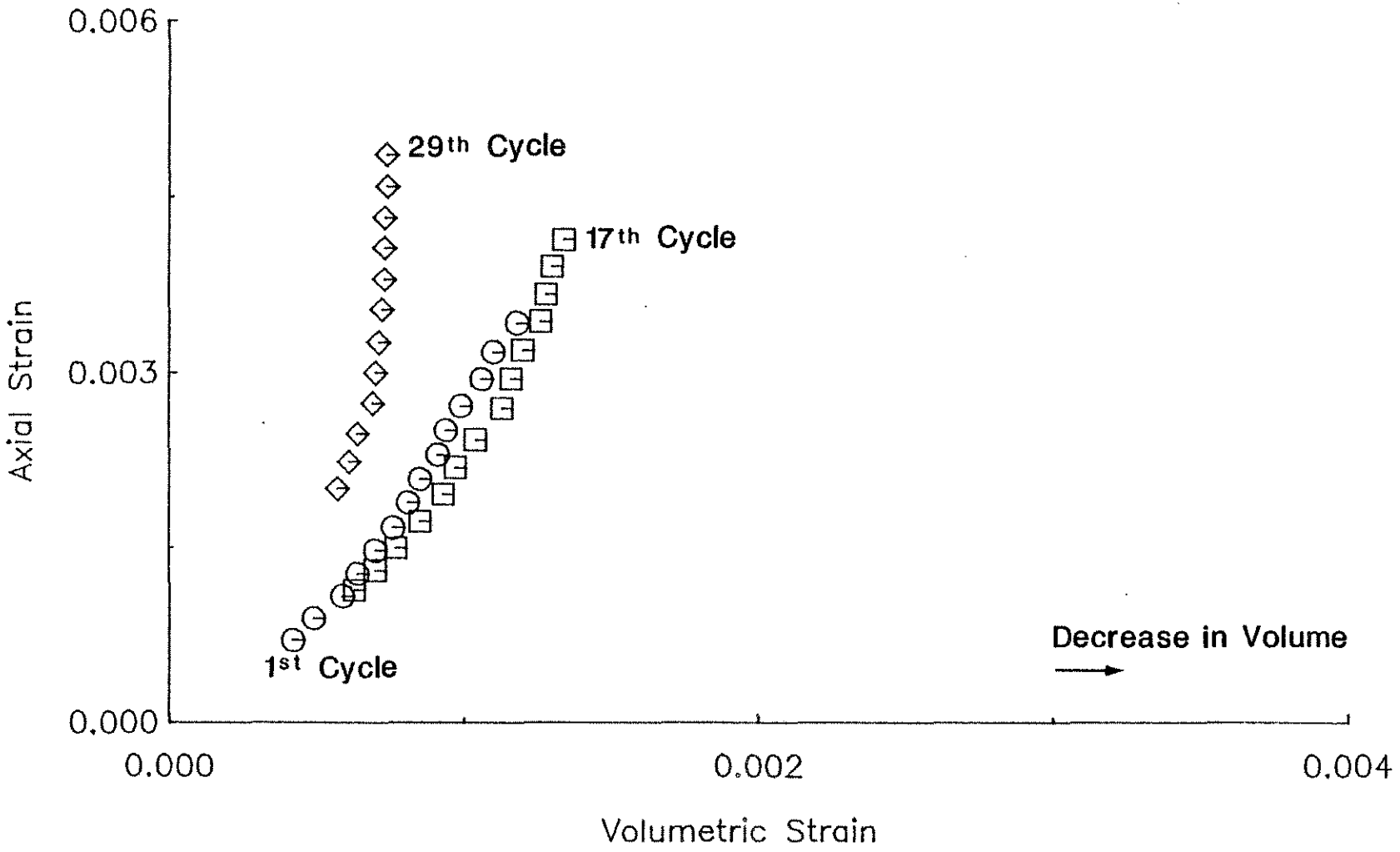

Fig. 2.21. Volumetric Strain versus Axial STrain for Cyclic Loading: 1st, 17th and 29th Cycles; Cement Paste with a W/C = 0.5: Specimen 19A-1/P-0.5/C

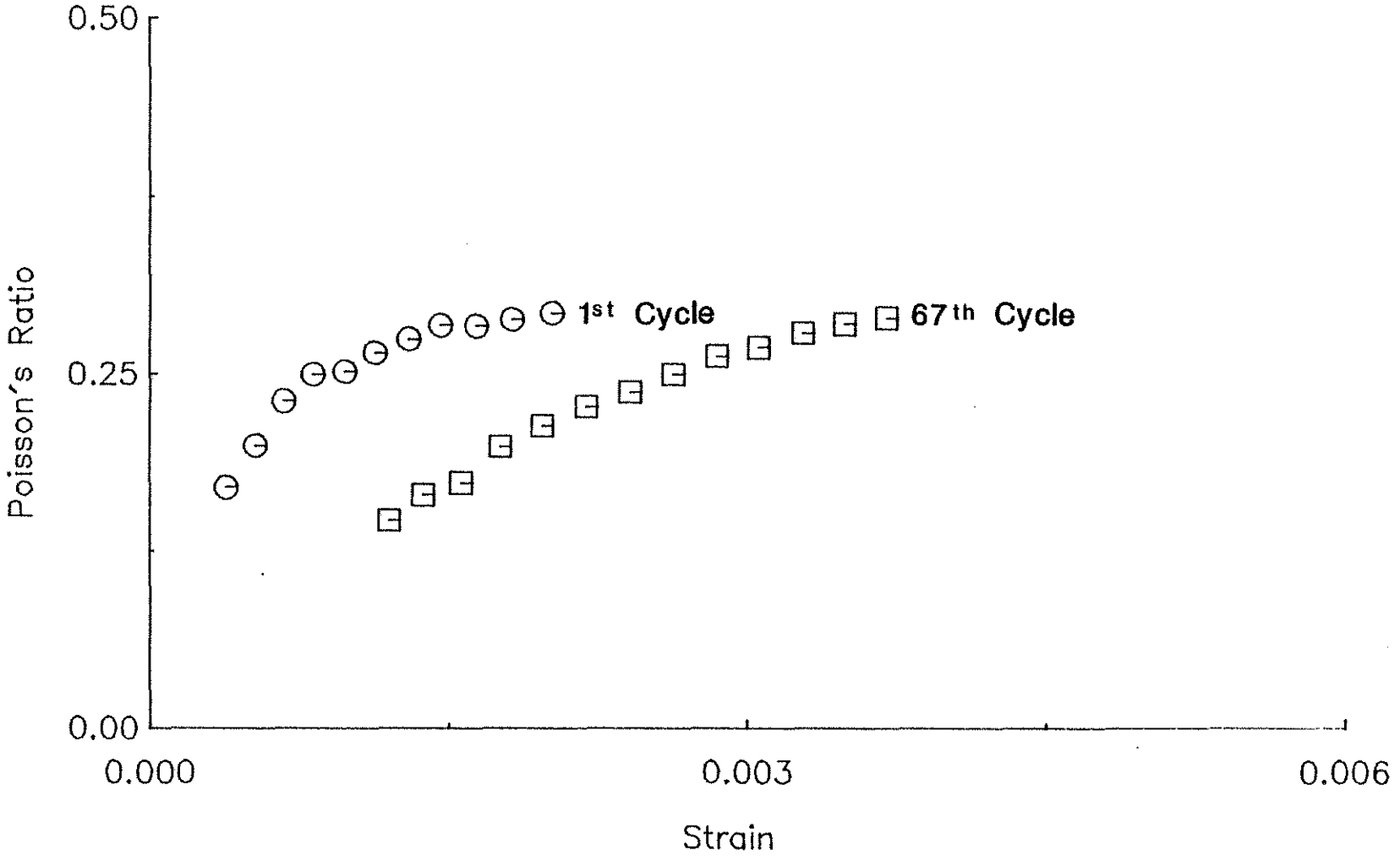

Fig. 2.22. Poisson's Ratio versus Axial Strain for Cyclic Loading: 1st and 67th Cycles; Cement Paste with a W/C = 0.5: Specimen 18-5/P-0.5/C

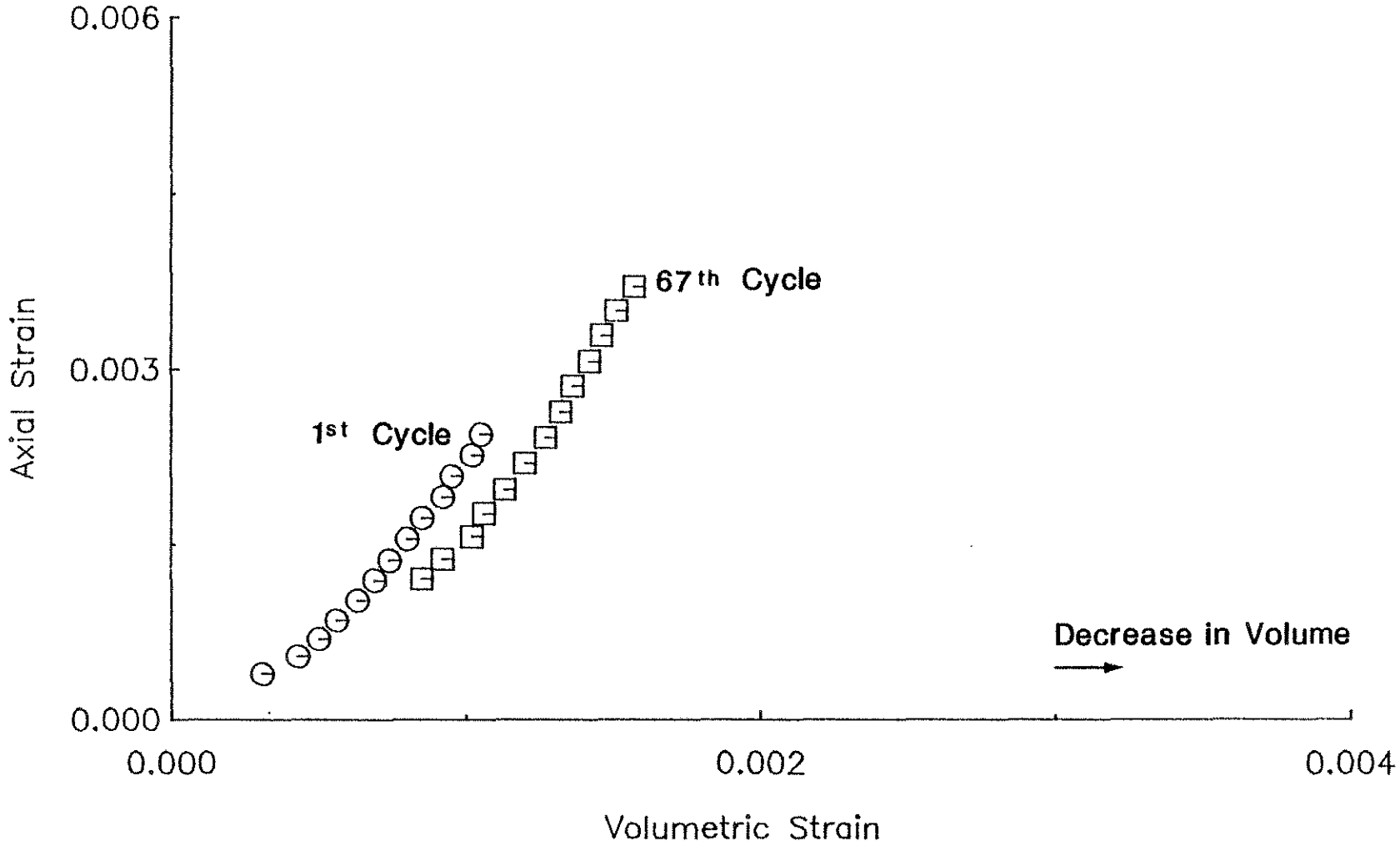

Fig. 2.23. Volumetric Strain versus Axial Strain for Cyclic Loading: 1st and 67th Cycles; Cement Paste with a W/C = 0.5: Specimen 18-5/P-0.5/C

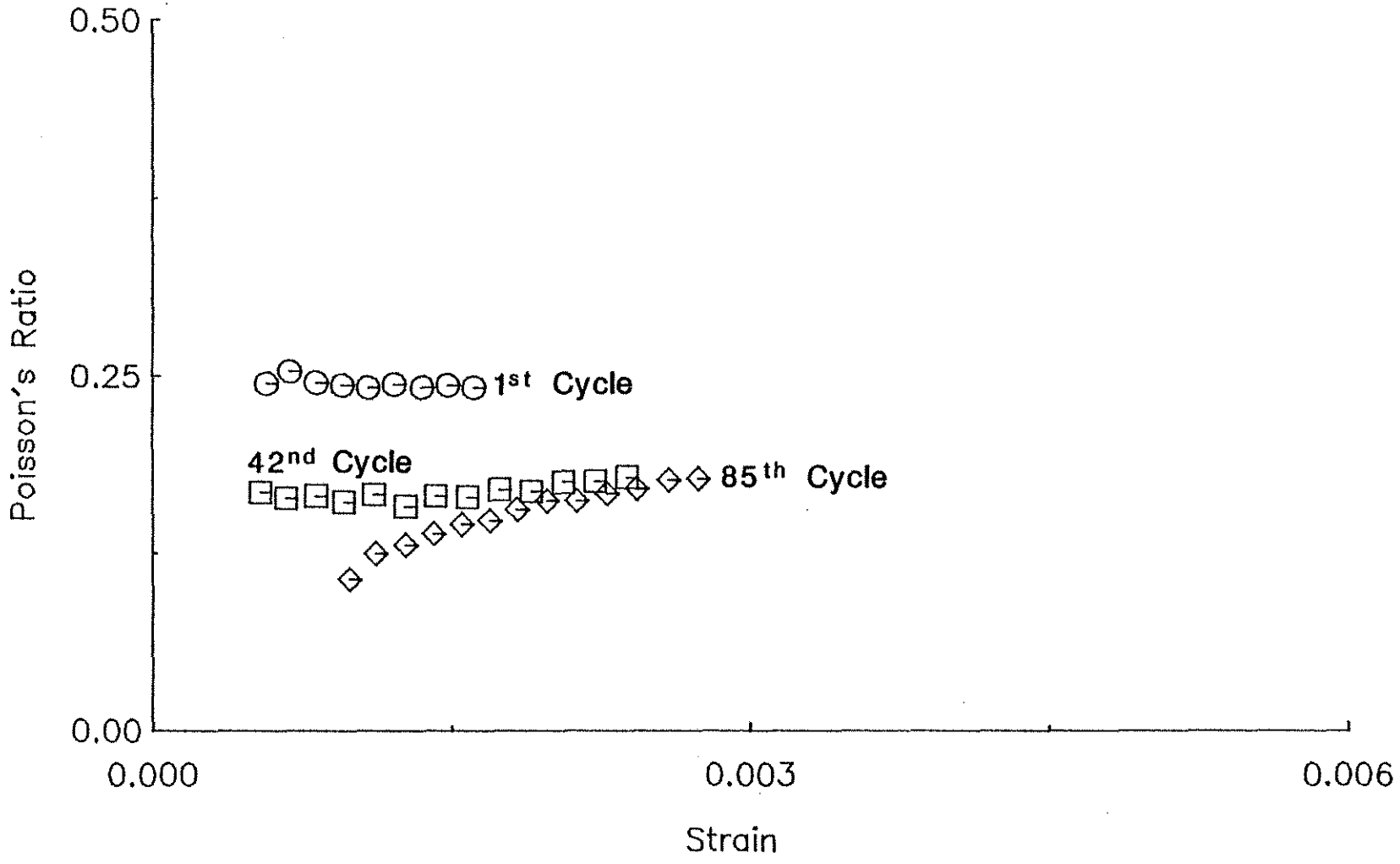

Fig. 2.24. Poisson's Ratio versus Axial Strain for Cyclic Loading: 1st, 42nd and 85th Cycles; Cement Paste with a W/C = 0.3: Specimen 21-5/P-0.3/C

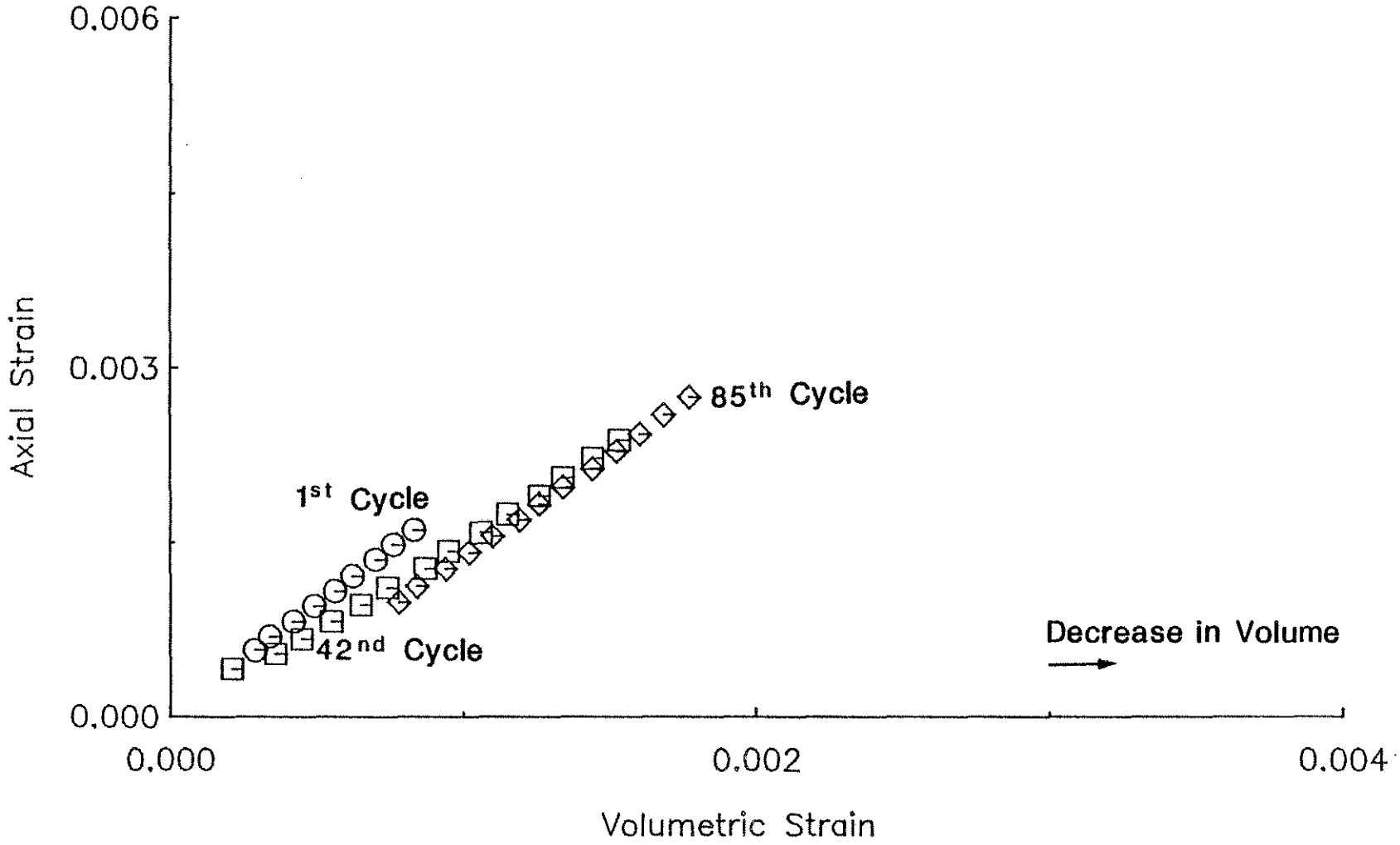

Fig. 2.25. Volumetric Strain versus Axial Strain for Cyclic Loading: 1st, 42nd and 85th Cycles; Cement Paste with a W/C = 0.3: Specimen 21-5/P-0.3/C

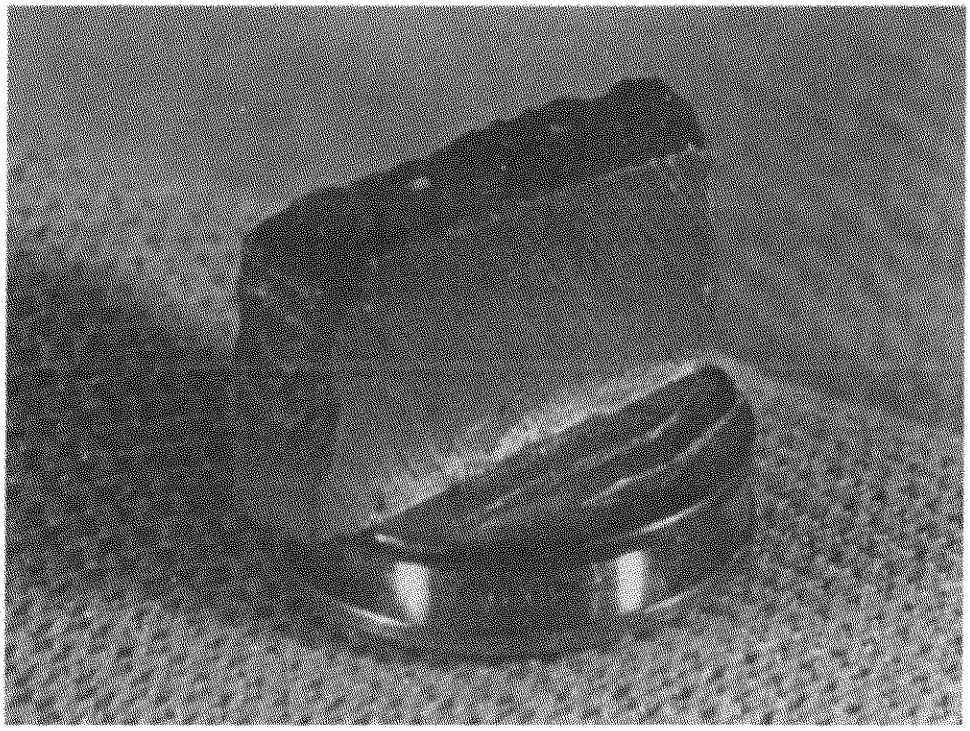

Fig. 2.26. Specimen as Mounted on Stud

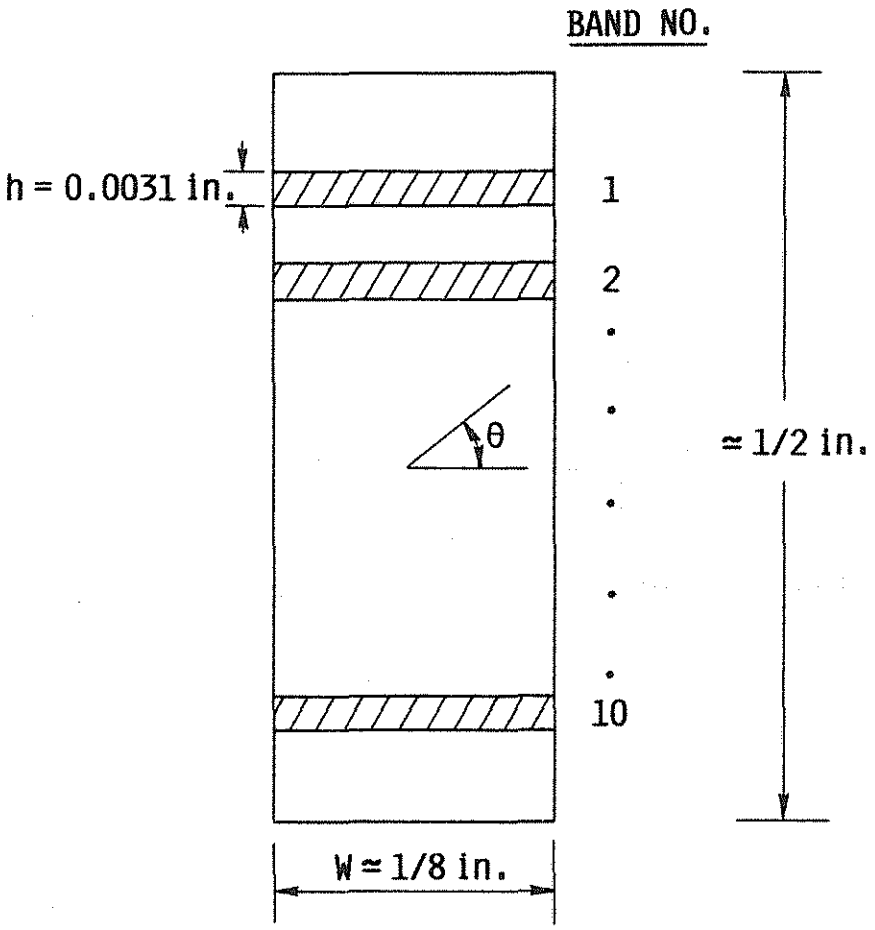

Fig. 2.27. Specimen as Positioned in SEM

Fig. 2.28. Type I Calcium Silicate Hydrate (CSH); Oven Dried Specimen; magnification = 5000x, μ marker =0.9 μm

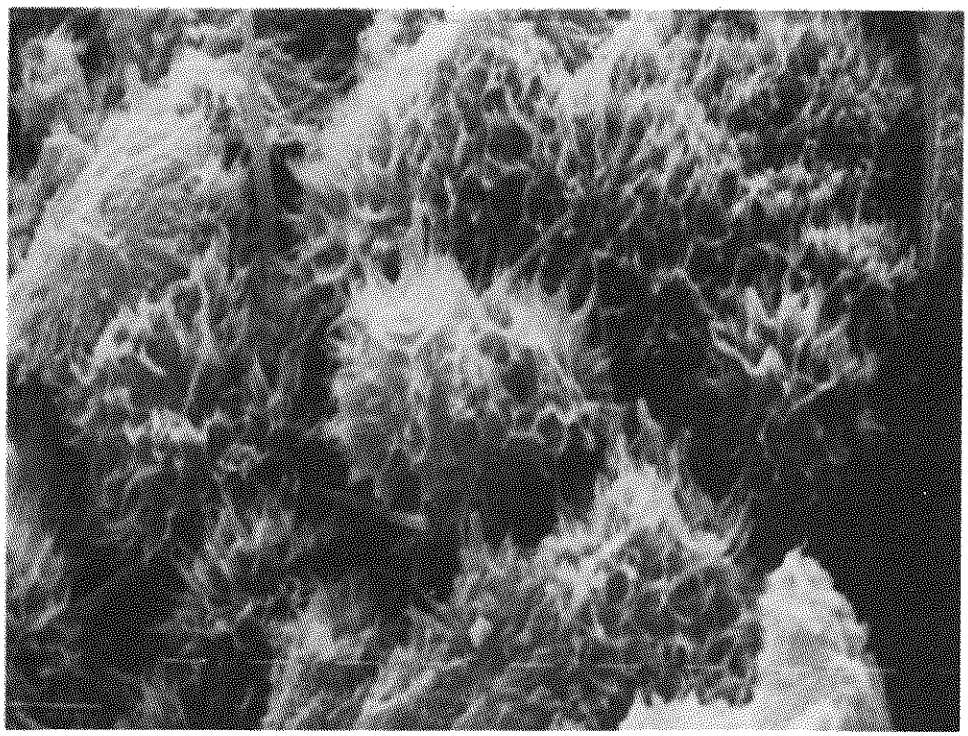

Fig. 2.29. Type I Calcium Silicate Hydrate (CSH); Solvent Replacement Dried Specimen; magnification = 5000x, μ marker = 0.9 μm

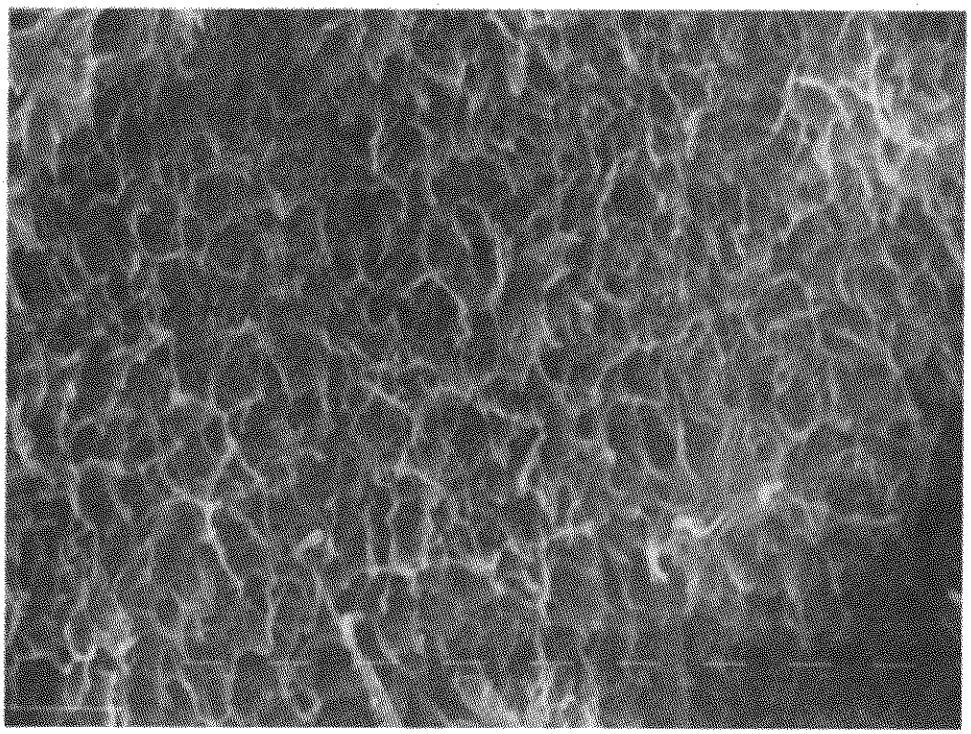

Fig. 2.30. Type II Calcium Silicate Hydrate (CSH); magnification = 5000x, μ marker = 0.9 μm

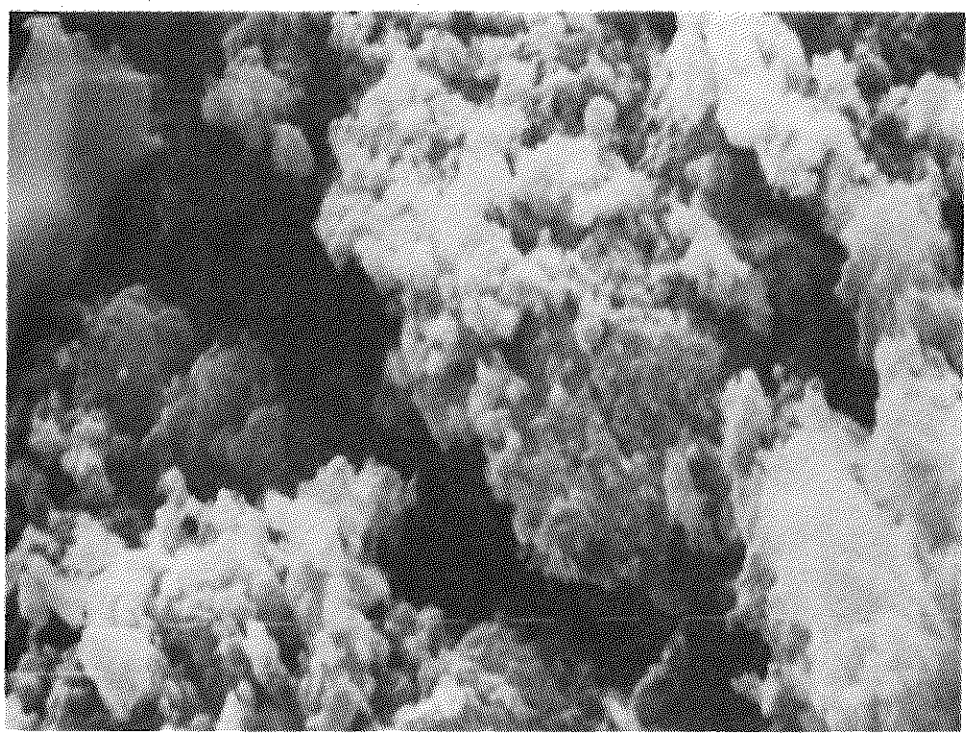

Fig. 2.31. Crack through type III Calcium Silicate Hydrate (CSH); magnification = 5000x, μ marker = 0.9 μm

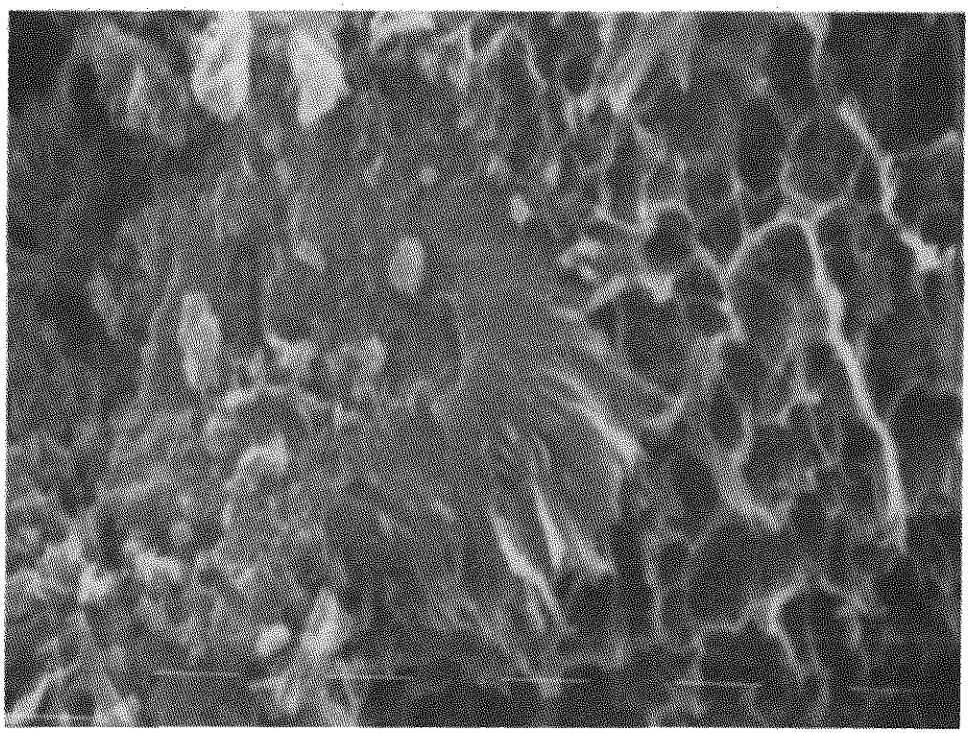

Fig. 2.32. Type IV Calcium Silicate Hydrate (CSH) or Inner Product Morphology (in center of micrograph); magnification = 10000x, μ marker = 0.9 μm

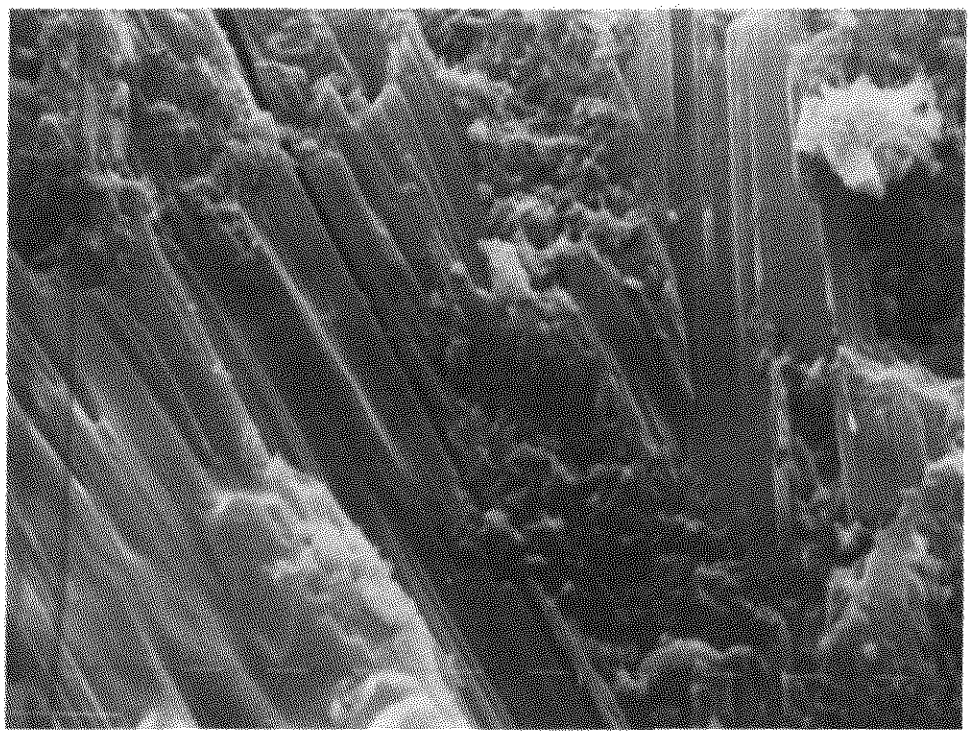

Fig. 2.33. Calcium Hydroxide (CH) with Crack Parallel to Cleavage Plane; magnification = 5000x, μ marker = 0.9 μm

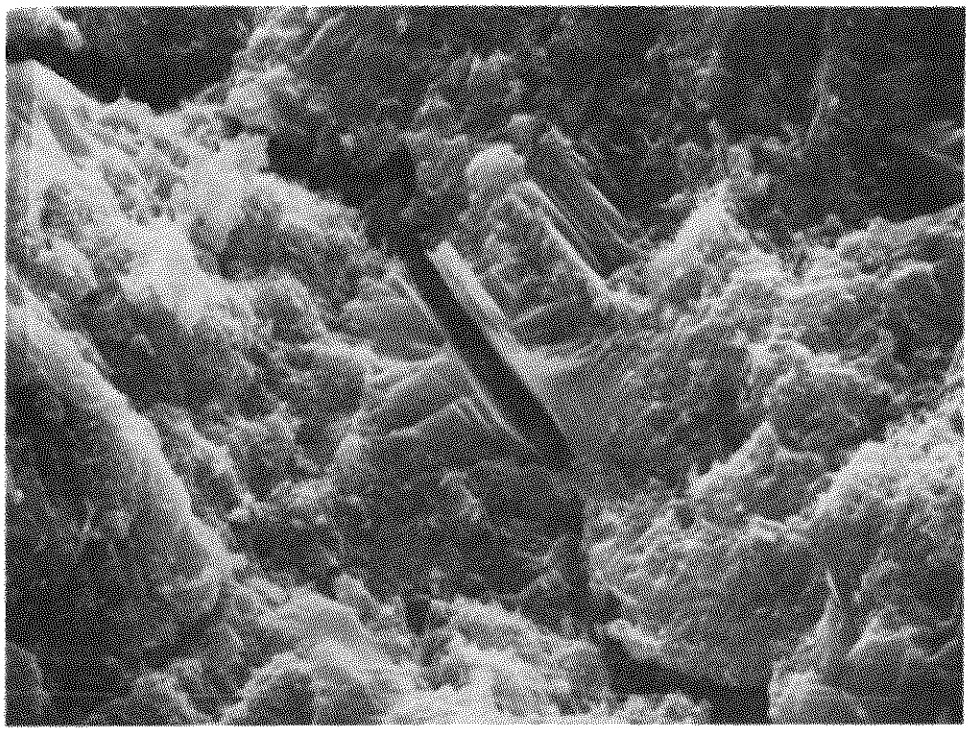

Fig. 2.34. Crack through type III CSH and CH Structures; magnification = 1250x, μ marker = 9.1 μm

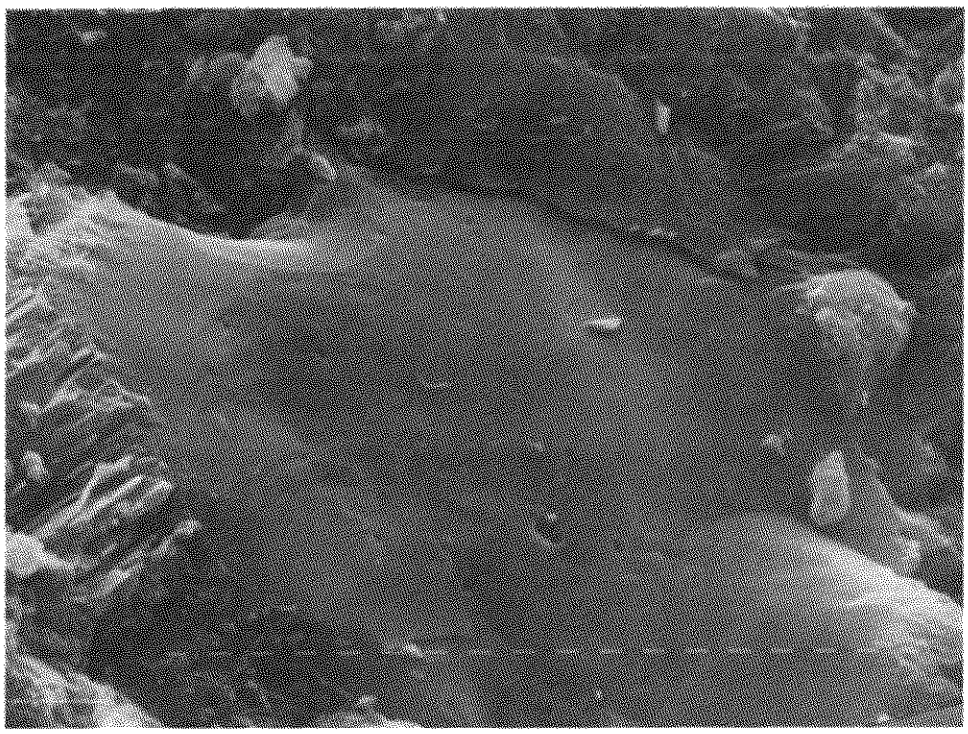

Fig. 2.35. Unhydrated Cement Grain (UHC); magnification = 2500x, μ marker = 0.9 μm

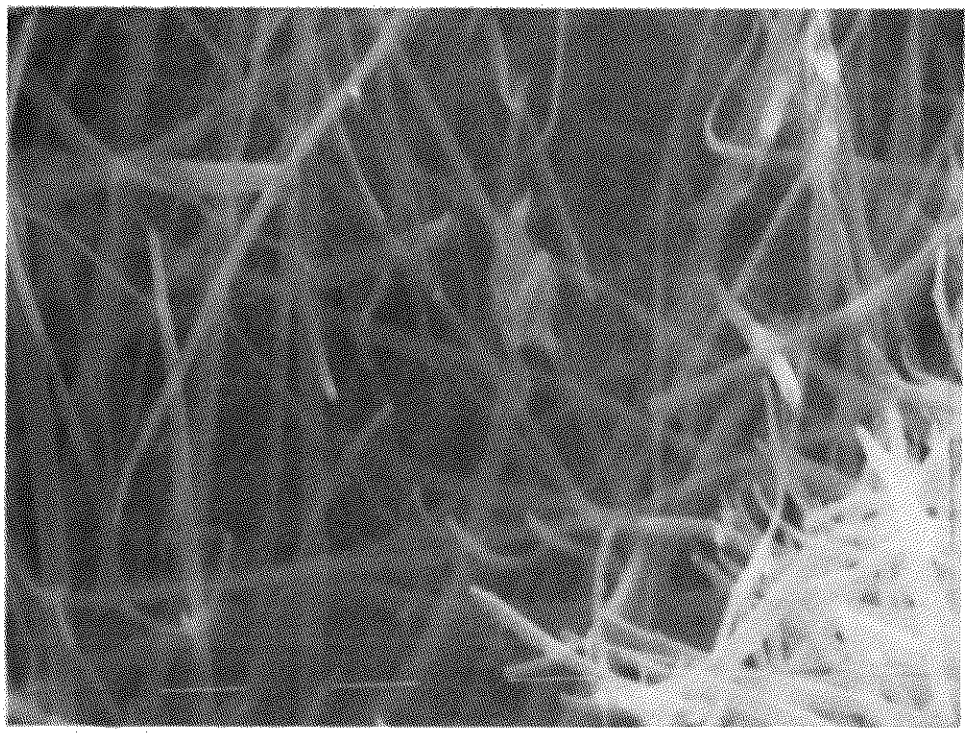

Fig. 2.36. Ettringite; magnification = 10000x, μ marker = 0.9 μm

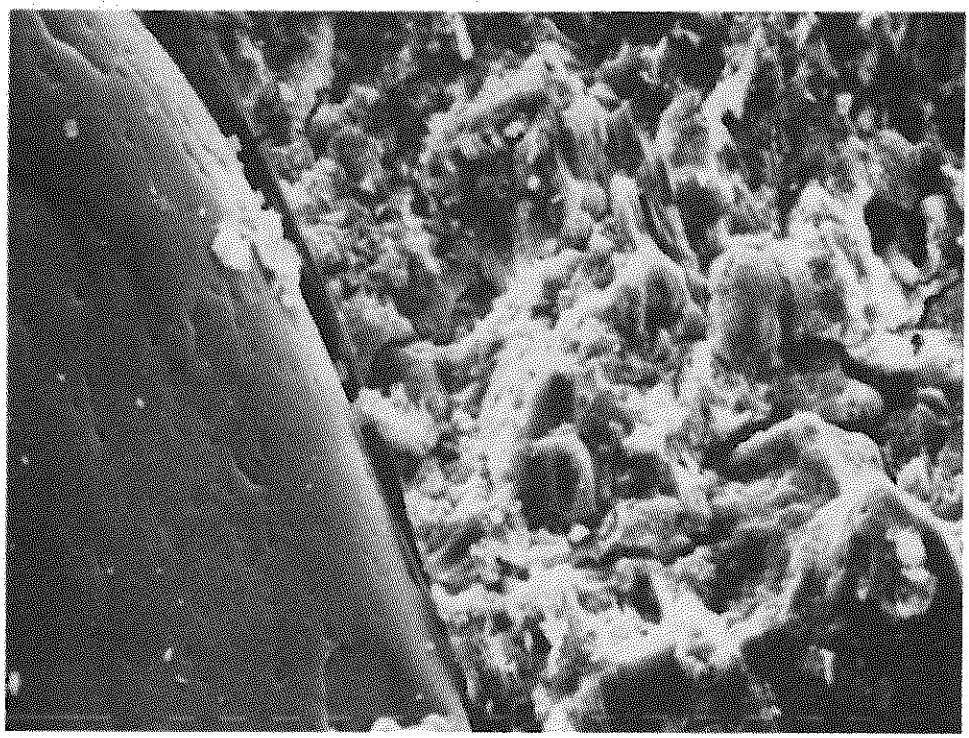

Fig. 2.37. Sand Grain (SG) Adjacent to type III CSH with Cracks at the Interface and withing the CSH; magnification = 320x, μ marker = 90.9 μm

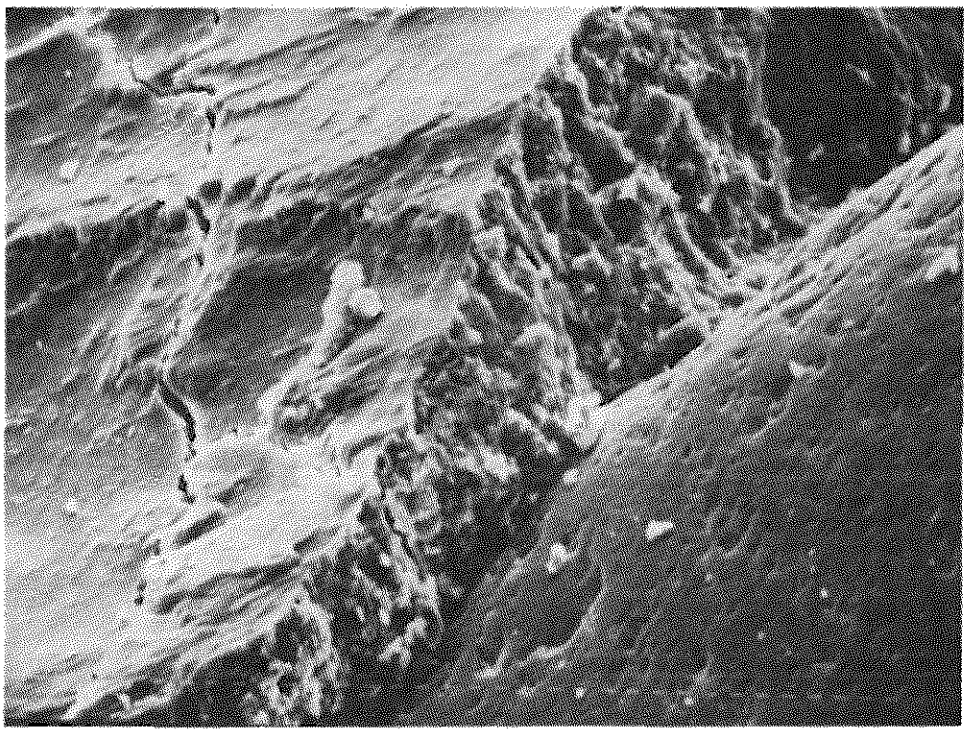

Fig. 2.38. Sand Grain (SG) Adjacent to type III CSH with Cracks at the Interface and withing the CSH; magnification = 160x, μ marker = 90.9 μm

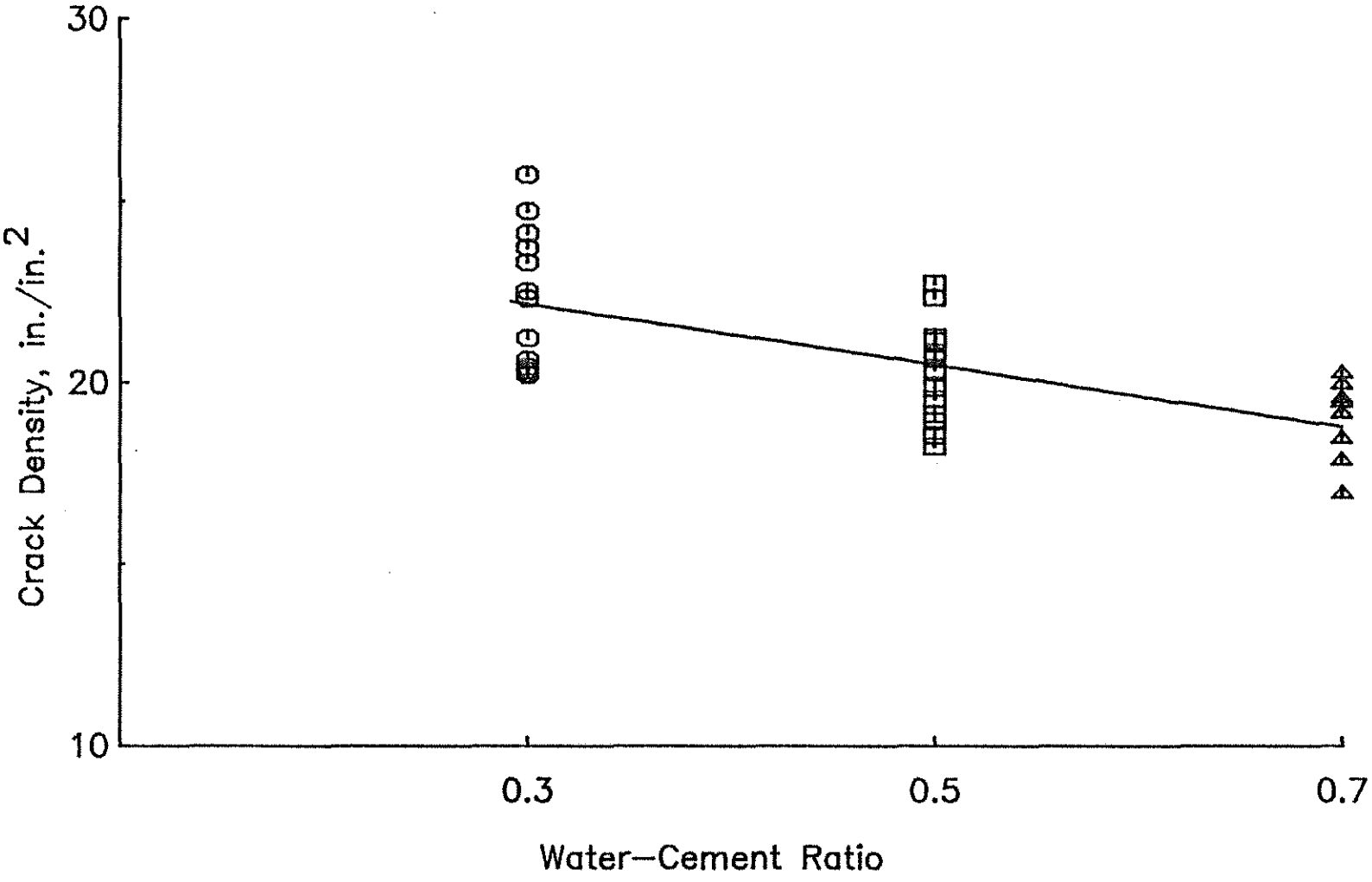

Fig. 2.39. Crack Density versus Water-Cement Ratio for Nonloaded Cement Paste Specimens

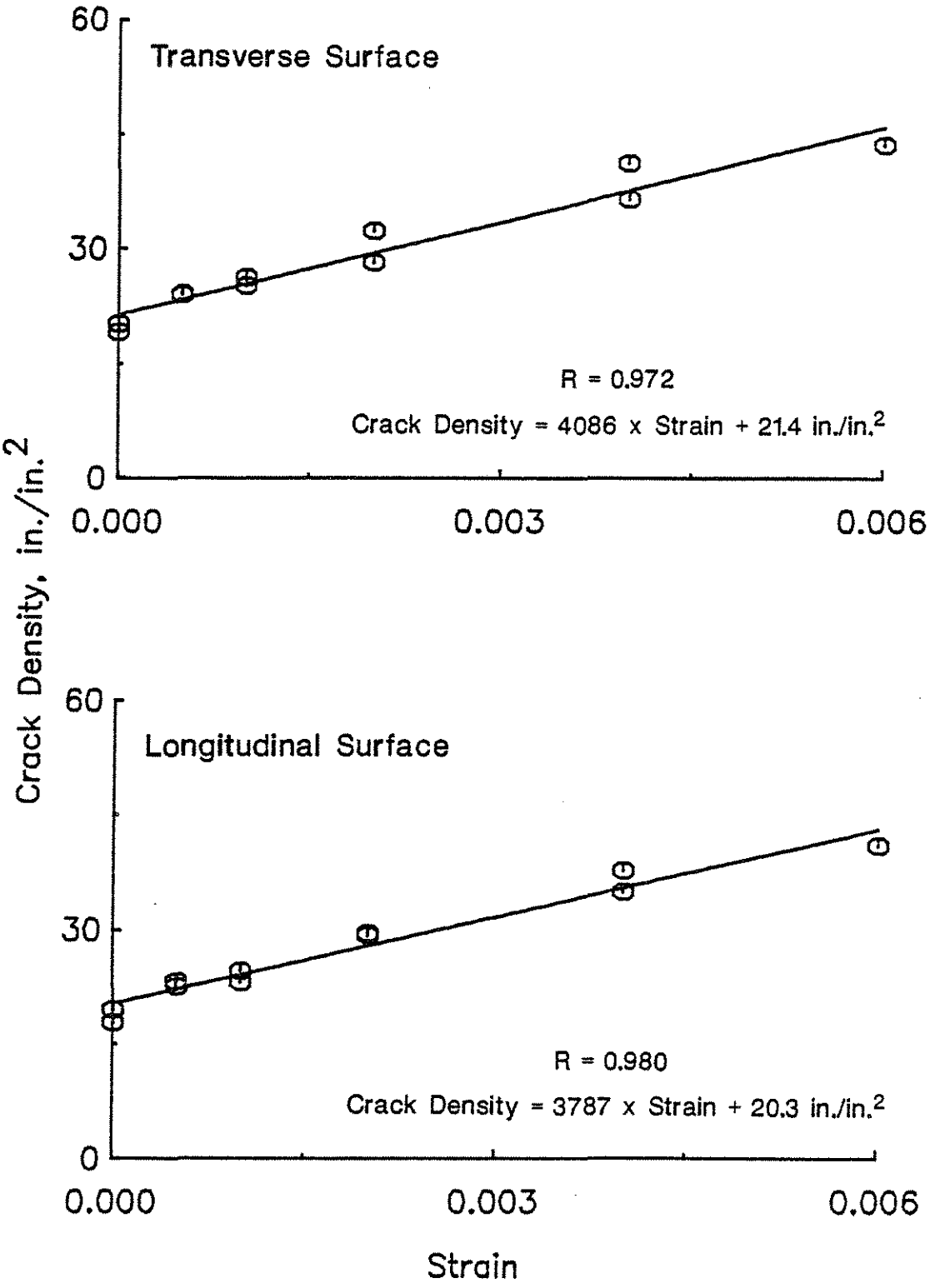

Fig. 2.40. Crack Density versus Strain for Monotonic Loading of Cement Paste with a W/C = 0.7; Transverse and Longitudinal Surfaces

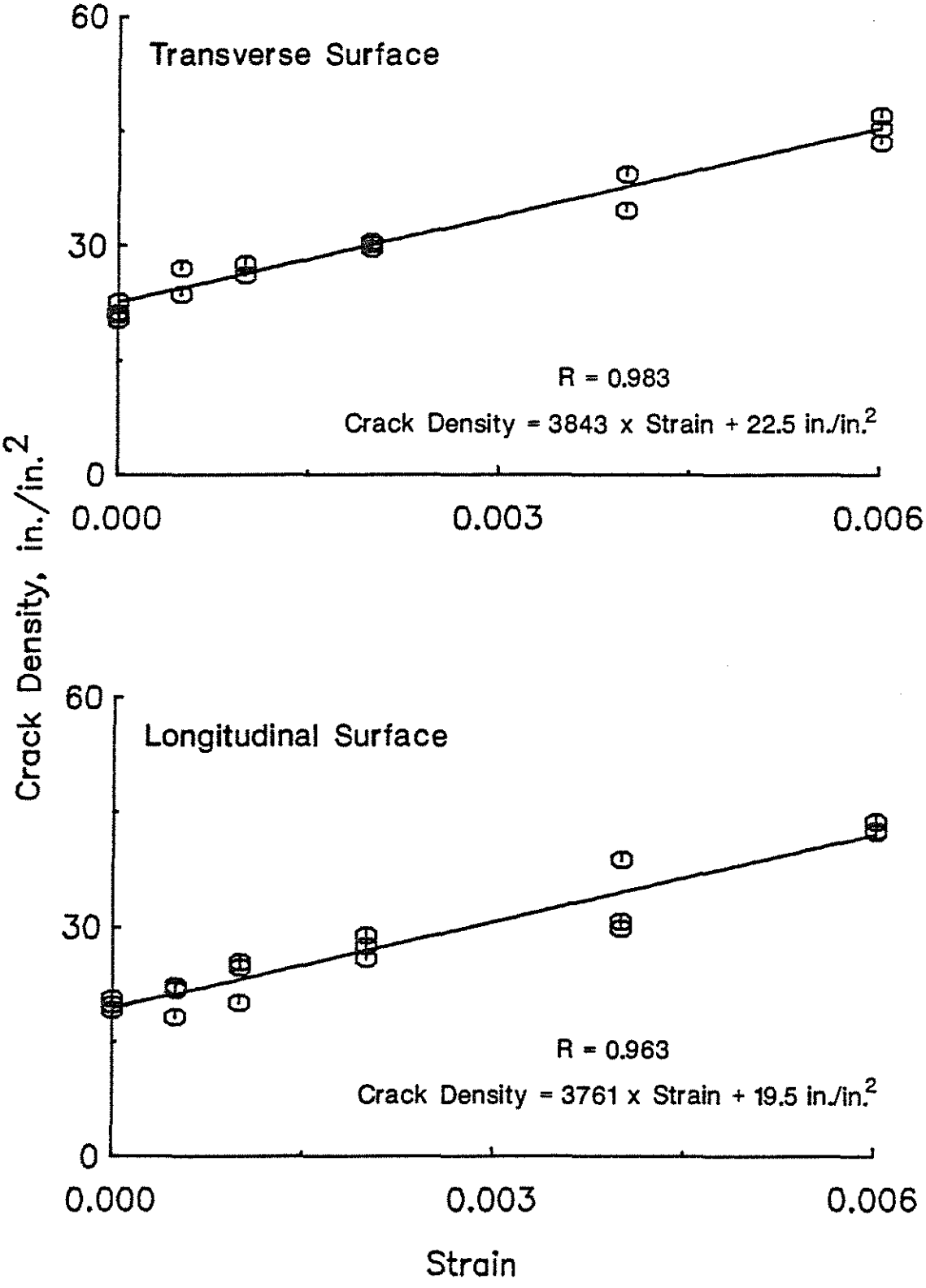

Fig. 2.41. Crack Density versus Strain for Monotonic Loading of Cement Paste with a W/C = 0.5; Transverse and Longitudinal Surfaces

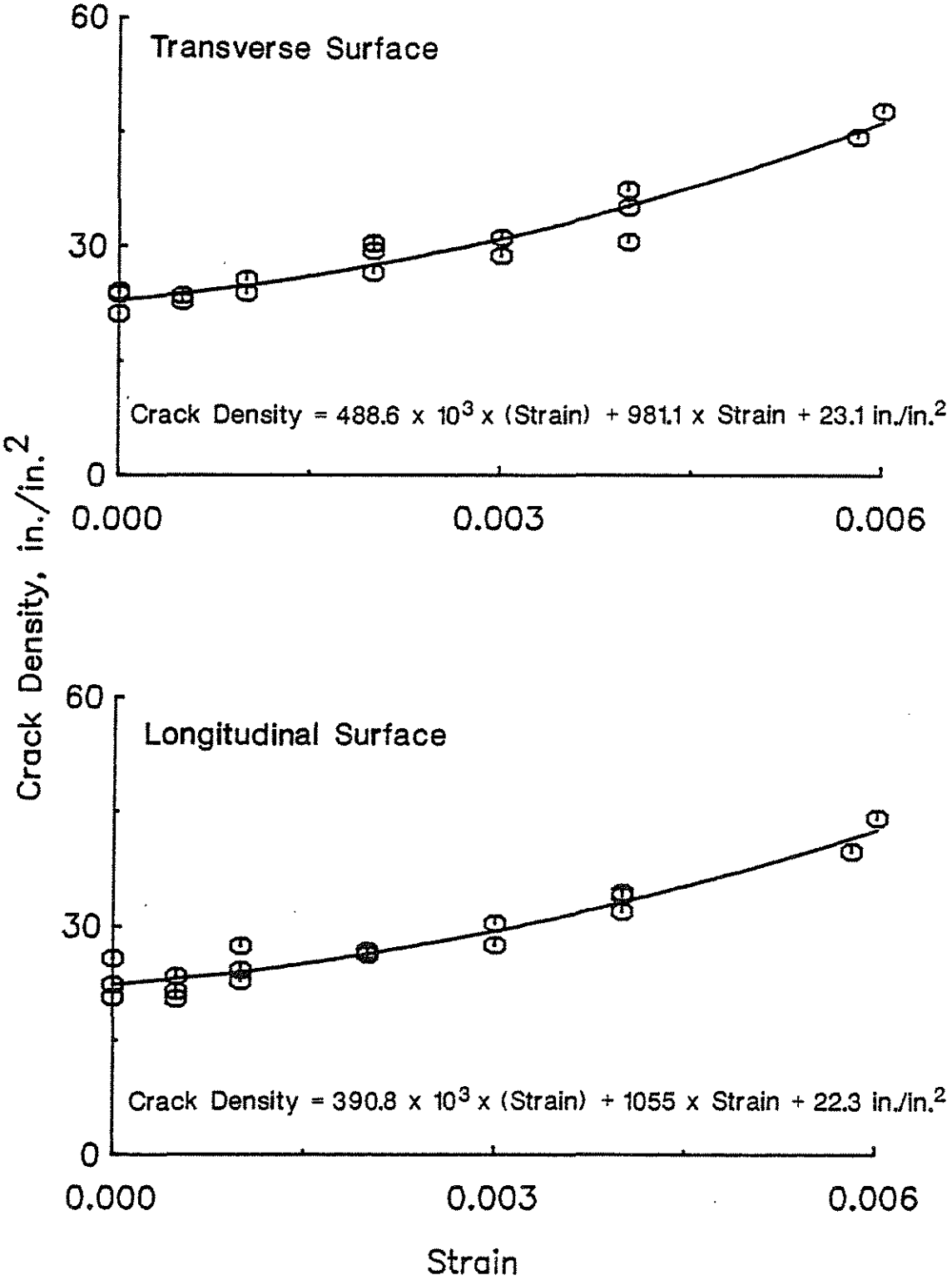

Fig. 2.42. Crack Density versus Strain for Monotonic Loading of Cement Paste with a W/C = 0.3; Transverse and Longitudinal Surfaces

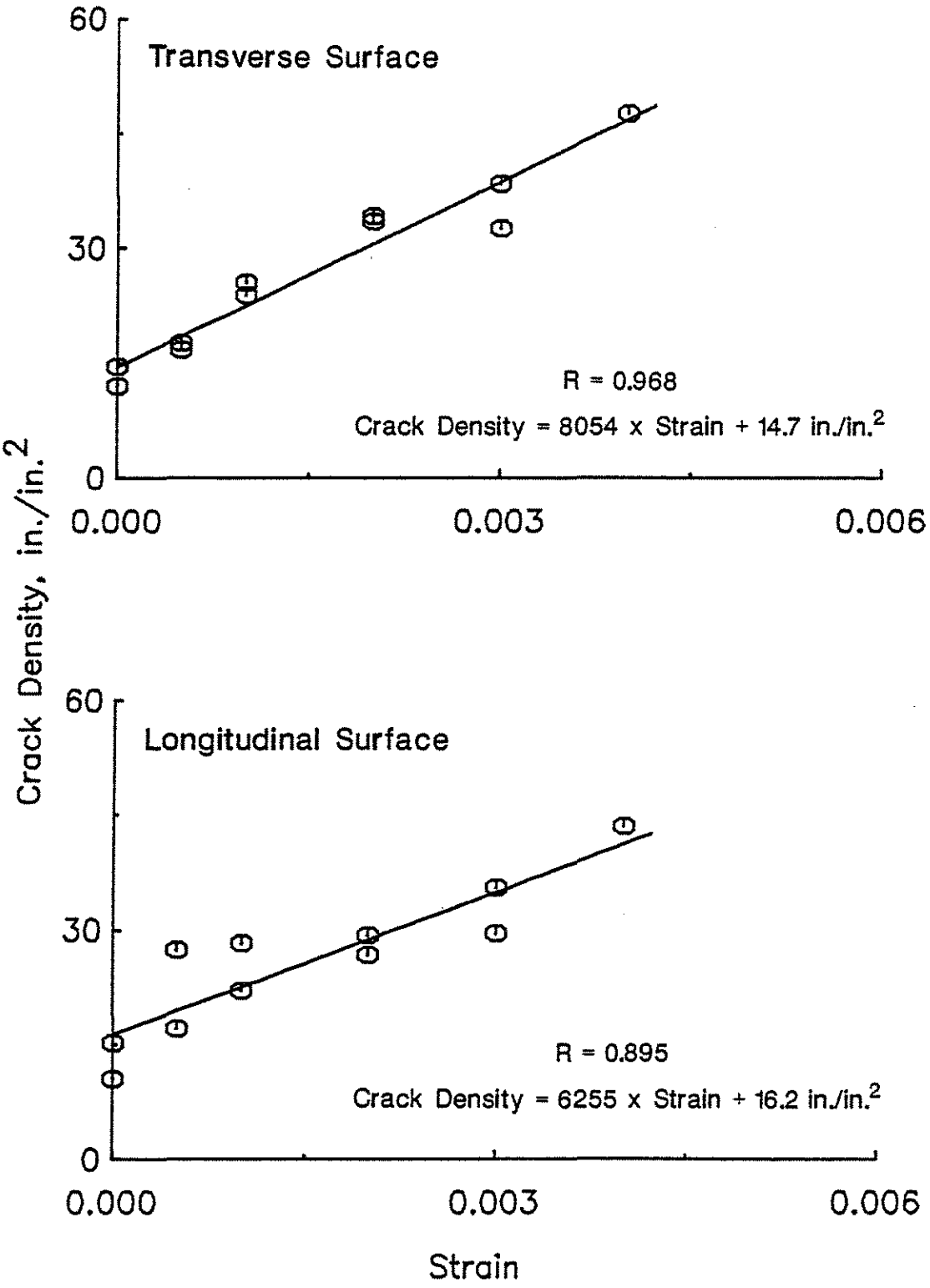

Fig. 2.43. Crack Density versus Strain on Monotonic Loading of Mortar with a W/C = 0.5; Transverse and Longitudinal Surfaces

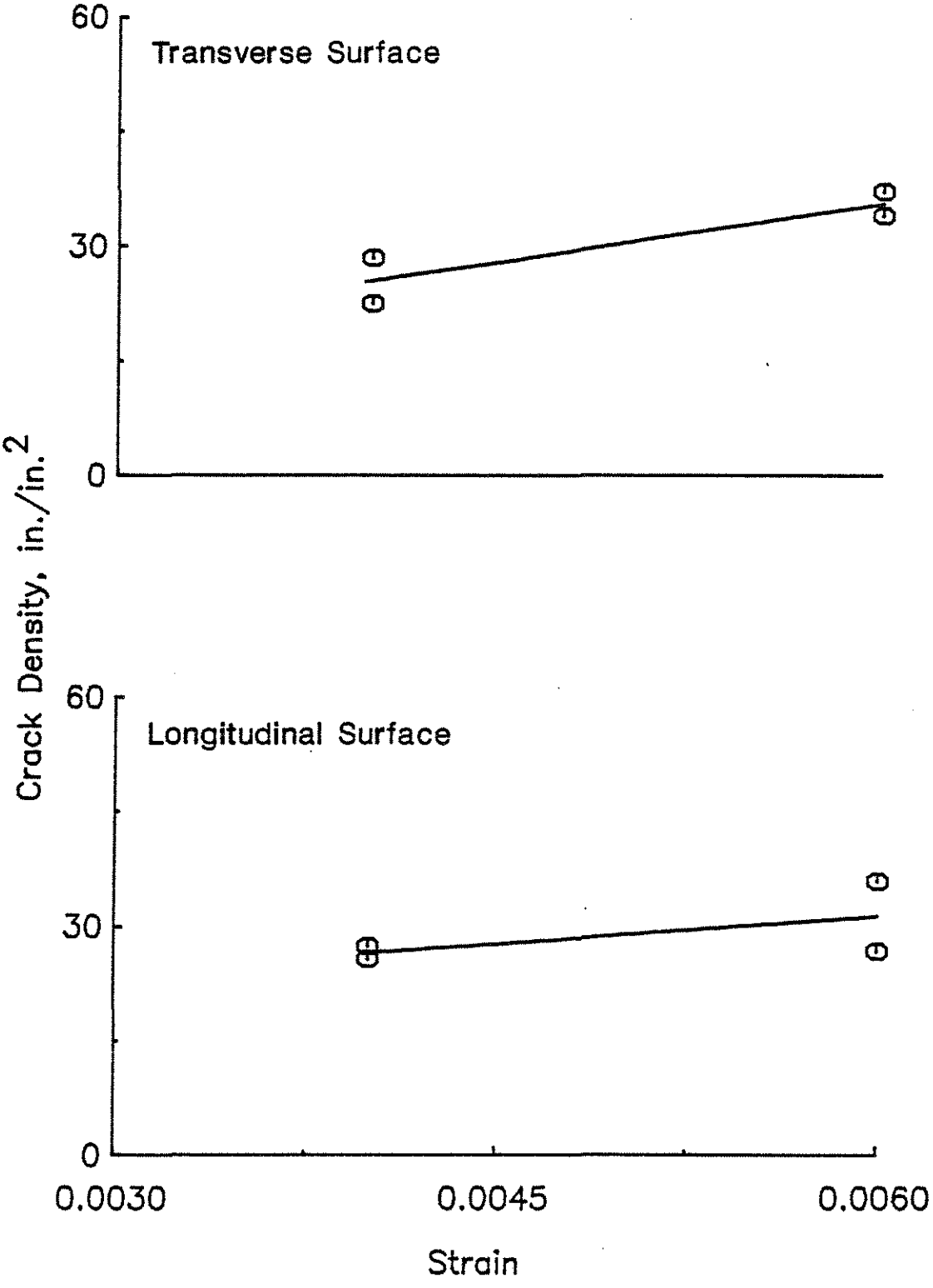

Fig. 2.44. Crack Density versus Strain for Sustained Loading of Cement Paste with a W/C = 0.5; Transverse and Longitudinal Surfaces

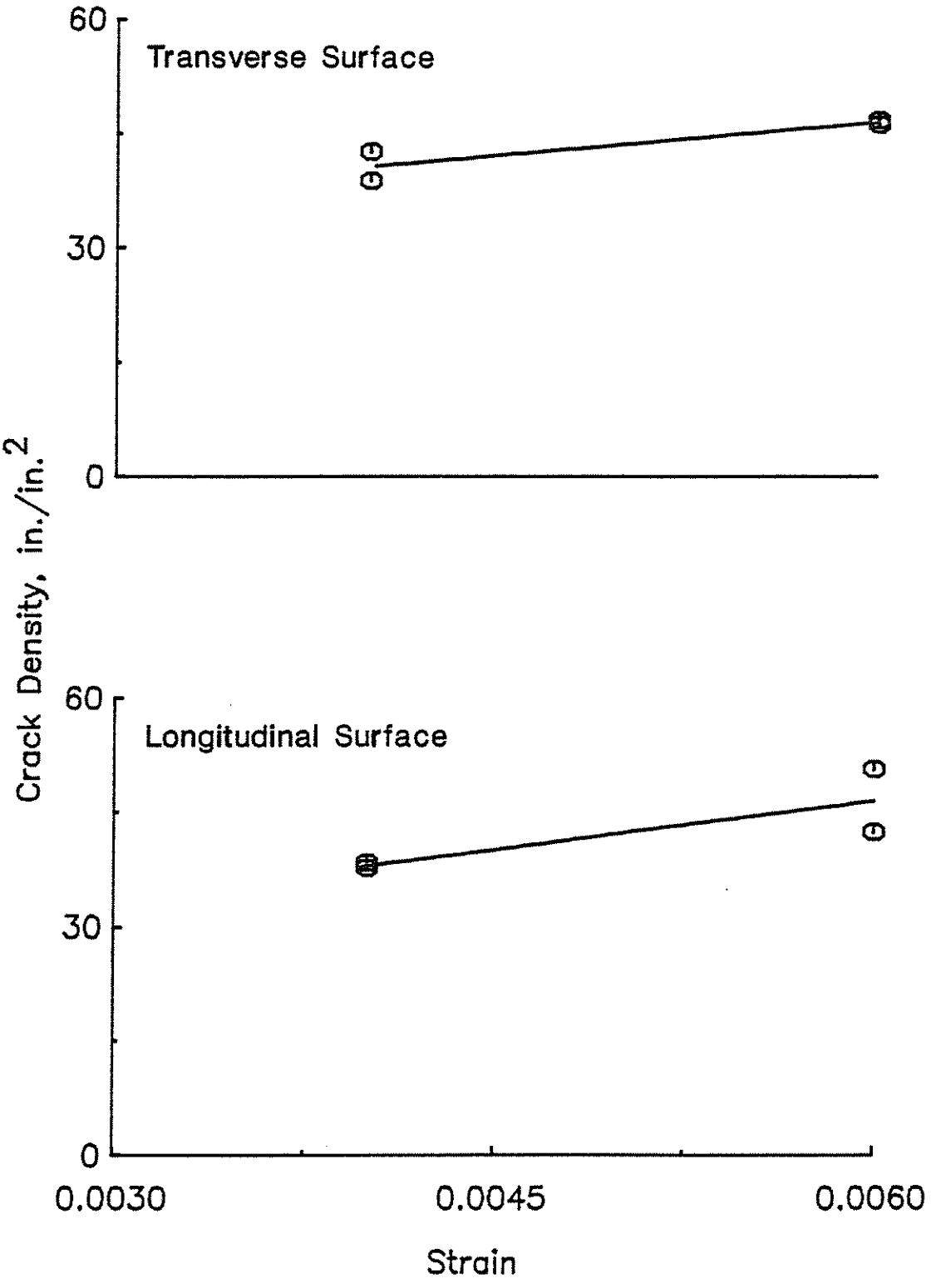

Fig. 2.45. Crack Density versus Strain for Sustained Loading of Cement Paste with a W/C = 0.3; Transverse and Longitudinal Surfaces

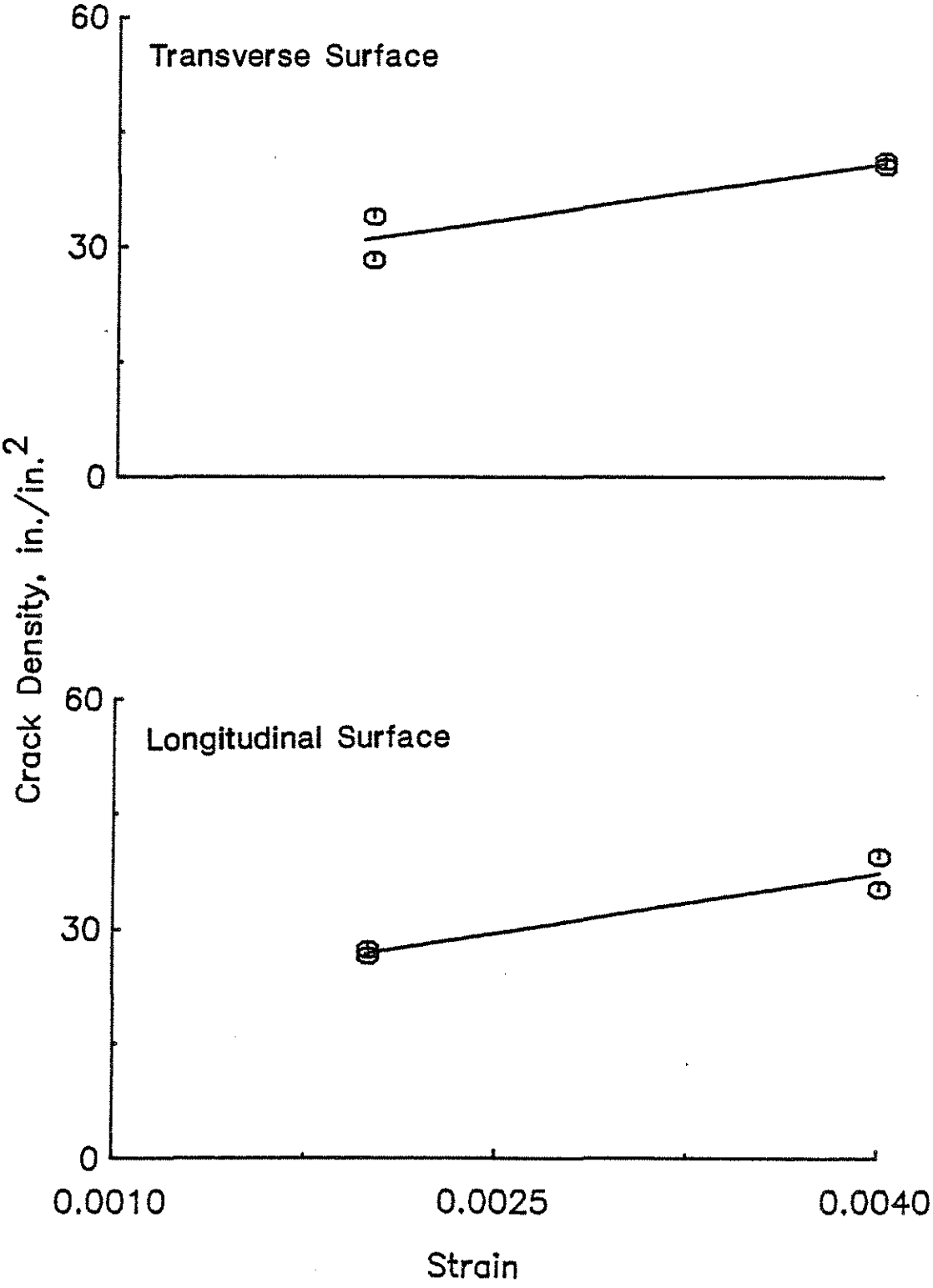

Fig. 2.46. Crack Density versus Strain for Cyclic Loading of Cement Paste with a W/C = 0.5; Transverse and Longitudinal Surfaces

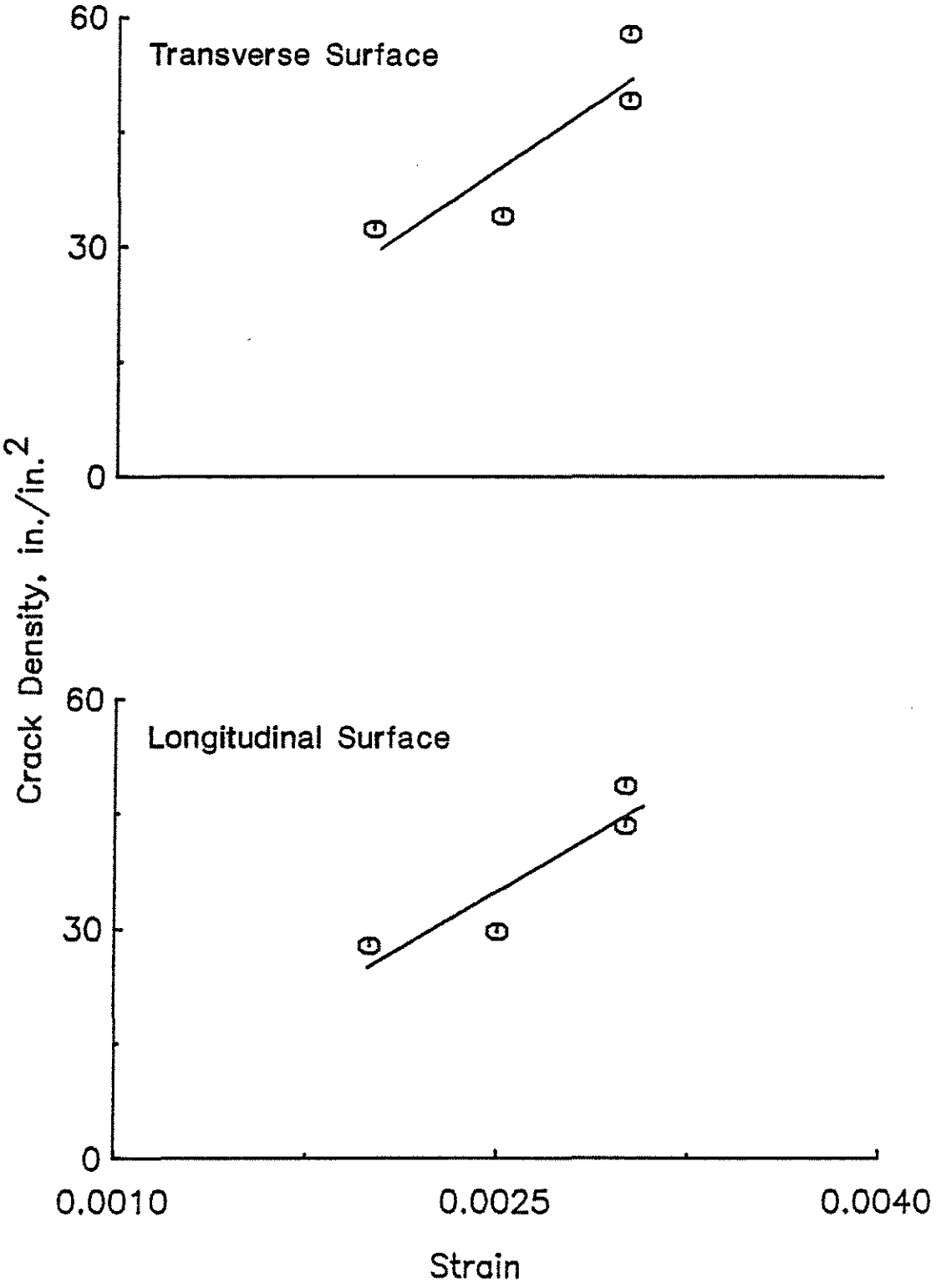

Fig. 2.47. Crack Density versus Strain for Cyclic Loading of Cement Paste with a W/C = 0.3; Transverse and Longitudinal Surfaces

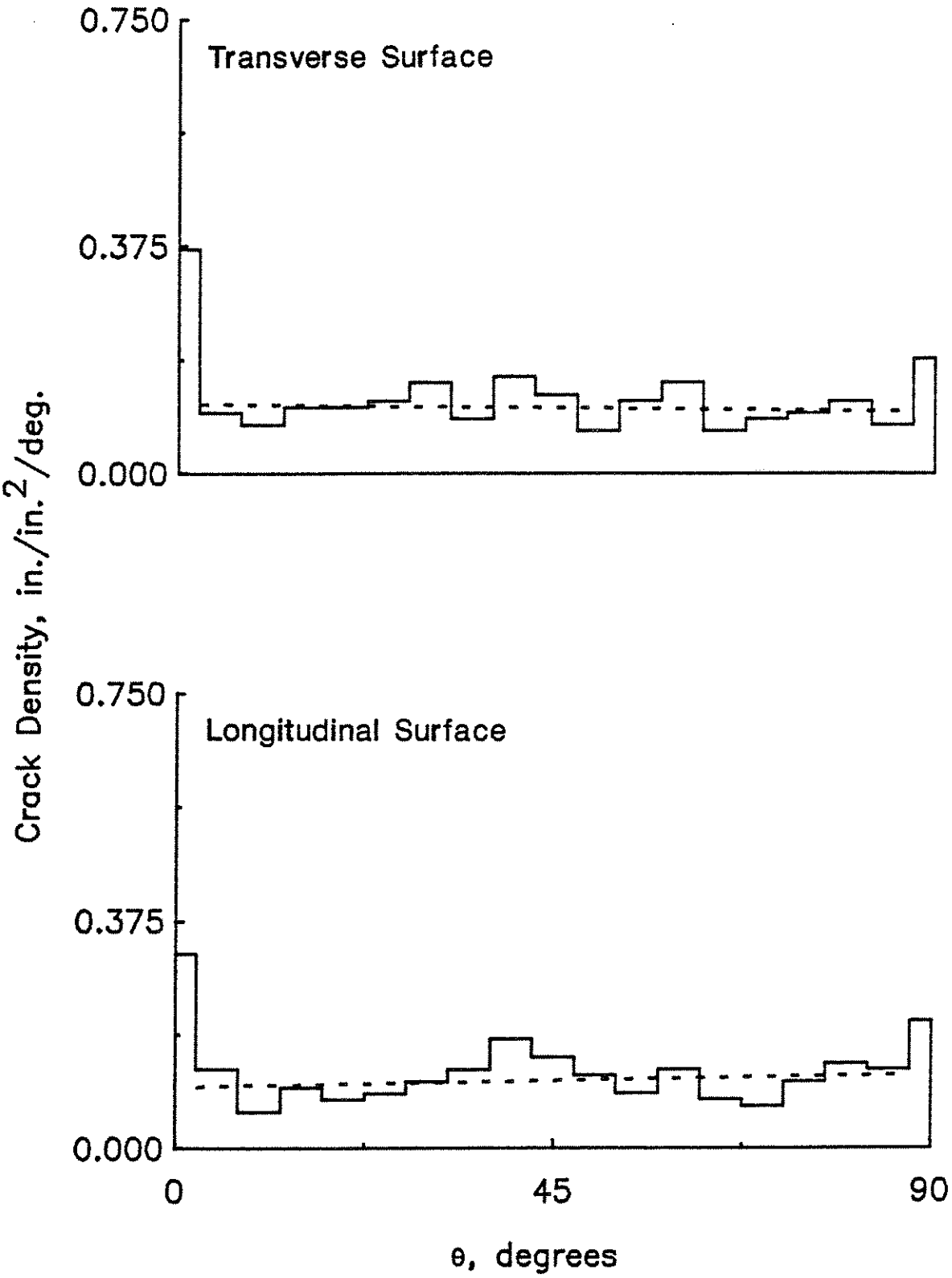

Fig. 2.48. Crack Density versus Trace Angle for Transverse and Longitudinal Surfaces of Nonloaded Cement Paste with a W/C = 0.5

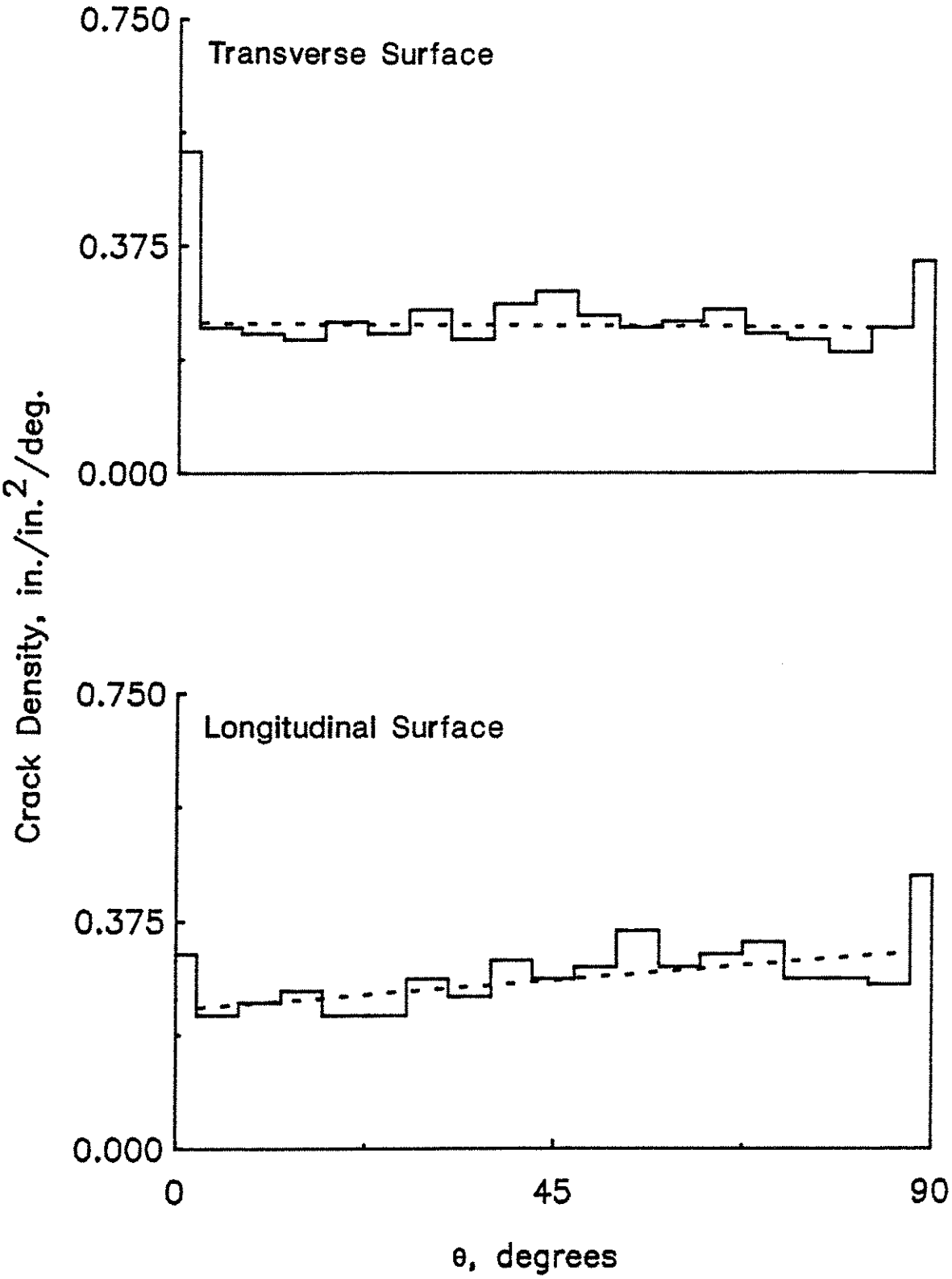

Fig. 2.49. Crack Density versus Trace Angle for Transverse and Longitudinal Surfaces of Monotonically Loaded Cement Paste with a W/C = 0.5; Strain = 0.006

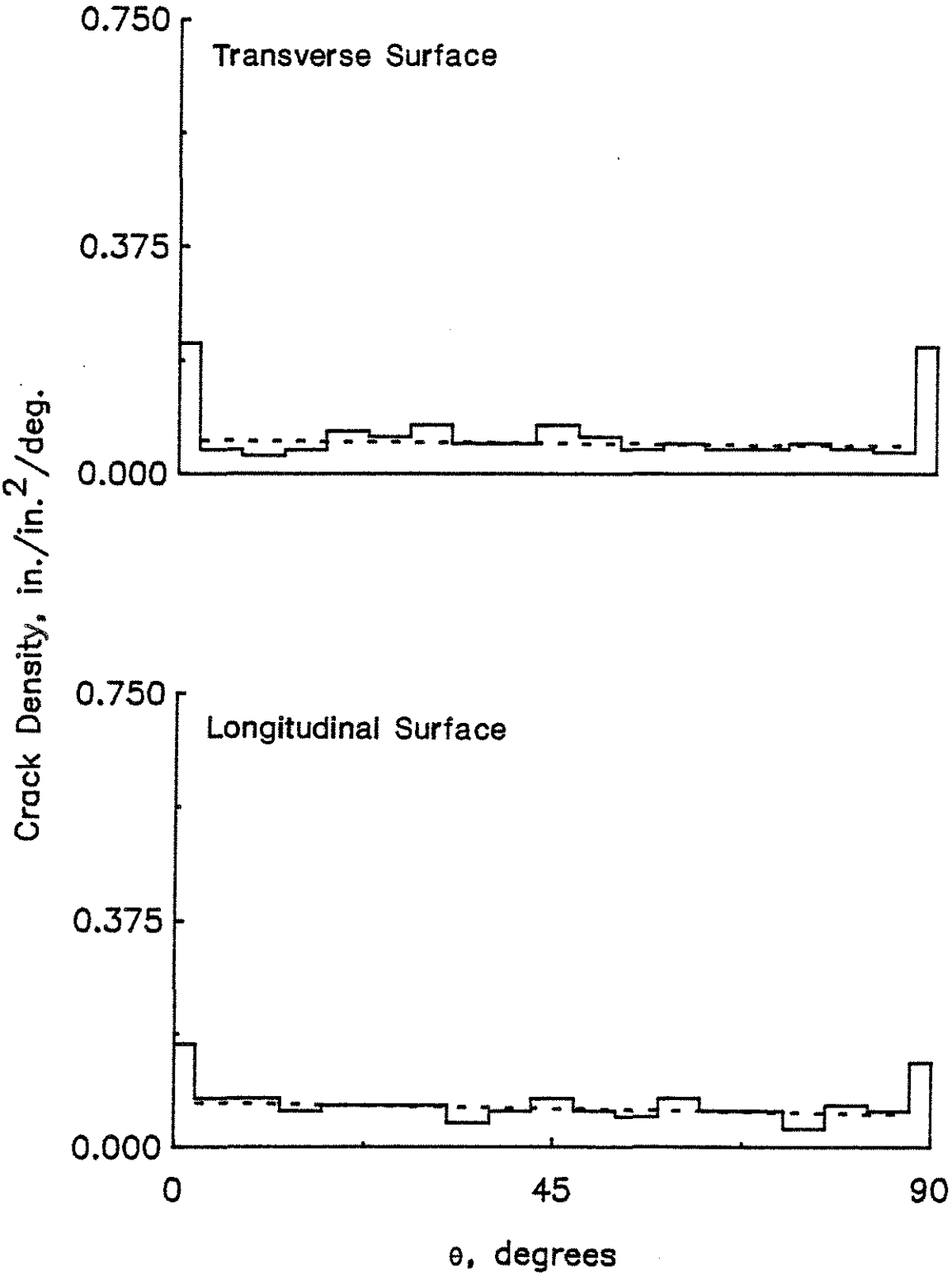

Fig. 2.50. Crack Density versus Trace Angle for Transverse and Longitudinal Surfaces of Nonloaded Mortar with a W/C = 0.5

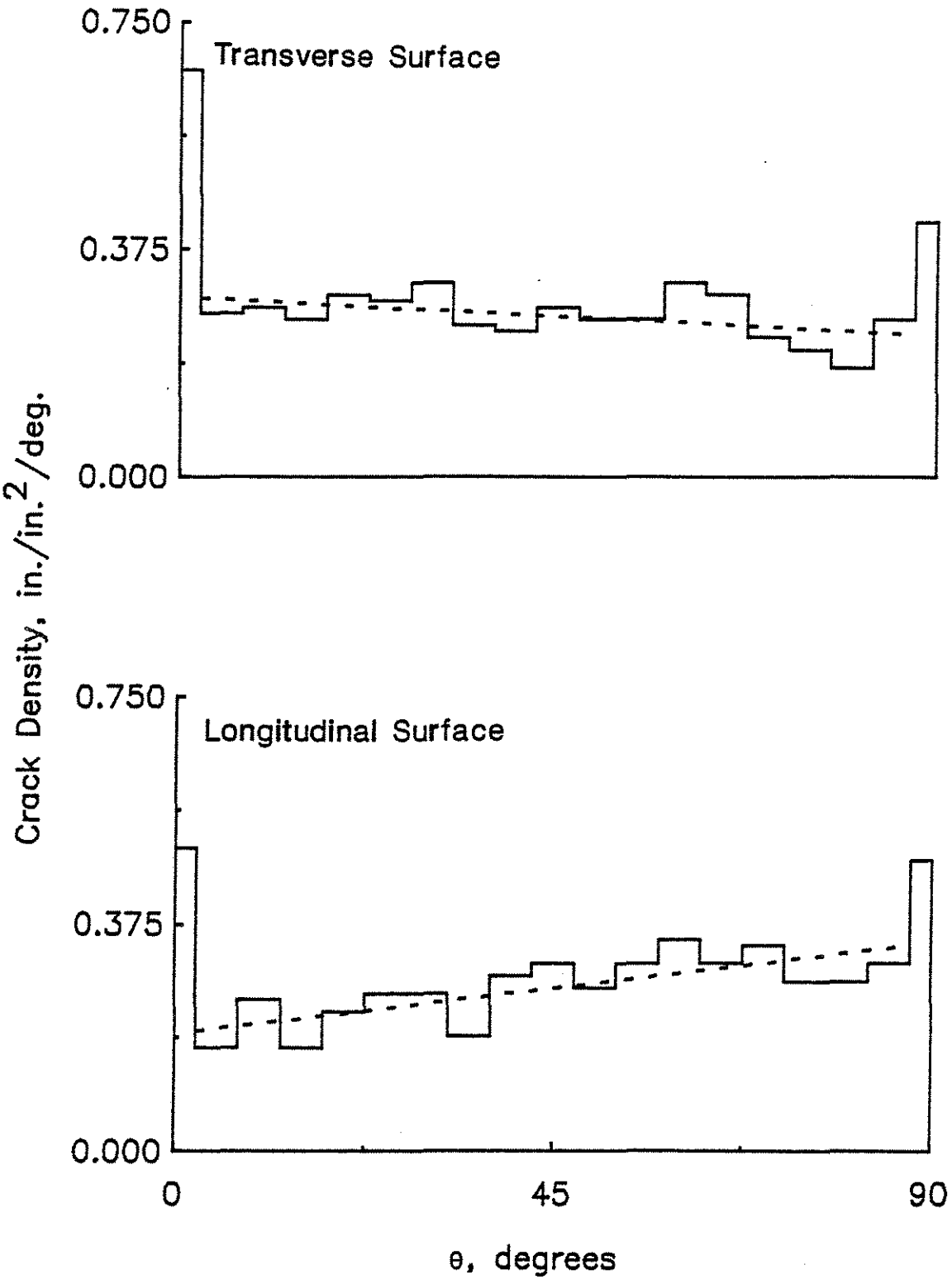

Fig. 2.51. Crack Density versus Trace Angle for Transverse and Longitudinal Surfaces of Monotonically Loaded Mortar with a W/c = 0.5; Strain = 0.004

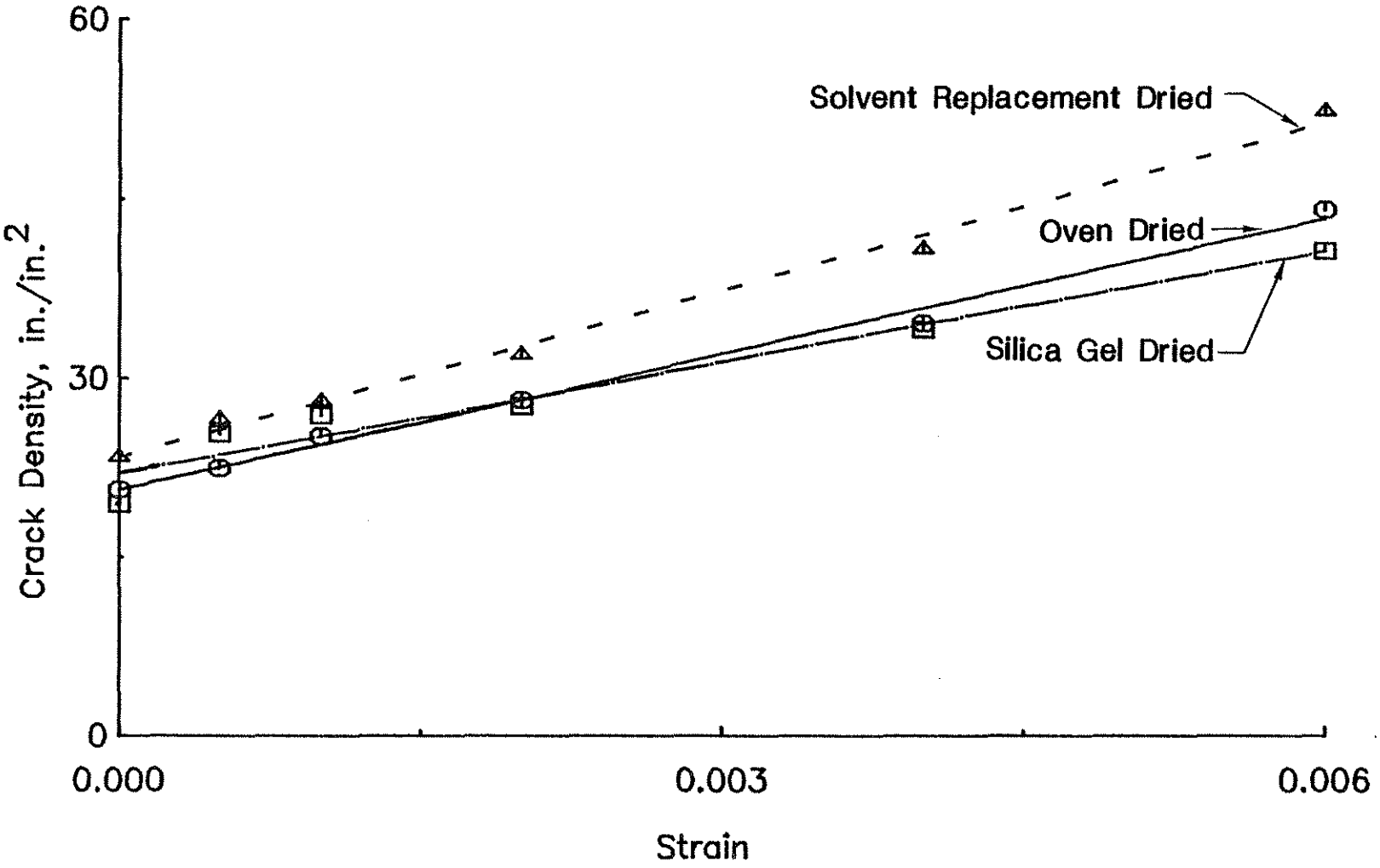

Fig. 2.52. Crack Density versus Strain for Transverse Surfaces of Oven Dried, Solvent Replacement Dried, and Silica Gel Dried Cement Paste Specimens with a W/C = 0.5; Monotonic Loading

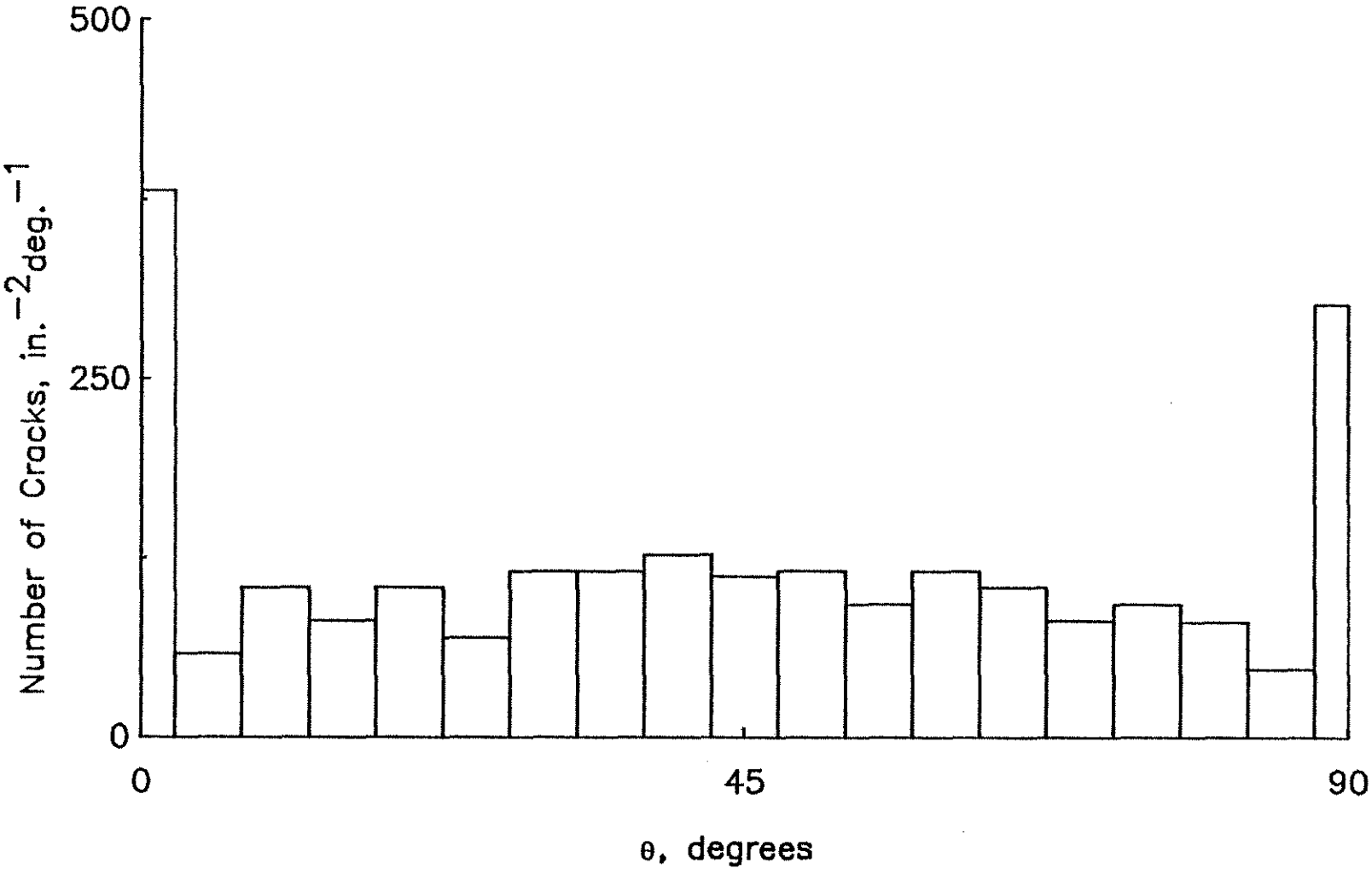

Fig. 3.1. Variation of Number of Cracks per Unit Area per Degree with Trace Angle; Transverse Surface of Nonloaded Cement Paste with a W/C = 0.5

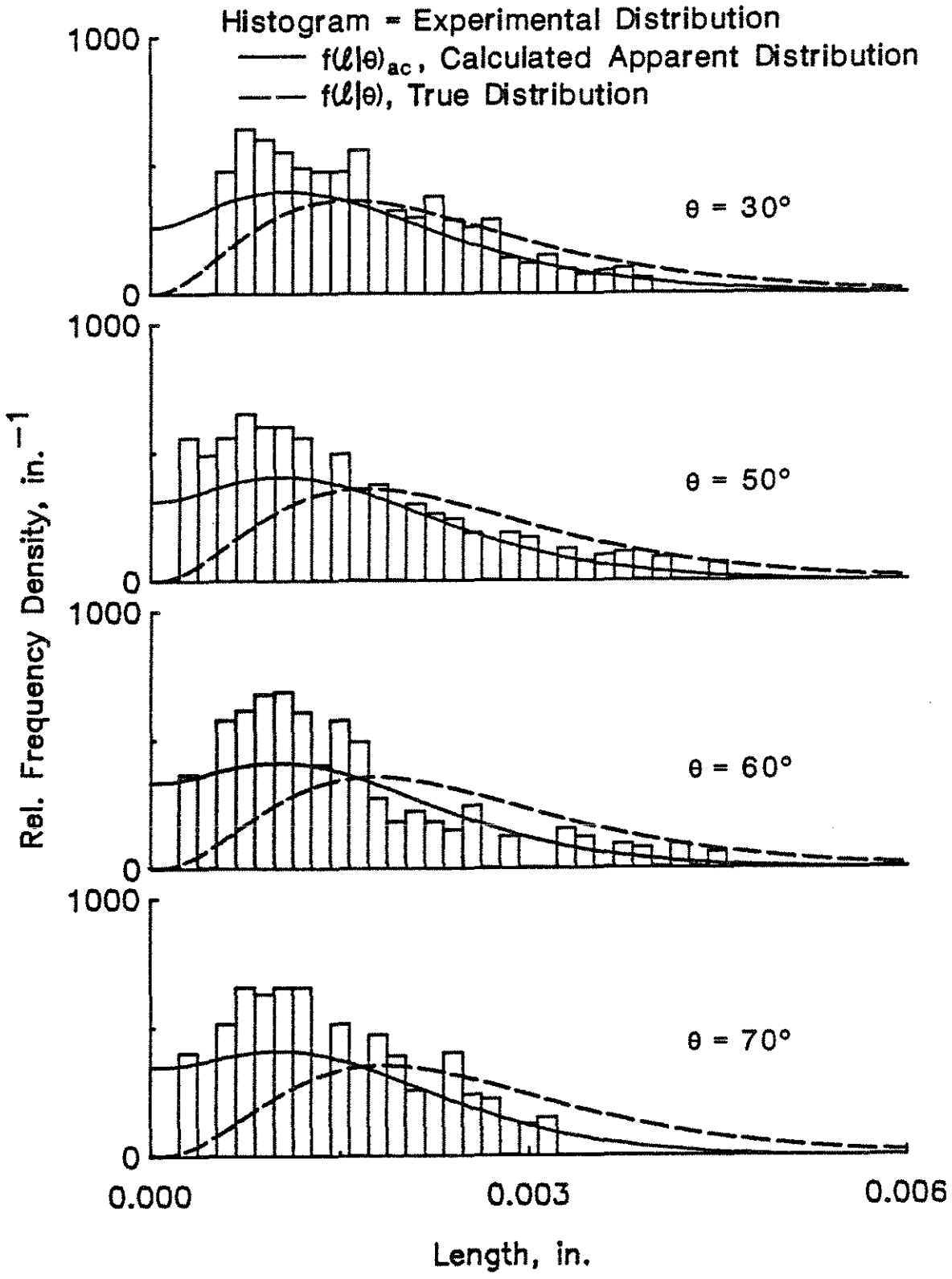

Fig. 3.2. Apparent and True Trace Length Distributions for Cement Paste with a W/C = 0.5; Monotonic Loading: Strain = 0.004

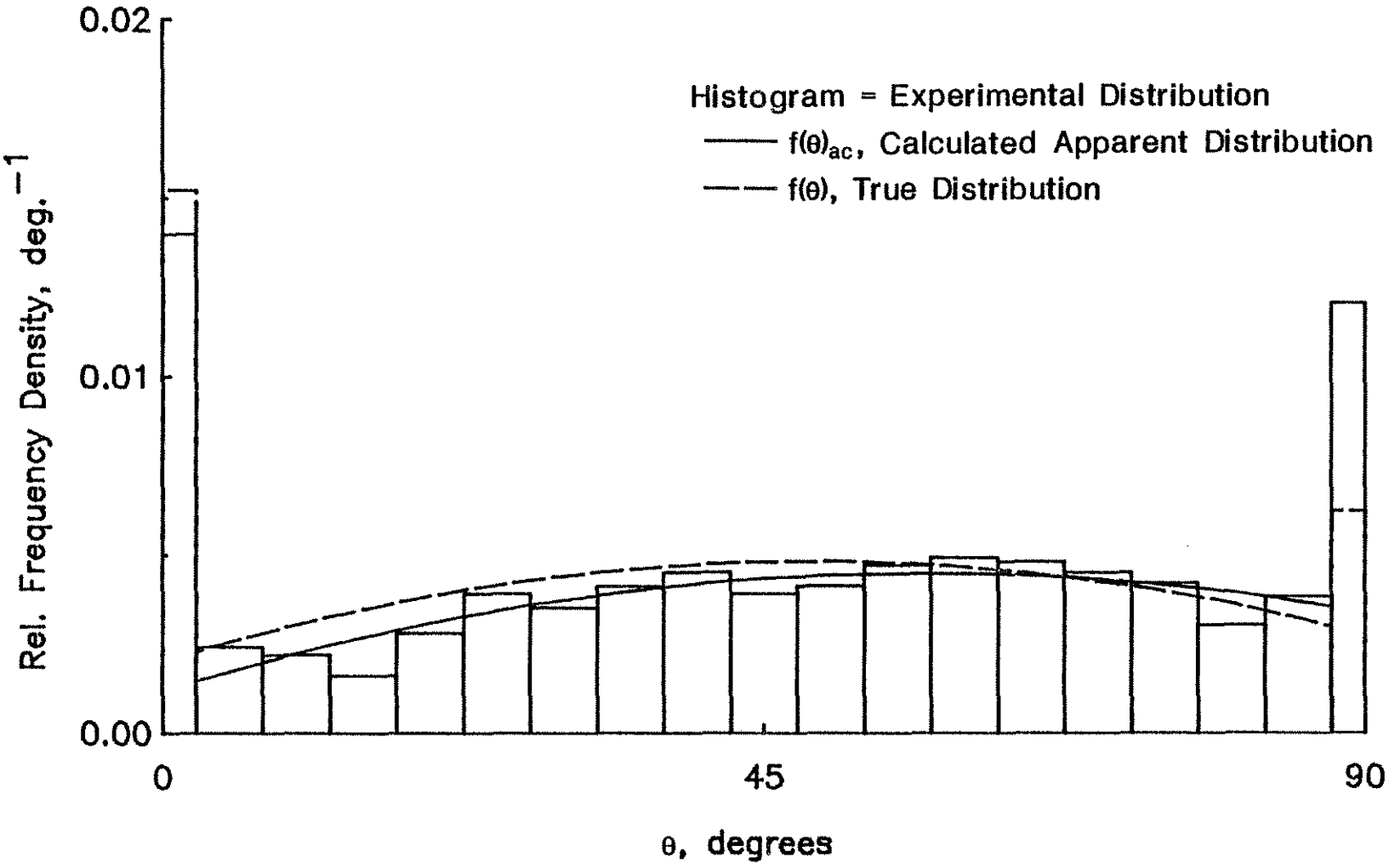

Fig. 3.3. Apparent and True Trace Angle Distributions for Cement Paste with a W/C = 0.5; Monotonic Loading: Strain = 0.004

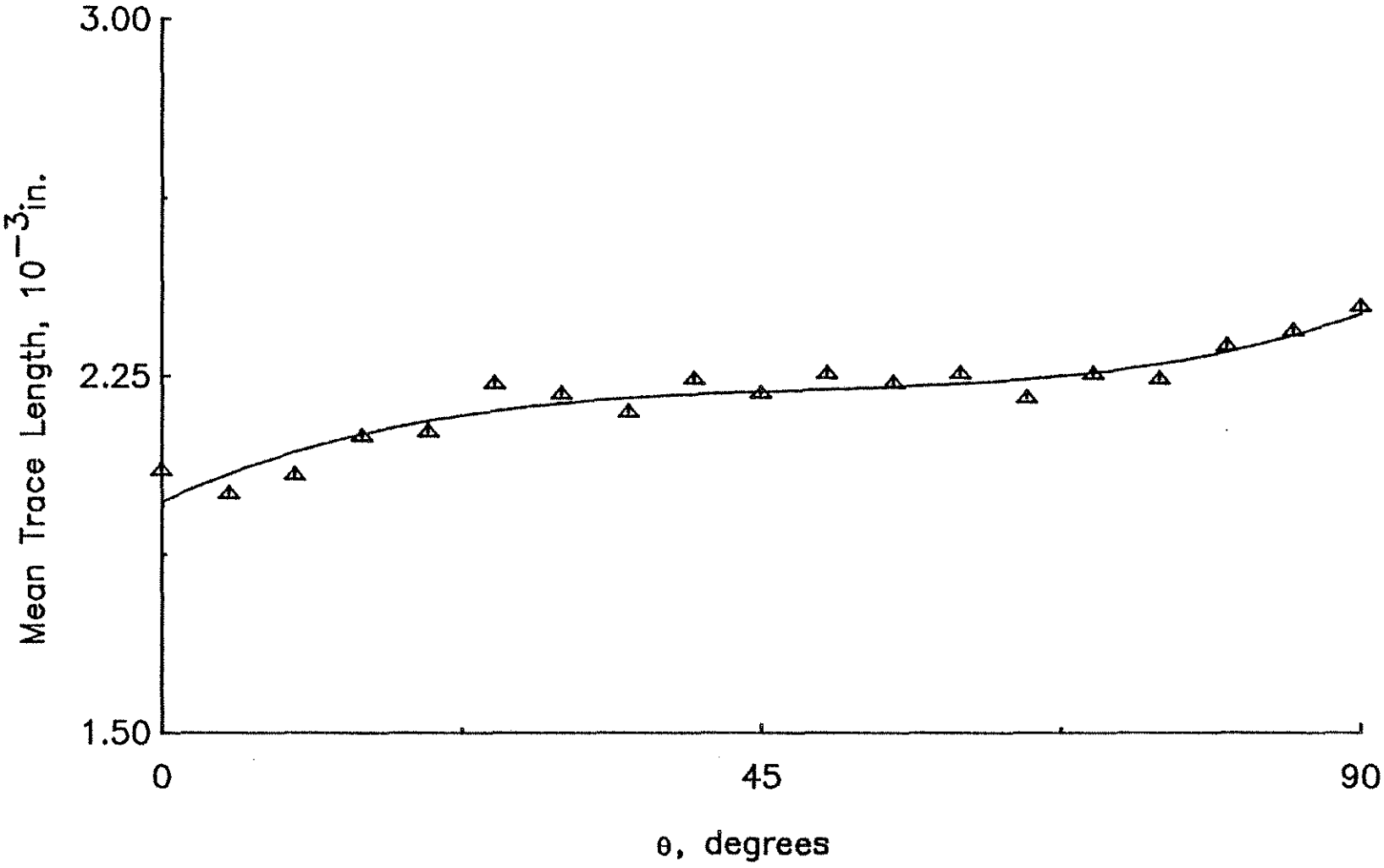

Fig. 3.4. Mean Trace Length versus Trace Angle for Transverse Surface of Cement Paste with a W/C = 0.5; Monotonic Loading: Strain = 0.004

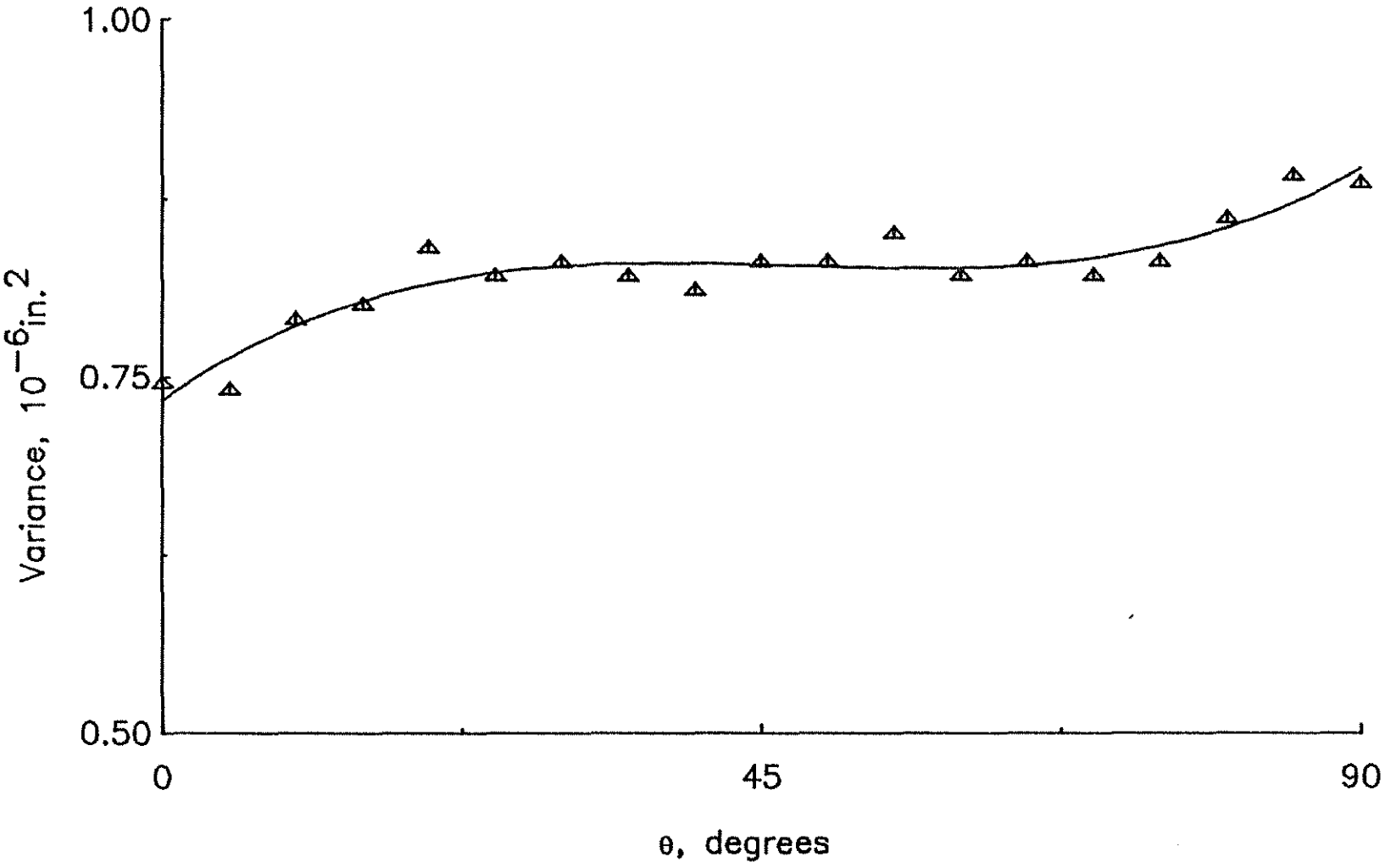

Fig. 3.5. Variance of Trace Length Distribution versus Trace Angle for Transverse Surface of Cement Paste with a W/C = 0.5; Monotonic Loading: Strain = 0.004

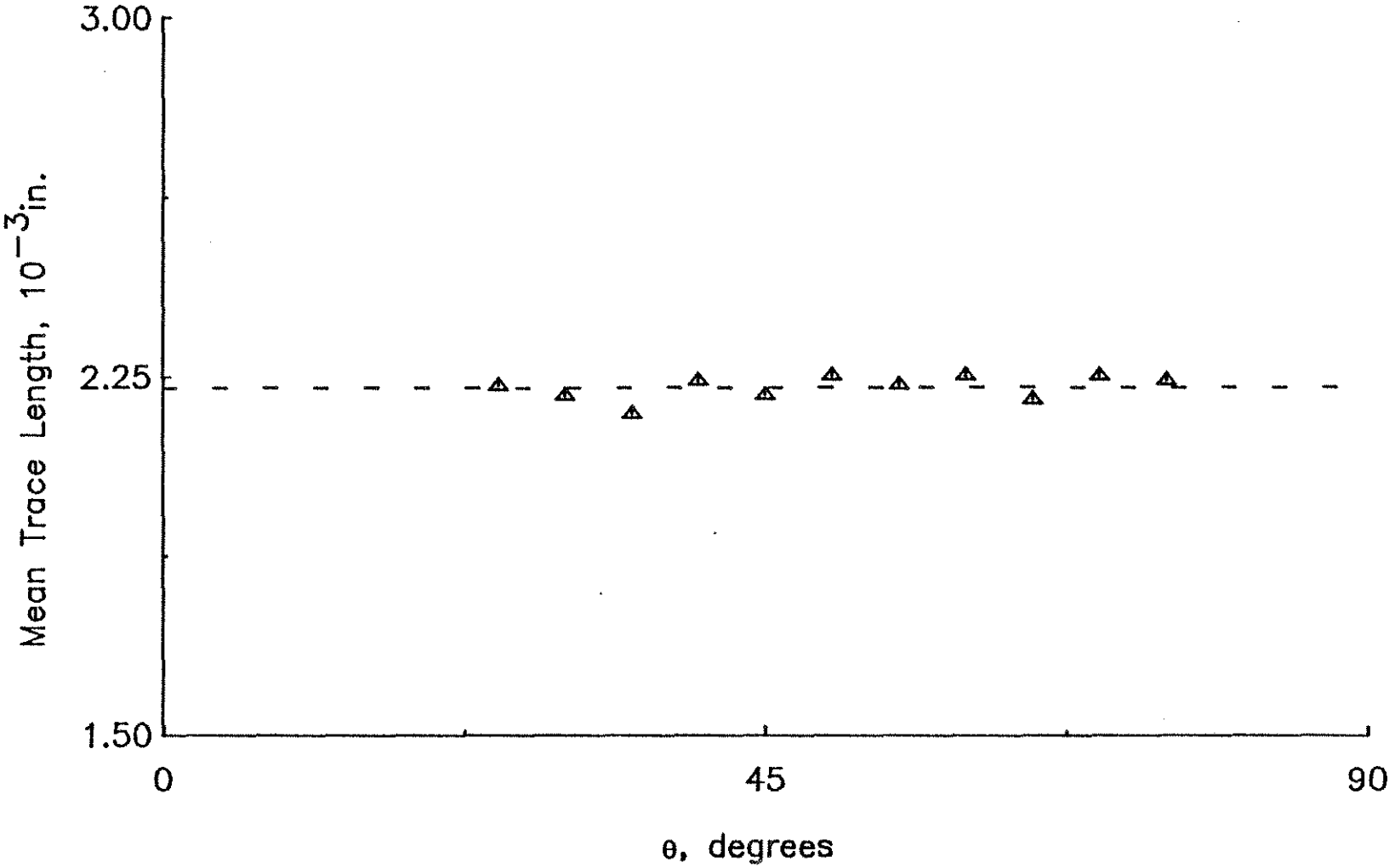

Fig. 3.6. Modified Experimental Mean Trace Length, $\langle \ell \rangle_T$, versus Trace Angle for Transverse Surface of Cement Paste with a W/C = 0.5; Monotonic Loading: Strain = 0.004

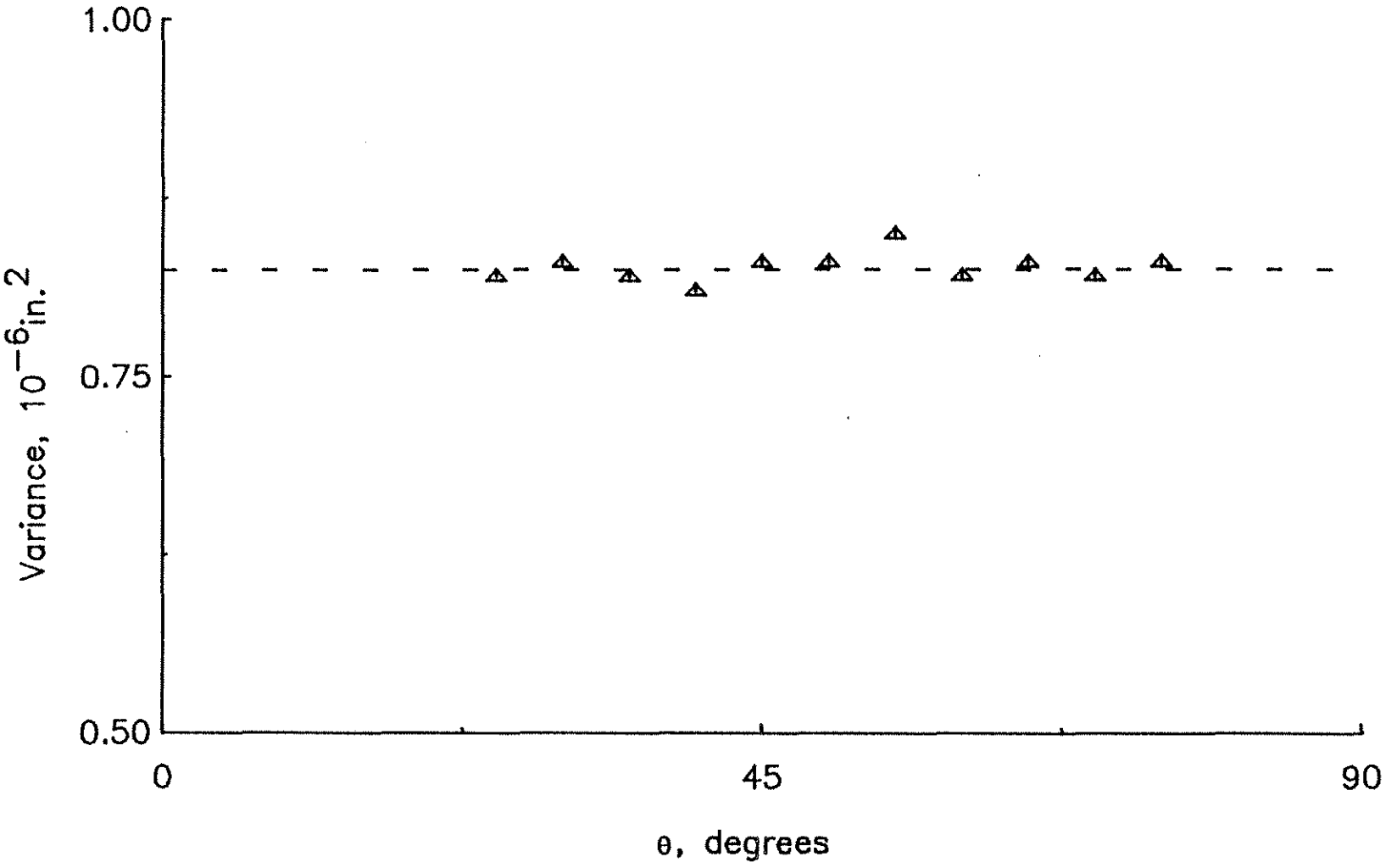

Fig. 3.7. Modified Experimental Variance of Trace Length Distribution, $var(\ell)_T$, versus Trace Angle for Transverse Surface of Cement Paste with a W/C = 0.5; Monotonic Loading: Strain = 0.004

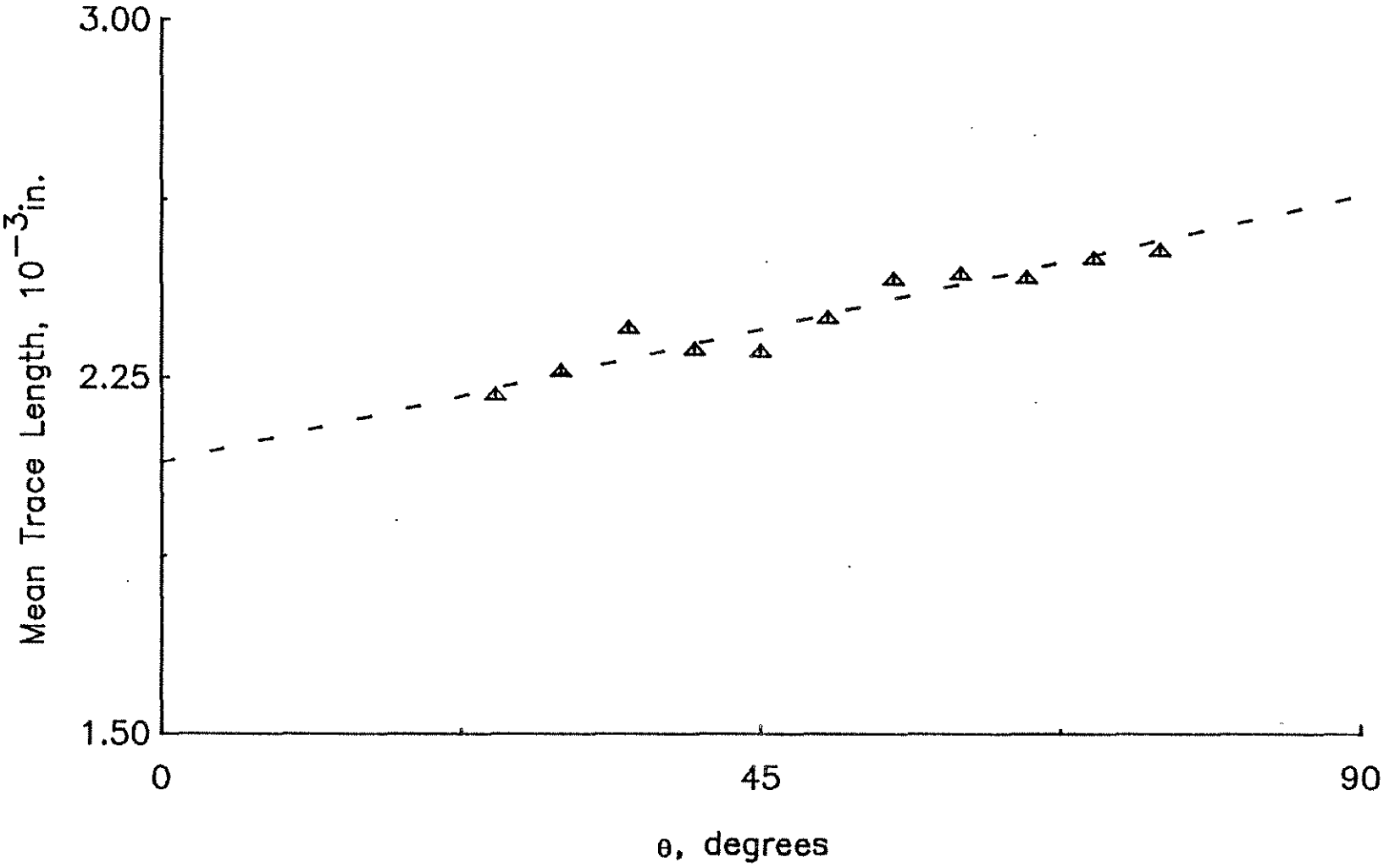

Fig. 3.8. Modified Experimental Mean Trace Length, $\langle \ell \rangle_L$, versus Trace Angle for Longitudinal Surface of Cement Paste with a W/C = 0.5; Monotonic Loading: Strain = 0.004

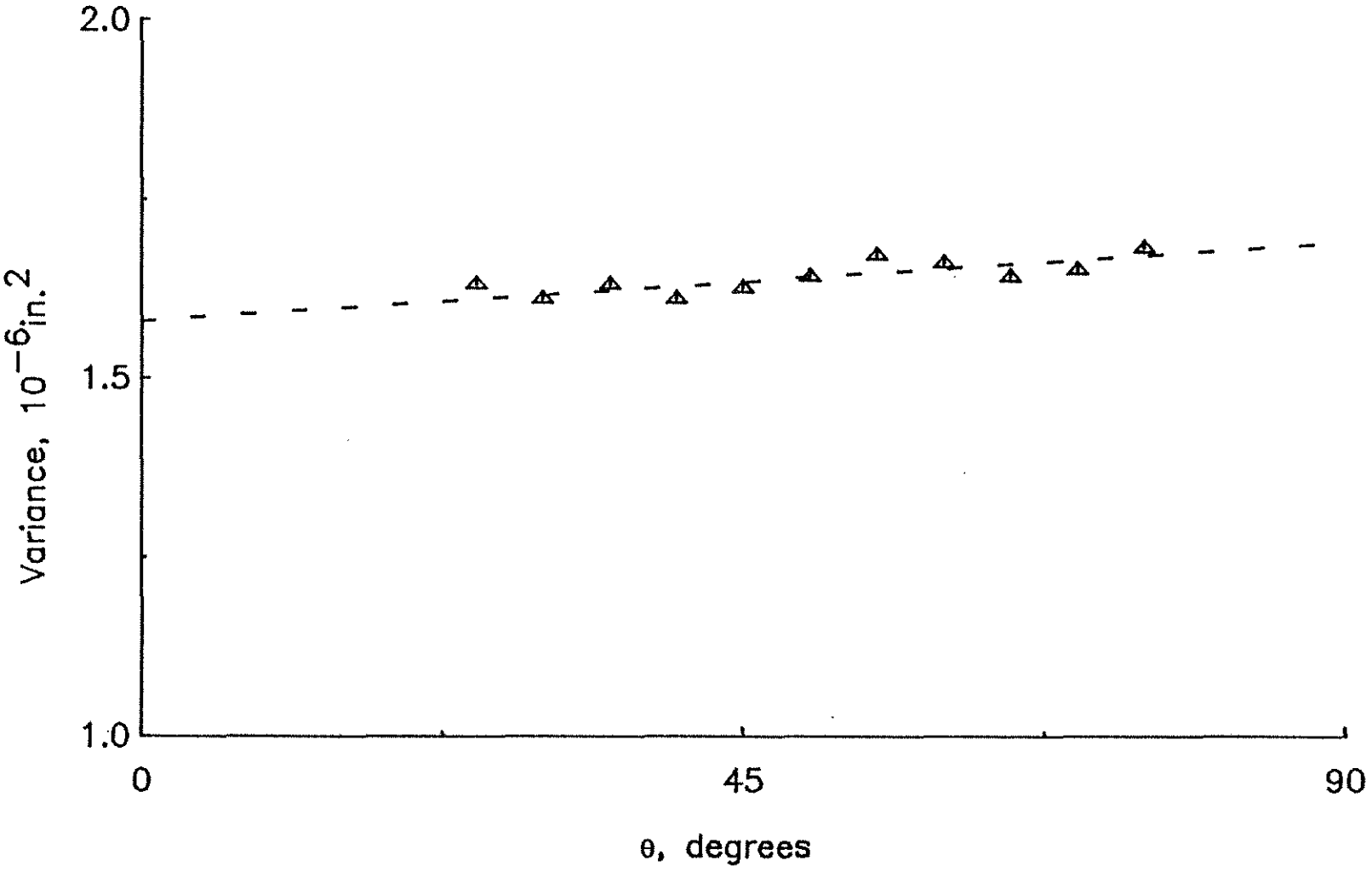

Fig. 3.9. Modified Experimental Variance of Trace Length Distribution, var $(\ell_\theta)_L$, versus Trace Angle for Longitudinal Surface of Cement Paste with a W/C = 0.5; Monotonic Loading: Strain = 0.004

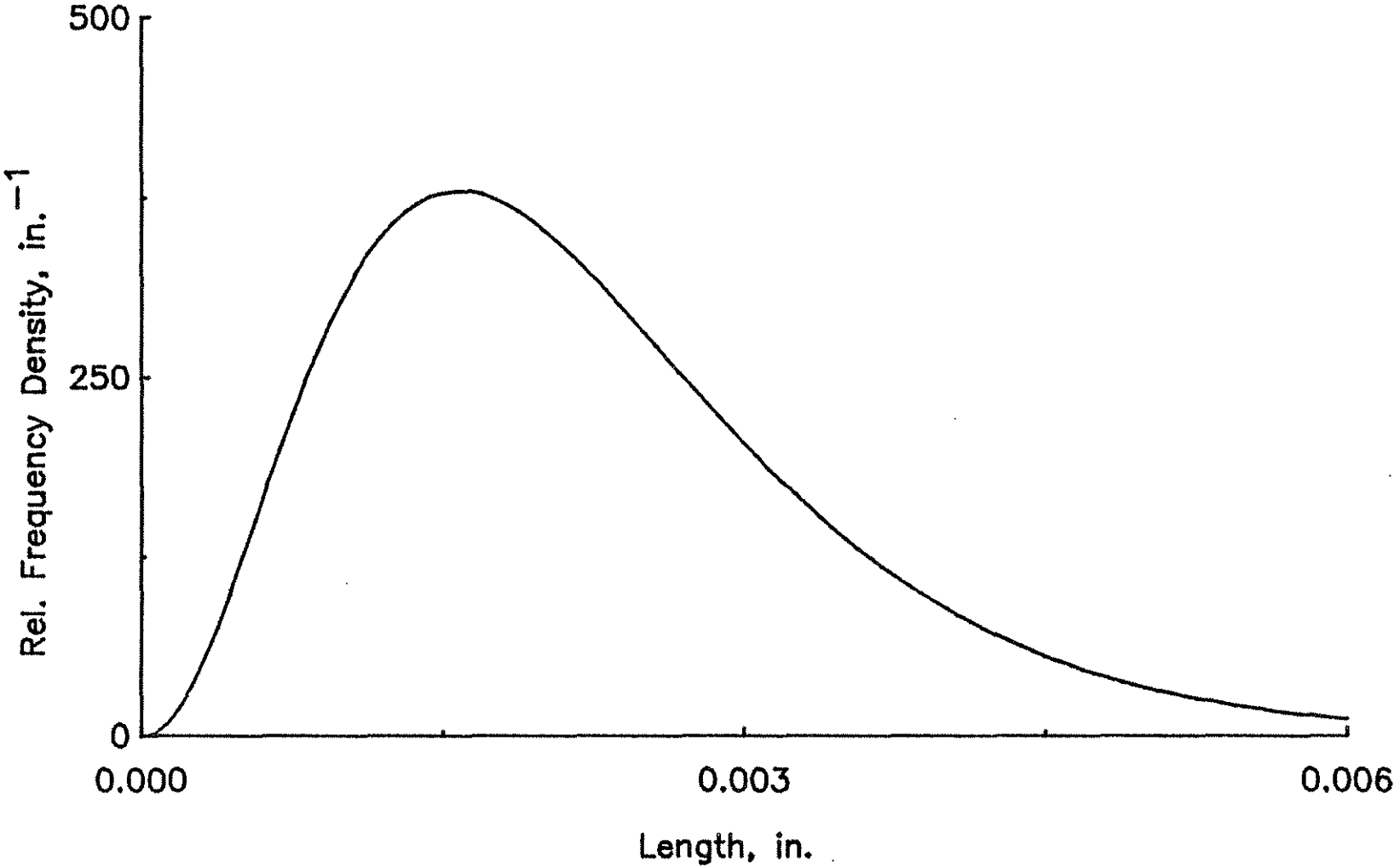

Fig. 3.10. Modified Experiment Trace Length Distribution, $f\langle\ell\rangle_T$, for Transverse Surface of Cement Paste with a W/C = 0.5; Monotonic Loading: Strain = 0.004

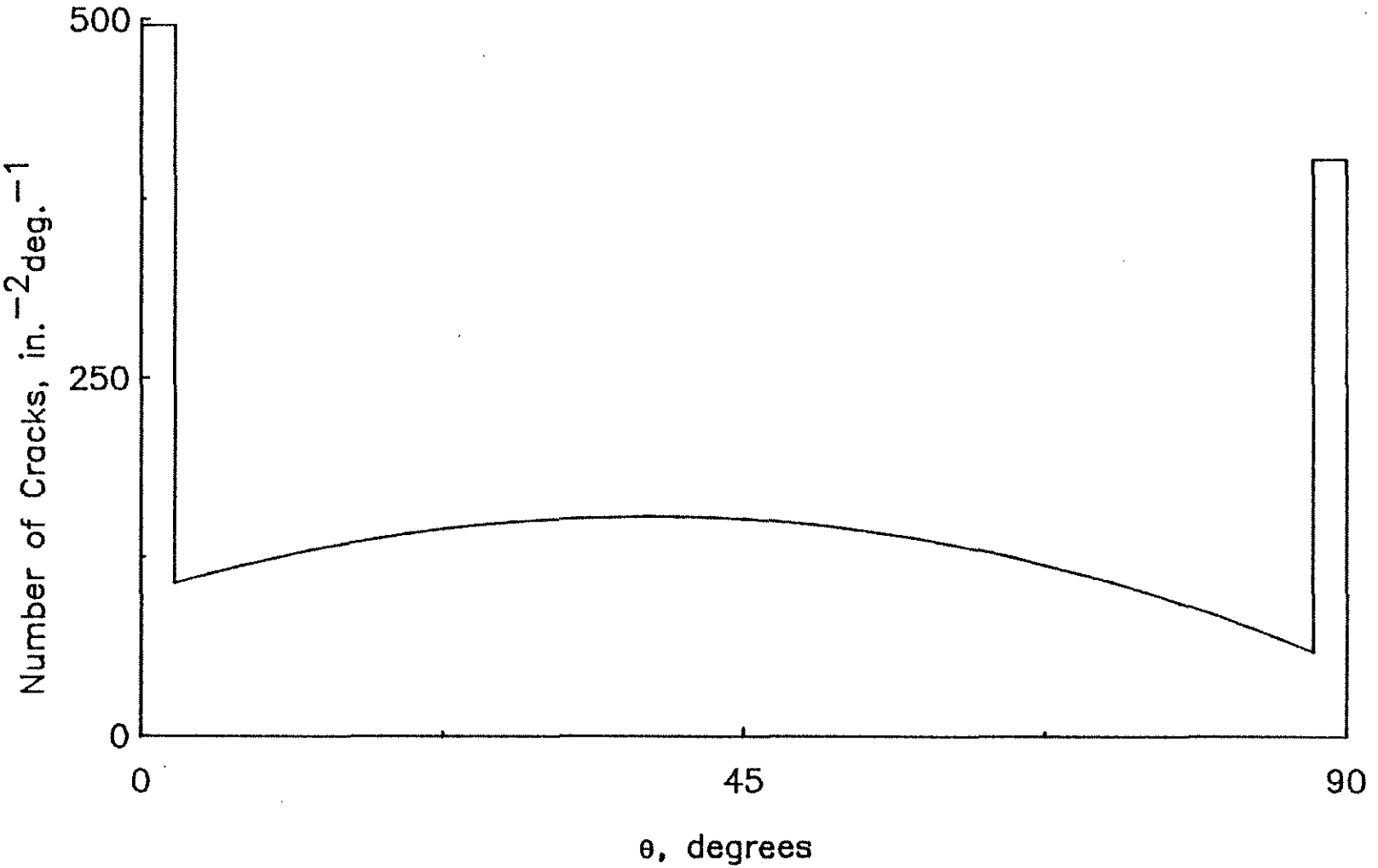

Fig. 3.11. Variation of Number of Cracks per Unit Area per Degree with Trace Angle; Transverse Surface of Cement Paste with a W/C = 0.5; Monotonic Loading: Strain = 0.004

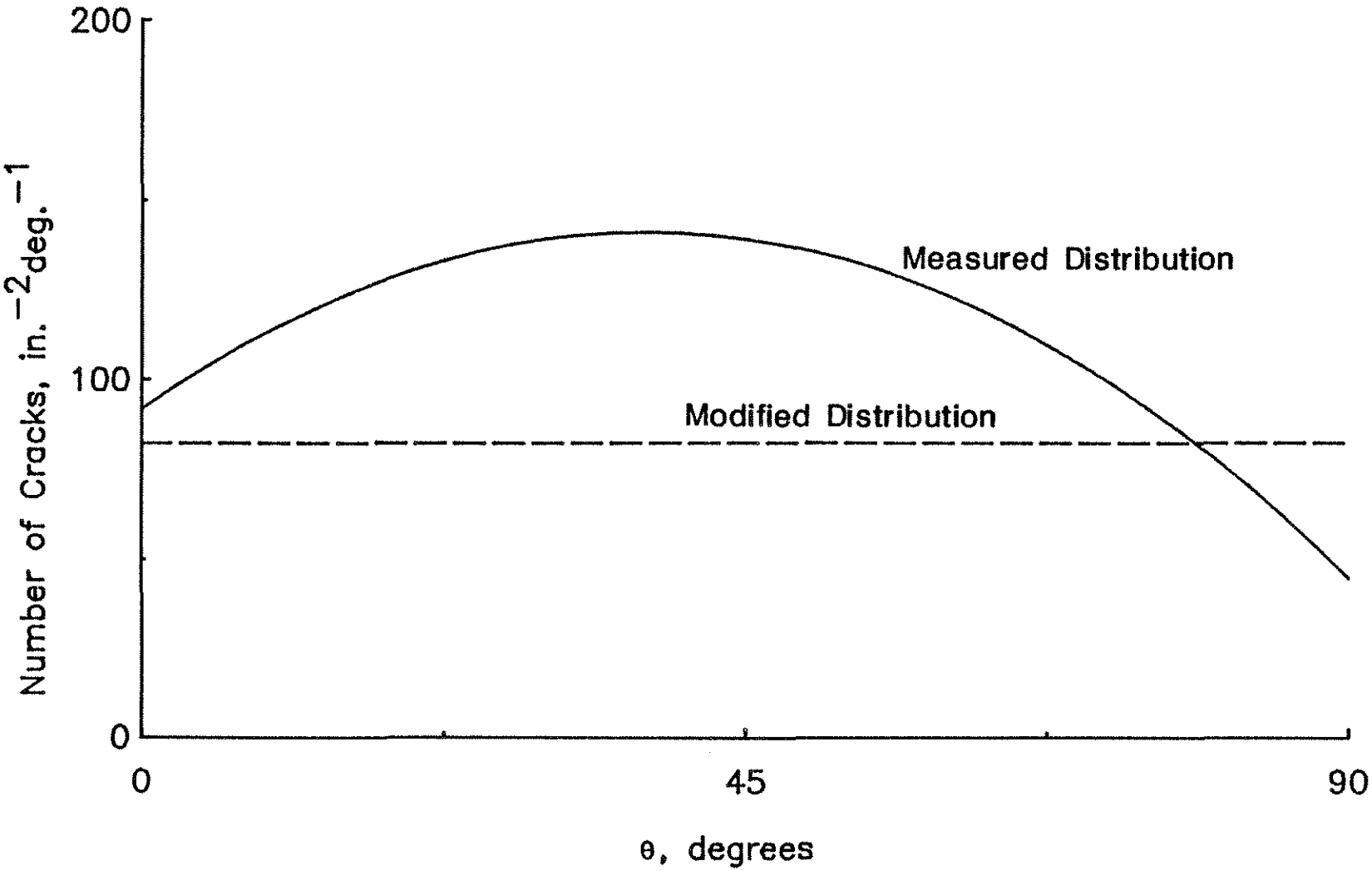

Fig. 3.12. Distributions of Measured, $\bar{m}_\theta$, and Modified, m_θ, Numbers of Cracks per Unit Area per Degree on Transverse Surface of Cement Paste with a W/C = 0.5; Monotonic Loading: Strain = 0.004

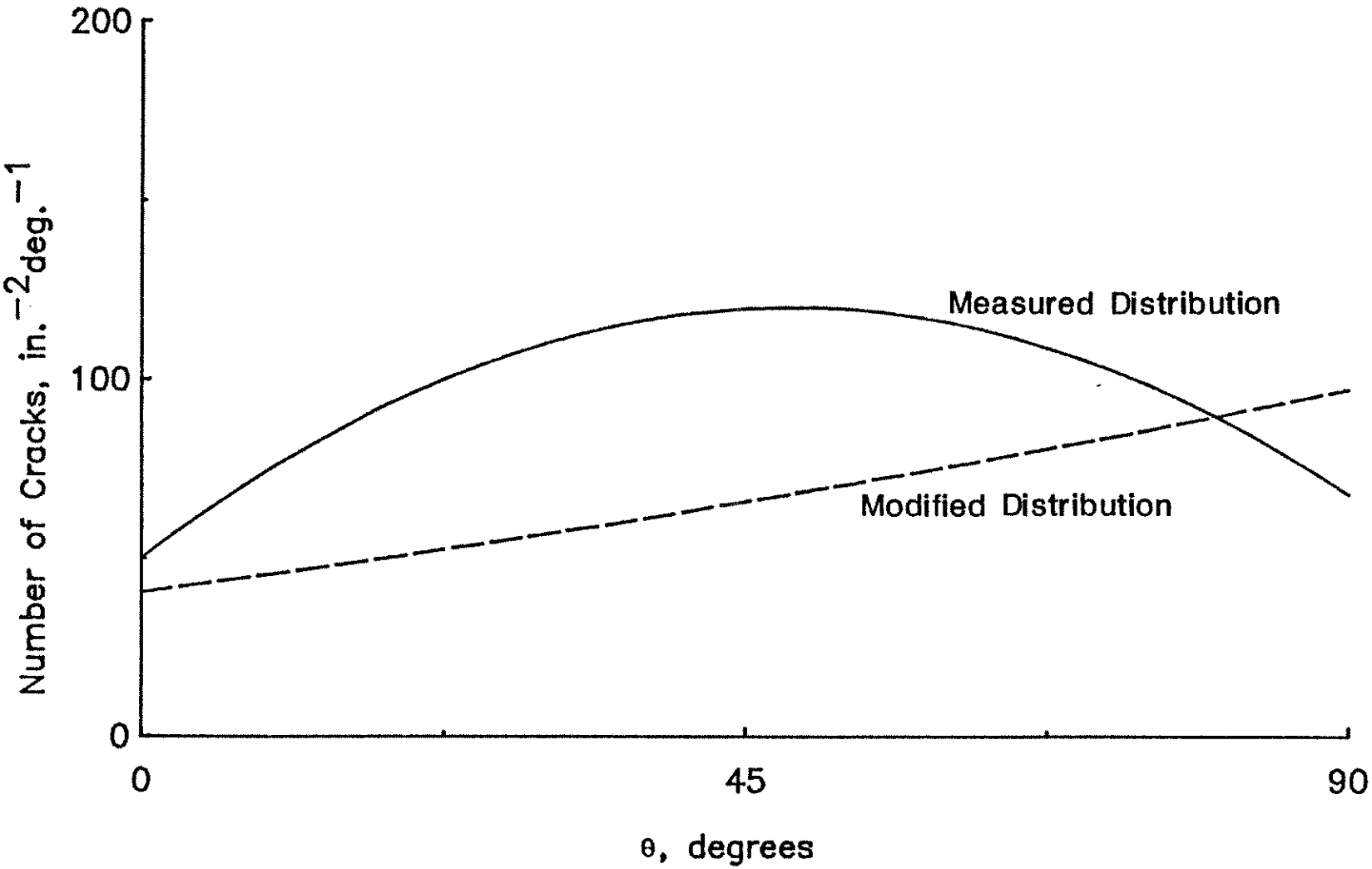

Fig. 3.13. Distributions of Measured, $\bar{m}_\theta$, and Modified, m_θ, Numbers of Cracks per Unit Area per Degree on Longitudinal Surface of Cement Paste with a W/C = 0.5; Monotonic Loading: Strain = 0.004

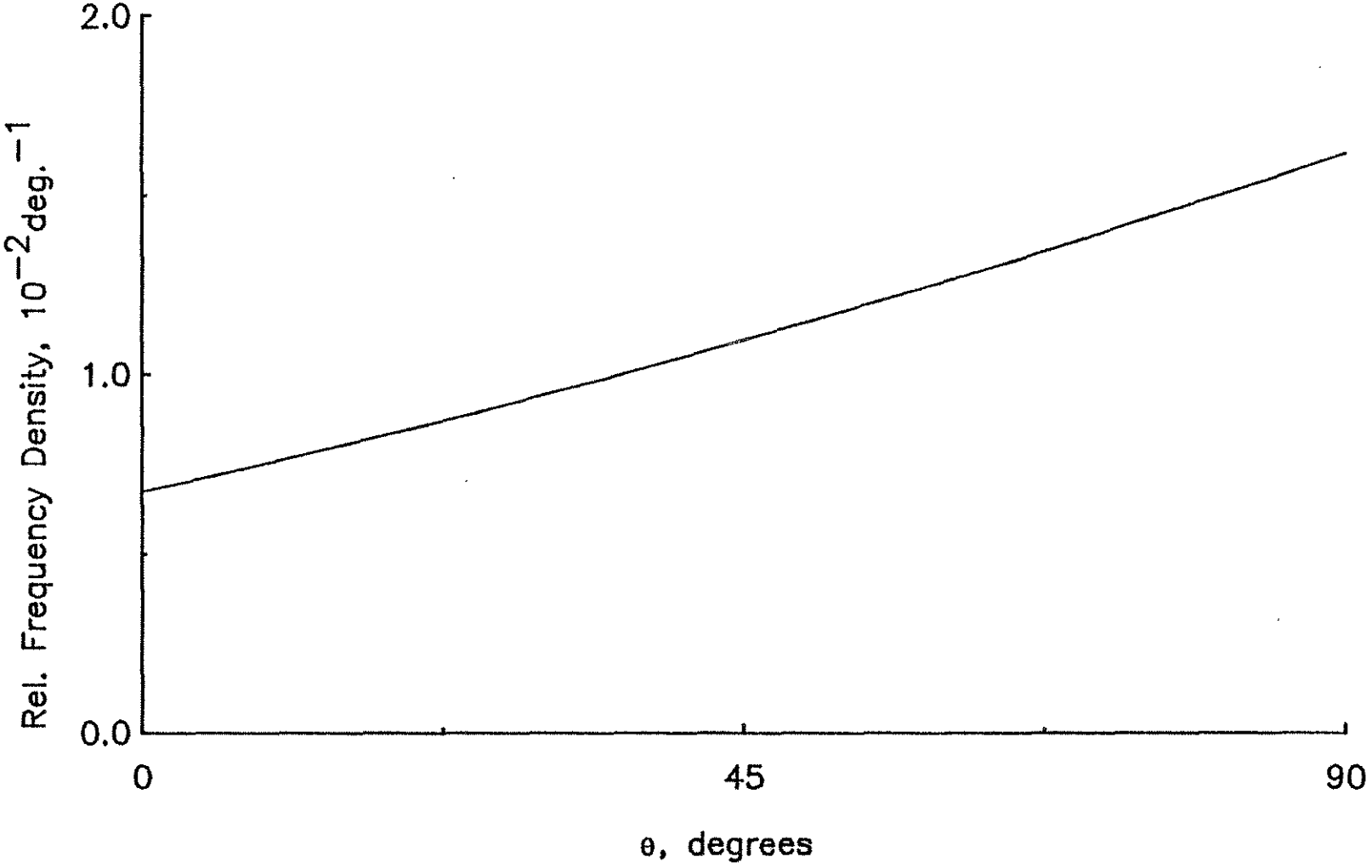

Fig. 3.14. Modified Experimental Trace Angle Distribution of Cracks, $f(\theta)_L$, for Longitudinal Surface of Cement Paste with a W/C = 0.5; Monotonic Loading: Strain = 0.004

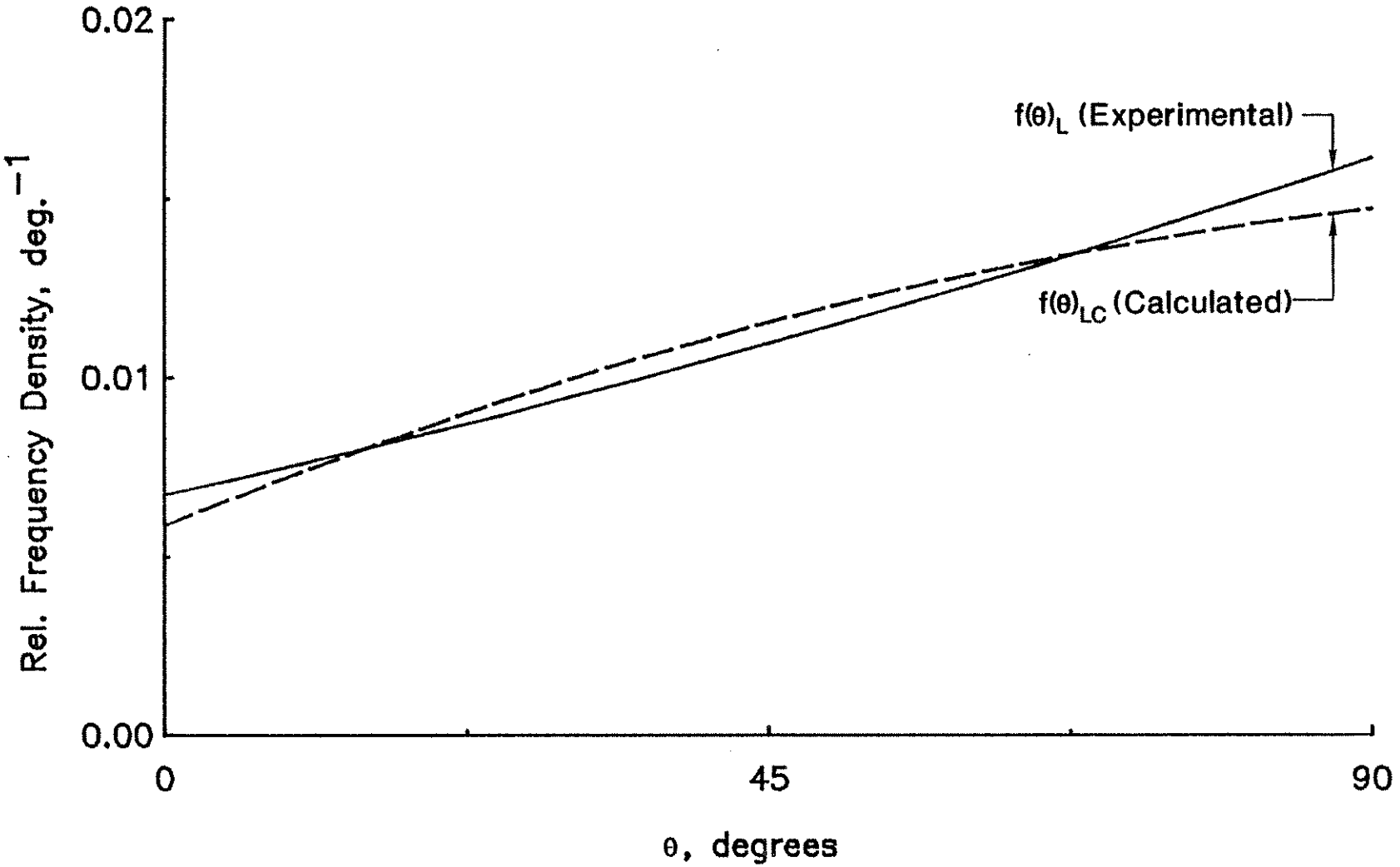

Fig. 3.15. Modified Experimental and Calculated Trace Angle Distributions for Longitudinal Surface of Cement Paste with a W/C = 0.5; Monotonic Loading: Strain = 0.004

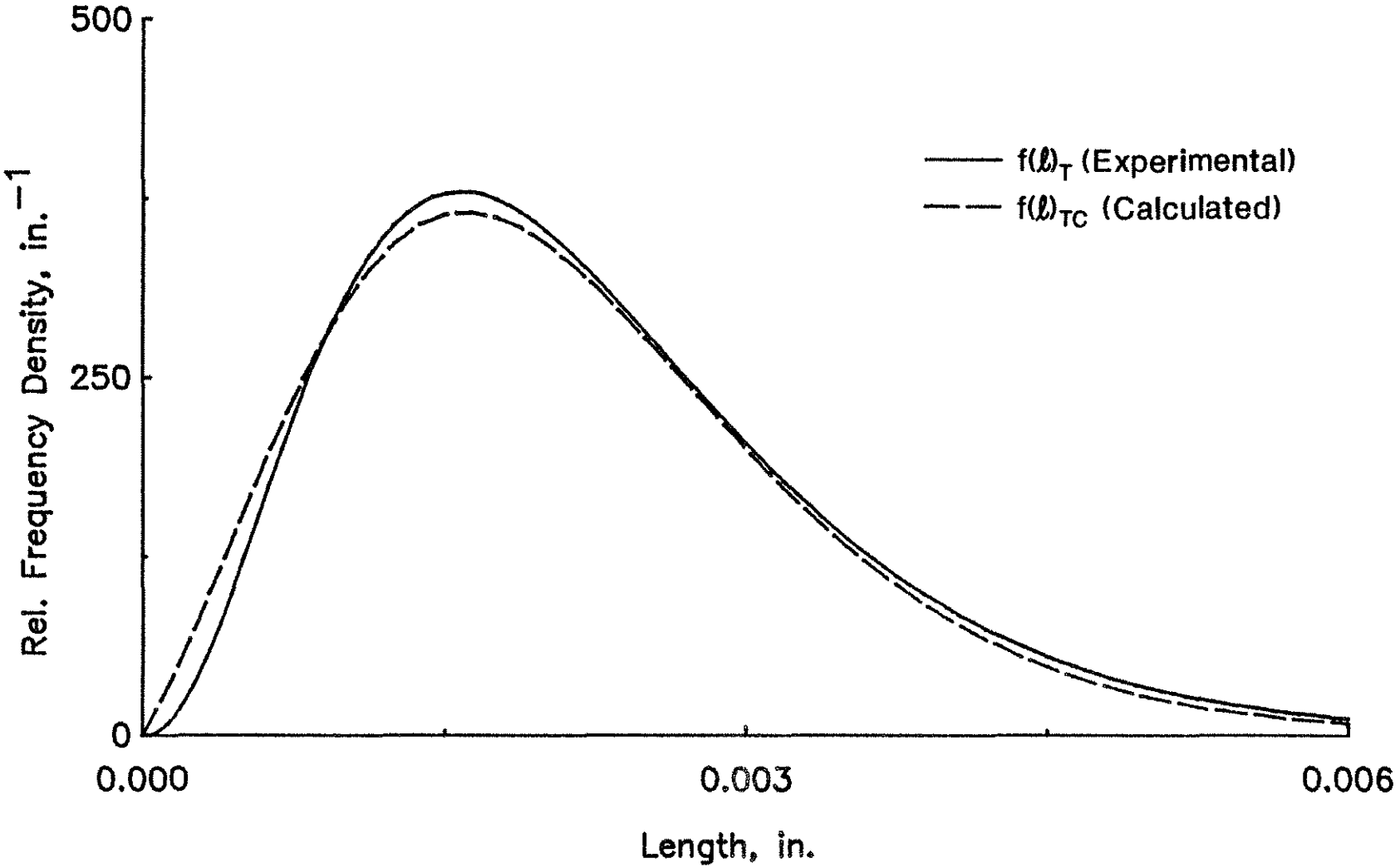

Fig. 3.16. Modified Experimental and Calculated Trace Length Distributions for Transverse Surface of Cement Paste with a W/C = 0.5; Monotonic Loading: Strain = 0.004

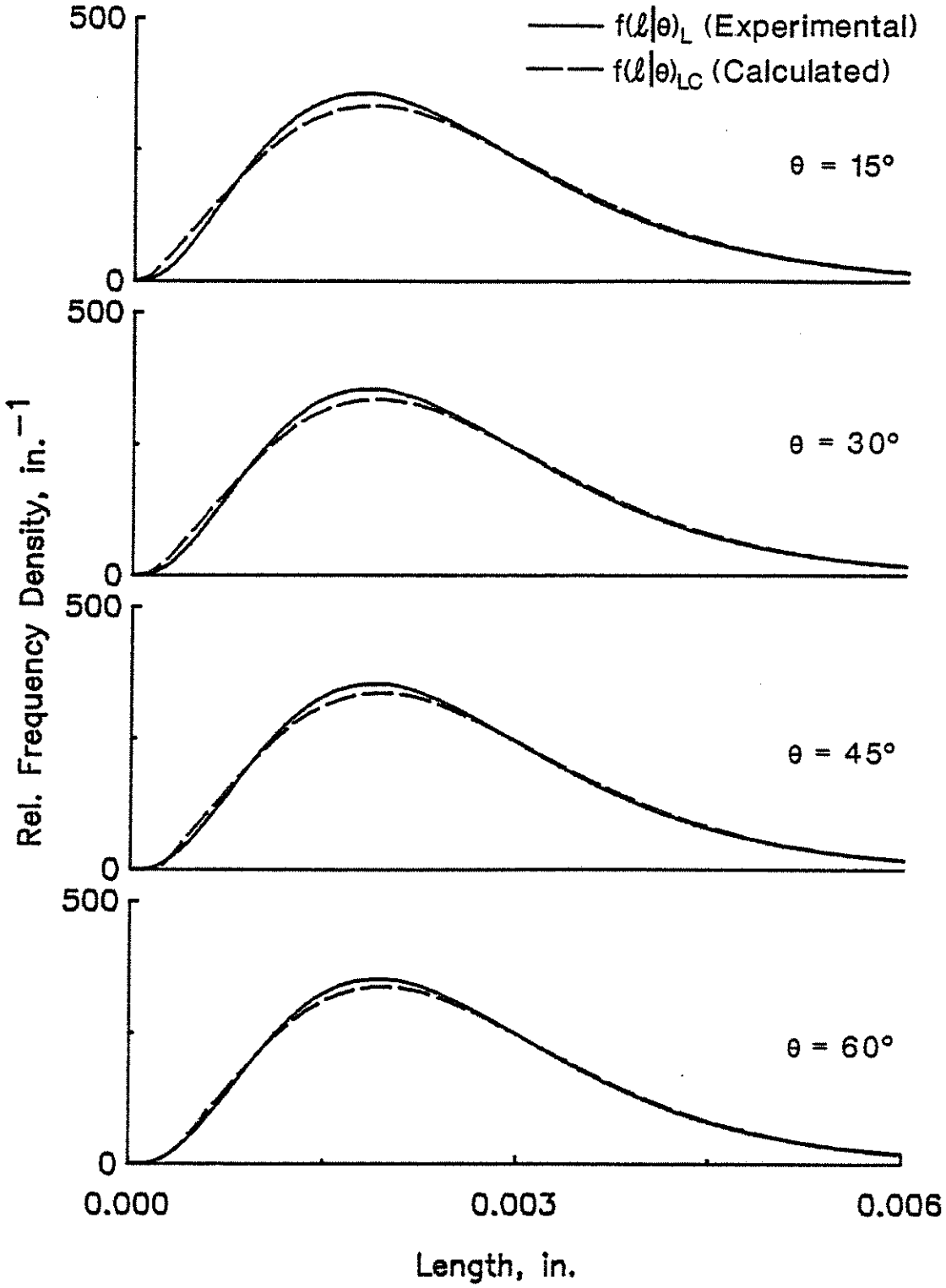

Fig. 3.17. Modified Experimental and Calculated Trace Length Distributions for Longitudinal Surface of Cement Paste with a W/C = 0.5; Monotonic Loading: Strain = 0.004

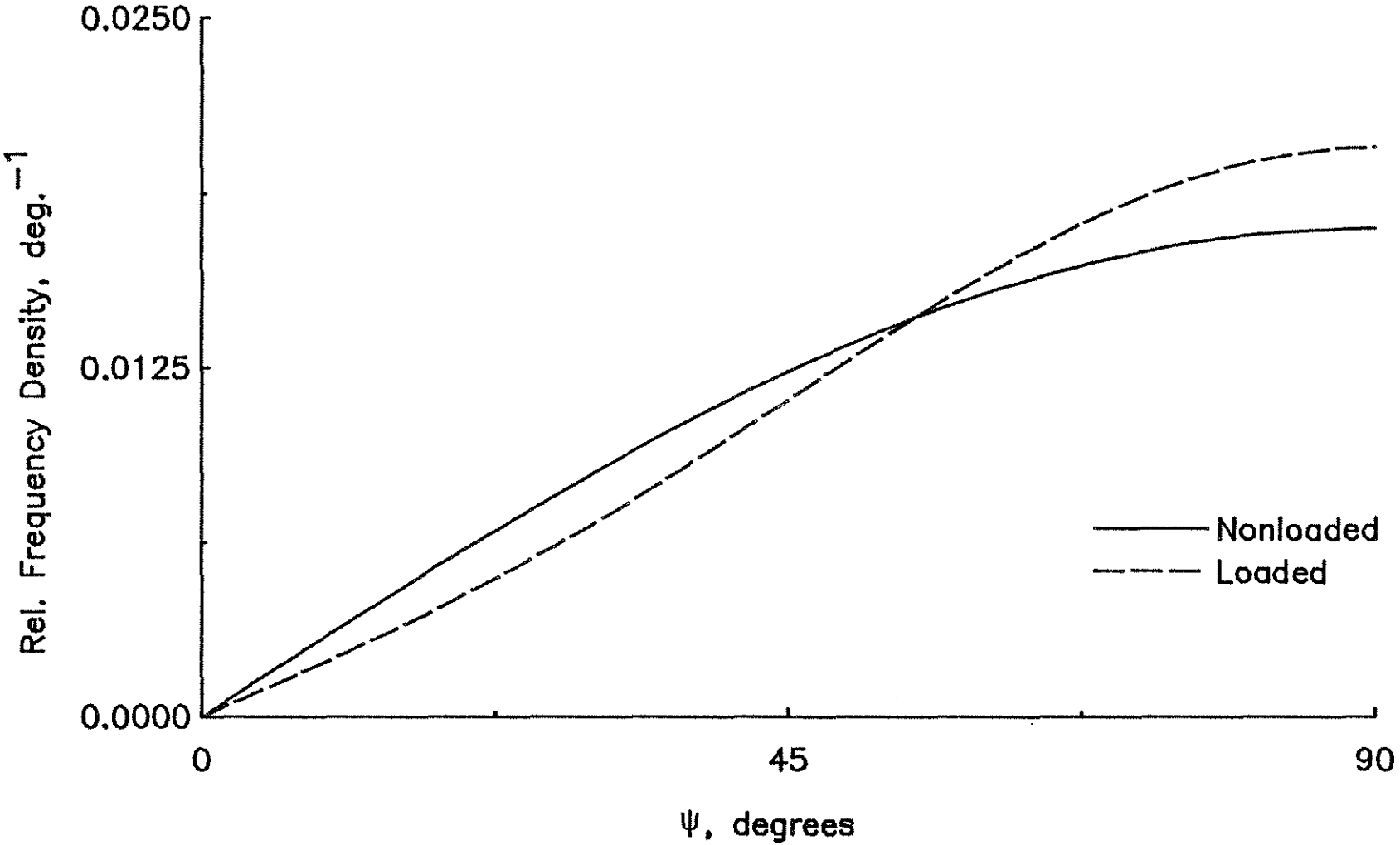

Fig. 3.18. Crack Orientation Distributions, f(ψ), for Nonloaded and Loaded (Strain = 0.004) Cement Pastes with a W/C = 0.5

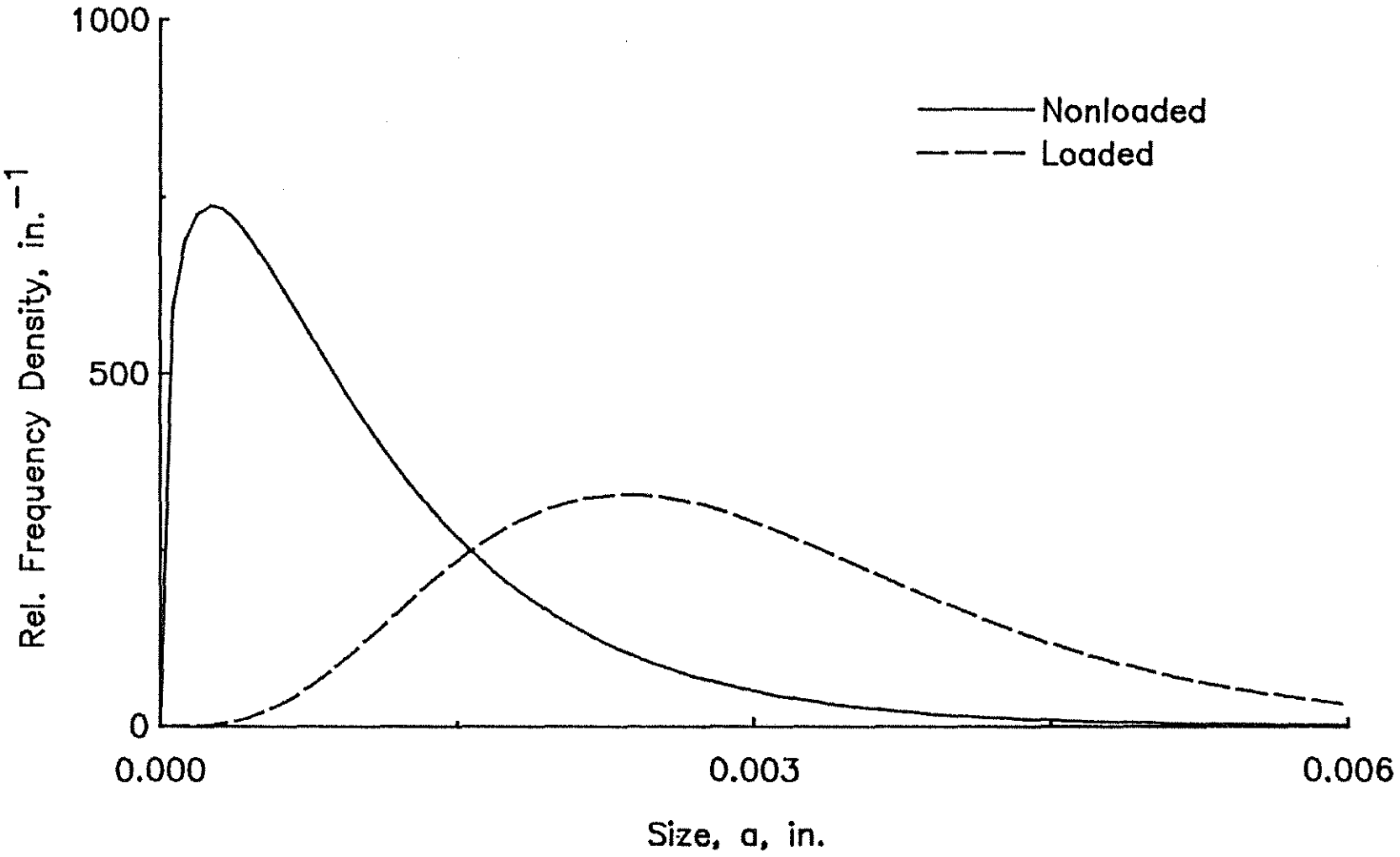

Fig. 3.19. Crack Size Distributions, $f(a|\psi)$, for Nonloaded and Loaded (Strain = 0.004) Cement Pastes with a W/C = 0.5, = 60°

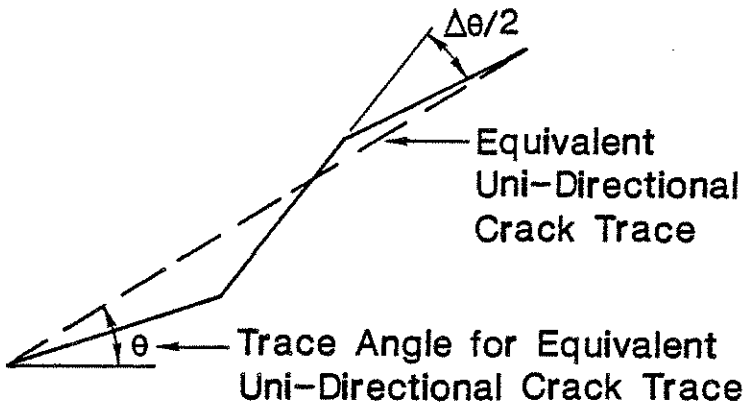

Fig. 3.20. Multi- and Uni-Directional Crack Traces

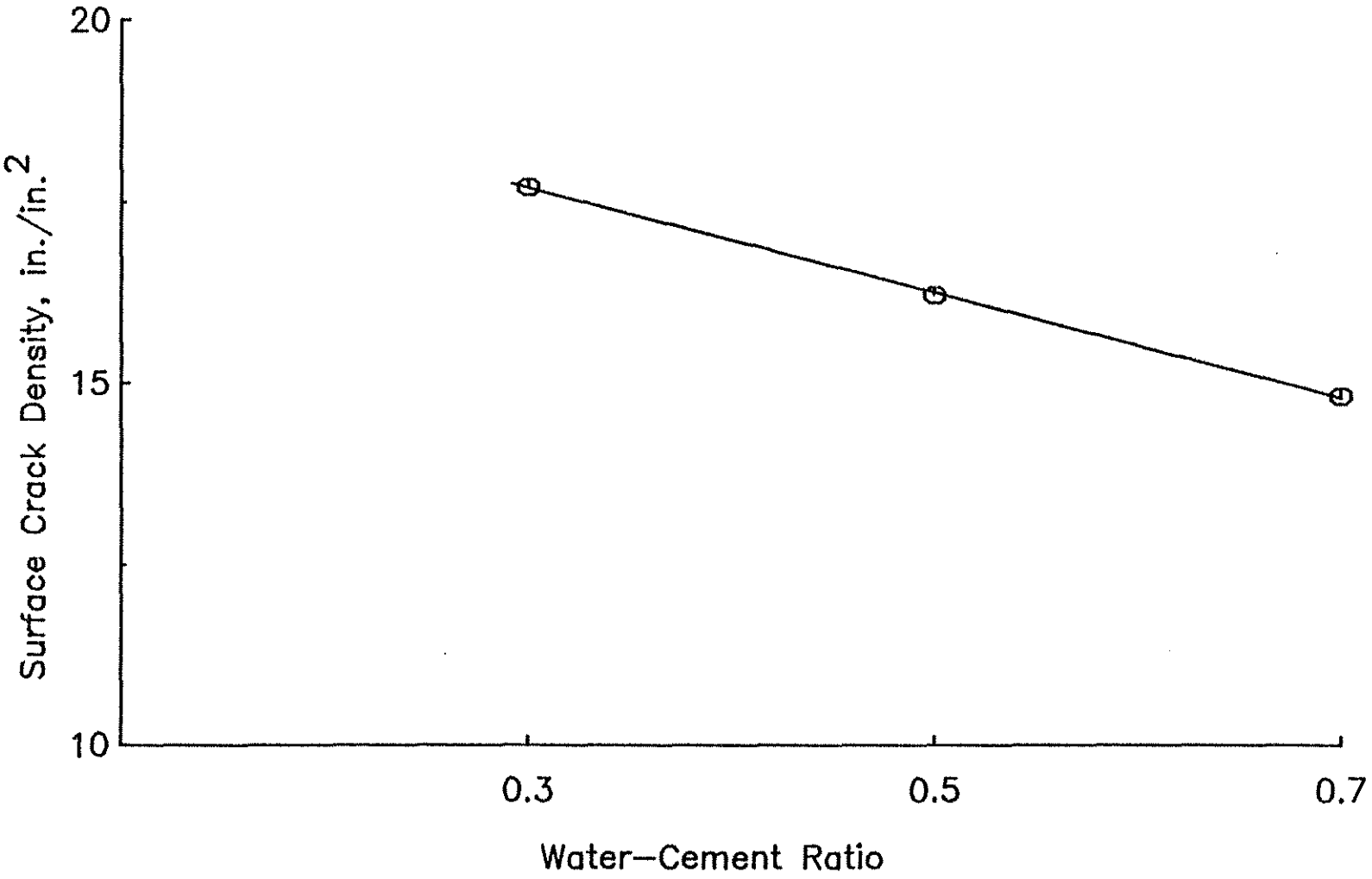

Fig. 3.21. Surface Crack Density versus Water-Cement Ratio for Nonloaded Cement Paste

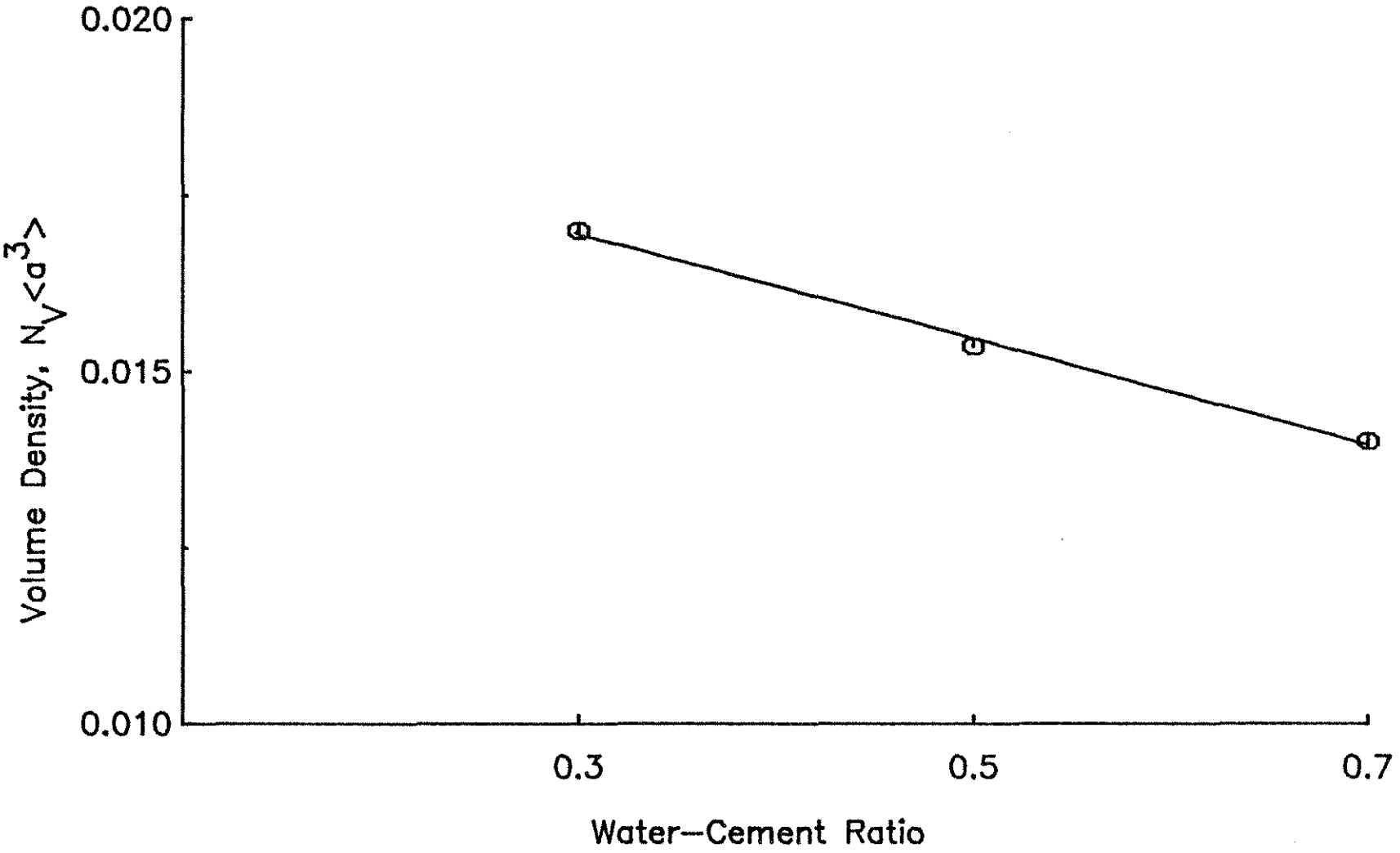

Fig. 3.22. Measure of Volumetric Crack Density, $N_V\langle a^3\rangle$, versus Water-Cement Ratio for Nonloaded Cement Paste

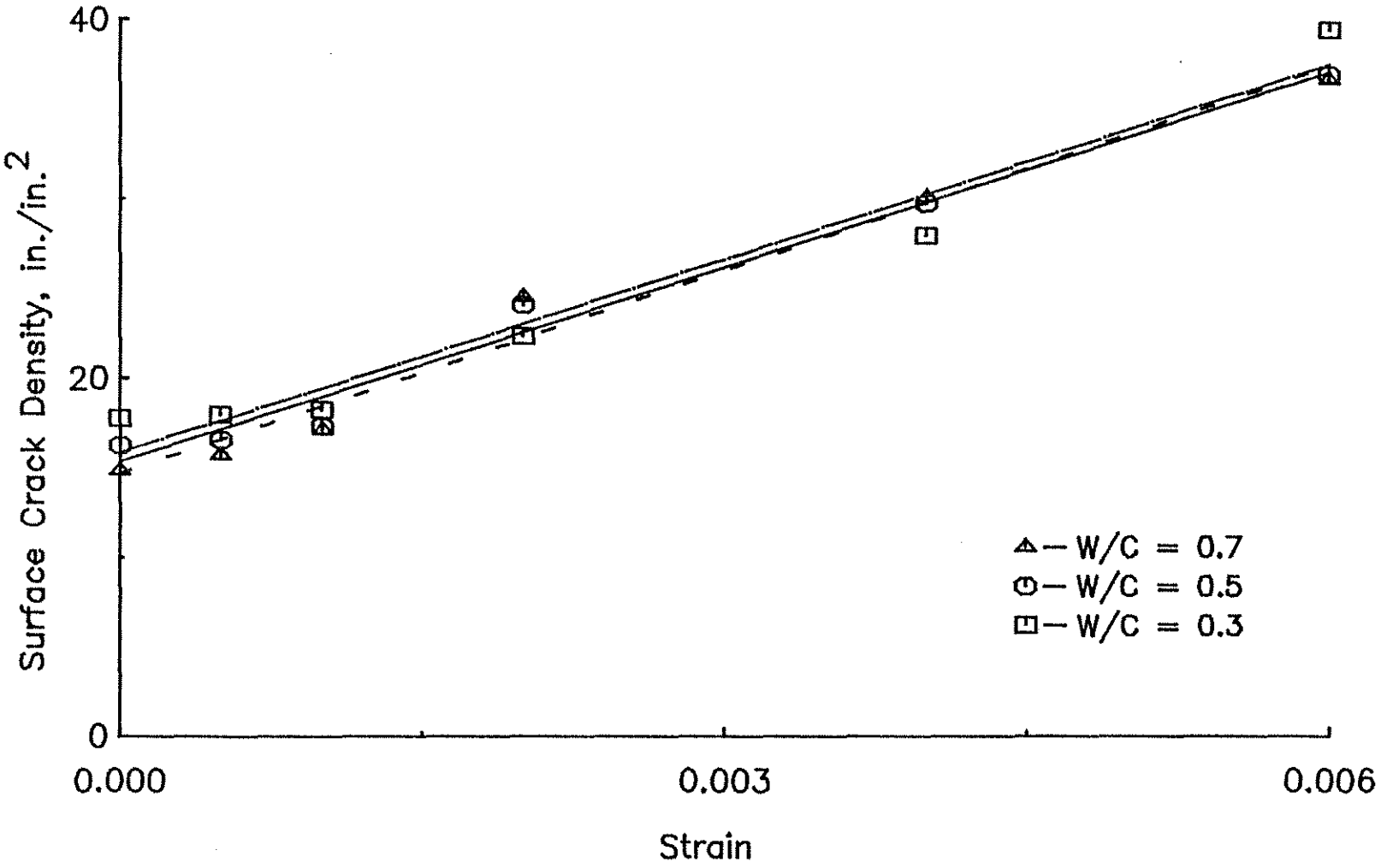

Fig. 3.23. Surface Crack Density, $M_T\langle\ell\rangle_T$, versus Strain for Monotonic Loading of Cement Pastes with W/C = 0.7, 0.5 and 0.3

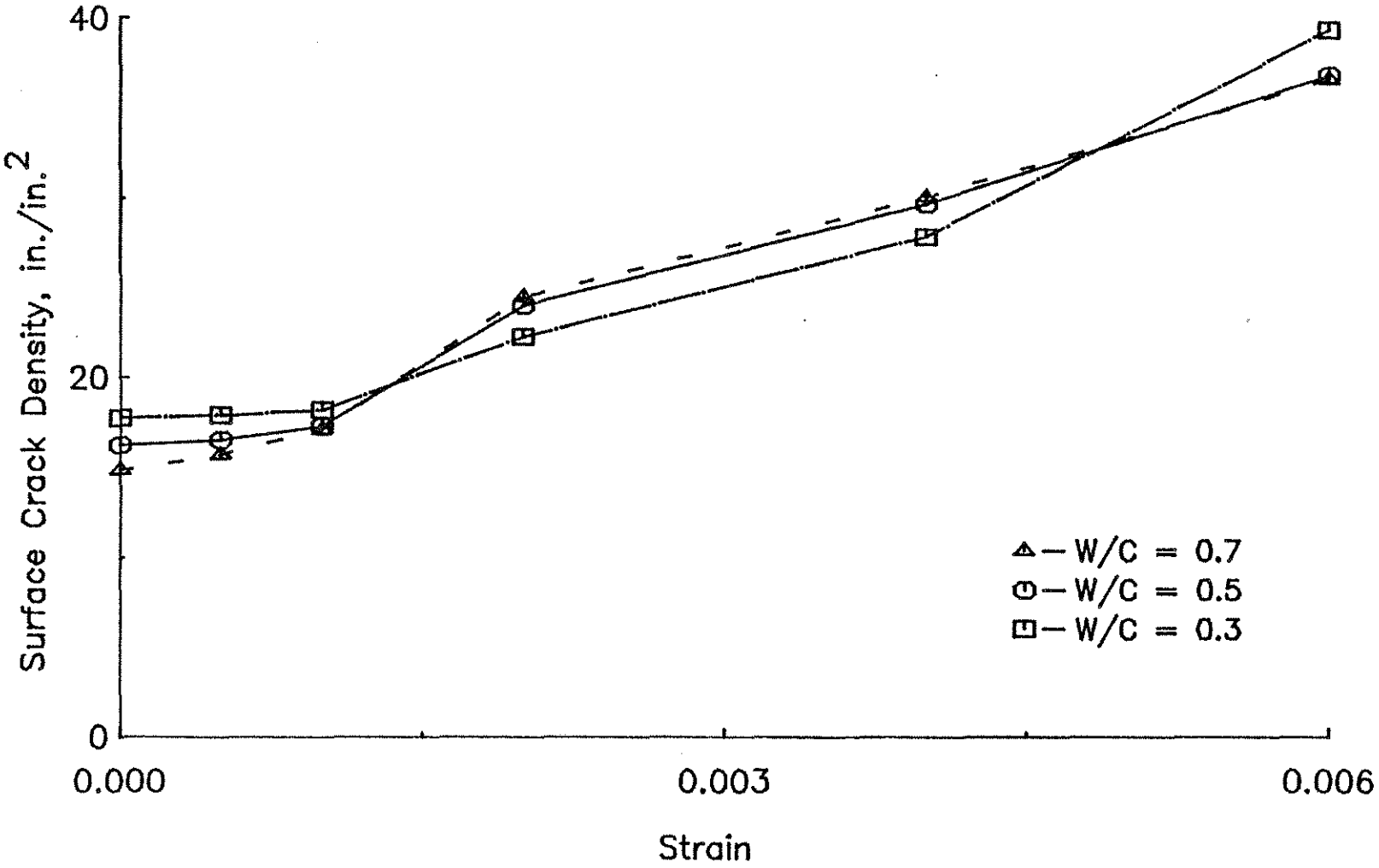

Fig. 3.24. Surface Crack Density, $M_T\langle\ell\rangle_T$, versus Strain for Monotonic Loading of Cement Pastes with W/C = 0.7, 0.5 and 0.3

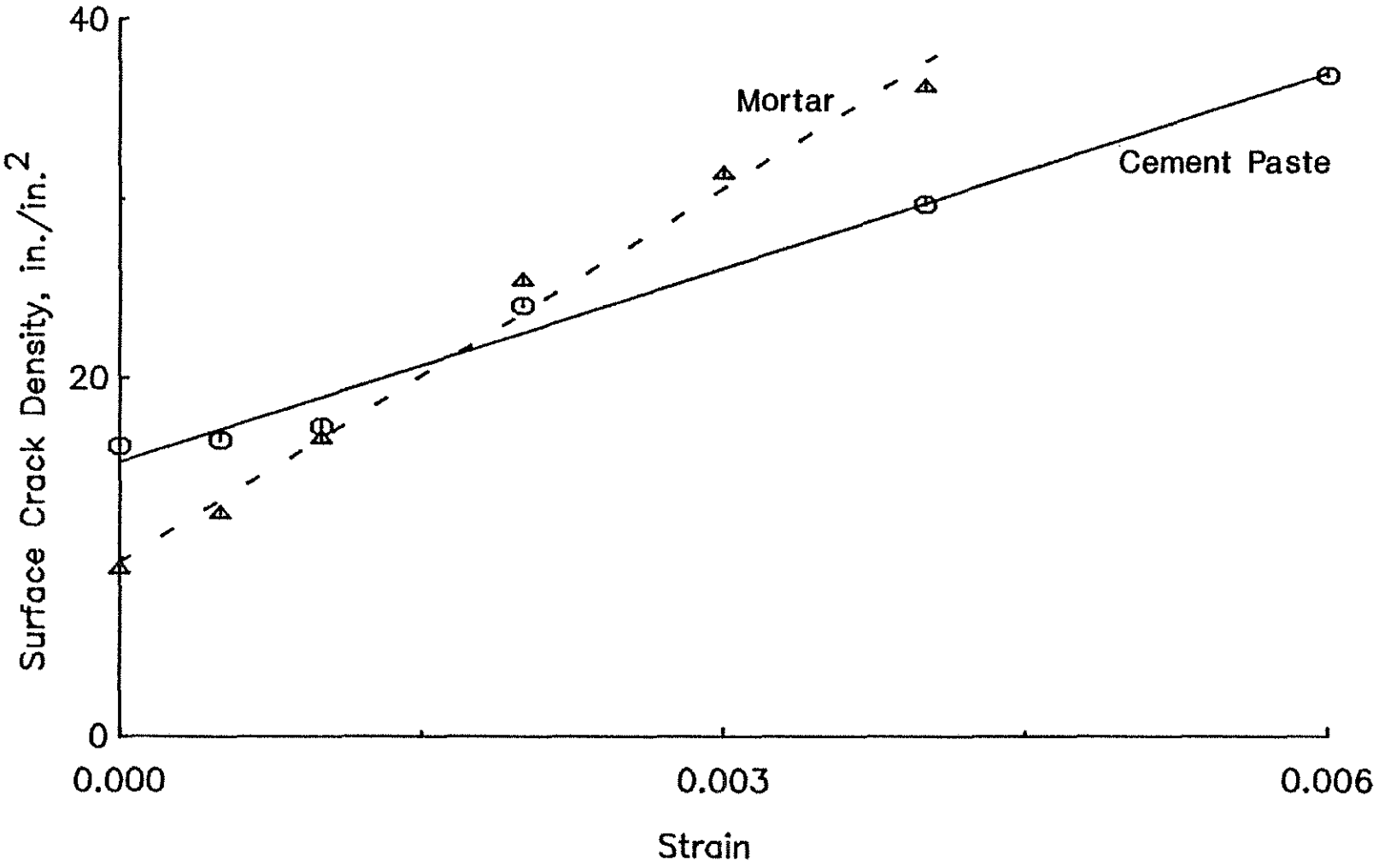

Fig. 3.25. Surface Crack Density, $M_T\langle\ell\rangle_T$, versus Strain for Monotonic Loading of Cement Paste and Mortar with a W/C = 0.5

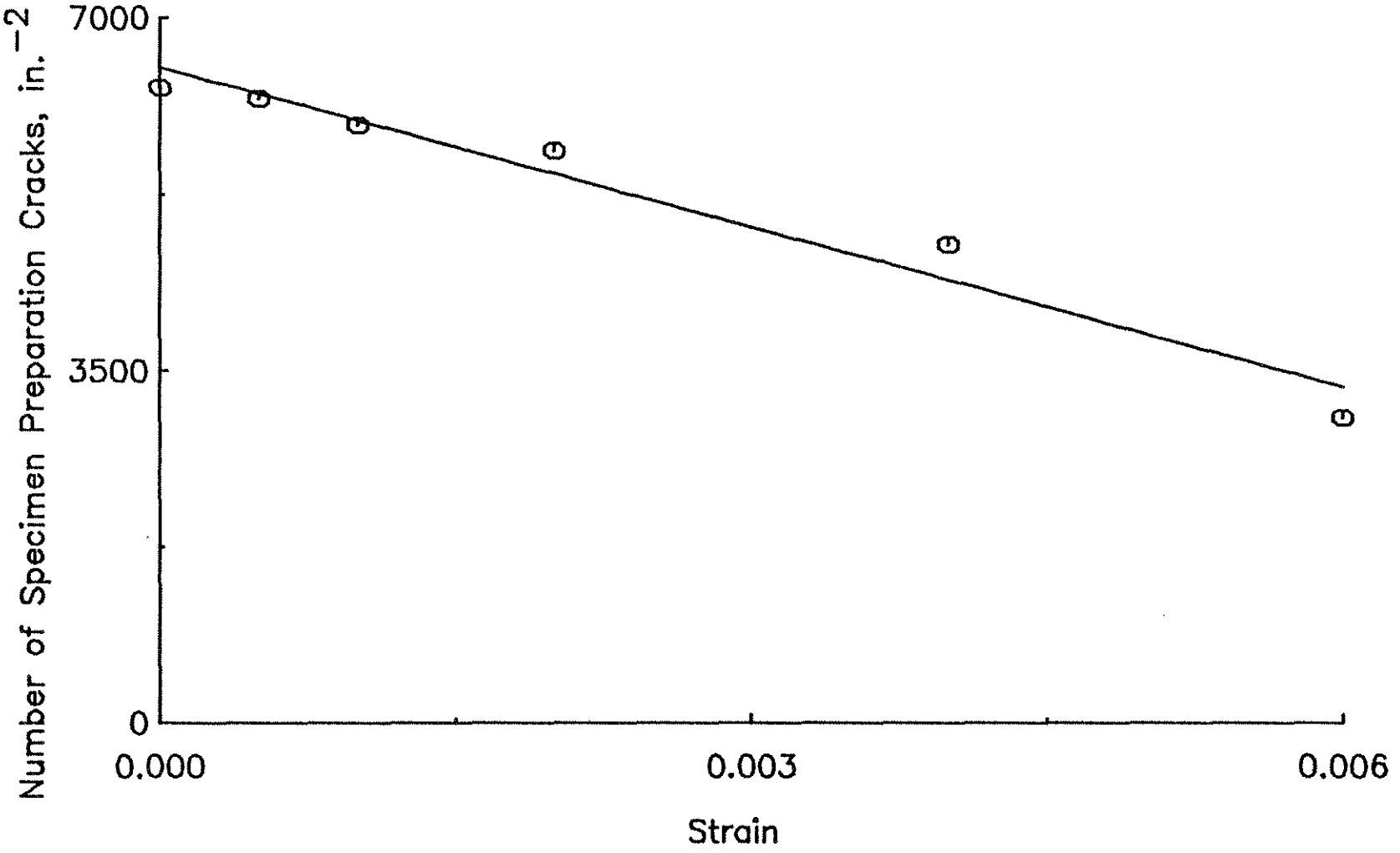

Fig. 3.26. Number of Specimen Preparation Cracks per Unit Area versus Strain for Monotonic Loading of Cement Paste with a W/C = 0.5

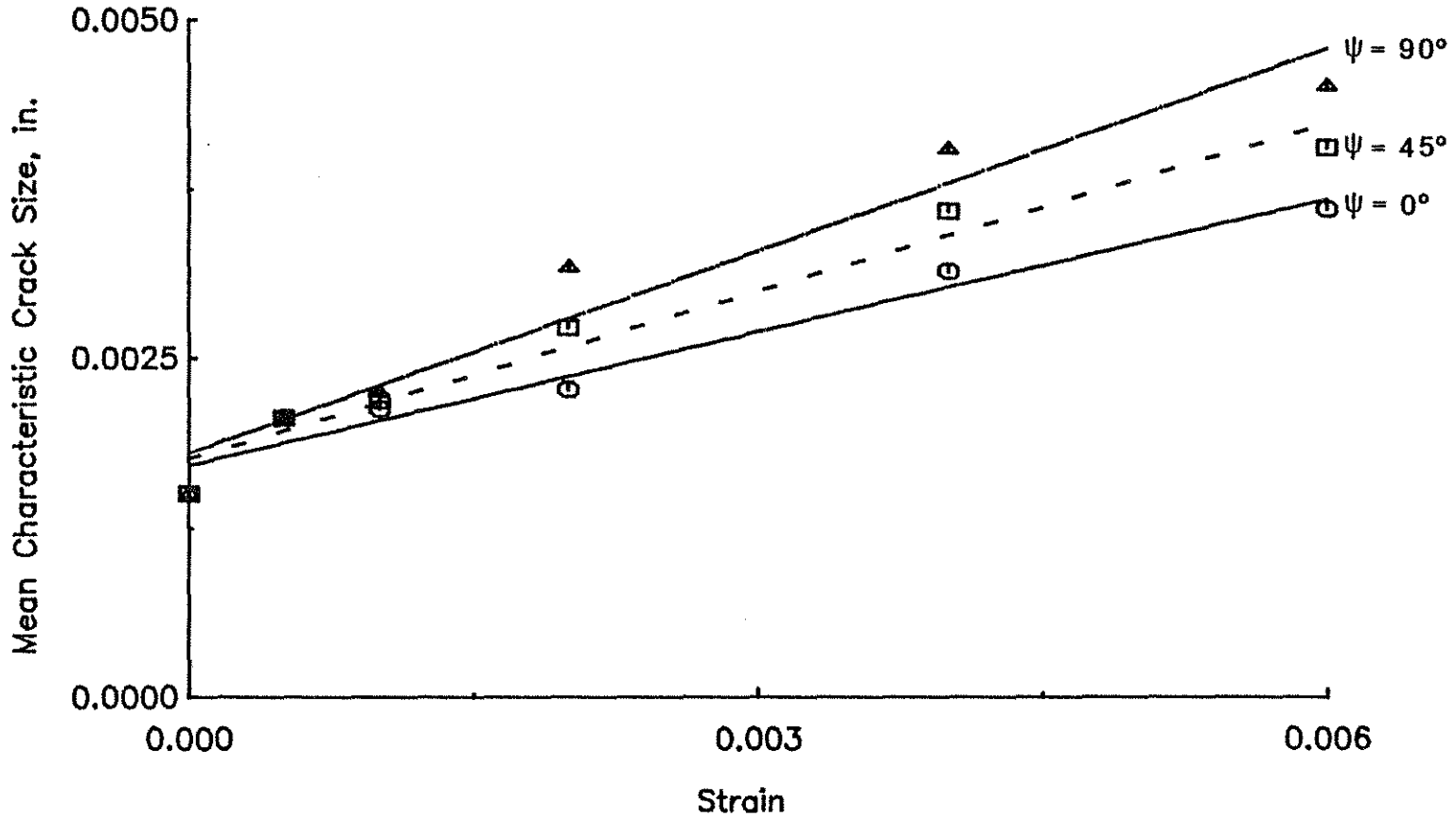

Fig. 3.27. Mean Characteristic Crack Size, $\langle a_\psi \rangle$, versus Strain for Monotonic Loading of Cement Paste with a W/C = 0.5

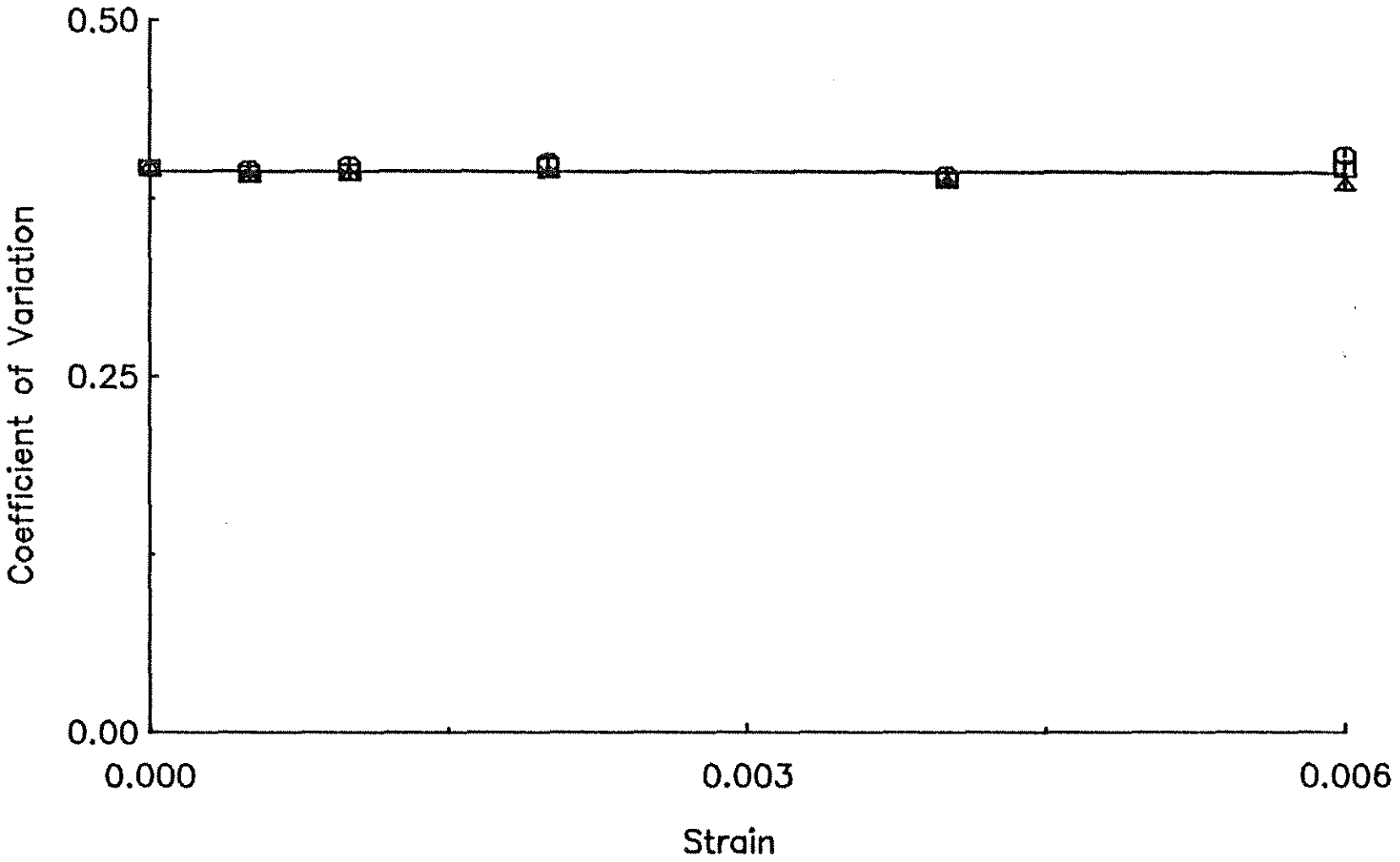

Fig. 3.28. Coefficient of Variation versus Strain for Monotonic Loading of Cement Paste with a W/C = 0.5

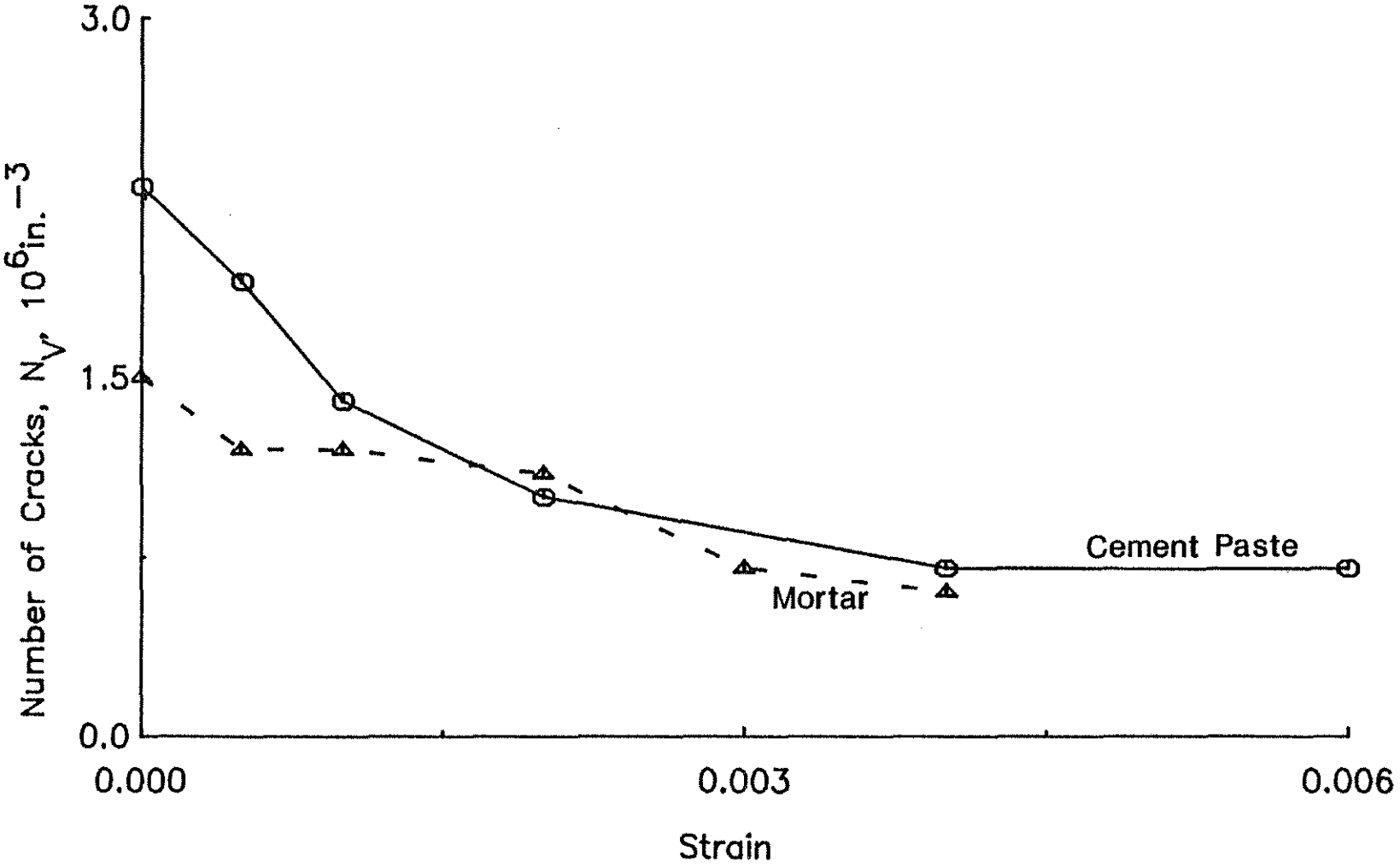

Fig. 3.29. Number of Cracks per Unit Volume, N_V, versus Strain for Monotonic Loading of Cement Paste and Mortar with a W/C = 0.5

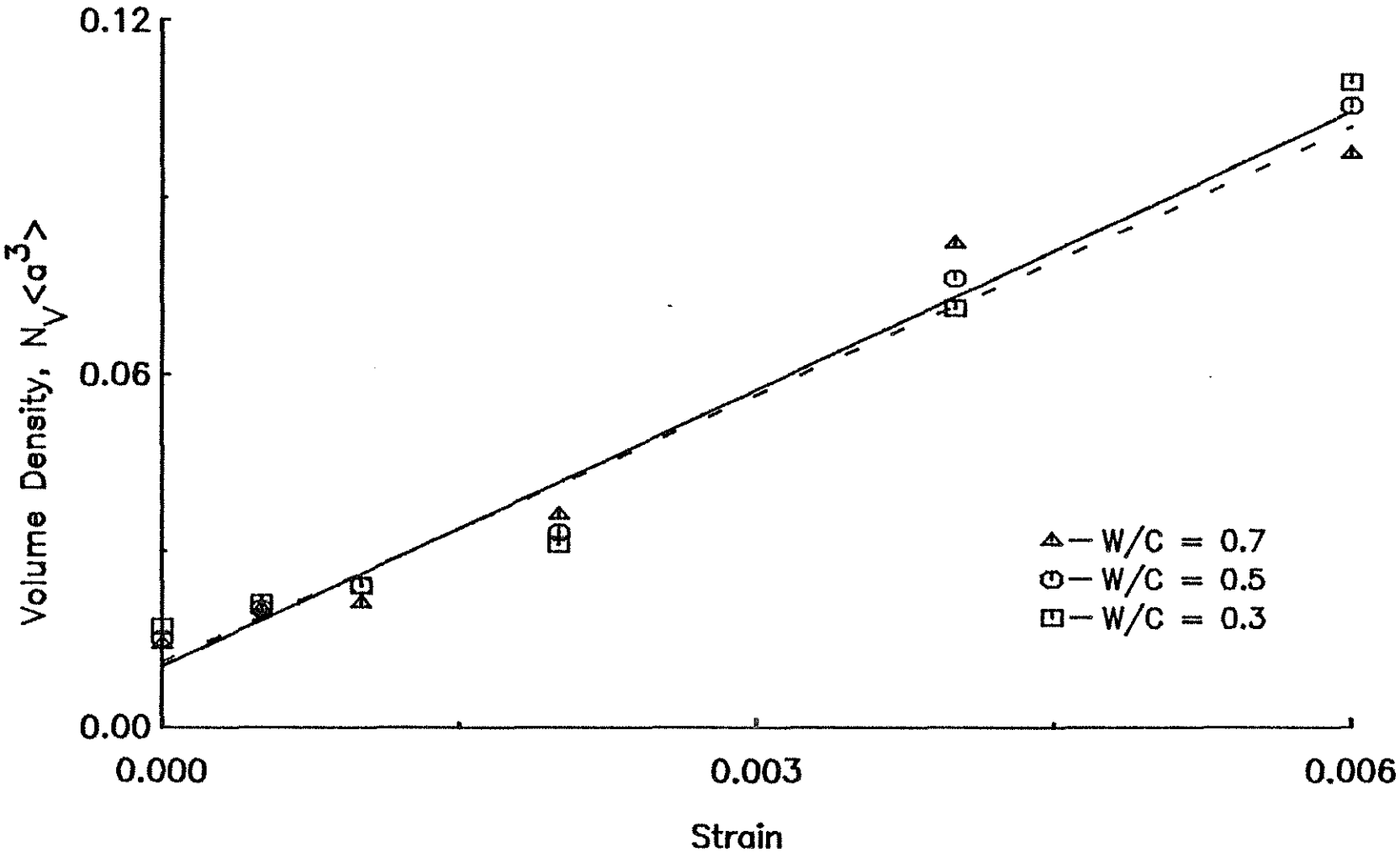

Fig. 3.30. Measure of Volumetric Crack Density, $N_V\langle a^3\rangle$, versus Strain for Monotonic Loading of Cement Pastes with W/C = 0.7, 0.5 and 0.3

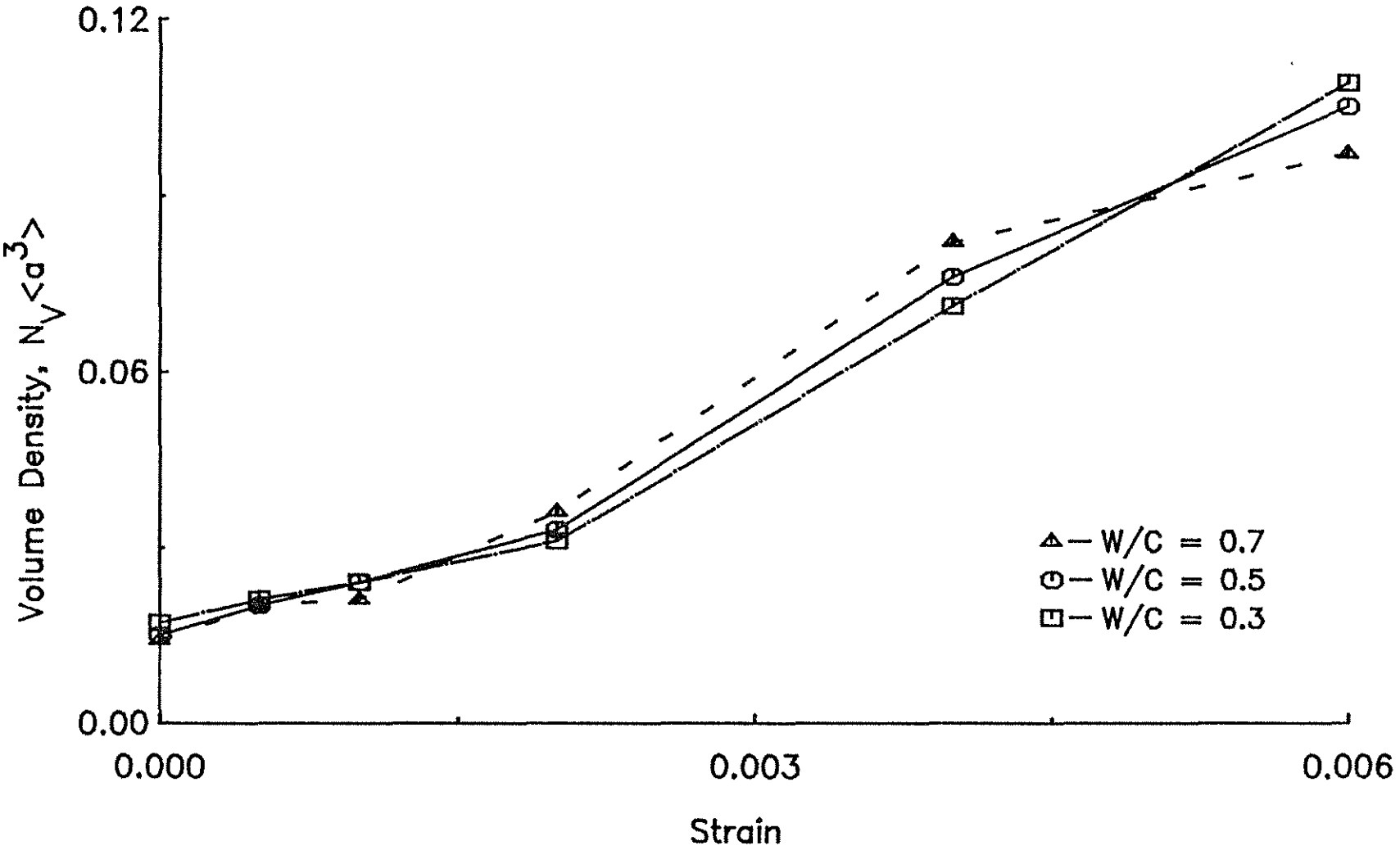

Fig. 3.31. Measure of Volumetric Crack Density, $N_V\langle a^3\rangle$, versus Strain for Monotonic Loading of Cement Pastes with W/C = 0.7, 0.5 and 0.3

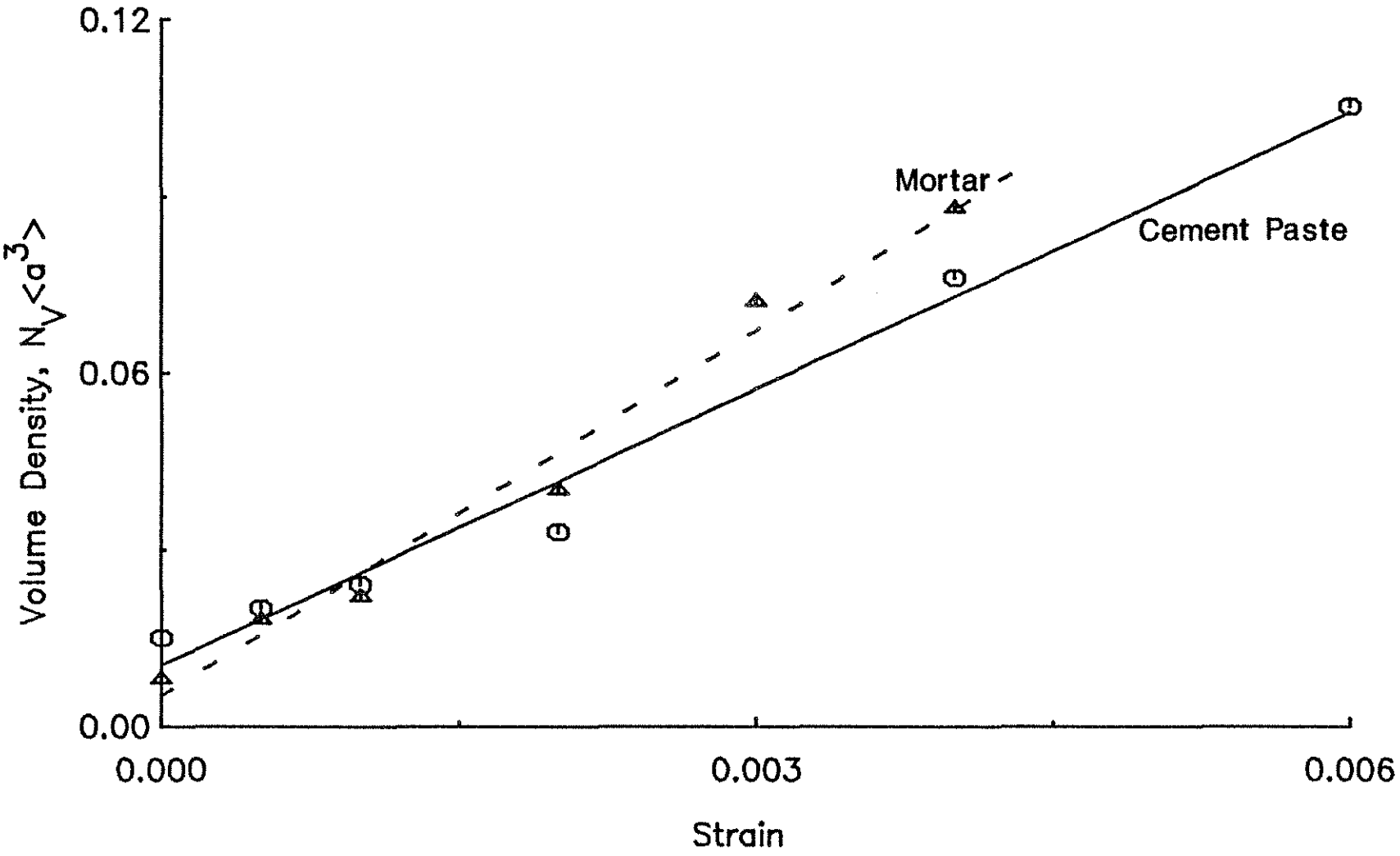

Fig. 3.32. Measure of Volumetric Crack Density, $N_V\langle a^3\rangle$, versus Strain for Monotonic Loading of Cement Paste and Mortar with a W/C = 0.5

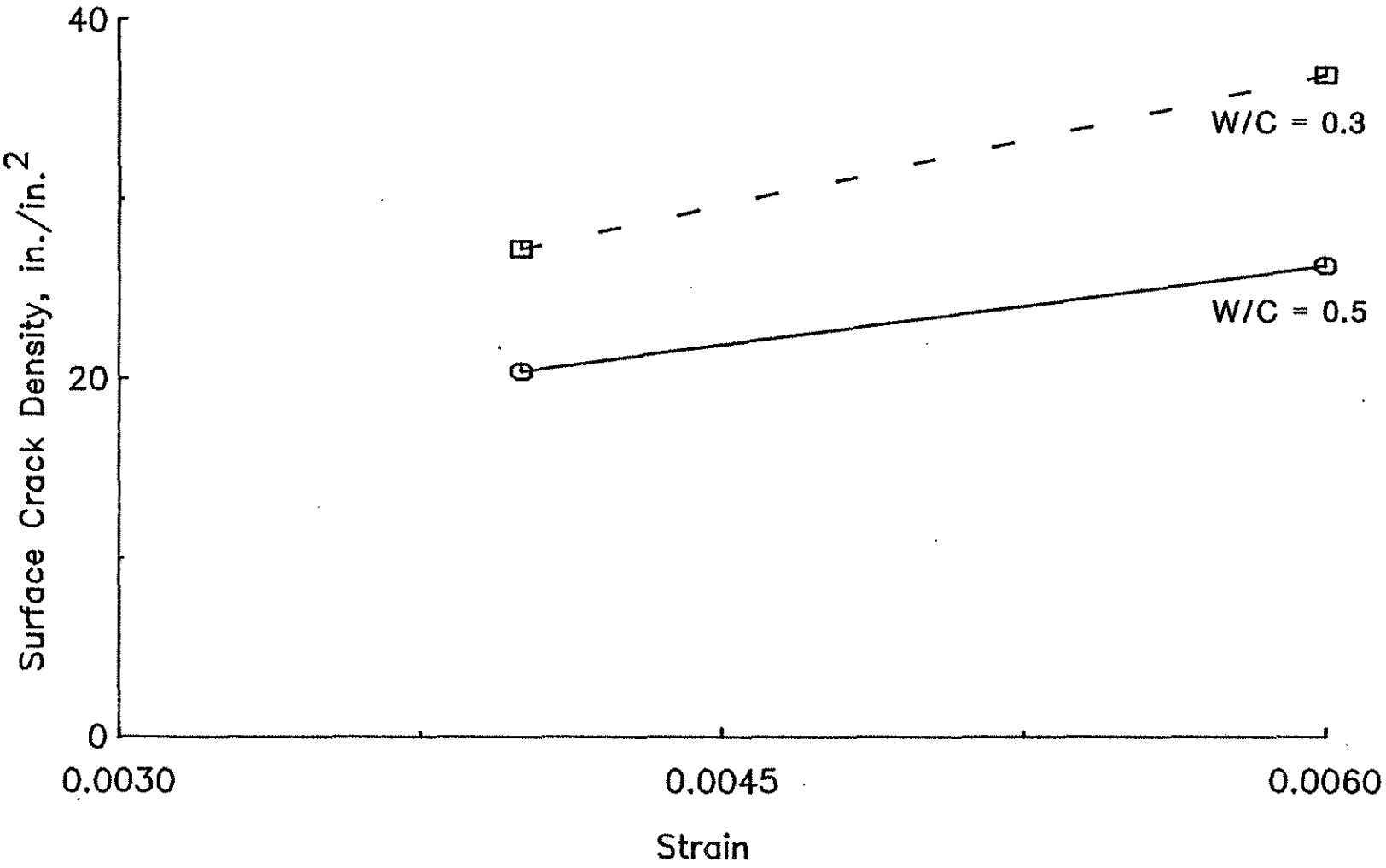

Fig. 3.33. Surface Crack Density, $M_T\langle\ell\rangle_T$, versus Strain for Sustained Loading of Cement Pastes with W/C = 0.5 and 0.3

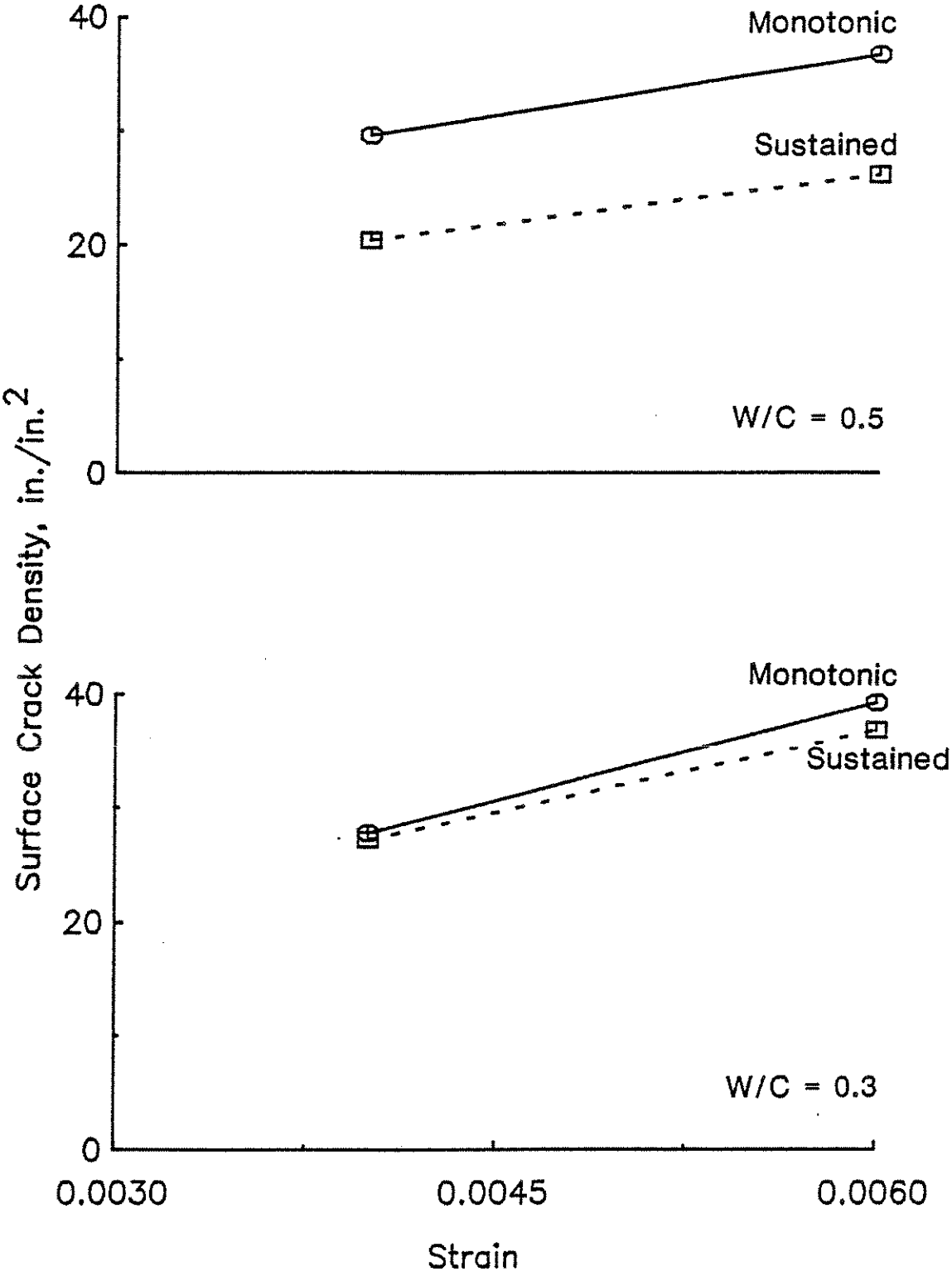

Fig. 3.34. Surface Crack Density, $M_T\langle\ell\rangle_T$, versus Strain for Monotonic and Sustained Loading of Cement Pastes with W/C = 0.5 and 0.3

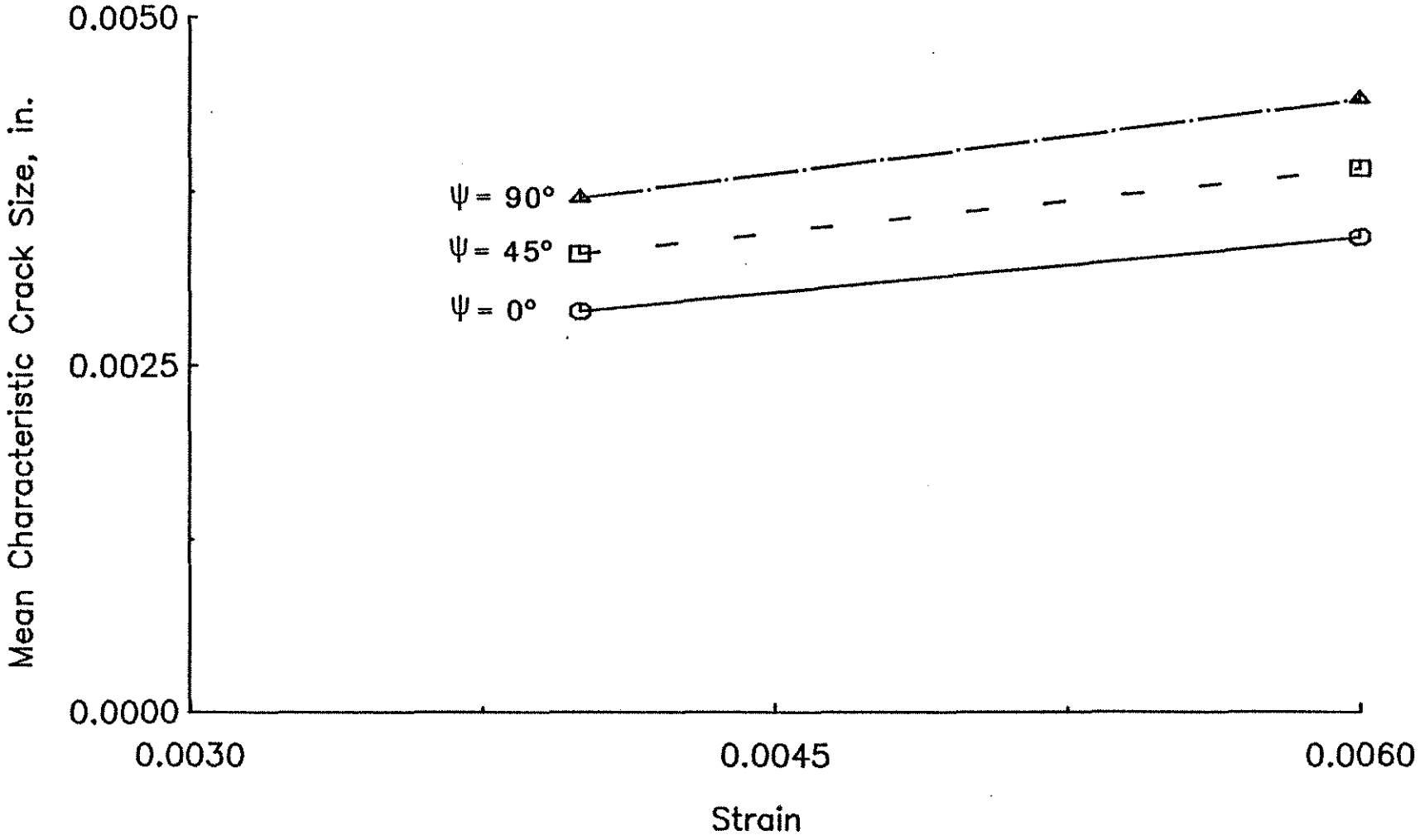

Fig. 3.35. Mean Characteristic Crack Size, $\langle a_\psi \rangle$, versus Strain for Sustained Loading of Cement Paste with a W/C = 0.5

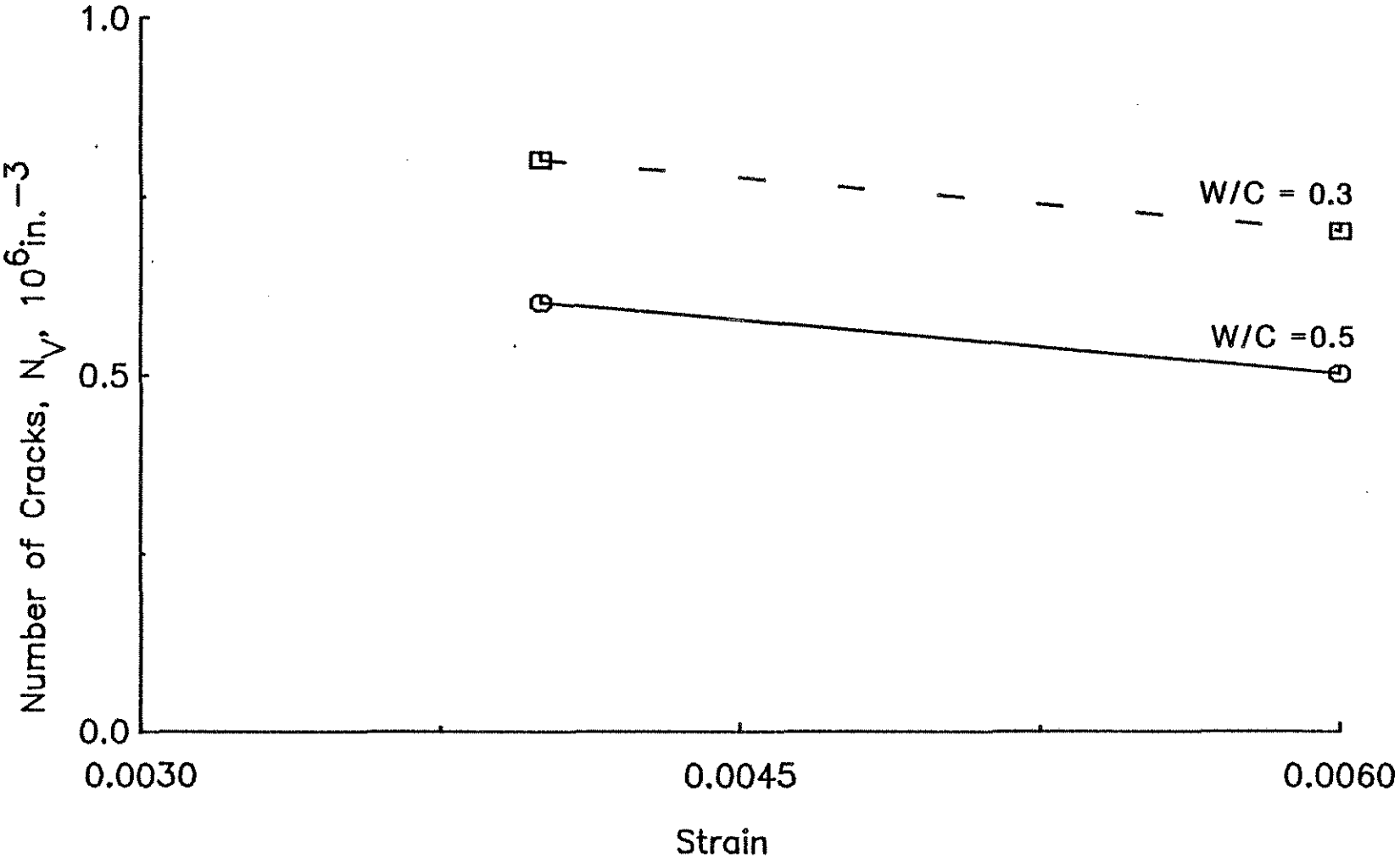

Fig. 3.36. Number of Cracks per Unit Volume versus Strain for Sustained Loading of Cement Pastes with W/C = 0.5 and 0.3

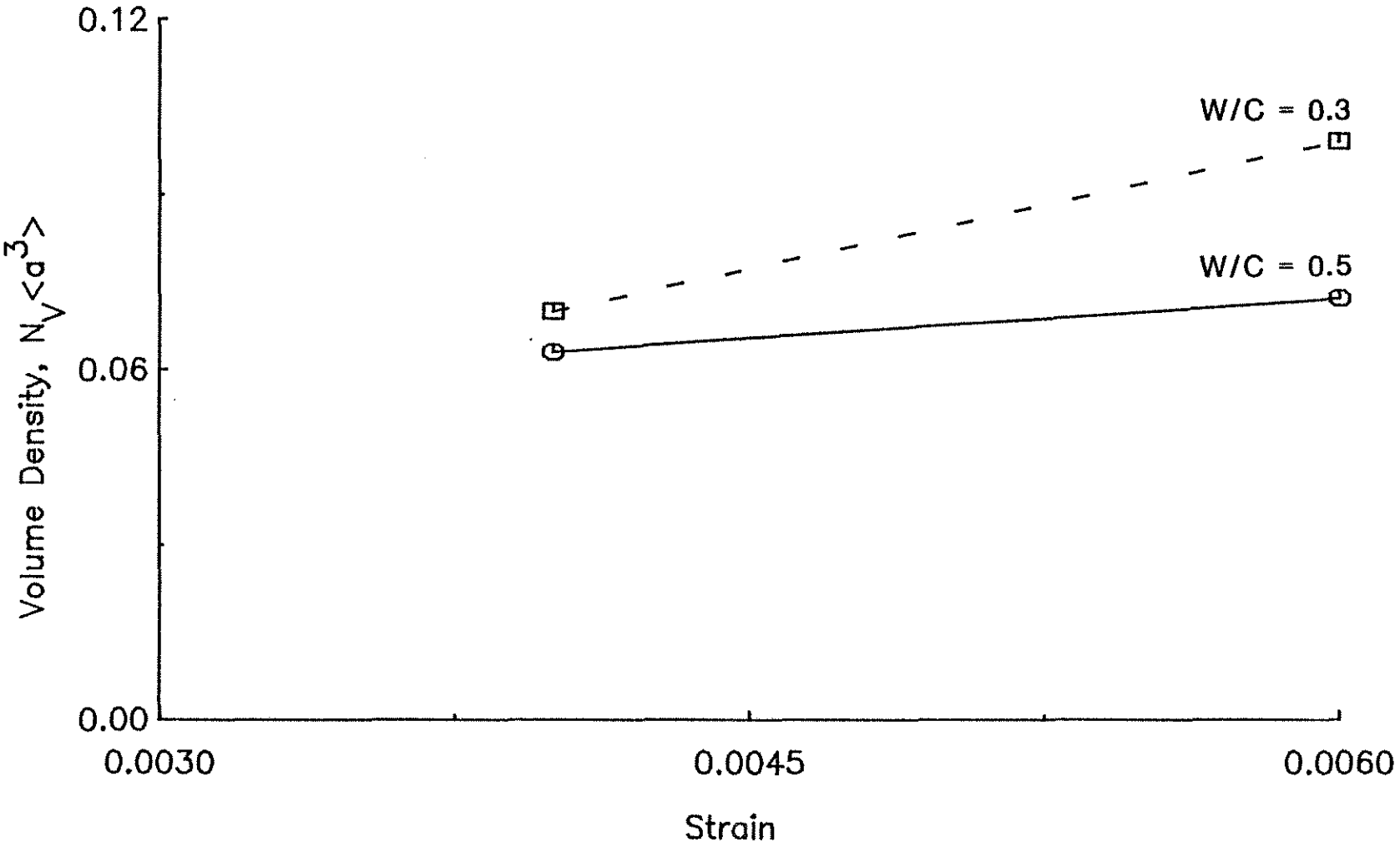

Fig. 3.37. Measure of Volumetric Crack Density, $N_V\langle a^3\rangle$, for Sustained Loading of Cement Pastes with W/C = 0.5 and 0.3

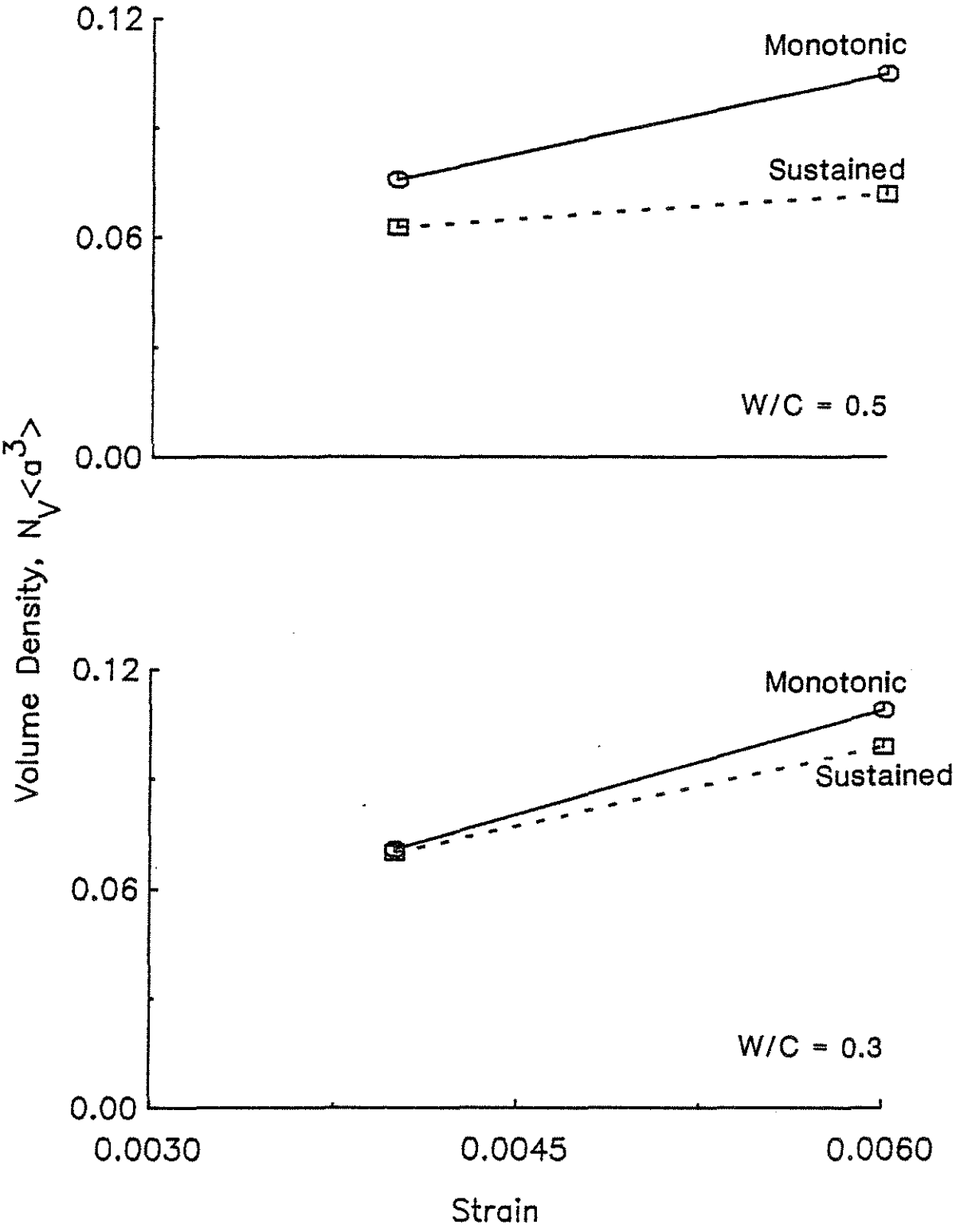

Fig. 3.38. Measure of Volumetric Crack Density, $N_V\langle a^3\rangle$, versus Strain for Monotonic and Sustained Loading of Cement Pastes with W/C = 0.5 and 0.3

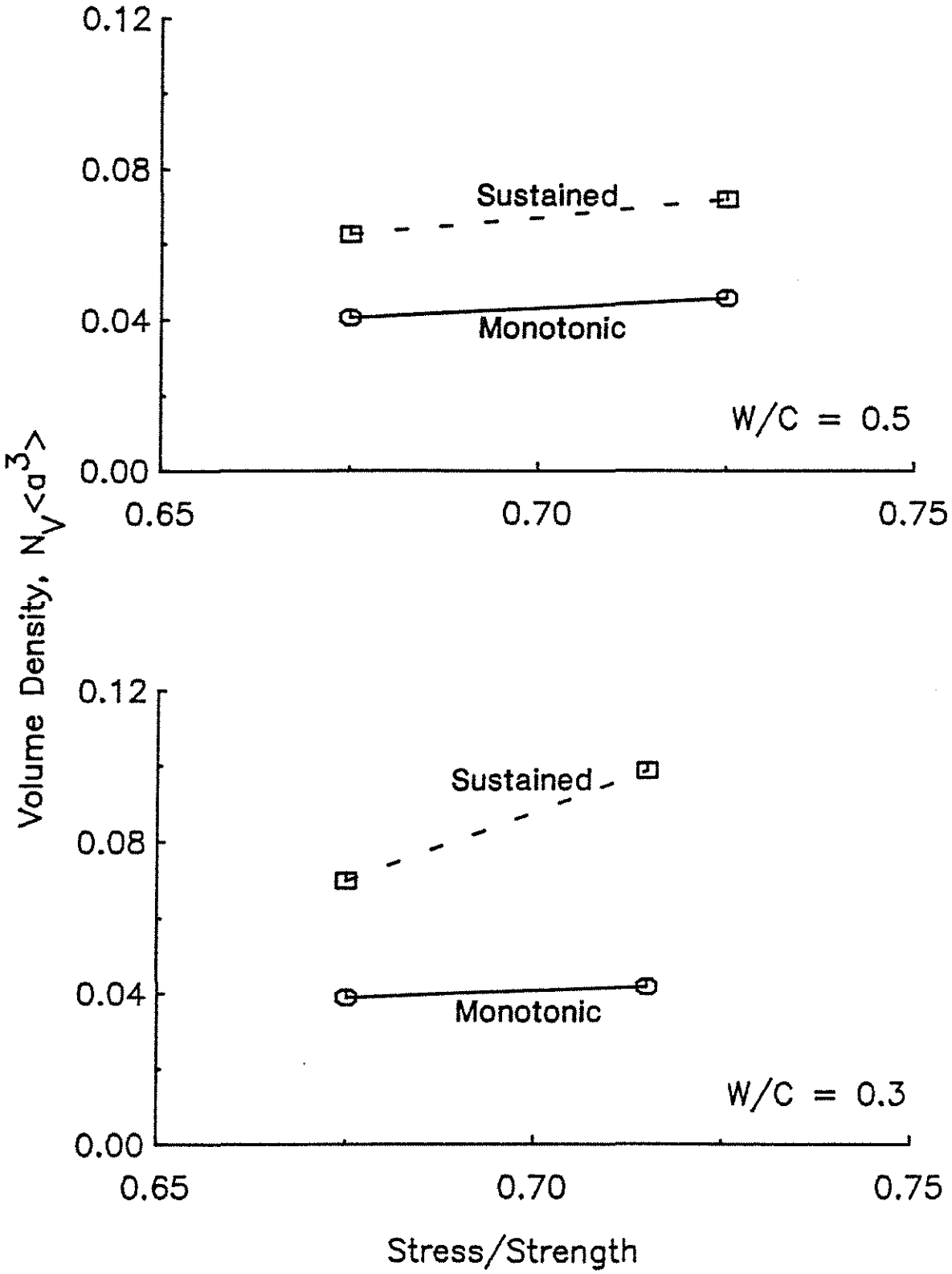

Fig. 3.39. Measure of Volumetric Crack Density, $N_V\langle a^3\rangle$, versus Stress-Strength Ratio for Monotonic and Sustained Loading of Cement Pastes with W/C = 0.5 and 0.3

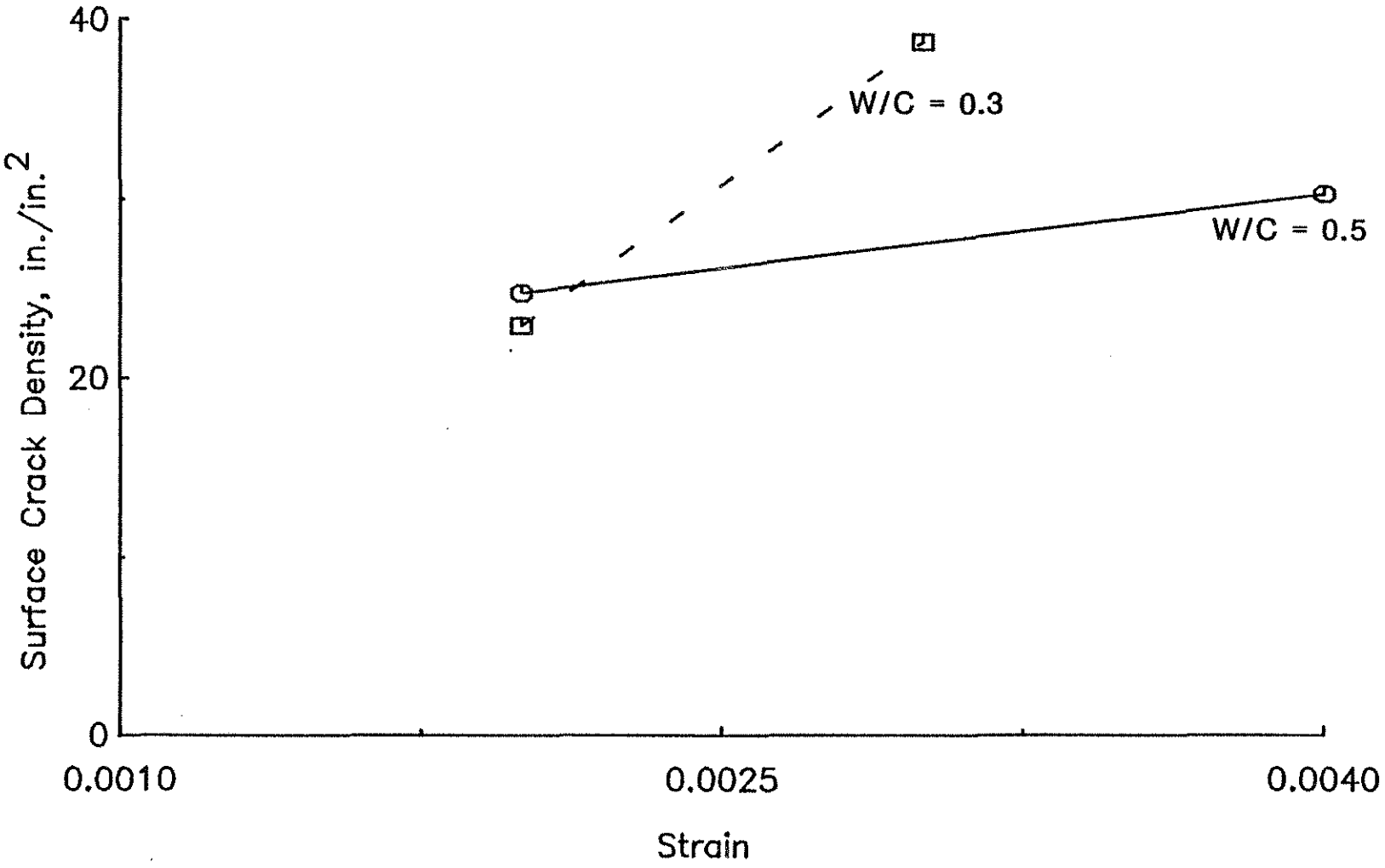

Fig. 3.40. Surface Crack Density, $M_T\langle \ell \rangle_T$, versus Strain for Cyclic Loading of Cement Pastes with W/C = 0.5 and 0.3

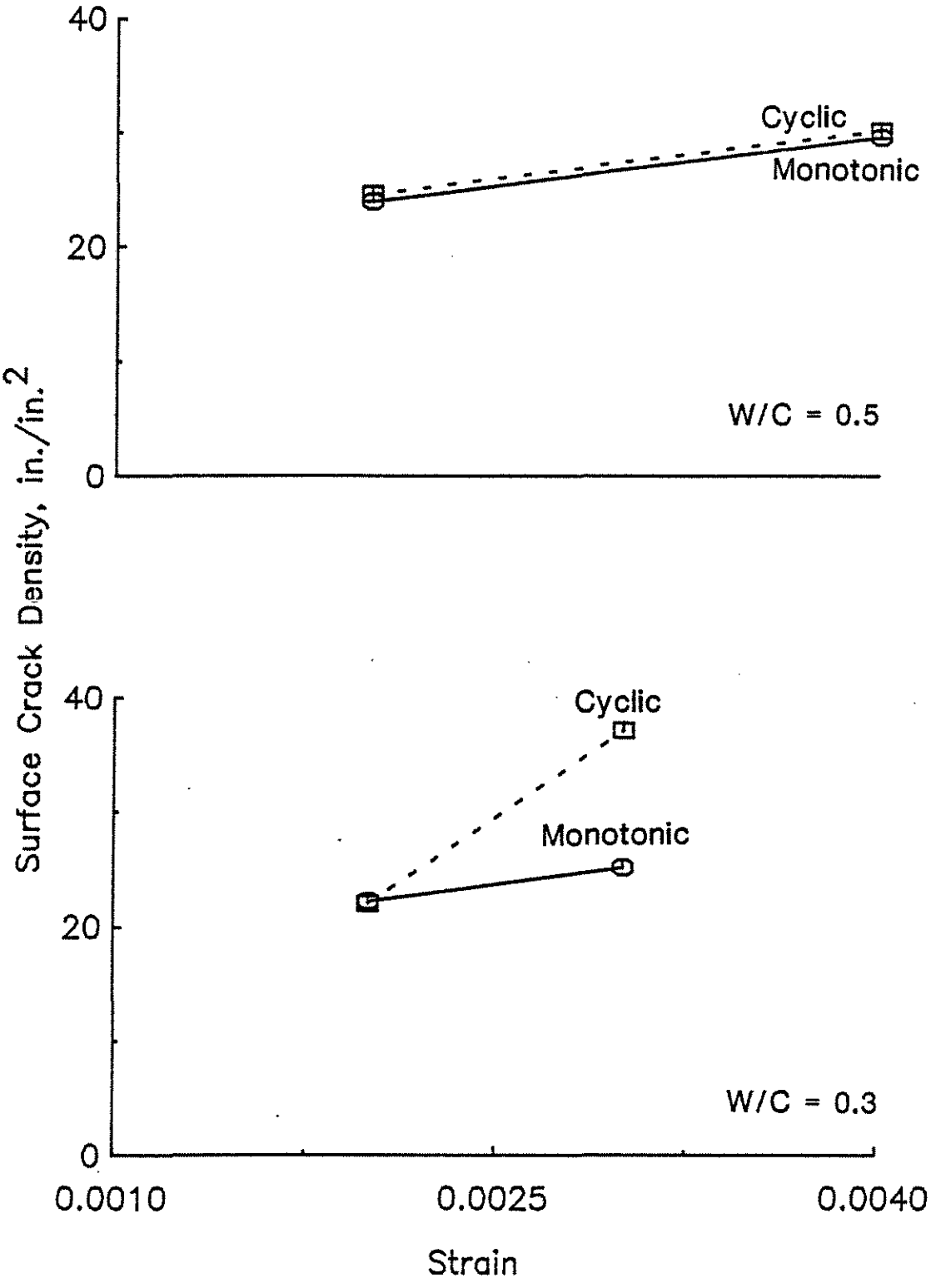

Fig. 3.41. Surface Crack Density, $M_T\langle\ell\rangle_T$, versus Strain for Monotonic and Sustained Loading of Cement Pastes with W/C = 0.5 and 0.3

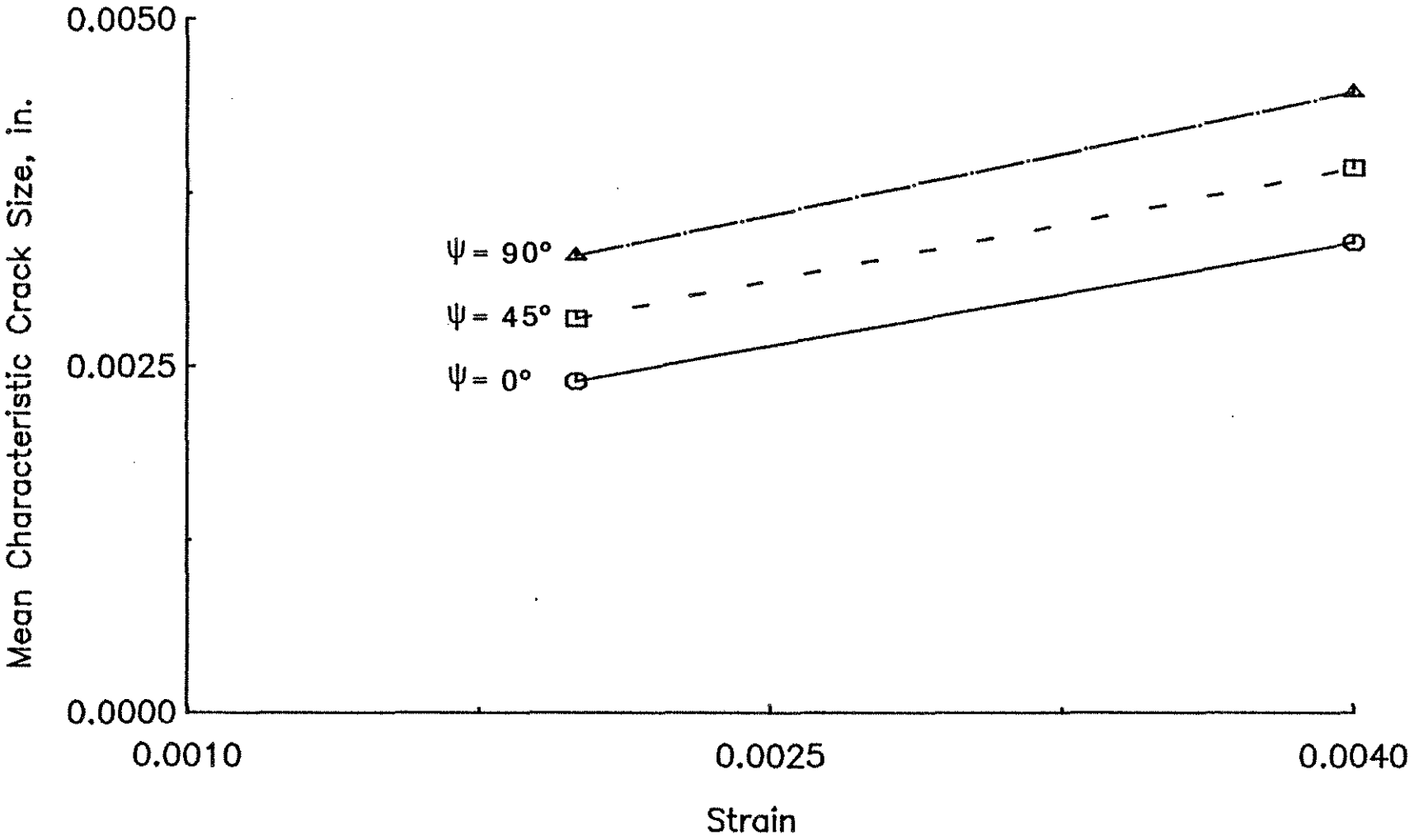

Fig. 3.42. Mean Characteristic Crack Size, $\langle a_\psi \rangle$, versus Strain for Cyclic Loading of Cement Paste with a W/C = 0.5

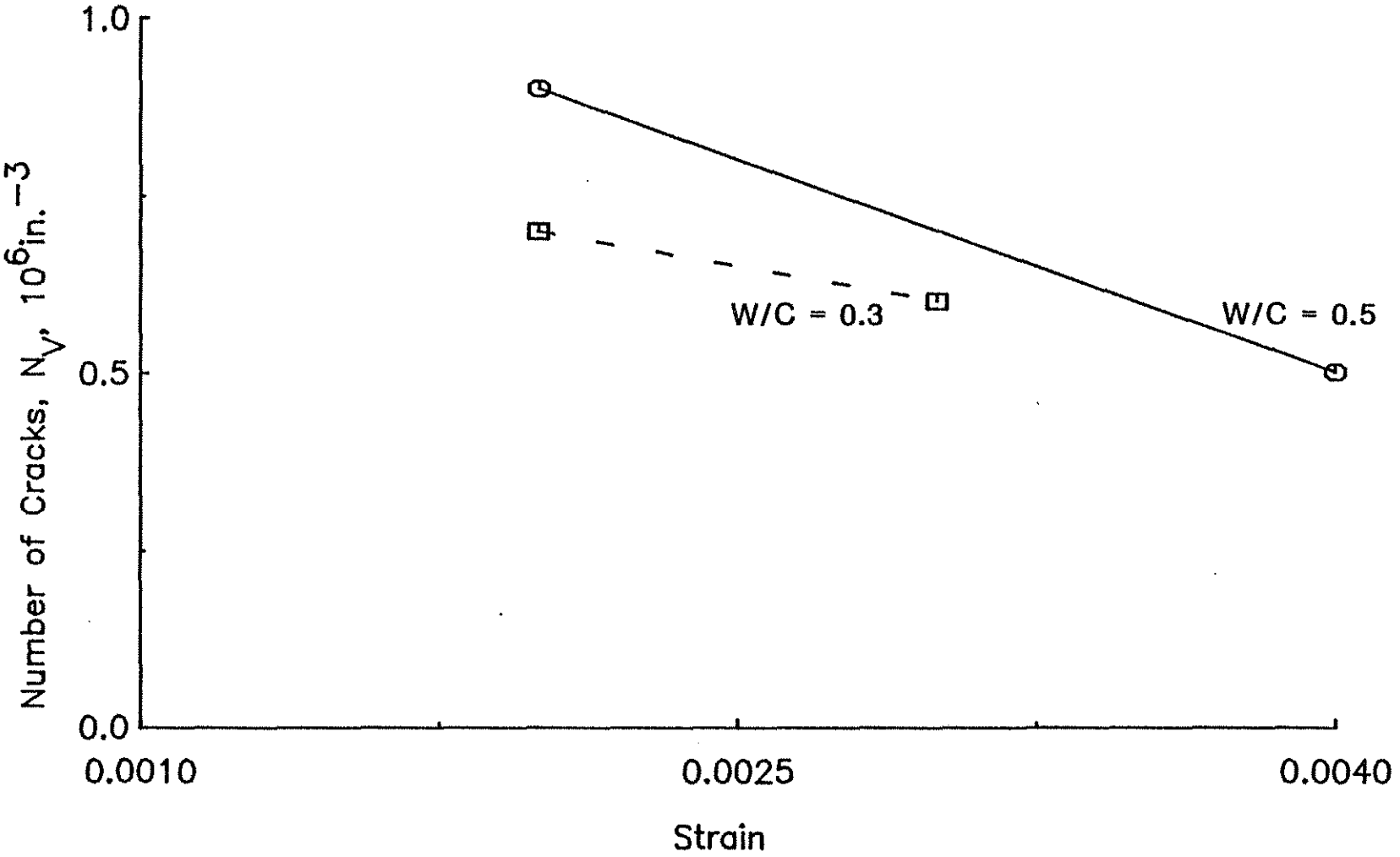

Fig. 3.43. Number of Cracks per Unit Volume, N_V, versus Strain for Cyclic Loading of Cement Pastes with W/C = 0.5 and 0.3

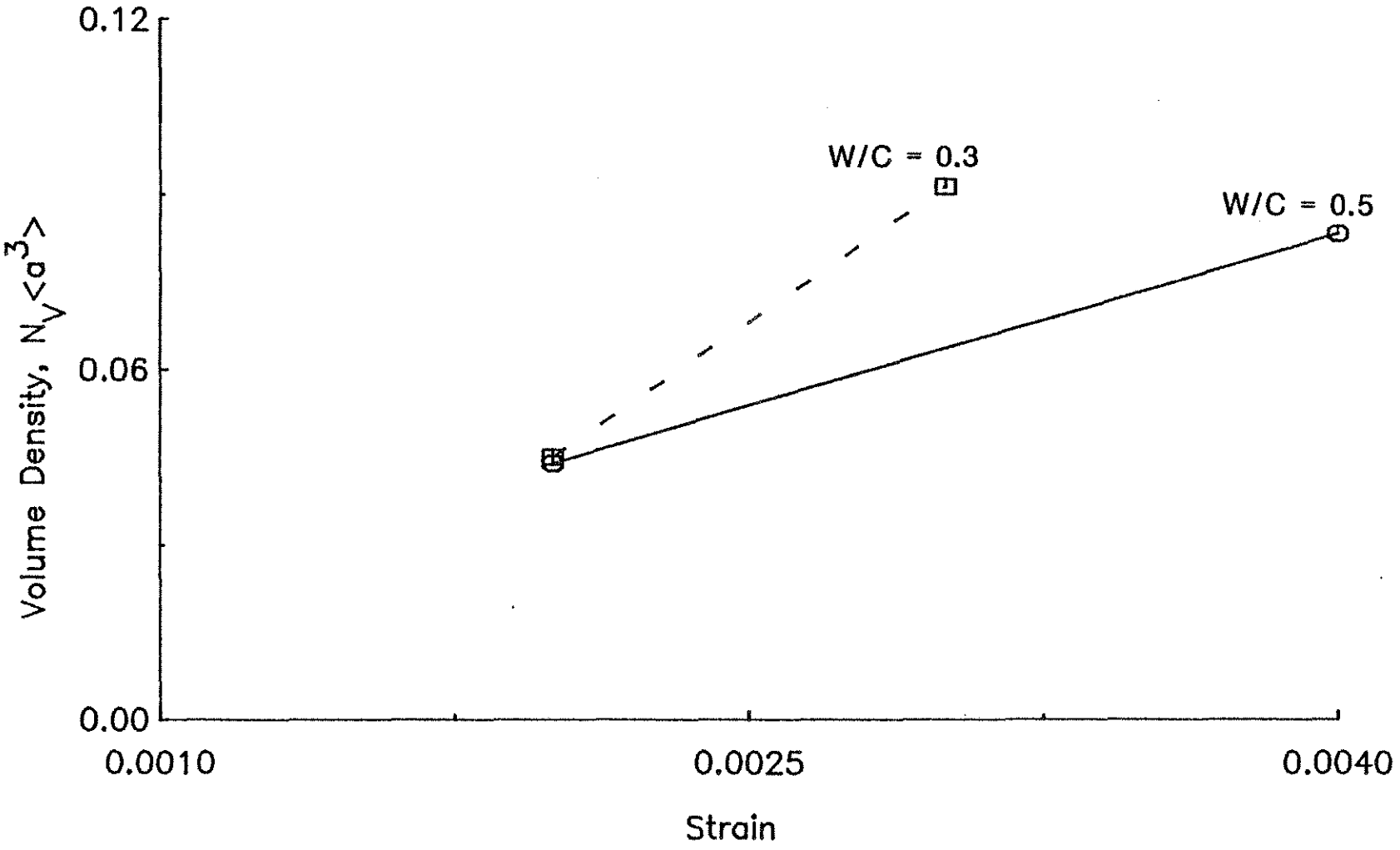

Fig. 3.44. Measure of Volumetric Crack Density, $N_V\langle a^3\rangle$, versus Strain for Cyclic Loading of Cement Pastes with W/C = 0.5 and 0.3

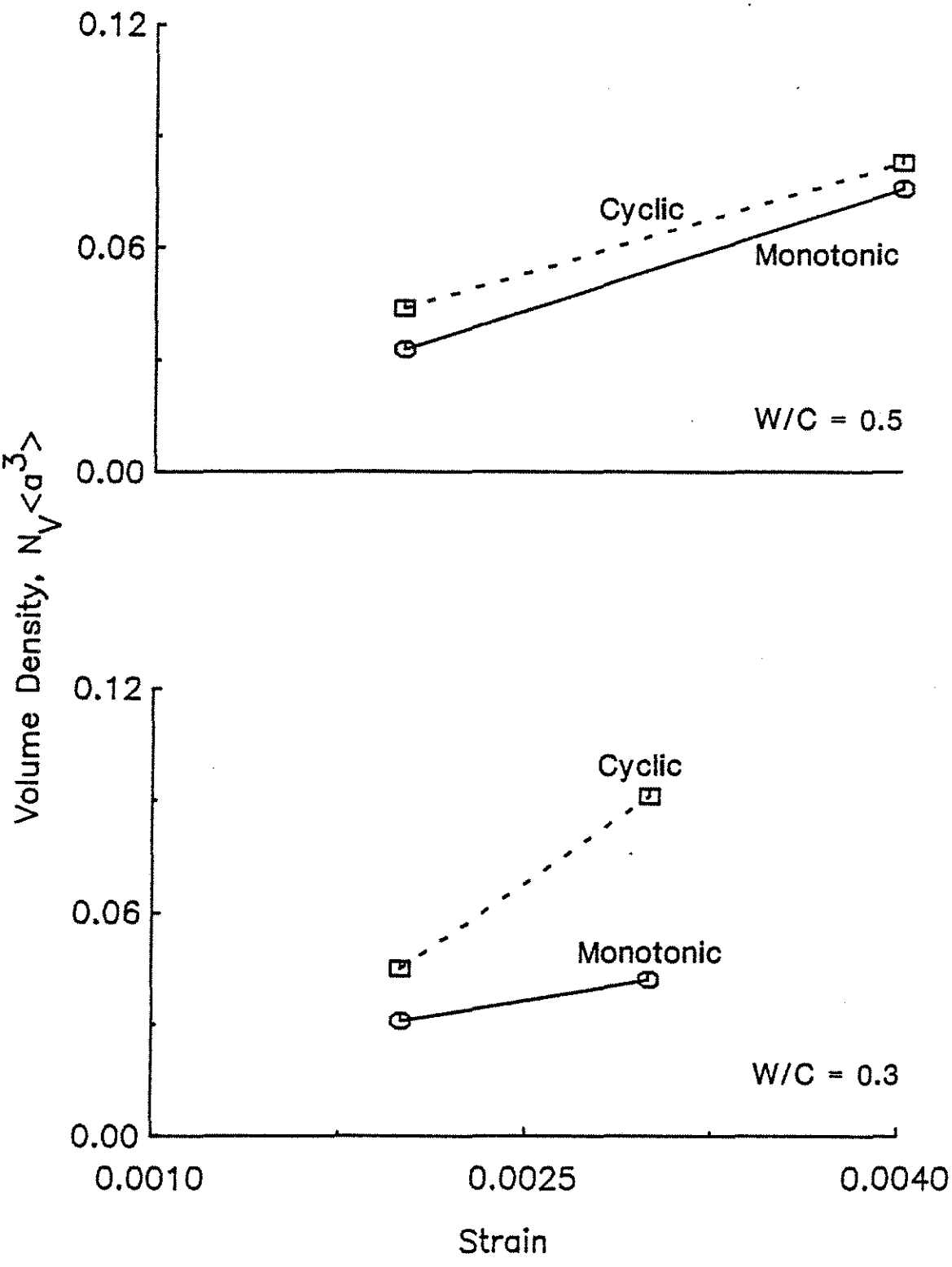

Fig. 3.45. Measure of Volumetric Crack Density, $N_V\langle a^3\rangle$, versus Strain for Monotonic and Cyclic Loading of Cement Pastes with W/C = 0.5 and 0.3

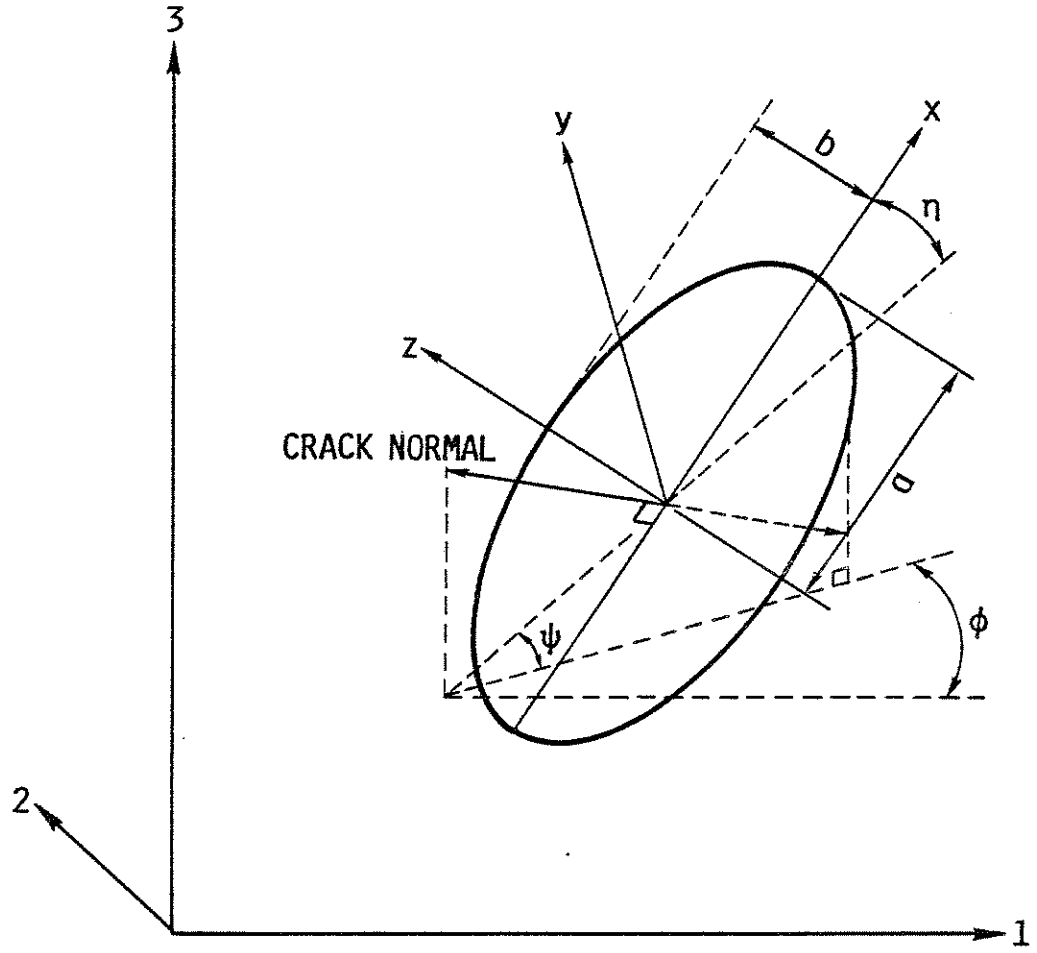

Fig. 4.1. Elliptic Crack and Principal Material Directions

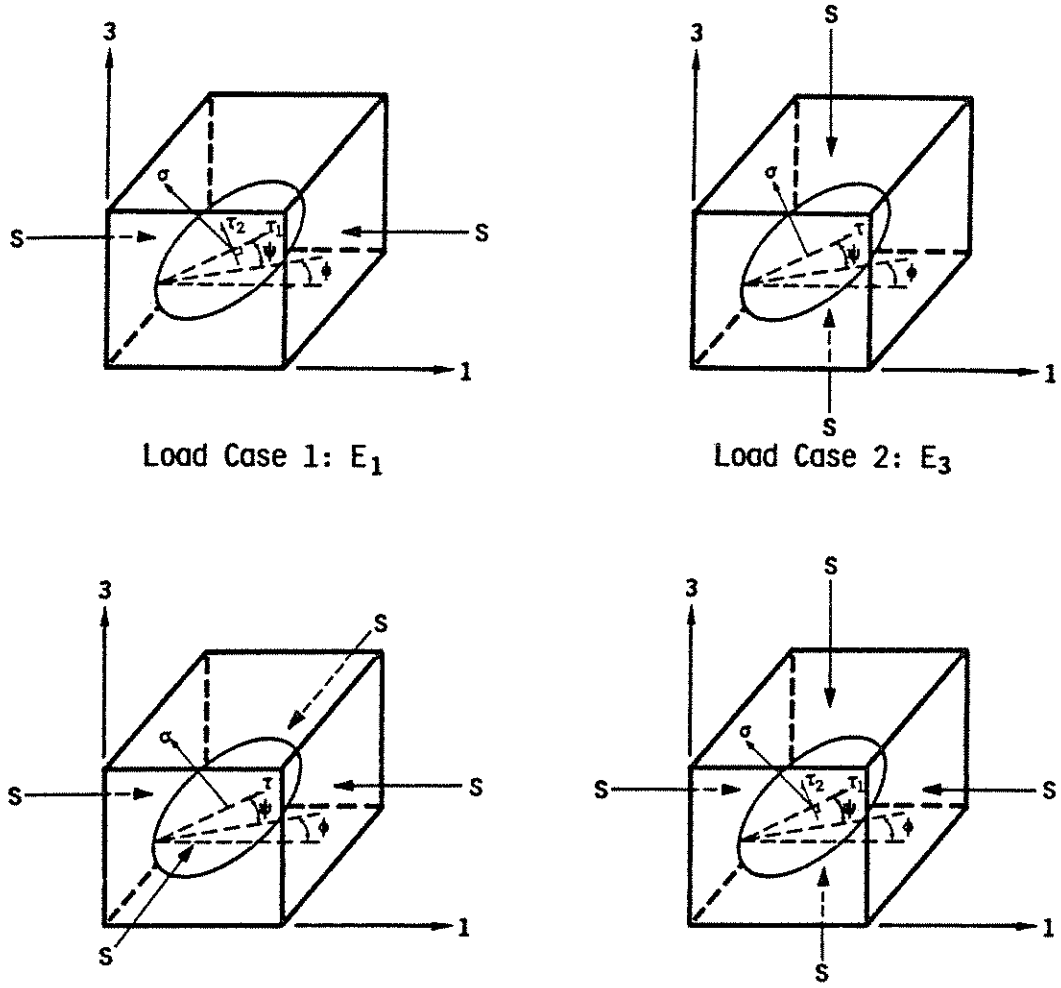

Fig. 4.2. Applied Stresses for Determining Effective Moduli

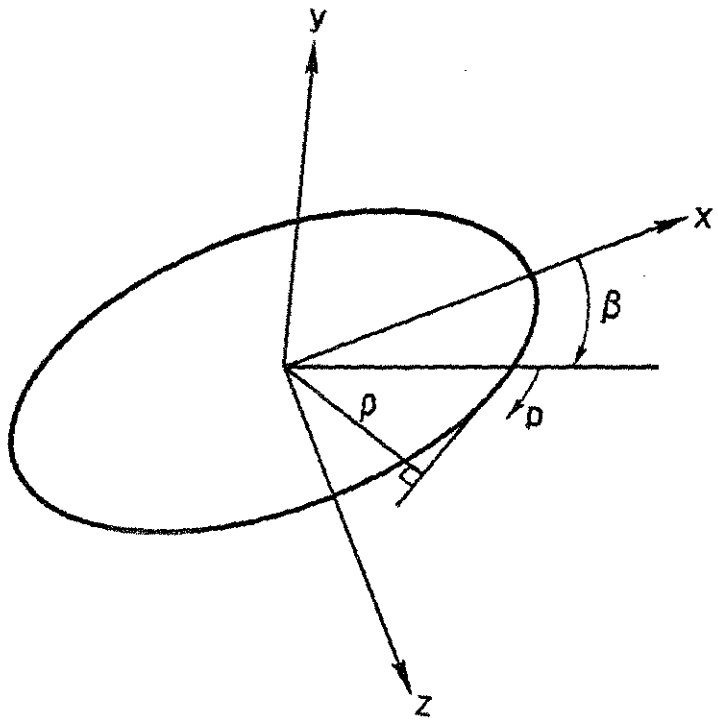

Fig. 4.3. Crack-based Coordinates

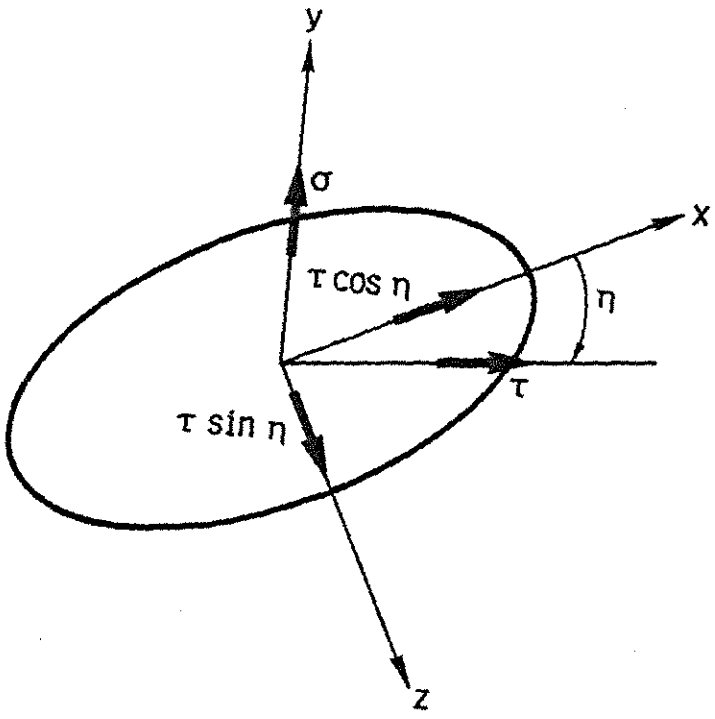

Fig. 4.4. Elliptic Crack and Resolved Stresses

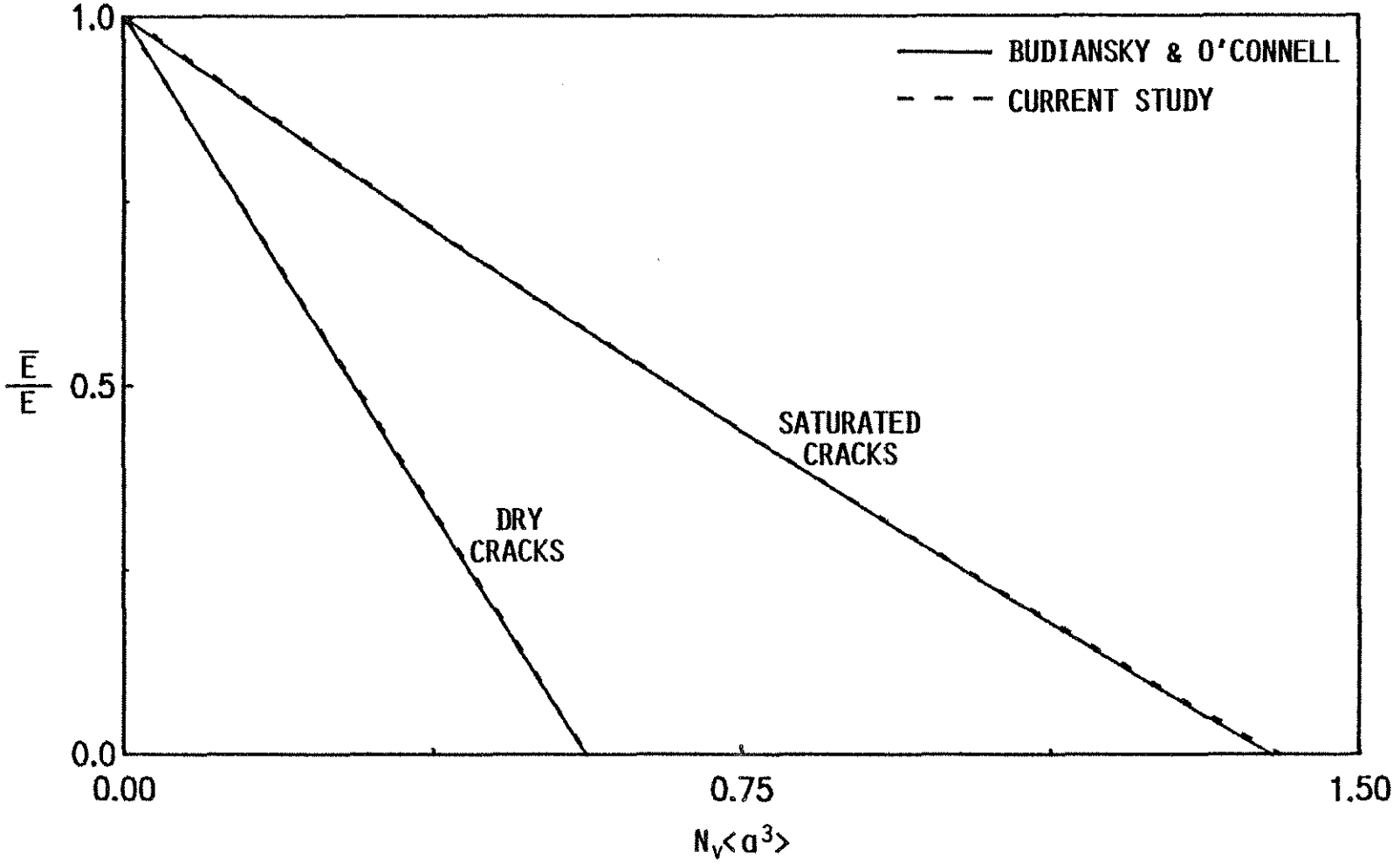

Fig. 4.5. Effective Stiffness Modulus; Dry or Saturated Circular Cracks in an Isotropic Solid

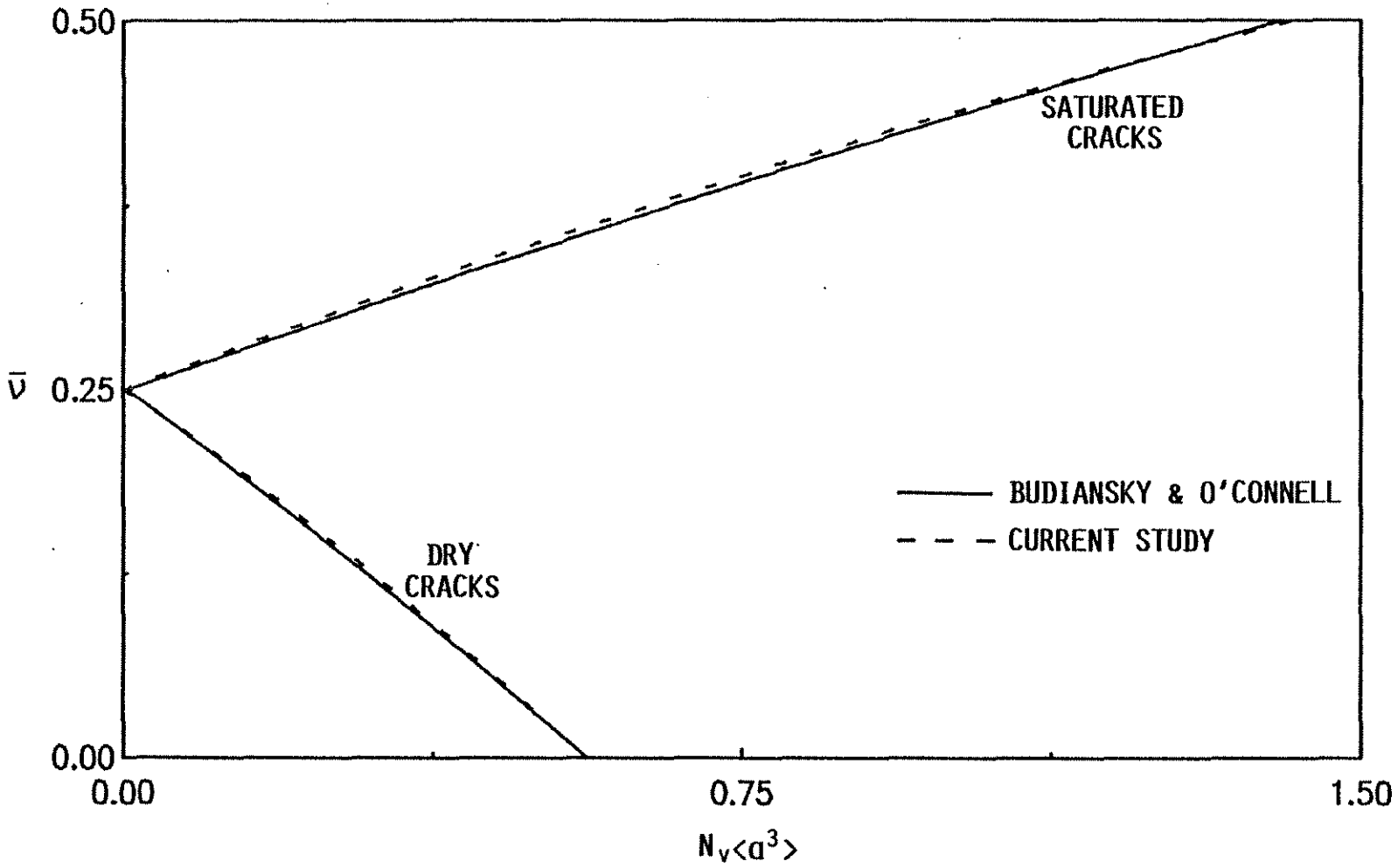

Fig. 4.6. Effective Poisson's Ratio; Dry or Saturated Circular Cracks in an Isotropic Solid

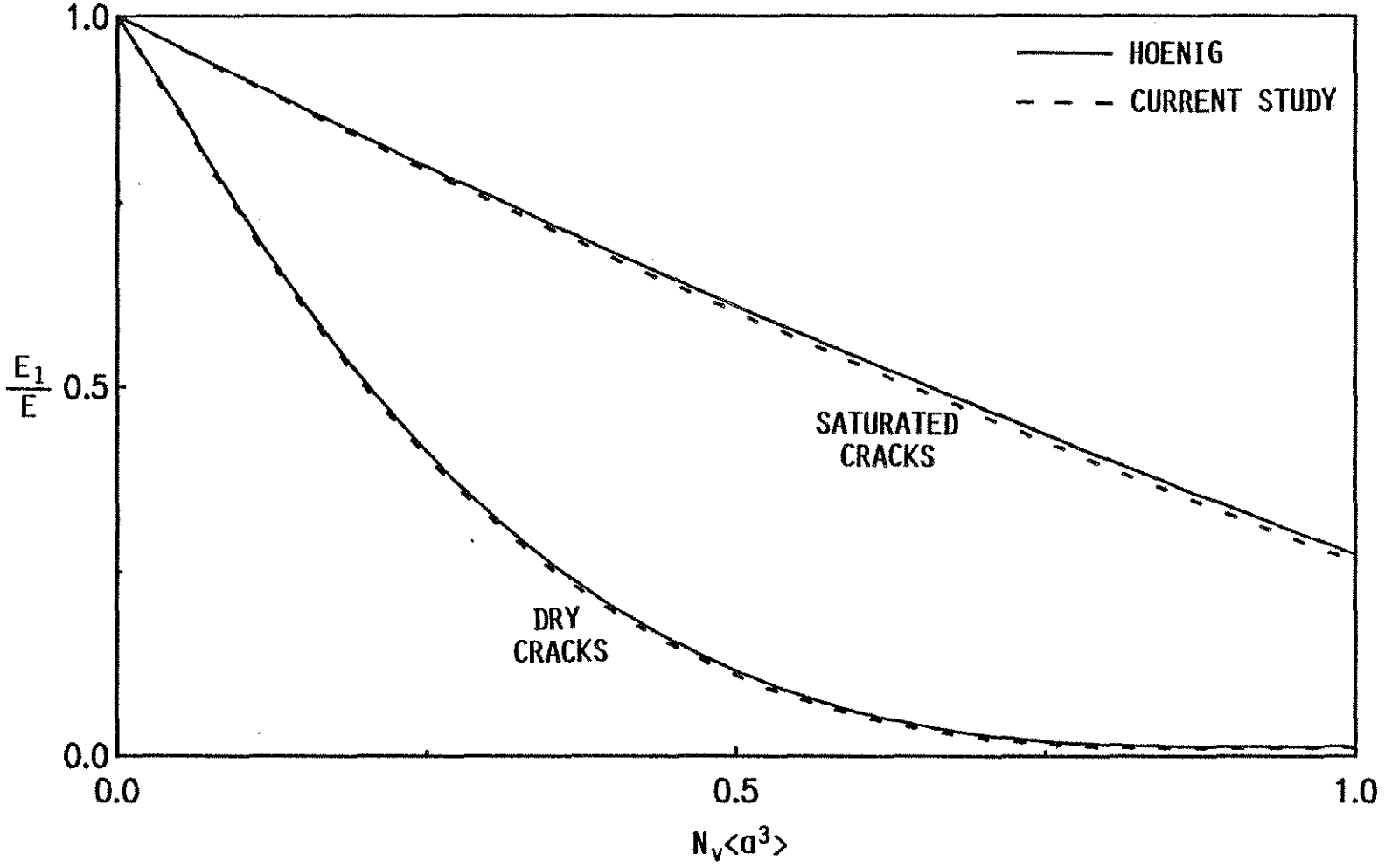

Fig. 4.7. Effective Stiffness Modulus; Dry or Saturated Circular Cracks in a Cylindrically Transverse Isotropic Solid

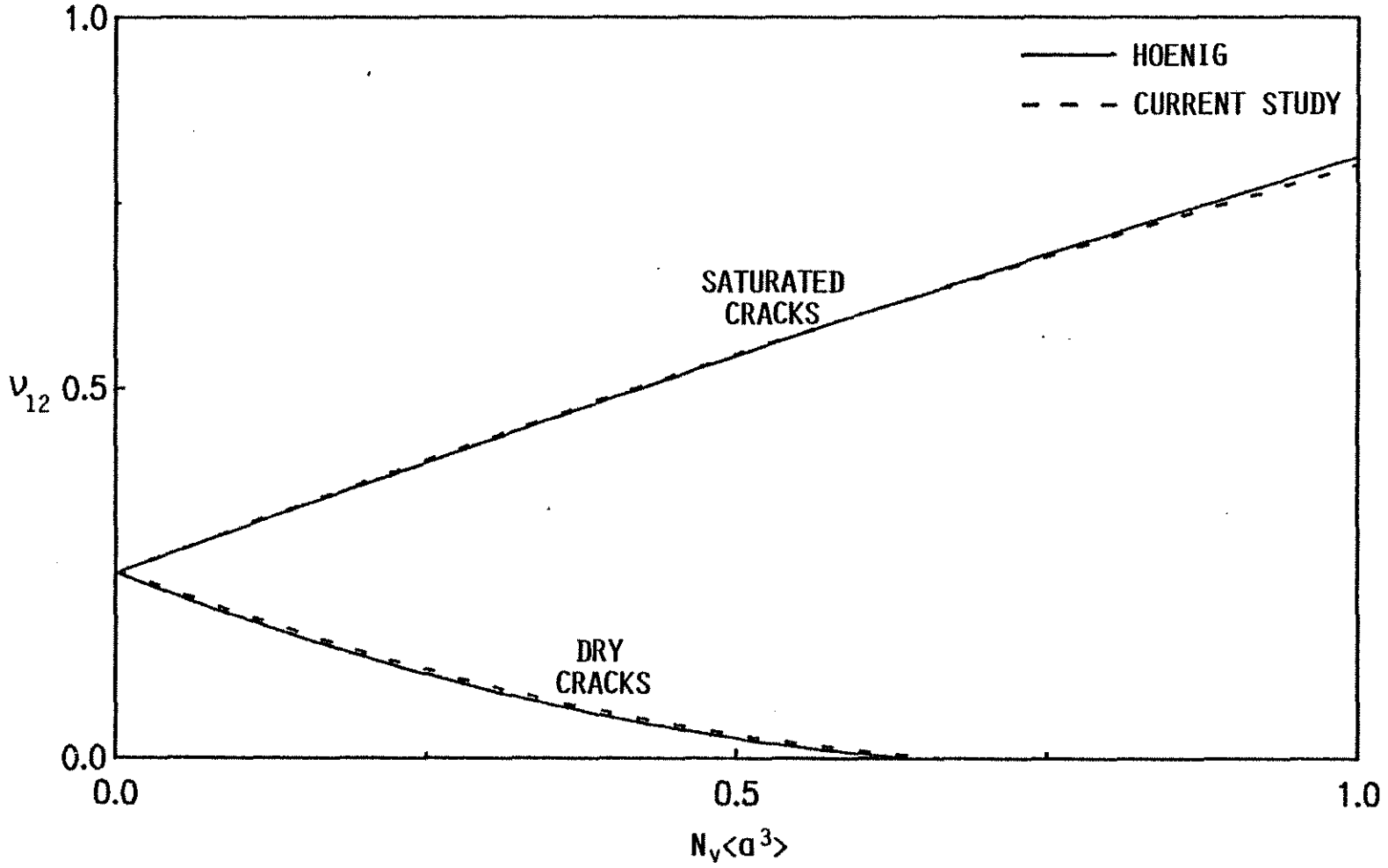

Fig. 4.8. Effective Poisson's Ratio; Dry or Saturated Circular Cracks in a Cylindrically Transverse Isotropic Solid

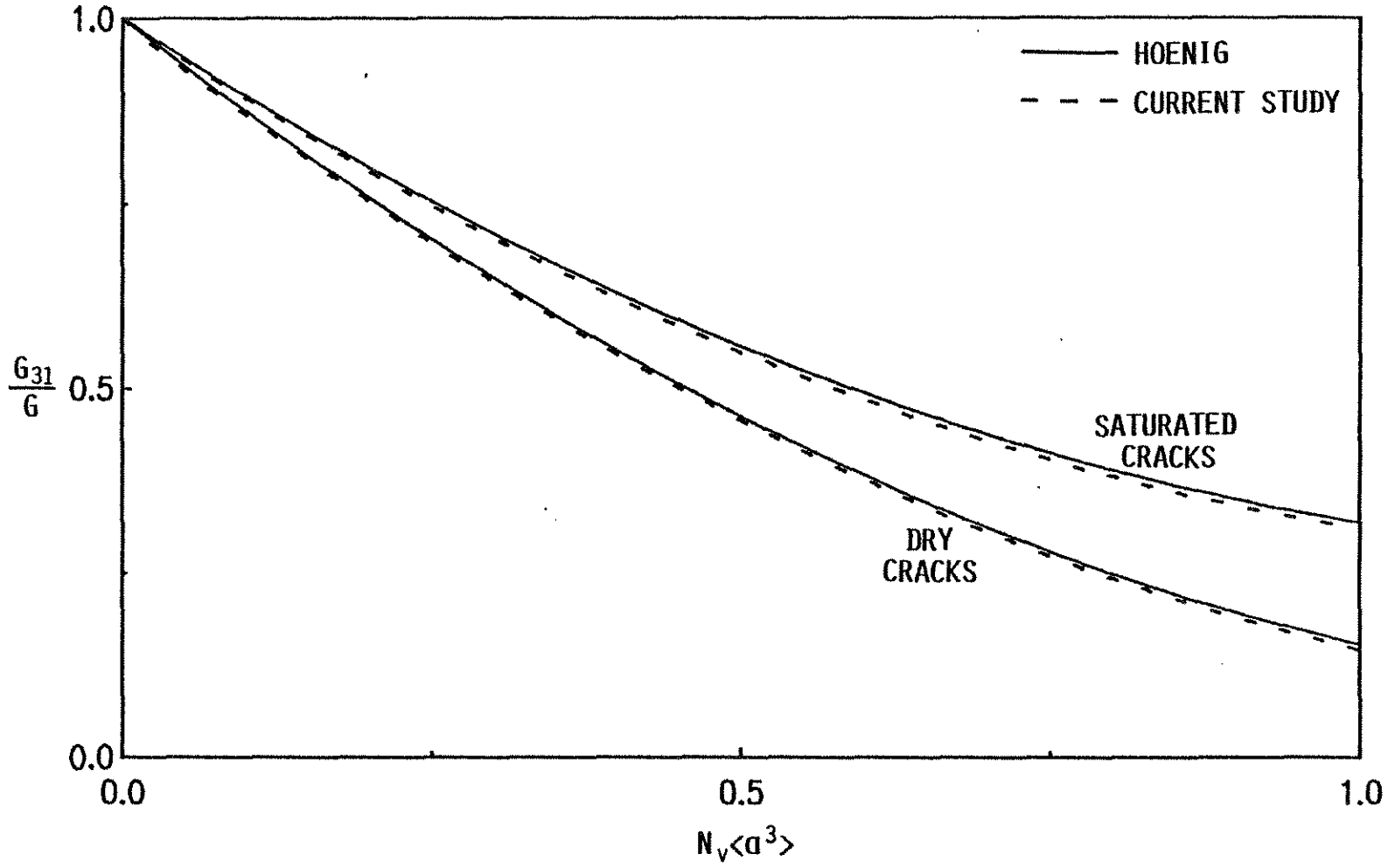

Fig. 4.9. Effective Shear Modulus; Dry or Saturated Circular Cracks in a Cylindrically Transverse Isotropic Solid

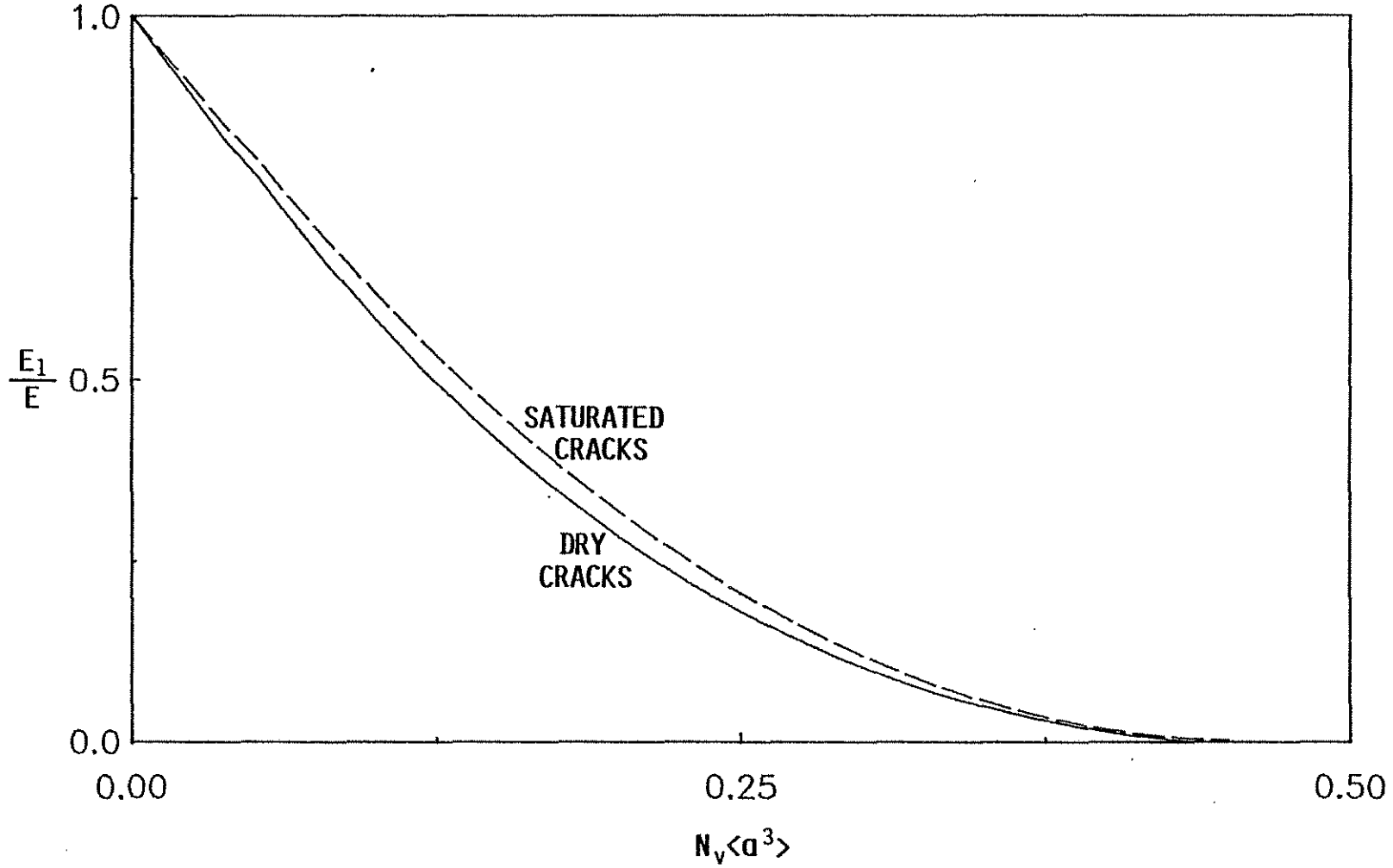

Fig. 4.10. Effective Stiffness Modulus; Dry or Saturated Circular Cracks in a Transversely Isotropic Solid; K = -0.3

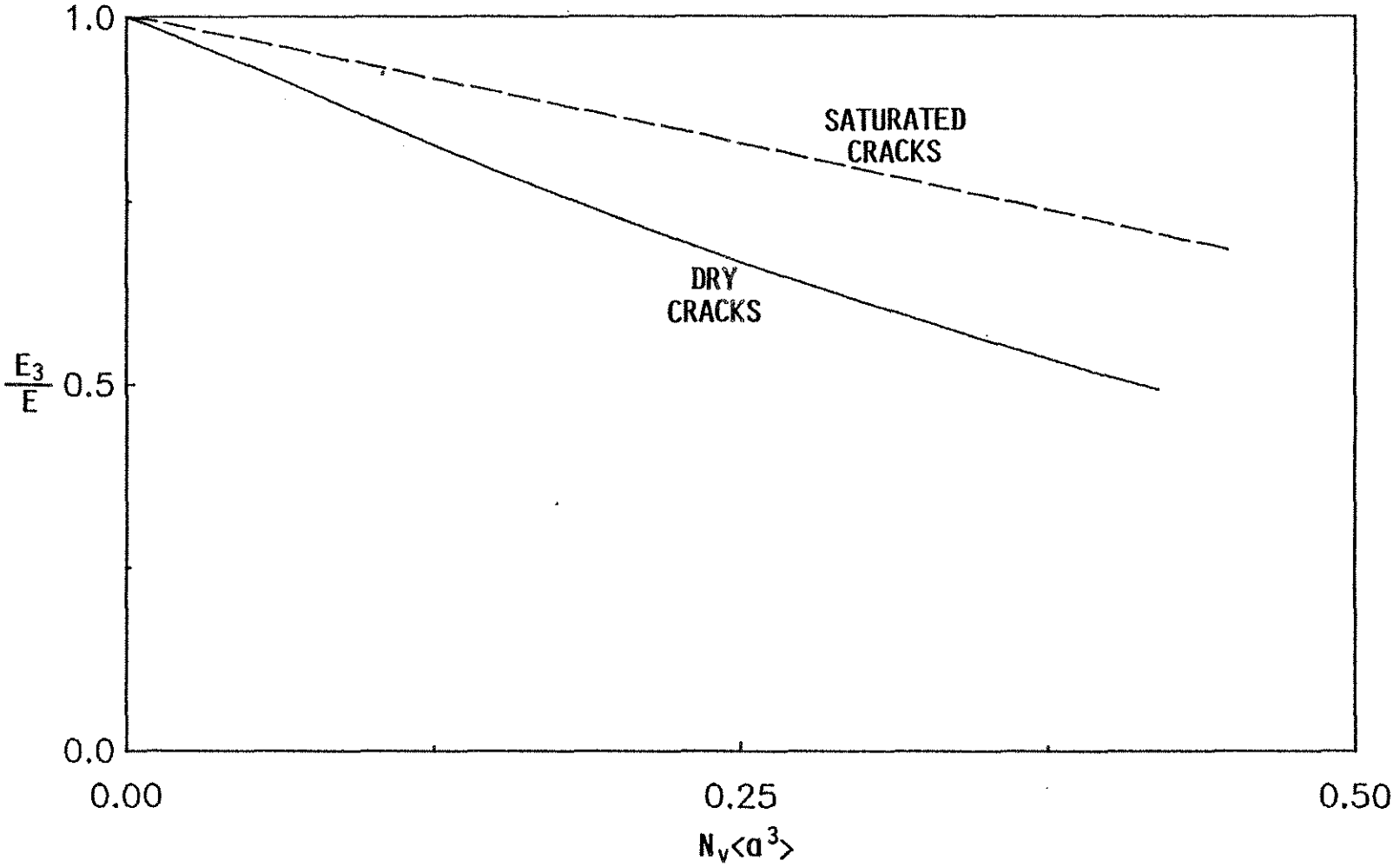

Fig. 4.11. Effective Stiffness Modulus; Dry or Saturated Circular Cracks in a Transversely Isotropic Solid; K = -0.3

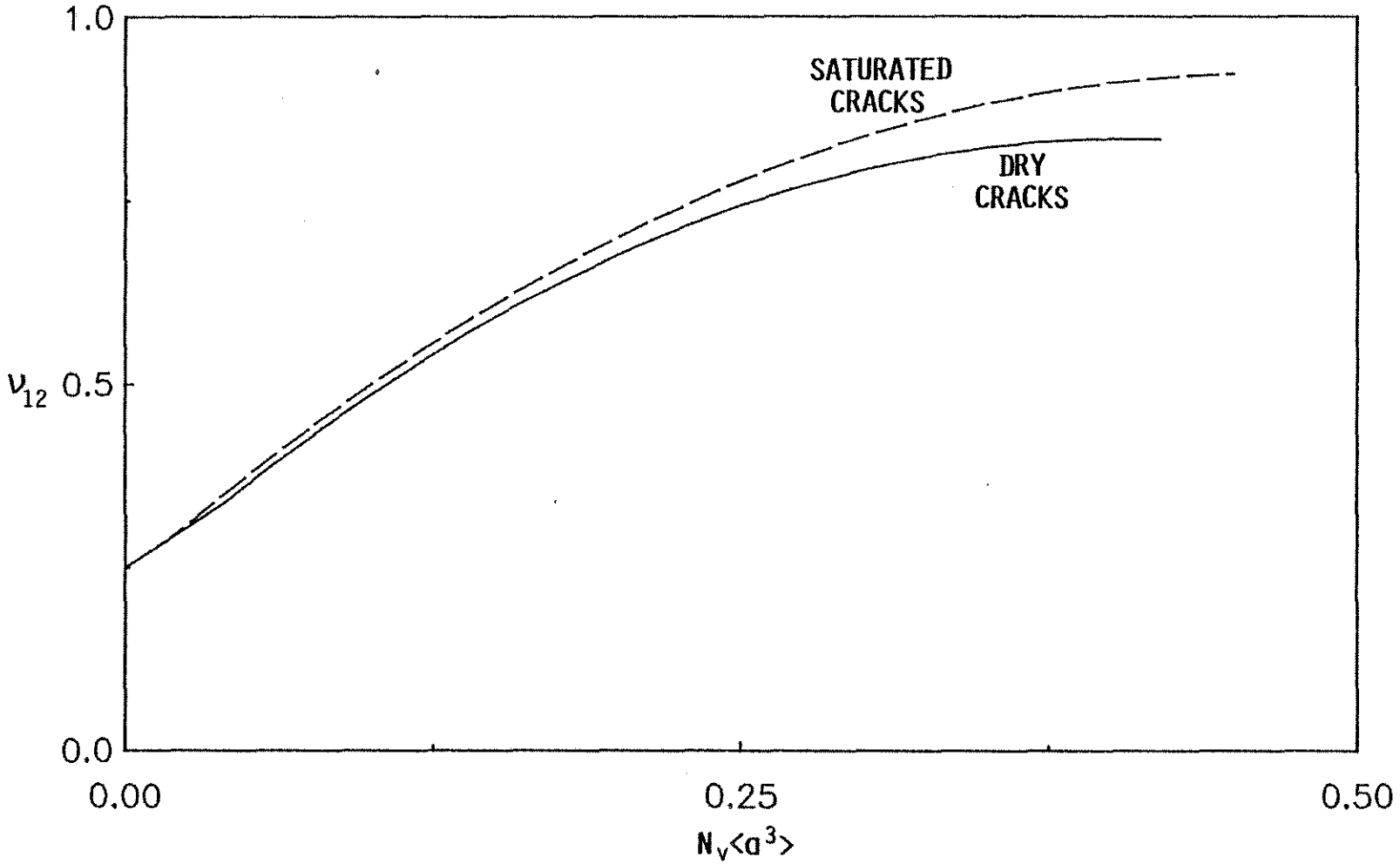

Fig. 4.12. Effective Poisson's Ratio; Dry or Saturated Circular Cracks in a Transversely Isotropic Solid; K = -0.3

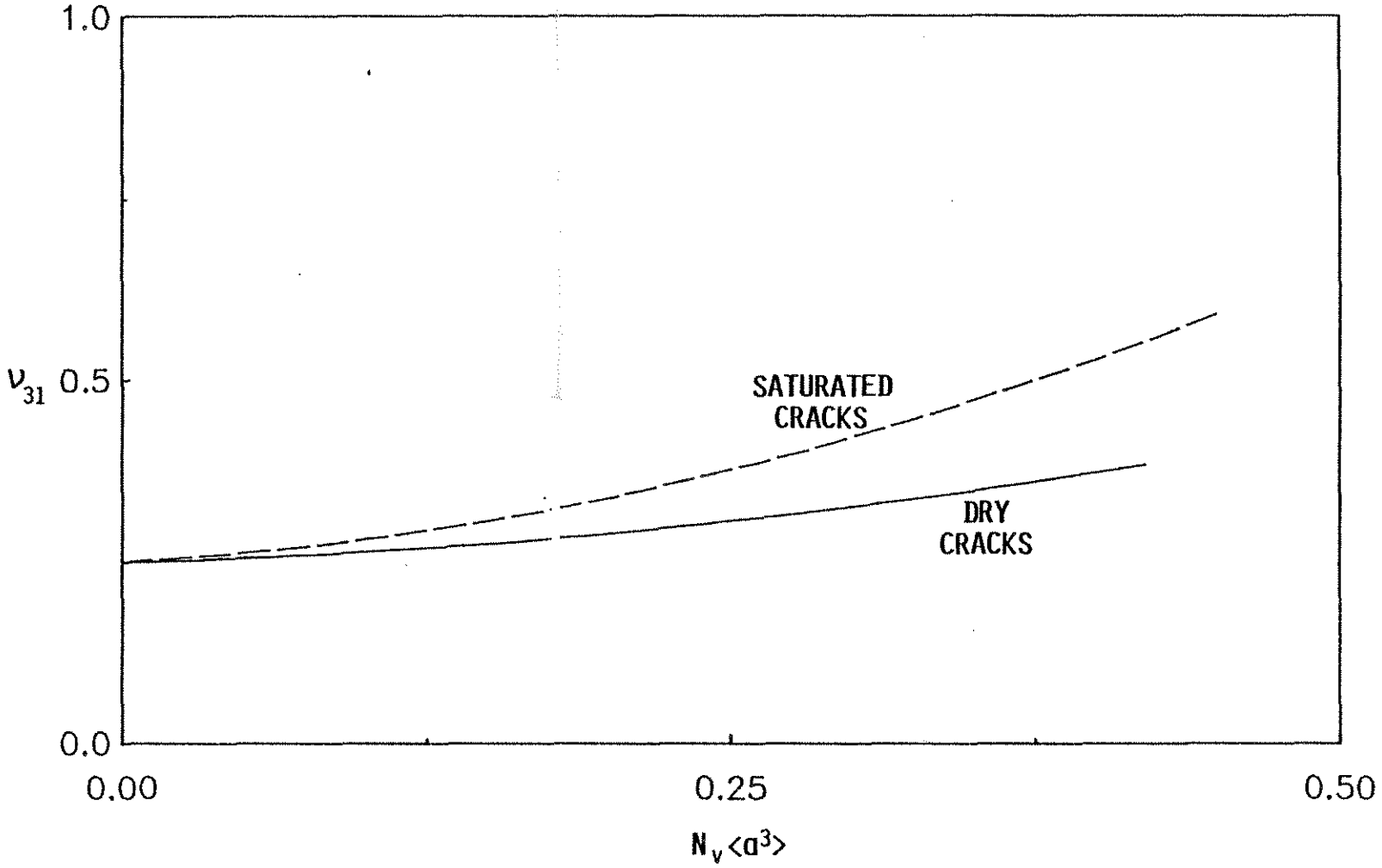

Fig. 4.13. Effective Poisson's Ratio; Dry or Saturated Circular Cracks in a Transversely Isotropic Solid; K = -0.3

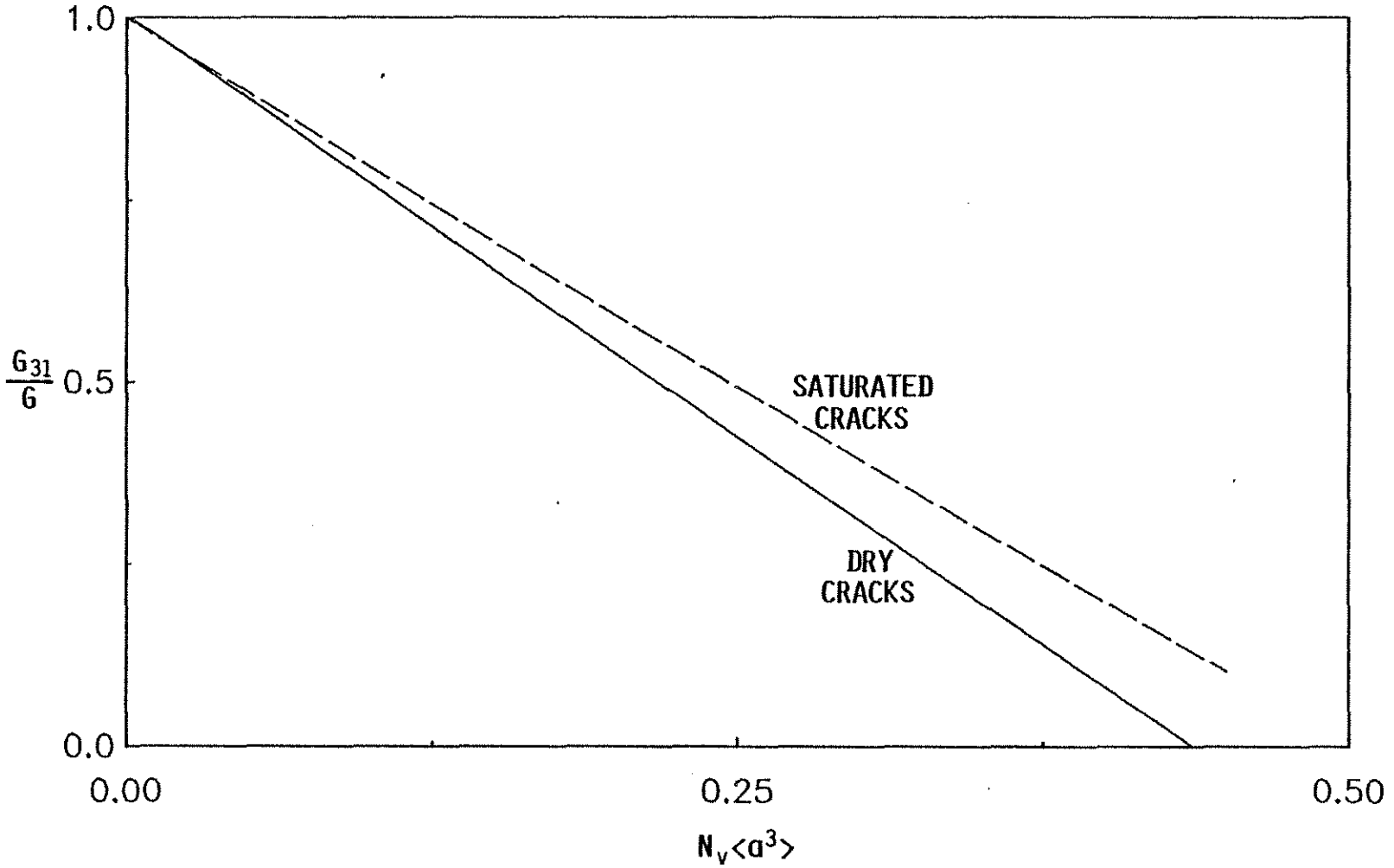

Fig. 4.14. Effective Shear Modulus; Dry or Saturated Circular Cracks in a Transversely Isotropic Solid; K = -0.3

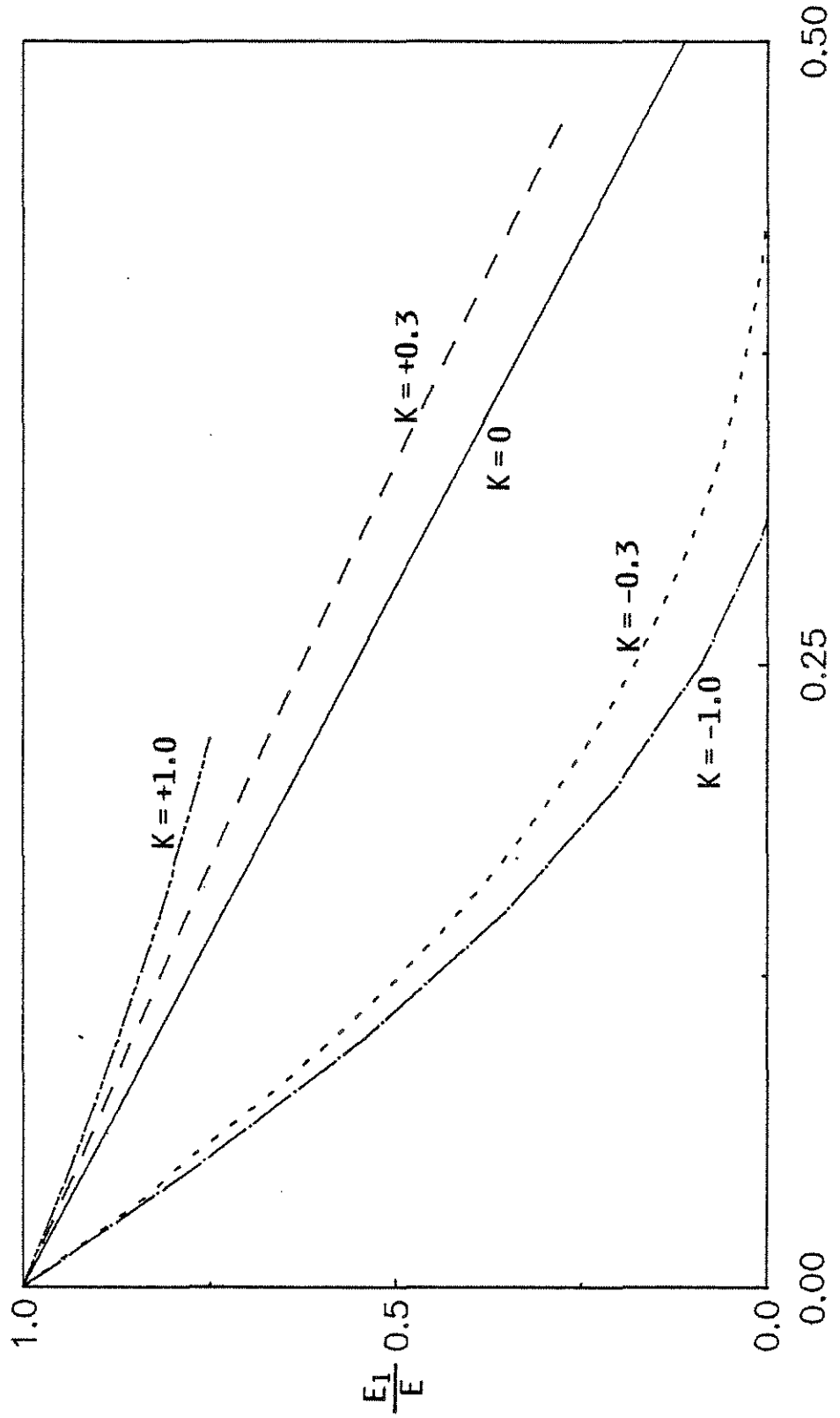

Fig. 4.15. Effective Stiffness Modulus; Dry Circular Cracks in a Transversely Isotropic Solid; K = -0.3

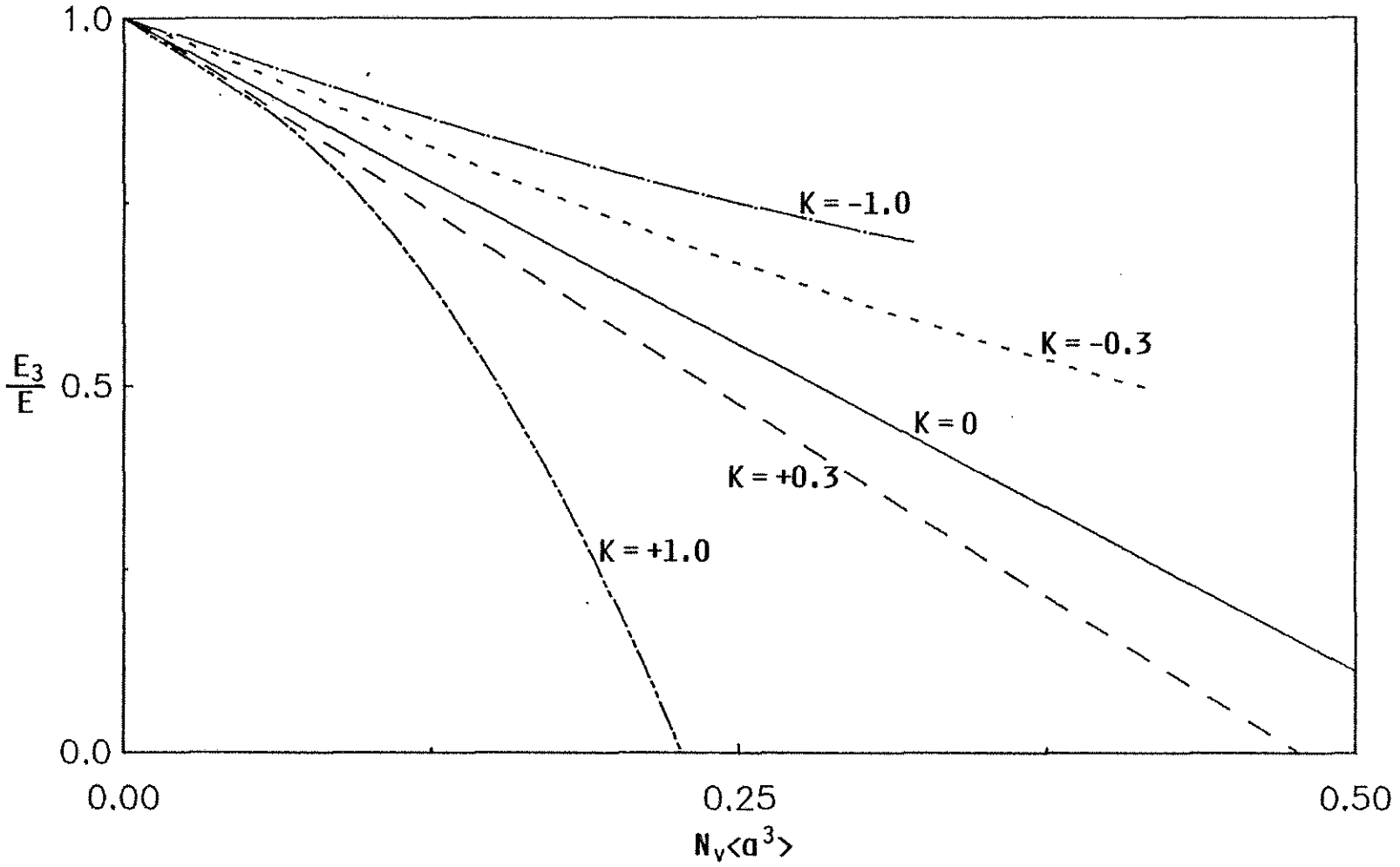

Fig. 4.16. Effective Stiffness Modulus; Dry Circular Cracks in a Transversely Isotropic Solid; K = -0.3

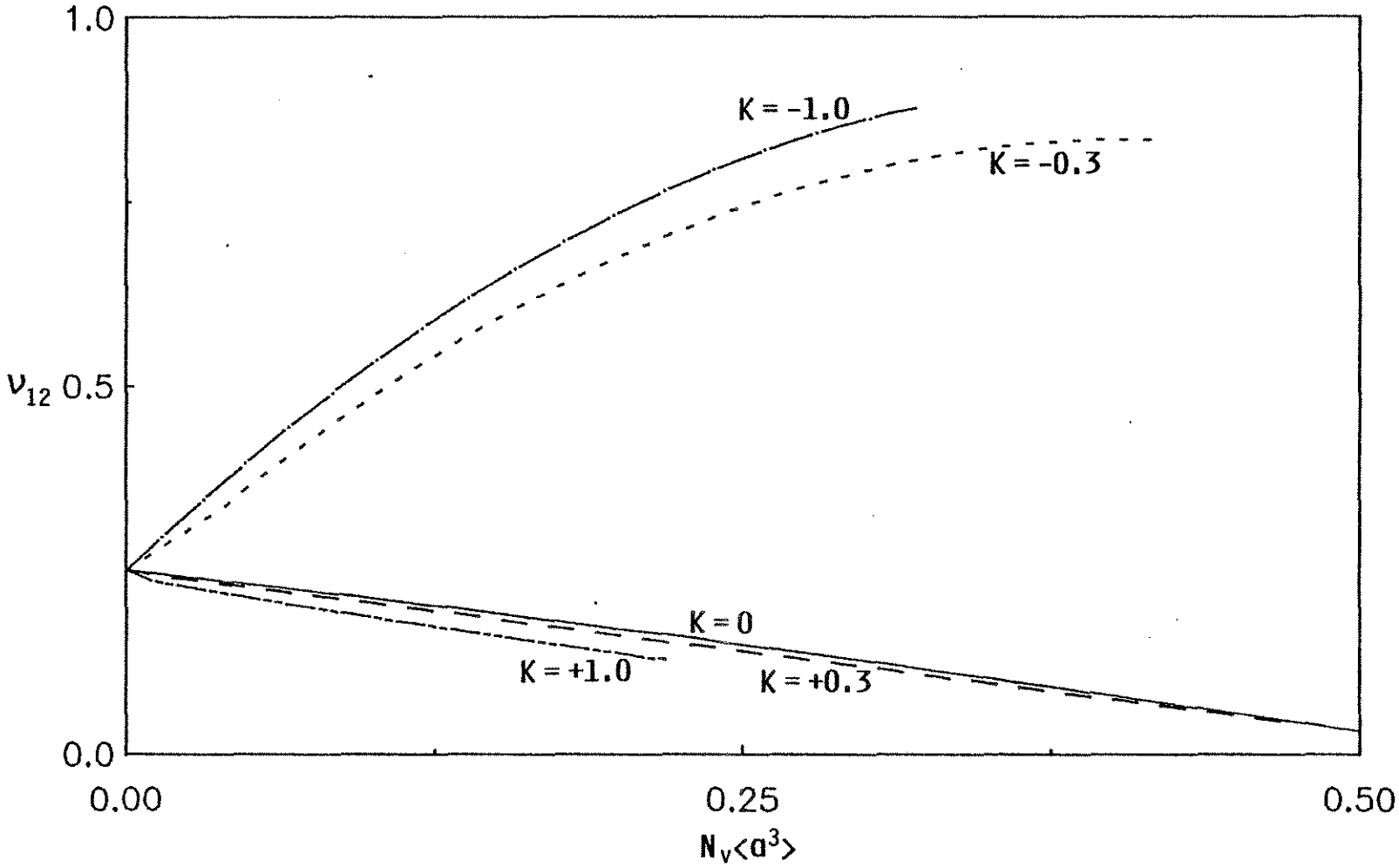

Fig. 4.17. Effective Poisson's Ratio; Dry Circular Cracks in a Transversely Isotropic Solid

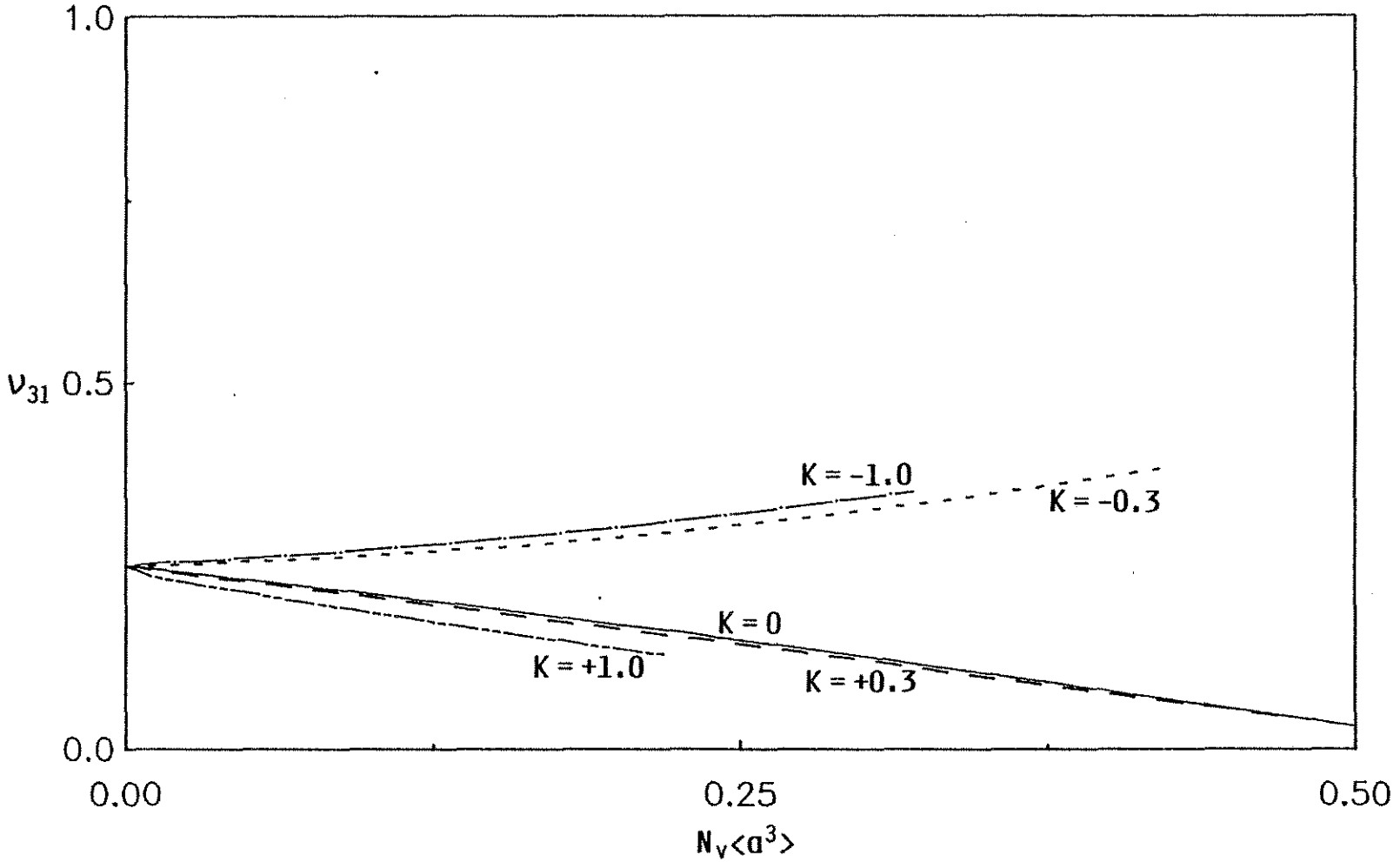

Fig. 4.18. Effective Poisson's Ratio; Dry Circular Cracks in a Transversely Isotropic Solid

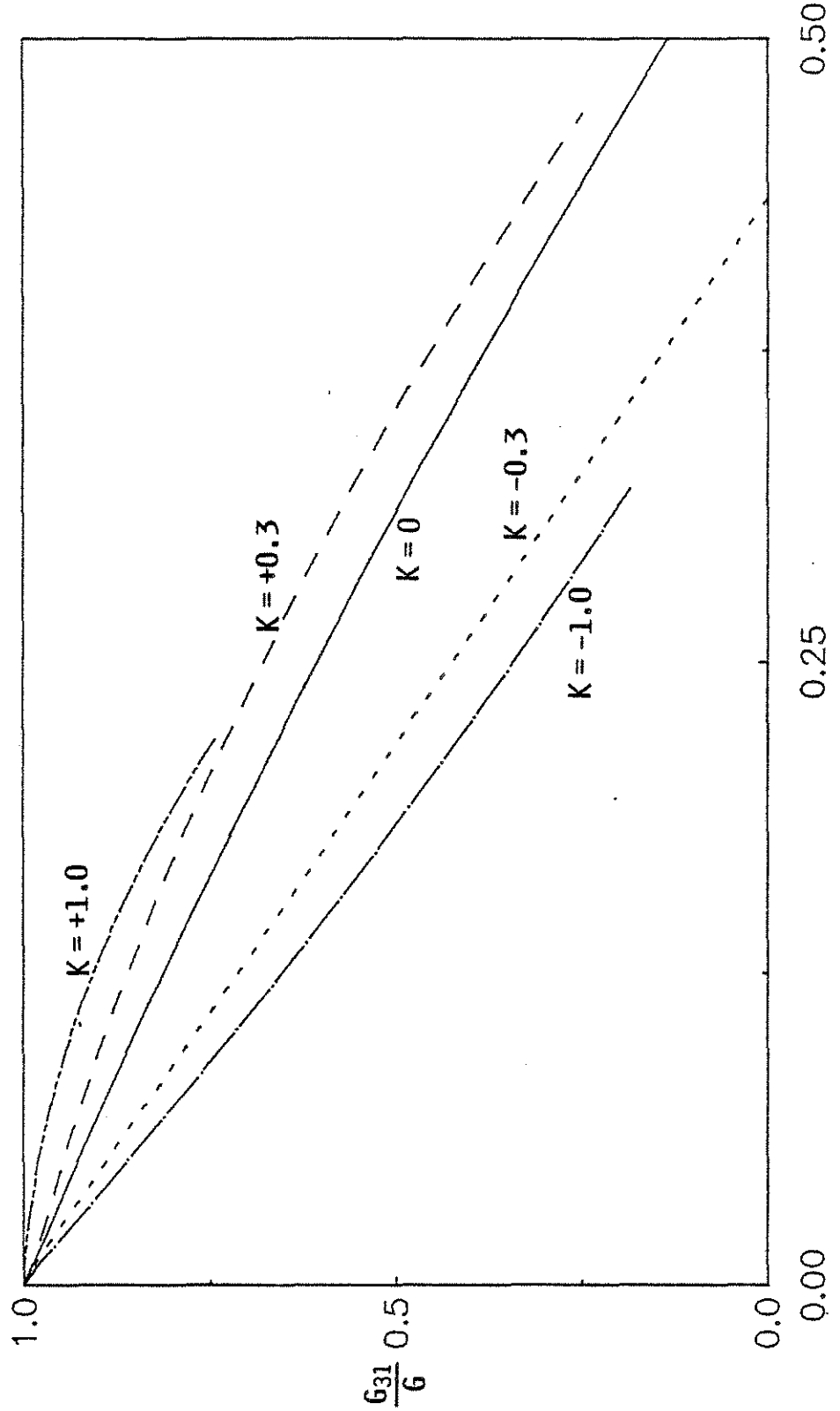

Fig. 4.19. Effective Shear Modulus; Dry Circular Cracks in a Transversely Isotropic Solid

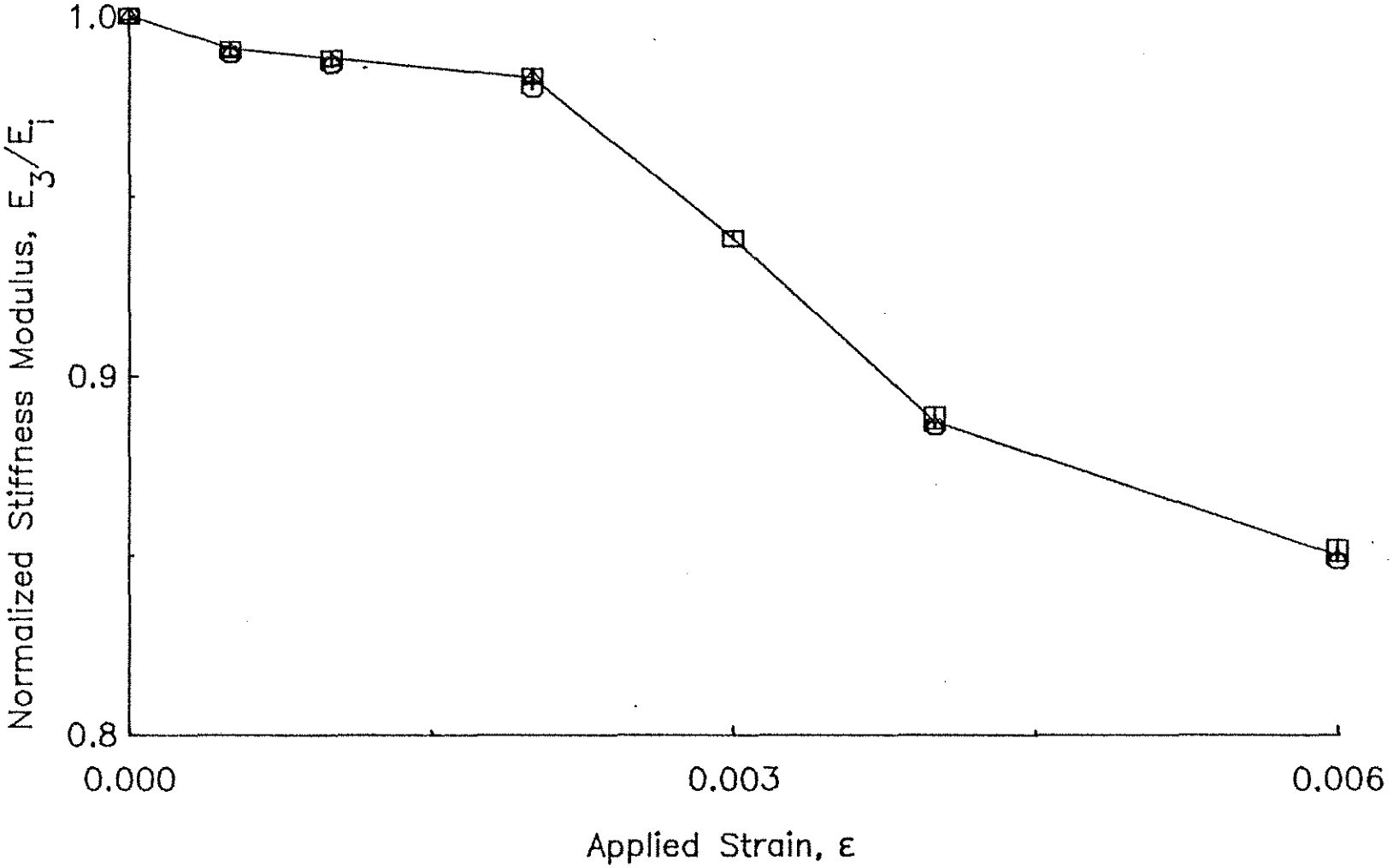

Fig. 5.1. Normalized Stiffness Modulus versus Applied Strain for Monotonic Loading of Cement Pastes with W/C = 0.7, 0.5 and 0.3; Dry Cracks

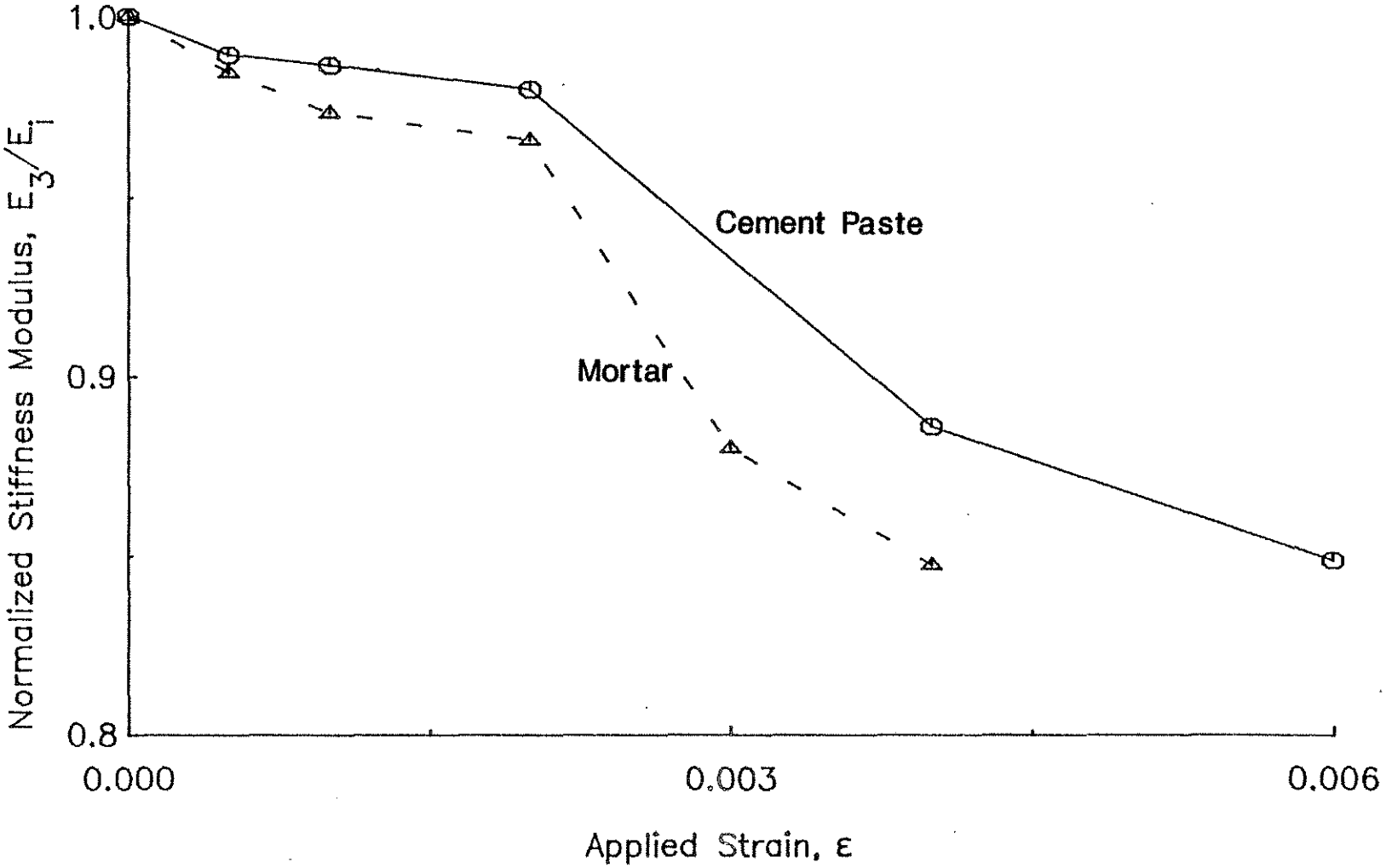

Fig. 5.2. Normalized Stiffness Modulus versus Applied Strain for Monotonic Loading of Cement Paste and Mortar with a W/C = 0.5; Dry Cracks

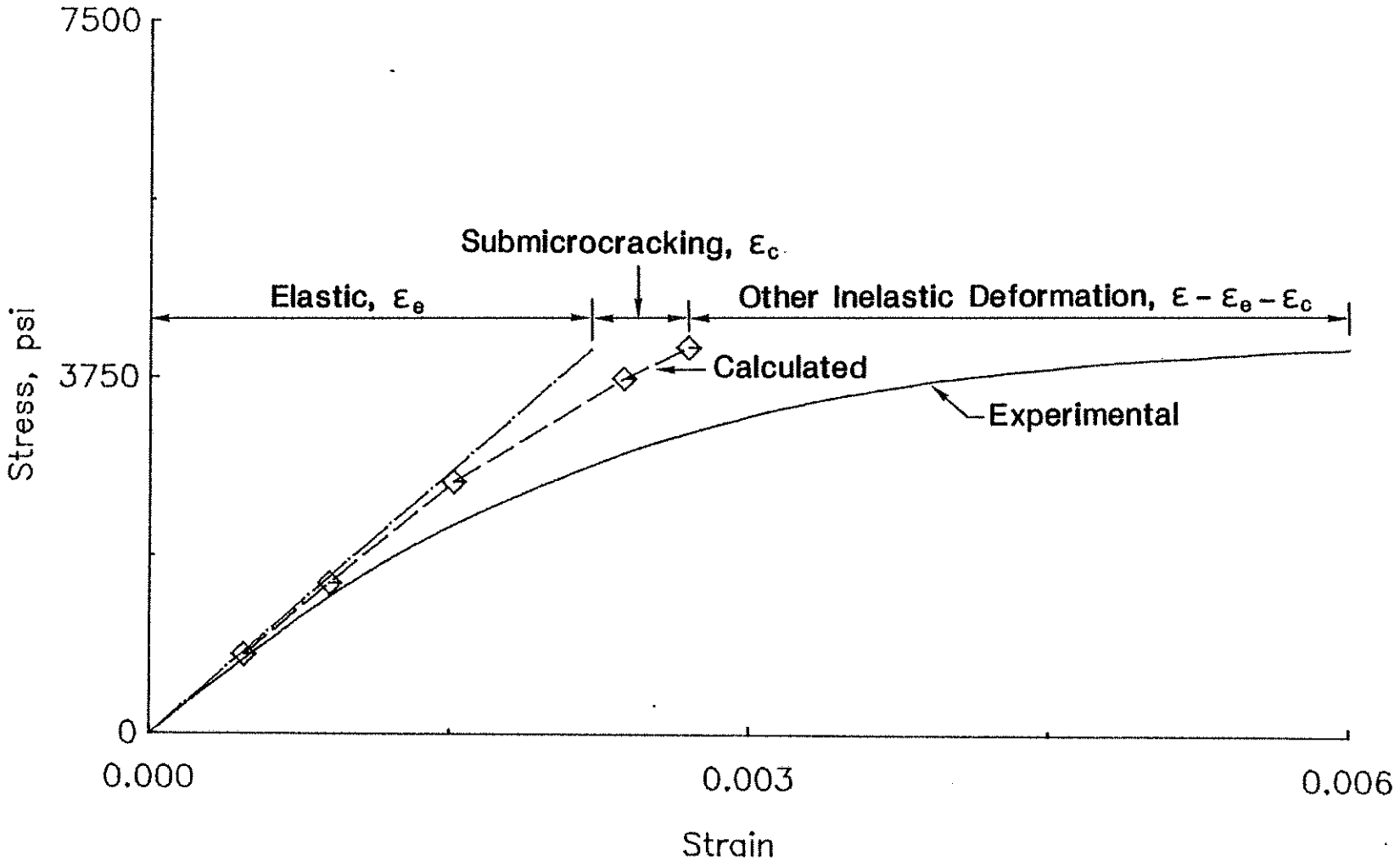

Fig. 5.3. Experimental and Calculated Stress-Strain Relationships for Monotonic Loading of Cement Paste with a W/C = 0.7. (Calculated STress-Strain Relationship is Based on an Elastic Matrix; Dry Cracks)

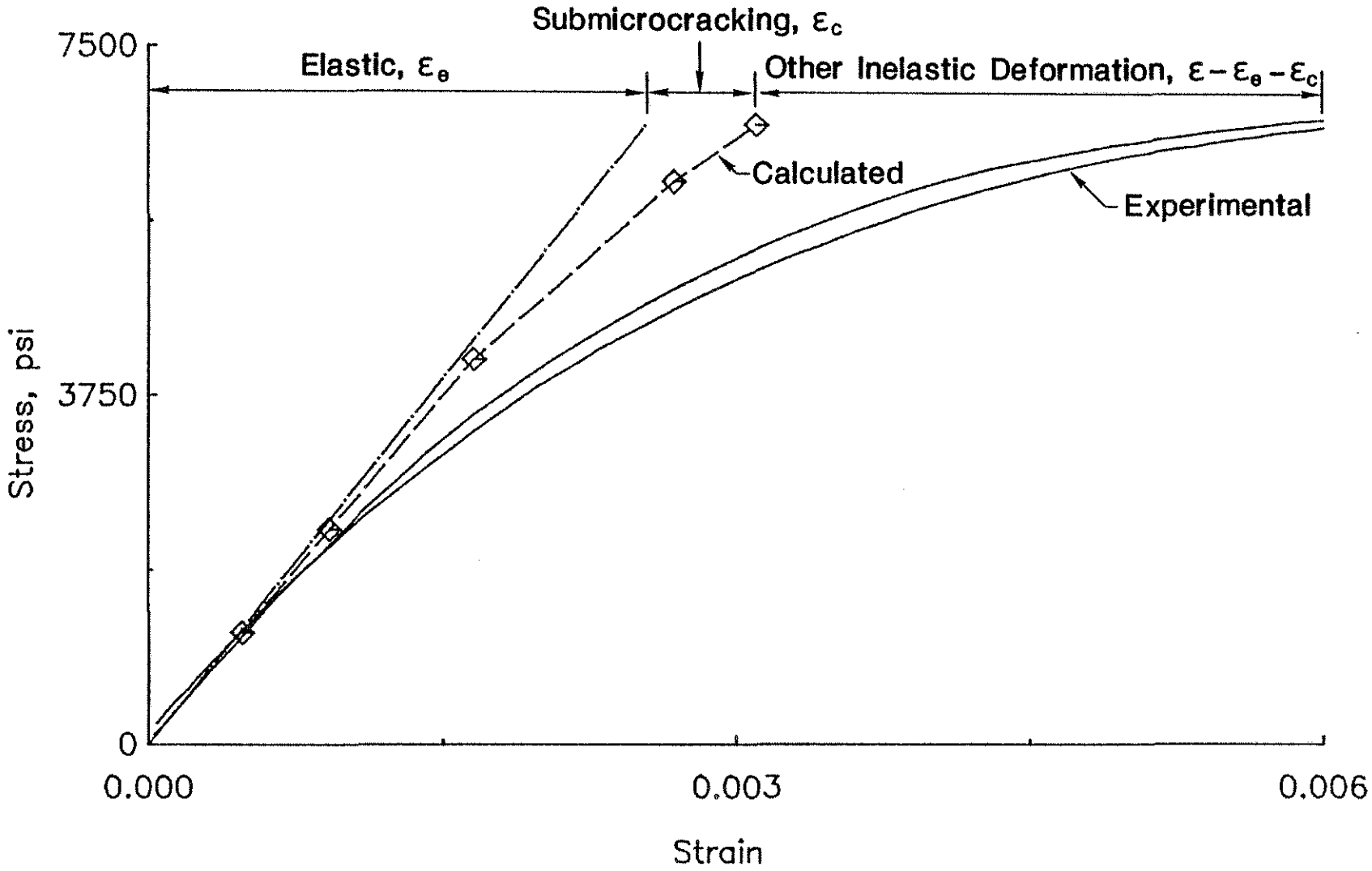

Fig. 5.4. Experimental and Calculated Stress-Strain Relationships for Monotonic Loading of Cement Paste with a W/C = 0.5. (Calculated Stress-Strain Relationship is Based on an Elastic Matrix; Dry Cracks)

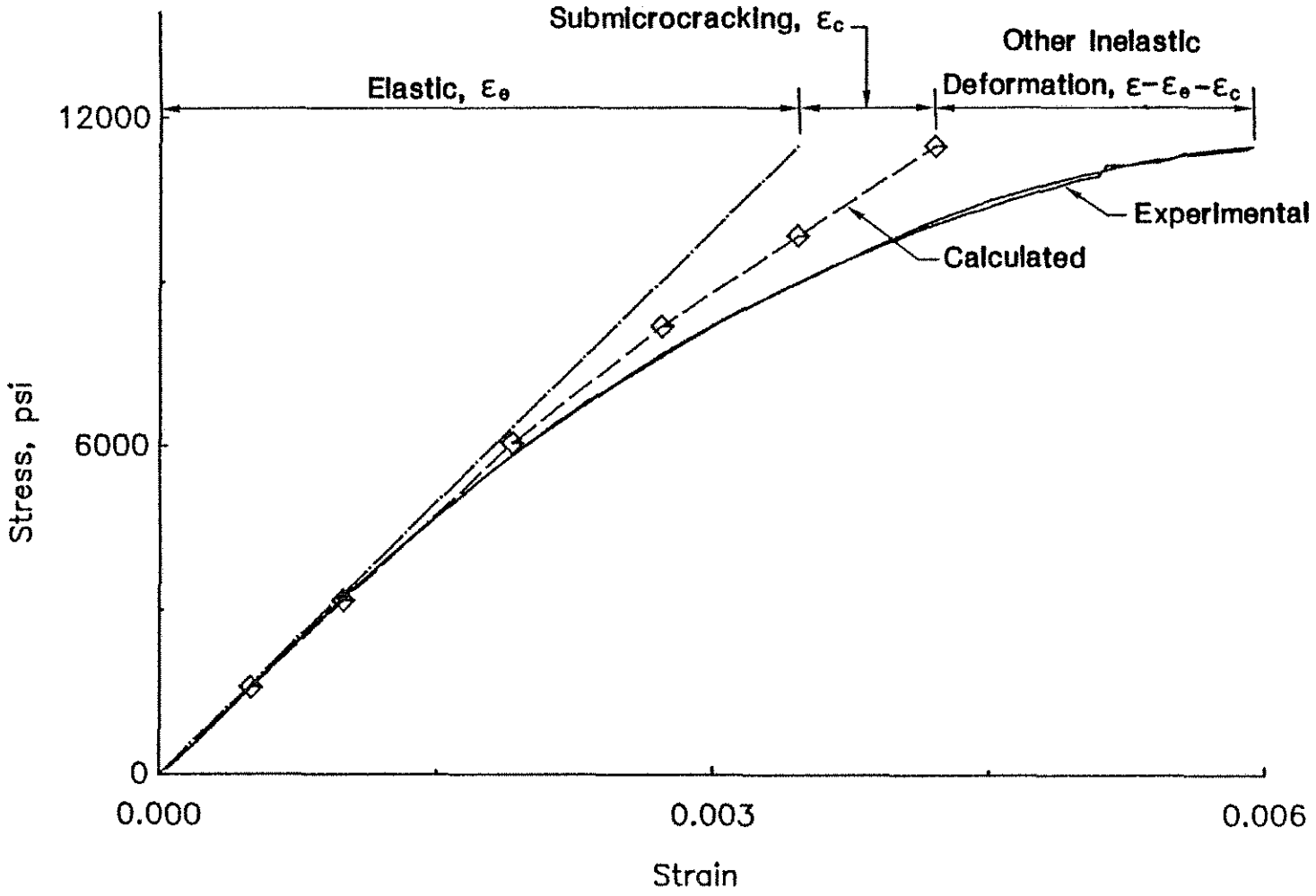

Fig. 5.5. Experimental and Calculated Stress-Strain Relationships for Monotonic Loading of Cement Paste with a W/C = 0.3. (Calculated Stress-Strain Relationship is Based on an Elastic Matrix; Dry Cracks)

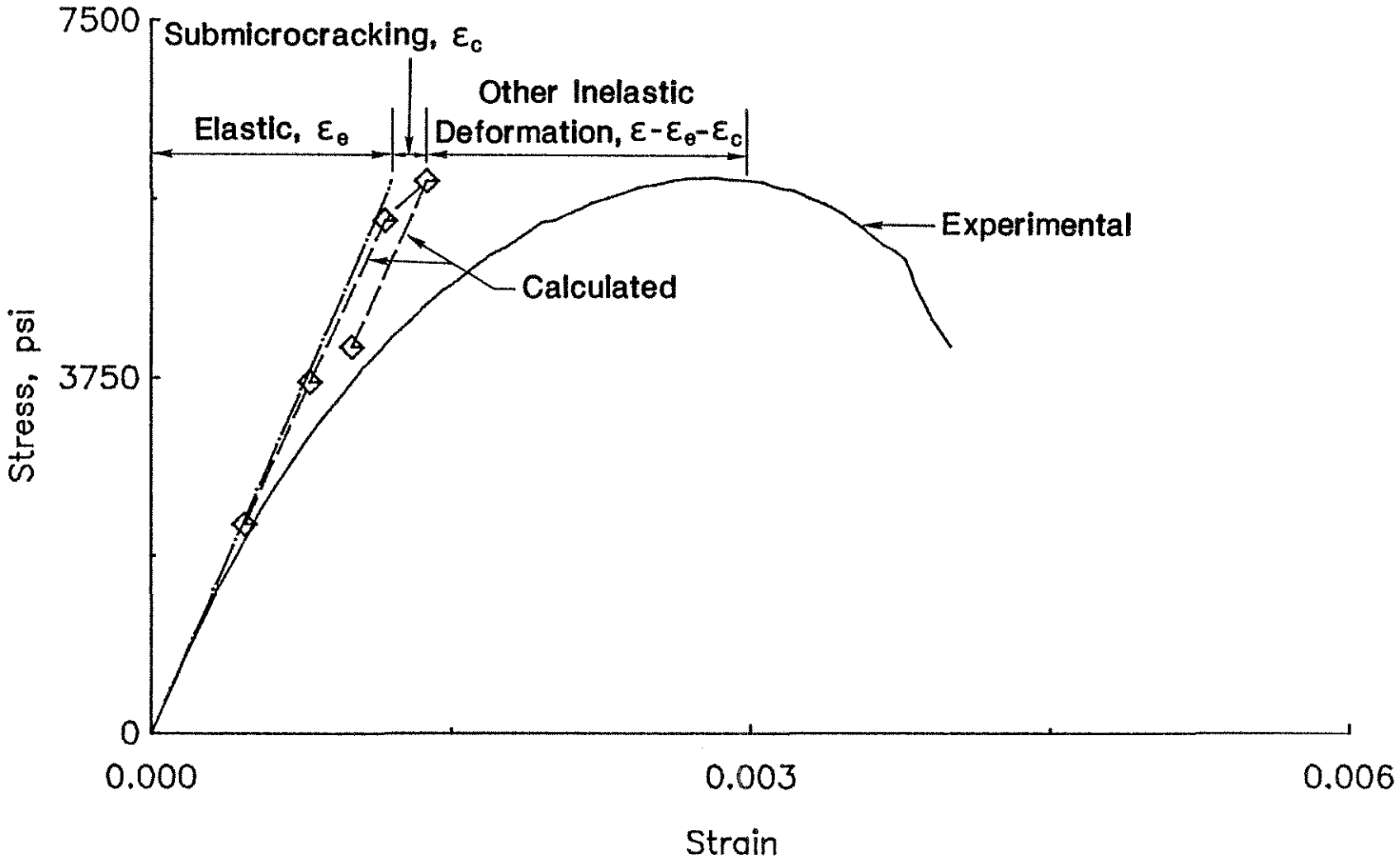

Fig. 5.6. Experimental and Calculated Stress-Strain Relationships for Monotonic Loading of Mortar with a W/C = 0.5. (Calculated Stress-Strain Relationship is Based on an Elastic Matrix; Dry Cracks)

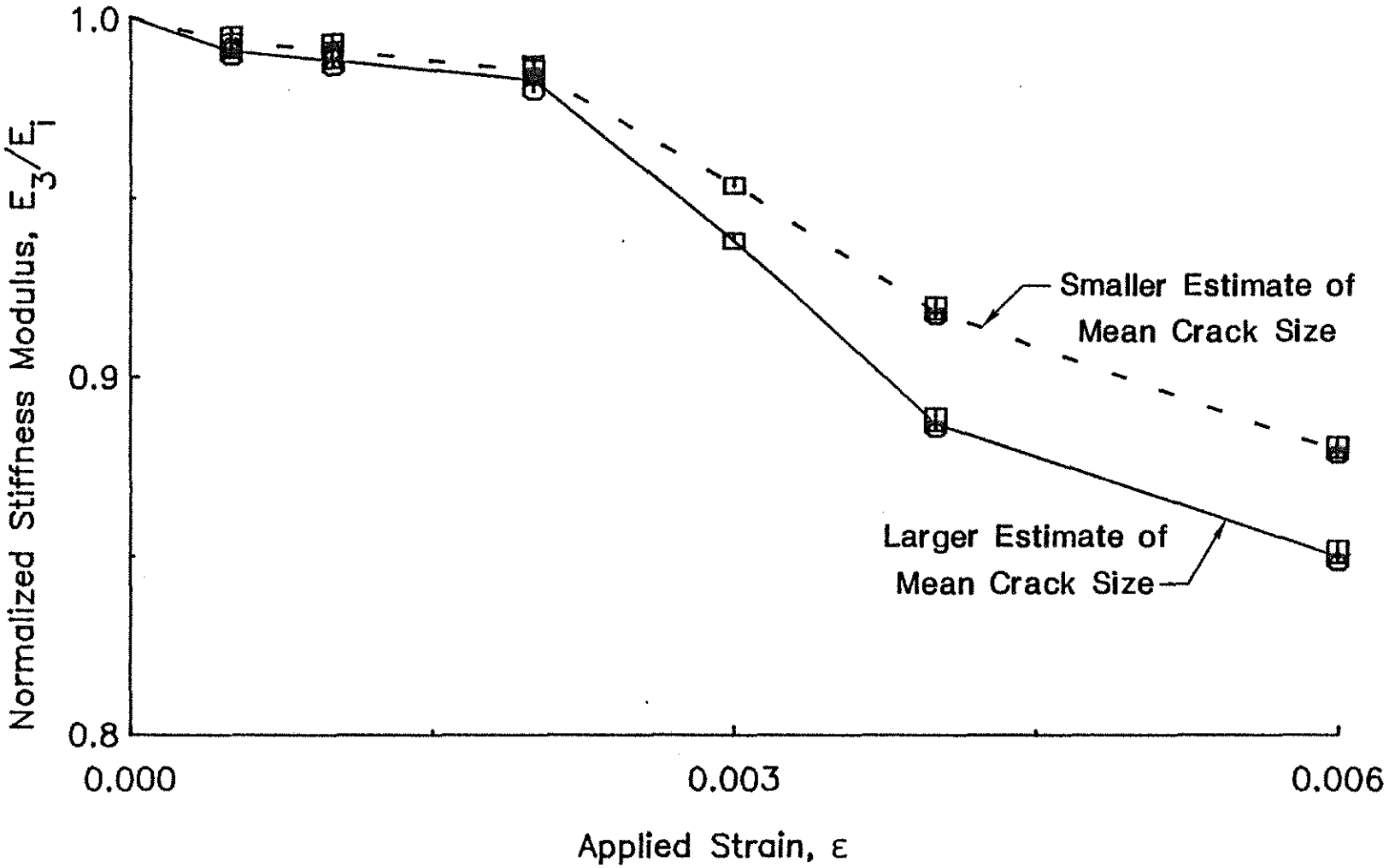

Fig. 5.7. Comparison of Values of Normalized Stiffness Modulus Corresponding to the Smaller and Larger Estimates of Mean Crack Size; Monotonic Loading of Cement Pastes with W/C = 0.7, 0.5 and 0.3; Dry Cracks

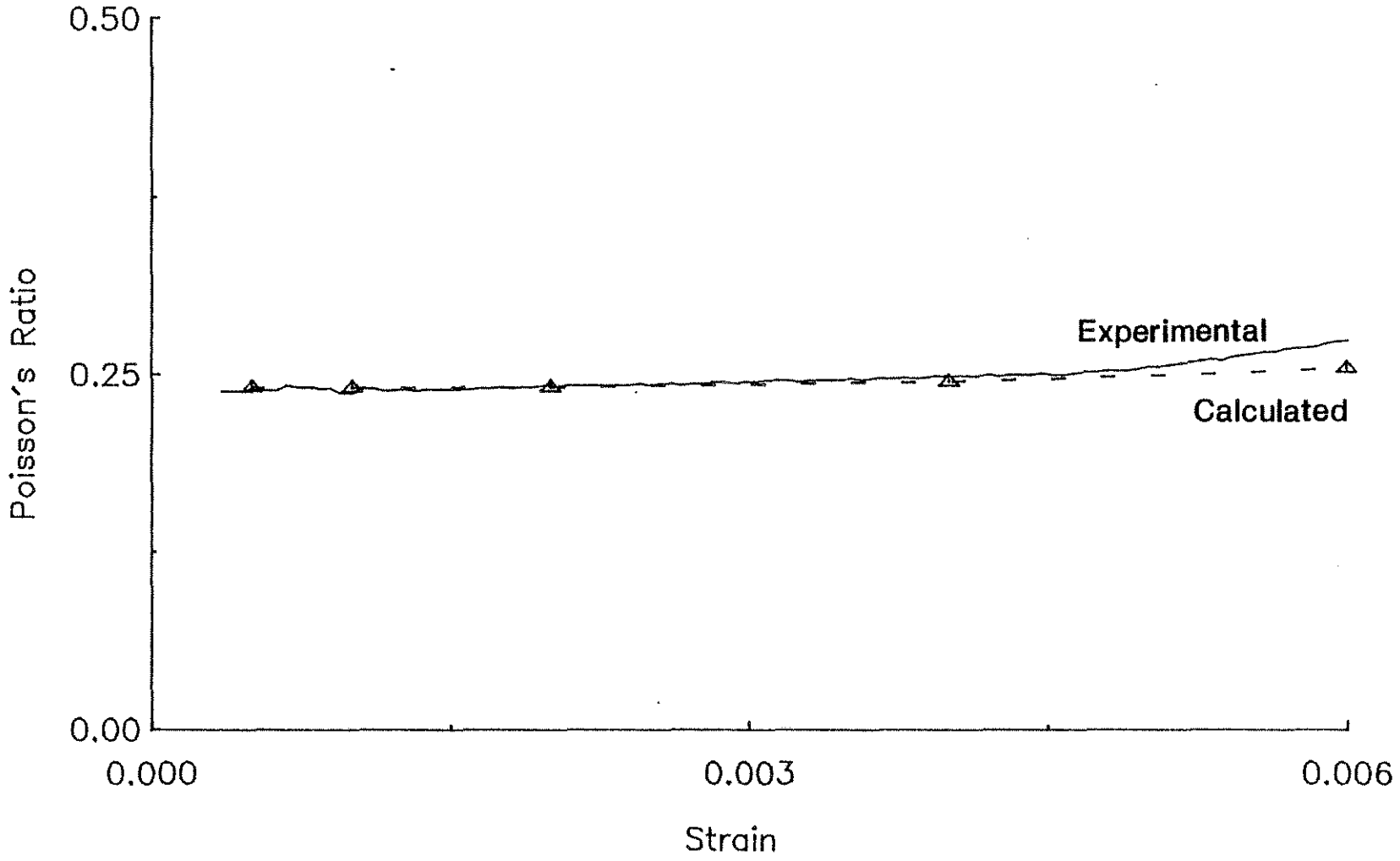

Fig. 5.8. Experimental and Calculated Poisson's Ratios versus Applied Strain for Monotonic Loading of Cement Paste with a W/C = 0.5. (Calculated Poisson's Ratios are Based on an Elastic Matrix; Dry Cracks)

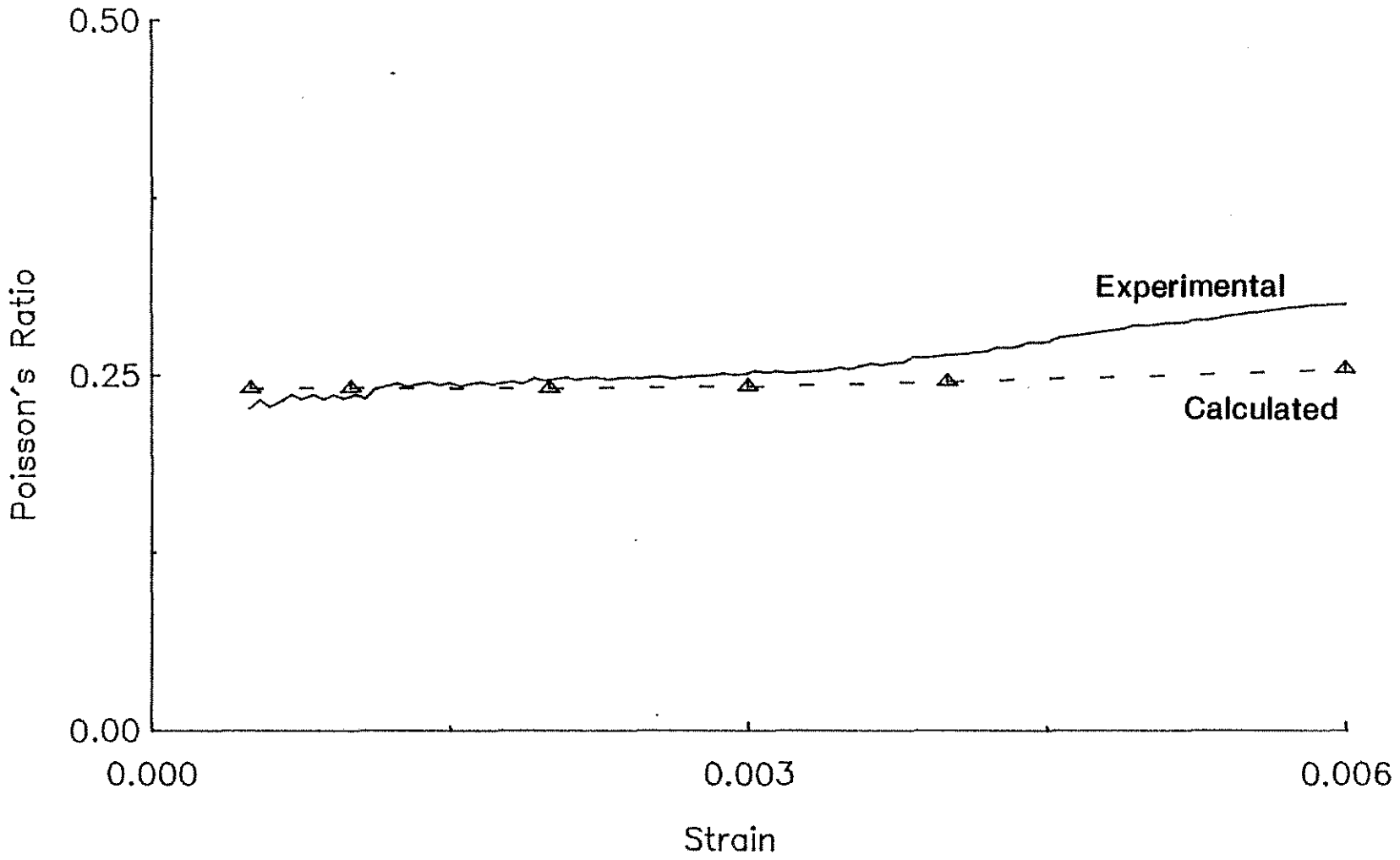

Fig. 5.9. Experimental and Calculated Poisson's Ratios versus Applied Strain for Monotonic Loading of Cement Paste with a W/C = 0.3. (Calculated Poisson's Ratios are Based on an Elastic Matrix; Dry Cracks)

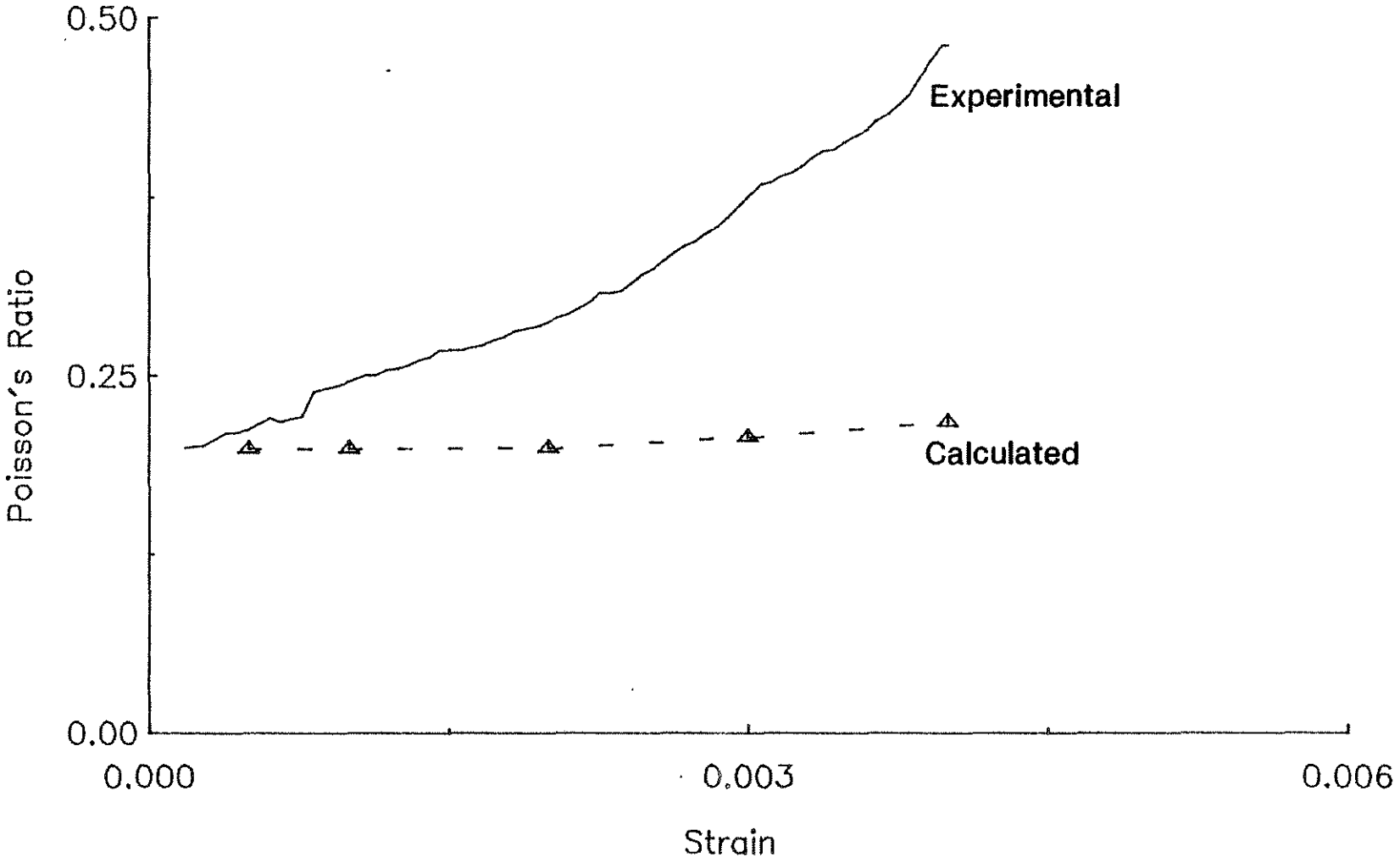

Fig. 5.10. Experimental and Calculated Poisson's Ratios versus Applied Strain for Monotonic Loading of Mortar with a W/C = 0.5. (Calculated Poisson's Ratios are Based on an Elastic Matrix; Dry Cracks)

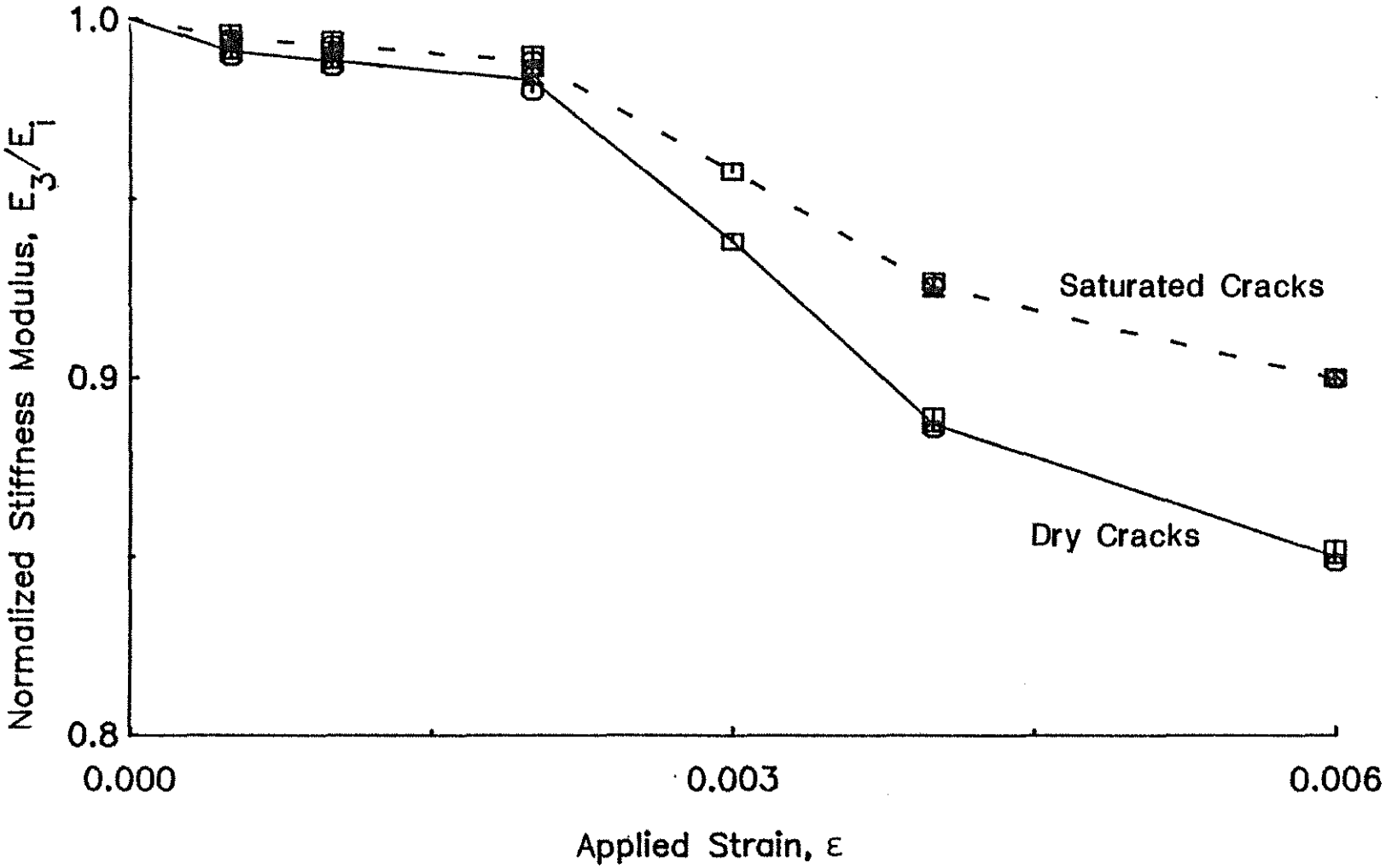

Fig. 5.11. Comparison of Values of Normalized Stiffness Modulus for Dry and Saturated Cracks; Monotonic Loading of Cement Pastes with W/C = 0.7, 0.5 and 0.3

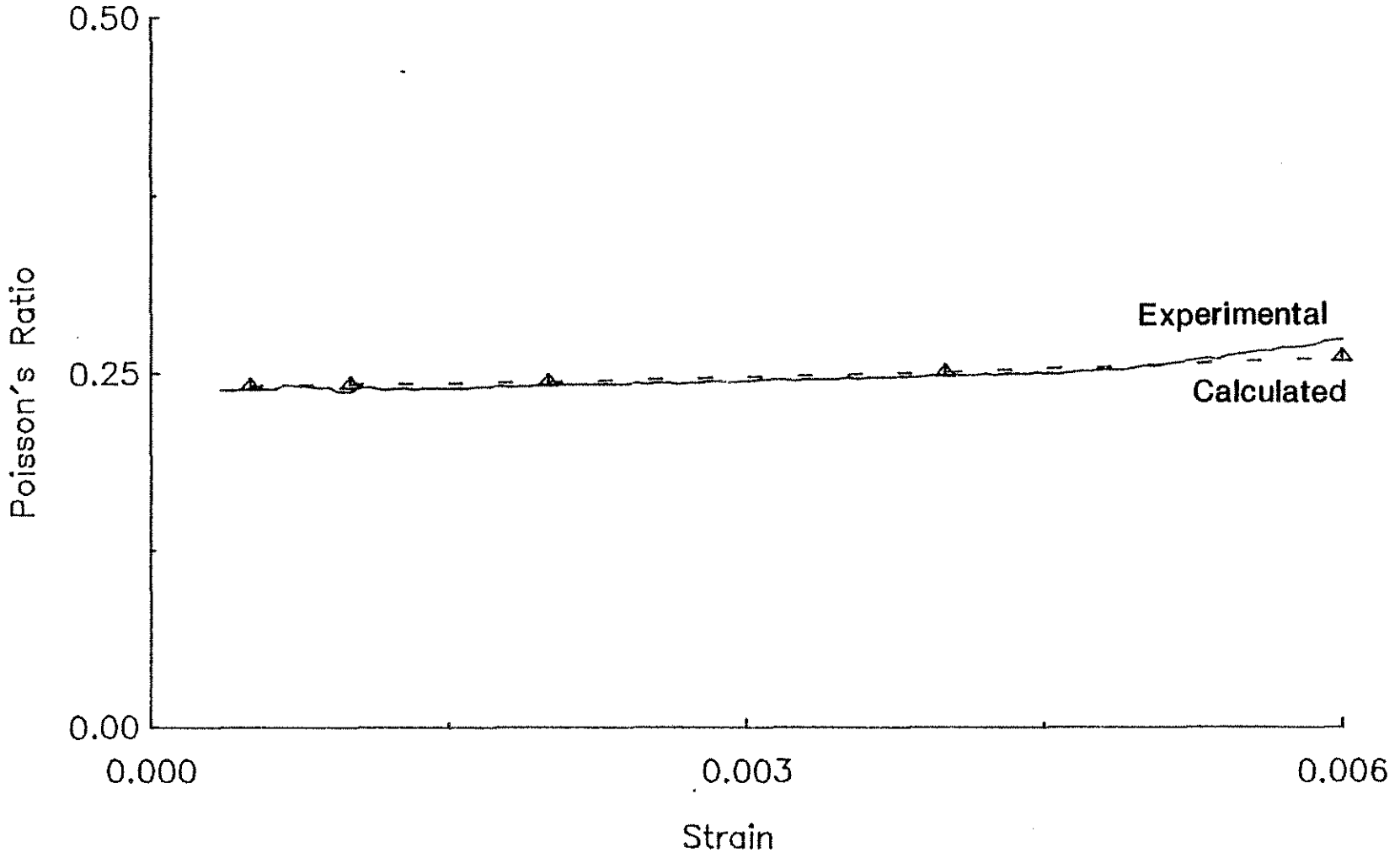

Fig. 5.12. Experimental and Calculated Poisson's Ratios versus Applied Strain for Monotonic Loading of Cement Paste with a W/C = 0.5. (Calculated Poisson's Ratios are Based on an Elastic Matrix; Saturated Cracks)

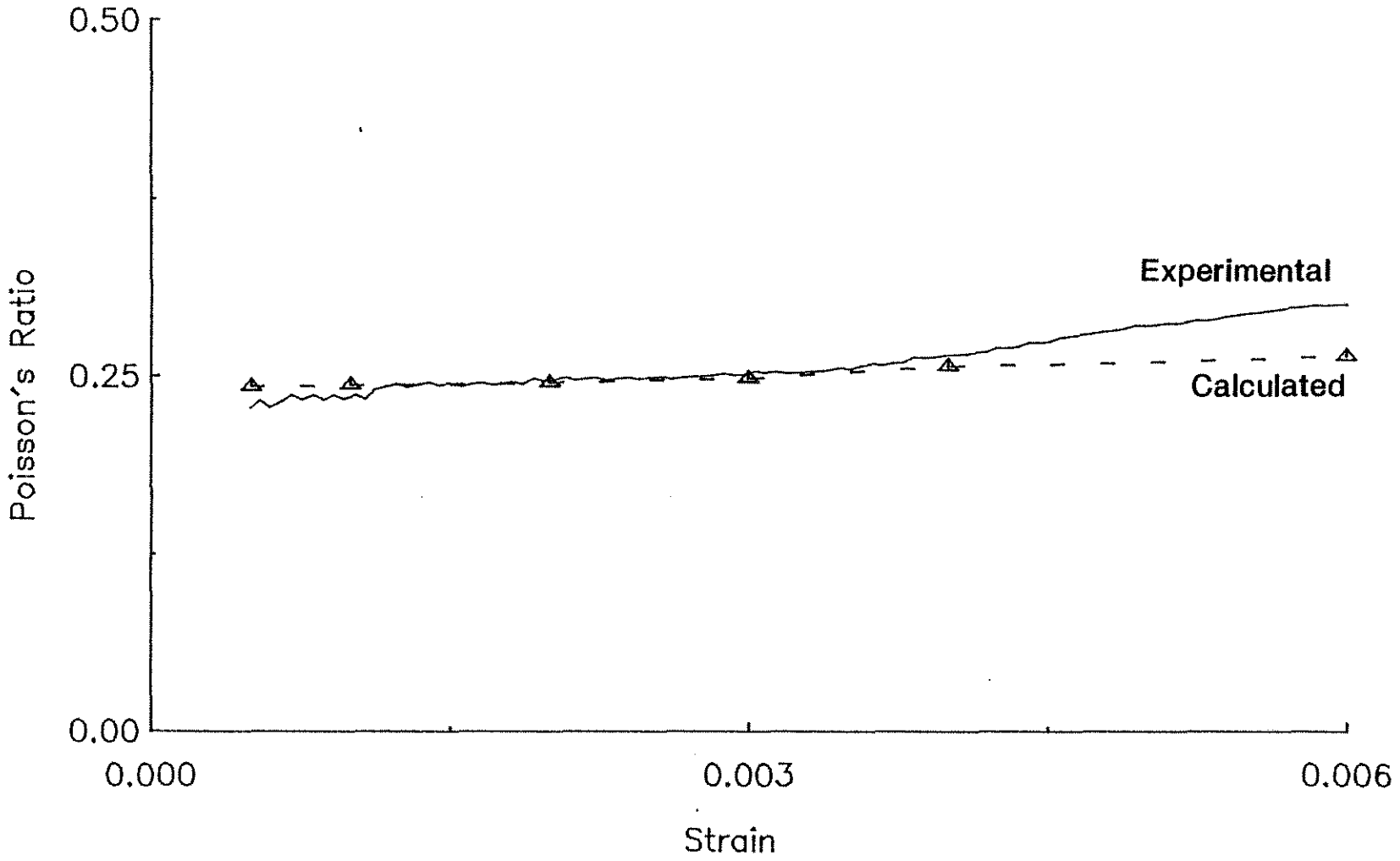

Fig. 5.13. Experimental and Calculated Poisson's Ratios versus Applied Strain for Monotonic Loading of Cement Paste with a W/C = 0.3. (Calculated Poisson's Ratios are Based on an Elastic Matrix; Saturated Cracks)

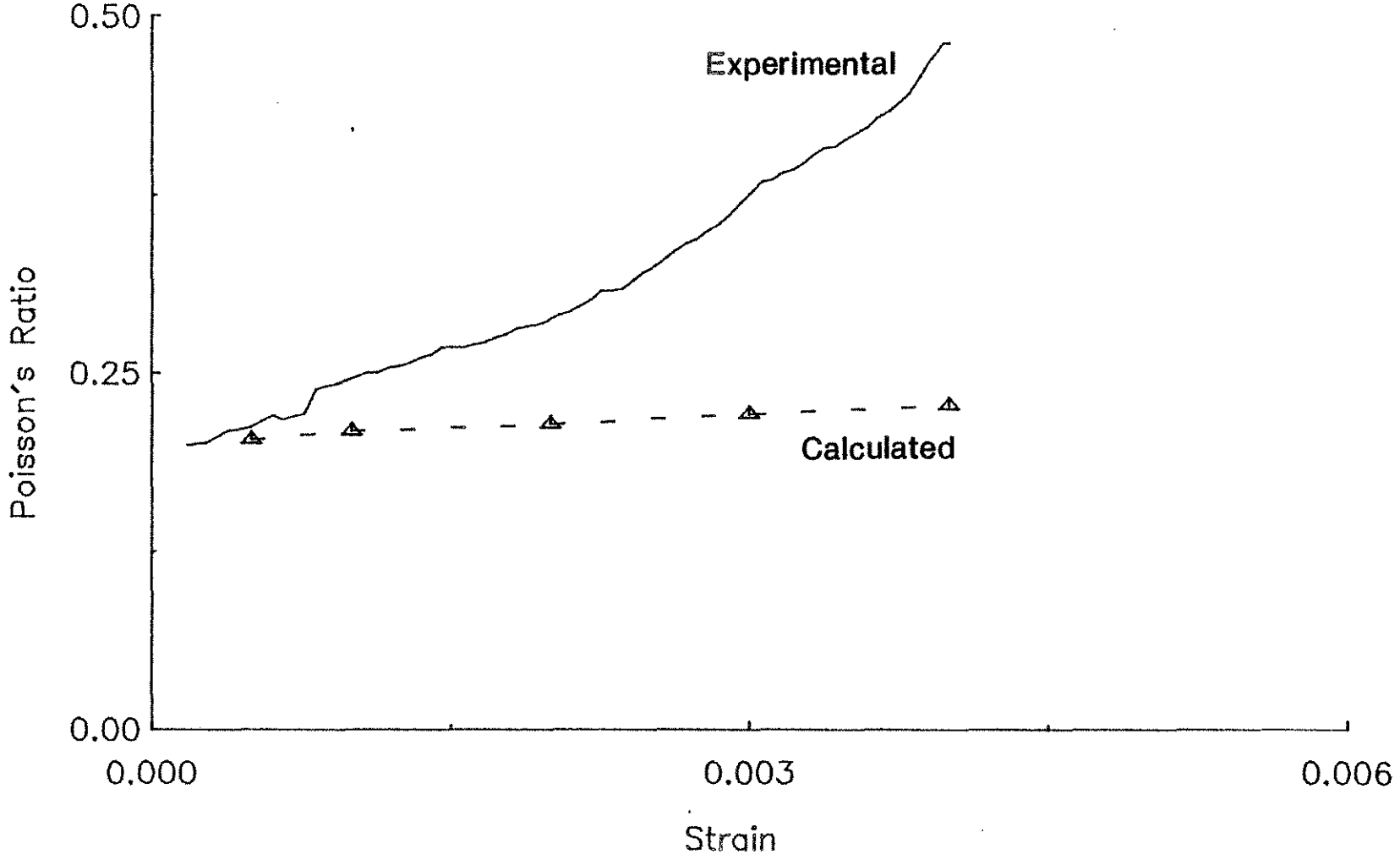

Fig. 5.14. Experimental and Calculated Poisson's Ratios versus Applied Strain for Monotonic Loading of Mortar with a W/C = 0.5. (Calculated Poisson's Ratios are Based on an Elastic Matrix; Saturated Cracks)

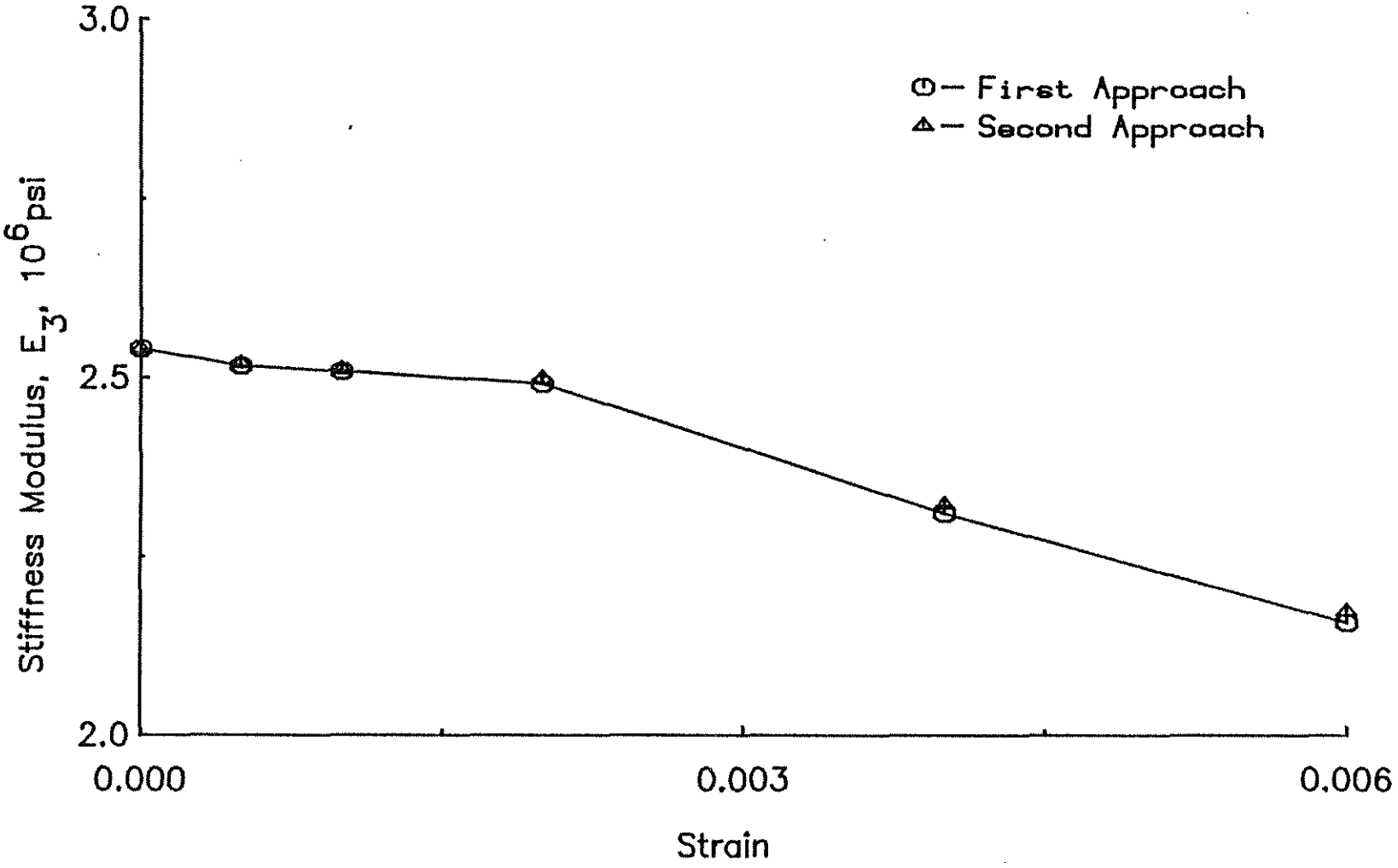

Fig. 5.15. Comparison of Values of Stiffness Modulus Calculated in Accordance with the First and Second Approaches; Monotonic Loading of Cement Paste with a W/C = 0.5; Dry Cracks

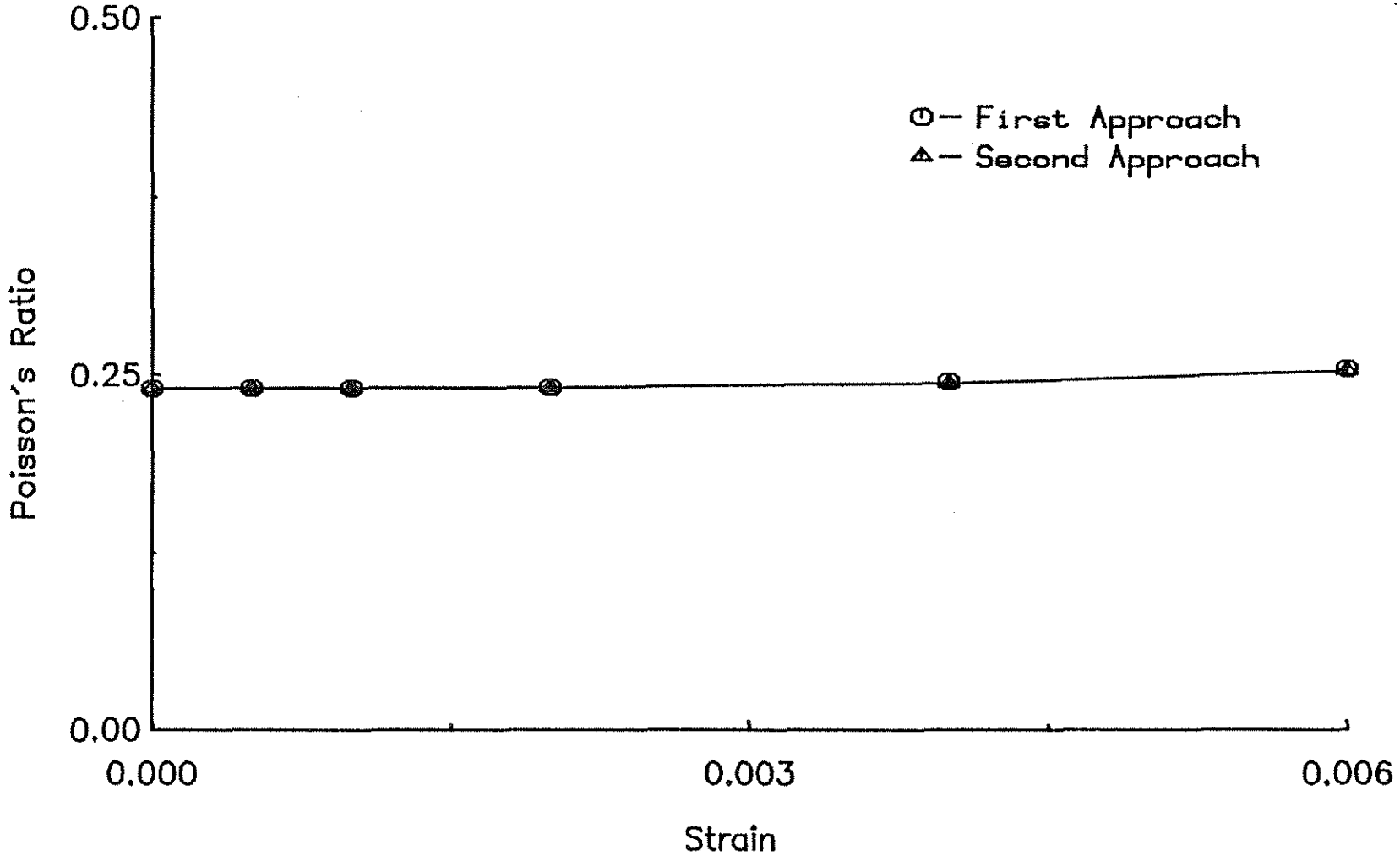

Fig. 5.16. Comparison of Values of Poisson's Ratios Calculated in Accordance with the First and Second Approaches; Monotonic Loading of Cement Paste with a W/C = 0.5; Dry Cracks

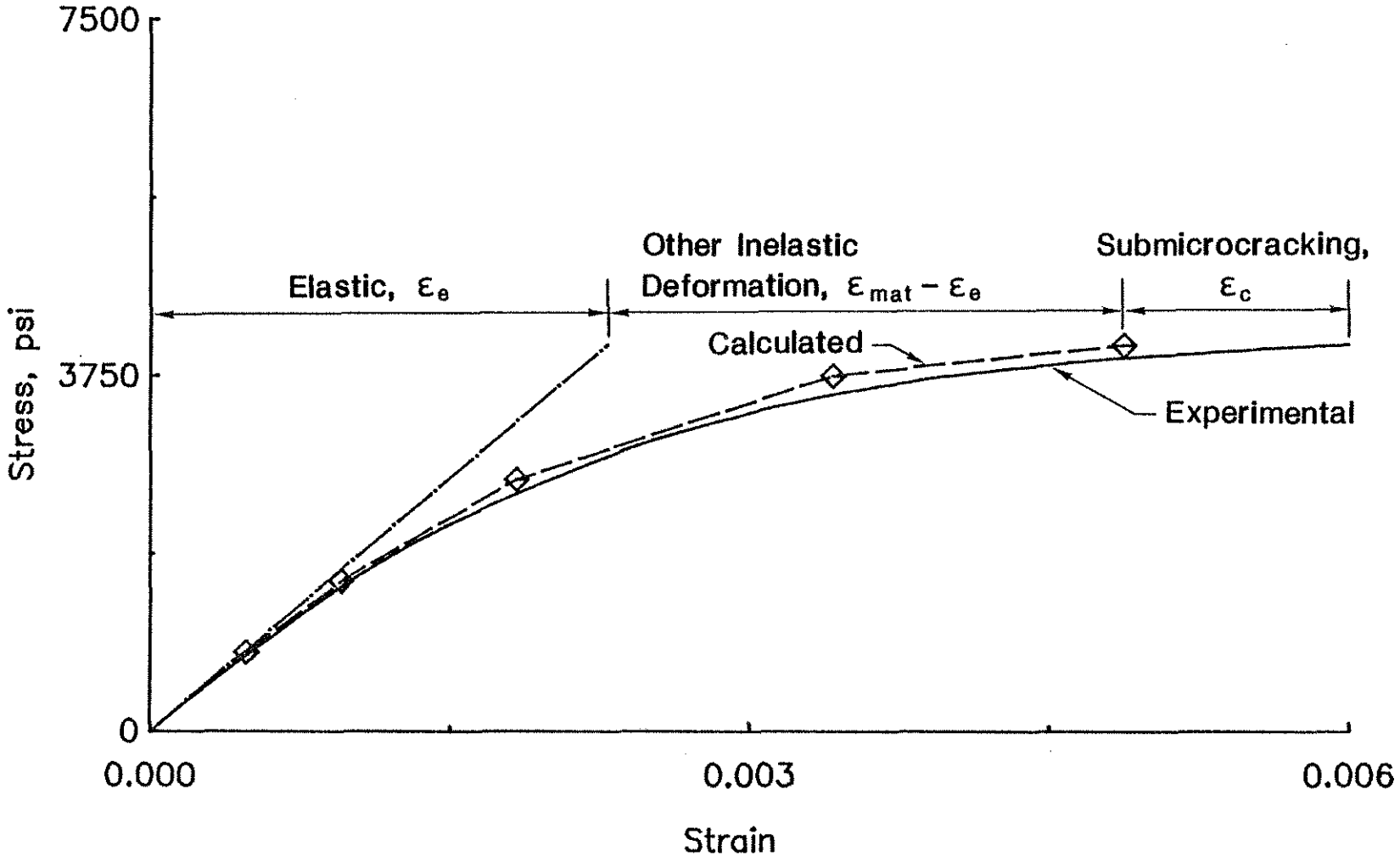

Fig. 5.17. Experimental and Calculated Stress-Strain Relationships for Monotonic Loading of Cement Paste with a W/C = 0.7. (Calculated Stress-Strain Relationship is Based on an Inelastic Matrix)

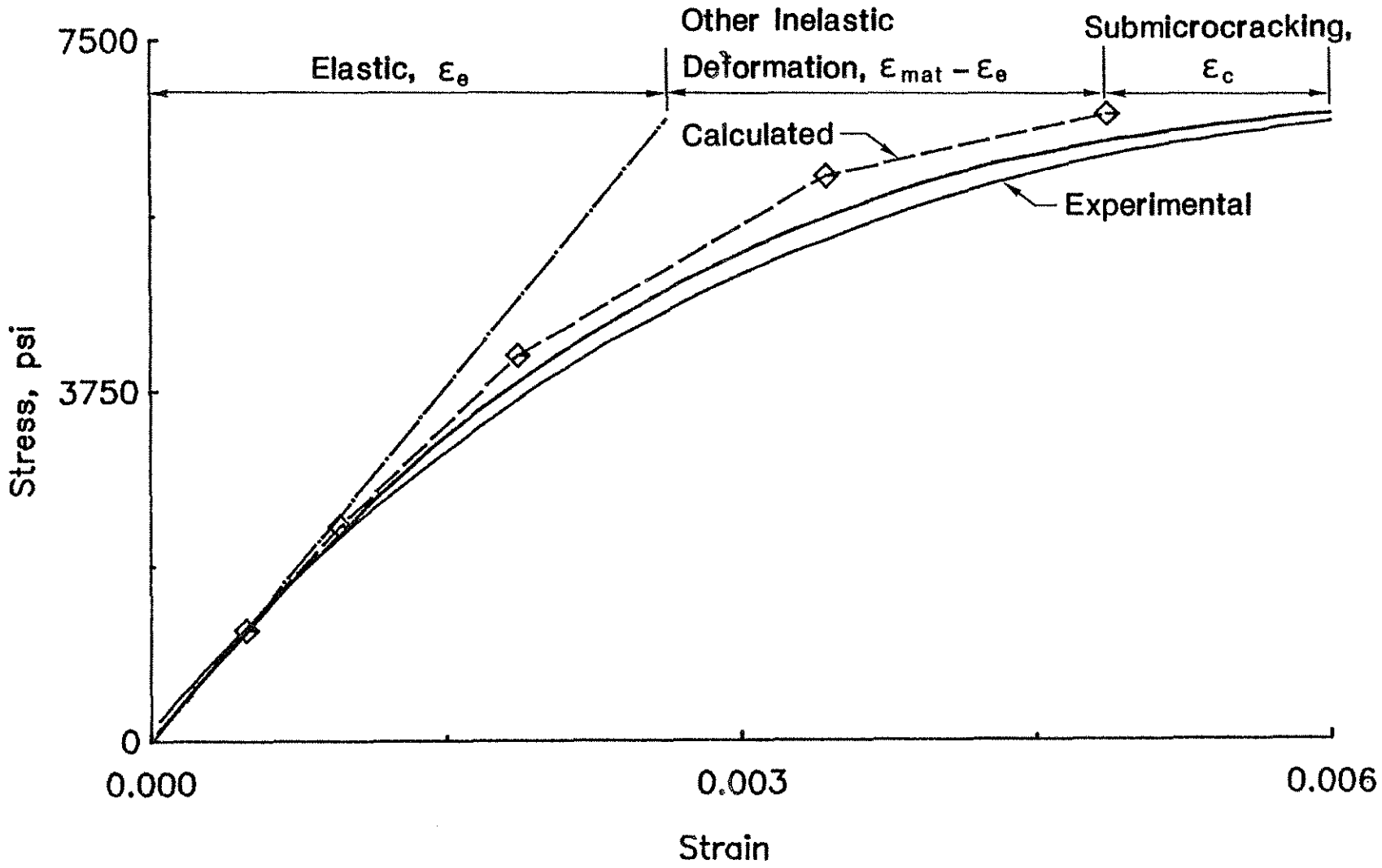

Fig. 5.18. Experimental and Calculated Stress-Strain Relationships for Monotonic Loading of Cement Paste with a W/C = 0.5. (Calculated Stress-Strain Relationship is Based on an Inelastic Matrix)

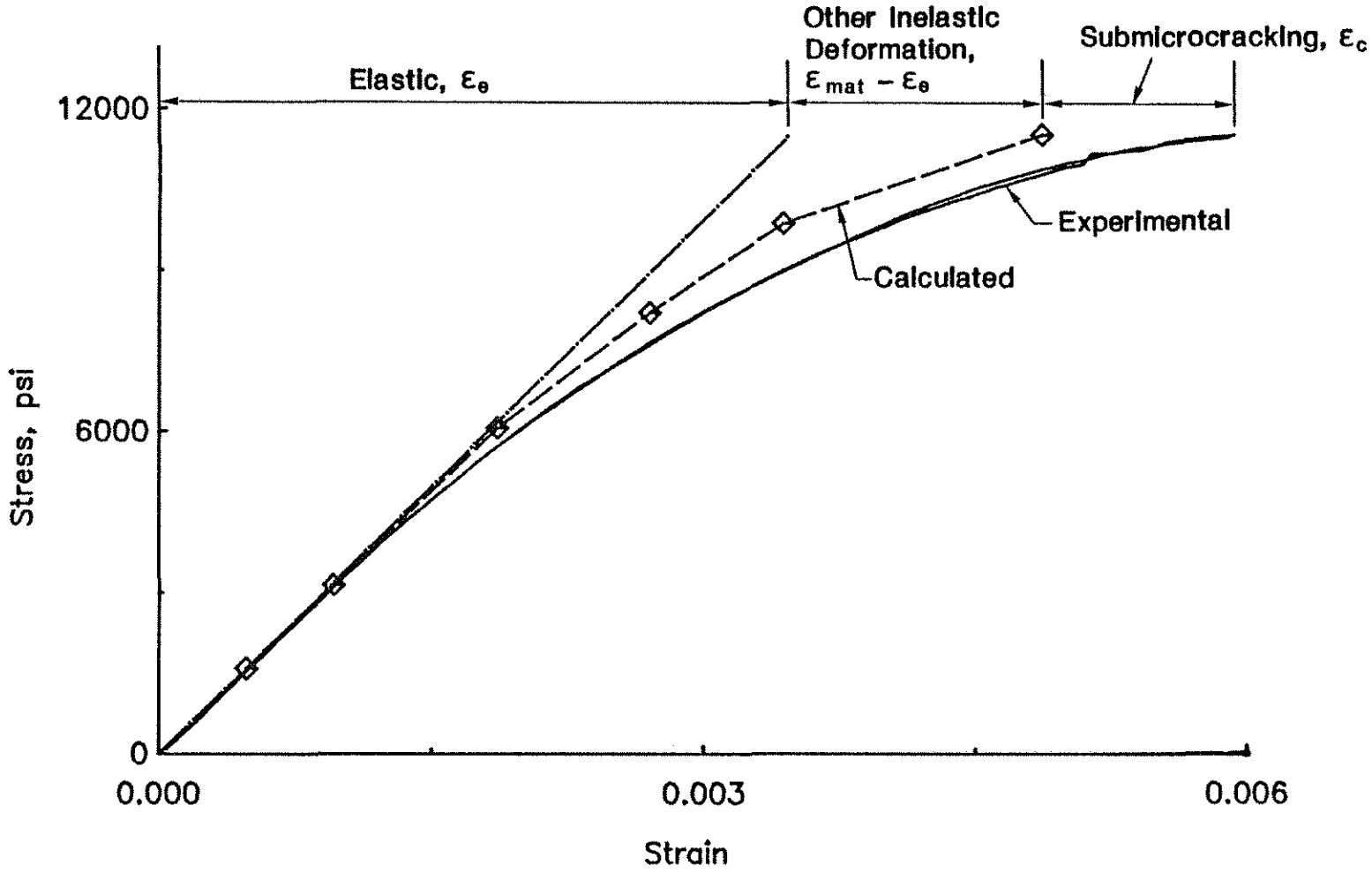

Fig. 5.19. Experimental and Calculated Stress-Strain Relationships for Monotonic Loading of Cement Paste with a W/C = 0.3. (Calculated Stress-Strain Relationship is Based on an Inelastic Matrix)

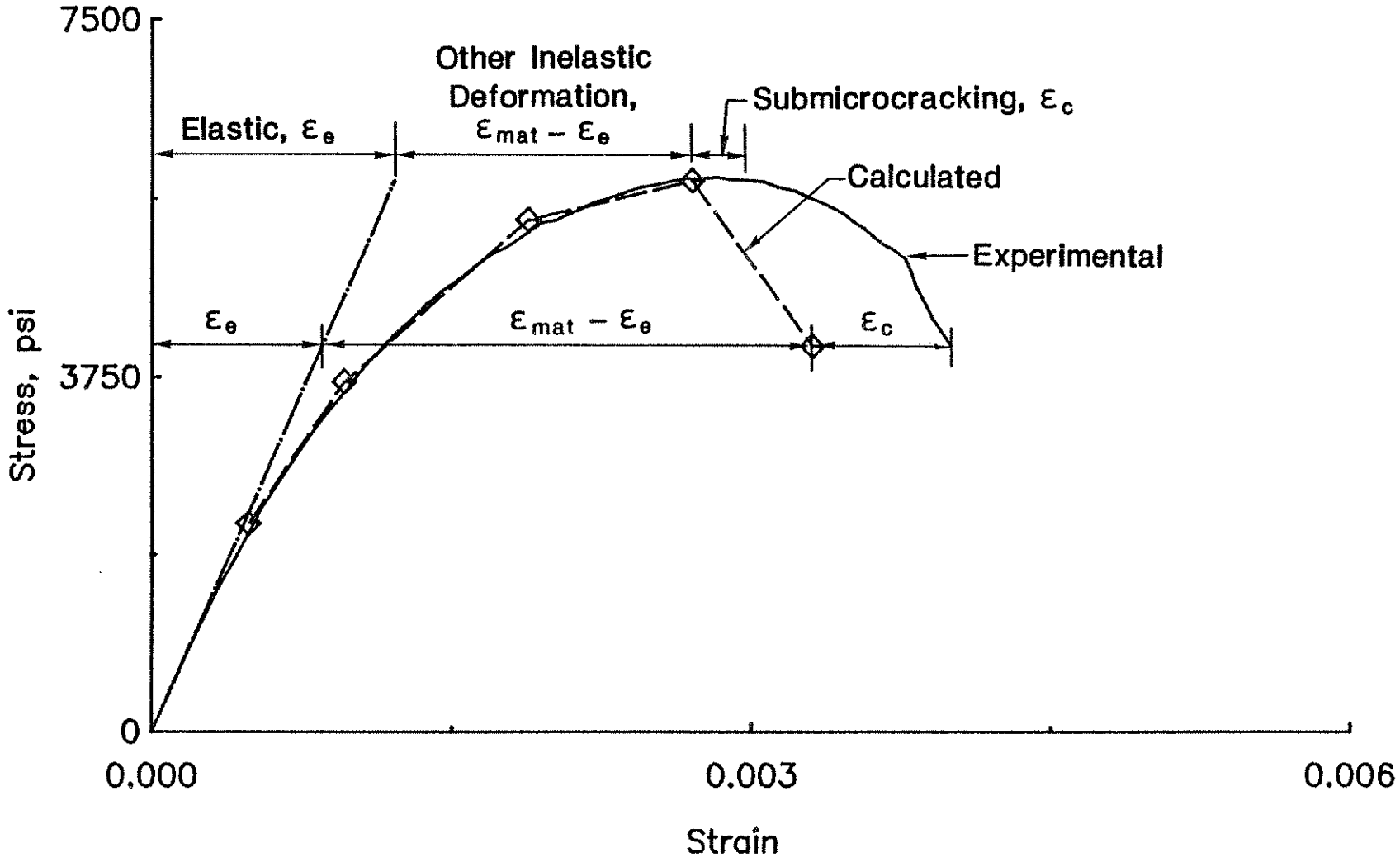

Fig. 5.20. Experimental and Calculated Stress-Strain Relationships for Monotonic Loading of Mortar with a W/C = 0.5. (Calculated Stress-Strain Relationship is Based on Inelastic Matrix)

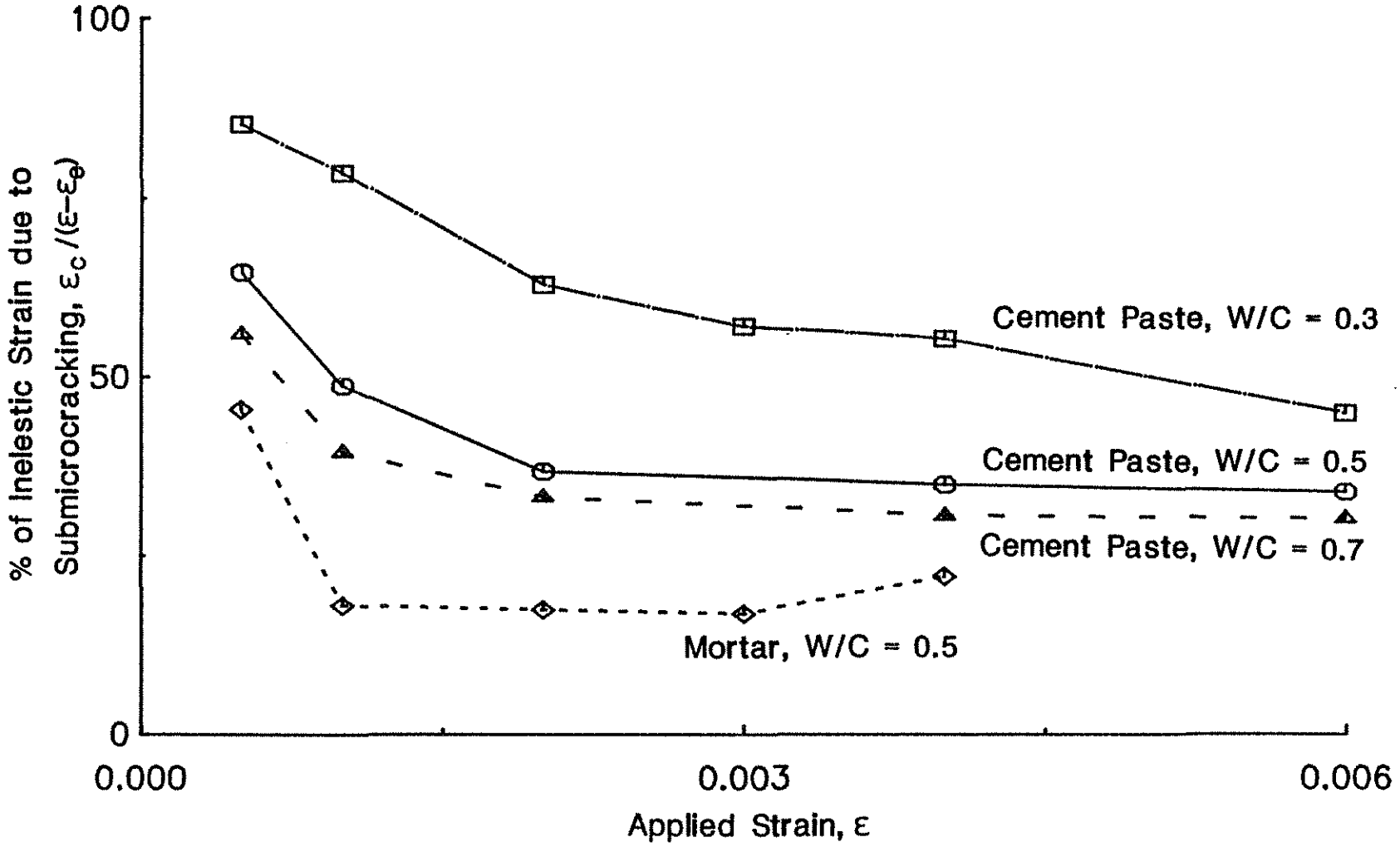

Fig. 5.21. Percentage of Inelastic Strain Due to Submicrocracking versus Applied Strain for Monotonic Loading of Cement Paste with W/C = 0.7, 0.5 and 0.3, and Mortar with a W/C = 0.5

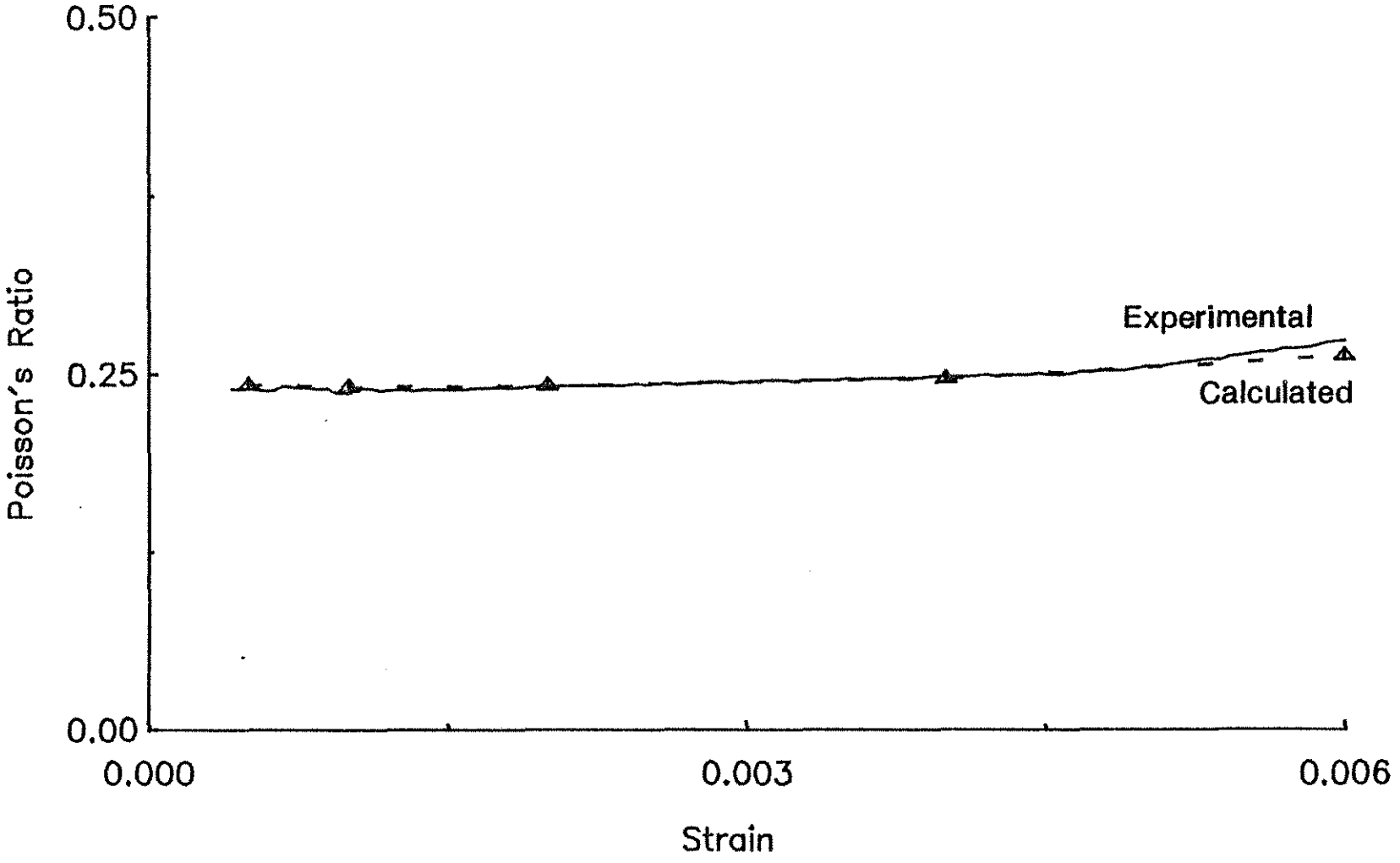

Fig. 5.22. Experimental and Calculated Poisson's Ratios versus Applied Strain for Monotonic Loading of Cement Paste with a W/C = 0.5. (Calculated Poisson's Ratios are Based on an Inelastic Matrix)

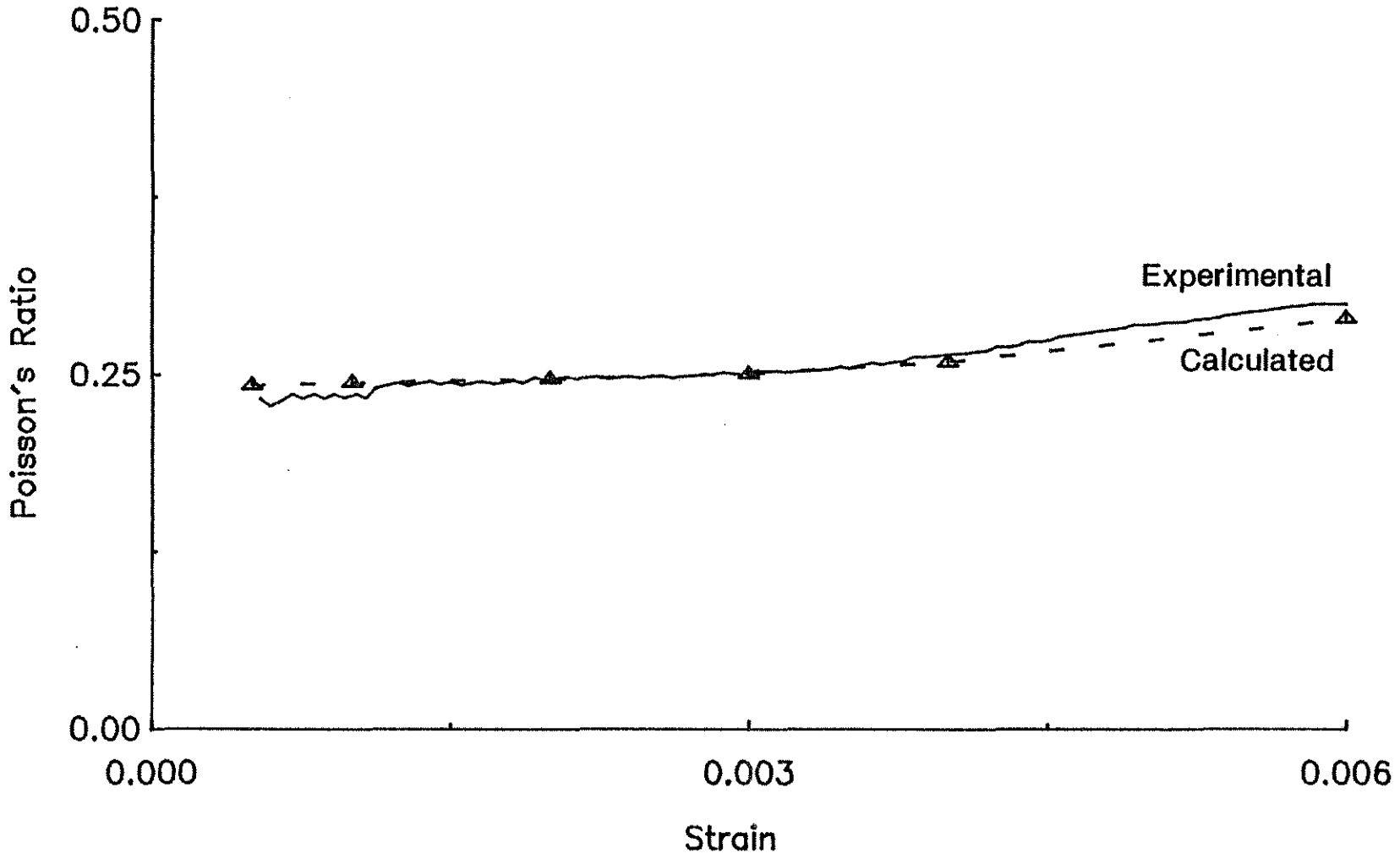

Fig. 5.23. Experimental and Calculated Poisson's Ratios versus Applied Strain for Monotonic Loading of Cement Paste with a W/C = 0.3. (Calculated Poisson's Ratios are Based on an Inelastic Matrix)

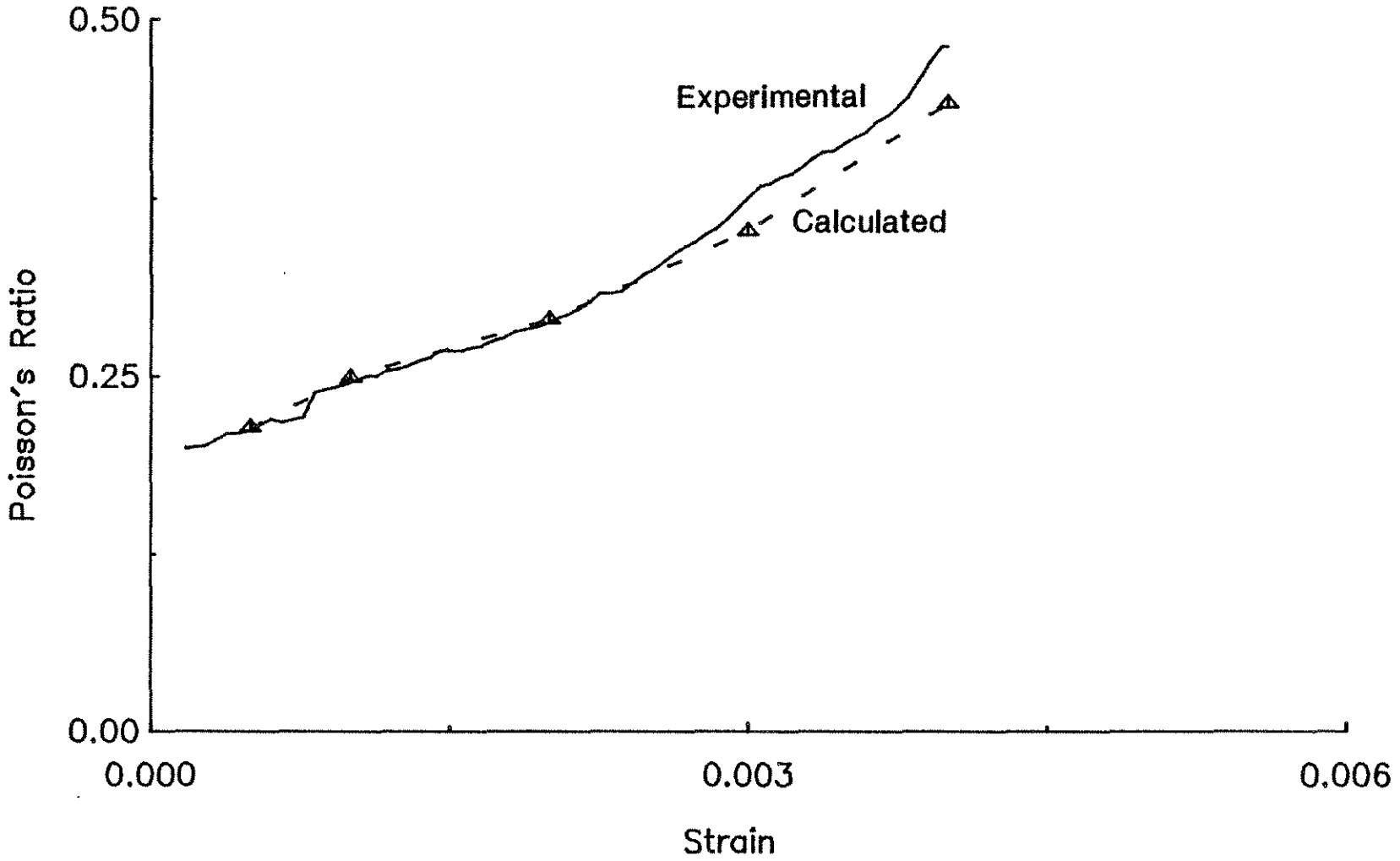

Fig. 5.24. Experimental and Calculated Poisson's Ratios versus Applied Strain for Monotonic Loading of Mortar with a W/C = 0.5. (Calculated Poisson's Ratios are Based on an Inelastic Matrix)

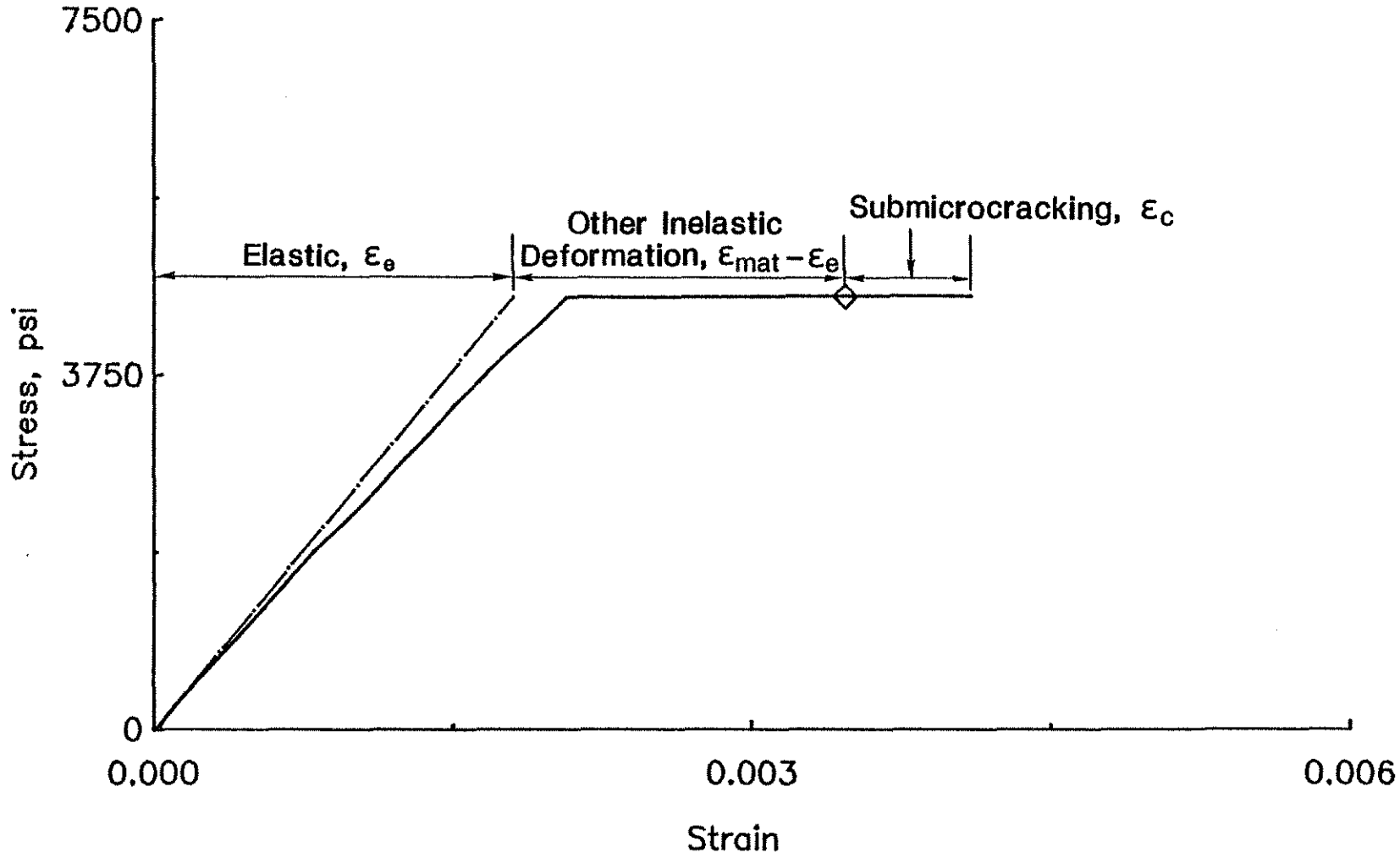

Fig. 5.25. Experimental Stress-Strain Curve and Calculated Strain in Inelastic Matrix Material for Sustained Loading of Cement Paste with a W/C = 0.5; Applied Strain = 0.004

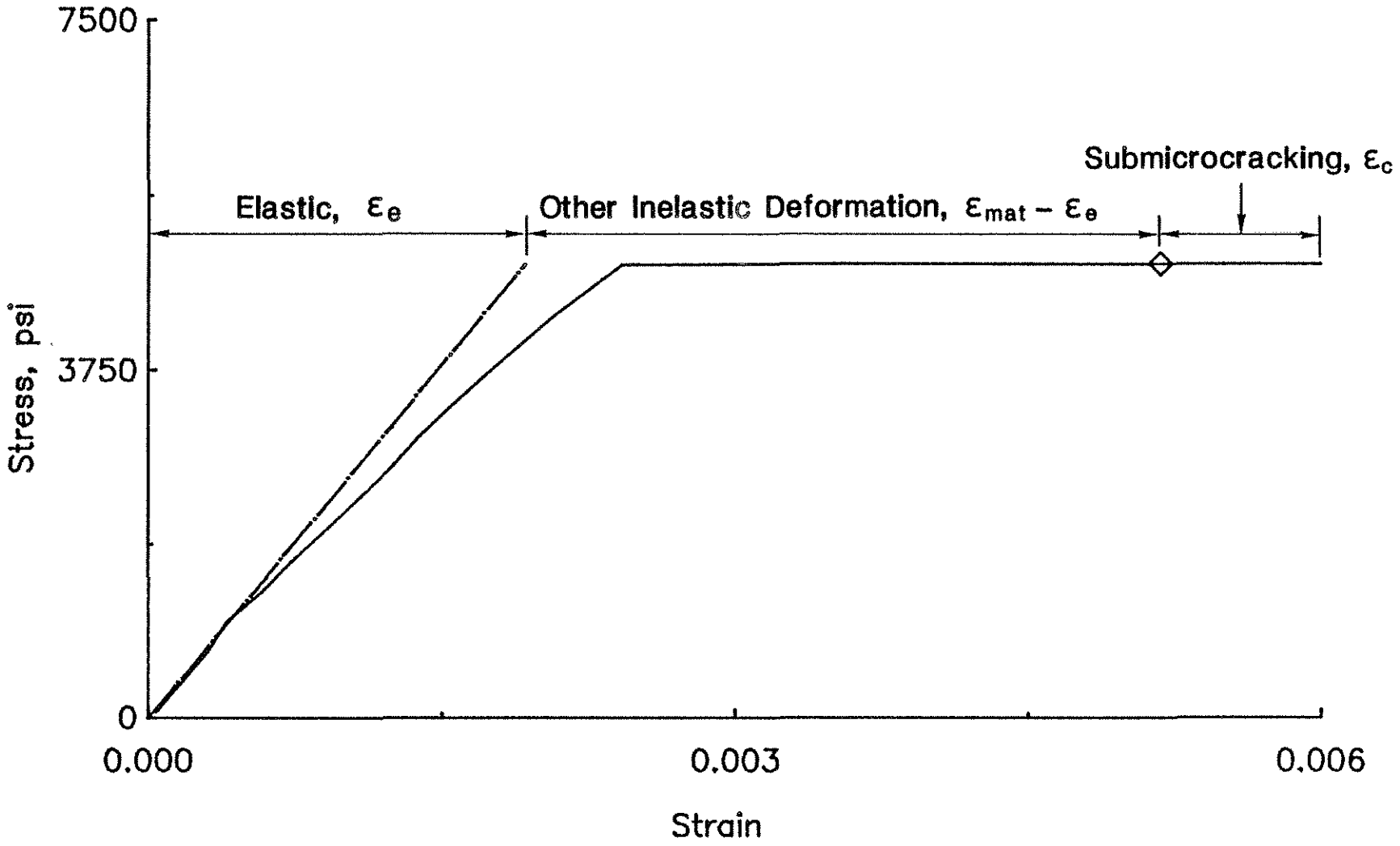

Fig. 5.26. Experimental Stress-Strain Curve and Calculated Strain in Inelastic Matrix Material for Sustained Loading of Cement Paste with a W/C = 0.5; Applied Strain = 0.006

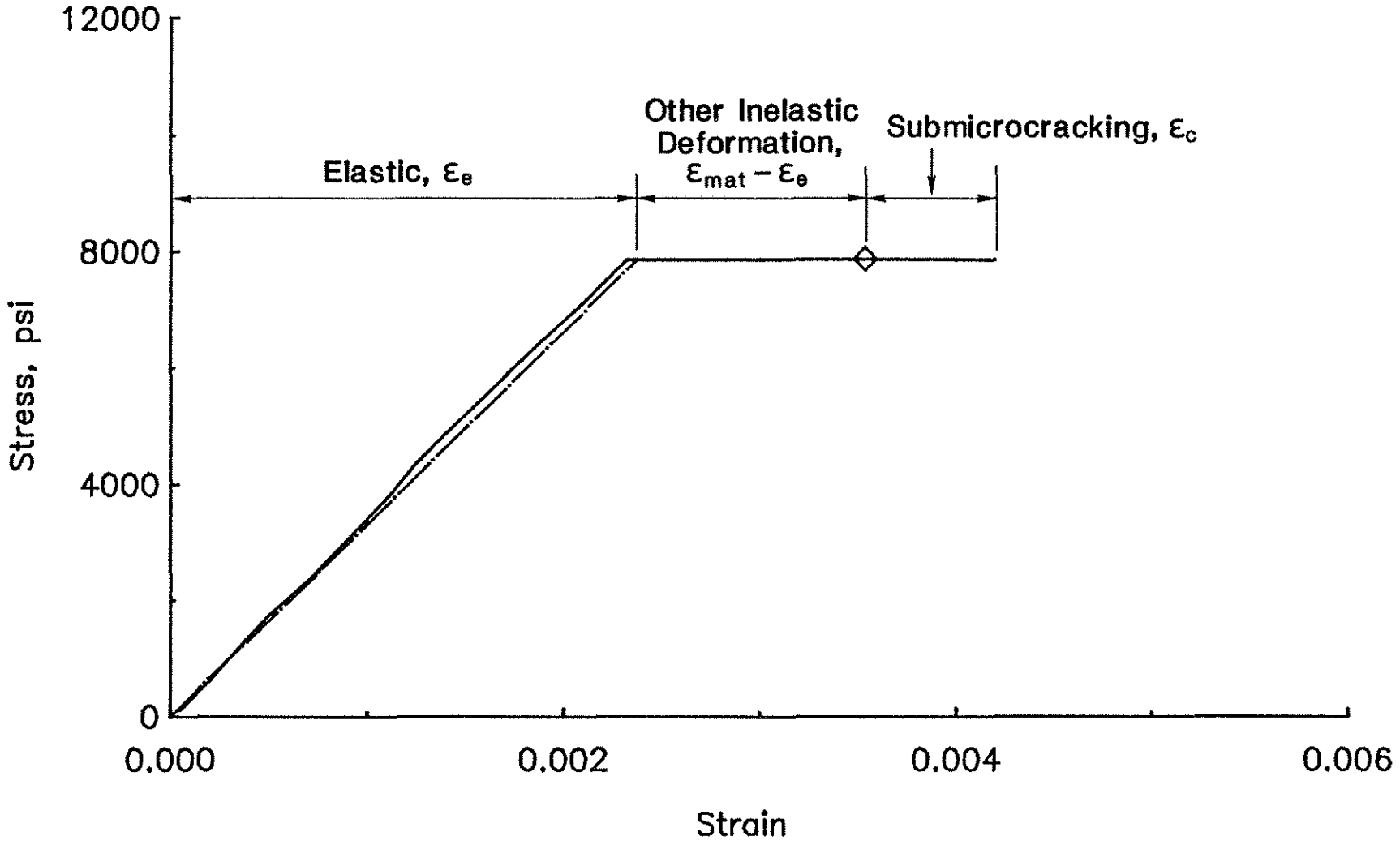

Fig. 5.27. Experimental Stress-Strain Curve and Calculated Strain in Inelastic Matrix Material for Sustained Loading of Cement Paste with a W/C = 0.3; Applied Strain = 0.004

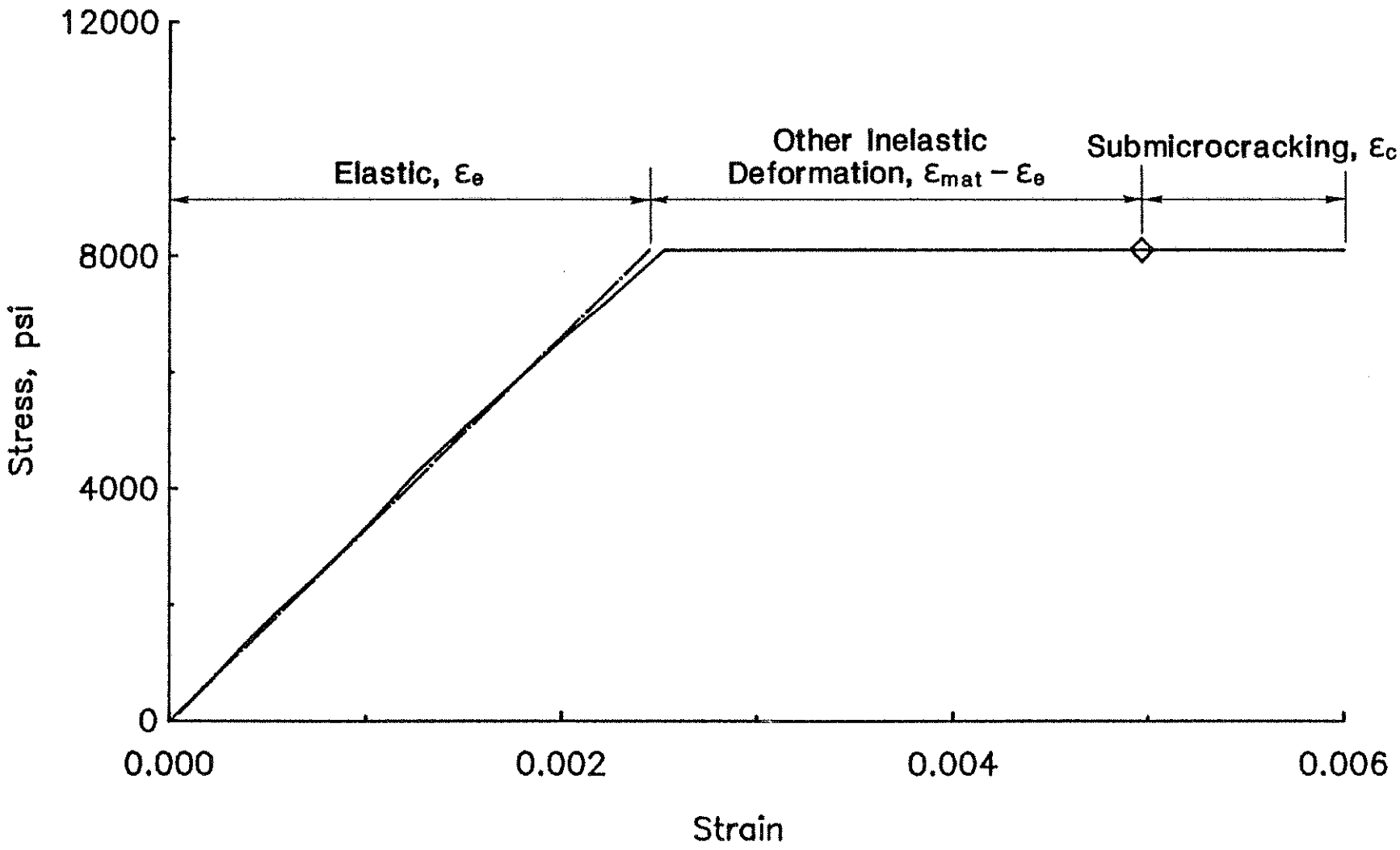

Fig. 5.28. Experimental Stress-Strain Curve and Calculated Strain in Inelastic Matrix Material for Sustained Loading of Cement Paste with a W/C = 0.3; Applied Strain = 0.006

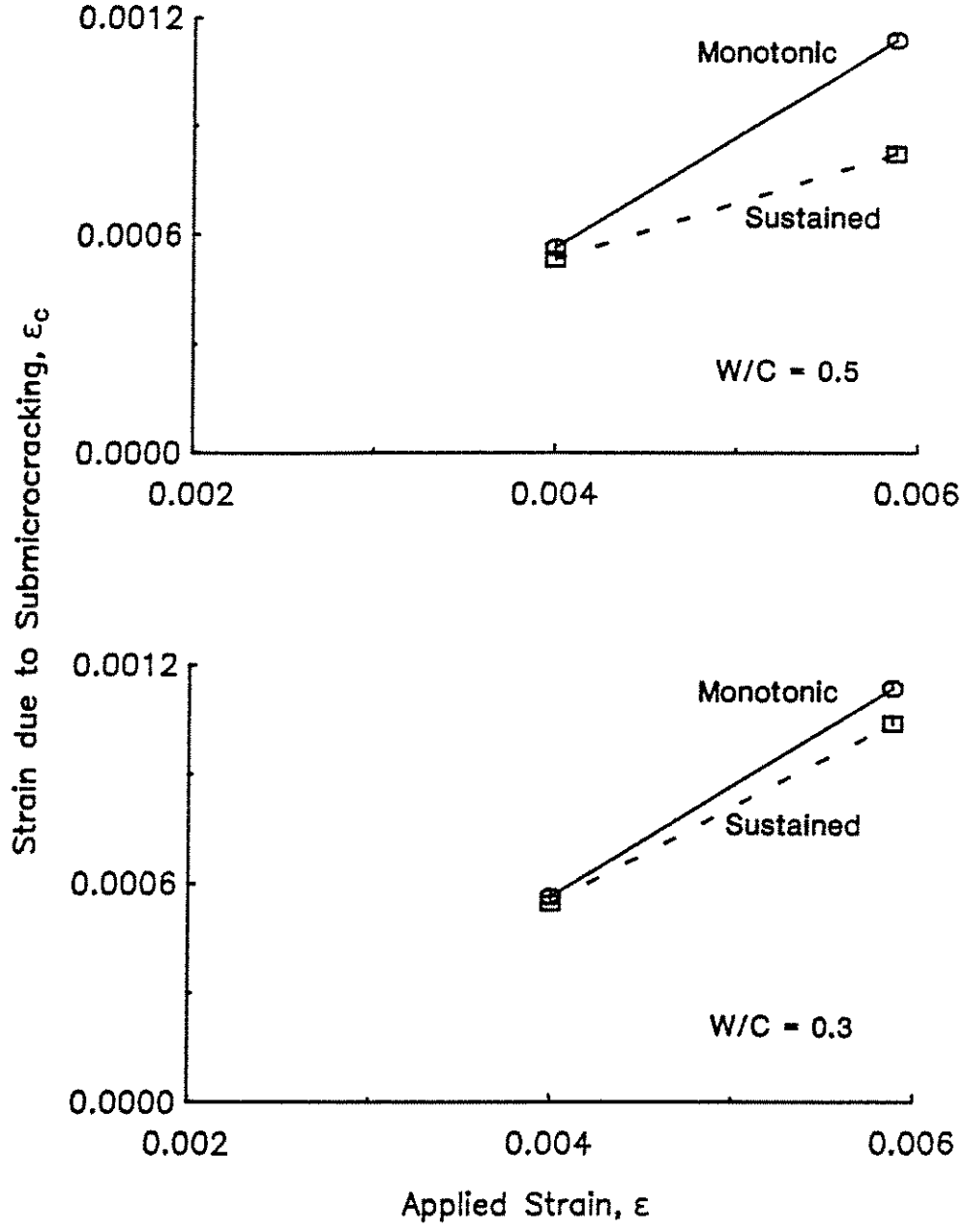

Fig. 5.29. Comparison of Calculated Strains Due to Submicrocracking for Monotonic and Sustained Loading of Cement Pastes (W/C = 0.5 and 0.3) at the same Applied Strain. (Calculated Strains are Based on an Inelastic Matrix)

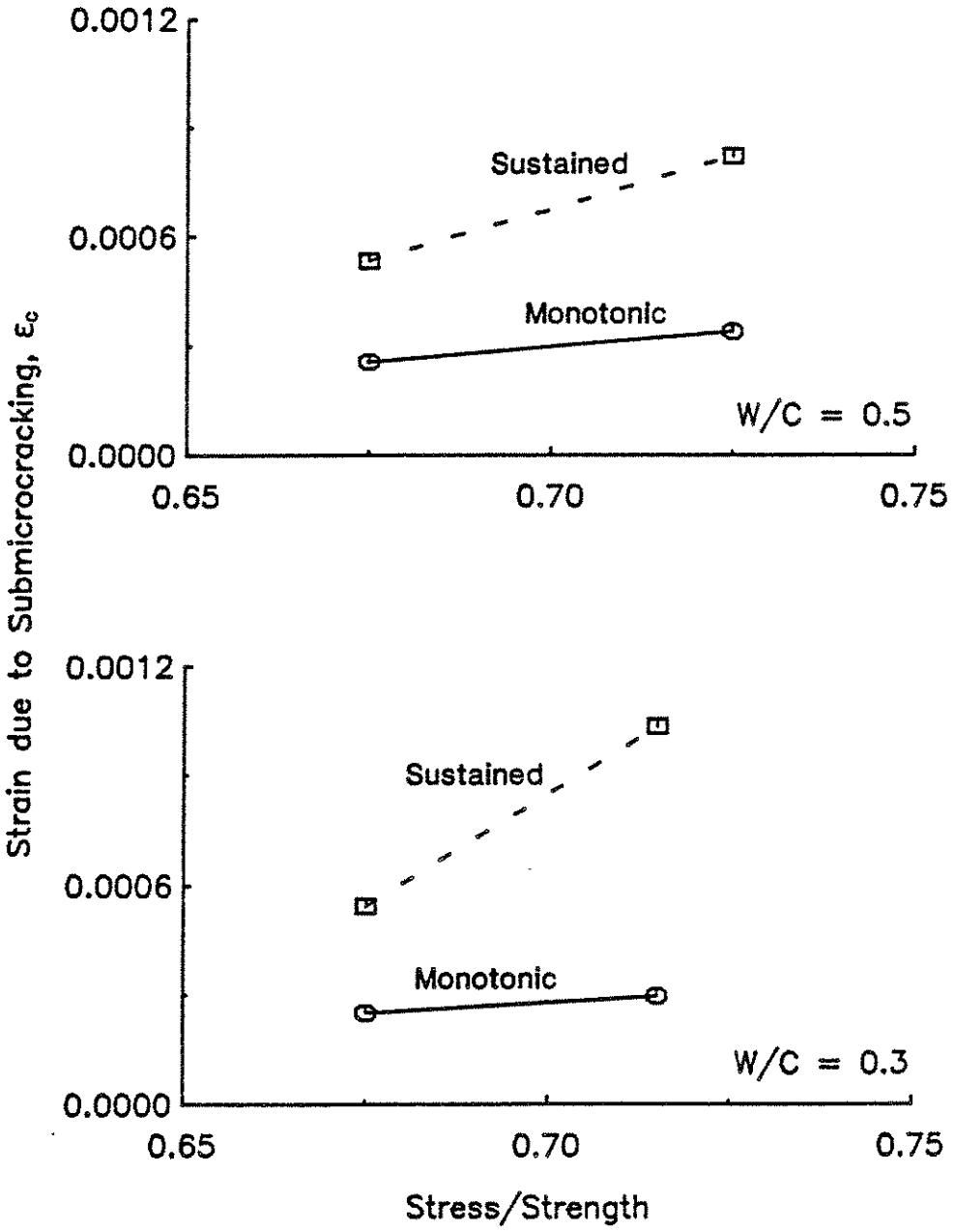

Fig. 5.30. Comparison of Calculated Strains Due to Submicrocracking for Monotonic and Sustained Loading of Cement Pastes (W/C = 0.5 and 0.3) at the same Stress-Strength Ratio. (Calculated Strains are Based on an Inelastic Matrix)

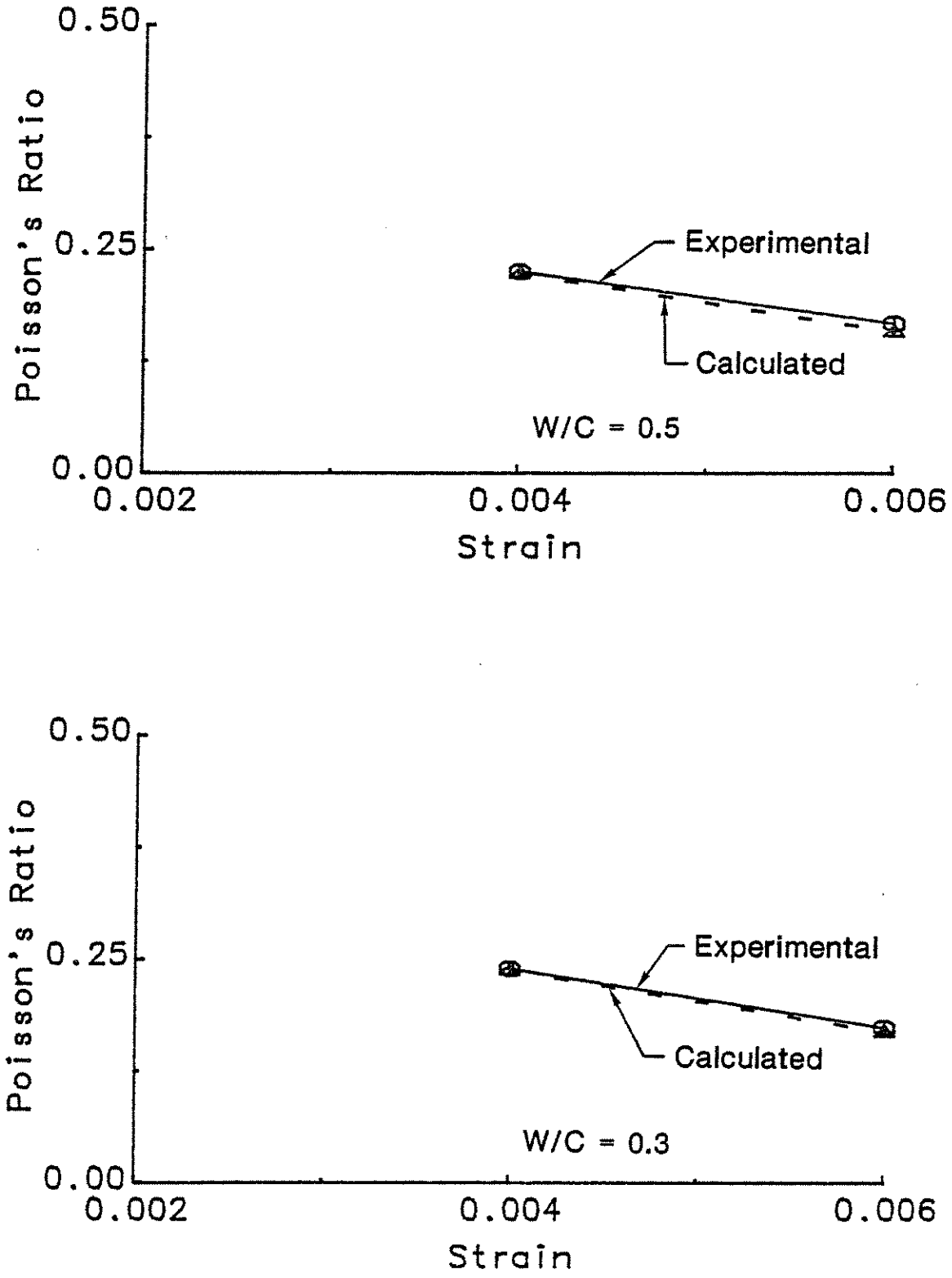

Fig. 5.31. Experimental and Calculated Poisson's Ratios versus Applied Strain for Sustained Loading of Cement Pastes (W/C = 0.5 and 0.3). (Calculated Poisson's Ratios are Based on an Inelastic Matrix)

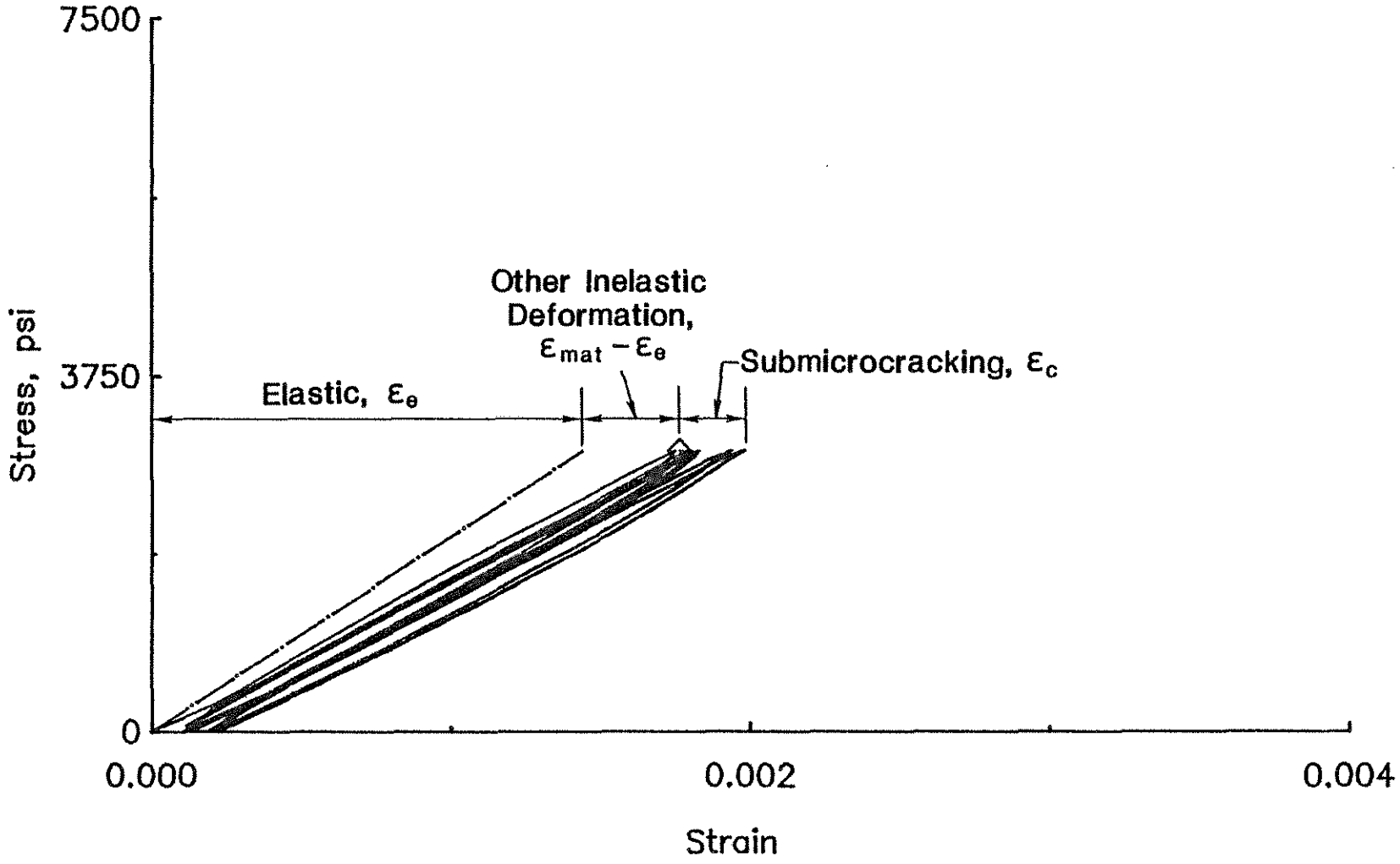

Fig. 5.32. Experimental Stress-Strain Curve and Calculated Strain in Inelastic Matrix Material for Cyclic Loading of Cement Paste with a W/C = 0.5; Applied Strain = 0.002

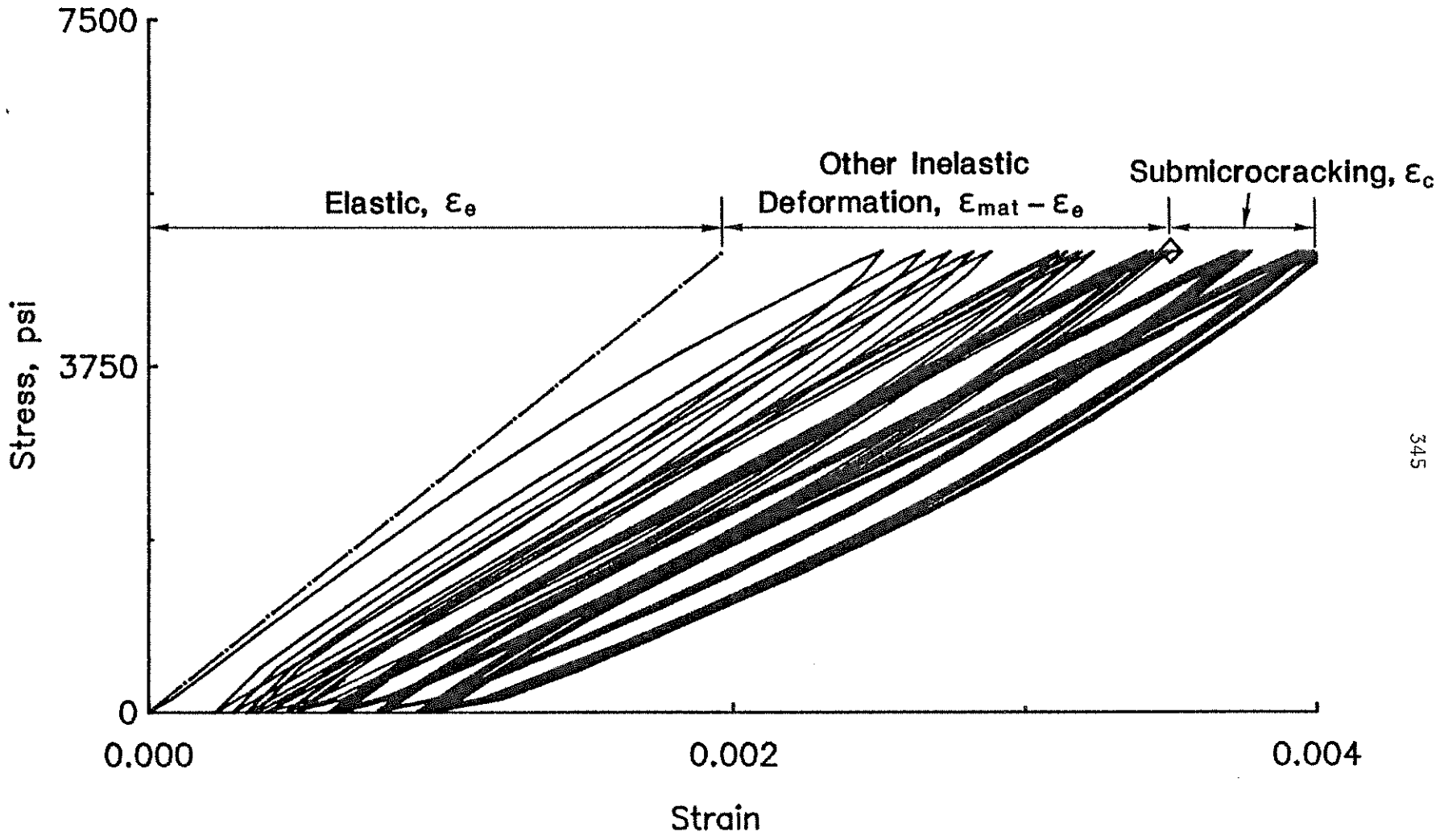

Fig. 5.33. Experimental Stress-Strain Curve and Calculated Strain in Inelastic Matrix Material for Cyclic Loading of Cement Paste with a W/C = 0.5; Applied Strain = 0.004

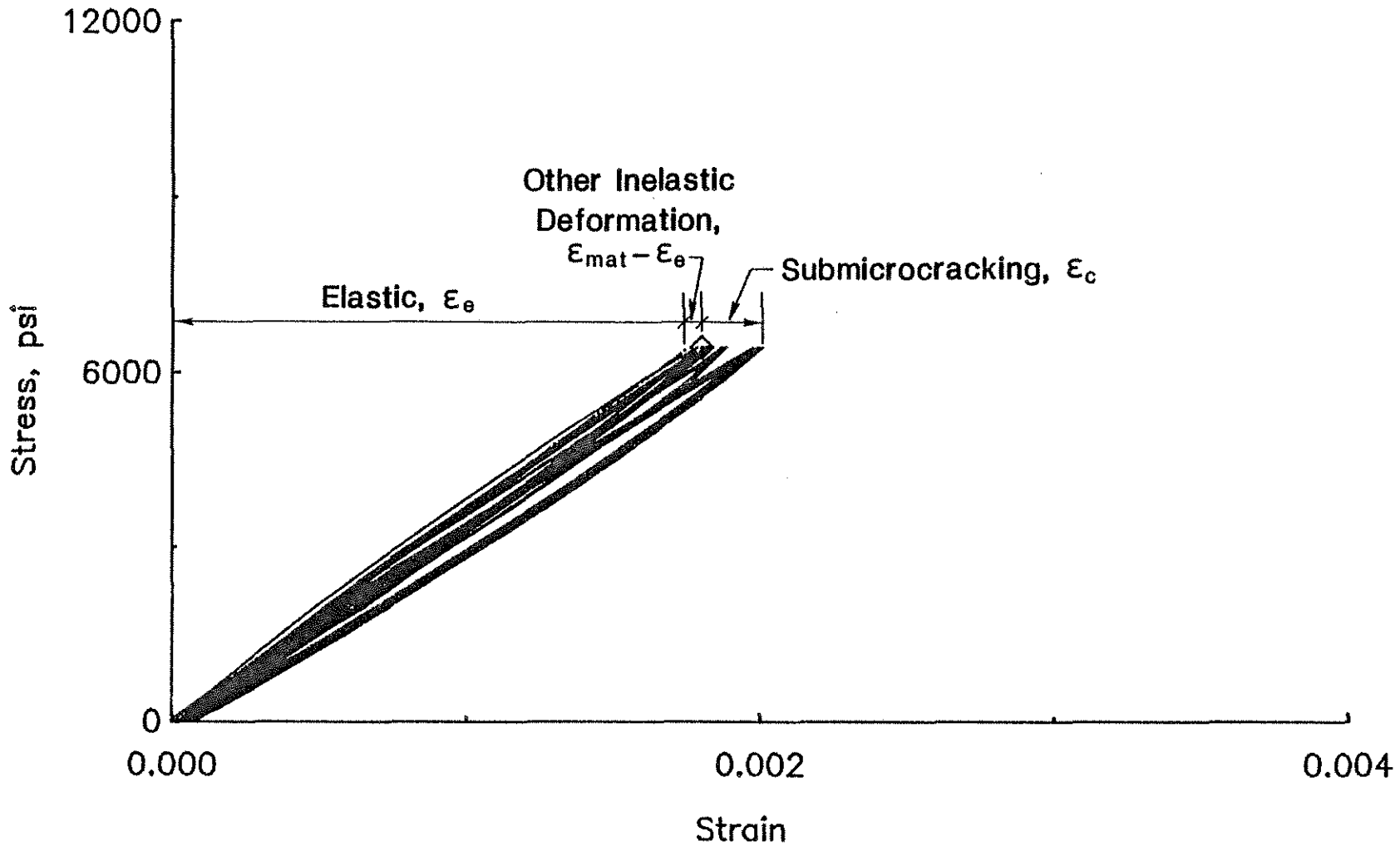

Fig. 5.34. Experimental Stress-Strain Curve and Calculated Strain in Inelastic Matrix Material for Cyclic Loading of Cement Paste with a W/C = 0.3; Applied Strain = 0.002

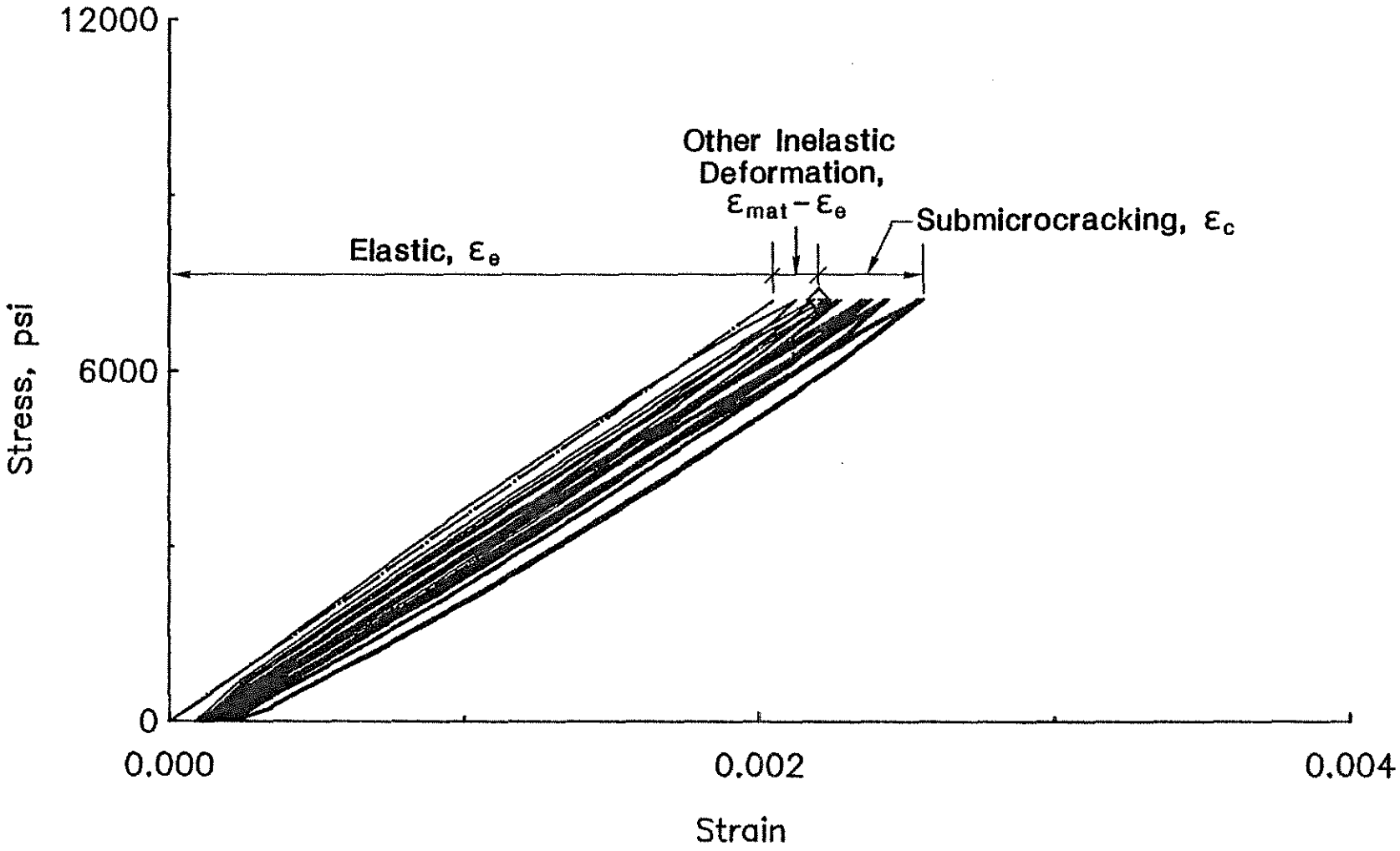

Fig. 5.35. Experimental Stress-Strain Curve and Calculated Strain in Inelastic Matrix Material for Cyclic Loading of Cement Paste with a W/C = 0.3; Applied Strain = 0.0025

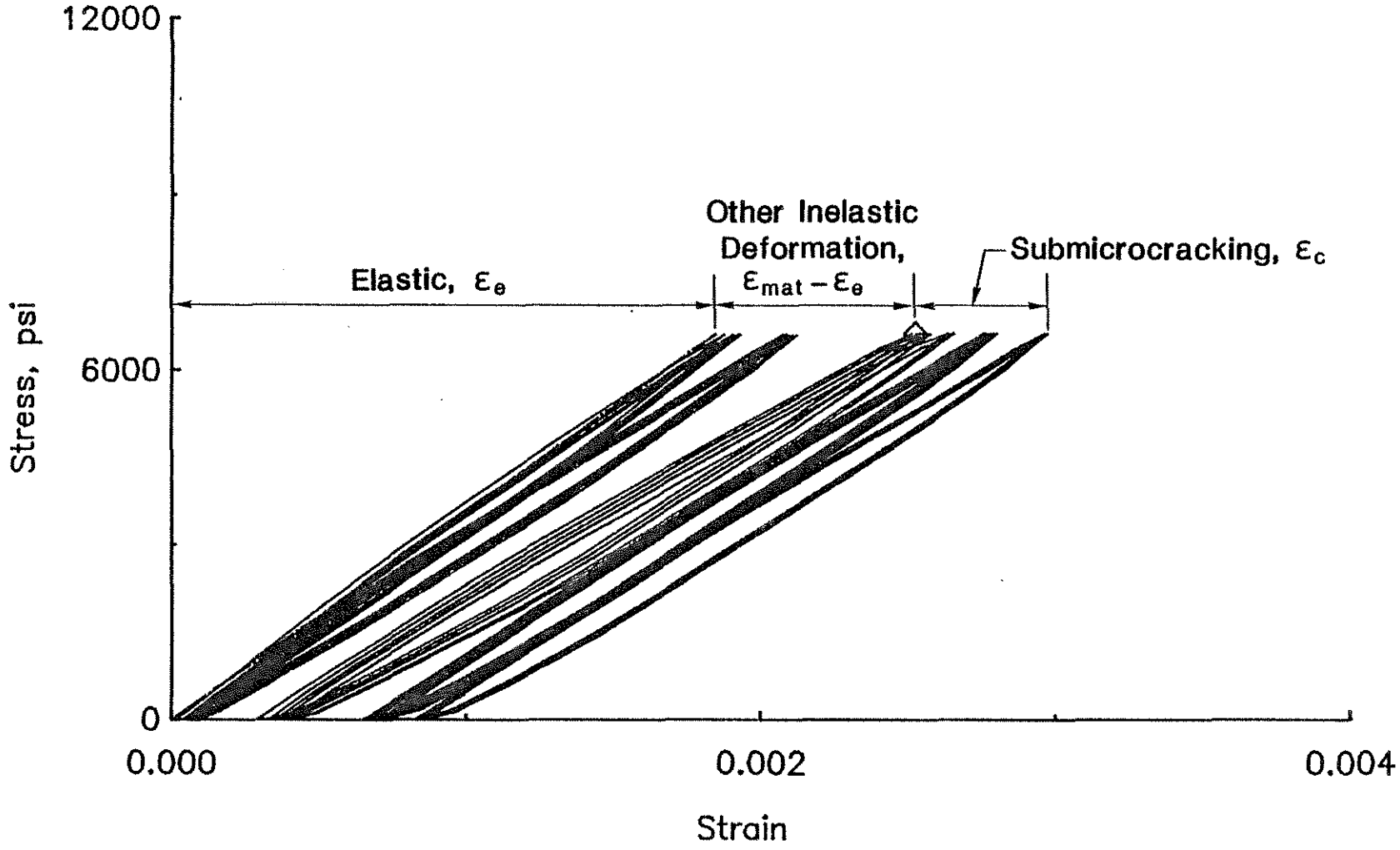

Fig. 5.36. Experimental Stress-Strain Curve and Calculated Strain in Inelastic Matrix Material for Cyclic Loading of Cement Paste with a W/C = 0.3; Applied Strain = 0.003

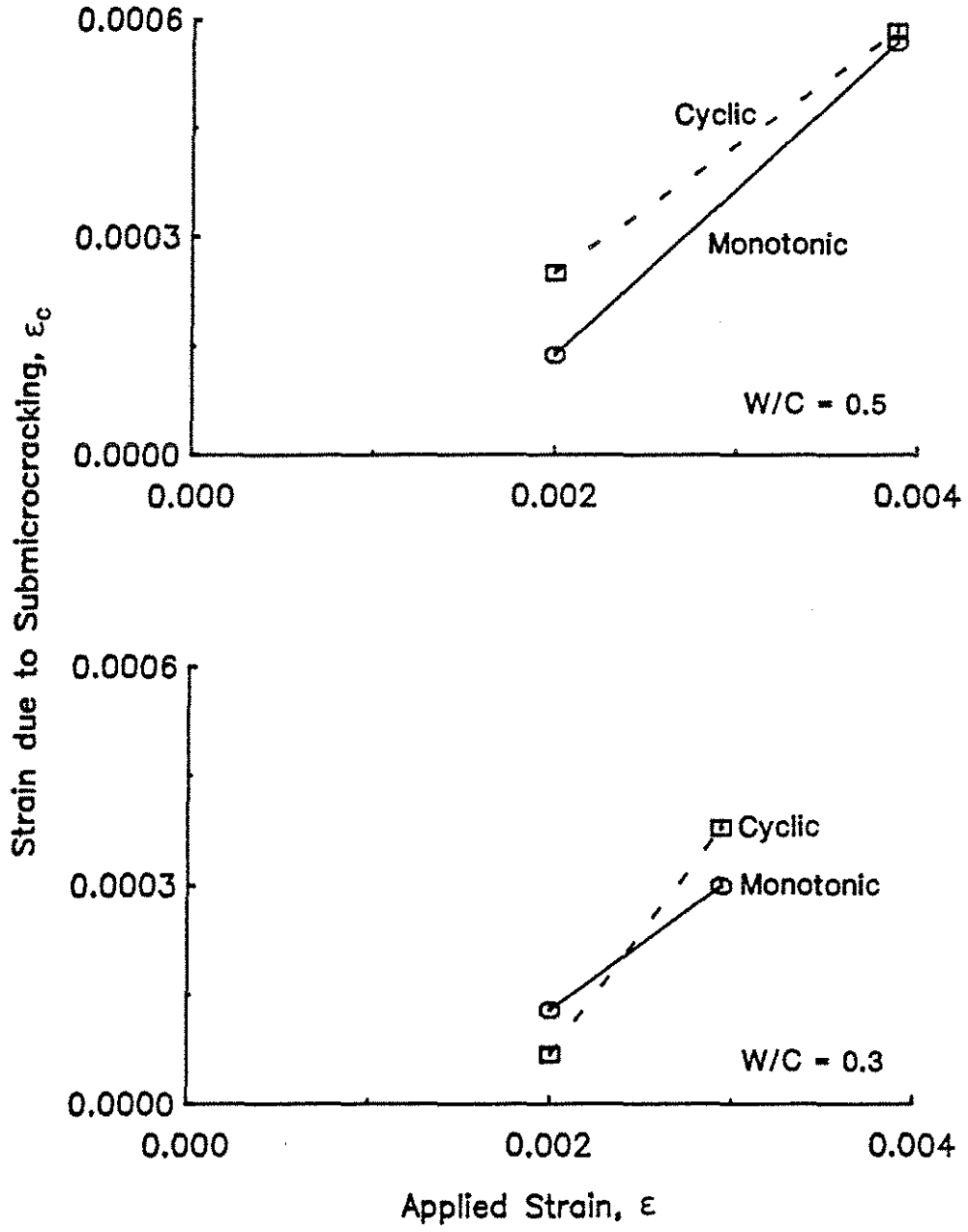

Fig. 5.37. Comparison of Calculated Strains Due to Submicrocracking for Monotonic and Cyclic Loading of Cement Pastes (W/C = 0.5 and 0.3) at the Same Applied Strain. (Calculated Strains are Based on an Inelastic Matrix)

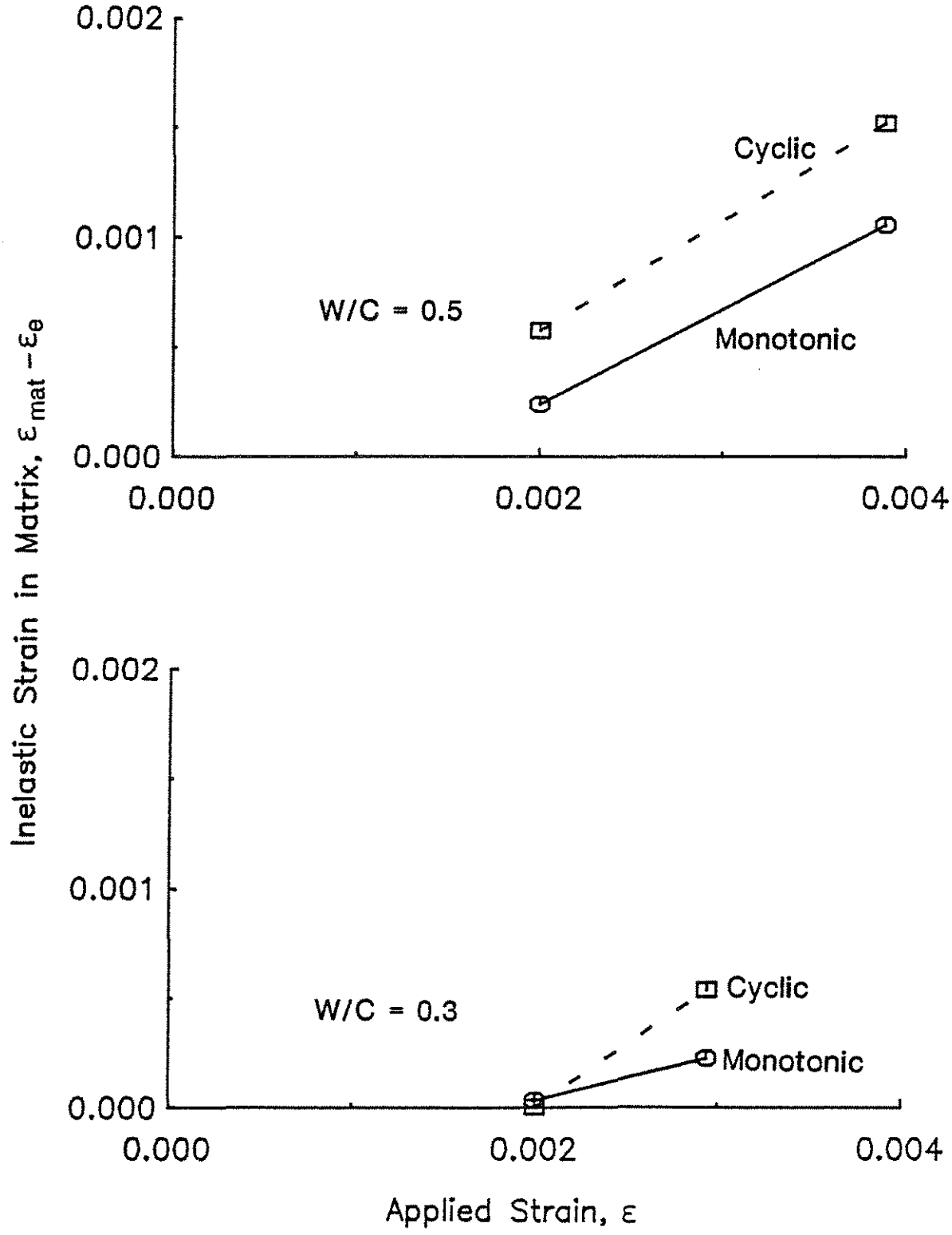

Fig. 5.38. Comparison of Inelastic Strains in Matrix for Monotonic and Cyclic Loading of Cement Pastes (W/C = 0.5 and 0.3) at the Same Applied Strain. (Calculated Strains are Based on an Inelastic Matrix)

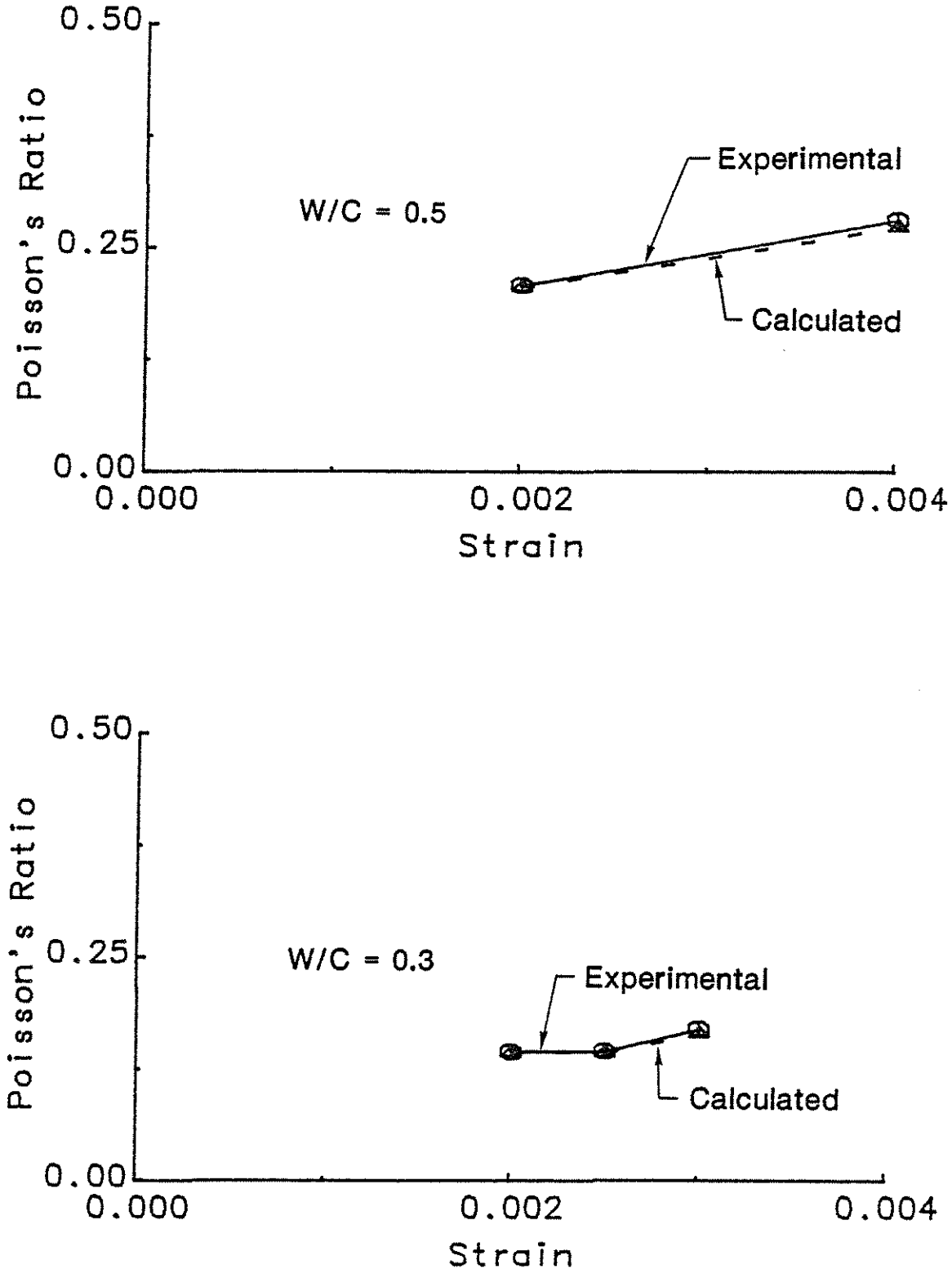

Fig. 5.39. Experimental and Calculated Poisson's Ratios versus Applied Strain for Cyclic Loading of Cement Pastes (W/C = 0.5 and 0.3). (Calculated Poisson's Ratios are Based on an Inelastic Matrix)

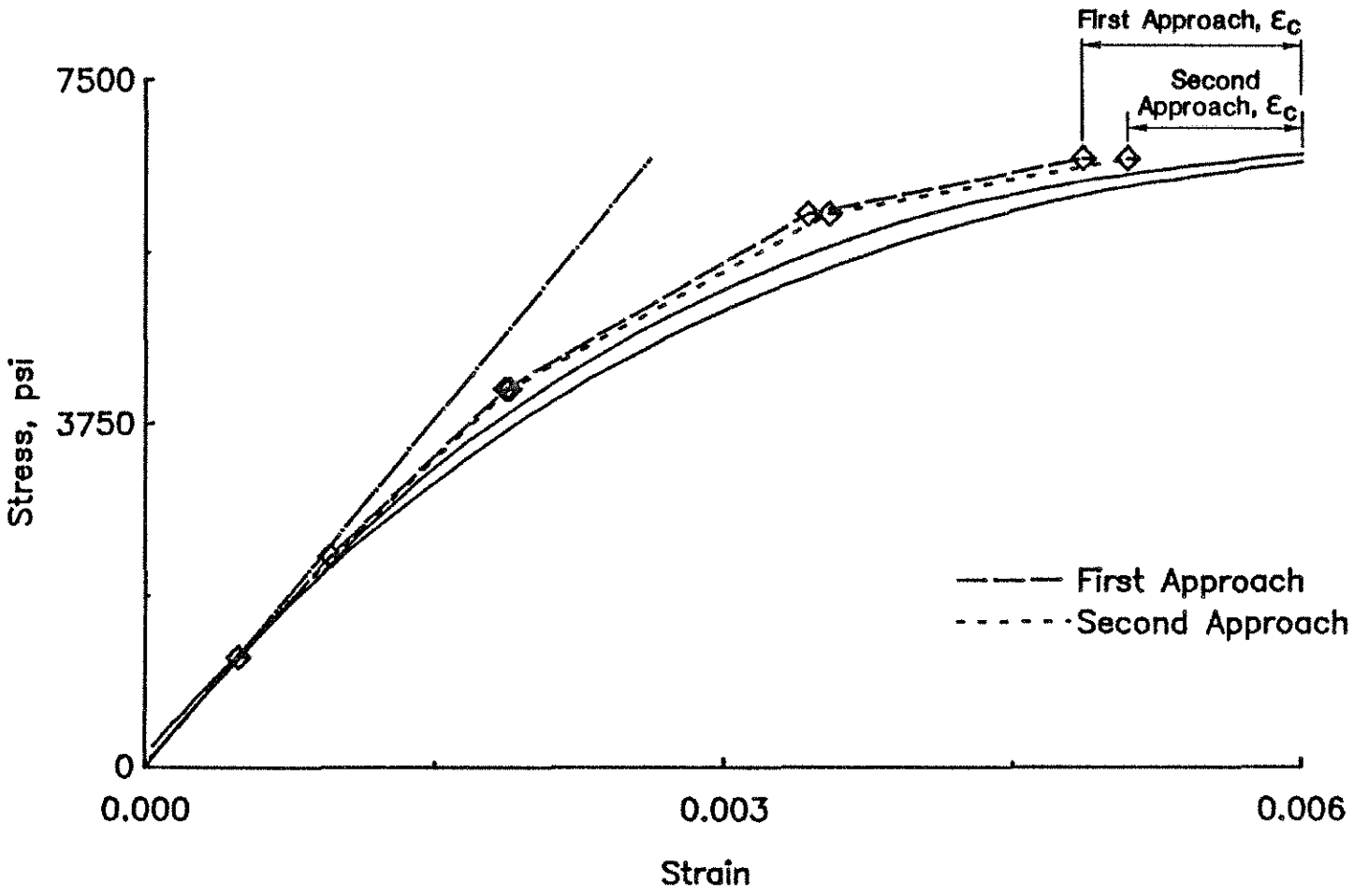

Fig. 5.40. Calculated Stress-Strain Relationships for First and Second Approaches (Based on an Inelastic Matrix) Compared with Experimental Curves. Monotonic Loading of Cement Paste with a W/C = 0.5

APPENDIX A

KEY TO SPECIMEN IDENTIFICATION

The specimens are identified as follows:

Identification: i-j/X-R/L

in which

i = batch number

j = specimen number, in batch i

X = type of specimen

R = water-cement ratio

L = type of load regime

Type of specimen - X

P = cement paste

M = mortar

Type of load regime - L

NL = nonloaded

M = monotonic loading

S = sustained loading

C = cyclic loading

Example: 8-4/P-0.5/M

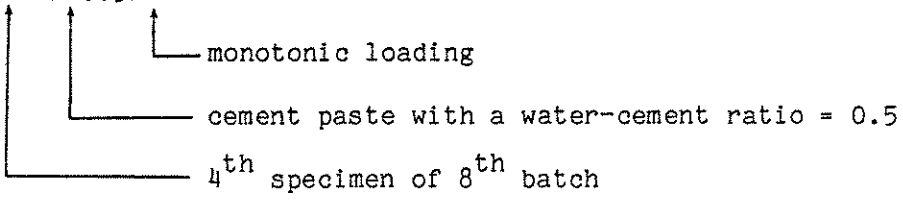

APPENDIX B

NOTATION

a	major semi-axis of an elliptic crack or "characteristic" crack size
a_{min}	smallest characteristic crack size that gives a trace length of ℓ on a plane
a_L	projected length, on longitudinal plane, of the major semi-axis of an elliptic crack
a_T	projected length, on transverse plane, of the major semi-axis of an elliptic crack
$\langle a_\psi \rangle$	mean characteristic crack size for each crack orientation ψ
b	minor semi-axis of an elliptic crack
b_L	projected length, on longitudinal plane, of the minor semi-axis of an elliptic crack
b_T	projected length, on transverse plane, of the minor semi-axis of an elliptic crack
B_L	boundary length per unit area of traces of three-dimensional objects on longitudinal plane
B_T	boundary length per unit area of traces of three-dimensional objects on transverse plane
c_{ij}	elements of compliance matrix in global coordinates
c'_{ij}	elements of compliance matrix in crack coordinates
$[C]$	compliance matrix in global coordinates
$[C']$	compliance matrix in crack coordinates
$C_{k\ell}$	second order tensor used in calculating stress-intensity factors
d_{ij}	elements of stiffness matrix in global coordinates
d'_{ij}	elements of stiffness matrix in crack coordinates
E	stiffness modulus of uncracked material
$\bar{E}$	stiffness modulus of an isotropic cracked material

E_i	stiffness modulus prior to loading
E_{mat}	stiffness modulus of matrix material (material between submicroscopic cracks)
E_1	stiffness modulus in the plane of isotropy, for a transversely isotropic cracked material
E_3	stiffness modulus in the direction of applied stress, for a transversely isotropic cracked material
$f(a\|\psi)$	three-dimensional crack size distribution for each crack orientation ψ
$f(\ell)_T$	modified experimental crack trace length distribution on transverse surface
$f(\ell)_{Tc}$	calculated crack trace length distribution on transverse surface
$f(\ell\|\theta)$	true crack trace length distribution for each trace angle θ
$f(\ell\|\theta)_a$	apparent crack trace length distribution for each trace angle θ
$f(\ell\|\theta)_{ac}$	calculated apparent crack trace length distribution for each trace angle θ
$f(\ell\|\theta)_L$	modified experimental crack trace length distribution on longitudinal surface for each trace angle θ
$f(\ell\|\theta)_{Lc}$	calculated crack trace length distribution on longitudinal surface for each trace angle θ
$f(\theta)$	true crack trace angle distribution
$f(\theta)_a$	apparent crack trace angle distribution
$f(\theta)_{ac}$	calculated apparent crack trace angle distribution
$f(\theta)_L$	modified experimental crack trace angle distribution on longitudinal surface
$f(\theta)_{Lc}$	calculated crack trace angle distribution on longitudinal surface
$f(\psi)$	three-dimensional crack orientation distribution
G	shear modulus of uncracked material
$\bar{G}$	shear modulus of an isotropic cracked material

G_{12}	shear modulus in the plane of isotropy, for a transversely isotropic cracked material
G_{31}	shear modulus in the direction of applied stress, for a transversely isotropic cracked material
h	height of viewing area in SEM
J_1, J_1'	energy release rates associated with Mode I crack deformation in the case of dry and saturated cracks, respectively
J_2	energy release rate associated with Mode II crack deformation
J_3	energy release rate associated with Mode III crack deformation
k_i	generalized notation for stress-intensity factors, K_I, K_{II}, K_{III}
K	measure of degree of anisotropy for three-dimensional crack distributions
K_I	stress-intensity factors for Mode I crack deformation
K_{II}	stress-intensity factors for Mode II crack deformation
K_{III}	stress-intensity factors for Mode III crack deformation
K_f	bulk modulus of fluid in cracks
K_m	bulk modulus of cracked material
ℓ	crack trace length
$\langle \ell \rangle_L$	modified experimental mean crack trace length on longitudinal surface
$\langle \ell \rangle_T$	modified experimental mean crack trace length on transverse surface
$\langle \ell_\theta \rangle$	true mean crack trace length for each trace angle θ
$\langle \ell_\theta \rangle_a$	apparent mean crack trace length for each trace angle θ
$\langle \ell_\theta \rangle_L$	modified experimental mean crack trace length on longitudinal surface for each trace angle θ
m_θ	modified experimental number of cracks per unit area per degree

$\bar{m}_\theta$	measured number of cracks per unit area per degree
M	true number of cracks per unit area
M_a	apparent number of cracks per unit area
$M_{a\theta}$	apparent number of cracks per unit area for each trace angle θ
M_L	modified experimental number of cracks per unit area on longitudinal surface
M_T	modified experimental number of craks per unit area on transverse surface
M_θ	true number of cracks per unit area for each trace angle θ
$\bar{M}_L$	number of cracks per unit area on longitudinal surface before modification
$\bar{M}_T$	number of cracks per unit area on transverse surface before modification
$M_L\langle\ell\rangle_L$	crack density on longitudinal surface
$M_T\langle\ell\rangle_T$	crack density on transverse surface
n	number of cracks in viewing area with a given trace length and trace angle
n_1	number of cracks that lie fully within the viewing area
n_2	number of cracks that lie partially within the viewing area
n_θ	number of cracks in viewing area with a trace angle of $\theta \pm d\theta/2$
N	total number of cracks in viewing area
N_{jk}	second order tensor used in calculating stress-intensity factors
N_V	number of cracks per unit volume
$N_V\langle a^3\rangle$	measure of volumetric crack density
p	distance measured along crack perimeter
p_{jk}	second order tensor used in calculating stress-intensity factors

P_i	applied stress acting on cracked solid
Q_{ij}	second order tensor used in calculating stress-intensity factors
r	crack aspect ratio = b/a
r_L	aspect ratio of crack projection on longitudinal plane
r_T	aspect ratio of crack projection on transverse plane
R	correlation coefficient
R_{jk}	second order tensor used in calculating stress-intensity factors
s	applied normal stress acting on cracked solid; also distance between crack centroid and intersecting plane
s_{max}	maximum value of s for which a plane intersects a crack
s_{jk}	real component of tensor p_{jk}
t_{jk}	imaginary component of tensor p_{jk}
$[T_\varepsilon]$	strain transformation matrix
$[T_\varepsilon]^T$	transpose of strain transformation matrix
$[T_\sigma]$	stress transformation matrix
$[T_\sigma]^T$	transpose of stress transformation matrix
u	crack displacement along major axis
U	Airy's stress function
U_{jk}	real component of tensor N_{jk}
v	applied shear stress acting on cracked solid; also crack displacement normal to crack plane
v_c	volume of crack
$var(a_\psi)$	variance of crack size distribution for each crack orientation ψ
$var(\ell)_T$	modified experimental variance of crack trace length distribution on transverse surface
$var(\ell_\theta)$	true variance of crack trace length distribution for each trace angle θ

$var(\ell_\theta)_a$	apparent variance of crack trace length distribution for each trace angle θ
$var(\ell_\theta)_L$	modified experimental variance of crack trace length distribution on longitudinal surface for each trace angle θ
V	volume of cracked material
V_{jk}	imaginary component of tensor N_{jk}
w	width of viewing area in SEM; also crack displacement along minor axis
w_c	crack width
$W_f(a,\psi)$	crack energy parameter due to fluid within cracks
$W_i(a,\psi)$	crack energy parameter for each load case
x,y,z	local reference frame of crack
x_1,x_2	coordinates of points at which longitudinal and transverse planes intersect boundaries of crack projections
y_1,y_2	distances of center of crack trace from center of viewing area; also coordinates of points at which longitudinal and transverse planes intersect boundaries of crack projections
y_m	y_1 coordinate corresponding to smallest crack size that has a given trace length on longitudinal plane
z_1,z_2	complex variable solutions for equilibrium and compatibility equations
α,β	parameters of gamma distribution
$\alpha_1,\alpha_2,\alpha_3$	real parts of solutions for equilibrium and compatibility equations
β_1,β_2,β_3	imaginary parts of solutions for equilibrium and compatibility equations
γ_{xy}	shear strain associated with Mode II crack deformation
γ_{xz},γ_{yz}	shear strains associated with Mode III crack deformation
$\gamma_{12},\gamma_{23},\gamma_{31}$	shear strains in principal material directions
$\Delta\ell$	interval at which crack trace lengths are recorded

$\Delta\theta$	interval at which crack trace angles are recorded
$\Delta\Phi$	strain energy change due to cracks
$\Delta\Phi_i$	strain energy change due to cracks, for each load case
ε	applied axial (longitudinal) strain
ε_c	strain due to submicroscopic cracks
ε_e	strain due to elastic deformation = σ/E_i
ε_{ec}	elastic strain plus cracking strain = σ/E_3
ε_{mat}	strain in matrix material = σ/E_{mat}
ε_t	lateral strain
ε_v	volumetric strain = $\varepsilon - 2\varepsilon_t$
$\varepsilon_x, \varepsilon_y$	normal strains associated with Modes I and II crack deformations
$\varepsilon_1, \varepsilon_2, \varepsilon_3$	normal strains in principal material directions
η	angular rotation of crack about its normal
η_L	projection of angle η on longitudinal plane
η_T	projection of angle η on transverse plane
θ	crack trace angle
μ_1, μ_2, μ_3	complex roots of equilibrium and compatibility equations
ν	Poisson's ratio of uncracked material
$\bar{\nu}$	Poisson's ratio of an isotropic cracked material
ν_{mat}	Poisson's ratio of matrix material
ν_{12}	Poisson's ratio in the plane of isotropy, for a transversely isotropic cracked material
ν_{31}	Poisson's ratio in a plane perpendicular to the plane of isotropy
ξ	energy change associated with a single crack
ρ	perpendicular distance from crack centroid to a point on the crack perimeter

σ	stress normal to crack plane
σ_f	hydrostatic stress due to fluid within cracks
σ_x, σ_y	normal stresses associated with Modes I and II crack deformations
$\sigma_1, \sigma_2, \sigma_3$	normal stresses in principal material directions
τ	stress tangential to crack plane
τ_{xy}	shear stress associated with Mode II crack deformation
τ_{xz}, τ_{yz}	shear stresses associated with Mode III crack deformation
τ_1, τ_2	perpendicular components of stress which acts tangential to crack plane
$\tau_{12}, \tau_{23}, \tau_{31}$	shear stresses in principal material directions
ϕ	crack angular coordinate which varies in a full circle about the longitudinal axis
Φ	strain energy of uncracked solid under a prescribed loading
Φ_c	strain energy of cracked solid under a prescribed loading
ψ	three-dimensional crack orientation

APPENDIX C
CORRECTION OF WINDOW SIZE DISTORTION OF CRACK DISTRIBUTIONS ON PLANE SECTIONS

C.1 INTRODUCTION

The problem studied here deals with the estimation of true surface distributions from measurements of lengths and angles of cracks (or straws, needles, etc.) on a plane section, where only a portion of the plane section is visible within the field of view, or window. This problem stems from a scanning electron microscope study of load-induced cracks in cement paste and mortar.

The window width, w, is very large and has no effect on the problem (Fig. C.1). However, the window height, h, is finite. Segments of some cracks will therefore lie outside the window, and hence their measured lengths will be shorter than their true lengths, causing the length distribution to be skewed towards low values. A crack whose center is located outside the viewing area may have a portion within the field of view. A crack centered at the same point, but at a lower angle, θ, may lie completely outside the viewing area. The observed or apparent number of cracks at low angles will therefore be relatively lower than the number at high angles, resulting in the angle distribution being skewed towards $\theta = 90°$. This implies that the apparent number of cracks at low angles is less than the true number and the apparent number at high angles is greater than the true number. The true surface distributions of crack length and crack angle on plane sections of opaque bodies are required in order to accurately estimate crack distributions in three-dimensions.

In the following analysis, the concepts of mathematical statistics [31] and geometrical probability [48] are used to establish relationships between the observed or apparent distributions and the true distributions. Procedures are established for estimating the true distributions. Examples based on a study of load-induced cracks in cement paste and mortar are given to illustrate the results of the procedures.

It is shown that the total length of cracks per unit area is unaffected by the window height. A guideline is provided to determine if the window analysis is required for a given window height.

C.2 ESTIMATES OF THE TRUE SURFACE DISTRIBUTIONS OF CRACK LENGTH AND CRACK ANGLE

C.2.1 True Surface Distribution of Crack Length

The derivations that follow are aimed at establishing a relationship between the apparent and true distributions of crack length. The form of the true distribution, as well as its mean and variance, is required. An iterative procedure is used to determine the true distribution.

If $f(\ell,\theta)$ is the true joint relative frequency density of a crack length and angle on a plane, then $f(\ell,\theta)d\ell d\theta$ is the probability that a crack has a true length of $\ell \pm d\ell/2$ and an angle of $\theta \pm d\theta/2$. The true number of such cracks in a unit area is

$$M\, f(\ell,\theta)d\ell d\theta \tag{C.1}$$

in which M is the true number of cracks per unit area. The ranges of ℓ and θ are

$$0 < \ell < \infty$$

$$0 \leq \theta \leq \pi$$

such that

$$\int_0^{\infty} \int_0^{\pi} f(\ell,\theta)d\theta d\ell = 1 \tag{C.2}$$

The number of cracks, n, in the viewing area with a measured length of $\ell_i \pm d\ell/2$ and an angle of $\theta \pm d\theta/2$ is the sum of two components, n_1 and n_2. n_1 is the number of cracks that lie fully within the window and n_2 is the number that lie partially within the window.

In order for cracks with a length of $\ell_i \pm d\ell/2$ and an angle of $\theta \pm d\theta/2$ to lie fully within the viewing area, their centers must not be further than a distance of $\pm y_1$ from the center of the viewing area (see the crack labelled A in Fig. C.1).

$$y_1 = \frac{1}{2}(h - \ell_i \sin\theta) \tag{C.3}$$

in which $\ell_i < h/\sin\theta$.

From Eq. (C.1), $n_1 = M\, f(\ell_i,\theta)d\ell d\theta\; w\; 2y_1 =$

$$M\, w\, (h-\ell_i \sin\theta)\, f(\ell_i,\theta)d\ell d\theta \qquad (C.4)$$

Type B and C cracks (Fig. C.1) contribute to n_2. Type B cracks are those with a measured length equal to $\ell_i \pm d\ell/2$ ($\ell_i < h/\sin\theta$) projecting into the viewing area. Type C cracks are those with a true length of $\ell \geq h/\sin\theta$ and a measured length exactly equal to $h/\sin\theta$ and which have centers not further than a distance of $\pm y_2$ from the window center. Fig. C.1 shows a type C crack which has its center at a distance of y_2 above the window center.

$$y_2 = \frac{1}{2}\,\ell\sin\theta - h/2 \qquad (C.5)$$

The number of type B cracks that have a true length of $\ell \pm d\ell/2$ and an angle of $\theta \pm d\theta/2$ and have tips within a region $d\ell\sin\theta$ wide (i.e., tips within the region $\ell_i\sin\theta \pm d\ell\sin\theta/2$ from the edge of the window) is equal to the number of cracks with centers within a region of the same width. This number is

$$M\, f(\ell,\theta)d\ell d\theta\; w\; d\ell\sin\theta \qquad (C.6)$$

for each edge of the viewing area.

To obtain the total number of type B cracks which contribute to n_2, Eq. (C.6) is integrated for all $\ell \geq \ell_i$ to give

$$2\, M\, w \sin\theta\, d\ell\, d\theta \int_{\ell_i}^{\infty} f(\ell,\theta)d\ell \qquad (C.7)$$

Type C cracks will contribute to n_2 only if cracks with a measured length, ℓ_i, exactly equal to $h/\sin\theta$ are being considered. In this case, the contribution to n_2 of type C cracks with a true length of $\ell \pm d\ell/2$ and an angle of $\theta \pm d\theta/2$ is

$$M\, f(\ell,\theta)d\ell d\theta\; w\; 2y_2 \qquad (C.8)$$

The total number of type C cracks is obtained by integrating Eq. (C.8) for all $\ell \geq h\sin\theta$ to give

$$M\ w\ d\theta \int_{h/\sin\theta}^{\infty} (\ell\sin\theta - h) f(\ell,\theta) d\ell \tag{C.9}$$

If h is not large enough in relation to the mean crack length for a particular angle, the number of type C cracks [given by Eq. (C.9)] will appear as a spike at $h/\sin\theta$ in the measured length distribution for the given angle (Fig. C.2). A spike cannot be handled adequately with this analysis. The absence of a spike (implying a negligible number of type C cracks) is desirable and indicates that the window height is adequate for the cracks being measured; (i.e. few cracks have a length of $\ell > h/\sin\theta$).

In the absence of a significant number of type C cracks, the number of cracks in the viewing area with a measured length of $\ell_i \pm d\ell/2$ and an angle of $\theta \pm d\theta/2$ is obtained by summing Eq. (C.4) and (C.7).

$$n = Mw(h-\ell_i\sin\theta) f(\ell_i,\theta) d\ell d\theta + 2Mw\sin\theta d\ell d\theta \int_{\ell_i}^{\infty} f(\ell,\theta) d\ell \tag{C.10a}$$

or

$$n = Mwd\theta\left[(h-\ell_i\sin\theta) f(\ell_i,\theta) + 2\sin\theta \int_{\ell_i}^{\infty} f(\ell,\theta) d\ell\right] d\ell \tag{C.10b}$$

If $f(\ell|\theta)_a$ is the apparent relative frequency density of a measured length for a given angle, then $f(\ell_i|\theta)_a d\ell$ is the probability that a crack has a measured length of $\ell_i \pm d\ell/2$ for a given θ.

$$f(\ell_i|\theta)_a d\ell = \frac{\text{Number of cracks with } \ell_i \pm d\ell/2,\ \theta \pm d\theta/2}{\text{Number of cracks with } \theta \pm d\theta/2} = \frac{n}{n_\theta} \tag{C.11}$$

The number of cracks for a particular angle is obtained by integrating Eq. (C.10b) for all ℓ. The number of cracks with $\theta \pm d\theta/2$ is

$$n_\theta = M\ w\ d\theta \int_o^{\infty} \left[(h-\ell\sin\theta) f(\ell,\theta) + 2\sin\theta \int_{\ell}^{\infty} f(\ell,\theta) d\ell\right] d\ell \tag{C.12}$$

Eq. (C.12) can be simplified using the following statistical relation [31].

$$f(\ell,\theta) = f(\ell|\theta)\ f(\theta) \tag{C.13}$$

in which $f(\ell|\theta)$ is the true relative frequency density of a crack length for a given angle and $f(\theta)$ is the true relative frequency density of a crack

angle. Substituting Eq. (C.13) into Eq. (C.12), the number of cracks with $\theta \pm d\theta/2$ is

$$n_\theta = M\ w\ f(\theta)\ d\theta \int_o^\infty \left[(h-\ell\sin\theta)f(\ell|\theta) + 2\sin\theta \int_\ell^\infty f(\ell|\theta)d\ell\right]d\ell \qquad (C.14)$$

Eq. (C.14) can be further simplified by using the technique of integration by parts to show that

$$\int_o^\infty \ell f(\ell|\theta)d\ell = \int_o^\infty \int_\ell^\infty f(\ell|\theta)d\ell d\ell \qquad (C.15)$$

Substituting Eq. (C.15) into Eq. (C.14), the number of cracks with $\theta \pm d\theta/2$ is

$$n_\theta = M\ w\ f(\theta)d\theta\left[h \int_o^\infty f(\ell|\theta)d\ell + \sin\theta \int_o^\infty \ell f(\ell|\theta)d\ell\right] \qquad (C.16)$$

However in Eq. (C.16), $\int_o^\infty f(\ell|\theta)d\ell = 1$, and $\int_o^\infty \ell f(\ell|\theta)d\ell$ is the true mean crack length at θ; i.e. $\langle\ell_\theta\rangle = \int_o^\infty \ell f(\ell|\theta)d\ell$. Hence the number of cracks with angle $\theta \pm d\theta/2$ is

$$n_\theta = M\ w\ f(\theta)d\theta(h + \langle\ell_\theta\rangle\sin\theta) \qquad (C.17)$$

The statistical relation expressed in Eq. (C.13) is substituted into Eq. (C.10b) to give

$$n = M\ w\ f(\theta)d\theta\left[(h-\ell_i\sin\theta)f(\ell_i|\theta) + 2\sin\theta\int_{\ell_i}^\infty f(\ell|\theta)d\ell\right]d\ell \qquad (C.18)$$

Substitution of Eq. (C.17) and (C.18) into Eq. (C.11) yields

$$f(\ell_i|\theta)_a = \frac{(h-\ell_i\sin\theta)f(\ell_i|\theta) + 2\sin\theta\int_{\ell_i}^\infty f(\ell|\theta)d\ell}{h + \langle\ell_\theta\rangle\sin\theta} \qquad (C.19)$$

In Eq. (C.19), ℓ may be substituted in place of ℓ_i, since the expression is valid for any measured length.

$$f(\ell|\theta)_a = \frac{(h-\ell\sin\theta)f(\ell|\theta) + 2\sin\theta\int_\ell^\infty f(\ell|\theta)d\ell}{h + \langle\ell_\theta\rangle\sin\theta} \qquad (C.20)$$

The apparent mean crack length at θ is given by

$$\langle \ell_\theta \rangle_a = \int_0^\infty \ell f(\ell|\theta)_a d\ell \tag{C.21}$$

By substituting Eq. (C.20) into Eq. (C.21) and evaluating the integral, the true mean crack length at θ can be determined in terms of a measurable quantity, $\langle \ell_\theta \rangle_a$.

$$\langle \ell_\theta \rangle = \frac{h\langle \ell_\theta \rangle_a}{h - \langle \ell_\theta \rangle_a \sin\theta} \tag{C.22}$$

in which h must be greater than $\langle \ell_\theta \rangle_a \sin\theta$.

The variance of the apparent length distribution for a given θ can be expressed as

$$\text{var}(\ell_\theta)_a = \int_0^\infty (\ell - \langle \ell_\theta \rangle_a)^2 f(\ell|\theta)_a d\ell \tag{C.23}$$

Substituting Eq. (C.20) into Eq. (C.23) and evaluating the integral, the variance of the true length distribution for a given θ is

$$\text{var}(\ell_\theta) = \frac{\langle \ell_\theta \rangle}{\langle \ell_\theta \rangle_a} \text{var}(\ell_\theta)_a - \langle \ell_\theta \rangle(\langle \ell_\theta \rangle - \langle \ell_\theta \rangle_a) + \frac{\sin\theta}{3h} \int_0^\infty \ell^3 f(\ell|\theta) d\ell \tag{C.24}$$

In Eq. (C.24), $\langle \ell_\theta \rangle_a$ and $\text{var}(\ell_\theta)_a$ are respectively the mean and variance of the apparent length distribution and are therefore known quantities.

In order to estimate the true crack length distribution, $f(\ell|\theta)$, the form of $f(\ell|\theta)$, mean crack length, $\langle \ell_\theta \rangle$, and variance, $\text{var}(\ell_\theta)$, must be known. $\langle \ell_\theta \rangle$ can be obtained from Eq. (C.22). The form and variance of $f(\ell|\theta)$, however, cannot be obtained directly, requiring the use of an iterative procedure. The objective of the procedure is to calculate an apparent distribution based on an assumed form of the true distribution. If a close match is obtained between the known (experimental) and calculated apparent distributions, then the assumed form of the true distribution is the correct one. Since only some of the true crack lengths will be longer than their corresponding measured lengths, as an initial guess, it is reasonable to

assume that the true length distribution, $f(\ell|\theta)$, is similar in form to the known apparent length distribution.

The procedure for estimating the true length distribution is outlined as follows.

1. Assume that $f(\ell|\theta)$ is similar in form to the known apparent length distribution.
2. The mean and variance of $f(\ell|\theta)$ are $\langle \ell_\theta \rangle$ and $\text{var}(\ell_\theta)$, respectively. $\langle \ell_\theta \rangle$ is obtained from Eq. (C.22). As an initial guess, assume that $\text{var}(\ell_\theta) = \text{var}(\ell_\theta)_a$.
3. Calculate the true variance, $\text{var}(\ell_\theta)$, using Eq. (C.24).
4. If the computed variance is not equal to the assumed variance, recompute $\text{var}(\ell_\theta)$ from Eq. (C.24) using the variance calculated in Step 3.
5. Repeat Steps 3 and 4 until the assumed and computed variances are equal.
6. Substitute $f(\ell|\theta)$, with parameters $\langle \ell_\theta \rangle$ and $\text{var}(\ell_\theta)$, into Eq. (C.20) in order to calculate $f(\ell|\theta)_a$.
7. A "goodness of fit" test, based on the chi-square distribution [31], is used to determine if there is a close agreement between the known and calculated apparent distributions. A close agreement implies that a good estimate of $f(\ell|\theta)$ has been obtained.
8. If the "goodness of fit" test fails, assume a true distribution with a different form. Repeat Steps 2 to 7.

An example based on a study of load-induced cracks in cement paste and mortar is presented in Section C.2.3 to illustrate the results of the above procedure.

C.2.2 True Surface Distribution of Crack Angle

In the following derivation, a relationship is established between the apparent and true distributions of crack angles. An iterative procedure is described for determining the true distribution.

If $f(\theta)_a$ is the apparent relative frequency density of a measured angle, then $f(\theta)_a d\theta$ is the probability that an observed crack has a measured angle of $\theta \pm d\theta/2$.

$$f(\theta)_a d\theta = \frac{\text{Number of cracks with } \theta \pm d\theta/2}{\text{Number of cracks for all } \theta} = \frac{n_\theta}{N} \qquad \text{(C.25)}$$

The number of cracks with an angle of $\theta \pm d\theta/2$ is given by Eq. (C.17) as

$$n_\theta = M\, w\, f(\theta)d\theta(h + \langle \ell_\theta \rangle \sin\theta) \tag{C.26}$$

Integrating Eq. (C.26), the number of cracks for all θ is

$$N = M\, w \int_0^\pi (h + \langle \ell_\theta \rangle \sin\theta) f(\theta) d\theta \tag{C.27}$$

By noting that $\int_0^\pi f(\theta)d\theta = 1$, Eq. (C.27) is simplified to become:

$$N = M\, w\left[h + \int_0^\pi \langle \ell_\theta \rangle \sin\theta\, f(\theta)d\theta\right] \tag{C.28}$$

Substituting Eq. (C.26) and (C.28) into Eq. (C.25),

$$f(\theta)_a = \frac{(h + \langle \ell_\theta \rangle \sin\theta) f(\theta)}{h + \int_0^\pi \langle \ell_\theta \rangle \sin\theta\, f(\theta)d\theta} \tag{C.29}$$

In Eq. (C.29), the true angle distribution, $f(\theta)$, is the only unknown. An iterative procedure is used to estimate $f(\theta)$. The objective of the procedure is similar to that in the case of the length distribution. An apparent distribution is calculated based on an assumed expression for the true angle distribution. If a close match is obtained between the known and calculated apparent distributions, then the assumed expression for the true distribution is the correct estimate.

The procedure for estimating the true angle distribution is outlined as follows.

1. Assume an expression for $f(\theta)$. As described in the introduction, the true number of cracks at low angles will be greater than the apparent number and the true number at high angles will be less than the apparent number. This information serves as a guide in determining an assumed expression for $f(\theta)$.
2. Compute $f(\theta)_a$ using Eq. (C.29).
3. A "goodness of fit" test, based on the chi-square distribution, is used to determine if there is a close agreement between the known and calculated apparent distributions.

4. Repeat Steps 1 to 3 until the "goodness of fit" test in Step 3 is successful. The true angle distribution which satisfies the test is the correct estimate of $f(\theta)$.

In the following section, examples based on a study of load-induced cracks in cement paste and mortar are presented in order to illustrate the results of the procedures for obtaining the true length and angle distributions.

C.2.3 Examples

The examples presented in this section are based on the results obtained in a study of load-induced cracks in cement paste and mortar.

Cement paste and mortar specimens are loaded in compression to selected stress levels and then unloaded. Fractured surfaces of the loaded specimens are then viewed in a scanning electron microscope (SEM). Within the SEM, the fractured surfaces are scanned horizontally, and crack lengths and angles are measured at a magnification of 1250x. Only the portions of cracks within the field of view are measured in order to obtain an accurate estimate of the density of cracks within the scanned areas. Apparent distributions of crack length and crack angle are obtained from the data. Typical apparent distributions are represented by the histograms in Fig. C.3 and C.4. The particular length distribution illustrated represents cracks measured at angles, θ, between 47.5° and 52.5°. Angles of θ and $180°-\theta$ are grouped together. The data in the histograms, along with the results of the analysis, are summarized in Tables C.1 and C.2.

The procedures described in Sections C.2.1 and C.2.2 are used to obtain calculated apparent distributions. Calculations are performed using a computer, and all integrals are numerically evaluated using Gaussian quadrature [72]. Four integration points over a length range of 0.0 to 0.006 in. are sufficient for these results. A level of significance of 0.05 is used for the "goodness of fit" tests.

The calculated apparent length distribution, $f(\ell|\theta)_a$, is obtained by assuming that the true length distribution, $f(\ell|\theta)$, has the form of a gamma distribution. This form of distribution gives a close match between the calculated apparent distribution and the histogram, as shown in Fig. C.3. As expected, the estimated true length distribution is shifted to the right of the apparent distribution.

In Fig. C.4, it is observed that the known apparent angle distribution (the histogram) has spikes near 0° and 90°. These spikes are mainly due to specimen preparation (sawing, drying, and fracturing) prior to viewing in the SEM. In using the procedure described in section C.2.2 to determine the true angle distribution, $f(\theta)$, trial expressions need to be assumed for $f(\theta)$. Due to the discontinuous form of the known apparent distribution, constant functions are assumed for $f(\theta)$ from 0° to 2.5° and from 87.5° to 90°, while a quadratic function is assumed over the middle eighty-five degree range. This form of $f(\theta)$, as shown in Fig. C.4, gives a close match between the calculated apparent distribution and the histogram. A comparison of the true and the apparent angle distributions in Fig. C.4 shows that, as expected, the true number of cracks at low angles is greater than the apparent number and the true number at high angles is less than the apparent number.

C.3 ESTIMATE OF THE TRUE NUMBER OF CRACKS PER UNIT AREA

As explained in the introduction and illustrated in the example (Fig. C.4), the apparent number of cracks at low angles is less than the true number and the apparent number at high angles is greater than the true number. The apparent number of cracks per unit area should, therefore, not be expected to equal the actual number of cracks per unit area. In the following analysis, the true number of cracks per unit area is estimated.

The apparent number of cracks on a plane section is given by Eq. (C.28) as

$$N = M\, w\left[h + \int_0^{\pi} \langle \ell_\theta \rangle \sin\theta f(\theta) d\theta\right] \tag{C.30}$$

Rearranging Eq. (C.30), the true number of cracks per unit area, M, is

$$M = \frac{N}{w\left[h + \int_0^{\pi} \langle \ell_\theta \rangle \sin\theta f(\theta) d\theta\right]} \tag{C.31}$$

The apparent number of cracks per unit area, M_a, is given by

$$M_a = \frac{N}{w\, h} \tag{C.32}$$

By comparing Eq. (C.31) and (C.32), it is noted that $M_a > M$. This observation may be intuitive by examination of Fig. C.1. It may also be easily demonstrated by referring to Fig. C.5. In the figure, a plane section of unit area is shown with eight cracks, i.e. $M = 8$. If the hatched area is not visible within the field of view, the two horizontal cracks in this area will be completely invisible. The apparent number of cracks within the window will be 6 and the apparent number per unit area will be

$$M_a = \frac{6}{(1)(1/2)} = 12$$

Hence, $M_a > M$. The effect of a finite window size is therefore to overestimate the number of cracks per unit area on a plane section.

C.4 TOTAL LENGTH OF CRACKS PER UNIT AREA

The following proof shows that the total length of all cracks per unit area is unaffected by the window height.

The number of cracks with an angle of $\theta \pm d\theta/2$ is given by Eq. (C.17) as

$$n_\theta = M\, w\, f(\theta)d\theta(h + \langle \ell_\theta \rangle \sin\theta) \tag{C.33}$$

The apparent number of cracks per unit area with an angle of $\theta \pm d\theta/2$ is

$$M_{a\theta} = \frac{n_\theta}{wh} \tag{C.34}$$

Substituting Eq. (C.33) into Eq. (C.34),

$$M_{a\theta} = \frac{1}{h}[Mf(\theta)d\theta(h + \langle \ell_\theta \rangle \sin\theta)] \tag{C.35}$$

Eq. (C.22) for $\langle \ell_\theta \rangle$ is substituted into Eq. (C.35) to obtain

$$M_{a\theta} = \frac{1}{h}\left[Mf(\theta)d\theta\left(h + \frac{h\langle \ell_\theta \rangle_a}{h - \langle \ell_\theta \rangle_a \sin\theta}\right)\sin\theta\right] \tag{C.36}$$

Multiplying both sides of Eq. (C.36) by $\langle \ell_\theta \rangle_a$ and simplifying, the apparent total length per unit area of cracks with an angle of $\theta \pm d\theta/2$ is

$$M_{a\theta} \langle \ell_\theta \rangle_a = Mf(\theta)d\theta \frac{h\langle \ell_\theta \rangle_a}{h - \langle \ell_\theta \rangle_a \sin\theta} \tag{C.37}$$

The true total length per unit area of cracks with an angle of $\theta \pm d\theta/2$ is

$$M_\theta \langle \ell_\theta \rangle = Mf(\theta)d\theta \langle \ell_\theta \rangle \tag{C.38}$$

Substitution of Eq. (C.22) for $\langle \ell_\theta \rangle$ into the right hand side of the above equation gives

$$M_\theta \langle \ell_\theta \rangle = Mf(\theta)d\theta \frac{h\langle \ell_\theta \rangle_a}{h - \langle \ell_\theta \rangle_a \sin\theta} \tag{C.39}$$

The right hand sides of Eq. (C.37) and (C.39) are identical. Hence,

$$M_{a\theta} \langle \ell_\theta \rangle_a = M_\theta \langle \ell_\theta \rangle \tag{C.40}$$

Since Eq. (C.40) is true for all θ, it follows that the total length of all cracks per unit area is unaffected by the window height.

C.5 DETERMINING IF THE WINDOW ANALYSIS IS REQUIRED

The following discussion addresses the question of how big the window height, h, must be so that the apparent and the true crack distributions are approximately the same. Eq. (C.22), which relates the apparent and the true mean crack lengths, provides a guide in answering this question.

The true mean crack length is expressed in Eq. (C.22) as

$$\langle \ell_\theta \rangle = \frac{h\langle \ell_\theta \rangle_a}{h - \langle \ell_\theta \rangle_a \sin\theta} \tag{C.41}$$

in which h must be greater than $\langle \ell_\theta \rangle_a \sin\theta$. Eq. (C.41) is rearranged to become

$$\frac{\langle \ell_\theta \rangle_a}{\langle \ell_\theta \rangle} = 1 - \frac{1}{h/\langle \ell_\theta \rangle_a \sin\theta} \tag{C.42}$$

The relationship expressed in Eq. (C.42) is shown in Fig. C.6, and it indicates that for the apparent and the true mean crack lengths to be approximately the same, the ratio of the window height to the projected height of the apparent mean crack length must be extremely large.

For the apparent and the true distributions to be exactly the same, the total plane surface must be visible within the window. In practical situations involving the use of microscopes, the window height will be small in comparison to the height of the plane surface under view. This is because portions of the plane surface may have to be viewed at a high magnification in order to obtain a good resolution. Hence, correction of the window size distortion of the surface distributions may be required in most practical situations. However, if the ratio $h/\langle \ell_\theta \rangle_a \sin\theta$ is very large for all θ, the differences between the apparent and the true crack parameters may be so small that the correction may not be needed. For example, as Eq. (C.42) indicates, if $h/\langle \ell_\theta \rangle_a \sin\theta = 100$, the difference between the apparent and the true mean crack lengths is only 1%.

For a given window height and an apparent mean length of cracks with an angle of θ, Eq. (C.42), therefore, provides a guide to determine if the window size distortion needs to be corrected. In border line cases, it is possible that a given window size, h, may be satisfactory for lower values of θ, but may be too narrow for higher values.

C.6 SUMMARY

True distributions of cracks (or straws, needles, etc.) on a plane section may not be obtained directly if only a portion of the plane section is visible within the field of view. The procedures used to estimate the true distributions are presented. These procedures are based on the concepts of geometrical probability and statistics. Relationships are established between the observed and the true distributions, and iterative techniques are employed to estimate the true distributions. For a given window height, a guideline is provided to determine if the window size distortion needs to be corrected.

It is shown that the total length of cracks per unit area on a plane section is not affected by the window size.

True estimates of crack parameters on plane sections of opaque bodies are required if crack parameters in three-dimensions are to be accurately estimated.

TABLE C.1

LENGTH DISTRIBUTION DATA FOR CRACK ANGLES, θ, FROM 47.5° to 52.5°.

Observed Dist. : $\langle \ell_\theta \rangle_a = 0.98\times10^{-3}$in. $\quad \mathrm{var}(\ell_\theta)_a = 2.80\times10^{-7}$in.^{2}

True Dist. : $\langle \ell_\theta \rangle = 1.22\times10^{-3}$in. $\quad \mathrm{var}(\ell_\theta) = 2.45\times10^{-7}$in.^{2}

$f(\ell|\theta) = 1.23\times10^{20}\ \ell^5\ e^{-4953\ell}$

Length, 10^{-3}in.	Relative Frequency Density, in.$^{-1}$		
	Observed	Calculated Apparent	True
0.00	0.0	310.9	0.0
0.15	0.0	313.7	4.4
0.30	555.6	357.3	67.7
0.45	555.6	477.1	244.4
0.60	954.9	631.6	489.9
0.75	740.7	749.7	711.3
0.90	740.7	788.8	841.9
1.05	555.6	747.8	865.7
1.20	740.7	650.9	802.9
1.35	341.6	528.4	688.3
1.50	505.6	405.0	554.5
1.65	0.0	295.5	424.8
1.80	475.6	206.8	312.2
1.95	120.0	140.5	221.6
2.10	200.2	92.2	152.7
2.25	0.0	58.8	102.6
2.40	170.2	36.5	67.4

TABLE C.2. ANGLE DISTRIBUTION DATA.

$$f(\theta) = \begin{cases} 1.85\times10^{-2} & 0°\leq\theta\leq2.5° \\ -1.42\times10^{-6}\theta^2 + 1.07\times10^{-4}\theta + 3.72\times10^{-3} & 2.5°\leq\theta\leq87.5° \\ 1.50\times10^{-2} & 87.5°\leq\theta\leq90° \end{cases}$$

Angle,	Relative Frequency Density, 10^{-2} deg.$^{-1}$		
degrees	Observed	Calculated Apparent	True
1.25	1.429	1.428	1.850
5.00	0.275	0.273	0.422
10.00	0.385	0.337	0.465
15.00	0.220	0.394	0.501
20.00	0.495	0.443	0.529
25.00	0.330	0.486	0.551
30.00	0.549	0.521	0.565
35.00	0.549	0.550	0.573
40.00	0.604	0.571	0.573
45.00	0.533	0.585	0.566
50.00	0.659	0.592	0.552
55.00	0.440	0.592	0.531
60.00	0.672	0.585	0.503
65.00	0.604	0.571	0.468
70.00	0.385	0.549	0.425
75.00	0.549	0.521	0.376
80.00	0.495	0.485	0.319
85.00	0.385	0.443	0.256
88.75	1.813	1.813	1.500

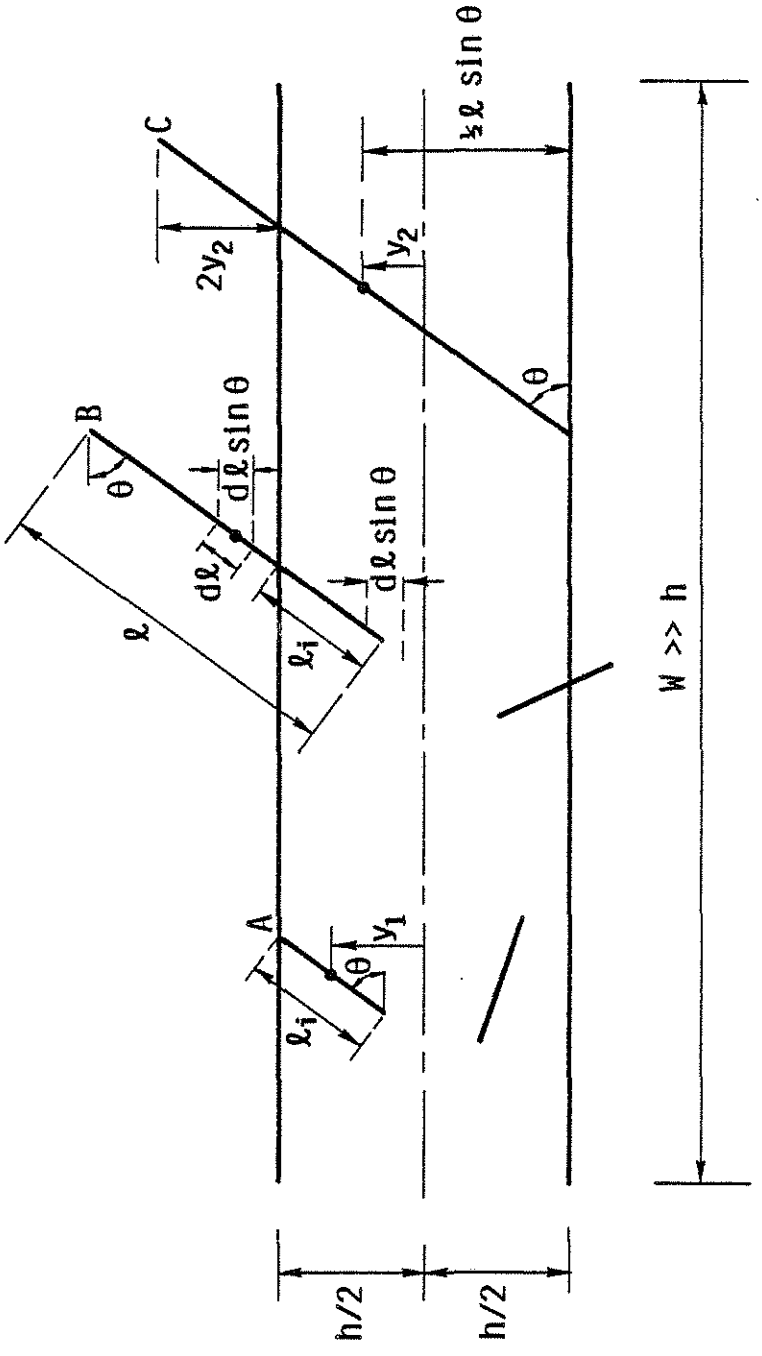

Fig. C.1. Cracks Viewed Through Window

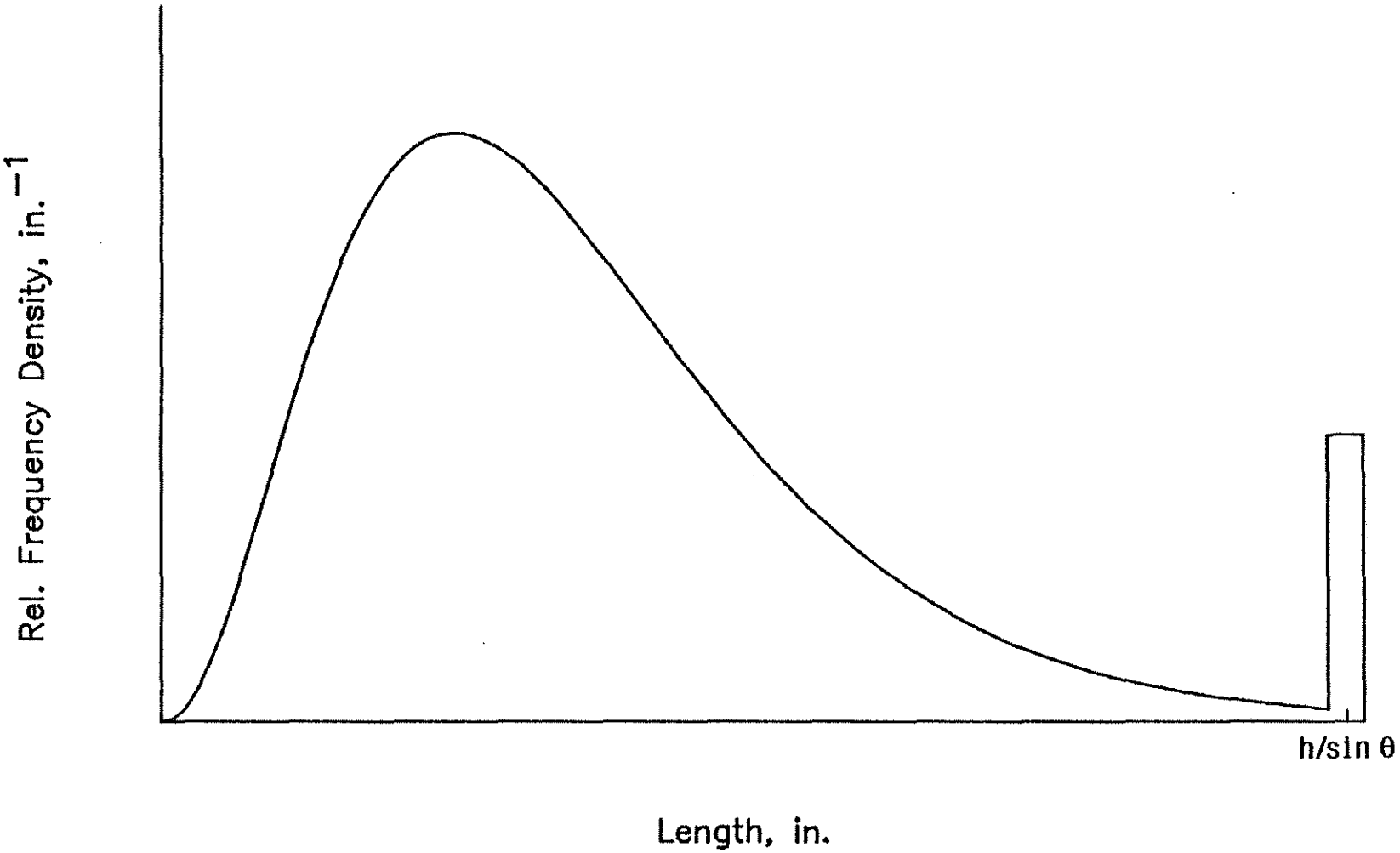

Fig. C.2. Measured Length Distribution for a Given θ, where the Window Height is Too Small

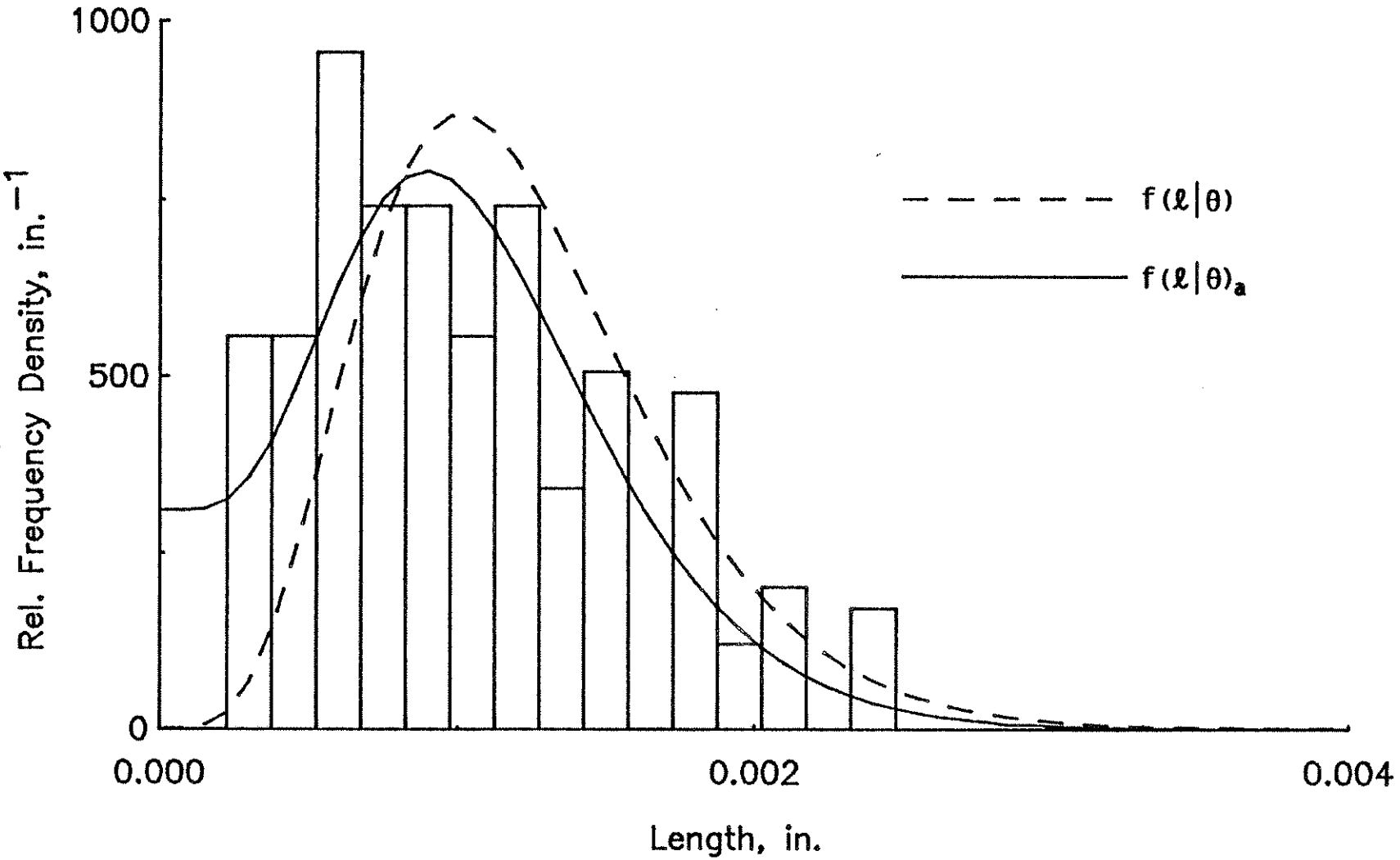

Fig. C.3. Apparent and True Length Distributions

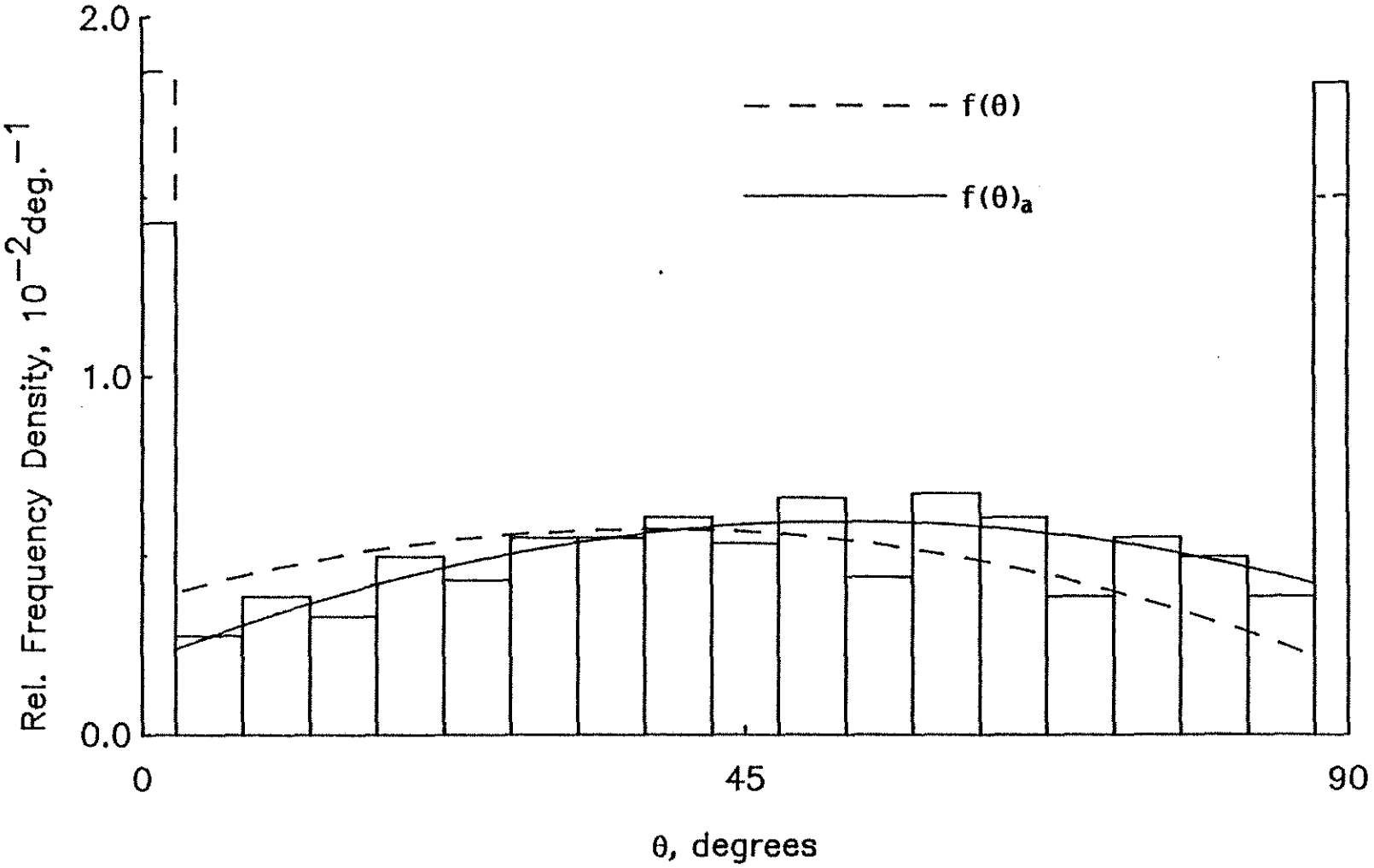

Fig. C.4. Apparent and True Angle Distributions

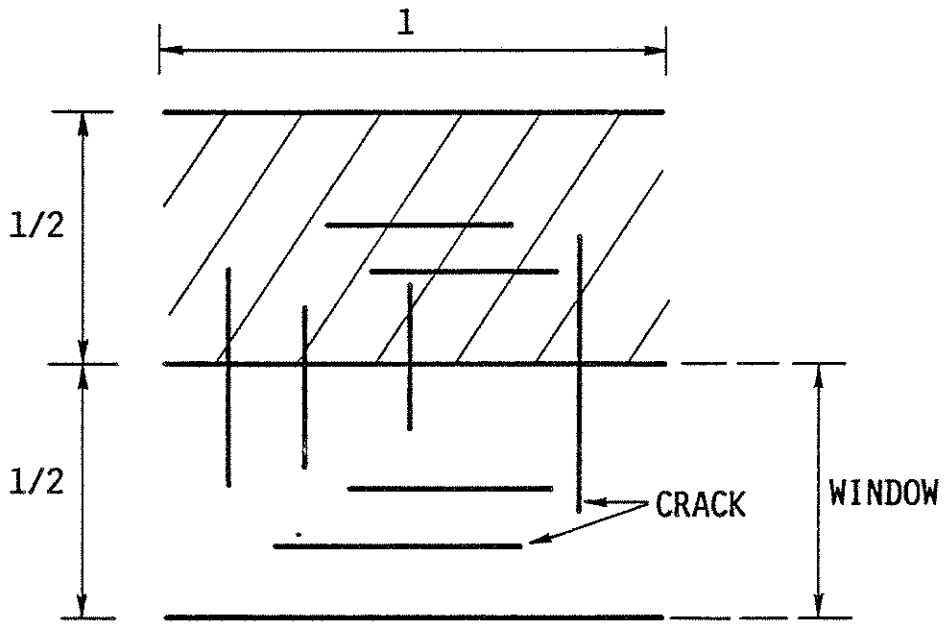

Fig. C.5. Cracks on a Plane Section

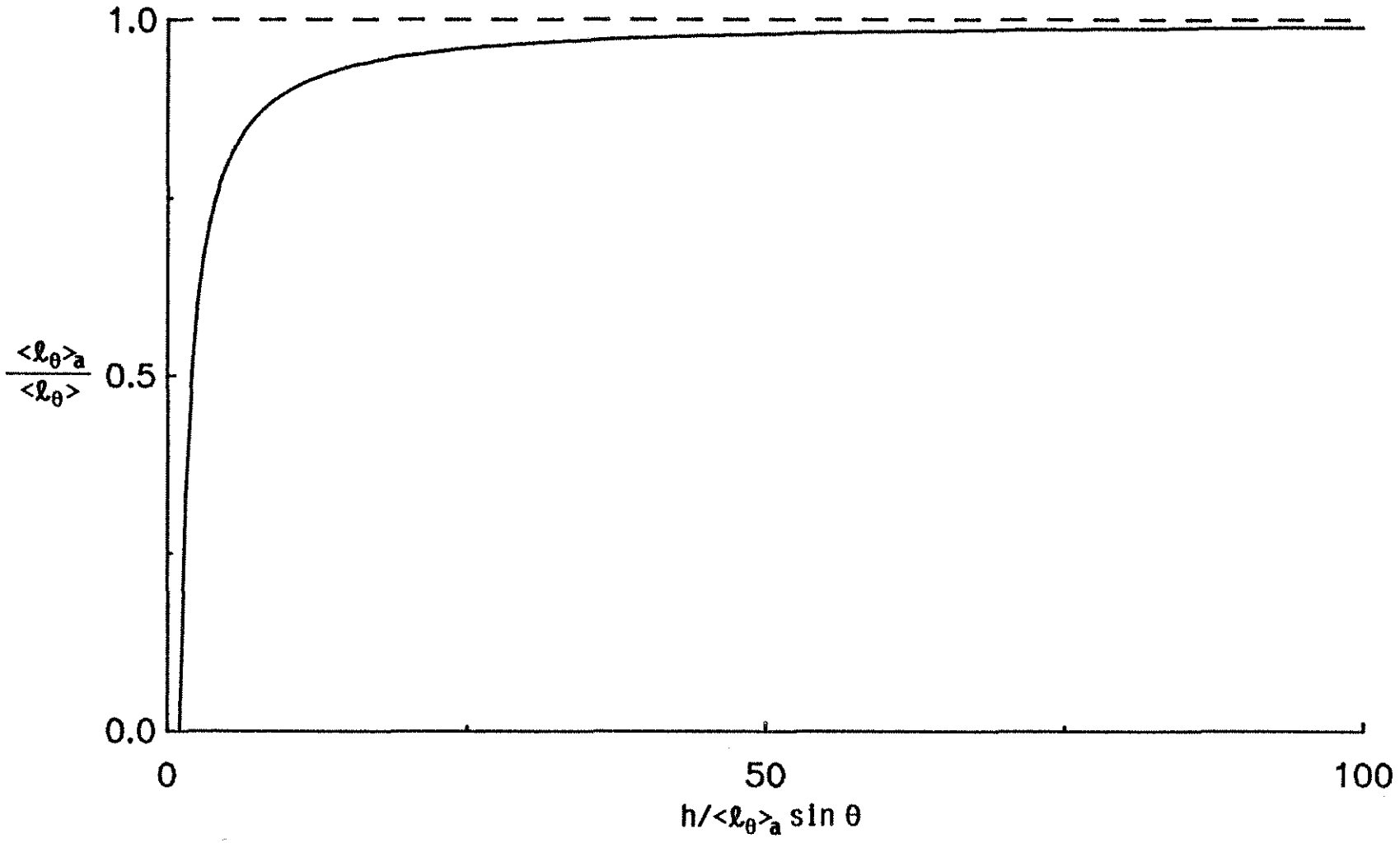

Fig. C.6. Variation of Apparent Mean Length with Window Height

APPENDIX D
CONVERSION OF CRACK DISTRIBUTIONS ON PLANE SECTIONS TO SPATIAL DISTRIBUTIONS

D.1 INTRODUCTION

The analysis presented here involves the conversion of crack trace distributions on plane sections of a transversely isotropic body to three-dimensional crack distributions. In such a body, the orientation and size distributions of cracks are symmetric about one axis of the body. The cracked body is assumed to be opaque so that only crack traces on the exterior of the body can be obtained experimentally. This analysis was developed as part of a study of load-induced cracks in cement paste and mortar, in which an estimate of the three-dimensional crack distribution was required to gain a full understanding of the material response.

A number of investigators [1,25,26,36,44,60,74,83,99] have used the concepts of stereology to develop methods for determining numerical densities and size distributions of inclusions from information obtained on plane sections of a structure. These methods are mainly applicable to systems in which the orientation distributions of the inclusions are isotropic with respect to the structure space [98]. In an isotropic system of inclusions or cracks, all orientations occur with equal likelihood and size distribution is independent of orientation. Weibel [98] has shown how the orientation distribution of inclusions in a transversely isotropic body can be estimated from information obtained on two mutually perpendicular plane sections of the body. Seaman, Curran and Crewdson [75] extended the method of Kaechele and Tetelman [44] to establish a statistical procedure to transform observed crack traces on a single plane section of a transversely isotropic body to a spatial crack distribution. The procedure is limited to circular cracks with a size distribution that is independent of crack orientation.

The current study establishes an iterative procedure for estimating spatial crack distributions for transversely isotropic systems. The crack size distribution can vary with orientation. The cracks are assumed to have a general elliptic planform. The analysis may also apply to similarly shaped inclusions. An example based on a study of load-induced cracks in

cement paste and mortar is provided to illustrate the results of the procedure.

D.2 OVERVIEW OF THE METHOD OF ANALYSIS

In this analysis, the concepts of mathematical statistics [31], geometrical probability [48] and stereology [94,98] are used to establish relationships between spatial distributions of crack size and orientation and surface distributions of crack trace length and angle on plane sections. First, each relationship is obtained in a form which is valid for a structure in which the size and the orientation distributions of the cracks are generally anisotropic with respect to the structure space. Relevant assumptions are made to reduce the general relationships to simpler forms which are valid for a transversely isotropic system of cracks. The derivations are presented in terms of continuous frequency distribution functions. The distribution functions of crack trace lengths and angles are those that describe crack distributions on two mutually perpendicular plane sections of a cracked body. The plane sections are the longitudinal and the transverse planes which are respectively parallel and perpendicular to the longitudinal (or loading) axis of a cracked body (Fig. D.1). For a transversely isotropic system, the longitudinal axis is the axis of symmetry for the crack size and orientation distributions.

To obtain the three-dimensional crack parameters for a transversely isotropic system, the orientation distribution of the cracks must be determined. In this regard, a Marriott distribution function [98], which describes the orientation distribution of transversely isotropic systems with mild degrees of anisotropy, is assumed. This distribution has the property that it can be determined from a knowledge of the length of crack traces on longitudinal and transverse plane sections. The solution procedure is not limited to any particular form of trace length or size distribution.

The geometric expressions which are required to establish relationships between spatial and surface distributions are derived in Appendix E.

D.3 RELATIONSHIPS BETWEEN 2-D AND 3-D CRACK DISTRIBUTIONS

In this study, each crack is assumed to be elliptic, as shown in Fig. D.1, with a major semi-axis length of a and a minor semi-axis length of b.

The size of an elliptic crack will be represented by the length of its major axis. The length of the major semi-axis, a, is therefore designated as the "characteristic crack size". The aspect ratio of the crack, r, is defined as the ratio b/a, and its value is assumed to be same for all cracks. The aspect ratio varies between 0 and 1. A value of 1 indicates a circular crack.

ψ, ϕ and η are the angular coordinates of the crack. ψ is the angle between the plane of the crack and the transverse plane; it is also the angle that the normal to the crack surface makes with the longitudinal axis of the body. ϕ is the angle between a plane defined by the projection, on a transverse plane, of the normal to the crack and the longitudinal axis and a selected longitudinal plane. ϕ varies in a full circle about the longitudinal axis. The angle η defines the degree of rotation of the crack about its normal. For $\eta = 0$, the plane defined by the major axis of the crack and the crack normal is parallel to the longitudinal axis and perpendicular to the transverse plane, while $\eta = \pi/2$ when the major axis is parallel to the transverse plane. For a circular crack ($r = 1$), η is not defined since every axis of the crack is a major axis.

When a plane intersects a crack, a crack trace length, ℓ, and angle, θ, are obtained, as shown in Fig. D.2 for a longitudinal plane intersecting an elliptic crack. The crack angle, θ, on a transverse plane is equal to $\phi \pm \pi/2$, as can be seen in Fig. D.3.

If $f(a,\psi,\phi,\eta)$ is the joint relative frequency density of crack size and orientation, then $f(a,\psi,\phi,\eta)da d\psi d\phi d\eta$ is the probability that a crack has a major semi-axis length of $a \pm da/2$ and an orientation of $\psi \pm d\psi/2$, $\phi \pm d\phi/2$, $\eta \pm d\eta/2$. The number of such cracks in a unit volume is

$$N_V \, f(a,\psi,\phi,\eta)da d\psi d\phi d\eta \qquad (D.1)$$

in which N_V is the total number of cracks per unit volume. The ranges of a, ψ, ϕ and η are

$$0 < a < \infty$$

$$0 \leq \psi \leq \pi/2$$

$$0 \leq \phi \leq 2\pi$$

$$-\eta' \leq \eta \leq \eta'$$

such that

$$\int_{-\eta'}^{\eta'} \int_0^{2\pi} \int_0^{\pi/2} \int_0^{\infty} f(a,\psi,\phi,\eta)\,da\,d\psi\,d\phi\,d\eta = 1 \qquad (D.2)$$

In the discussions that follow, the relationship of spatial distributions to surface angle distributions are derived first, followed by relationships to surface length distributions. Finally, the total number of cracks per unit volume, N_V, is estimated from the total length of cracks per unit area on longitudinal and transverse planes. In a subsequent section, these relationships will be used to obtain an estimate of spatial distributions based on observed surface distributions.

D.3.1 Relationships between Spatial Distributions and Surface Angle Distributions

D.3.1.1 Longitudinal Plane

For a crack which intersects a given plane, s is the distance between the crack centroid and the plane, and s_{max} is the maximum distance for which an intersection can be obtained. s_{max} is a function of a, ψ, ϕ and η; i.e. $s_{max} = s_{max}(a,\psi,\phi,\eta)$. The expression for s_{max} is given later in this section.

The number of cracks with given values of a, ψ, ϕ and η which intersect a longitudinal plane of unit area and therefore lie within a distance of $s \leq s_{max}$ from both sides of the plane is

$$2\,N_V\,f(a,\psi,\phi,\eta)\,da\,d\psi\,d\phi\,d\eta\,s_{max} \qquad (D.3)$$

For all a, ψ, ϕ and η, the number of cracks with an angle of $\theta \pm d\theta/2$ on the plane is

$$\int_{-\eta'}^{\eta'} \int_0^{\pi} \int_0^{\infty} 2N_V\left[f\{a,\psi(\theta,\phi),\phi,\eta\}d\psi\,s_{max}\right]da\,d\phi\,d\eta \qquad (D.4)$$

in which ψ is defined over a range which limits the cracks to a trace angle of $\theta \pm d\theta/2$. Only cracks with $\psi \geq \theta$ can give a trace angle of θ on the plane. An expression which relates θ to ψ and ϕ is given later in this section. The total number of cracks which intersect the plane is

$$\int_{-\eta'}^{\eta'} \int_0^{\pi} \int_0^{\pi/2} \int_0^{\infty} 2N_V\left[f(a,\psi,\phi,\eta)\,s_{max}\right]da\,d\psi\,d\phi\,d\eta \qquad (D.5)$$

If $f(\theta)$ is the relative frequency density of a crack angle on the plane, then $f(\theta)d\theta$ is the probability that a crack intersects the plane with an angle of $\theta \pm d\theta/2$; $0 \leq \theta \leq \pi/2$.

$$f(\theta)d\theta = \frac{\text{Number of cracks with } \theta \pm d\theta/2}{\text{Total number of cracks which intersect the plane}} \tag{D.6}$$

Substituting Eq. (D.4) and (D.5) into Eq. (D.6),

$$f(\theta)d\theta = \frac{\int_{-\eta'}^{\eta'} \int_0^{\pi} \int_0^{\infty} [f(a,\psi(\theta,\phi),\phi,\eta)d\psi\ s_{max}]da d\phi d\eta}{\int_{-\eta'}^{\eta'} \int_0^{\pi} \int_0^{\pi/2} \int_0^{\infty} f(a,\psi,\phi,\eta)\ s_{max} da d\psi d\phi d\eta} \tag{D.7}$$

Substituting $d\psi = \frac{\partial\psi}{\partial\theta}\, d\theta$ into Eq. (D.7),

$$f(\theta) = \frac{\int_{-\eta'}^{\eta'} \int_0^{\pi} \int_0^{\infty} f(a,\psi(\theta,\phi),\phi,\eta) \mid \partial\psi/\partial\theta \mid s_{max} da d\phi d\eta}{\int_{-\eta'}^{\eta'} \int_0^{\pi} \int_0^{\pi/2} \int_0^{\infty} f(a,\psi,\phi,\eta)\ s_{max} da d\psi d\phi d\eta} \tag{D.8}$$

The joint distribution, $f(a,\psi,\phi,\eta)$, is expressed in terms of conditional distributions [31] as follows.

$$f(a,\psi,\phi,\eta) = f(a|\psi,\phi,\eta)\ f(\psi|\phi,\eta)\ f(\phi|\eta)\ f(\eta) \tag{D.9}$$

Substituting Eq. (D.9) into Eq. (D.8),

$$f(\theta) = \frac{\int_{-\eta'}^{\eta'} \int_0^{\pi} \int_0^{\infty} f(a|\psi(\theta,\phi),\phi,\eta) f(\psi(\theta,\phi)|\phi,\eta) f(\phi|\eta) f(\eta) \left|\frac{\partial\psi}{\partial\theta}\right| s_{max} da d\phi d\eta}{\int_{-\eta'}^{\eta'} \int_0^{\pi} \int_0^{\pi/2} \int_0^{\infty} f(a|\psi,\phi,\eta) f(\psi|\phi,\eta) f(\phi|\eta) f(\eta) s_{max} da d\psi d\phi d\eta} \tag{D.10}$$

For a general anisotropic system of cracks, Eq. (D.10) gives the relationship between the spatial distributions and the angle distribution on the longitudinal plane.

In a transversely isotropic system, the crack size distribution is independent of ϕ, and the distribution in ϕ is uniform. It is assumed in the current analysis that the distribution in η is uniform. Therefore, the characteristic crack size, a, and the variance of the crack size distribution, var(a), are, in general, functions of ψ only; i.e. $a = a(\psi) = a_{\psi}$,

$\text{var}(a) = \text{var}(a_\psi)$. $f(\phi)$ and $f(\eta)$ are constant functions and therefore Eq. (D.10) becomes

$$f(\theta) = \frac{\int_{-\eta'}^{\eta'} \int_0^{\pi} \int_0^{\infty} f(a|\psi(\theta,\phi))\, f(\psi(\theta,\phi)) \mid \partial\psi/\partial\theta \mid s_{max}\, da\, d\phi\, d\eta}{\int_{-\eta'}^{\eta'} \int_0^{\pi} \int_0^{\pi/2} \int_0^{\infty} f(a|\psi)\, f(\psi)\, s_{max}\, da\, d\psi\, d\phi\, d\eta} \tag{D.11}$$

As shown in Appendix E, the relationship between θ, ψ and ϕ on the longitudinal plane is given by

$$\cos\theta = \cos\psi\,(1 - \sin^2\psi \sin^2\phi)^{-1/2} \tag{D.12}$$

Differentiation of Eq. (D.12) gives

$$\frac{\partial\psi}{\partial\theta} = \frac{\cos\phi}{1 - \cos^2\theta \sin^2\phi} \tag{D.13}$$

Also in Appendix E, s_{max} is expressed as

$$s_{max} = \frac{a_T\,[r_T^2 \cos(\phi+\eta_T) + \sin(\phi+\eta_T)\tan(\phi+\eta_T)]}{[r_T^2 + \tan^2(\phi+\eta_T)]^{1/2}} \tag{D.14}$$

in which $a_T = a\,(\sin^2\eta + \cos^2\eta \cos^2\psi)^{1/2}$

$$\tan\eta_T = \tan\eta/\cos\psi \;;\; \psi \neq \pi/2 \tag{D.15}$$

$$r_T = r\left(\frac{\cos^2\eta + \sin^2\eta \cos^2\psi}{\sin^2\eta + \cos^2\eta \cos^2\psi}\right)^{1/2}$$

a_T is the projected length on a transverse plane of the major semi-axis of the crack, η_T is the projection of the angle η on a transverse plane, and r_T is the aspect ratio of the projection of the crack on a transverse plane.

The evaluation of Eq. (D.11) requires that the size distribution of the cracks, $f(a|\psi)$, be known. However, the equation can be simplified so that its evaluation depends only on a knowledge of the mean size of the cracks. In Eq. (D.11), since only $f(a|\psi)$ and s_{max} are functions of a, both the numerator and the denominator can be simplified by noting that the mean

value of s_{max} for all cracks at a particular orientation, ψ, is directly dependent upon the mean crack size, $\langle a_\psi \rangle$. In the numerator,

$$\langle s_{max} \rangle_{\psi(\theta,\phi)} = \int_0^\infty s_{max} f(a|\psi(\theta,\phi))da \tag{D.16a}$$

In the denominator,

$$\langle s_{max} \rangle_{\psi} = \int_0^\infty s_{max} f(a|\psi)da \tag{D.16b}$$

Eq. (D.11) then becomes

$$f(\theta) = \frac{\int_{-\eta'}^{\eta'} \int_0^\pi f(\psi(\theta,\phi)) \; | \; \partial\psi/\partial\theta \; | \; \langle s_{max} \rangle_{\psi(\theta,\phi)} \; d\phi d\eta}{\int_{-\eta'}^{\eta'} \int_0^\pi \int_0^{\pi/2} f(\psi) \langle s_{max} \rangle_{\psi} \; d\psi d\phi d\eta} \tag{D.17}$$

If the mean crack size, $\langle a_\psi \rangle$, is known, $\langle s_{max} \rangle$ in the numerator and denominator of Eq. (D.17) can be determined using Eq. (D.14) and (D.15). Eq. (D.17) is therefore independent of $f(a|\psi)$. The numerator of Eq. (D.17) is evaluated by using Eq. (D.12) to express ψ in terms of θ and ϕ.

The evaluation of Eq. (D.17) is illustrated by considering the case of an isotropic system of cracks. In this case, the use of polar coordinates [98] yields

$$f(\psi) = \sin \psi \tag{D.18}$$

Substitution of Eq. (D.18) into Eq. (D.17) should give a uniform distribution in θ since all orientations occur with equal likelihood. The result is shown in Fig. D.4. ψ and θ have units of degrees. It is observed in Fig. D.4 that a uniform distribution is computed over the range of θ from about 10° to 90°. The non-uniform distribution over the range of θ from 0° to about 10° is due to the nature of Eq. (D.18). This equation gives $f(\psi) = 0$ if $\psi = 0°$. But $\psi = 0°$ also corresponds to $\theta = 0°$ [see Eq. (D.12)]. Hence Eq. (D.17) is zero for $\theta = 0°$ resulting in the non-uniform distribution over low angles. In evaluating Eq. (D.17), it is therefore recommended that $f(\theta)$ be computed over the range of θ from 10° to 90° and the results extrapolated to include the range from 0° to 10°. The forms of the integrands in Eq. (D.17) do not allow direct integration. Gaussian quadrature

[72] is therefore used for the numerical evaluation of Eq. (D.17). Four integration points are sufficient for these results.

D.3.1.1.1 Marriott Distribution

The orientation distribution of a transversely isotropic system of three-dimensional objects with a mild degree of anisotropy can be described by a Marriott distribution [98]. This distribution is expressed as

$$f(\psi) = \frac{1}{1 - K/3} (1 + K \cos 2\psi) \sin \psi \qquad (D.19)$$

$$-1 \leq K \leq 1$$

K is a measure of the degree of anisotropy and is given by

$$K = \frac{4[(B_L/B_T) - 1]}{2(B_L/B_T) - 1} \qquad (D.20a)$$

in which $\frac{2}{3} \leq \frac{B_T}{B_L} \leq \frac{6}{5}$

B_L and B_T are the boundary lengths of the objects per unit area on longitudinal and transverse planes respectively. The boundary length of a three-dimensional object is the perimeter of the trace of the object obtained on a plane section. If the object is a crack, the trace on a plane section is a line. Hence, the boundary length of a crack is twice its trace length on a plane section. B_L and B_T, therefore, are respectively equal to two times the total crack trace length per unit area on longitudinal and transverse planes; i.e. $B_L = 2 M_L \langle \ell \rangle_L$, $B_T = 2 M_T \langle \ell \rangle_T$, in which M_L and M_T are the number of cracks per unit area on longitudinal and transverse planes respectively, and $\langle \ell \rangle_L$ and $\langle \ell \rangle_T$ are the mean crack trace lengths on longitudinal and transverse planes respectively. Eq. (D.20a) can therefore be written in the following form:

$$K = \frac{4[(M_L \langle \ell \rangle_L / M_T \langle \ell \rangle_T) - 1]}{2(M_L \langle \ell \rangle_L / M_T \langle \ell \rangle_T) - 1} \qquad (D.20b)$$

in which $\frac{2}{3} \leq \frac{M_T \langle \ell \rangle_T}{M_L \langle \ell \rangle_L} \leq \frac{6}{5}$

Defining "high angles" as angles, ψ, close to 90° and "low angles" as ψ close to 0°, a negative K indicates a system in which more cracks are oriented at high angles than at low angles, while a positive K indicates a system in which fewer cracks are oriented at high angles than at low angles. For K = 0, Eq. (D.19) reduces to Eq. (D.18), the equation for an isotropic distribution of orientations..

Fig. D.5 provides comparisons between the orientation, ψ, and the surface angle, θ, distributions for an isotropic system of cracks (K = 0) and those for a transversely isotropic system in which K = -0.5. The surface angle distributions are determined using Eq. (D.17). The orientation distribution of the transversely isotropic system is skewed more towards high angles than the corresponding distribution for the isotropic system. The computed surface angle distribution for the transversely isotropic system correctly indicates that more cracks are oriented at high angles than at low angles.

If $M\langle\ell\rangle$ is obtained on longitudinal and transverse plane sections of a cracked body, the Marriott distribution provides an estimate of the orientation distribution. It will be shown later how Eq. (D.17), (D.19) and (D.20b) can be used with expressions relating spatial distributions and surface length distributions, to establish a procedure for estimating the crack size distribution, $f(a|\psi)$, aspect ratio, r, and the range of η for a transversely isotropic system of cracks.

D.3.1.2 Transverse Plane

The trace angle, θ, on a transverse plane is equal to $\phi \pm \pi/2$ (see Fig. D.3). Hence, the distributions in θ and $\phi \pm \pi/2$ are equal.

$$f(\theta) = f(\phi \pm \pi/2) \qquad (D.21)$$

For a transversely isotropic system of cracks, the distribution in ϕ is equal to the distribution in $\phi \pm \pi/2$. The distributions in θ and ϕ are therefore equal.

$$f(\theta) = f(\phi) \qquad (D.22)$$

D.3.2 Relationships between Spatial Distributions and Surface Length Distributions

D.3.2.1 Longitudinal Plane.

For a general transversely isotropic system of cracks, the trace length distribution on a longitudinal plane will vary with trace angle. For convenience, the derivations that follow are in terms of the number of cracks with given values of trace length and angle.

The number of cracks with given values of a, ψ, ϕ and η that have centers within a distance of s ± ds/2 from both sides of a longitudinal plane of unit area and give a trace length of ℓ ± dℓ/2 and a trace angle of θ ± dθ/2 on the plane is

$$2\, N_V\, f\big(a(\ell,\psi,\phi,\eta),\psi(\theta,\phi),\phi,\eta\big)\,da\,d\psi\,d\phi\,d\eta\,ds \tag{D.23}$$

in which a and ψ are limited to those values that give a trace length of ℓ ± dℓ/2 and an angle of θ ± dθ/2, respectively, on the plane. For all a, ψ, ϕ and η, the number of cracks that give a length of ℓ ± dℓ/2 and an angle of θ ± dθ/2 on the plane is

$$\int_{-\eta'}^{\eta'} \int_0^{\pi} \int_{a_{min}}^{\infty} 2N_V\big[f\big(a(\ell,\psi,\phi,\eta),\psi(\theta,\phi),\phi,\eta\big)d\psi\; ds\big]\,da\,d\phi\,d\eta \tag{D.24}$$

in which a_{min} is the smallest characteristic crack size that gives a length of ℓ on the plane and is a function of ℓ, ψ, ϕ and η. The expression for a_{min} is given later in this section. The total number of cracks which intersect the plane with an angle of θ ± dθ/2 is given by Eq. (D.4) as

$$\int_{-\eta'}^{\eta'} \int_0^{\pi} \int_0^{\infty} 2N_V\big[f\big(a,\psi(\theta,\phi),\phi,\eta\big)d\psi\; s_{max}\big]\,da\,d\phi\,d\eta \tag{D.25}$$

If $f(\ell|\theta)$ is the relative frequency density of a crack length on the plane for a given angle, then $f(\ell|\theta)d\ell$ is the probability that a crack intersects the plane with a length of ℓ ± dℓ/2 for a given θ.

$$f(\ell|\theta)d\ell = \frac{\text{Number of cracks with } \ell \pm d\ell/2,\ \theta \pm d\theta/2}{\text{Number of cracks which intersect the plane with } \theta \pm d\theta/2} \tag{D.26}$$

Substituting Eq. (D.24) and (D.25) into Eq. (D.26),

$$f(\ell|\theta)d\ell = \frac{\int_{-\eta'}^{\eta'}\int_0^{\pi}\int_{a_{min}}^{\infty} [f(a(\ell,\psi,\phi,\eta),\psi(\theta,\phi),\phi,\eta)d\psi\ ds]dad\phi d\eta}{\int_{-\eta'}^{\eta'}\int_0^{\pi}\int_0^{\infty} [f(a,\psi(\theta,\phi),\phi,\eta)d\psi\ s_{max}]dad\phi d\eta} \tag{D.27}$$

Substituting $ds = \frac{\partial s}{\partial \ell}\, d\ell$ into Eq. (D.27),

$$f(\ell|\theta) = \frac{\int_{-\eta'}^{\eta'}\int_0^{\pi}\int_{a_{min}}^{\infty} f(a(\ell,\psi,\phi,\eta),\psi(\theta,\phi),\phi,\eta)\ \left|\frac{\partial s}{\partial \ell}\right|\ dad\phi d\eta}{\int_{-\eta'}^{\eta'}\int_0^{\pi}\int_0^{\infty} f(a,\psi(\theta,\phi),\phi,\eta)\ s_{max} dad\phi d\eta} \tag{D.28}$$

Eq. (D.9) is substituted into Eq. (D.28) to obtain

$$f(\ell|\theta) = \frac{\int_{-\eta'}^{\eta'}\int_0^{\pi}\int_{a_{min}}^{\infty} f(a(\ell,\psi,\phi,\eta)|\psi(\theta,\phi),\phi,\eta)f(\psi(\theta,\phi)|\phi,\eta)f(\phi|\eta)f(\eta)\left|\frac{\partial s}{\partial \ell}\right| dad\phi d\eta}{\int_{-\eta'}^{\eta'}\int_0^{\pi}\int_0^{\infty} f(a|\psi(\theta,\phi),\phi,\eta)f(\psi(\theta,\phi)|\phi,\eta)f(\phi|\eta)f(\eta)s_{max} dad\phi d\eta} \tag{D.29}$$

Eq. (D.29) is valid for a general anisotropic system of cracks.

For transverse isotropy and the assumption that the crack distribution is uniform in η, Eq. (D.29) becomes

$$f(\ell|\theta) = \frac{\int_{-\eta'}^{\eta'}\int_0^{\pi}\int_{a_{min}}^{\infty} f(a(\ell,\psi,\phi,\eta)|\psi(\theta,\phi))\ f(\psi(\theta,\phi))\ \left|\frac{\partial s}{\partial \ell}\right|\ dad\phi d\eta}{\int_{-\eta'}^{\eta'}\int_0^{\pi}\int_0^{\infty} f(a|\psi(\theta,\phi))\ f(\psi(\theta,\phi))\ s_{max}\ dad\phi d\eta} \tag{D.30}$$

Eq. (D.30) is evaluated by using Eq. (D.12) to express ψ in terms of θ and ϕ. s_{max} is given by Eq. (D.14). From the geometric relations derived in Appendix E,

$$a_{min} = \frac{y_m}{r_T \tan(\phi+\eta_T)}\left[\frac{r_T^2 + \tan^2(\phi+\eta_T)}{\sin^2\eta + \cos^2\eta\cos^2\psi}\right]^{1/2} \tag{D.31}$$

in which $$y_m = \frac{\ell\cos\theta\tan(\phi+\eta_T)[\sin^2(\phi+\eta_T) + r_T^2\cos^2(\phi+\eta_T)]}{2\sin(\phi+\eta_T)\tan(\phi+\eta_T) + r_T^2\cos(\phi+\eta_T)}$$

η_T and r_T are defined previously in Eq. (D.15). Since the numerator of Eq. (D.30) requires an integration over crack sizes, $\frac{\partial s}{\partial \ell}$ needs to be expressed as a function of the characteristic crack size. This is accomplished in Appendix E by considering the projection of the crack on a transverse plane. $\frac{\partial s}{\partial \ell}$ is expressed as

$$\frac{\partial s}{\partial \ell} = \frac{\partial s}{\partial a_T} \frac{\partial a_T}{\partial \ell} \tag{D.32}$$

in which a_T is the projected length on a transverse plane of the major semi-axis of the crack and is defined previously in Eq. (D.15). The derivative on the right hand side of Eq. (D.32) are expressed in Eq. (E.63) through (E.68) of Appendix E.

The nature of surface trace length distributions obtained using Eq. (D.30) can be illustrated using assumed spatial distributions. For an orientation distribution in which the degree of anisotropy, K = -0.5 [Eq. (D.19)], and for a crack size distribution which is independent of ψ [i.e. $f(a|\psi) = f(a)$], Eq. (D.30) gives the distribution of crack trace length on the longitudinal plane shown in Fig. D.6. As expected, the mean trace length on the plane, $\langle \ell_\theta \rangle$, is smaller than the mean crack size, $\langle 2a \rangle$.

D.3.2.2 Transverse Plane

For a transversely isotropic system of cracks, the trace length distribution on a transverse plane will not vary with trace angle. Therefore in the following derivations, the number of cracks with a given value of trace length is summed over all trace angles.

The number of cracks with given values of a, ψ, ϕ and η that have centers within a distance of s ± ds/2 from both sides of a transverse plane of unit area and give a trace length of ℓ ± dℓ/2 on the plane is

$$2 N_V f\left(a(\ell,\psi,\eta),\psi,\phi,\eta\right) da d\psi d\phi d\eta \, ds \tag{D.33}$$

in which a is limited to those values that give a length of ℓ ± dℓ/2 on the plane. For all a, ψ, ϕ and η, the number of cracks that give a length of ℓ ± dℓ/2 on the plane is

$$\int_{-\eta'}^{\eta'} \int_{0}^{\pi} \int_{0}^{\pi/2} \int_{a_{min}}^{\infty} 2N_V[f(a(\ell,\psi,\eta),\psi,\phi,\eta)\ ds]da d\psi d\phi d\eta \tag{D.34}$$

in which a_{min} is the smallest characteristic crack size that gives a length of ℓ on the plane and is a function of ℓ, ψ and η. The expression for a_{min} is derived in Appendix E and given later in this section. The total number of cracks which intersect the plane is

$$\int_{-\eta'}^{\eta'} \int_{0}^{\pi} \int_{0}^{\pi/2} \int_{0}^{\infty} 2N_V[f(a,\psi,\phi,\eta)\ s_{max}]da d\psi d\phi d\eta \tag{D.35}$$

If $f(\ell)$ is the relative frequency density of a crack length on the plane, then $f(\ell)d\ell$ is the probability that a crack intersects the plane with a length of $\ell \pm d\ell/2$.

$$f(\ell)d\ell = \frac{\text{Number of cracks with } \ell \pm d\ell/2}{\text{Total number of cracks which intersect the plane}} \tag{D.36}$$

Substituting Eq. (D.34) and (D.35) into Eq. (D.36),

$$f(\ell)d\ell = \frac{\int_{-\eta'}^{\eta'} \int_{0}^{\pi} \int_{0}^{\pi/2} \int_{a_{min}}^{\infty} [f(a(\ell,\psi,\eta),\psi,\phi,\eta)\ ds]da d\psi d\phi d\eta}{\int_{-\eta'}^{\eta'} \int_{0}^{\pi} \int_{0}^{\pi/2} \int_{0}^{\infty} [f(a,\psi,\phi,\eta)\ s_{max}]\ da d\psi d\phi d\eta} \tag{D.37}$$

Substituting $ds = \frac{\partial s}{\partial \ell} d\ell$ into Eq. (D.37),

$$f(\ell) = \frac{\int_{-\eta'}^{\eta'} \int_{0}^{\pi} \int_{0}^{\pi/2} \int_{a_{min}}^{\infty} f(a(\ell,\psi,\eta),\psi,\phi,\eta)\ \left|\frac{\partial s}{\partial \ell}\right|\ da d\psi d\phi d\eta}{\int_{-\eta'}^{\eta'} \int_{0}^{\pi} \int_{0}^{\pi/2} \int_{0}^{\infty} f(a,\psi,\phi,\eta)\ s_{max}\ da d\psi d\phi d\eta} \tag{D.38}$$

Eq. (D.9) is substituted into Eq. (D.38) to obtain

$$f(\ell) = \frac{\int_{-\eta'}^{\eta'} \int_{0}^{\pi} \int_{0}^{\pi/2} \int_{a_{min}}^{\infty} f(a(\ell,\psi,\eta)|\psi,\phi,\eta) f(\psi|\phi,\eta) f(\phi|\eta) f(\eta) \left|\frac{\partial s}{\partial \ell}\right| da d\psi d\phi d\eta}{\int_{-\eta'}^{\eta'} \int_{0}^{\pi} \int_{0}^{\pi/2} \int_{0}^{\infty} f(a|\psi,\phi,\eta) f(\psi|\phi,\eta) f(\phi|\eta) f(\eta) s_{max}\, da d\psi d\phi d\eta} \tag{D.39}$$

Eq. (D.39) is for a general anisotropic system of cracks.

For a transversely isotropic system of cracks, and the assumption that the crack distribution is uniform in η, Eq. (D.39) is simplified to become

$$f(\ell) = \frac{\int_{-\eta'}^{\eta'} \int_{0}^{\pi/2} \int_{a_{min}}^{\infty} f(a(\ell,\psi,\eta)|\psi)\, f(\psi)\, |\, \partial s/\partial \ell\, |\, da d\psi d\eta}{\int_{-\eta'}^{\eta'} \int_{0}^{\pi/2} \int_{0}^{\infty} f(a|\psi)\, f(\psi)\, s_{max}\, da d\psi d\eta} \tag{D.40}$$

The geometric relations in Appendix E give

$$s_{max} = a_L\, (1 + r_L^2 \tan^2\eta_L)^{-1/2}\, (r_L^2 \sin\eta_L \tan\eta_L + \cos\eta_L) \tag{D.41}$$

in which $a_L = a\, (\sin^2\eta + \cos^2\eta \sin^2\psi)^{1/2}$

$$\tan\eta_L = \tan\eta/\sin\psi \; ; \; \psi \neq 0 \tag{D.42}$$

$$r_L = r \left(\frac{\cos^2\eta + \sin^2\eta \sin^2\psi}{\sin^2\eta + \cos^2\eta \sin^2\psi}\right)^{1/2}$$

a_L is the projected length on a longitudinal plane of the major semi-axis of the crack, η_L is the projection of the angle η on a longitudinal plane, and r_L is the aspect ratio of the projection of the crack on a longitudinal plane. The smallest a that gives a length of ℓ on the plane is derived in Appendix E as

$$a_{min} = \frac{\ell\, (\cos^2\eta_L + r_L^2 \sin^2\eta_L)\, (1 + r_L^2 \tan^2\eta_L)^{1/2}}{2\, r_L (\cos\eta_L + r_L^2 \sin\eta_L \tan\eta_L)\, (\sin^2\eta + \cos^2\eta \sin^2\psi)^{1/2}} \tag{D.43}$$

The derivative, $\frac{\partial s}{\partial \ell}$, in the numerator of Eq. (D.40) needs to be expressed as a function of the characteristic crack size. In Appendix E, this relationship is obtained by considering the projection of the crack on a longitudinal plane. $\frac{\partial s}{\partial \ell}$ is expressed as

$$\frac{\partial s}{\partial \ell} = \frac{\partial s}{\partial a_L} \frac{\partial a_L}{\partial \ell} \tag{D.44}$$

The expressions for the derivatives on the right hand side of Eq. (D.44) are given by Eq. (E.70) through (E.75) of Appendix E.

The nature of the surface trace length distributions obtained using Eq. (D.40) can be illustrated using the same assumed spatial distributions used previously for the longitudinal plane [K = -0.5 and $f(a|\psi) = f(a)$]. Eq.

(D.40) gives the distribution of crack lengths on the transverse plane shown in Fig. D.7. As in the case of the longitudinal plane, the mean trace length on the transverse plane, $\langle \ell \rangle$, is smaller than the mean crack size, $\langle 2a \rangle$.

D.3.3 Estimate of the Total Number of Cracks per Unit Volume.

Weibel [98] has shown that based on the Marriott distribution, the surface area per unit volume of flattened structures can be expressed as

$$S_V = \frac{4}{3\pi} (B_T + 2 B_L) \tag{D.45a}$$

in which B_T and B_L are the boundary lengths per unit area of sections of the structures on transverse and longitudinal planes, respectively. In the case of cracks, B_T and B_L are respectively equal to two times the total crack trace length per unit area on transverse and longitudinal planes (see section D.3.1.1.1). Eq. (D.45a) can therefore be written as

$$S_V = \frac{8}{3\pi} (M_T \langle \ell \rangle_T + 2 M_L \langle \ell \rangle_L) \tag{D.45b}$$

in which $M_T \langle \ell \rangle_T$ and $M_L \langle \ell \rangle_L$ are, respectively, the total crack trace length per unit area on transverse and longitudinal planes.

If the elliptic cracks have a mean surface area of $\langle \pi ab \rangle$ over all orientations, then

$$S_V = 2 N_V \langle \pi ab \rangle$$

or

$$S_V = 2 N_V \pi r \langle a^2 \rangle \tag{D.46}$$

in which N_V is the number of cracks per unit volume, r is the aspect ratio of the cracks, and $\langle a^2 \rangle$ is the mean squared value of the characteristic crack size over all orientations; i.e.

$$\langle a^2 \rangle = \int_0^\infty \int_0^{\pi/2} a^2 f(a|\psi) f(\psi) d\psi da \tag{D.47}$$

Equating (D.45b) and (D.46) and rearranging,

$$N_V = \frac{4}{3\pi^2 r\langle a^2\rangle}\left(M_T\langle \ell\rangle_T + 2\,M_L\langle \ell\rangle_L\right) \tag{D.48}$$

In Eq. (D.48), the total crack trace lengths per unit area ($M\langle \ell\rangle$) on transverse and longitudinal planes are measurable quantities. $\langle a^2\rangle$ can be determined from Eq. (D.47) if the crack size and orientation distributions are known. For a transversely isotropic system of cracks, Eq. (D.48) can therefore be used to estimate the number of cracks per unit volume. The procedure for determining distributions $f(a|\psi)$ and $f(\psi)$ is described in the following section.

D.4 PROCEDURE FOR ESTIMATING 3-D CRACK PARAMETERS

The expressions relating spatial crack distributions to surface distributions on longitudinal and transverse planes, can be used to estimate the three-dimensional crack distributions for a transversely isotropic system of cracks based on observations of surface crack traces. Specifically, the procedure that follows provides estimates of the distributions of crack orientation and size, $f(\psi)$ and $f(a|\psi)$, the mean characteristic size of cracks as a function of ψ, $\langle a_\psi\rangle$, the variance of the crack size distribution, $\mathrm{var}(a_\psi)$, the crack aspect ratio, r, and the range of the angle η. It is assumed that crack trace distributions have been obtained on longitudinal and transverse planes of the cracked body.

An iterative procedure is used in order to estimate the spatial crack parameters. The procedure is set up in terms of the three equations [(D.17), (D.30), and (D.40)] which relate spatial crack distributions to surface distributions on longitudinal and transverse plane sections of a cracked body. The Marriott distribution which is described in Section D.3.1 for a mildly anisotropic system, is assumed. In using this distribution, the restriction on the degree of anisotropy (i.e. $-1 \leq K \leq 1$) must be satisfied.

The procedure is based on minimizing the sum of the squared differences between observed surface distributions and calculated distributions that are obtained from assumed spatial distributions. As an initial guess, the relationship between mean trace length and trace angle on the longitudinal plane is used as a guide to the form of $f(a|\psi)$ and the values of $\langle a_\psi\rangle$. Similarly, values of $\mathrm{var}(a_\psi)$ may be assumed. The assumed spatial distributions which minimize the sum of the squared differences between the observed

and calculated surface distributions are the correct estimates based on the assumed form of $f(a|\psi)$. The procedure may be repeated with different forms of $f(a|\psi)$. The spatial distributions and the form of $f(a|\psi)$ which enable the minimization process to attain a global minimum are the desired estimates.

The procedure is outlined as follows.

1. Determine the degree of anisotropy, K, from Eq. (D.20b) using the total lengths of cracks per unit area, $M\langle\ell\rangle$, obtained on longitudinal and transverse plane sections of the cracked body. $f(\psi)$ is then obtained from Eq. (D.19).
2. Assume a form for the crack size distribution, $f(a|\psi)$, such as a gamma distribution.
3. Assume expressions for $\langle a_\psi \rangle$ and $\text{var}(a_\psi)$ as functions of crack orientation.
4. By varying the crack aspect ratio, r, compute the trace angle distribution on the longitudinal plane, $f(\theta)_{Lc}$, using Eq. (D.17) with $-\pi/2 \leq \eta \leq \pi/2$. Determine the r which minimizes the sum of the squared differences between the observed, $f(\theta)_L$, and computed, $f(\theta)_{Lc}$, trace angle distributions. This sum is expressed as

$$\sum_{\theta} [f(\theta)_L - f(\theta)_{Lc}]^2 \Delta\theta \qquad \text{(D.49)}$$

$\Delta\theta$ is the interval for recording the trace angles. Change the range of η and again determine the r which minimizes Eq. (D.49). Continue this process until Eq. (D.49) cannot be minimized further. The value of r and the range of η for which Eq. (D.49) is fully minimized, are the estimates to be used in the following steps.

5. Use Eq. (D.40) to compute the trace length distribution on the transverse plane, $f(\ell)_{Tc}$. An improved estimate of the variance of $f(a|\psi)$ is obtained by assuming trial values for $\text{var}(a_\psi)$ until the sum of the squared differences between the observed, $f(\ell)_T$, and computed, $f(\ell)_{Tc}$, trace length distributions is minimized. This sum is expressed as

$$\sum_{\ell} [f(\ell)_T - f(\ell)_{Tc}]^2 \Delta\ell \qquad \text{(D.50)}$$

$\Delta\ell$ is the interval for recording the trace lengths.

6. Compute the trace length distribution on the longitudinal plane, $f(\ell|\theta)_{Lc}$, using Eq. (D.30). Calculate the sum, over all trace angles, of the squared differences between the observed, $f(\ell|\theta)_L$, and computed, $f(\ell|\theta)_{Lc}$, trace length distributions. This sum is expressed as

$$\sum_{\theta} \left\{ \sum_{\ell} \left[f(\ell|\theta)_L - f(\ell|\theta)_{Lc} \right]^2 \Delta\ell \right\} \tag{D.51}$$

7. Return to Step 3 and repeat the process until the values computed from Eq. (D.51) reach a global minimum. The parameters $\langle a_\psi \rangle$, $\text{var}(a_\psi)$, r, and the range of η which produce this global minimum are the best estimates for the three-dimensional crack distribution based on the form of $f(a|\psi)$ assumed in Step 2.
8. The iterative process may be restarted at Step 2 by assuming a different form for $f(a|\psi)$. The form of $f(a|\psi)$ and the corresponding values of $\langle a_\psi \rangle$, $\text{var}(a_\psi)$, r, and the range of η which minimize Eq. (D.51) are the desired estimates.

If the cracks are assumed to be circular, the procedure becomes simplified since Step 4 is no longer required.

D.4.1 Example

In order to illustrate the results of the procedure described above, an example based on a study of load-induced cracks in cement paste and mortar is presented. In the example, angles have units of degrees. Computations are performed on a computer, and all integrals are evaluated numerically using Gaussian quadrature. Four integration points are sufficient for these results.

Cement paste and mortar specimens are loaded in compression to selected stress levels and then unloaded. Longitudinal and transverse fractured surfaces of the loaded specimens are then viewed using a scanning electron microscope (SEM). Crack trace lengths and angles are measured at a magnification of about 1250x. Only portions of cracks within the field of view are measured in order to obtain an accurate estimate of the density of cracks within the scanned areas. As a result of the finite size of the viewing area, the trace length and angle distributions are distorted. These

distortions are corrected as described in Appendix C. The trace distributions are also modified to account for the effects of specimen preparation prior to viewing in the SEM (see Chapter 3). The experimental trace distributions for a specimen of cement paste (age 28 days, water-cement ratio = 0.5) loaded to a strain of 0.002 are summarized in Tables D.1 and D.2 and used in this example. The trace length distributions on both the transverse and longitudinal planes are best described by the gamma distribution. This distribution is represented as

$$f(\ell|\theta)_L = \frac{1}{\beta^{\alpha}\Gamma(\alpha)}\,\ell^{\alpha-1}\,e^{-\ell/\beta} \tag{D.52}$$

in which α and β are functions of the mean and the variance of the distribution, in this case $\langle\ell\rangle$ or $\langle\ell_\theta\rangle$ and $\mathrm{var}(\ell)$ or $\mathrm{var}(\ell_\theta)$.

$$\alpha = \frac{\langle\ell\rangle^2}{\mathrm{var}(\ell)} \qquad \beta = \frac{\mathrm{var}(\ell)}{\langle\ell\rangle} \tag{D.53}$$

$\Gamma(\alpha)$ is the gamma function and is defined as

$$\Gamma(\alpha) = \int_0^{\infty} y^{\alpha-1}\,e^{-y}\,dy \tag{D.54}$$

Gaussian quadrature with four integration points over the range of y from 0 to 50 is sufficient for the integration in Eq. (D.54).

For the longitudinal plane, representative values for the trace length distributions are given in Table D.2 for trace angles of 15°, 30° and 60°. Values of the relative frequency density for other trace angles can be obtained using Eq. (D.52) and the values of $\langle\ell_\theta\rangle_L$ and $\mathrm{var}(\ell_\theta)_L$ given in Table D.2.

In Fig. D.8, the experimental trace angle distribution indicates that the orientations of the crack traces are skewed towards the longitudinal direction. The degree of anisotropy also shows that the spatial distribution is skewed toward the longitudinal direction. K is -0.16 as determined using Eq. (D.20b). The value of K falls within the required range of -1 to 1, indicating that the Marriott distribution is valid.

As observed in Fig. D.8-D.10, the calculated surface distributions, obtained from the converged solution for the spatial distributions, closely match the distributions obtained from the experimental data. Selected

values for the calculated surface distributions are also given in Tables D.1 and D.2.

For the spatial distributions, crack size varies with crack orientation. The best form of the size distribution, $f(a|\psi)$, turns out to be a gamma distribution [Eq. (D.52)].

$$f(a|\psi) = \frac{1}{\beta^{\alpha}\Gamma(\alpha)} a^{\alpha-1} e^{-a/\beta} \tag{D.55}$$

with $a = a_{\psi}$. α, β and Γ are defined in Eq. (D.53) and (D.54). For this example, the values of the estimated crack parameters are:

$r = 0.9 \qquad \eta' = 0°$

$\langle a_{\psi} \rangle = 1.0\times10^{-5}\psi + 1.55\times10^{-3}$ in. $\quad var(a_{\psi}) = 1.6\times10^{-9}\psi + 1.4\times10^{-6}$ in.^{2}

$f(\psi) = 0.95(1 - 0.16\cos 2\psi)\sin\psi$

To obtain the total number of cracks per unit volume, N_V, the calculated spatial distributions are used in Eq. (D.47) to determine $\langle a^2 \rangle$. The value of N_V [Eq. (D.48)] is 2.3×10^6 cracks per cubic in.

D.5 SENSITIVITY OF THE MODEL TO ERRORS IN TRACE LENGTH PARAMETERS

In this section, the sensitivity of the estimated three-dimensional crack size parameters to errors in the surface crack trace length parameters is investigated.

A trace length distribution of known form is adequately described by its mean, $\langle \ell \rangle$, and variance, $var(\ell)$. The corresponding three-dimensional parameters which describe a size distribution of known form are $\langle a_{\psi} \rangle$ and $var(a_{\psi})$. For errors of 10%, 20% and 30% in the trace length parameters used in the previous example, estimates of $\langle a_{\psi} \rangle$ and $var(a_{\psi})$ are obtained.

Table D.3 illustrates the results. A 30% overestimation of $\langle \ell \rangle$ results in a 43.8% overestimation of $\langle a_{\psi} \rangle$, while a 30% underestimation of $\langle \ell \rangle$ results in a 39.2% underestimation of $\langle a_{\psi} \rangle$. This implies that errors made in the measurement of trace lengths can result in larger errors in estimated crack sizes. The effect of an overestimation (or underestimation) of $\langle \ell \rangle$ on

var(a_ψ) is very small, as evidenced by the 2.6% overestimation of var(a_ψ) for a 30% overestimation of $\langle \ell \rangle$.

On the other hand, a 30% overestimation or underestimation of var(ℓ) has a large effect on var(a_ψ) and a very small effect on $\langle a_\psi \rangle$. A 30% overestimation of var(ℓ) results in overestimations of var(a_ψ) and $\langle a_\psi \rangle$ of 72.3% and 1.4%, respectively, while a 30% underestimation of var(ℓ) results in underestimations of 68.4% and 1.0%, respectively..

This example reinforces the fact that the data on surface crack traces must be obtained accurately in order to obtain a close estimate of the spatial crack distribution.

D.6 SUMMARY

The three-dimensional distributions of cracks or similarly shaped inclusions in opaque bodies cannot be obtained directly from experimental measurements. By using the concepts of statistics, geometrical probability, and stereology, relationships have been obtained between spatial and surface distributions of cracks. These relationships are used to establish an iterative procedure for estimating three-dimensional crack parameters for a transversely isotropic system of cracks, using crack trace distributions on longitudinal and transverse sections of the cracked body.

Results from a study of load-induced cracks in cement paste and mortar are provided to illustrate the use of the procedure.

TABLE D.1

TRACE ANGLE DISTRIBUTIONS FOR THE LONGITUDINAL PLANE.

(CEMENT PASTE WITH A WATER-CEMENT RATIO = 0.5; STRAIN = 0.002)

Angle,	Relative Frequency Density, 10^{-2}deg.$^{-1}$	
degrees	Experimental	Calculated
0	0.97	0.91
5	0.99	0.94
10	1.00	0.97
15	1.02	0.99
20	1.03	1.02
25	1.05	1.04
30	1.06	1.07
35	1.08	1.09
40	1.10	1.11
45	1.11	1.13
50	1.13	1.15
55	1.14	1.16
60	1.16	1.18
65	1.17	1.19
70	1.19	1.21
75	1.21	1.22
80	1.22	1.23
85	1.24	1.23
90	1.25	1.24

TABLE D.2

EXPERIMENTAL AND CALCULATED TRACE LENGTH DISTRIBUTIONS.

(CEMENT PASTE WITH A WATER-CEMENT RATIO = 0.5; STRAIN = 0.002)

Transverse Plane: $\langle \ell \rangle_T = 2.01 \times 10^{-3}$ in. $\quad \mathrm{var}(\ell)_T = 1.37 \times 10^{-6}$ in.^{2}

Longitudinal Plane: $\langle \ell_\theta \rangle_L = 0.75 \times 10^{-5}\theta + 1.90 \times 10^{-3}$ in.

$\mathrm{var}(\ell_\theta)_L = 1.15 \times 10^{-9}\theta + 1.35 \times 10^{-6}$ in.^{2}

Length,	Relative Frequency Density, in.$^{-1}$							
10^{-3}in.	Tran. Plane		Longitudinal Plane					
			$\theta = 15°$		$\theta = 30°$		$\theta = 60°$	
	Exp.	Cal.	Exp.	Cal.	Exp.	Cal.	Exp.	Cal.
0.0	0	0	0	0	0	0	0	0
0.5	202	156	89	110	76	95	59	66
1.0	374	301	254	242	238	232	212	212
1.5	396	364	345	319	339	317	325	310
2.0	333	343	346	329	349	332	350	336
2.5	247	276	294	289	301	296	311	305
3.0	169	199	225	228	233	235	245	245
3.5	110	131	160	165	167	171	178	180
4.0	68	81	108	112	113	117	121	124
4.5	41	47	70	72	73	75	79	80
5.0	24	26	44	45	46	47	49	50
5.5	14	14	27	26	28	28	30	30
6.0	8	7	16	15	17	16	18	17

TABLE D.3

SENSITIVITY OF 3-D CRACK SIZE PARAMETERS TO ERRORS IN TRACE LENGTH PARAMETERS.

Overestimation (Underestimation) of $\langle \ell \rangle$, %	Resulting Overestimation (Underestimation) of $\langle a_\psi \rangle$, %	Resulting Overestimation (Underestimation) of $var(a_\psi)$, %
10	14.1	0.7
20	28.6	1.8
30	43.8	2.6
(10)	(12.5)	(0.6)
(20)	(25.3)	(1.4)
(30)	(39.2)	(2.2)

Overestimation (Underestimation) of $var(\ell)$, %	Resulting Overestimation (Underestimation) of $\langle a_\psi \rangle$, %	Resulting Overestimation (Underestimation) of $var(a_\psi)$, %
10	0.4	24.8
20	0.9	49.2
30	1.4	72.3
(10)	(0.1)	(22.7)
(20)	(0.5)	(46.5)
(30)	(1.0)	(68.4)

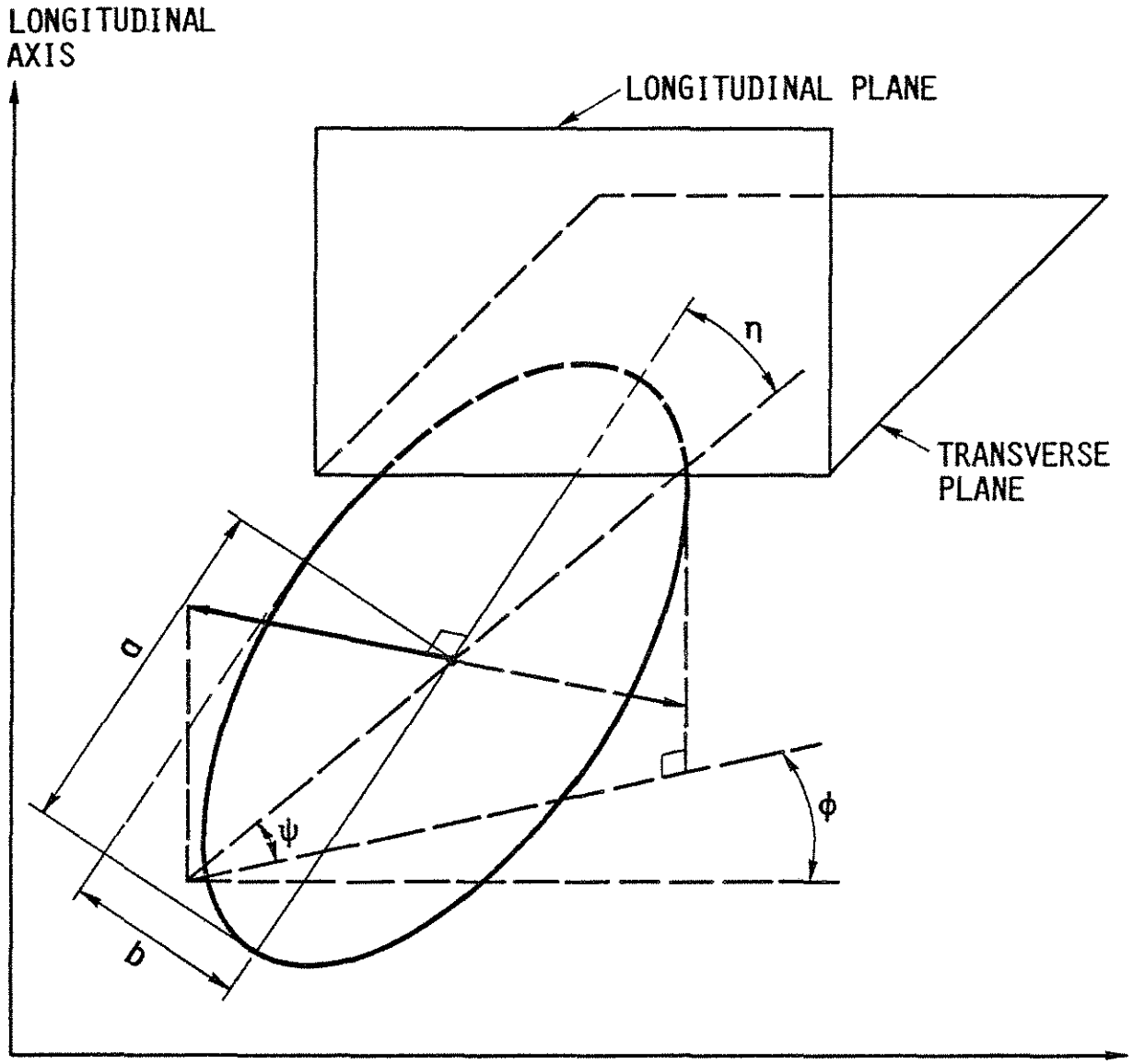

Fig. D.1. Elliptic Crack and Intersecting Planes

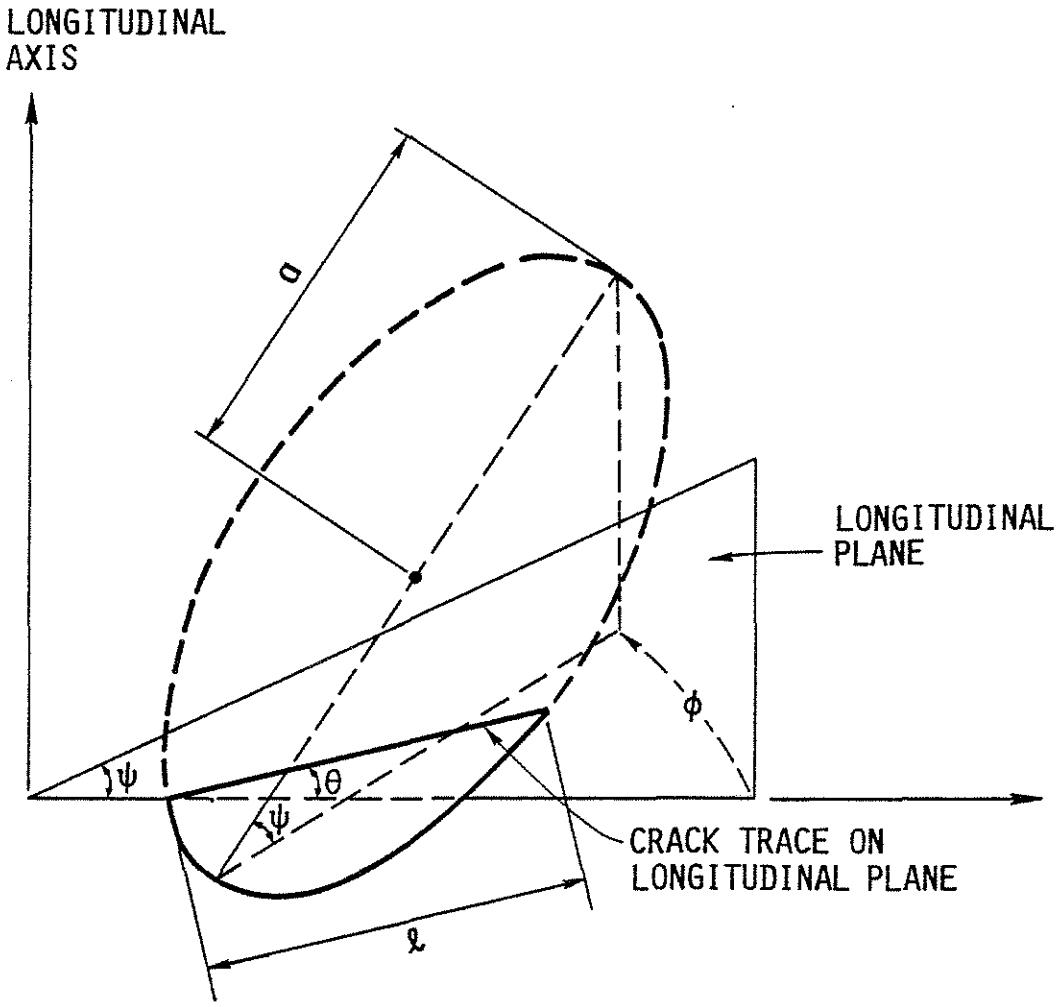

Fig. D.2. Longitudinal Plane Intersecting an Elliptic Crack

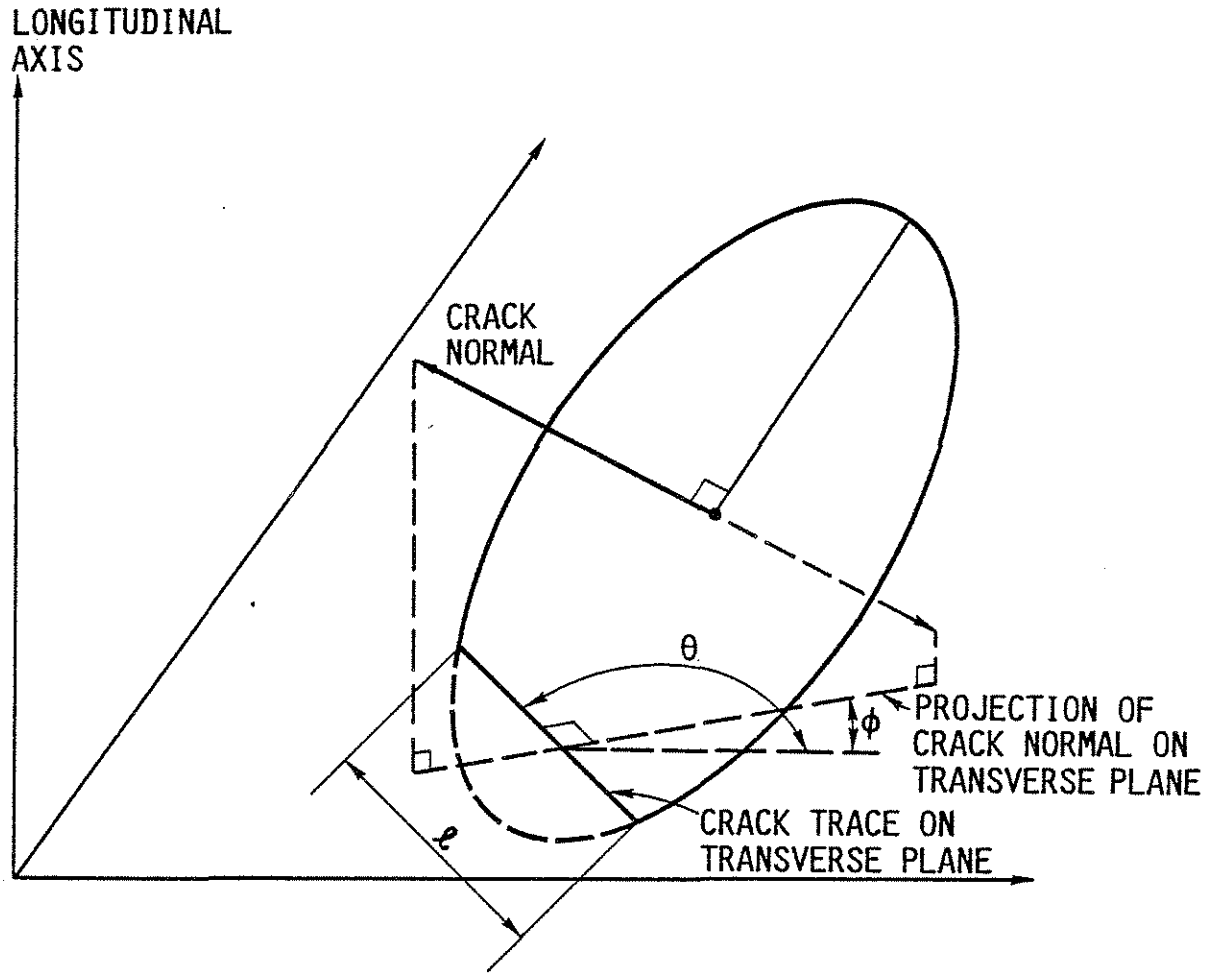

Fig. D.3. Transverse Plane Intersecting an Elliptic Crack

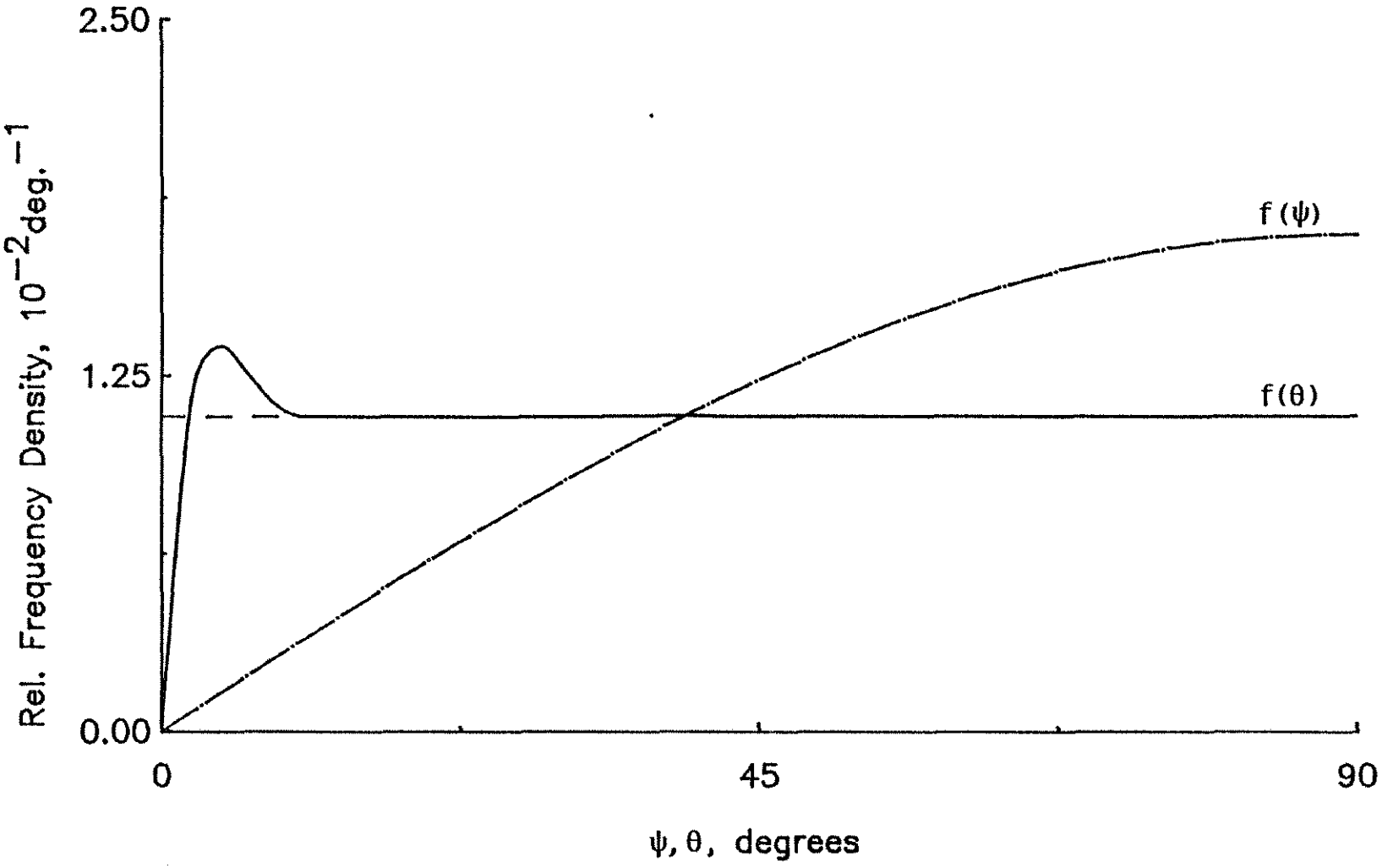

Fig. D.4. Orientation and Surface Angle Distributions for an Isotropic System of Cracks

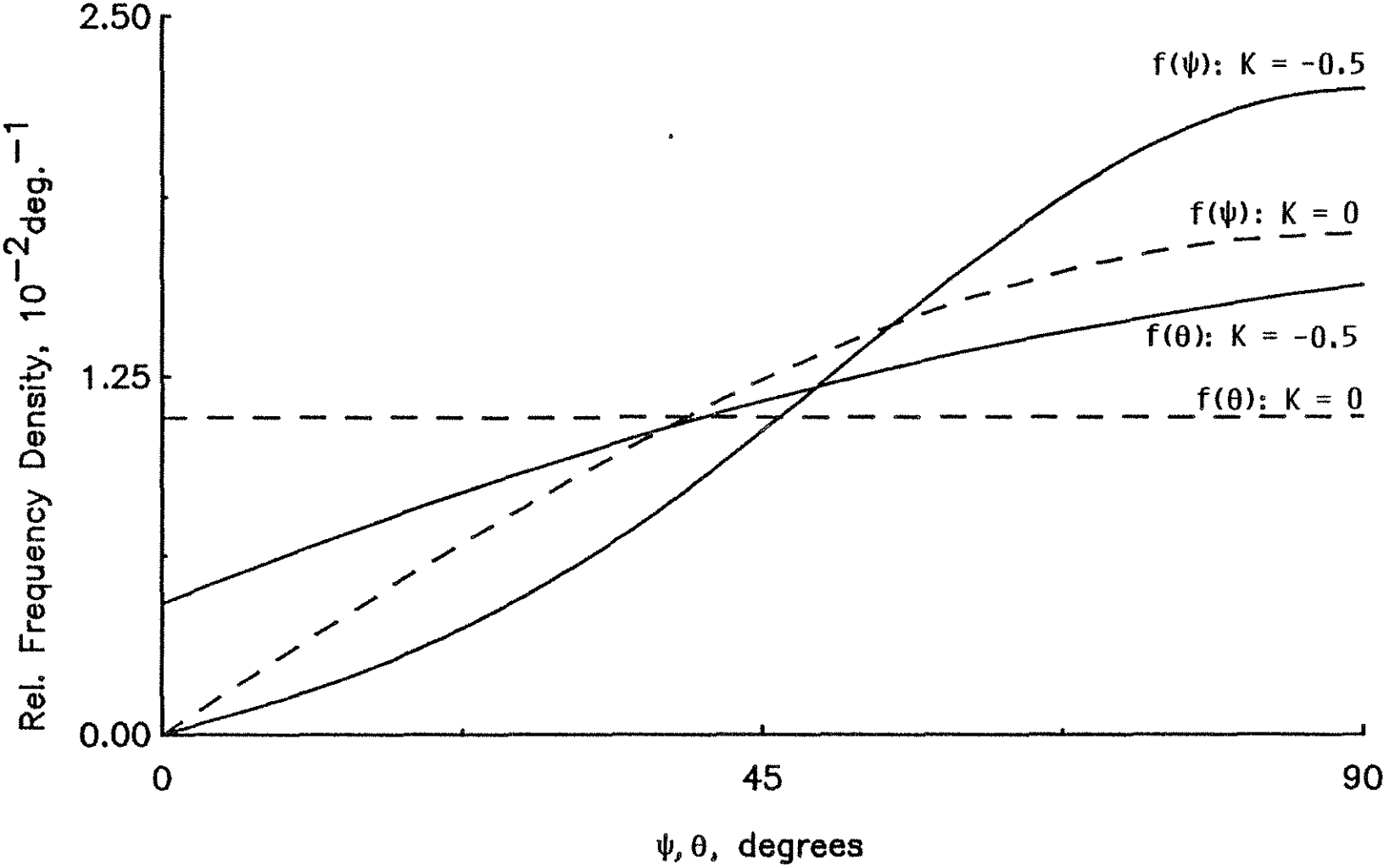

Fig. D.5. Orientation and Surface Angle Distribution for Isotropic and Transversely Isotropic Systems of Cracks

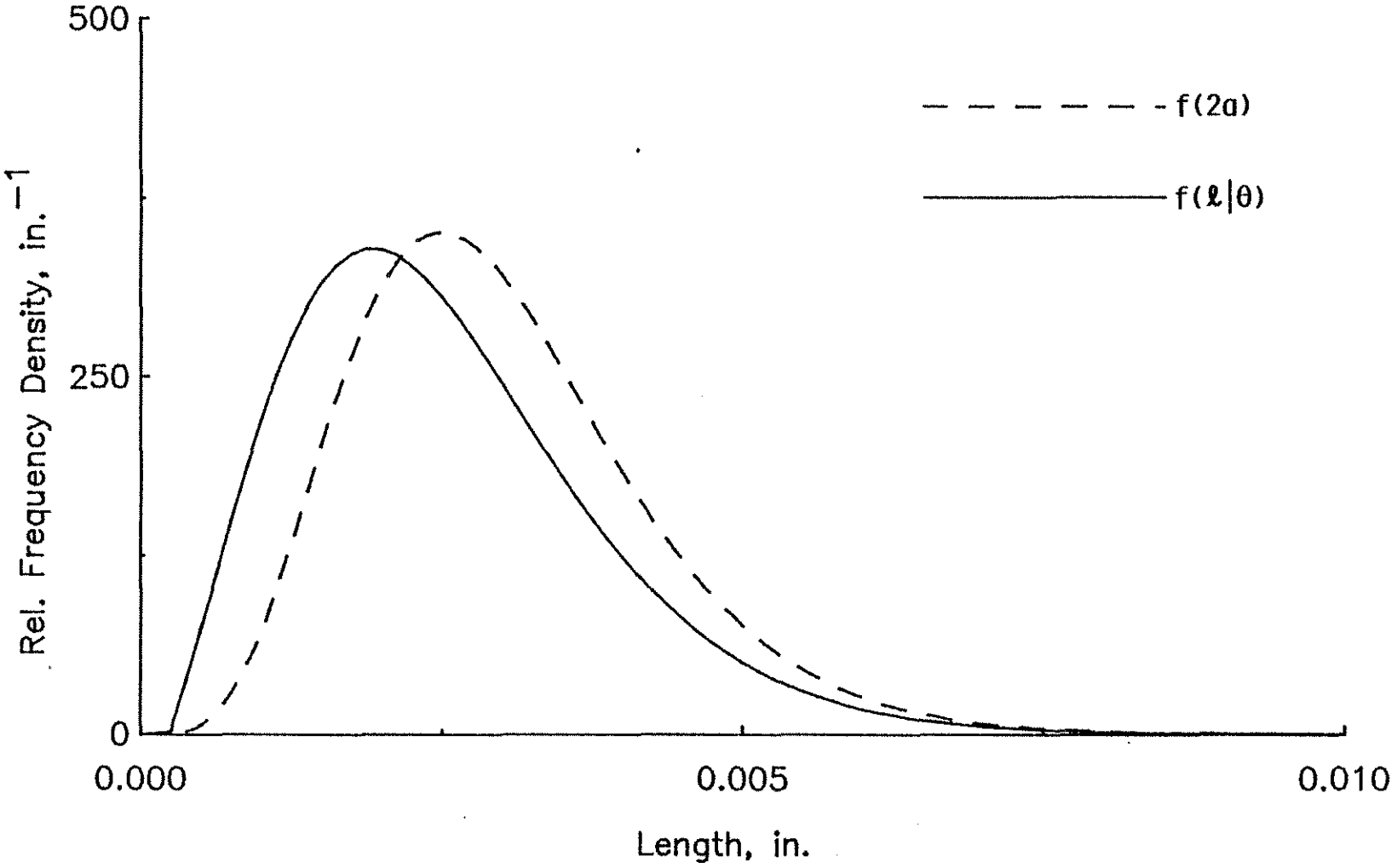

Fig. D.6. Crack Size, 2a, and Longitudinal Surface Length, ℓ, Distributions; θ = 30°

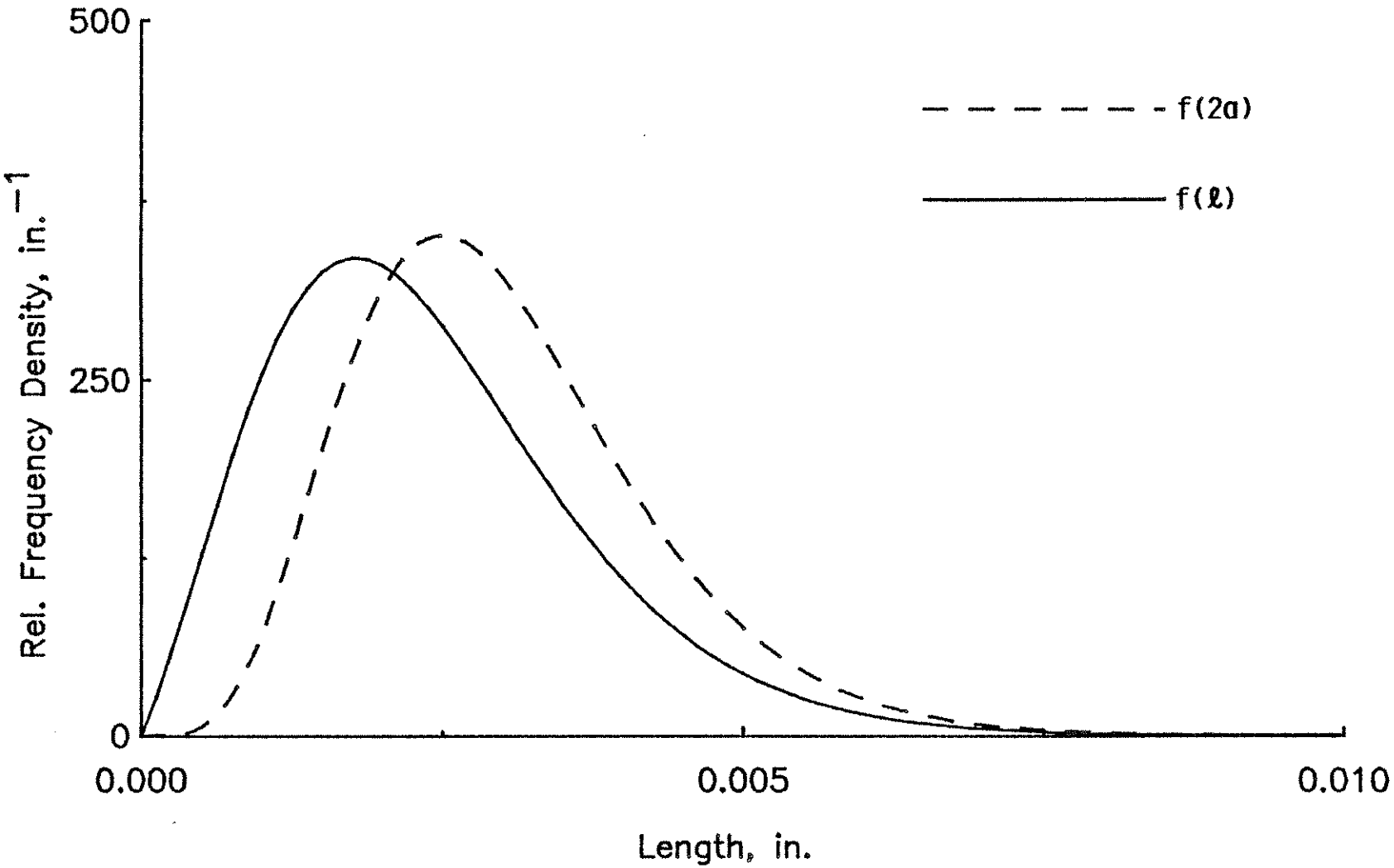

Fig. D.7. Crack Size, 2a, and Transverse Surface Length, ℓ, Distributions

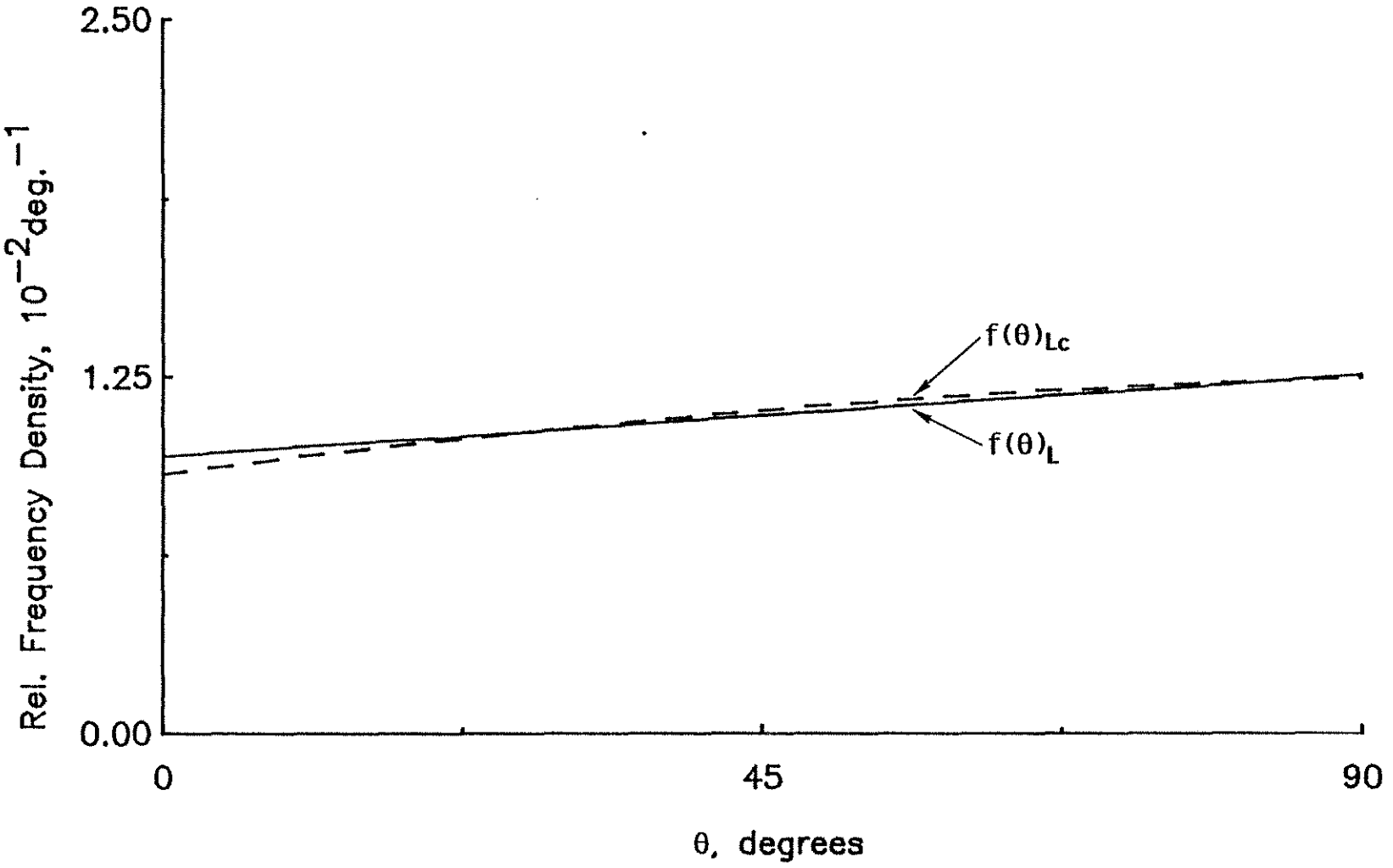

Fig. D.8. Comparison of Experimental, $f(\theta)_L$, and Calculated, $f(\theta)_{Lc}$, Trace Angle Distributions on a Longitudinal Plane

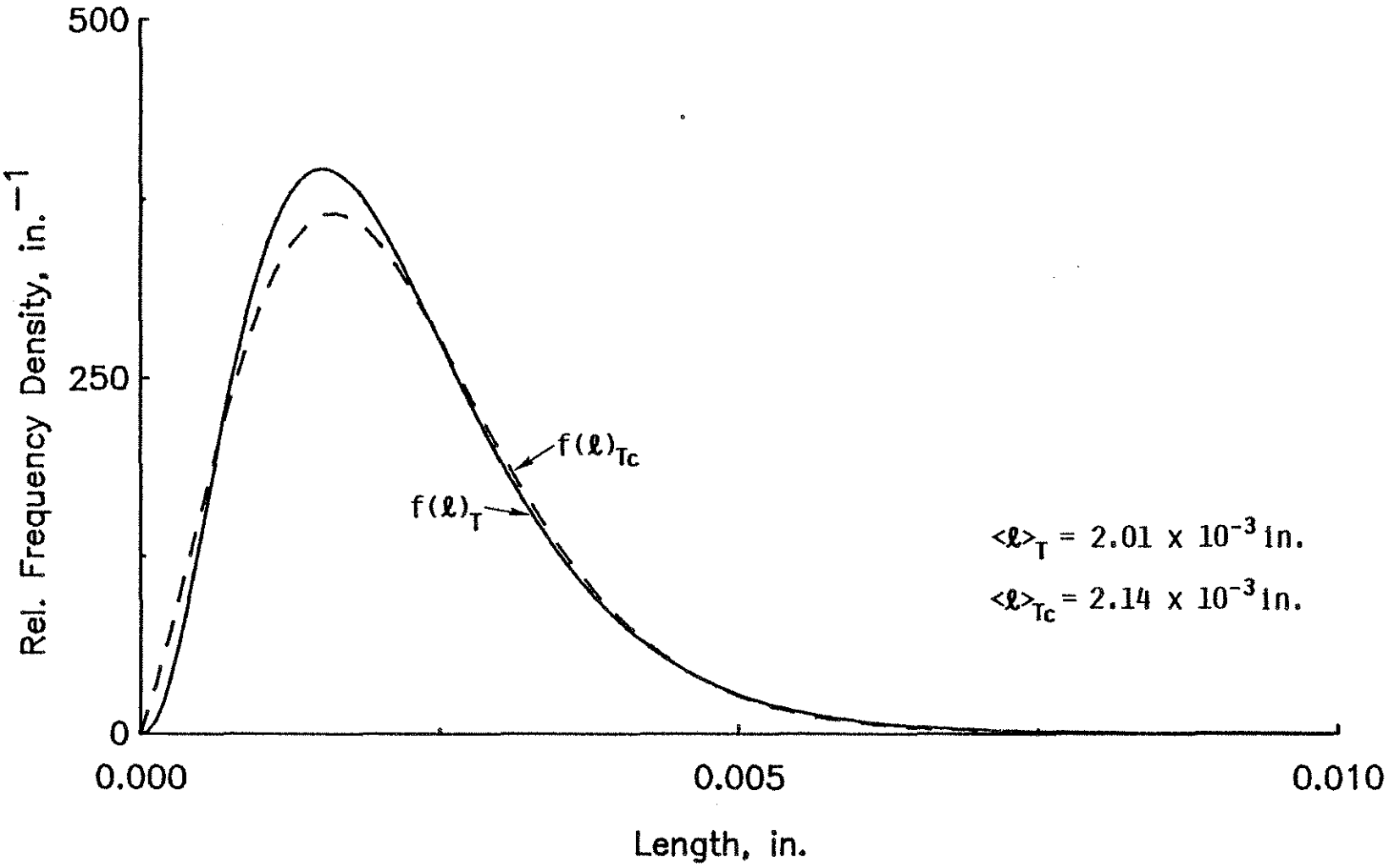

Fig. D.9. Comparison of Experimental, $f(\ell)_T$, and Calculated, $f(\ell)_{Tc}$, Trace Length Distributions on a Transverse Plane

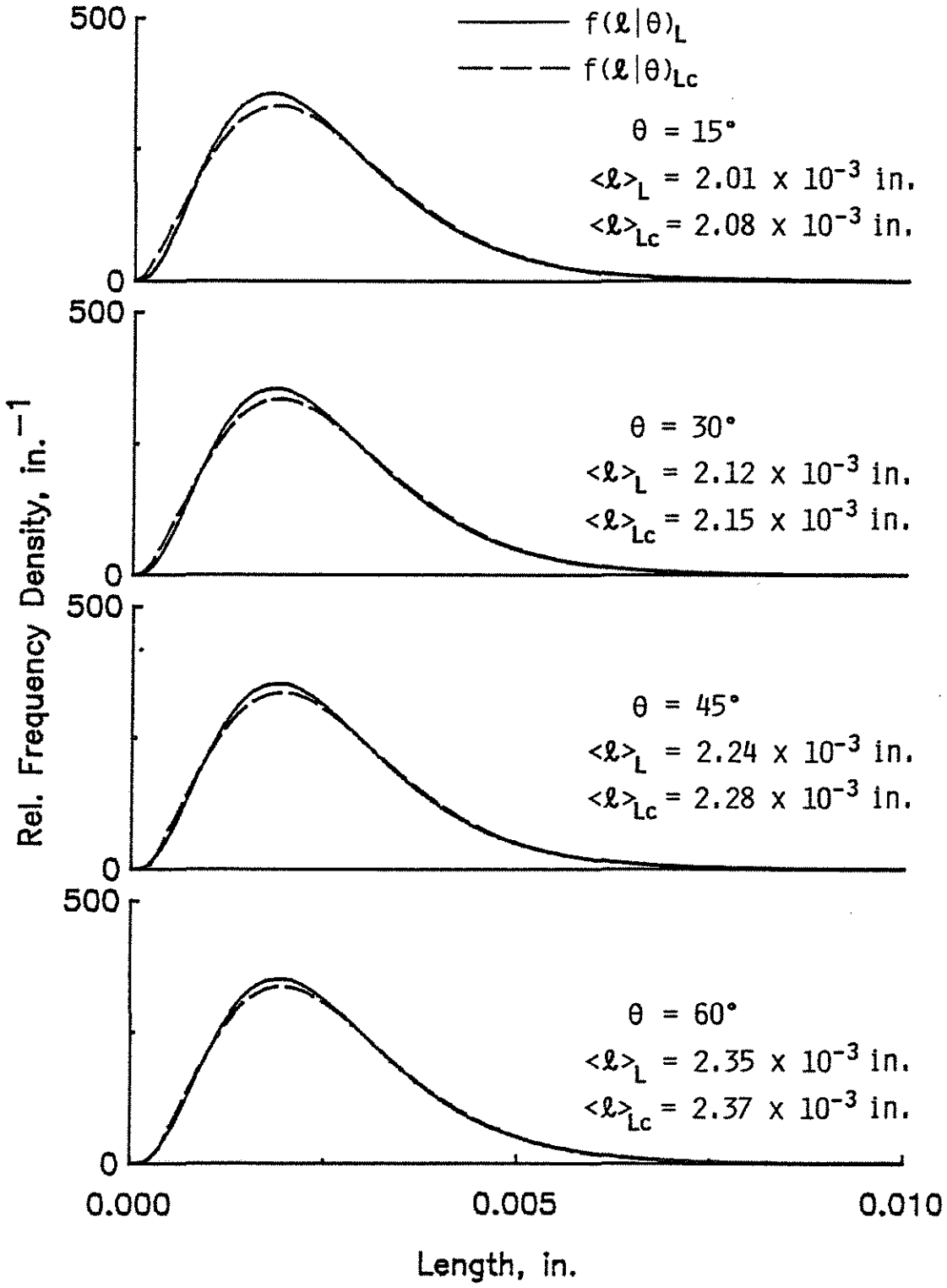

Fig. D.10. Comparison of Experimental, $f(\ell|\theta)_L$, and Calculated, $f(\ell|\theta)_{Lc}$, Trace Length Distributions on a Longitudinal Plane

APPENDIX E
GEOMETRIC RELATIONS FOR CONVERTING CRACK DISTRIBUTIONS ON PLANE SECTIONS TO SPATIAL DISTRIBUTIONS.

E.1 INTRODUCTION

The relationships established in Appendix D between spatial and surface distributions of cracks require geometrical expressions relating crack sizes and orientations to crack trace lengths and angles on longitudinal and transverse plane sections of a cracked body. In this appendix, expressions are derived that relate surface and spatial crack parameters for an elliptic crack. The dimensions and the angular coordinates of the 3-D cracks and the corresponding parameters for the crack traces are as defined in Appendix D.

In deriving relationships which involve the characteristic crack size, projections of the elliptic crack on longitudinal and transverse planes are considered. These projections are also ellipses. This fact is used in order to simplify the derivations.

E.2 DERIVATION OF GEOMETRIC RELATIONS

The relationships established in Appendix D between spatial and surface distributions of cracks, require expressions for (1) the trace angle, θ, as a function of the angular coordinates, ψ and ϕ, (2) the rate of change of ψ with respect to θ, $\partial\psi/\partial\theta$, (3) s_{max} which is the maximum distance between a crack centroid and a given plane for which the plane intersects the crack, (4) a_{min} which is the smallest characteristic crack size that gives a trace length of ℓ on a plane, and (5) the rate of change of s with respect to ℓ, $\partial s/\partial \ell$.

Expressions relating the crack trace angle on a longitudinal plane, θ, to the angular coordinates of the three-dimensional crack are derived first, followed by derivations involving the characteristic crack size, a.

E.2.1 Relationship between Crack Trace Angle on a Longitudinal Plane, θ, and Angular Coordinates of a 3-D Crack, ψ and ϕ

The crack trace angle on a longitudinal plane, θ, is related to the angular coordinates of the three-dimensional crack, ψ and ϕ, by means of the labelled triangles in Fig. E.1. Note that variations in η (Fig. D.1) do not affect θ.

From triangles ACD and ABD,

$$AC \sin \psi = AB \sin \theta$$

$$\frac{AC}{AB} = \frac{\sin \theta}{\sin \psi} \tag{E.1}$$

$$BD = AB \cos \theta \tag{E.2}$$

From triangle BCD,

$$BC = BD \sin \phi \tag{E.3}$$

Substituting Eq. (E.2) into Eq. (E.3) and rearranging,

$$\frac{BC}{AB} = \cos \theta \sin \phi \tag{E.4}$$

From triangle ABC,

$$\sin \beta = \frac{BC}{AB} \tag{E.5}$$

$$\cos \beta = \frac{AC}{AB} \tag{E.6}$$

Equating (E.4) and (E.5),

$$\sin \beta = \cos \theta \sin \phi \tag{E.7}$$

But $\cos^2 \beta = 1 - \sin^2 \beta$ (E.8)

Substituting Eq. (E.7) into Eq. (E.8),

$$\cos \beta = (1 - \cos^2 \theta \sin^2 \phi)^{1/2} \tag{E.9}$$

Equating (E.1), (E.6) and (E.9),

$$\frac{\sin \theta}{\sin \psi} = (1 - \cos^2 \theta \sin^2 \phi)^{1/2} \tag{E.10}$$

Rearranging Eq. (E.10),

$$\cos\theta = \cos\psi\,(1 - \sin^2\psi\,\sin^2\phi)^{-1/2} \tag{E.11}$$

$$0 \leq \theta,\ \psi \leq \pi/2$$

$$0 \leq \phi \leq 2\pi$$

The rate of change of ψ with respect to θ is obtained by differentiating Eq. (E.11).

$$\frac{\partial\psi}{\partial\theta} = \frac{\cos\phi}{1 - \cos^2\theta\,\sin^2\phi} \tag{E.12}$$

E.2.2 Relationships between s_{max} and crack parameters

For a crack that intersects a plane, the maximum distance between the crack centroid and the longitudinal or the transverse plane, s_{max}, can be expressed in terms of the size and the angular coordinates of the crack.

Fig. E.2 shows an inclined elliptic crack with major semi-axis length a and minor semi-axis length b. The crack has been rotated through an angle n about a normal to the crack plane. The expression for s_{max} with respect to the longitudinal plane is obtained by considering the projection of the inclined crack on a transverse plane, while the expression for s_{max} with respect to the transverse plane is obtained by considering the projection of the crack on a longitudinal plane. Fig. E.3 and E.4 show the projections of the crack on transverse and longitudinal planes, respectively. The coordinates of points on the boundary of each projected crack are defined in terms of x-y axes, with the origin at the crack centroid. In both Fig. E.3 and E.4, OT is the distance between the crack centroid and the plane; i.e. OT = s. For each plane, s_{max} is obtained by expressing s in terms of the coordinates of one of the points at which the plane intersects the boundary of the projected crack.

In the derivations that follow, the lengths of the major and minor semi-axes of the projected cracks are determined in terms of the size and the angular coordinates of the inclined crack. The aspect ratios of the projected cracks are then obtained. Finally, s_{max} is expressed as a function of the size, the aspect ratio, and the angular coordinates of the projected cracks. The longitudinal plane is considered first.

E.2.2.1 Longitudinal Plane

Consider triangle OAC of Fig. E.2 and its projection on a transverse plane, triangle OEF, shown in Fig. E.5. In Fig. E.2,

$$\begin{aligned} OA &= a \\ AC &= a \sin \eta \\ OC &= a \cos \eta \end{aligned} \tag{E.13}$$

In Fig. E.5,

$$\begin{aligned} EF &= AC = a \sin \eta \\ OF &= OC \cos \psi = a \cos \eta \cos \psi \end{aligned} \tag{E.14}$$

The right angle triangle OEF gives

$$a_T^2 = a^2 (\sin^2 \eta + \cos^2 \eta \cos^2 \psi) \tag{E.15}$$

in which a_T is the projected length, on a transverse plane, of the major semi-axis of the crack. Triangle OEF also gives

$$\tan \eta_T = \frac{EF}{OF} = \frac{\tan \eta}{\cos \psi} \tag{E.16}$$

in which η_T is the projection of the angle η on a transverse plane.

Consider triangle OBD of Fig. E.2 and its projection on a transverse plane, triangle OGD, as shown in Fig. E.6. In Fig. E.2,

$$\begin{aligned} OB &= b \\ BD &= b \sin \eta \\ OD &= b \cos \eta \end{aligned} \tag{E.17}$$

In Fig. E.6,

$$GD = BD \cos \psi = b \sin \eta \cos \psi \tag{E.18}$$

The right angle triangle OGD gives

$$b_T^2 = b^2 \, (\cos^2\eta + \sin^2\eta \cos^2\psi) \tag{E.19}$$

Dividing Eq. (E.19) by Eq. (E.15), the aspect ratio of the projection of the crack on a transverse plane is

$$r_T = r \left(\frac{\cos^2\eta + \sin^2\eta \cos^2\psi}{\sin^2\eta + \cos^2\eta \cos^2\psi}\right)^{1/2} \tag{E.20}$$

In Fig. E.3, which shows the projection of the inclined elliptic crack on a transverse plane, if $P(x_1, y_1)$ is one of the points at which the longitudinal plane intersects the boundary of the projected crack, the equation of the projection of the crack on a transverse plane is

$$\frac{x_1^2}{a_T^2} + \frac{y_1^2}{b_T^2} = 1 \tag{E.21}$$

Since $r_T^2 = b_T^2/a_T^2$, Eq. (E.21) becomes

$$x_1^2 = a_T^2 - y_1^2/r_T^2 \tag{E.22}$$

In order to obtain an expression for s_{max}, s must be expressed in terms of the coordinates of P. If OP = d in Fig. E.3, triangle AOP gives

$$OP = d = y_1/\cos\alpha \tag{E.23}$$

and $$\tan\alpha = x_1/y_1 \tag{E.24}$$

Angle TOB = $\phi+\eta_T$, hence

$$OT = s = d \cos(\phi+\eta_T-\alpha) \tag{E.25}$$

Substituting Eq. (E.23) and (E.24) into Eq. (E.25),

$$s = y_1 \cos(\phi+\eta_T) + x_1 \sin(\phi+\eta_T) \tag{E.26}$$

Substituting Eq. (E.22) into Eq. (E.26),

$$s = y_1 \cos(\phi+\eta_T) + \left(a_T^2 - y_1^2/r_T^2\right)^{1/2} \sin(\phi+\eta_T) \tag{E.27}$$

The value of y_1 which corresponds to s_{max} is obtained by differentiating Eq. (E.27) with respect to y_1 and setting the resulting expression to zero.

$$\frac{\partial s}{\partial y_1} = \cos(\phi+\eta_T) - \frac{y_1 \sin(\phi+\eta_T)}{r_T^2 \left(a_T^2 - y_1^2/r_T^2\right)^{1/2}} = 0 \tag{E.28}$$

Upon solving Eq. (E.28) for y_1,

$$(y_1)_{s_{max}} = r_T^2 a_T^2 \left[r_T^2 + \tan^2(\phi+\eta_T)\right]^{-1/2} \tag{E.29}$$

Eq. (E.29) is substituted in place of y_1 in Eq. (E.27) to obtain s_{max}.

$$s_{max} = a_T\left[r_T^2+\tan^2(\phi+\eta_T)\right]^{-1/2}\left[r_T^2\cos(\phi+\eta_T)+\sin(\phi+\eta_T)\tan(\phi+\eta_T)\right] \tag{E.30}$$

in which a_T, η_T and r_T are given by Eq. (E.15), (E.16), and (E.20), respectively.

E.2.2.2 Transverse Plane

Consider triangle OAC (Fig. E.2) and its projection on a longitudinal plane, triangle MAC, shown in Fig. E.7.

$$\begin{aligned} AC &= a \sin\eta \\ MC &= OC \sin\psi = a \cos\eta \sin\psi \end{aligned} \tag{E.31}$$

The right angle triangle MAC gives

$$a_L^2 = a^2 \left(\sin^2\eta + \cos^2\eta \sin^2\psi\right) \tag{E.32}$$

in which a_L is the projected length, on a longitudinal plane, of the major semi-axis of the crack. Triangle MAC also gives

$$\tan\eta_L = \frac{AC}{MC} = \frac{\tan\eta}{\sin\psi} \tag{E.33}$$

in which η_L is the projection of the angle η on a longitudinal plane.

Consider triangle OBD (Fig. E.2) and its projection on a longitudinal plane, triangle MBT, as shown in Fig. E.8.

$$MT = OD = b \cos \eta$$

$$BT = BD \sin \psi = b \sin \eta \sin \psi \tag{E.34}$$

The right angle triangle MBT gives

$$b_L^2 = b^2 (\cos^2\eta + \sin^2\eta \sin^2\psi) \tag{E.35}$$

Dividing Eq. (E.35) by Eq. (E.32), the aspect ratio of the projection of the crack on a longitudinal plane is

$$r_L = r \left(\frac{\cos^2\eta + \sin^2\eta \sin^2\psi}{\sin^2\eta + \cos^2\eta \sin^2\psi}\right)^{1/2} \tag{E.36}$$

In Fig. E.4, which shows the projection of the inclined elliptic crack on a longitudinal plane, if $P(x_2,y_2)$ is one of the points at which the transverse plane intersects the boundary of the projected crack, the equation of the projection of the crack on a longitudinal plane is

$$\frac{x_2^2}{a_L^2} + \frac{y_2^2}{b_L^2} = 1 \tag{E.37}$$

Since $r_L^2 = b_L^2/a_L^2$, Eq. (E.37) becomes

$$x_2^2 = a_L^2 - y_2^2/r_L^2 \tag{E.38}$$

In order to obtain an expression for s_{max}, s must be expressed in terms of the coordinates of P. If OP = d in Fig. E.4, triangle AOP gives

$$OP = d = y_2/\cos \alpha \tag{E.39}$$

and $$\tan \alpha = x_2/y_2 \tag{E.40}$$

Angle TOA = η_L, hence

$$OT = s = d \cos[\pi/2-(\eta_L+\alpha)] \tag{E.41}$$

Substituting Eq. (E.39) and (E.40) into Eq. (E.41),

$$s = y_2 \sin \eta_L + x_2 \cos \eta_L \tag{E.42}$$

Substituting Eq. (E.38) into Eq. (E.42),

$$s = y_2 \sin \eta_L + (a_L^2 - y_2^2/r_L^2)^{1/2} \cos \eta_L \tag{E.43}$$

The value of y_2 which corresponds to s_{max} is obtained by differentiating Eq. (E.43) with respect to y_2 and setting the resulting expression to zero.

$$\frac{\partial s}{\partial y_2} = \sin \eta_L - \frac{y_2 \cos \eta_L}{r_L^2 (a_L^2 - y_2^2/r_L^2)^{1/2}} = 0 \tag{E.44}$$

Upon solving Eq. (E.44) for y_2,

$$(y_2)_{s_{max}} = r_L^2 a_L^2 [r_L^2 + \tan^2(\phi+\eta_L)]^{-1/2} \tag{E.45}$$

Eq. (E.45) is substituted in place of y_2 in Eq. (E.43) to obtain s_{max}.

$$s_{max} = a_L (1 + r_L^2 \tan^2\eta_L)^{-1/2} (r_L^2 \sin \eta_L \tan \eta_L + \cos \eta_L) \tag{E.46}$$

in which a_L, η_L and r_L are given by Eq. (E.32), (E.33), and (E.36), respectively.

E.2.3 Relationships between a_{min} and crack parameters

For the smallest characteristic crack size, a_{min}, that gives a length of ℓ on a plane, the plane must pass through the crack centroid; i.e. s = 0. Relationships established in Section E.2.2 are used to obtain a_{min}. First, the characteristic crack size is expressed as a function of crack trace length on each plane. Then a_{min} is obtained by setting s = 0 in the resulting expression.

E.2.3.1 Longitudinal Plane

The characteristic crack size is expressed as a function of crack trace length on the longitudinal plane through the relationship given by Eq. (E.27).

Rearranging Eq. (E.27),

$$a_T = \left[\left(\frac{s - y_1 \cos(\phi+\eta_T)}{\sin(\phi+\eta_T)}\right)^2 + \frac{y_1^2}{r_T^2}\right]^{1/2} \qquad (E.47)$$

For a given trace length ℓ on the plane, if y_1 is expressed in terms of ℓ, Eq. (E.47) provides the relationship between the characteristic crack size and ℓ. y_1 is expressed in terms of ℓ as follows.

In Fig. E.3, let EF = t. Angle EPG = $\phi+\eta_T$. The x-coordinate of E is OA + AF, in which

$$OA = x_1$$

$$AF = PG = \ell \cos\theta \cos(\phi+\eta_T) \qquad (E.48)$$

Thus the coordinates of E are $[\ell \cos\theta \cos(\phi+\eta_T) + x_1, t]$. With these coordinates, Eq. (E.22) becomes

$$t^2 = r_T^2 \left[a_T^2 - (\ell \cos\theta \cos(\phi+\eta_T) + x_1)^2\right] \qquad (E.49)$$

From triangle PEG of Fig. E.3,

$$t + y_1 = \ell \cos\theta \sin(\phi+\eta_T) \qquad (E.50)$$

Rearranging and squaring both sides of Eq. (E.50),

$$t^2 = [\ell \cos\theta \sin(\phi+\eta_T) - y_1]^2 \qquad (E.51)$$

Equating (E.49) and (E.51) and substituting Eq. (E.22) and (E.47) for x_1 and a_T, respectively,

$$y_1 = \frac{\ell \cos\theta \tan(\phi+\eta_T)[\sin^2(\phi+\eta_T) + r_T^2\cos^2(\phi+\eta_T)] + 2\, s\, r_T^2}{2 \sin(\phi+\eta_T) \tan(\phi+\eta_T) + r_T^2 \cos(\phi+\eta_T)} \tag{E.52}$$

a_{min} is obtained by setting s = 0 in Eq. (E.47) and substituting the resulting expression into Eq. (E.15).

$$a_{min} = \frac{y_m}{r_T \tan(\phi+\eta_T)} \left[\frac{r_T^2 + \tan^2(\phi+\eta_T)}{\sin^2\eta + \cos^2\eta \cos^2\psi}\right]^{1/2} \tag{E.53}$$

in which y_m is obtained by setting s = 0 in Eq. (E.52).

$$y_m = \frac{\ell \cos\theta \tan(\phi+\eta_T)[\sin^2(\phi+\eta_T) + r_T^2 \cos^2(\phi+\eta_T)]}{2 \sin(\phi+\eta_T) \tan(\phi+\eta_T) + r_T^2 \cos(\phi+\eta_T)} \tag{E.54}$$

E.2.3.2 Transverse Plane

In the case of the transverse plane, the relationship given by Eq. (E.43) is used to express the characteristic crack size as a function of crack trace length on the plane.

Rearranging Eq. (E.43),

$$a_L = \left[\left(\frac{s - y_2 \sin\eta_L}{\cos\eta_L}\right)^2 + \frac{y_2^2}{r_L^2}\right]^{1/2} \tag{E.55}$$

For a given length ℓ on the plane, if y_2 is expressed in terms of ℓ, Eq. (E.55) provides the relationship between the characteristic crack size and ℓ. y_2 is expressed in terms of ℓ as follows.

In Fig. E.4, EP = ℓ and let EF = t. The x-coordinate of E is OA + AF, in which

$$\begin{aligned} OA &= x_2 \\ AF &= PG = \ell \sin\eta_L \end{aligned} \tag{E.56}$$

Thus the coordinates of E are ($\ell \sin\eta_L + x_2$, t). With these coordinates, Eq. (E.38) becomes

$$t^2 = r_L^2 \left[a_L^2 - (\ell \sin \eta_L + x_2)^2\right] \tag{E.57}$$

From triangle PEG of Fig. E.4,

$$t + y_2 = \ell \cos \eta_L \tag{E.58}$$

Rearranging and squaring both sides of Eq. (E.58),

$$t^2 = (\ell \cos \eta_L - y_2)^2 \tag{E.59}$$

Equating (E.57) and (E.59) and substituting Eq. (E.38) and (E.55) for x_2 and a_L respectively,

$$y_2 = \frac{\ell (\cos^2\eta_L + r_L^2 \sin^2\eta_L) + 2 s r_L^2 \tan \eta_L}{2 (\cos \eta_L + r_L^2 \sin \eta_L \tan \eta_L)} \tag{E.60}$$

a_{min} which gives a length of ℓ on the transverse plane is obtained by setting $s = 0$ in Eq. (E.55) and (E.60) and substituting the resulting expression into Eq. (E.32).

$$a_{min} = \frac{\ell (\cos^2\eta_L + r_L^2\sin^2\eta_L)(1 + r_L^2\tan^2\eta_L)^{1/2}}{2 r_L(\cos \eta_L + r_L^2\sin \eta_L\tan \eta_L)(\sin^2\eta + \cos^2\eta \sin^2\psi)^{1/2}} \tag{E.61}$$

E.2.4 Expressions for $\partial s/\partial \ell$

Since the equations for the relative frequency density of crack trace lengths on longitudinal and transverse planes require integrations over crack size (see Appendix D), $\partial s/\partial \ell$ needs to be expressed as a function of crack size. In the following derivations, $\partial s/\partial \ell$ is expressed as the product of two differentials which involve the characteristic crack size. Expressions are then obtained for these differentials by differentiating relationships established in Sections E.2.2 and E.2.3.

E.2.4.1 Longitudinal Plane

$\partial s/\partial \ell$ is expressed in terms of the projected length, on a transverse plane, of the major semi-axis of the crack, a_T, as

$$\frac{\partial s}{\partial \ell} = \frac{\partial s}{\partial a_T} \frac{\partial a_T}{\partial \ell} \tag{E.62}$$

$\partial s/\partial a_T$ in Eq. (E.62) is obtained by differentiating Eq. (E.27).

$$\frac{\partial s}{\partial a_T} = \cos(\phi+\eta_T) \frac{\partial y_1}{\partial a_T} + \sin(\phi+\eta_T) \left(a_T - \frac{y_1}{r_T^2} \frac{\partial y_1}{\partial a_T}\right) \left(a_T^2 - \frac{y_1^2}{r_T^2}\right)^{-1/2} \tag{E.63}$$

By substituting Eq. (E.27) in place of s in Eq. (E.52), y_1 is expressed as a function of a_T.

$$y_1 = \frac{1}{C} \left[AB + (A^2B^2 - CD)^{1/2}\right] \tag{E.64}$$

in which $A = 2 \sin(\phi+\eta_T)$

$$B = \ell \cos\theta \left[\sin^2(\phi+\eta_T) + r_T^2 \cos^2(\phi+\eta_T)\right]$$

$$C = A^2 + 4 r_T^2 \cos^2(\phi+\eta_T)$$

$$D = B^2 - 4 a_T^2 r_T^4 \cos^2(\phi+\eta_T)$$

a_T, η_T and r_T are defined previously in Eq. (E.15), (E.16), and (E.20), respectively. $\partial y_1/\partial a_T$ in Eq. (E.63) is obtained by differentiating Eq. (E.64).

$$\frac{\partial y_1}{\partial a_T} = \frac{B^2 - D}{a_T (Cy_1 - AB)} \tag{E.65}$$

In Eq. (E.62), $$\frac{\partial a_T}{\partial \ell} = \frac{\partial a_T}{\partial y_1} \frac{\partial y_1}{\partial \ell} \tag{E.66}$$

Differentiating Eq. (E.47) with respect to y_1,

$$\frac{\partial a_T}{\partial y_1} = \frac{1}{a_T} \left[\frac{\cos(\phi+\eta_T) \left(y_1 \cos(\phi+\eta_T) - s\right)}{\sin^2(\phi+\eta_T)} + \frac{y_1}{r_T^2}\right] \tag{E.67}$$

in which s and y_1 are given by Eq. (E.27) and (E.64), respectively.

Differentiating Eq. (E.52) with respect to ℓ,

$$\frac{\partial y_1}{\partial \ell} = \frac{\cos\theta \tan(\phi+\eta_T) \left[\sin^2(\phi+\eta_T) + r_T^2 \cos^2(\phi+\eta_T)\right]}{2 \left[\sin(\phi+\eta_T) \tan(\phi+\eta_T) + r_T^2 \cos(\phi+\eta_T)\right.} \tag{E.68}$$

$\partial s/\partial \ell$ is therefore obtained from Eq. (E.62) by evaluating Eq. (E.63) through (E.68).

E.2.4.2 Transverse Plane

$\partial s/\partial \ell$ is expressed in terms of the projected length, on a longitudinal plane, of the major semi-axis of the crack, a_L, as

$$\frac{\partial s}{\partial \ell} = \frac{\partial s}{\partial a_L} \frac{\partial a_L}{\partial \ell} \tag{E.69}$$

$\partial s/\partial a_L$ in Eq. (E.69) is obtained by differentiating Eq. (E.43).

$$\frac{\partial s}{\partial a_L} = \sin \eta_L \frac{\partial y_2}{\partial a_L} + \cos \eta_L \left(a_L - \frac{y_2}{r_L^2} \frac{\partial y_2}{\partial a_L}\right) \left(a_L^2 - \frac{y_2^2}{r_L^2}\right)^{-1/2} \tag{E.70}$$

By substituting Eq. (E.43) in place of s in Eq. (E.60), y_2 is expressed as a function of a_L.

$$y_2 = \frac{1}{C} \left[AB + (A^2B^2 - CD)^{1/2}\right] \tag{E.71}$$

in which $A = 2 \cos \eta_L$

$$B = \ell \left[\cos^2\eta_L + r_L^2 \sin^2\eta_L\right]$$

$$C = A^2 + 4 r_L^2 \sin^2\eta_L$$

$$D = B^2 - 4 a_L^2 r_L^4 \sin^2\eta_L$$

a_L, η_L and r_L are defined previously in Eq. (E.32), (E.33), and (E.36), respectively. Hence $\partial y_2/\partial a_L$ in Eq. (E.70) is obtained by differentiating Eq. (E.71).

$$\frac{\partial y_2}{\partial a_L} = \frac{B^2 - D}{a_L\,(Cy_2 - AB)} \tag{E.72}$$

In Eq. (E.69), $$\frac{\partial a_L}{\partial \ell} = \frac{\partial a_L}{\partial y_2}\,\frac{\partial y_2}{\partial \ell} \tag{E.73}$$

Differentiating Eq. (E.55) with respect to y_2,

$$\frac{\partial a_L}{\partial y_2} = \frac{1}{a_L}\left[\frac{\sin \eta_L\,(y_2 \sin \eta_L - s)}{\cos^2 \eta_L} + \frac{y_2}{r_L^2}\right] \tag{E.74}$$

in which s and y_2 are given by Eq. (E.43) and (E.71), respectively. Differentiating Eq. (E.60) with respect to ℓ,

$$\frac{\partial y_2}{\partial \ell} = \frac{\cos^2 \eta_L + r_L^2 \sin^2 \eta_L}{2\,(\cos \eta_L + r_L^2 \sin \eta_L \tan \eta_L)} \tag{E.75}$$

$\partial s/\partial \ell$ is therefore obtained from Eq. (E.69) by evaluating Eq. (E.70) through (E.75).

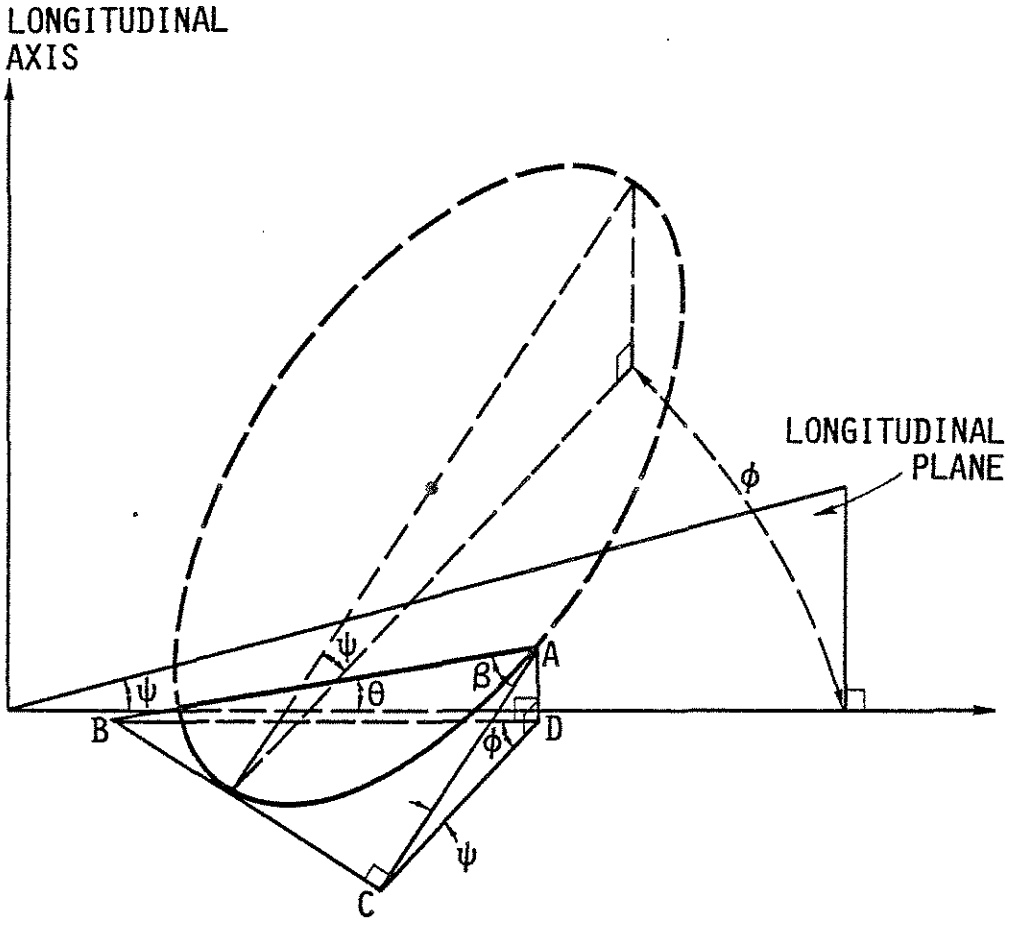

Fig. E.1. Sketch for Determining the Relationship Between 2-D and 3-D Angles

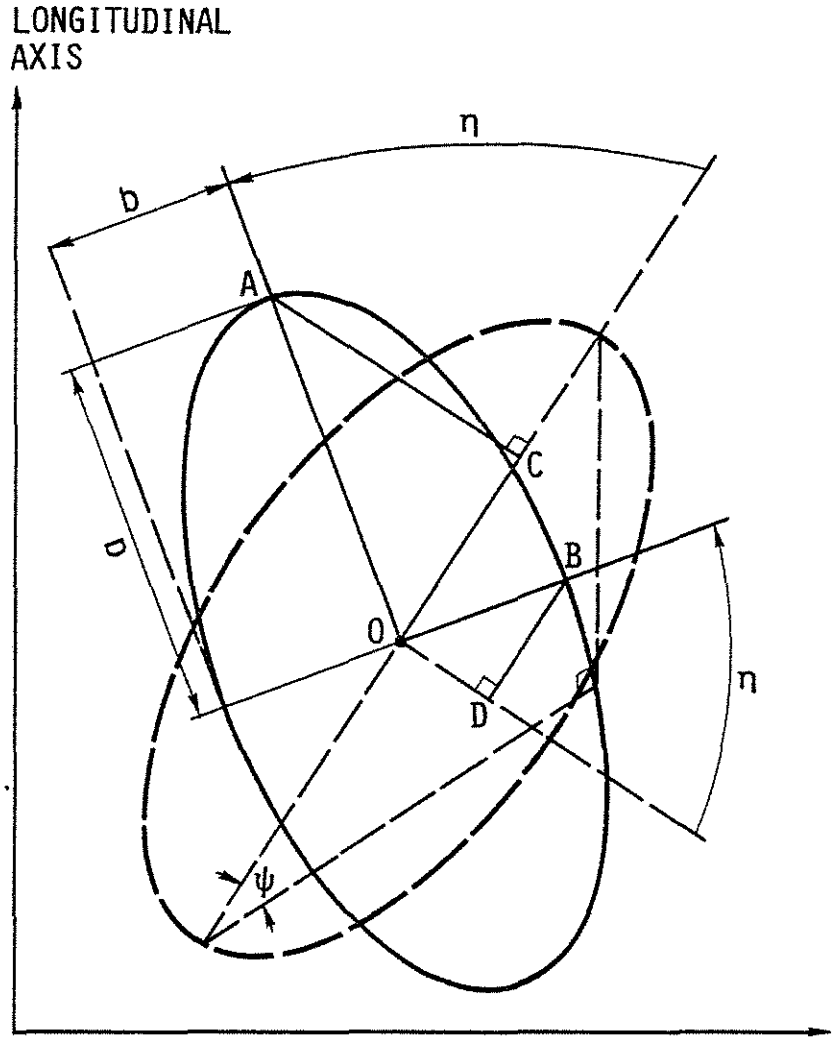

Fig. E.2. Rotation of Crack about Normal through its Centroid

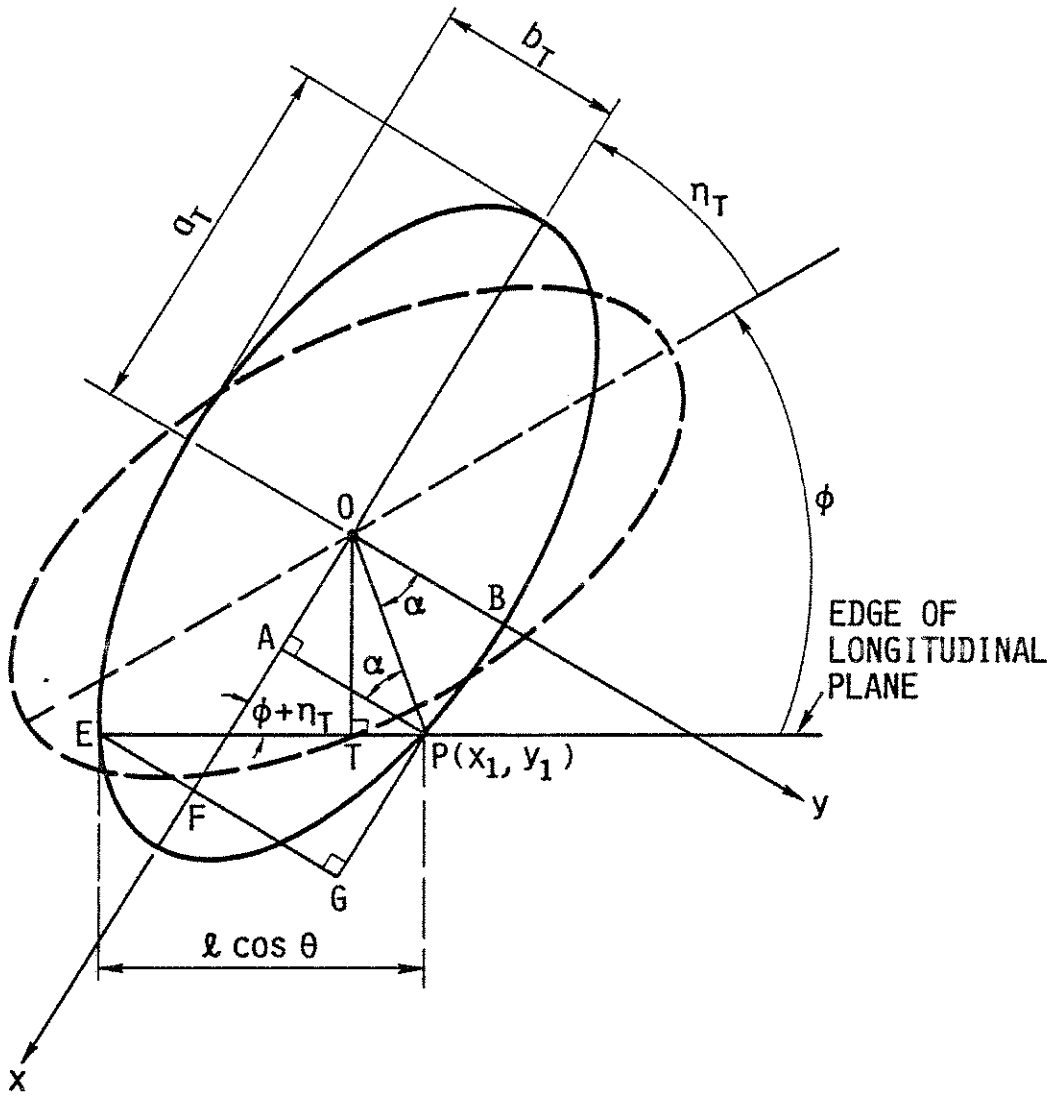

Fig. E.3. Projection of Crack on Transverse Plane

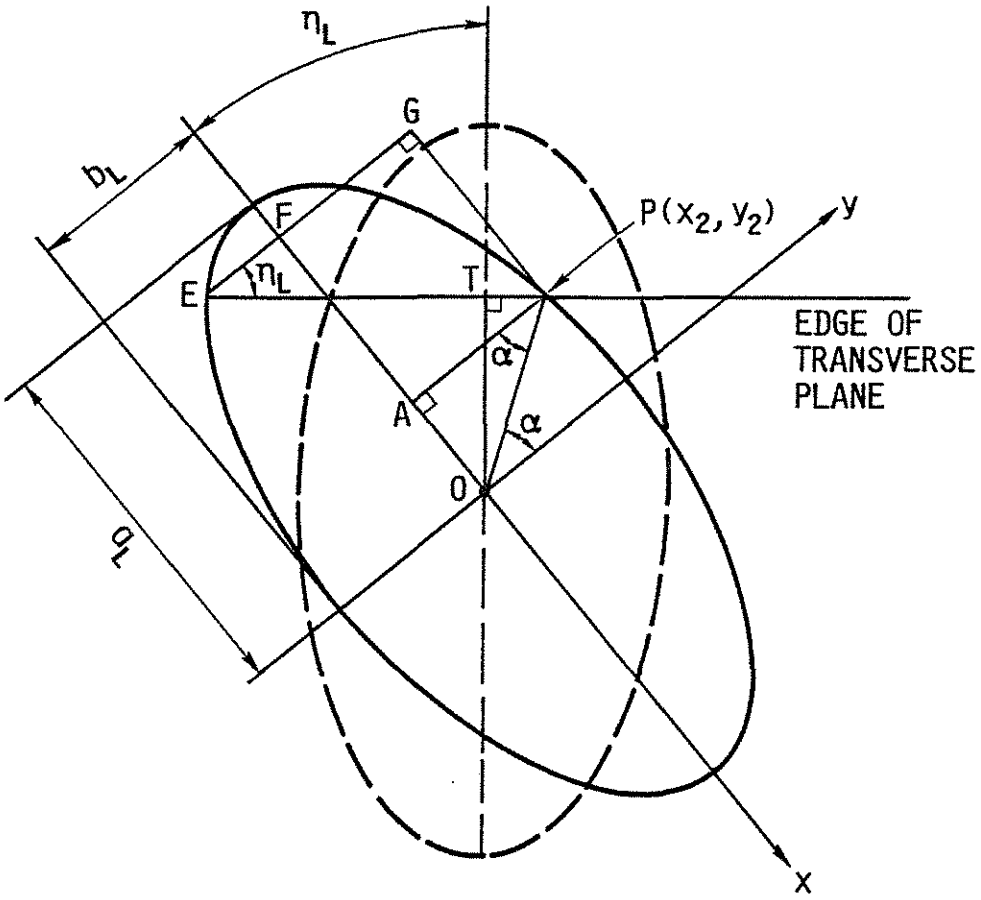

Fig. E.4. Projection of Crack on Longitudinal Plane

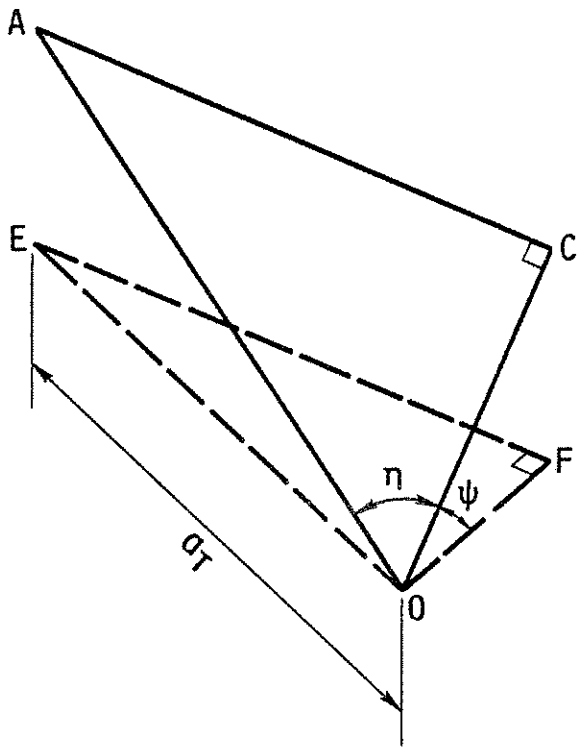

Fig. E.5. Projection of Triangel OAC (Fig. E.2) on Transverse Plane

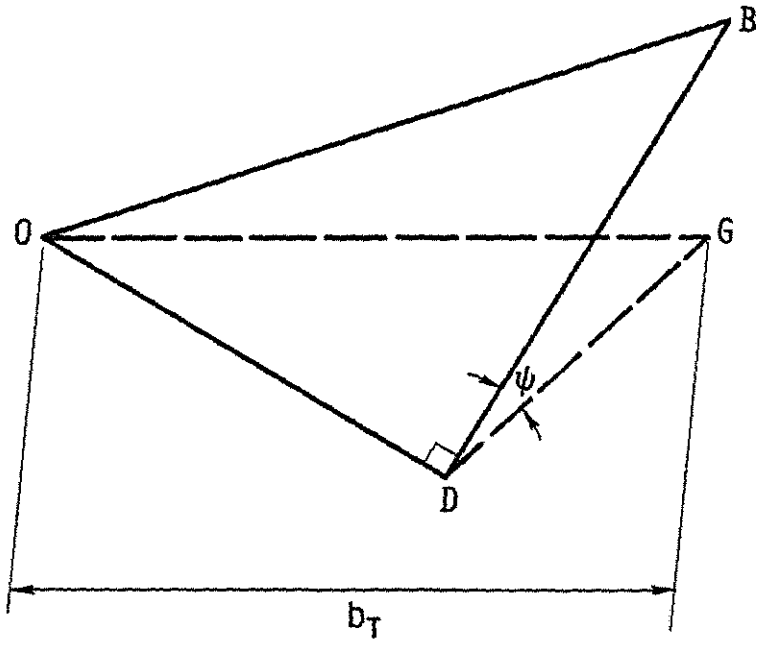

Fig. E.6. Projection of Triangle OBD (Fig. E.2) on Transverse Plane

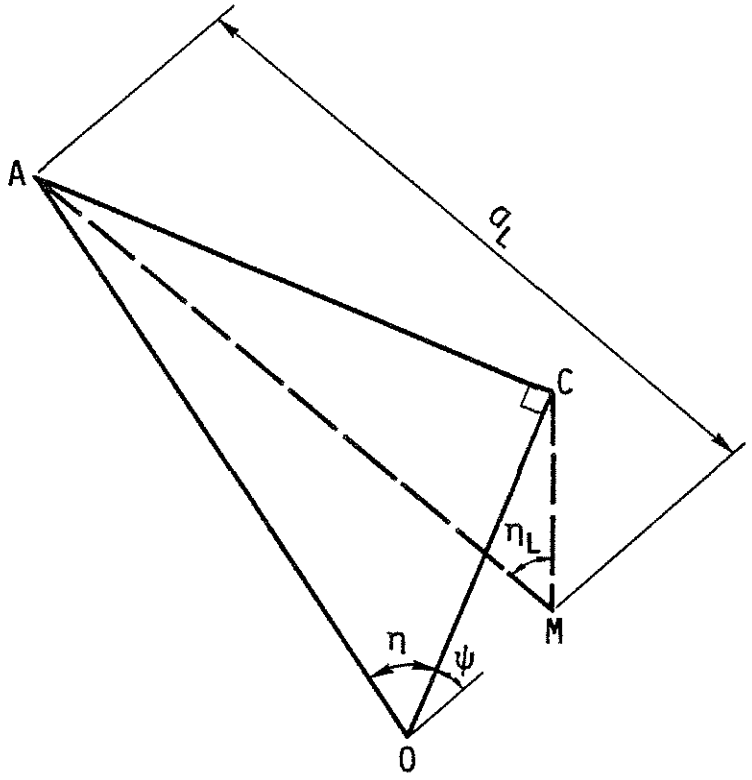

Fig. E.7. Projection of Triangle OAC (Fig. E.2) on Longitudinal Plane

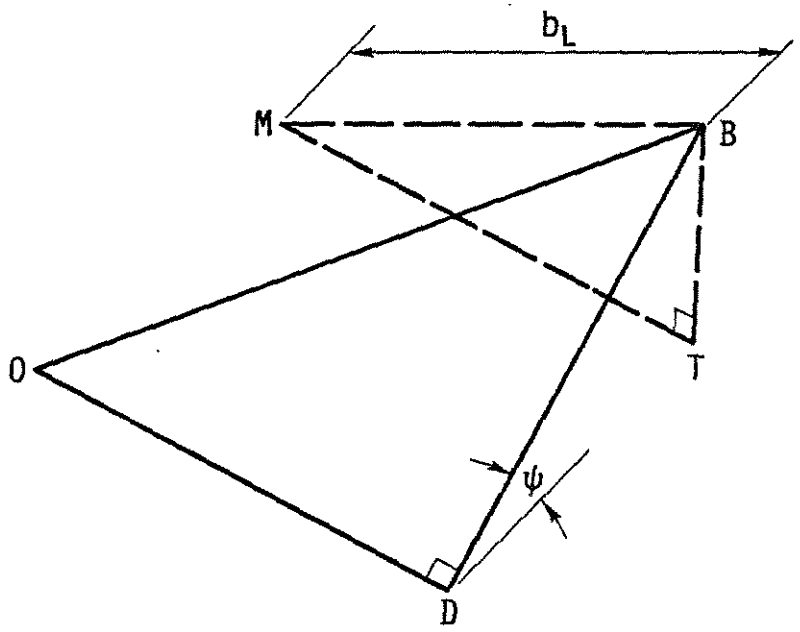

Fig. E.8. Projection of Triangle OBD (Fig. E.2) on Longitudinal Plane